Gesellschaft für Mikro- und Nanoelektronik

The Society for Micro- and Nanoelectronics

Biennial Report

2005 – 2006

Vienna, October 2007

Gesellschaft für Mikro- und Nanoelektronik

The Society for Micro- and Nanoelectronics

Biennial Report

2005 – 2006

Society for Micro- and Nanoelectronics
c/o Vienna University of Technology
Institute of Sensor and Actuator Systems
Gusshausstrasse 27-29/366, A-1040 Vienna, Austria

Vienna, October 2007

Editor: Karl Riedling

Layout: Claudia Benedela
Karl Riedling

ISBN: 978-3-901578-18-2

c/o Technische Universität Wien
Institut für Sensor- und Aktuatorsysteme
Gusshausstraße 27-29/366, A-1040 Wien

The Society for Micro- and Nanoelectronics (GMe — Gesellschaft für Mikro- und Nanoelektronik)

E. Gornik, K. Riedling

Gesellschaft für Mikro- und Nanoelektronik,
c/o Institut für Sensor- und Aktuatorsysteme,
TU Wien
Gußhausstraße 27 – 29, A-1040 Wien

Goals of the Society for Micro- and Nanoelectronics

The Society for Micro- and Nanoelectronics (GMe) has been founded in 1985 as "*Society for Microelectronics - Gesellschaft für Mikroelektronik*" with the aim to "*support microelectronics technology and its applications*" in Austria. With the shift of the focus in research from micro to nano technologies the goals of the GMe changed accordingly. Therefore, the GMe has changed its name into "*Society for Micro- and Nanoelectronics — Gesellschaft für Mikro- und Nanoelektronik*" in 2003.

The GMe defines its tasks as follows:

- Support of university-based "high-tech" research in the areas of micro- and nanoelectronics, semiconductor technology, sensors, and opto-electronics;
- Operation of research facilities;
- Support and consulting for industry, in particular, for small and medium enterprises, within the area of micro- and nanoelectronics.

The central task of the GMe is to provide an internationally competitive *infra-structure* in the area of micro- and nanoelectronics technology. The GMe allocates funds to maintain research projects in the fields of semiconductor technology, sensors, opto-electronics, and ASIC design. Thus the infra-structure support generates a base for research projects that are funded by other funding agencies.

Activities of the Society

Due to funding constraints, the present focal point activity of the GMe is the operation of university-based laboratories for microelectronics technology, where its main task is the operation of the cleanroom laboratories in Vienna and Linz. The GMe has coordinated the construction of the Center for Micro- and Nanostructures (ZMNS — *Zentrum für Mikro- und Nanostrukturen*; previously, MISZ — *Mikrostrukturzentrum*) in Vienna; the funds were supplied by the Austrian Federal Ministry of Science and Research. The GMe now finances a significant part of the operation costs for the cleanroom laboratories in Vienna and Linz.

Microelectronics Technology — Cleanroom Vienna

The following university institutes receive support within this focal point activity:

- University of Technology Vienna:
  - Institute of Solid State Electronics
  - Photonics Institute
  - Institute of Sensor and Actuator Systems

Microelectronics Technology — Cleanroom Linz

The following university institutes receive support within this focal point activity:

- Johannes Kepler University Linz:
  - Institute of Semiconductor and Solid State Physics

Other Activities of the Society

Both in 2005 and 2006, the GMe has organized two seminars of its own, the "GMe Forum 2005" and the "GMe Workshop 2006", respectively:

GMe Forum 2005:

Thursday, March 17, 2005

10:00 – 10:30	Welcome, Coffee
	Opening:
10:30 – 11:00	E. GORNIK (President of the GMe)
	P. SKALICKY (President of the Vienna University of Technology)
	Nanoelectromechanical Systems:
11:00 – 11.45	R. BLICK: *From Classical Mechanics to Quantum-Electro-Mechanics*
11:45 – 12:30	Ch. HIEROLD: *From MEMS to NEMS*
12:30 – 14:00	Lunch Break
	Micromachining with Femtolasers:
14:00 – 14:45	A. ISEMANN: *Micromachining with Femtolasers*
	Bioelectronics:
14:45 – 15:30	H.U. DODT: *Bioelectronics and Bioimaging - New Approaches for the Investigation of Brain Microcircuits*
15:30 – 16:00	Coffee Break
	Spintronics:
16:00 – 16:45	L. ALFF: *Spintronics: A New Spin for the World of Electronics*
	Carbon Nanotubes:
16:45 – 17:30	W. HÖNLEIN: *Carbon Nanotubes – A Successor to Silicon Technology?*
17:30 – 17:45	Break
	Evening Session:
17:45 – 18:00	E. GORNIK: *Presentation of the Activities of the GMe*
18:00 – 19:00	Panel Discussion: "*Who supports technology in Austria?*"

Friday, March 18, 2005

	Technology:
09:00 – 09:45	R. MINIXHOFER: *Semiconductor Process Simulation*
09:45 – 10:30	H. OKORN-SCHMIDT: *Using Extreme Sono-Effects to Improve on the Selectivity of Particle Removal to Microelectronic Structure Damage below 65 nm*
10:30 – 11:00	A. LUGSTEIN: *Focused Ion Beam Technology*
11:00 – 11:30	Coffee Break
	Quantum Devices:
11:30 – 12:00	T. MÜLLER: *Carrier Dynamics at Quantum Dots*
	Opto-Electronics:
12:00 – 12:30	K. HINGERL: *Photonic Crystals: Optical materials for the 21st century*
12:30 – 13:00	G. SPRINGHOLZ: *Lead-Salt Lasers*
	Sensors:
13:00 – 13:30	D. ROCHA: *Sensor Interface Electronics*
	Poster Exhibition:
13:30	Snacks and Poster Exhibition

GMe Workshop 2006:

Friday, October 13, 2006

09.00 – 10.00	Registration; Coffee
10.00 – 10.15	Opening
10.15 – 11.00	K. EBERL: *GaAs based High Power Laser Diodes from Lumics*
11.00 – 11.30	M. BÖBERL *et al.*: *Narrow-band lead salt photodetectors and solution-processible nanocrystal photodetectors for the midinfrared*
11.30 – 12.00	K. UNTERRAINER *et al.*: *Optical properties of IR quantum dots*
12.00 – 13.30	Lunch Break
13.30 – 14.15	S. CHRISTIANSEN: *Semiconductor nanowires: properties and applications*
14.15 – 14.45	A. LUGSTEIN *et al.*: *Synthesis of nanowires in room temperature ambient with a focused ion beam*
14.45 – 15.15	G. Chen *et al.*: *Initial stage of the 2D-3D transition of a strained Ge layer on a pit-patterned Si(001) template – Progress in Quantum Dot Array (QDA)*
15.15 – 15.45	S. Kostner *et al.*: *On-Chip Cytometric Detection of Single Biological Cells Using Integrated Photodiodes*
15.45 – 16.00	Coffee
16.00 – 18.00	Poster Session

In addition, the GMe was the official coordinator of the "28th International Conference on the Physics of Semiconductors" (ICPS 2006 – http://www.icps2006.at/), which has taken place in Vienna from the 24th to the 28th July 2006. The ICPS 2006 was a successful international event with 1320 registered participants, eight plenary and 44 invited speakers which took place at the Vienna Hofburg.

One of the declared tasks of the GMe is to provide information on current Austrian academic activities in the field of microelectronics to industry, in particular to Austrian small- and medium enterprises (SMEs). To enhance the distribution of the results of the research work done with GMe support, the GMe has put the contents of its annual reports — 1995 through 2006 — and the proceedings of the latest seminars organized by the GMe on its Web server. This server provides a variety of search facilities into the reports, thus acting as a Microelectronics Knowledge Base. The GMe Web server is available under the address http://gme.tuwien.ac.at/ .

The Biennial Report for 2005 – 2006 of the Society for Micro- and Nanoelectronics

The GMe is currently supporting the microelectronics technology activities of the cleanroom laboratories in Vienna and Linz. All projects described in this report were carried out in the cleanrooms in Vienna and Linz, respectively, and in special sensor technology laboratories closely associated with the Center for Micro- and Nanostructures in Vienna. They are *not* specific projects of the GMe but were funded by a variety of other sources. They all have in common that they use the infra-structure provided by the GMe. It would therefore not have been possible to carry out these projects without the support by the GMe.

Contents

Microelectronics Technology — Cleanroom Vienna

Contents

Cleanroom Vienna

G. Strasser, W. Schrenk

**Center for Micro- and Nanostructures
of the Vienna University of Technology,
Floragasse 7, A-1040 Vienna, Austria**

In this report a summary of the main activities in the ZMNS TU Wien (*Zentrum für Mikro- und Nanostrukturen der Technischen Universität Wien*) during the years 2005 and 2006 will be given. Within this report we describe projects making intensive use of the cleanroom and the available technologies within. This includes state of the art growth of III-V nanostructures and silicon processing, structuring techniques utilizing standard contact lithography, the production of patterned masks, dry etching and plasma enhanced chemical vapor deposition, electron beam writing, focused ion beam etching and depositing, and various metallization techniques. A major part of the mission of the ZMNS is the development and production of microelectronic, optoelectronic, and nanoelectronic prototype devices. A list of the people involved in the cleanroom activities is added. The list of scientific publications published last year is a direct measure of the activities within the ZMNS cleanroom.

Introduction

An overview of the main research efforts with a high need of technological input is presented within this scientific report. This summary includes the majority of experimental projects of the solid state electronics institute (*Festkörperelektronik TU Wien*) and the photonics institute (*Photonik TU Wien*) during the last two years. All the projects described below like transport studies in low dimensional semiconductor nanostructures, scanning probe spectroscopy, realization of new and improved optoelectronic devices, quantum cascade lasers, THz sources, and the characterization of microelectronic devices take full advantage of the technologies installed in the cleanroom of the ZMNS (*Reinraum des Zentrums für Mikro-und Nanostrukturen der TU Wien*). A detailed up-to-date list of the existing cleanroom equipment including benchmark data are given on the actual webpage of the cleanroom (http://zmns.tuwien.ac.at/).

To structure the yearly increasing number of various activities within the cleanroom of the ZMNS, six research areas are introduced, namely:

- Optoelectronics & THz technology
- Quantum Dots and Nanowires
- Transport in III-V Semiconductors
- Silicon Device Testing
- Focused Ion Beam and Electron Beam Developments
- Novel Characterization Techniques and Devices

To satisfy this variety of topics and demonstrate e.g. optoelectronic devices as well as basic research and the development of new tools for semiconductor industries, different technologies have to be kept at state of the art performance.

This includes growth of semiconductor nanostructures (molecular beam epitaxy and advanced nanowire growth techniques), as well as a complete process line including structure definition (lithography), structure transfer (reactive ion etching, focused ion

beam etching and deposition, wet chemical etching techniques) and coating with metals and/or dielectrics (plasma-enhanced chemical vapor deposition, sputtering, electron gun evaporation, focused ion beam deposition). Surface morphology as well as local carrier concentrations probing is done with a conventional Atomic Force Microscope (AFM) in combination with a Scanning Capacitance Microscopy (SCM) extension.

In 2006, a new electron beam lithography system and an atomic layer deposition system had been installed, extending the possibilities in nanostructure fabrication.

All the equipment necessary for the above mentioned technologies needs the cleanroom environment (cooling, filtered air, constant temperature and humidity, high quality water, different inert gases) as well as periodic maintenance of the equipment and the cleanroom itself, e.g. pumping systems (rotary pumps, turbo pumps), exhaust filtering, liquid nitrogen, and cleaning and repair. Testing of the cleanroom quality and adjustment (laminar airflow, filters, cooling, humidity, and temperature) is done periodically.

For a more general overview the listed projects and the attached publication list may give more insides on the broad range of activities in our facility.

Research Activities

Optoelectronics and THz Technology

Quantum Dots and Nanowires

Transport in III-V Semiconductors

Silicon Device Testing

Focused Ion Beam and Electron Beam Developments

Novel Characterization Techniques and Devices

Project Information

Project Manager

Ao.Univ.Prof. Dr. Gottfried Strasser

Institut für Festkörperelektronik und ZMNS
Floragasse 7
A-1040 Wien

Project Group

Last Name	First Name	Status	Remarks
Abermann	Stephan	dissertation	
Andrews	A. Maxwell	postdoc	
Auer	Erwin	univ. ass.	
Austerer	Maximilian	dissertation	
Bae	Kim Heung	dissertation	
Benz	Alexander	student	
Bertagnolli	Emmerich	o. prof.	
Blaho	Matej	dissertation	
Bychikhin	Sergey	postdoc	
Brezna	Wolfgang	postdoc	
Coquelin	Michael	dissertation	
Dalibor	Kovac	dissertation	
Darmo	juraj	univ. ass.	
Dominizi	Karl	student	
Dubec	Viktor	dissertation	
Dzigal	Elvira	technician	
Fasching	Gernot	dissertation	
Fischer	Markus	dissertation	
Gebhard	Thomas	dissertation	
Golka	Sebastian	dissertation	
Gornik	Erich	o. prof.	
Heer	Michael	dissertation	
Hobler	Gerhard	ao. prof.	
Hochleitner	Gottfried	student	
Hoffmann	Leonard	dissertation	
Hyun	Youn-Joo	dissertation	
Klang	Pavel	postdoc	
Köck	Thomas	student	

Last Name	First Name	Status	Remarks
Kröll	Josef	dissertation	
Kröll	Peter	technician	
Kuzmik	Ian	postdoc	
Lugstein	Alois	ass. Prof.	
Mujagic	Elvis	student	
Müller	Thomas	univ. ass.	
Nobile	Michele	dissertation	
Otto	Gustav	dissertation	
Özcan	Soner	dissertation	
Pacher	Christoph	dissertation	
Parz	Wolfgang	dissertation	
Pogany	Dionyz	ao. prof.	
Pozzovivo	Gianmauro	dissertation	
Prinzinger	Johannes	technician	
Riegler	Erich	technician	
Roch	Tomas	postdoc	
Schartner	Stefan	dissertation	
Schinnerl	Markus	technician	
Schenold	Helmut	technician	
Schöndorfer	Christoph	dissertation	
Schramböck	Matthias	dissertation	
Schrenk	Werner	cleanroom director	
Schrey	Frederik	dissertation	
Smoliner	Jürgen	ao. prof.	
Steiger	Andreas	dissertation	
Steinmair	Matthias	dissertation	
Strasser	Gottfried	ao. prof.	
Svarc	Markus	student	
Tamosiunas	Vincas	postdoc	
Unterrainer	Karl	prof.	
Wanzenböck	Heinz	ass. Prof.	
Zahel	Thomas	student	
Zobl	Reinhard	postdoc	

Publications in Reviewed Journals

1. S. Abermann, W. Brezna, J. Smoliner, E. Bertagnolli:
"*Nanoscopic versus macroscopic C-V characterization of high-k - MOCVD ZrO2 thin films*";
Microelectronic Engineering, **83** (2006), S. 1055 - 1057.

2. S. Abermann, C. Jordan, M. Harasek, E. Bertagnolli:
"*Processing and simulation of few nm thick high-k dielectric films*";
Microelectronic Engineering, **83** (2006), S. 1571 - 1572.

3. M. Austerer, C. Pflügl, S. Golka, W. Schrenk, A. M. Andrews, T. Roch, G. Strasser:
"*Coherent 5.35 µm surface emission from a GaAs-based distributed feedback quantum-cascade laser*";
Applied Physics Letters, **88** (2006), S. 1211041 - 1211043.

4. M. Austerer, S. Schartner, C. Pflügl, A. M. Andrews, T. Roch, W. Schrenk, G. Strasser:
"*Second-harmonic generation in GaAs-based qunatum cascade lasers*";
Physica E, **35** (2006), S. 234 - 240.

5. E. Baumann, F. Giorgetta, D. Hofstetter, S. Golka, W. Schrenk, G. Strasser, L. Kirste, E. Feltin, J. Carlin, N. Grandjean:
"Near infrared absorption and room temperature photovoltaic response in AlN/GaN superlattices grown by metal-organic vapour-phase epitaxy";
Applied Physics Letters, **89** (2006), S. 0411061 - 0411063.

6. e. Bogner, K. Dominizi, P. Hagl, E. Bertagnolli, M. Wirth, F. Gabor, W. Brezna, H. D. Wanzenböck:
"*Bridging the gap - Biocompatibility of microelectronic materials*";
Acta Biomaterialia, **2** (2006), 2; S. 229 - 237.

7. W. Brezna, M. Fischer, H. D. Wanzenböck, E. Bertagnolli, J. Smoliner:
"*Electron beam deposited SiO2 investigated by Scanning Capacitance Microscopy*";
Applied Physics Letters, **88** (2006), S. 1221161 - 1221163.

8. M. Coquelin, C Pacher, M. Kast, G. Strasser, E. Gornik:
"*Wannier-Stark level anticrossing in biperiodic superlattices*";
Physica Status Solidi (b), **14** (2006), S. 3692 - 3695.

9. G. Fasching, A. Benz, R. Zobl, A.M. Andrews, T. Roch, W. Schrenk, G. Strasser, V Tamosiunas, K. Unterrainer:
"*Microcavity THz quantum cascade laser*";
Physica E, **32** (2006), S. 316 - 319.

10. G. Fasching, F. Schrey, T. Roch, A.M. Andrews, W. Brezna, J. Smoliner, G. Strasser, K. Unterrainer:
"*Single InAs/GaAs quantum dots: photoncurrent and cross-sectional AFM analysis*";
Physica E, **32** (2006), S. 183 - 186.

11. M. Fischer, H. D. Wanzenböck, J. Gottsbachner, S. Müller, W. Brezna, M. Schramböck, E. Bertagnolli:
"*Direct-Writing with a Focused Electron Beam*";
Microelectronic Engineering, **83** (2006), S. 784 - 787.

12. S. Golka, C. Pflügl, W. Schrenk, G. Strasser, C. Skierbiszewski, M. Siekacz, I. Grzegory, S. Porowski:
"*Negative differential resistance in dislocation-free GaN/AlGaN double-barrier diodes grown on bulk GaN*";
Applied Physics Letters, **88** (2006), S. 1721061 - 1721063.

13. M. Heer, V. Dubec, S. Bychikhin, D. Pogany, E. Gornik, M. Frank, A. Konrad, J. Schulz:
"*Analysis of triggering behaviour of high voltage CMOS LDMOS clamps and SCRs during ESD induced latch-up*";
Microelectronics Reliability, **46** (2006), S. 1591 - 1596.

14. G. Hobler, K. Bourdelle, T. Akatsu:
"*Random and channeling stopping power of H in Si below 100keV*";
Nuclear Instruments & Methods B, **242** (2006), S. 617 - 619.

15. D. Kovac, G. Hobler:
"Investigation of the impact of defect models on Monte Carlo simulations of RBS/C spectra";
Nuclear Instruments & Methods B, **249** (2006), S. 776 - 779.

16. J. Kuzmik, S. Bychikhin, D. Pogany, C. Gaquière, E. Morvan:
"*Current conduction and saturation mechanism in AlGaN/GaN ungated structures*";
Journal of Applied Physics, **99** (2006), S. 1237201 - 1237207.

17. J. Kuzmik, T. Kostopoulos, G. Konstantinidis, J. Carlin, A. Georgakilas, D. Pogany:
"*InAlN/GaN HEMTs: A first insight into technological optimization*";
IEEE Transactions on Electron Devices, **53** (2006), 3; S. 422 - 426.

18. A. Lugstein, B. Basnar, W. Brezna, M. Weil, S. Golka, E. Bertagnolli:
"*Advanced nanopattern formation by a subtrative self-organization process with focused ion beams*";
Nuclear Instruments & Methods B, **242** (2006), S. 93 - 95.

19. A. Lugstein, J. Bernardi, C. Tomastik, E. Bertagnolli:
"*Synthesis of nanowires in room temperature ambient: A focused ion beam approach*";
Applied Physics Letters, **88** (2006), S. 1631141 - 1631143.

20. P Moens, S. Bychikhin, D. Pogany:
"*Ruggedness of integrated VDMOS transistors under TLP stress*";
IEEE Transactions on Device and Materials Reliability, **6** (2006), 3; S. 393 - 398.

21. O. Moutanabbir, B. Terreault, M. Chicoine, J. Simpson, T. Zahel, G. Hobler:
"*Hydrogen/Deuterium-defect complexes involved in the ion cutting of Si (0 0 1) at the sub-100 nm scale*";
Physica B, **376** (2006), S. 36 - 40.

22. T. Müller, G. Strasser, K. Unterrainer:
"Ultrafast spectral hole burning spectroscopy of exciton spin flip processes in InAs/GaAs quantum dots";
Applied Physics Letters, **88** (2006), 192105.

23. G. Otto, G. Hobler, L. Palmetshofer, K Mayerhofer, K Piplits, H. Hutter:
"*Dose-rate dependence of damage formation in Si by N implantation as determined from channeling profile measurements*";
Nuclear Instruments & Methods B, **242** (2006), S. 667 - 669.

24. G. Otto, G. Hobler, L. Palmetshofer, P. Pongratz:
"Amorphous pocktes in Si: Comparison of coupled molecular dynamics and TEM image contrast simulations with experimental results";
angenommen für Nuclear Instruments & Methods B.

25. G. Otto, G. Hobler, P. Pongratz, L. Palmetshofer:
"s there an influence of ion-beam-induced interfacial amorphization on the a/c-interface depth in silicon at common implantation energies?";
Nuclear Instruments & Methods B, **253** (2006), S. 227 - 231.

26. C. Pflügl, M. Austerer, S. Golka, W. Schrenk, A. M. Andrews, T. Roch, G. Strasser:
"*Second-harmonic generation in three-well and bound-to-continuum GaAs-based quantum-cascade lasers*";
Applied Physics B, **85** (2006), S. 231 - 234.

27. D. Rakoczy, G. Strasser, J. Smoliner:
"Cross Sectional Ballistic Electron Emission Microscopy for Schottky Barrier Height Profiling on Heterostructures";
Journal of Applied Physics, **45** (2006), 3B; S. 2204 - 2207.

28. S. Schartner, S. Golka, C. Pflügl, W. Schrenk, A. M. Andrews, T. Roch, G. Strasser:
"*Band structure mapping of photonic crystal intersubband detectors*";
Applied Physics Letters, **89** (2006), S. 1511071 - 1511073.

29. S. Schartner, S. Golka, C. Pflügl, W. Schrenk, G. Strasser:
"*Deeply etched waveguides structures for quantum cascade lasers*";
Microelectronic Engineering, **83** (2006), S. 1163 - 1166.

30. C. Schöndorfer, A. Lugstein, E. Bertagnolli:
"*Focused Ion Beam induced Nanodot and Nanofiber Growth*";
Microelectronic Engineering, **83** (2006), S. 1491 - 1494.

31. M. Schramböck, A. M. Andrews, T. Roch, W. Schrenk, A. Lugstein, G. Strasser:
"*Nano-patterning and growth of self-assembled quantum dots*";
Microelectronics Journal, **37** (2006), S. 1532 - 1543.

32. M. Schramböck, W. Schrenk, T. Roch, A. M. Andrews, M. Austerer, G. Strasser:
"*Self organized InAs quantum dots grown on patterned GaAs substrates*";
Microelectronic Engineering, **83** (2006), S. 1573 - 1576.

33. F. Schrey F., D. Nguyen, N. Regnault, R. Ferreira, G. Bastard, G. Strasser, K. Unterrainer:
"*Optical properties of IR quantum dot detectors with miniband tunnel extraction*";
angenommen für Journal of Applied Physics 2006 (2006).

34. H. D. Wanzenböck, C. Ostermaier, A Gruen, B. Eichinger, M. Karner, E. Bertagnolli:
"*Dot-array implantation for patterned doping of semiconductors*";
Nuclear Instruments & Methods B, **242** (2006), S. 257 - 260.

Talks and Poster Presentations (with Proceedings):

1. R. Heer, J. Smoliner, J. Bornemeier, H. Brückl:
"*Temperature Dependent Ballistic Electron Transport in Spin Valve Transistors*";
Vortrag: International Conference on Nonequilibrium Carrier Dynamics in Semiconductors (HCIS), Chicago, USA; 24.07.2005 - 29.07.2005; in:
"*Nonequilibrium Carrier Dynamics in Semiconductors/Proceedings of the 14 International Conference*", (2006), S. 159 - 162.

2. A. M. Andrews, T. Roch, G. Fasching, W. Schrenk, R. Zobl, K. Unterrainer, G. Strasser:
"*Growth Optimization of GaAs-based Quantum Cascade Laser for Terahertz Emission*";
Poster: 14th International Winterschool on New Developments in Solid State Physics, Mauterndorf; 13.02.2006 - 17.02.2006; in: "*Book of Abstracts*", (2006), S. 148.

3. M. Austerer, S. Schartner, S. Golka, C. Pflügl, W. Schrenk, A. M. Andrews, T. Roch, G. Strasser, R. Green, L.R. Wilson, J.W. Cockburn, A.B. Krysa, J.S. Roberts:
"*Single mode quantum cascade lasers*";
Poster: 14th International Winterschool on New Developments in Solid State Physics, Mauterndorf; 13.02.2006 - 17.02.2006; in: "*Book of Abstracts*", (2006), S. 149 - 150.

4. G. Fasching, A. Benz, A.M. Andrews, K. Unterrainer, R. Zobl, T. Roch, W. Schrenk, G. Strasser, V Tamosiunas:
"*Microcavity THz quantum cascade laser*";
Poster: 14th International Winterschool on New Developments in Solid State Physics, Mauterndorf, Austria; 13.02.2006 - 17.02.2006; in: "*Book of Abstract*", (2006), S. 151.

5. T. Gebhard, F. Schrey F., G. Strasser, K. Unterrainer, M. Pires, S. Landi, P. Souza:
"*Intraband transitions in InAs/InGaAs/InP quantum dots for infrared photodetection*";
Poster: 14th International Winterschool on New Developments in Solid State Physics, Mauterndorf, Austria; 13.02.2006 - 17.02.2006; in: "*Book of Abstract*", (2006), S. 81 - 82.

6. J. Kröll, J. Darmo, K. Unterrainer, S. Dhillon, C. Sirtori:
"*70. Optical processes in terhaertz quantum-cascade laser waveguides*";
Poster: 14th International Winterschool on New Developments in Solid State Physics, Mauterndorf, Austria; 13.02.2006 - 17.02.2006; in: "*Book of Abstract*", (2006), S. 152.

7. T. Müller, G. Strasser, K. Unterrainer:
"*Ultrafast spectral hole burning spectroscopy of exciton spin relaxation in InAs/GaAs quantum dots*";
Poster: 14th International Winterschool on New Developments in Solid State Physics, Mauterndorf, Austria; 13.02.2006 - 17.02.2006; in: "*Book of Abstract*", (2006), S. 89 - 90.

8. M. Schramböck, W. Schrenk, T. Roch, A. M. Andrews, M. Austerer, A. Lugstein, G. Strasser:
"*Nano-patterning and growth of self-assembled nano-structures*";
Poster: 14th International Winterschool on New Developments in Solid State Physics, Mauterndorf; 13.02.2006 - 17.02.2006; in: "*Book of Abstracts*", (2006), S. 139.

9. F.F. Schrey, E. Magerl, G. Fasching, G. Strasser, K. Unterrainer:
"*Ultrafast intersublevel spectroscopy of a single InAs Quantum Dot*";
Poster: 14th International Winterschool on New Developments in Solid State Physics, Mauterndorf, Austria; 13.02.2006 - 17.02.2006; in: "*Book of Abstract*", (2006), S. 91 - 92.

10. G. Strasser:
"*Nonlinear effects in quantum cascade lasers*";
Vortrag: 14th International Winterschool on New Developments in Solid State Physics, Mauterndorf (eingeladen); 13.02.2006 - 17.02.2006; in: "*Book of Abstracts*", (2006), S. 34.

11. M. Schramböck, A. M. Andrews, T. Roch, W. Schrenk, A. Lugstein, G. Strasser:
"*Nano-patterning and growth of self-assembled quantum dots*";
Poster: 6th International Workshop on Epitaxial Semiconductors on Patterned Substrates and Novel Index Surfaces, Nottingham, Great Britain; 03.04.2006 - 05.04.2006; in: "*Book of Abstract*", (2006), S. 56.

12. A. M. Andrews, G. Fasching, A. Benz, T. Roch, W. Schrenk, K. Unterrainer, G. Strasser:
"*Ga-As-based Quantum Cascade Laser for Dual Frequency Terahertz Emission*";
Vortrag: Materials Research Society Spring Meeting (MRS), San Francisco, USA; 17.04.2006 - 21.04.2006; in: "*MRS Spring Meeting Abstracts*", (2006), S. 231.

13. A. Benz, G. Fasching, K. Unterrainer, R. Zobl, A.M. Andrews, T. Roch, W. Schrenk, G. Strasser:

"*Quantum-Mechanical designed Terahertz Laser*";
Poster: Junior Scientist Conference 2006, Vienna, University of Technology, Wien; 19.04.2006 - 21.04.2006; in: "*Proceedings*", (2006), 3-902463-05-8; S. 91 - 92.

14. S. Schartner, S. Golka, M. Austerer, C. Pflügl, W. Schrenk, G. Strasser:
"*Photonic Crystal Cavities for Quantum Cascade Lasers*";
Poster: Junior Scientist Conference 2006, Wien; 19.04.2006 - 21.04.2006; in: "*Proceedings of the Junior Scientist Conference 2006*", (2006), S. 169 - 170.

15. M. Schramböck, A. M. Andrews, T. Roch, W. Schrenk, A. Lugstein, G. Strasser:
"*Nano-patterning and growth of self-assembled nano-structures*";
Poster: Junior Scientist Conference 2006, Wien; 19.04.2006 - 21.04.2006; in: "*Proceedings of the Junior Scientist Conference 2006*", (2006), S. 171 - 172.

16. J. Kröll, K. Unterrainer:
"*Quantum cascade laser dynamics probed by broad-band Terahertz pulses*";
Poster: Junior Scientist Conference 2006, Vienna, University of Technology; 19.04.2006 - 21.04.2006; in: "*Proceedings*", (2006), ISBN 3-902463-05-8; S. 311 - 312.

17. P. Schwaha, R. Heinzl, W. Brezna, J. Smoliner, H. Enichlmair, R. Minixhofer, T. Grasser:
"*Leakage Current Analysis of a Real World Silicon-Silicon Dioxide Capacitance*";
Vortrag: International Caracas Conference on Devices, Circuits and Systems (ICCDCS), Playa del Carmen; 26.04.2006 - 28.04.2006; in: "*Proceedings International Caribbean Conference on Devices, Circuits and Systems*", (2006), ISBN: 1-4244-0042-2; S. 365 - 370.

18. J. Kuzmik, S. Bychikhin, R. Lossy, H. Würfl, M. di Forte Poisson, J. Teyssier, C. Gaquière, D. Pogany:
"*Investigation of the cooling effect introduced by the airbridge structure in the multifinger AlGaN/GaN HEMTs*";
Vortrag: Workshop on Compound Semiconductor Devices and Integrated Circuits (WOCSDICE), Fiskebäckskil, Schweden; 14.05.2006 - 17.05.2006; in: "*Abstract Book WOCSDICE*", (2006), S. 181 - 183.

19. M. Austerer, C. Pflügl, S. Golka, S. Schartner, W. Schrenk, T. Roch, A. M. Andrews, G. Strasser:
"*Surface Emission of Intracavity Frequency-Doubled Light from Quantum Cascade Lasers*";
Vortrag: CLEO/QELS, Long Beach, California, USA; 21.05.2006 - 26.05.2006; in: "*Conference Programm*", (2006).

20. J. Kröll, J. Darmo, K. Unterrainer, S. Dhillon, C. Sirtori, X. Marcadet, M. Calligaro:
"*Terahertz time-domain spectroscopy of a quantum cascade laser*";
Vortrag: CLEO/QELS, Long Beach California, USA; 21.05.2006 - 26.05.2006; in: "*Postdeadline papers*", (2006), ISBN 1-55752-815-2; 2 S.

21. J. Kuzmik, J. Carlin, T. Kostopoulos, G. Konstantinidis, S. Bychikhin, A. Georgakilas, D. Pogany:
"*InAlN/(In)GaN HEMTs for high power applications (Ultragan project)*";
Vortrag: MIKON 2006, Workshop on GaN Devices, Krakow, Poland (eingeladen); 22.05.2006 - 24.05.2006; in: "*Workshop on GaN Devices*", (2006), S. 1 - 14.

22. M. Rudan, S. Reggiani, E. Gnani, G. Baccarani, C. Corvasce, M. Ciappa, M. Stecher, D. Pogany, E. Gornik:
"*Physical Models for Smart-Power Devices*";
Vortrag: International Conference on Mixed Design of Integrated Circuits and Systems (MIXDES), Gdynia, Poland (eingeladen); 22.06.2006 - 24.06.2006; in:

"*Proceedings of the International Conference on Mixed Design of Integrated Circuits and Systems*", (2006), S. 28 - 33.

23. J. Kröll, J. Darmo, K. Unterrainer:
"*Optical controll of terahertz lasers*";
Vortrag: 12th International Conference on Applied Physics of Condensed Matter, Mala Lucivna, Slovak Republic; 21.06.2006 - 23.06.2006; in: "*Proceedings*", (2006), S. 296 - 300.

24. A. M. Andrews, T. Roch, M. Schramböck, M. Austerer, W. Schrenk, G. Strasser:
"*Growth of InAs Quantum Dots for GaAs-based Quantum Cascade Lasers*";
Vortrag: Physics of Intersubband Semiconductor Emitters Summer School (POISE), Palazzone di Cortona, Italy; 25.06.2006 - 30.06.2006; in: "*Programme and Abstracts*", (2006).

25. M. Austerer, S. Schartner, S. Golka, C. Pflügl, W. Schrenk, A. M. Andrews, T. Roch, G. Strasser:
"*Surface emitting quantum cascade lasers*";
Poster: Physics of Intersubband Semiconductor Emitters Summer School (POISE), Palazzone di Cortona, Italy; 25.06.2006 - 30.06.2006; in: "*Programme and Abstracts*", (2006).

26. A. Benz, G. Fasching, A.M. Andrews, K. Unterrainer, T. Roch, W. Schrenk, G. Strasser:
"*The influence of doping on the performance of THz-QCLs*";
Vortrag: Physics of Intersubband Semiconductor Emitters, Summer School, Cortona, Italy; 25.06.2006 - 30.06.2006; in: "*Programme and Abstracts*", (2006), S. 2.

27. M. Nobile, M. Austerer, S. Schartner, A. M. Andrews, T. Roch, W. Schrenk, G. Strasser:
"*Improvement of Second Harmonic Generation by modal phase-matching in nonlinear MIR quantum cascade lasers*";
Poster: Physics of Intersubband Semiconductor Emitters Summer School (POISE), Palazzone di Cortana, Italy; 25.06.2006 - 30.06.2006; in: "*Programme and Abstracts*", (2006).

28. S. Schartner, M. Austerer, M. Nobile, S. Golka, C. Pflügl, T. Roch, A. M. Andrews, W. Schrenk, G. Strasser:
"*Farfied investigation on quantum cascade lasers*";
Poster: Physics of Intersubband Semiconductor Emitters Summer School (POISE), Cortona, Italien; 25.06.2006 - 30.06.2006; in: "*Abstract Book*", (2006).

29. D. Stehr, S. Winnerl, M. Helm, A. M. Andrews, T. Roch, G. Strasser:
"*Picosecond dynamics of interminiband transitions in doped GaAs/AlGaAs superlattices*";
Vortrag: Physics of Intersubband Semiconductor Emitters Summer School (POISE), Palazzone di Cortana, Italy; 25.06.2006 - 30.06.2006; in: "*Programme and Abstracts*", (2006).

30. G. Strasser, A. M. Andrews, M. Austerer, A. Benz, G. Fasching, S. Golka, M. Nobile, C. Pflügl, T. Roch, S. Schartner, M. Schramböck, W. Schrenk, K. Unterrainer:
"*Advanced Device Fabrication for High-Performance Cascade Lasers*";
Vortrag: Physics of Intersubband Semiconductor Emitters Summer School (POISE), Palazzone di Cortona, Italy; 25.06.2006 - 30.06.2006; in: "*Programme and Abstracts*", (2006).

31. H. D. Wanzenböck, M. Fischer, G. Hochleitner, W. Brezna, J. Smoliner, E. Bertagnolli:

"*High quality Silicon Dioxide by EBID*";
Poster: First International Workshop on Electron Beam Induced Deposition, Delft, Niederlande; 25.06.2006 - 27.06.2006; in: "*First International Workshop on Electron Beam Induced Deposition*", (2006), S. 24 - 25.

32. S. Abermann, J. Efavi, G. Sjoblom, M. Lemme, J. Olsson, E. Bertagnolli:
"*Impact of Al-, Ni-, TiN-, and Mo metal gates on MOCVD-grown HfO2 and ZrO2 high-k dielectrics*";
als Vortrag angenommen für: Workshop on Dielectrics in Microelectronics (WODIM), Santa Tecla, Italy; 26.06.2006 - 28.06.2006; in: "*Microelectronics Reliability*".

33. K. Cico, J. Kuzmik, D. Gregusova, T. Lalinsky, D. Pogany, K. Fröhlich:
"*Optimization and performance of Al2O3/GaN metal-oxide-semiconductor structures*";
Poster: Workshop on Dielectrics in Microelectronics (WODIM), Santa Tecla, Italy; 26.06.2006 - 28.06.2006; in: "*Book of Abstracts*", (2006), S. 209 - 210.

34. S. Abermann, G. Sjoblom, J. Efavi, M. Lemme, A. Lugstein, E. Auer, H. Gottlob, M. Schmidt, J. Olsson, E. Bertagnolli:
"*Comparative study on the impact of TiN and Mo metal gates on MOCVD-grown HfO2 and ZrO2 high- dielectrics for CMOS technology*";
Poster: 28th International Conference on the Physics of Semiconductors, Wien; 24.07.2006 - 28.07.2006; in: "*Proceedings of the 28th International Conference on the Physics of Semiconductors*", (2006).

35. G. Fasching, A. Benz, A.M. Andrews, K. Unterrainer, R. Zobl, W. Schrenk, G. Strasser, V Tamosiunas:
"*Dual-mode microdisk terahertz quantum-cascade lasers*";
Poster: 28th International Conference on the Physics of Semiconductors, Vienna, Austria; 24.07.2006 - 28.07.2006; in: "*Programme and Abstracts*", (2006), S. 182 - 183.

36. T. Gebhard, P. Souza, F. Schrey, G. Strasser, K. Unterrainer:
"*Polarization dependence of absorption and photocurrent in QDIPs*";
Poster: 28th International Conference on the Physics of Semiconductors, Vienna, Austria; 24.07.2006 - 28.07.2006; in: "*Book of Abstracts*", (2006), S. 76.

37. J. Kuzmik, S. Bychikhin, R. Lossy, H. Würfl, M. di Forte Poisson, J. Teyssier, C. Gaquière, E. Kohn, D. Pogany:
"*Thermal boundary resistance between GaN layer and different substrates determined by transient electrical and optical methods*";
Poster: International Conference on Physics of Semiconductor (ICPS), Wien; 24.07.2006 - 28.07.2006; in: "*Book of Abstracts*", (2006), S. 306.

38. J. Kuzmik, S. Bychikhin, E. Pichonat, C. Gaquière, E. Morvan, D. Pogany:
"*Influence of surface trapping on determination of electron saturation velocity in AlGaN/GaN structure*";
Poster: International Conference on Physics of Semiconductor (ICPS), Wien; 24.07.2006 - 28.07.2006; in: "*Book of Abstracts*", (2006), S. 307.

39. T. Müller, T. Moldaschl, G. Strasser, K. Unterrainer:
"*Ultrafast spectral hole burning spectroscopy of exciton spin relaxation in quantum dots*";
Vortrag: 28th International Conference on the Physics of Semiconductors, Vienna, Austria; 24.07.2006 - 28.07.2006; in: "*Programme and Abstracts*", (2006), S. 368 - 369.

40. S. Reggiani, E. Gnani, M. Rudan, G. Baccarani, S. Bychikhin, J. Kuzmik, D. Pogany, E. Gornik, M. Denison, N. Jensen, G. Groos, M. Stecher:

"*Experimental investigation on carrier dynamics at the thermal breakdown*";
Poster: International Conference on Physics of Semiconductor (ICPS), Wien; 24.07.2006 - 28.07.2006; in: "*Book of Abstracts*", (2006), S. 366 - 367.

41. C. Schöndorfer, A. Lugstein, L. Bischoff, Y.J. Hyun, P. Pongratz, E. Bertagnolli:
"*A new metallic nanowire growth technique utilizing focused ion beams*";
Poster: International Conference on Physics of Semiconductor (ICPS), Wien, Österreich; 24.07.2006 - 28.07.2006; in: "*International Conference on Physics of Semiconductor Programm*", (2006).

42. T. Gebhard, P. Souza, F. Schrey, G. Strasser, K. Unterrainer, M. Pires, S. Landi, A.J. Lopes, J.M. Villas-Boas, N. Studart:
"*Polarization dependence of intraband transitions in QDIPs*";
Poster: International Conference on Superlattices, Nano-Structures and Nano-Devices, Istanbul, Türkei; 30.07.2006 - 04.08.2006; in: "*Abstract Book*", (2006), S. 187.

43. S. Özcan, T. Roch, G. Strasser, J. Smoliner, R. Franke, T. Fritz:
"*Ballistic Electron Emission Microscopy/Spectroscopy on Au/Titanylphthalocyanine/GaAs Heterostructures*";
als Poster angenommen für: International Conference on Nanoscience and Technology (ICNT), Basel, Switzerland; 30.07.2006 - 04.08.2006; in: "*Proceedings of the International Conference on Nanoscience and Technology*".

44. P. Souza, T. Gebhard, F. Schrey F., G. Strasser, K. Unterrainer, M. Pires, S. Landi, J.M. Villas-Boas, N. Studart:
"*Polarization dependence of photocurrent in InAs/InGaAs/InP quantum-dot infrared photodetectors*";
Vortrag: SBCCI 2006, Ouro Preto, Brazil; 28.08.2006; in: "*Tagungsband*", (2006), S. 1 - 7.

45. M. Heer, S. Bychikhin, V. Dubec, D. Pogany, E. Gornik, L. Zullino, A. Andreini, G. Meneghesso:
"*Analysis of triggering behavior of low voltage BCD single and multi-finger gc-NMOS ESD protection devices*";
Vortrag: EOS/ESD Symposium 2006, Tucson, USA; 10.09.2006 - 15.09.2006; in: "*Proceedings of the EOS/ESD Symposium 2006*", (2006), S. 275 - 284.

46. E. Pichonat, J. Kuzmik, S. Bychikhin, D. Pogany, M. Poisson, B. Grimbert, C. Gaquière:
"Temperature analysis of AlGaN/GaN High-Electron- Mobility Transistors using micro-Raman scattering spectroscopy and Transient Interferometric Mapping";
Poster: European Microwave Integrated Circuits Conference, Manchester, UK; 10.09.2006 - 13.09.2006; in: "Proceedings of the first European Microwave Integrated Circuits Conference", (2006), S. 54 - 57.

47. S. Abermann, J. Efavi, G. Sjoblom, M. Lemme, J. Olsson, E. Bertagnolli:
"*Processing and evaluation of metal gate/high-k/Si capacitors*";
als Poster angenommen für: International Conference of Micro- and Nano-Engineering 2006, Barcelona, Spain; 17.09.2006 - 20.09.2006; in: "*Proceedings of the 32st International Conference on Micro- and Nano-Engineering*", (2006).

48. J. Darmo, J. Kröll, K. Unterrainer:
"*Time-domain spectroscopy of THz quantum cascade lasers: Theoretical and experimental aspects*";
Vortrag: IRMMW-THz 2006, Shanghai, China; 18.09.2006 - 22.09.2006; in: "*Conference Digest*", (2006), 1-4244-0400-2; S. 154.

49. J. Kröll, J. Darmo, K. Unterrainer, S. Dhillon, C. Sirtori, X. Marcadet, M. Calligaro:
"*Coherent probing of quantum cascade laser emission by terahertz time-domain*

spectroscopy";
Vortrag: IRMMW-THz 2006, Shanghai, China; 18.09.2006 - 22.09.2006; in: "*Conference Digest*", (2006), 1-4244-0400-2; S. 154.

50. E. Bertagnolli:
"*Nanopattern Formation with Focused Ion Beams*";
Vortrag: 16th International Workshop on Inelastic Ion-Surface Collisions (IISC-16), Hernstein (eingeladen); 17.09.2006 - 22.09.2006; in: "*Book of Abstracts*", (2006), S. 95.

51. G. Hochleitner, M. Fischer, H. D. Wanzenböck, R. Heer, H. Brückl, E. Bertagnolli:
"*Electron-beam-induced direct deposition of magnetic nanostructures*";
Vortrag: MNE2006 - Micro- and Nano-Engineering 2006 - 32nd International Conference, Barcelona, Spain; 17.09.2006 - 20.09.2006; in: "*Book of Abstracts*", (2006).

52. C. Schöndorfer, A. Lugstein, L. Bischoff, Y.J. Hyun, P. Pongratz, E. Bertagnolli:
"*FIB induced growth of antimony nanowires*";
Poster: International Conference of Micro- and Nano-Engineering 2006, Barcelona, Spain; 17.09.2006 - 20.09.2006; in: "*Book of Abstracts*", (2006), S. 595 - 596.

53. M. Schramböck, A. M. Andrews, T. Roch, W. Schrenk, G. Strasser:
"*In-based Quantum Dots on AlxGa1-xAs Surfaces*";
Poster: International Conference of Micro- and Nano-Engineering 2006, Barcelona, Spanien; 17.09.2006 - 20.09.2006; in: "*Book of Abstracts*", (2006), S. 597 - 598.

54. J. Kuzmik, S. Bychikhin, D. Pogany:
"*Electrical and thermal transient effects in GaN-based HEMT devices*";
Vortrag: European Workshop on III-Nitride Semiconductor Materials and Devices, Crete, Greece (eingeladen); 18.09.2006 - 20.09.2006; in: "*Book of Abstracts*", (2006), S. 15 - 16.

55. H. D. Wanzenböck, B. Lendl, E. Bertagnolli:
"*Custom-tailored microfluidics in transparent CaF2*";
Poster: International Conference on Ion Beam Modification of Materials (IBMM), Taormina, Italy; 18.09.2006 - 22.09.2006; in: "*15th Intl. Conference on ion Beam Modification of Materials*", (2006).

56. S. Schartner, M. Austerer, C. Pflügl, T. Roch, A. M. Andrews, W. Schrenk, G. Strasser:
"*Intersubband nonlinearities in GaAs-based quantum cascade lasers*";
als Vortrag angenommen für: Optics East 2006, Boston, USA (eingeladen); 01.10.2006 - 04.10.2006; in: "*Abstract Book & Proceedings SPIE*".

57. S. Schartner, M. Austerer, M. Nobile, S. Golka, C. Pflügl, T. Roch, A. M. Andrews, W. Schrenk, G. Strasser:
"*Farfied investigation on quantum cascade lasers*";
als Poster angenommen für: GMe-Workshop 2006, Wien; 12.10.2006; in: "*Abstract Book, GMe-Workshop*", (2006).

58. S. Abermann, G. Sjoblom, J. Efavi, M. Lemme, A. Lugstein, E. Auer, H. Gottlob, M. Schmidt, J. Olsson, E. Bertagnolli:
"*Comparative study on the impact of TiN and Mo metal gates on MOCVD-grown HfO2 and ZrO2 high- dielectrics for CMOS technology*";
Poster: GMe-Workshop 2006, Wien; 13.10.2006; in: "*Proceedings of the GMe-Workshop 2006*", (2006).

59. S. Özcan, T. Roch, G. Strasser, J. Smoliner, R. Franke, T. Fritz:
"*Ballistic Electron Emission Microscopy/Spectroscopy on Au/Titanylphthalocyanine/GaAs Heterostructures*";

als Poster angenommen für: GMe-Workshop 2006, Wien; 13.10.2006; in: "*Proceedings GMe-Workshop 2006*", (2006).

60. C. Schöndorfer, A. Lugstein, E. Bertagnolli:
"*Focused Ion Beam induced Nanodot and Nanowire Growth*";
als Poster angenommen für: GMe-Workshop 2006, Wien; 13.10.2006; in: "*GMe-Workshop 2006*".

61. K. Cico, J. Kuzmik, D. Gregusova, T. Lalinsky, A. Georgakilas, D. Pogany, K. Fröhlich:
"*Rapid thermal annealing and performance of Al2O3/GaN metal-oxide-semiconductor structures*";
Poster: International Conference on Advanced Semiconductor Devices and Microsystems (ASDAM), Smolenice Castle, Slovakia; 16.10.2006 - 18.10.2006; in: "*Conference Proceedings of the sixth International Conference on Advanced Semiconductor Devices and Microsystems*", (2006), S. 197 - 200.

62. D. Pogany, J. Kuzmik, S. Bychikhin, E. Pichonat, C. Gaquière, K. Andersson, C. Fager, J. Teyssier, J. Würfl, M. di Forte Poisson:
"*Thermal Characterization of HF power FETs*";
Vortrag: Target Days (TARGET), Frascati, Italy; 16.10.2006 - 18.10.2006; in: "*Target Days 2006, Book of Proceedings*", (2006), S. 31 - 34.

63. J. Kuzmik, J. Carlin, A. Kostopoulos, G. Konstantinidis, G. Pozzovivo, A. Georgakilas, D. Pogany:
"*Gate-lag and drain-lag effects in InAlN/GaN and GaN/InAlN/GaN HEMTs*";
Poster: International Workshop on Nitride Semiconductors 2006, Kyoto, Japan; 22.10.2006 - 27.10.2006; in: "*Technical Digest*", (2006), S. 302.

64. S. Golka, L. Hoffmann, M. Austerer, C. Pflügl, W. Schrenk, G. Strasser:
"*Deep etching of waveguiding structures in intersubband devices*";
Poster: Workshop of the Austrian Networks for Nanosciences and Nanotechnology, Krems; 21.11.2006 - 22.11.2006; in: "*Abstract Book*", (2006), S. 96 - 97.

65. S. Schartner, S. Golka, M. Austerer, A. M. Andrews, W. Schrenk, G. Strasser:
"*Photonic crystal mid infradred photodetectors*";
Poster: Workshop of the Austrian Networks for Nanosciences and Nanotechnology, Krems; 21.11.2006 - 22.11.2006; in: "*Abstract Book*", (2006), S. 154.

66. M. Schramböck, A. M. Andrews, T. Roch, W. Schrenk, G. Strasser:
"*In-based Quantum Dots on AlxGa1-xAs Surfaces*";
Poster: Workshop of the Austrian Networks for Nanosciences and Nanotechnology, Krems; 21.11.2006 - 22.11.2006; in: "*Book of Abstracts*", (2006), S. 98 - 99.

67. A. M. Andrews, M. Schramböck, T. Roch, M. Austerer, W. Schrenk, G. Strasser:
"*InAs Quantum Dots for Intersubband Devices*";
Vortrag: MRS Fall Meeting, Boston, MA, USA; 27.11.2006 - 01.12.2006; in: "*Program*", (2006).

68. C. Schöndorfer, A. Lugstein, Y.J. Hyun, P. Pongratz, E. Bertagnolli:
"*Focused Ion Beam Induced Growth of Antimony Nanowires*";
Vortrag: MRS Fall Meeting, Boston, USA; 27.11.2006 - 01.12.2006; in: "*2006 MRS Fall Meeting Abstracts*", (2006).

Talks and Poster Presentations (without Proceedings):

1. A. M. Andrews, T. Roch, G. Fasching, W. Schrenk, R. Zobl, K. Unterrainer, G. Strasser:
"*Growth Optimization of GaAs-based Quantum Cascade Laser for Terahertz*

Emission";
Poster: 14th International Winterschool on New Developments in Solid State Physics, Mauterndorf; 13.02.2006 - 17.02.2006; in: "*Book of Abstracts*", (2006), S. 148.

2. M. Austerer, S. Schartner, S. Golka, C. Pflügl, W. Schrenk, A. M. Andrews, T. Roch, G. Strasser, R. Green, L.R. Wilson, J.W. Cockburn, A.B. Krysa, J.S. Roberts:
"*Single mode quantum cascade lasers*";
Poster: 14th International Winterschool on New Developments in Solid State Physics, Mauterndorf; 13.02.2006 - 17.02.2006; in: "*Book of Abstracts*", (2006), S. 149 - 150.

3. G. Fasching, A. Benz, A.M. Andrews, K. Unterrainer, R. Zobl, T. Roch, W. Schrenk, G. Strasser, V Tamosiunas:
"*Microcavity THz quantum cascade laser*";
Poster: 14th International Winterschool on New Developments in Solid State Physics, Mauterndorf, Austria; 13.02.2006 - 17.02.2006; in: "*Book of Abstract*", (2006), S. 151.

4. T. Gebhard, F. Schrey F., G. Strasser, K. Unterrainer, M. Pires, S. Landi, P. Souza:
"*Intraband transitions in InAs/InGaAs/InP quantum dots for infrared photodetection*";
Poster: 14th International Winterschool on New Developments in Solid State Physics, Mauterndorf, Austria; 13.02.2006 - 17.02.2006; in: "*Book of Abstract*", (2006), S. 81 - 82.

5. J. Kröll, J. Darmo, K. Unterrainer, S. Dhillon, C. Sirtori:
"*70. Optical processes in terhaertz quantum-cascade laser waveguides*";
Poster: 14th International Winterschool on New Developments in Solid State Physics, Mauterndorf, Austria; 13.02.2006 - 17.02.2006; in: "*Book of Abstract*", (2006), S. 152.

6. T. Müller, G. Strasser, K. Unterrainer:
"*Ultrafast spectral hole burning spectroscopy of exciton spin relaxation in InAs/GaAs quantum dots*";
Poster: 14th International Winterschool on New Developments in Solid State Physics, Mauterndorf, Austria; 13.02.2006 - 17.02.2006; in: "*Book of Abstract*", (2006), S. 89 - 90.

7. M. Schramböck, W. Schrenk, T. Roch, A. M. Andrews, M. Austerer, A. Lugstein, G. Strasser:
"*Nano-patterning and growth of self-assembled nano-structures*";
Poster: 14th International Winterschool on New Developments in Solid State Physics, Mauterndorf; 13.02.2006 - 17.02.2006; in: "*Book of Abstracts*", (2006), S. 139.

8. F. Schrey, F. Schrey F., E. Magerl, G. Fasching, G. Strasser, K. Unterrainer:
"*Ultrafast intersublevel spectroscopy of a single InAs Quantum Dot*";
Poster: 14th International Winterschool on New Developments in Solid State Physics, Mauterndorf, Austria; 13.02.2006 - 17.02.2006; in: "*Book of Abstract*", (2006), S. 91 - 92.

9. G. Strasser:
"*Nonlinear effects in quantum cascade lasers*";
Vortrag: 14th International Winterschool on New Developments in Solid State Physics, Mauterndorf (eingeladen); 13.02.2006 - 17.02.2006; in: "*Book of Abstracts*", (2006), S. 34.

10. M. Schramböck, A. M. Andrews, T. Roch, W. Schrenk, A. Lugstein, G. Strasser:
"*Nano-patterning and growth of self-assembled quantum dots*";

Poster: 6th International Workshop on Epitaxial Semiconductors on Patterned Substrates and Novel Index Surfaces, Nottingham, Great Britain; 03.04.2006 - 05.04.2006; in: "*Book of Abstract*", (2006), S. 56.

11. A. M. Andrews, G. Fasching, A. Benz, T. Roch, W. Schrenk, K. Unterrainer, G. Strasser:
"*Ga-As-based Quantum Cascade Laser for Dual Frequency Terahertz Emission*";
Vortrag: Materials Research Society Spring Meeting (MRS), San Francisco, USA; 17.04.2006 - 21.04.2006; in: "*MRS Spring Meeting Abstracts*", (2006), S. 231.

12. A. Benz, G. Fasching, K. Unterrainer, R. Zobl, A.M. Andrews, T. Roch, W. Schrenk, G. Strasser:
"*Quantum-Mechanical designed Terahertz Laser*";
Poster: Junior Scientist Conference 2006, Vienna, University of Technology, Wien; 19.04.2006 - 21.04.2006; in: "*Proceedings*", (2006), 3-902463-05-8; S. 91 - 92.

13. J. Kröll, K. Unterrainer:
"*Quantum cascade laser dynamics probed by broad-band Terahertz pulses*";
Poster: Junior Scientist Conference 2006, Vienna, University of Technology; 19.04.2006 - 21.04.2006; in: "*Proceedings*", (2006), ISBN 3-902463-05-8; S. 311 - 312.

14. S. Schartner, S. Golka, M. Austerer, C. Pflügl, W. Schrenk, G. Strasser:
"*Photonic Crystal Cavities for Quantum Cascade Lasers*";
Poster: Junior Scientist Conference 2006, Wien; 19.04.2006 - 21.04.2006; in: "*Proceedings of the Junior Scientist Conference 2006*", (2006), S. 169 - 170.

15. M. Schramböck, A. M. Andrews, T. Roch, W. Schrenk, A. Lugstein, G. Strasser:
"*Nano-patterning and growth of self-assembled nano-structures*";
Poster: Junior Scientist Conference 2006, Wien; 19.04.2006 - 21.04.2006; in: "*Proceedings of the Junior Scientist Conference 2006*", (2006), S. 171 - 172.

16. P. Schwaha, R. Heinzl, W. Brezna, J. Smoliner, H. Enichlmair, R. Minixhofer, T. Grasser:
"*Leakage Current Analysis of a Real World Silicon-Silicon Dioxide Capacitance*";
Vortrag: International Caracas Conference on Devices, Circuits and Systems (ICCDCS), Playa del Carmen; 26.04.2006 - 28.04.2006; in: "*Proceedings International Caribbean Conference on Devices, Circuits and Systems*", (2006), ISBN: 1-4244-0042-2; S. 365 - 370.

17. S. Özcan, T. Roch, G. Strasser, R. Franke, T. Fritz:
"*Ballistic Electron Emission Microscopy/Spectroscopy on Au/Titanylphthalocyanine/GaAs Heterostructures*";
Vortrag: Infrared Optical Nanostructures workshop, Wien; 12.05.2006.

18. M. Schramböck, A. M. Andrews, T. Roch, W. Schrenk, M. Austerer, C. Schöndorfer, G. Strasser, M. Kast:
"*Alignment and growth of III-V semiconductor nano-structures*";
Vortrag: Infrared Optical Nanostructures workshop, Wien; 12.05.2006.

19. J. Kuzmik, S. Bychikhin, R. Lossy, H. Würfl, M. di Forte Poisson, J. Teyssier, C. Gaquière, D. Pogany:
"*Investigation of the cooling effect introduced by the airbridge structure in the multifinger AlGaN/GaN HEMTs*";
Vortrag: Workshop on Compound Semiconductor Devices and Integrated Circuits (WOCSDICE), Fiskebäckskil, Schweden; 14.05.2006 - 17.05.2006; in: "*Abstract Book WOCSDICE*", (2006), S. 181 - 183.

20. M. Austerer, C. Pflügl, S. Golka, S. Schartner, W. Schrenk, T. Roch, A. M. Andrews, G. Strasser:

"*Surface Emission of Intracavity Frequency-Doubled Light from Quantum Cascade Lasers*";
Vortrag: CLEO/QELS, Long Beach, California, USA; 21.05.2006 - 26.05.2006; in: "*Conference Programm*", (2006).

21. G. Fasching, A.M. Andrews, A. Benz, K. Unterrainer, R. Zobl, T. Roch, W. Schrenk, G. Strasser, V Tamosiunas:
"*Sub-wavelength terahertz quantum-cascade laser resonators*";
Vortrag: CLEO/QELS and PhAST 2006, Long Beach California, USA; 21.05.2006 - 26.05.2006.

22. J. Kröll, J. Darmo, K. Unterrainer, S. Dhillon, C. Sirtori, X. Marcadet, M. Calligaro:
"*Terahertz time-domain spectroscopy of a quantum cascade laser*";
Vortrag: CLEO/QELS, Long Beach California, USA; 21.05.2006 - 26.05.2006; in: "*Postdeadline papers*", (2006), ISBN 1-55752-815-2; 2 S.

23. T. Müller, G. Strasser, K. Unterrainer:
"*Exciton spin relaxation in semiconductor quantum dots*";
Poster: CLEO/QELS and PhAST 2006, Long Beach California, USA; 21.05.2006 - 26.05.2006.

24. J. Kuzmik, J. Carlin, T. Kostopoulos, G. Konstantinidis, S. Bychikhin, A. Georgakilas, D. Pogany:
"*InAlN/(In)GaN HEMTs for high power applications (Ultragan project)*";
Vortrag: MIKON 2006, Workshop on GaN Devices, Krakow, Poland (eingeladen); 22.05.2006 - 24.05.2006; in: "*Workshop on GaN Devices*", (2006), S. 1 - 14.

25. C. Pflügl, M. Austerer, S. Golka, S. Schartner, W. Schrenk, G. Strasser:
"*Nonlinear Light Generation in Quantum Cascade Lasers*";
Vortrag: Pontificia Universidade Católica do Rio de Janeiro, Rio de Janeiro, Brazil (eingeladen); 23.05.2006.

26. T. Müller, F. Schrey, G. Fasching, J. Darmo, J. Kröll, W. Parz, K. Unterrainer, A.M. Andrews, T. Roch, W. Schrenk:
"*Generation and application of THz radiation in semiconductor nanostructures*";
Vortrag: European Materials Research Society Spring Meeting, Nice, France (eingeladen); 29.05.2006 - 02.06.2006.

27. J. Kröll, J. Darmo, K. Unterrainer:
"*Optical controll of terahertz lasers*";
Vortrag: 12th International Conference on Applied Physics of Condensed Matter, Mala Lucivna, Slovak Republic; 21.06.2006 - 23.06.2006; in: "*Proceedings*", (2006), S. 296 - 300.

28. M. Rudan, S. Reggiani, E. Gnani, G. Baccarani, C. Corvasce, M. Ciappa, M. Stecher, D. Pogany, E. Gornik:
"*Physical Models for Smart-Power Devices*";
Vortrag: International Conference on Mixed Design of Integrated Circuits and Systems (MIXDES), Gdynia, Poland (eingeladen); 22.06.2006 - 24.06.2006; in: "*Proceedings of the International Conference on Mixed Design of Integrated Circuits and Systems*", (2006), S. 28 - 33.

29. A. M. Andrews, T. Roch, M. Schramböck, M. Austerer, W. Schrenk, G. Strasser:
"*Growth of InAs Quantum Dots for GaAs-based Quantum Cascade Lasers*";
Vortrag: Physics of Intersubband Semiconductor Emitters Summer School (POISE), Palazzone di Cortona, Italy; 25.06.2006 - 30.06.2006; in: "*Programme and Abstracts*", (2006).

30. M. Austerer, S. Schartner, S. Golka, C. Pflügl, W. Schrenk, A. M. Andrews, T. Roch, G. Strasser:

"*Surface emitting quantum cascade lasers*";
Poster: Physics of Intersubband Semiconductor Emitters Summer School (POISE), Palazzone di Cortona, Italy; 25.06.2006 - 30.06.2006; in: "*Programme and Abstracts*", (2006).

31. A. Benz, G. Fasching, A.M. Andrews, K. Unterrainer, T. Roch, W. Schrenk, G. Strasser:
"*The influence of doping on the performance of THz-QCLs*";
Poster: Physics of Intersubband Semiconductor Emitters, Summer School, Cortona, Italy; 25.06.2006 - 30.06.2006; in: "*Programme and Abstracts*", (2006), S. 2.

32. M. Martl, J. Darmo, J. Kröll, K. Unterrainer:
"*Terahertz surface plasmons:Time-domain analysis*";
Poster: Physics of Intersubband Semiconductor Emitters, Summer School, Palazzone die Cortona, Italy; 25.06.2006 - 30.06.2006; in: "*Programme and Abstracts*", (2006), S. 1 - 2.

33. M. Nobile, M. Austerer, S. Schartner, A. M. Andrews, T. Roch, W. Schrenk, G. Strasser:
"*Improvement of Second Harmonic Generation by modal phase-matching in nonlinear MIR quantum cascade lasers*";
Poster: Physics of Intersubband Semiconductor Emitters Summer School (POISE), Palazzone di Cortana, Italy; 25.06.2006 - 30.06.2006; in: "*Programme and Abstracts*", (2006).

34. S. Schartner, M. Austerer, M. Nobile, S. Golka, C. Pflügl, T. Roch, A. M. Andrews, W. Schrenk, G. Strasser:
"*Farfied investigation on quantum cascade lasers*";
Poster: Physics of Intersubband Semiconductor Emitters Summer School (POISE), Cortona, Italien; 25.06.2006 - 30.06.2006; in: "*Abstract Book*", (2006).

35. D. Stehr, S. Winnerl, M. Helm, A. M. Andrews, T. Roch, G. Strasser:
"*Picosecond dynamics of interminiband transitions in doped GaAs/AlGaAs superlattices*";
Vortrag: Physics of Intersubband Semiconductor Emitters Summer School (POISE), Palazzone di Cortana, Italy; 25.06.2006 - 30.06.2006; in: "*Programme and Abstracts*", (2006).

36. G. Strasser, A. M. Andrews, M. Austerer, A. Benz, G. Fasching, S. Golka, M. Nobile, C. Pflügl, T. Roch, S. Schartner, M. Schramböck, W. Schrenk, K. Unterrainer:
"*Advanced Device Fabrication for High-Performance Cascade Lasers*";
Vortrag: Physics of Intersubband Semiconductor Emitters Summer School (POISE), Palazzone di Cortona, Italy; 25.06.2006 - 30.06.2006; in: "*Programme and Abstracts*", (2006).

37. H. D. Wanzenböck, M. Fischer, G. Hochleitner, W. Brezna, J. Smoliner, E. Bertagnolli:
"*High quality Silicon Dioxide by EBID*";
Poster: First International Workshop on Electron Beam Induced Deposition, Delft, Niederlande; 25.06.2006 - 27.06.2006; in: "*First International Workshop on Electron Beam Induced Deposition*", (2006), S. 24 - 25.

38. S. Abermann, J. Efavi, G. Sjoblom, M. Lemme, J. Olsson, E. Bertagnolli:
"*Impact of Al-, Ni-, TiN-, and Mo metal gates on MOCVD-grown HfO2 and ZrO2 high-k dielectrics*";
als Vortrag angenommen für: Workshop on Dielectrics in Microelectronics

(WODIM), Santa Tecla, Italy; 26.06.2006 - 28.06.2006; in: "*Microelectronics Reliability*".

39. K. Cico, J. Kuzmik, D. Gregusova, T. Lalinsky, D. Pogany, K. Fröhlich:
"*Optimization and performance of Al2O3/GaN metal-oxide-semiconductor structures*";
Poster: Workshop on Dielectrics in Microelectronics (WODIM), Santa Tecla, Italy; 26.06.2006 - 28.06.2006; in: "*Book of Abstracts*", (2006), S. 209 - 210.

40. S. Abermann, G. Sjoblom, J. Efavi, M. Lemme, A. Lugstein, E. Auer, H. Gottlob, M. Schmidt, J. Olsson, E. Bertagnolli:
"*Comparative study on the impact of TiN and Mo metal gates on MOCVD-grown HfO2 and ZrO2 high- dielectrics for CMOS technology*";
Poster: 28th International Conference on the Physics of Semiconductors, Wien; 24.07.2006 - 28.07.2006; in: "*Proceedings of the 28th International Conference on the Physics of Semiconductors*", (2006).

41. J. Darmo, J. Kröll, K. Unterrainer:
"*Theoretical aspects of time-domain spectroscopy applied to semiconductor terahertz gain medium*";
Poster: International Conference on Physics of Semiconductor (ICPS), Vienna, Austria; 24.07.2006 - 28.07.2006; in: "*Book of Abstracts*", (2006), S. 183.

42. G. Fasching, A. Benz, A.M. Andrews, K. Unterrainer, R. Zobl, W. Schrenk, G. Strasser, V Tamosiunas:
"*Dual-mode microdisk terahertz quantum-cascade lasers*";
Poster: 28th International Conference on the Physics of Semiconductors, Vienna, Austria; 24.07.2006 - 28.07.2006; in: "*Programme and Abstracts*", (2006), S. 182 - 183.

43. T. Gebhard, P. Souza, F. Schrey, G. Strasser, K. Unterrainer:
"*Polarization dependence of absorption and photocurrent in QDIPs*";
Poster: 28th International Conference on the Physics of Semiconductors, Vienna, Austria; 24.07.2006 - 28.07.2006; in: "*Book of Abstracts*", (2006), S. 76.

44. J. Kuzmik, S. Bychikhin, R. Lossy, H. Würfl, M. di Forte Poisson, J. Teyssier, C. Gaquière, E. Kohn, D. Pogany:
"*Thermal boundary resistance between GaN layer and different substrates determined by transient electrical and optical methods*";
Poster: International Conference on Physics of Semiconductor (ICPS), Wien; 24.07.2006 - 28.07.2006; in: "*Book of Abstracts*", (2006), S. 306.

45. J. Kröll, J. Darmo, S. Dhillon, K. Unterrainer, C. Sirtori:
"*TuA1d: THz & quantum Cascade Structures*";
Vortrag: 28th International Conference on the Physics of Semiconductors, Vienna, Austria; 24.07.2006 - 28.07.2006; in: "*Programme and Abstracts*", (2006), S. 51.

46. J. Kuzmik, S. Bychikhin, E. Pichonat, C. Gaquière, E. Morvan, D. Pogany:
"*Influence of surface trapping on determination of electron saturation velocity in AlGaN/GaN structure*";
Poster: International Conference on Physics of Semiconductor (ICPS), Wien; 24.07.2006 - 28.07.2006; in: "*Book of Abstracts*", (2006), S. 307.

47. T. Müller, T. Moldaschl, G. Strasser, K. Unterrainer:
"*Ultrafast spectral hole burning spectroscopy of exciton spin relaxation in quantum dots*";
Vortrag: 28th International Conference on the Physics of Semiconductors, Vienna, Austria; 24.07.2006 - 28.07.2006; in: "*Programme and Abstracts*", (2006), S. 368 - 369.

48. S. Reggiani, E. Gnani, M. Rudan, G. Baccarani, S. Bychikhin, J. Kuzmik, D. Pogany, E. Gornik, M. Denison, N. Jensen, G. Groos, M. Stecher: "*Experimental investigation on carrier dynamics at the thermal breakdown*"; Poster: International Conference on Physics of Semiconductor (ICPS), Wien; 24.07.2006 - 28.07.2006; in: "*Book of Abstracts*", (2006), S. 366 - 367.

49. C. Schöndorfer, A. Lugstein, L. Bischoff, Y.J. Hyun, P. Pongratz, E. Bertagnolli: "*A new metallic nanowire growth technique utilizing focused ion beams*"; Poster: International Conference on Physics of Semiconductor (ICPS), Wien, Österreich; 24.07.2006 - 28.07.2006; in: "*International Conference on Physics of Semiconductor Programm*", (2006).

50. T. Gebhard, P. Souza, F. Schrey, G. Strasser, K. Unterrainer, M. Pires, S. Landi, A.J. Lopes, J.M. Villas-Boas, N. Studart: "*Polarization dependence of intraband transitions in QDIPs*"; Poster: International Conference on Superlattices, Nano-Structures and Nano-Devices, Istanbul, Türkei; 30.07.2006 - 04.08.2006; in: "*Abstract Book*", (2006), S. 187.

51. K. Unterrainer: "*Terahertz carrier dynamics*"; Vortrag: International Conference on Superlattices, Nano-Structures and Nano-Devices, Istanbul, Türkei (eingeladen); 30.07.2006 - 04.08.2006; in: "*Abstract Book*", (2006), S. 74.

52. S. Özcan, T. Roch, G. Strasser, J. Smoliner, R. Franke, T. Fritz: "*Ballistic Electron Emission Microscopy/Spectroscopy on Au/Titanylphthalocyanine/GaAs Heterostructures*"; Poster: International Conference on Nanoscience and Technology (ICNT), Basel Switzerland; 30.07.2006 - 04.08.2006.

53. S. Özcan, T. Roch, G. Strasser, J. Smoliner, R. Franke, T. Fritz: "*Ballistic Electron Emission Microscopy/Spectroscopy on Au/Titanylphthalocyanine/GaAs Heterostructures*"; als Poster angenommen für: International Conference on Nanoscience and Technology (ICNT), Basel, Switzerland; 30.07.2006 - 04.08.2006; in: "*Proceedings of the International Conference on Nanoscience and Technology*".

54. G. Pozzovivo, S. Golka, K. Cico, J. Kuzmik, W. Schrenk, G. Strasser, D. Pogany: "*Technology of InAlN/(In)GaN - based HEMT´s*"; Poster: Monte Verita´summer School, Wide-banbgap semiconductor quantum structure, Switzerland; 27.08.2006 - 01.09.2006.

55. G. Strasser: "*III-Nitride Resonant tunneling diodes*"; Vortrag: Monte Verita´summer School, Wide-banbgap semiconductor quantum structure, Switzerland (eingeladen); 27.08.2006 - 01.09.2006; in: "*Proceedings of the Monte Verita´summer school, wide-bandgap semiconductor quantum structure*", (2006).

56. P. Souza, T. Gebhard, F. Schrey F., G. Strasser, K. Unterrainer, M. Pires, S. Landi, J.M. Villas-Boas, N. Studart: "*Polarization dependence of photocurrent in InAs/InGaAs/InP quantum-dot infrared photodetectors*"; Vortrag: SBCCI 2006, Ouro Preto, Brazil; 28.08.2006; in: "*Tagungsband*", (2006), S. 1 - 7.

57. M. Heer, S. Bychikhin, V. Dubec, D. Pogany, E. Gornik, L. Zullino, A. Andreini, G. Meneghesso: "*Analysis of triggering behavior of low voltage BCD single and multi-finger gc-*

NMOS ESD protection devices";
Vortrag: EOS/ESD Symposium 2006, Tucson, USA; 10.09.2006 - 15.09.2006; in: "*Proceedings of the EOS/ESD Symposium 2006*", (2006), S. 275 - 284.

58. E. Pichonat, J. Kuzmik, S. Bychikhin, D. Pogany, M. Poisson, B. Grimbert, C. Gaquière:
"Temperature analysis of AlGaN/GaN High-Electron- Mobility Transistors using micro-Raman scattering spectroscopy and Transient Interferometric Mapping";
Poster: European Microwave Integrated Circuits Conference, Manchester, UK; 10.09.2006 - 13.09.2006; in: "Proceedings of the first European Microwave Integrated Circuits Conference", (2006), S. 54 - 57.

59. K. Unterrainer:
"*Phase-resolved stimulated emission from THz quantum cascade lasers*";
Vortrag: 2nd International Workshop on Quantum Cascade Lasers, Rosa Marina, Italy (eingeladen); 05.09.2006 - 10.09.2006; in: "*Abstract Book*", (2006), S. 42.

60. G. Strasser:
"*Vertical second-harmonic emission from QCLs*";
Vortrag: 2nd International Workshop on Quantum Cascade Lasers, Rosa Marina, Italy (eingeladen); 05.09.2006 - 10.09.2006; in: "*Abstract Book*", (2006), S. 80.

61. D. Pogany, J. Kuzmik, S. Bychikhin:
"*Thermal characterization of high frequency three and two terminal devices*";
Vortrag: European Microwave Week (EUMW), Manchester, UK (eingeladen); 10.09.2006.

62. J. Kuzmik, S. Bychikhin, D. Pogany:
"*Status and prospects in InAlN/(In)GaN HEMTs and nanosecond thermal analysis of III-Nitride devices*";
Vortrag: European Microwave Week (EUMW), Manchester, UK; 14.09.2006.

63. S. Abermann, J. Efavi, G. Sjoblom, M. Lemme, J. Olsson, E. Bertagnolli:
"*Processing and evaluation of metal gate/high-k/Si capacitors*";
als Poster angenommen für: International Conference of Micro- and Nano-Engineering 2006, Barcelona, Spain; 17.09.2006 - 20.09.2006; in: "*Proceedings of the 32st International Conference on Micro- and Nano-Engineering*", (2006).

64. E. Bertagnolli:
"*Nanopattern Formation with Focused Ion Beams*";
Vortrag: 16th International Workshop on Inelastic Ion-Surface Collisions (IISC-16), Hernstein (eingeladen); 17.09.2006 - 22.09.2006; in: "*Book of Abstracts*", (2006), S. 95.

65. G. Hochleitner, M. Fischer, H. D. Wanzenböck, R. Heer, H. Brückl, E. Bertagnolli:
"*Electron-beam-induced direct deposition of magnetic nanostructures*";
Vortrag: MNE2006 - Micro- and Nano-Engineering 2006 - 32nd International Conference, Barcelona, Spain; 17.09.2006 - 20.09.2006; in: "*Book of Abstracts*", (2006).

66. C. Schöndorfer, A. Lugstein, L. Bischoff, Y.J. Hyun, P. Pongratz, E. Bertagnolli:
"*FIB induced growth of antimony nanowires*";
Poster: International Conference of Micro- and Nano-Engineering 2006, Barcelona, Spain; 17.09.2006 - 20.09.2006; in: "*Book of Abstracts*", (2006), S. 595 - 596.

67. M. Schramböck, A. M. Andrews, T. Roch, W. Schrenk, G. Strasser:
"*In-based Quantum Dots on AlxGa1-xAs Surfaces*";
Poster: International Conference of Micro- and Nano-Engineering 2006, Barcelona, Spanien; 17.09.2006 - 20.09.2006; in: "*Book of Abstracts*", (2006), S. 597 - 598.

68. J. Kuzmik, S. Bychikhin, D. Pogany:
"*Electrical and thermal transient effects in GaN-based HEMT devices*";
Vortrag: European Workshop on III-Nitride Semiconductor Materials and Devices, Crete, Greece (eingeladen); 18.09.2006 - 20.09.2006; in: "*Book of Abstracts*", (2006), S. 15 - 16.

69. A. Lugstein, C. Schöndorfer, E. Bertagnolli:
"*Synthesis of nanowires in room temperature ambient with a focused ion beam*";
Vortrag: International Conference on Ion Beam Modification of Materials (IBMM), Taormina, Italy; 18.09.2006 - 22.09.2006.

70. H. D. Wanzenböck, B. Lendl, E. Bertagnolli:
"*Custom-tailored microfluidics in transparent CaF2*";
Poster: International Conference on Ion Beam Modification of Materials (IBMM), Taormina, Italy; 18.09.2006 - 22.09.2006; in: "*15th Intl. Conference on ion Beam Modification of Materials*", (2006).

71. S. Schartner, M. Austerer, C. Pflügl, T. Roch, A. M. Andrews, W. Schrenk, G. Strasser:
"*Intersubband nonlinearities in GaAs-based quantum cascade lasers*";
als Vortrag angenommen für: Optics East 2006, Boston, USA (eingeladen); 01.10.2006 - 04.10.2006; in: "*Abstract Book & Proceedings SPIE*".

72. M. Heer, V. Dubec, S. Bychikhin, D. Pogany, E. Gornik, M. Frank, A. Konrad, J. Schulz:
"*Analysis of triggering behaviour of high voltage CMOS LDMOS clamps and SCRs during ESD induced latch-up*";
Vortrag: European Symposium on Reliability of Electron Devices, Failure Physics and Analysis (ESREF), Wuppertal, Deutschland; 03.10.2006 - 06.10.2006.

73. S. Schartner, M. Austerer, M. Nobile, S. Golka, C. Pflügl, T. Roch, A. M. Andrews, W. Schrenk, G. Strasser:
"*Farfied investigation on quantum cascade lasers*";
als Poster angenommen für: GMe-Workshop 2006, Wien; 12.10.2006; in: "*Abstract Book, GMe-Workshop*", (2006).

74. S. Abermann, G. Sjoblom, J. Efavi, M. Lemme, A. Lugstein, E. Auer, H. Gottlob, M. Schmidt, J. Olsson, E. Bertagnolli:
"*Comparative study on the impact of TiN and Mo metal gates on MOCVD-grown HfO2 and ZrO2 high- dielectrics for CMOS technology*";
Poster: GMe-Workshop 2006, Wien; 13.10.2006; in: "*Proceedings of the GMe-Workshop 2006*", (2006).

75. S. Özcan, T. Roch, G. Strasser, J. Smoliner, R. Franke, T. Fritz:
"*Ballistic Electron Emission Microscopy/Spectroscopy on Au/Titanylphthalocyanine/GaAs Heterostructures*";
als Poster angenommen für: GMe-Workshop 2006, Wien; 13.10.2006; in: "*Proceedings GMe-Workshop 2006*", (2006).

76. C. Schöndorfer, A. Lugstein, E. Bertagnolli:
"*Focused Ion Beam induced Nanodot and Nanowire Growth*";
als Poster angenommen für: GMe-Workshop 2006, Wien; 13.10.2006; in: "*GMe-Workshop 2006*".

77. K. Cico, J. Kuzmik, D. Gregusova, T. Lalinsky, A. Georgakilas, D. Pogany, K. Fröhlich:
"*Rapid thermal annealing and performance of Al2O3/GaN metal-oxide-semiconductor structures*";
Poster: International Conference on Advanced Semiconductor Devices and Microsystems (ASDAM), Smolenice Castle, Slovakia; 16.10.2006 - 18.10.2006; in:

"*Conference Proceedings of the sixth International Conference on Advanced Semiconductor Devices and Microsystems*", (2006), S. 197 - 200.

78. D. Pogany, J. Kuzmik, S. Bychikhin, E. Pichonat, C. Gaquière, K. Andersson, C. Fager, J. Teyssier, J. Würfl, M. di Forte Poisson:
"*Thermal Characterization of HF power FETs*";
Vortrag: Target Days (TARGET), Frascati, Italy; 16.10.2006 - 18.10.2006; in:
"*Target Days 2006, Book of Proceedings*", (2006), S. 31 - 34.

79. J. Kuzmik, J. Carlin, A. Kostopoulos, G. Konstantinidis, G. Pozzovivo, A. Georgakilas, D. Pogany:
"*Gate-lag and drain-lag effects in InAlN/GaN and GaN/InAlN/GaN HEMTs*";
Poster: International Workshop on Nitride Semiconductors 2006, Kyoto, Japan; 22.10.2006 - 27.10.2006; in: "*Technical Digest*", (2006), S. 302.

80. S. Golka, L. Hoffmann, M. Austerer, C. Pflügl, W. Schrenk, G. Strasser:
"*Deep etching of waveguiding structures in intersubband devices*";
Poster: Workshop of the Austrian Networks for Nanosciences and Nanotechnology, Krems; 21.11.2006 - 22.11.2006; in: "*Abstract Book*", (2006), S. 96 - 97.

81. S. Schartner, S. Golka, M. Austerer, A. M. Andrews, W. Schrenk, G. Strasser:
"*Photonic crystal mid infradred photodetectors*";
Poster: Workshop of the Austrian Networks for Nanosciences and Nanotechnology, Krems; 21.11.2006 - 22.11.2006; in: "*Abstract Book*", (2006), S. 154.

82. M. Schramböck, A. M. Andrews, T. Roch, W. Schrenk, G. Strasser:
"*In-based Quantum Dots on AlxGa1-xAs Surfaces*";
Poster: Workshop of the Austrian Networks for Nanosciences and Nanotechnology, Krems; 21.11.2006 - 22.11.2006; in: "*Book of Abstracts*", (2006), S. 98 - 99.

83. A. M. Andrews, M. Schramböck, T. Roch, M. Austerer, W. Schrenk, G. Strasser:
"*InAs Quantum Dots for Intersubband Devices*";
Vortrag: MRS Fall Meeting, Boston, MA, USA; 27.11.2006 - 01.12.2006; in:
"*Program*", (2006).

84. C. Schöndorfer, A. Lugstein, Y.J. Hyun, P. Pongratz, E. Bertagnolli:
"*Focused Ion Beam Induced Growth of Antimony Nanowires*";
Vortrag: MRS Fall Meeting, Boston, USA; 27.11.2006 - 01.12.2006; in: "*2006 MRS Fall Meeting Abstracts*", (2006).

Doctor's Theses

1. F. Schrey:
"*High Resolution und Ultrafast Time-Domain Optical Spectroscopy of Self-Assembled Indium Arsenide Quantum Dots*";
Begutachter: K. Unterrainer, A. Scrinzi; Institut für Photonik, 2006; Rigorosum: 19.06.2006.

2. G. Fasching:
"*Microcavity terahertz quantum-cascade lasers and single quantum dot microdevices*";
Begutachter: K. Unterrainer, E. Gornik; Institut für Photonik, 2006; Rigorosum: 18.07.2006.

3. S. Golka:
"*Dry-etched intersubband devices for near- and mid-infrared optoelectronics*";
Begutachter: G. Strasser, K. Unterrainer; Institut für Festkörperelektronik, 2006; Rigorosum: 15.09.2006.

Diploma Works

1. J. Wissenwasser:
   "Der Einfluss wasserstoffbehafteter Siliziumprozessschritte auf die elektrischen Eigenschaften und die Zuverlässigkeit von Leistungshalbleiterbauelementen";
   Supervisor: E. Bertagnolli; Institut für Festkörperelektronik, 2006; Diplomprüfung: 13.01.2006.
2. A. Benz:
   "Optimierung von THz Quantum Cascade Lasers";
   Supervisor: K. Unterrainer, G. Fasching; Institut für Photonik, 2006; Diplomprüfung: 13.01.2006.
3. K. Dominizi:
   "Untersuchung von Biokompatibilität und Zelladhäsion an mikrostrukturierten Materialien der Halbleitertechnologie";
   Supervisor: E. Bertagnolli, H. D. Wanzenböck; Institut für Festkörperelektronik, 2006; Diplomprüfung: 10.03.2006.
4. T. Prikoszovits:
   "Terahertz Characterization and Imaging of Semiconductors";
   Supervisor: K. Unterrainer, J Darmo; Institut für Photonik, 2006; Diplomprüfung: 27.04.2006.
5. T.B. Moldaschl:
   "Ultrafast Spectral Hole Burning Spectroscopy of Excitonic Transitions in Self-Assembled Quantum Dots";
   Supervisor: K. Unterrainer, T. Müller; Institut für Photonik, 2006; Diplomprüfung: 23.11.2006.

Cooperations

1. JKU Linz, G. Bauer, W. Heiss, W. Jantsch, L. Palmetshofer, F. Schäffler
2. Universität Wien, H. Kauffmann, G. Kresse
3. TU Wien, H. Rauch, H. Hutter, P. Pongratz, G. Lendl
4. Universität für Bodenkultur Wien, U.Sleytr, D. Pum
5. Montanuniversität Leoben, F. Kuchar
6. Austrian Research Centers, H. Brückl
7. AMS-Unterbremstätten, H. Enichlmair, K. Tschernay, F. Unterleitner
8. Femtolasers, Wien, A. Stingl
9. High Q Laser, Hohenems, Dr. D. Kopf
10. IMS, Wien, E. Fantner, E. Platzgummer
11. AMIS, Oudenaarde, P. Moens, Belgien
12. Interuniversity Microelectronics Center (IMEC), Leuven, N. Mahadeva, Belgien
13. Siemens AG, E. Wolfgang, G. Sölkner, W. Maurer, A. Felder, Deutschland
14. Infineon München, M. Stecher, W. Stadler, Deutschland
15. ATMEL, Heilbronn, M. Graaf, Deutschland
16. TU-München, G. Abstreiter, P. Vogl, Deutschland
17. Universität Regensburg, W. Wegscheider, Deutschland

18. Friedrich-Schiller-Universität Jena, K. Gärtner, Deutschland
19. TU Braunschweig, D. Schneider, Deutschland
20. Technische Universität Berlin, D. Bimberg, Deutschland
21. Heinrich Hertz Institut, Berlin, H. Künzel, Deutschland
22. Paul Drude Institut, Berlin, H. Grahn, Deutschland
23. Institut für Kriststallzucht, Berlin, M. Albrecht, Deutschland
24. Universität Bremen, D. Hommel, Deutschland
25. Forschungszentrum Rossendorf, Dresden, M. Helm, Deutschland
26. Bosch, Reutlingen, W. Wilkening, Deutschland
27. XFAB, Erfurt, C. Foss, Deutschland
28. IZM Frauenhofer Institut, München, H. Grieser, Deutschland
29. Max Born Institut, Berlin, K. Reimann, M. Wörner, Deutschland
30. University Ulm, E. Kohn, Deutschland
31. University Darmstadt, D. Pavlidis, Deutschland
32. IZM Fraunhofer Institute, Munich, H. Gieser, H. Wolf, Deutschland
33. University of Armed Forces, Neubiberg, G. Groos, Deutschland
34. Research Center Jülich, Jülich, P. Kordos, Deutschland
35. WITEC, Ulm, O. Hollricher, Deutschland
36. MPI, Halle, U. Gösele, Deutschland
37. Imperial College, London, C. Phillips, England
38. Univ. Leeds, G. Davis, England
39. University of Sheffield, M. Skolnick, J. Cockburn, England
40. University of Surrey, B.N. Murdin, England
41. University Limoges, J.-P. Teyssier, Frankreich
42. University Lille, IEMN, De Jaeger, Frankreich
43. Centre National de la Recherche Scientific, Laboratoire de Microstructures et de Microelectronique, B. Etienne, Cedex, Frankreich
44. CEA, Grenoble, E. Monroy, Frankreich
45. Thales, Orsay , H. Page, D. Corbin, S. Delage, Frankreich
46. Universite Paris Sud, F. Julien, Frankreich
47. Universite Paris 7, C. Sirtori, Frankreich
48. FORTH, Crete, Konstantinidis, G. Georgakilas, Griechenland
49. Technische Universität Delft, P. Planken, Holland
50. Philips Neimegen, T. Smedes, Holland
51. Sub-Micron Center, Weizmann Institute, Rehovot, M. Heiblum, Israel
52. INFM-SNS Pisa, F. Beltram, A. Tredicucci, Italien
53. TASC Trient, L. Sorba, Italien
54. Universita Bari, G. Scamarcio, Italien

55. STMicroelectronics, A. Andreini, Italien
56. University Bologna, Bologna, G. Baccarani, S. Reggiani, Italien
57. Univ. Osaka, C. Hamaguchi, Japan
58. Univ. Nagoya, N. Sawaki, Japan
59. RIKEN, K. Ishibashi, Japan
60. Universite de Quebec, Quebec, B. Terreault, Kanada
61. TopGaN, Warschau, C. Skierbiszewski, S. Porowski, Polen
62. UniPress, Warschau, T. Suski, P. Perlin, Polen
63. Ioffe Physico-Technical Institute, St. Petersburg, Y. Ivanov, P. Rodin, Rußland
64. Herriot Watt University, Edinburgh, C. Pidgeon, Schottland
65. Univ. Glasgow, C. Ironside, Schottland
66. University Neuchatel, J. Faist, Schweiz
67. EPFL Lausanne, M. Ilegems, N Grandjean, Schweiz
68. ETH Zürich, W. Fichtner, Schweiz
69. Alpes Lasers, Neuchatel, A. Müller, Schweiz
70. EMPA, Thun, J. Michler, Schweiz
71. Slovak Academy of Sciences, Bratislava, Slowakei
72. Univ. of California, Lawrence Berkeley Laboratories, E. E. Haller , USA
73. Univ. of California, Los Angeles, S. Prussin, USA
74. Univ. of California, Santa Barbara, J. Allen, A. Gossard, M. Sherwin, USA
75. Columbia University, New York, H. Störmer, USA
76. Princeton University, C. Gmachl, S. Lyon, USA
77. Boston College, Boston, MA, K. Kempa, P. Bakshi, USA
78. EPI MBE Components, St. Paul, Minnesota, USA

Optimization of MBE Growth Parameters for GaAs-based THz Quantum Cascade Lasers

A.M. Andrews[1,2], T. Roch[2], A. Benz[1], G. Fasching[1], W. Schrenk[2], K. Unterrainer[1], G. Strasser[2]

[1]Institut für Photonik,
[2]Institut für Festkörperelektronik und Zentrum für Mikro- und Nanostrukturen,
Technical University of Vienna, A-1040 Wien

Introduction

Solid state terahertz (THz) lasers were made possible through the rapid progress in quantum cascade lasers (QCLs) [1]. Despite the advances in mid-infrared (MIR) QCLs [2], THz QCLs remain difficult to fabricate. The tolerances in alloy composition, layer thickness, and doping are lower for THz QCLs than their MIR counterparts. Typical THz structures can require more than a day to grow by MBE and a thickness change of a few percent will result in a non-lasing device.

In our QCL active region design, we use the phonon depletion scheme, shown in Fig. 1, to quickly depopulate the lower lasing level [3], to produce THz lasers that work above the critical liquid nitrogen temperature.

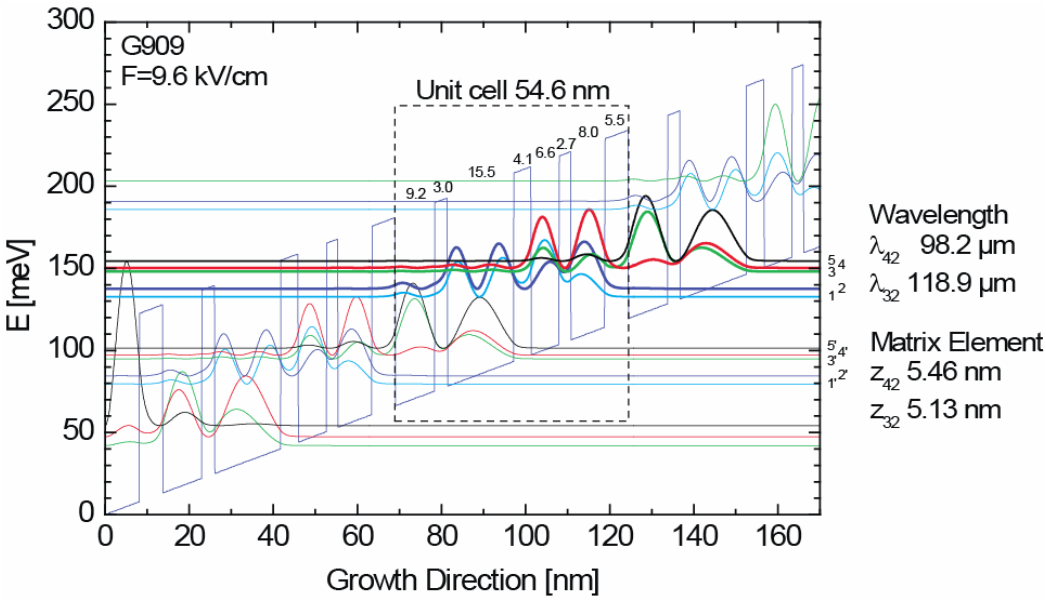

Fig. 1: Schematic of the conduction band structure (GaAs and $Al_{0.15}Ga_{0.85}As$) and electron wave functions in one unit cell of a 15 µm THz QCL active region with 271 cascade periods. This dual-wavelength design, 98.2 and 118.9 µm, results from the laser transitions from level 4 to 2 and 3 to 2. The rapid transition from level 1 to 5' emits one LO phonon.

Experiment and Results

The GaAs-based THz structures [4] were grown by solid-source molecular-beam epitaxy (MBE) in a modular GEN II. The MBE system has a vertical wagon wheel source configuration with four upward and four downward facing cells. Samples were grown on semi-insulating 3-inch GaAs substrates. Typical growth conditions used were substrate temperatures between 590 – 610°C with an As_4 pressure of $8x10^{-6}$ Torr. Original configuration, A, for the system was AC power supplies for all sources with the dual-filament Ga cell in the most upward facing position and the conical Al cell in the least upward facing position, approximately 90° from the Ga cell. The final configuration, B; uses a DC power supply for the Ga and exchanges the conical Al cell with a SUMO Al cell.

Due to the relatively low thickness tolerances, careful attention to growth conditions and their effect on wafer uniformity must be measured. Growth rate calibrations were first determined by reflected high energy electron diffraction (RHEED) oscillations and then further refined by the growth of either a singe superlattice or double superlattice measure *ex-situ* by high resolution x-ray diffraction (XRD). Shutter operations change the heat load of individual sources required to maintain specific cell temperatures by reflecting heat back into the cell. For example, the Ga cell initial growth rate upon opening the shutter was determined to be -10% of the steady state growth rate with a characteristic decay time of around 15 seconds. A second source of thickness error comes into account when growing 10 – 15 μm structures, and that is source material depletion. Due to the relatively low Al content of 15%, only the Ga depletion needs to be determined. By growing a growth rate calibration before and after the THz structure, the Ga depletion was measured to be 1% for every 10 μm of growth.

Due to the orientation of the sources, a non-rotated sample results in a thickness gradient of the desired thickness of +19% at the leading edge of the substrate to -21% at the trailing edge of the substrate for each source. This was confirmed by XRD for the growth of a non-rotated superlattice. Rotating the sample creates a more even thickness distribution across the wafer with a minimum every half rotation. After four rotations per epilayer, the average thickness error is slightly less than -1% at the edge. The total growth rate should be adjusted accordingly to maximize the usable area of the wafer when using epilayers on the order of a few or fractional monolayers.

N-type doping calibrations in the 10^{15} – 10^{16} cm^{-3} range are critical for THz QCLs, so a 4 μm Si-doped GaAs layer is grown on a semi-insulating $Al_xGa_{1-x}As$ barrier and GaAs substrate for each calibration. After 3 – 5 samples are measured, this produces reliable doping profiles with a 10% error.

Initial THz structures were grown with system configuration A, which produced broad peaks in XRD due to poor Ga flux stability, poor reproducibility, and no lasing devices. Two steps were taken to improve the THz structures: a switch to MBE configuration B along with the removal of Ga shutter operations, therefore no growth interrupts. This minimizes the flux variations for both thin layers and for long growths by using the dominant cell (Ga in this case) in steady state. The results are seen in the (002) XRD scan in Fig. 2. A 15 μm active region with 271 cascade periods is reproduced faithfully and what appear to be peak splitting, often seen in unstable long growths, are actually the diffraction peaks from the designed structure.

Table 1 summarizes the performance characteristics of the first four THz laser structures. The original 10-μm structure, 177 cascades, was designed to utilize both a surface plasmon and a double metal [5] waveguide by a 100 nm $Al_{0.55}Ga_{0.45}As$ lift-off layer and 800 nm bottom contact layer. To reduce the waveguide losses from the double-metal cladding and contacts, the active region was increased 50% to 15 μm, 271 cascades, doping reduced to $1.25e^{16}$ cm^{-3}, and the bottom contact layer thickness was reduced to 100 nm. The GaAs-based QCL has a large advantage over other material

systems when growing 10-15 μm active regions because lattice matching is not a critical factor.

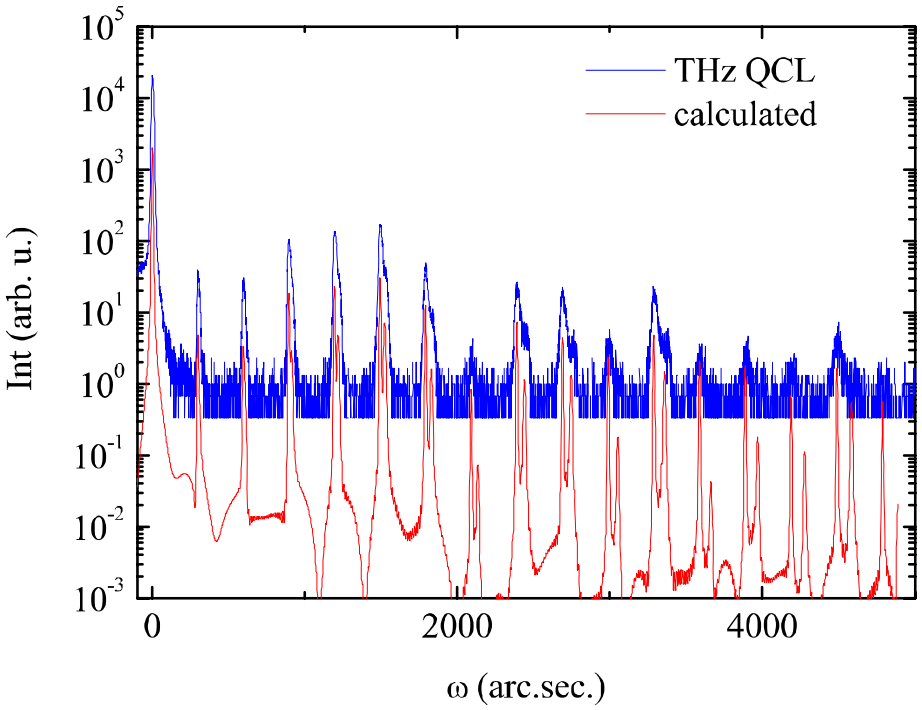

Fig. 2: X-ray diffraction (002) rocking curve of a 15 μm THz QCL active region with 271 cascade periods. The top (blue) curve is the measured scan and bottom (red) curve is the calculated diffraction pattern. What appear to be peak splitting are actually satellite peaks resulting from the designed structure.

Waveguide	J_{th} (kA/cm^2)	T_{max} Pulsed	T_{max} CW	Active Region	Doping (cm^{-3})
Surface Plasmon	1.88	88 K	-	10 μm	1.9e16
Double Metal	0.993	145 K	-	10 μm	1.9e16
Double Metal	0.506	145 K	25 K	15 μm	1.25e16
Double Metal	0.305	147 K	68 K	15 μm	8.0e15
Double Metal	0.205	133 K	72 K	15 μm	5.0e15

Table 1: Performance Characteristics of THz QCL with Decreasing Si Doping.

The double metal waveguide, due to strong mode confinement, resulted in a dramatic 50% reduction in J_{th} and pulsed operation T_{max}. The first three samples lased up to 145 K with a characteristic T_0 of 33 K. However, the continuous wave (CW) operation of the three samples differed greatly, with CW up to 25 K only in the initial low doped structures. A further reduction in doping resulted in a lower J_{th}, increased CW T_{max} of 72 K, at a cost of a reduction in the current operating range, output power, and pulsed T_{max}.

Conclusion

A 15-μm active region terahertz (2.86 THz) quantum cascade laser was optimized for maximum continuous wave temperature operation. Through the use of high-resolution x-ray diffraction, improved growth rate and doping calibrations, minimization of flux transients, a double-metal waveguide, and optimization of doping the threshold current was reduced from 1.88 to 0.205 kA/cm^2 and a maximum continuous wave operating temperature of 72K was achieved. The tolerable thickness variation in one cascade period was <1.1%.

References

[1] R. Köhler, A. Tredicucci, F. Beltram, H.E. Beere, E.H. Linfield, A.G. Davis, D.A. Ritchie, R.C. Jotti, and F. Rossi, Nature 417, 156 (2002)

[2] C. Pfluegl, M. Austerer, W. Schrenk, S. Golka, G. Strasser, R.P. Green, L.R. Wilson, J.W. Cockburn, A.B. Krysa, and J.S. Roberts, Appl. Phys. Lett. 86; 211102 (2005)

[3] S. Kumar, B.S. Williams, S. Kohen, Q. Hu, and J.L. Reno, Appl. Phys. Lett. 84, 2494 (2004)

[4] G. Fasching, A. Benz. K. Unterrainer, R. Zobel, A.M. Andrews, T. Roch, W. Schrenk, G. Strasser , Appl. Phys. Lett. 87, 211112 (2005).

[5] B.S. Williams, S. Kumar, H. Callebaut, Q. Hu, and J.L. Reno, Appl. Phys. Lett. 83, 2124 (2003).

Vertical Second-Harmonic Emission from Quantum Cascade Lasers

M. Austerer, S. Schartner, M. Nobile, W. Schrenk, A. M. Andrews, T. Roch, and G. Strasser

Zentrum für Mikro- und Nanostrukturen, TU Wien, Floragasse 7, A-1040 Vienna, Austria

We report surface emission of second-harmonic radiation generated in the cavity of GaAs/AlGaAs quantum cascade lasers. Intersubband nonlinearities in the active region of the quantum-cascade laser lead to second-harmonic generation. A distributed-feedback grating etched into to the top of the semiconductor surface provides for both single-mode fundamental laser operation and for surface-emission of the frequency-doubled light. The optical peak power from the surface is approx. 130 µW of SH light at 5.35 µm wavelength for ~1 Watt of fundamental optical power (10.7 µm) at liquid-nitrogen temperatures.

Introduction

Nonlinear light generation in quantum cascade lasers (QCLs) has first been demonstrated for the case of sum-frequency generation in the InGaAs/InAlAs material system [1], [2]. It has the potential to extend the emission wavelength region both to the high energy side by second-harmonic (SH) generation, and also to the low energy side by means of difference frequency generation. The latter process has not been demonstrated yet in QC lasers, whereas SH generation has already been combined with phase-matching schemes in order to increase the nonlinear conversion efficiency [3], [4]. In our work we used distributed-feedback (DFB) gratings in order to couple out the SH radiation via the surface of ridge lasers. The fundamental radiation is not coupled out from the surface, yielding vertical single-mode emission of SH light only.

Design and Fabrication

The laser material was grown by molecular beam epitaxy on n-doped GaAs substrates. It consists of a bound-to-continuum GaAs/AlGaAs active region and a double AlGaAs waveguide. The layer sequence of the heterostructure is as follows: 0.3 µm GaAs (n_{Si} = $4x10^{18}cm^{-3}$), 0.7 µm $Al_{0.9}Ga_{0.1}As$ (n_{Si} = $2.4x10^{17}cm^{-3}$), 2 µm GaAs (n_{Si} = $4x10^{16}cm^{-3}$), four stacks of 15 cascades of bound-to-continuum active cells, each stack separated from the next by 150 nm GaAs spacer layers, 2.2 µm GaAs (n_{Si} = $4x10^{16}cm^{-3}$), 0.7 µm $Al_{0.9}Ga_{0.1}As$ (n_{Si} = $2.4x10^{17}cm^{-3}$), 1 µm GaAs (n_{Si} = $4x10^{18}cm^{-3}$) and n-type GaAs substrate. The active region is described in detail in Ref. [5].

The DFB grating period, etch depth and duty cycle were optimized for efficient surface emission of the SH light. Our calculations yielded a grating period of 1.72 µm, an etch depth of 800 nm with a grating mark-space ratio of 0.6 and 200 nm of gold on the grating peaks only. The grating trenches were left void of metal in order to let the light couple out. The rectangular grating was transferred to the semiconductor by optical contact lithography and dry-etching. Ridge waveguides, 30 to 50 µm wide, were defined by dry-etched trenches. 300 nm of SiN_x were deposited for electrical insulation of the extended Ti/Au contact pads. The lasers were cut to approx. 2 mm long bars and indium soldered substrate down onto copper submounts. The measurements were performed

in a temperature controlled liquid-nitrogen cooled cryostat fitted with a ZnSe window. The fundamental and SH light was collected by uncoated ZnSe lenses and gold-coated off-axis parabolas and fed into a Bruker Fourier-Transform Infrared Spectrometer (FTIR). For the fundamental light a LN_2 cooled HgCdTe detector was used. The SH radiation was detected with a LN_2 cooled InSb detector fitted with an additional sapphire window to block all fundamental laser light.

Experimental

Sample Preparation

The DFB grating has a twofold function: It provides single-mode operation for the principal laser action, and couples out the second-harmonic radiation that is generated in the laser cavity by intersubband nonlinearities. The optical power at SH frequency is a function of the material second-order susceptibility χ_2 and the mismatch of the propagation constants between the fundamental and SH cavity modes. Fabry-Perot devices fabricated from the same semiconductor material show external linear-to-nonlinear conversion efficiencies $\eta_{nonlinear}$ between 10 and 130 $\mu W/W^2$ depending on the ridge width of the respective devices. We attribute that to varying phase-mismatches.

The surface-emitting DFB lasers show a $\eta_{nonlinear}$ of ~130 $\mu W/W^2$ for both facet and surface emissions. For a more detailed description of these devices refer to Ref. [6]. In Fig. 1 the light output vs. current characteristics of a typical DFB laser is shown. The investigated devices showed single mode operation on both the fundamental and SH wavelengths, as can be seen in Fig. 2. Due to the resonant nature of the DFB grating, the SH light exits the surface at nearly 90° from the ridge surface. The measurement of the exact emission angle could yield the exact difference in refractive indices for the fundamental and SH light. Furthermore the surface-emitting device allows to collect the SH radiation without the necessity of blocking filters for the fundamental frequency, as it is necessary when facet output is used.

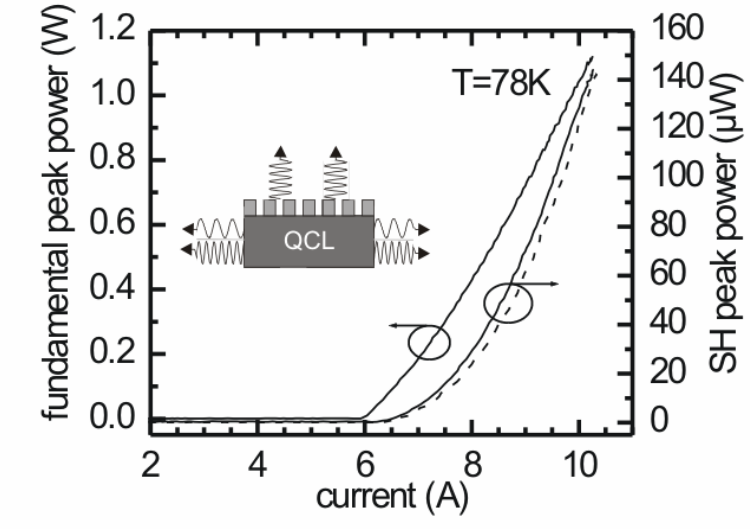

Fig. 1: Light output plotted against drive current for a 40 μm wide, 1.95 mm long device. The solid lines refer to single facet emission, the dashed line refers to vertical surface emission. Inset: A schematic depiction of the QC DFB laser ridge with fundamental (low-frequency arrows) and SH (high-frequency arrows) emissions.

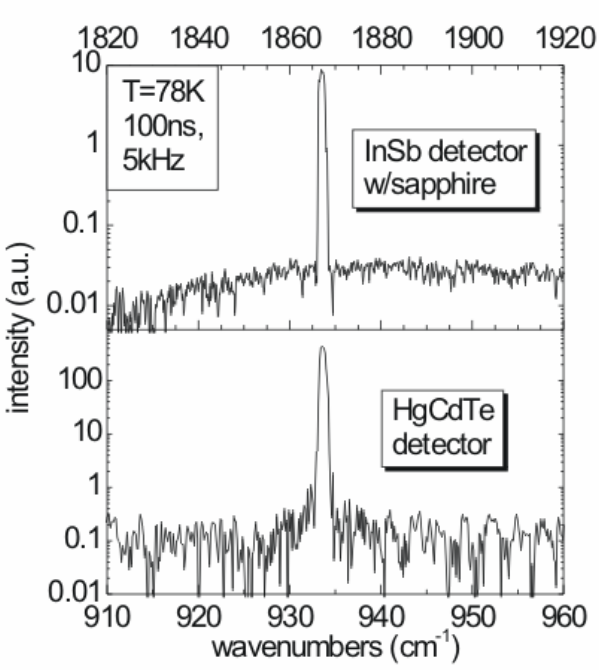

Fig. 2: Emission spectra from a 50 µm wide and 1.95 mm long device, collected from the facets. The laser was operated at 78 K under a pulsed bias of 8 A. The bottom trace shows the fundamental single-mode wavelength, whereas the top trace shows the signal at the second-harmonic frequency. The spectra were recorded with an FTIR in rapid-scan mode.

Conclusion

In conclusion we have shown that SH light generated in the cavity of a QC laser can be coupled out via the surface by means of a DFB grating. Surface gratings might also be useful for difference-frequency generation applications, or could be used for quasi-phase matching schemes, where destructive interference is suppressed by an appropriate grating.

Acknowledgements

We acknowledge the support by the EU-RTN project POISE, the Austrian FWF (ADLIS), the “Gesellschaft für Mikro- und Nanoelektronik” (GMe), and the MNA network.

References

[1] N. Owschimikow, C. Gmachl, A. Belyanin, V. Kocharovsky, D. L. Sivco, R. Colombelli, F. Capasso, and A. Y. Cho, Phys. Rev. Lett. 90, 043902 (2003)

[2] C. Gmachl, A. Belyanin, D. L. Sivco, M. L. Peabody, N. Owschimikow, A. M. Sergent, F. Capasso, and A. Y. Cho, IEEE J. Quantum Electron. 39, 1345 (2003)

[3] O. Malis, A. Belyanin, D. L.Sivco, M. L. Peabody, A. M. Sergent and A. Y. Cho, Appl. Phys. Lett. 84, 2721 (2004)

[4] M. A. Belkin, M. Troccoli, L. Diehl, F. Capasso, A. A. Belyanin, D. L. Sivco, and A. Y. Cho, Appl. Phys. Lett. 88, 201108 (2006)

[5] C. Pflügl, W. Schrenk, S. Anders, G. Strasser, C. Becker, C. Sirtori, Y. Bonetti, and A. Muller, Appl. Phys. Lett. 83, 4698 (2003)

[6] M. Austerer, C. Pflügl, S. Golka, W. Schrenk, A. M. Andrews, T. Roch, and G. Strasser, Appl. Phys. Lett. 88, 121104 (2006)

Second-Harmonic Emission from Quantum Cascade Lasers

M. Austerer, S. Schartner, M. Nobile, W. Schrenk, A. M. Andrews, T. Roch, G. Strasser

**Zentrum für Mikro- und Nanostrukturen, TU Wien,
Floragasse 7, A-1040 Vienna, Austria**

Introduction

The mid-infrared spectral region can be covered by quantum cascade (QC) semiconductor lasers, where the emission wavelength is tailored by bandstructure engineering. For a detailed review on QC lasers see Ref. [1]. Their emission energy is well below the band gaps of the hosting material system. Typical GaAs QC lasers operate in the mid-infrared regime with corresponding energies of ~100 meV, whereas the GaAs band gap is around 1.4 eV. That makes frequency-doubling inside the laser cavity feasible. Such intracavity second-harmonic (SH) generation is not possible in interband semiconductor lasers, where the SH radiation is strongly absorbed. The principle of nonlinear light generation in QC lasers was firstly demonstrated in 2003 [2], since then a lot of progress in this field has been made, such as the improvement of SH generation [3] and the demonstration of third-harmonic generation [4]. A crucial step was the achievement of phase-matching [5], [6], which was demonstrated by means of modal phase-matching in InP-based QC lasers. Another approach for higher conversion efficiencies is quasi phase-matching by periodically modulating the pump current along the QC laser ridge waveguide [7]. Besides up-conversion, other intracavity nonlinear effects are currently being investigated, such as Raman lasing [8] and anti-stokes [9] emission from QC lasers. The above nonlinear effects are due to higher-order susceptibilities of intersubband transitions. Although InP and GaAs, both of which are commonly used as host materials for QC lasers, have nonzero second-order susceptibilities, there is no resulting second-order polarization in the material for QC lasers. That is due to selection rules for intersubband transitions which allow gain only for TM polarized light, which in turn due to crystal symmetry cannot excite nonlinear polarization in the host material. However it was shown that QC lasers grown on ⟨111⟩ substrates, show sum-frequency generation due to bulk nonlinearity [10].

Bandstructure Engineering and Results

We have investigated second-harmonic and sum-frequency generation in three-well and bound-to-continuum GaAs based QC lasers. The discussed structures are regrowths of structures presented in Ref. [11] and [12] respectively. The second-harmonic generation in these samples is due to intersubband nonlinearities in the active regions of these devices. The optimization of QC active regions for intracavity second-harmonic generation is always jeopardized by the linear absorption that corrupts the laser operation at the fundamental frequency. However, three-well and bound-to-continuum active regions always have higher lying states that can resonantly enhance the second-order susceptibility of the respective QC active region.

The bandstructures discussed in this paper for the GaAs/AlGaAs material system are similar to the structures used for the InGaAs/InAlAs system. However the

GaAs/AlGaAs system offers the advantage of lattice matching for arbitrary $Al_xGa_{1-x}As$ alloy compositions. The highest Γ-valley conduction band offset can thus be reached for AlAs barriers. AlAs barriers have already been used in the past to improve the performance of QC lasers [13] – [15].

Our structure A uses AlAs barriers in the active region to design resonant intersubband transitions to generate frequency doubled light [16]. The Γ-valley conduction band edge of structure A together with the moduli squared of the relevant wavefunctions is shown in Fig. 1. The portion shown is similar to a typical three-well [11] QC active region, but with four AlAs barriers. The AlGaAs barriers in the injector regions have 45% Al-content. The wavefunctions are calculated in an effective mass approximation, where band non-parabolicity is taken into account by an energy-dependent effective mass. The lasing transition between levels 3 and 2 is calculated to an energy of 117 meV with a matrix element of z_{32} = 1.53 nm. Important nonlinear cascades are the level triplets 2–3–5a, 2–3–5b and 2–3–5c. To estimate the second-order susceptibility all three levels (2, 3, 5) have to be considered.

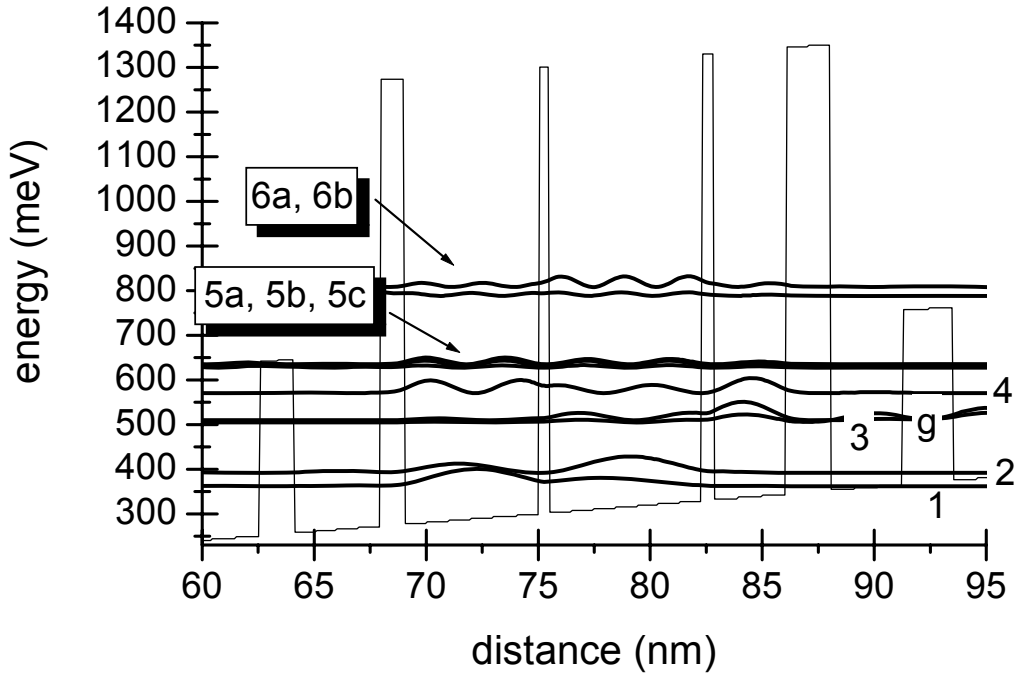

Fig. 1: Conduction band diagram and moduli squared of relevant wavefunctions in the active region of structure A. Important energy levels are labeled “1” through “6” for the active cell and “g” for the injector ground state. The layer thicknesses in nanometers for the GaAs quantum wells and AlAs barriers (italic type) from left to right *1.1*, 6, *0.5*, 6.8, *0.5*, 3.3, *1.9*; The injector bridging regions consist of $GaAs/Al_{0.45}Ga_{0.55}As$ superlattices.

Apart from the QC structure with AlAs barriers in the active region, we also investigated active regions with three-well (structure T) and bound-to-continuum (structure B) active regions, where all the barriers consisted of AlGaAs with 45% Al-content. The band-structures and moduli squared of the wavefunctions for these structures are plotted in Fig. 2. The lasing transition takes place between states 3 and 2. For a detailed description of the laser properties on the fundamental wavelength please refer to references [11] and [12].

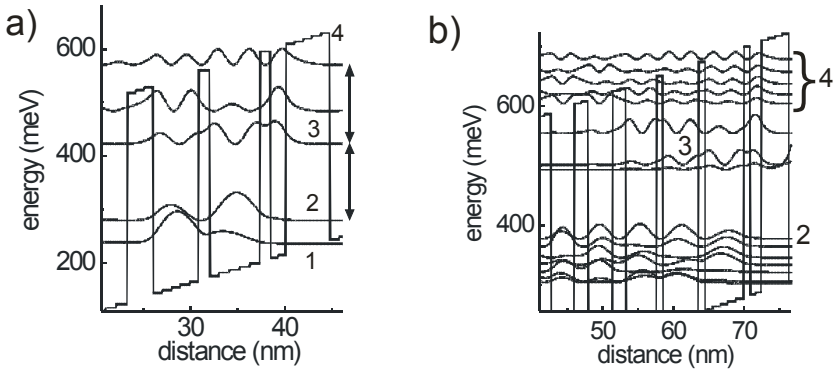

Fig. 2 Portions of the conduction band diagram and the moduli squared wavefunctions of structures a) T and b) B. The most important wavefunctions are labeled 1, 2, 3 and 4. Their functions are described in the text.

So far, SFG was only reported for three-well and two-well design active region QCLs [2], [3], [16]. We demonstrate structure B, where the situation differs qualitatively from these devices. Because the active region of the bound-to-continuum design consists of a superlattice with a thin pre-well, more states significantly contribute to sum-frequency generation. The calculated matrix elements between the involved states (2–4 and 3–4) are in the range of several Å. A feature of this structure, which was already discussed in ref. [12], is the high threshold current density. One reason for this is the strong linear resonant absorption in the active region. In this structure for lower applied fields (<35 kV/cm) the upper states are bound and thus the losses caused by linear absorption are too high to achieve lasing for the fundamental transition 3–2. However, if the electric field is increased these states are shifted towards the border of the barriers, lasing starts and because the states are still close to resonance a high second-order susceptibility is achieved, which leads to efficient sum-frequency generation in these devices.

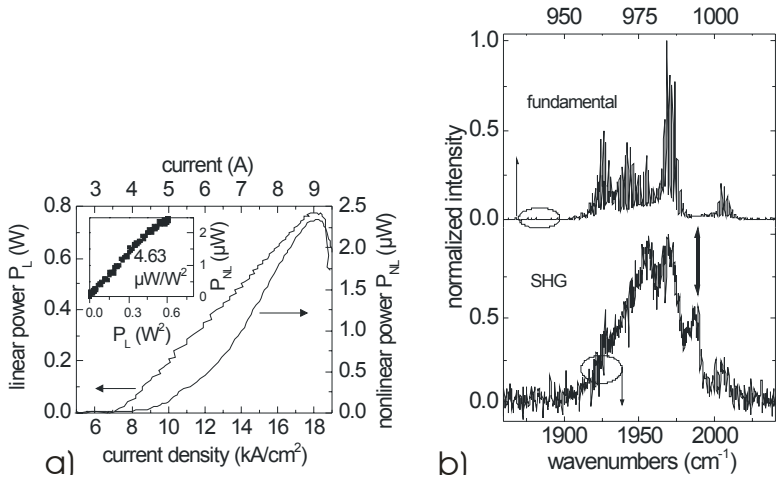

Fig. 3 Light output vs. current characteristics (a) of structure A and the corresponding spectra (b). The sum-frequency signal at 1980 cm-1 is indicated by the double-headed arrow.

The fundamental and nonlinear output powers of structure A as a function of drive current are shown in Fig. 3(a). The quadratic dependence of the nonlinear power on the

linear power can be clearly seen. When the nonlinear power is plotted as a function of the fundamental power squared, a linear function is obtained with a slope of ~5 μW/W^2 (see inset of Fig. 3(a)). In the spectra (Fig. 3(b)) we observe not only the frequency-doubled signal, but also a sum-frequency signal at ~1980 cm^{-1}, which arises from the two distinct Fabry-Perot combs at 980 cm^{-1} and 1000 cm^{-1}.

The bound-to-continuum active region shows the best conversion efficiency, possibly due to the multitude of upper states in the nonlinear cascade. Both the three-well designs with AlGaAs and AlAs barriers show approximately the same conversion efficiency, so there is no significant advantage with the additional barrier height provided by the AlAs material.

References

[1] C. Gmachl, F. Capasso, D. L. Sivco, and A. Y.Cho, Rep. Prog. Phys. 64, 1533 (2001)

[2] N. Owschimikow, C. Gmachl, A. Belyanin, V. Kocharovsky, D. L. Sivco, R. Colombelli, F. Capasso, and A. Y. Cho, Phys. Rev. Lett. 90, 043902 (2003)

[3] C. Gmachl, A. Belyanin, D. L. Sivco, M. L. Peabody, N. Owschimikow, A. M. Sergent, F. Capasso, and A. Y. Cho, IEEE J. Quantum Electron. 39, 1345 (2003)

[4] T. S. Mosely, A. Belyanin, C. Gmachl, D. L. Sivco, M. L. Peabody, and A.Y Cho, Opt. Express 12, 2976 (2004)

[5] O. Malis, A. Belyanin, D. L.Sivco, M. L. Peabody, A. M. Sergent and A. Y. Cho, Appl. Phys. Lett. 84, 2721 (2004)

[6] O. Malis, A. Belyanin, D. L. Sivco, J. Chen, A.M. Sergent, C. Gmachl and A. Y. Cho, Electron. Lett. 40, 1586 (2004)

[7] M. A. Belkin, M. Troccoli, L. Diehl, F. Capasso, A. Belyanin, and D. L. Sivco, in Conference on Lasers and Electro-Optics/Quantum Electronics (Optical Society of America, Washington, DC, 2005), QPDA1

[8] M. Troccoli, A. Belyanin, F. Capasso, E. Cubukcu, D. L. Sivco and A.Y. Cho, Nature 433, 845 (2005)

[9] H. Page, C. Becker, A. Robertson, G. Glastre, V. Ortiz, and C. Sirtori, Appl. Phys. Lett. 78, 3529 (2001)

[10] J.-Y. Bengloan, A. DeRossi, V. Ortiz, X. Marcadet, M. Calligaro, I. Maurin, and C. Sirtori, Appl. Phys. Lett. 84, 2019 (2004)

[11] H. Page, C. Becker, A. Robertson, G. Glastre, V. Ortiz, and C. Sirtori, Appl. Phys. Lett. 78, 3529 (2001)

[12] C. Pflügl, W. Schrenk, S. Anders, G. Strasser, C. Becker, C. Sirtori, Y. Bonetti, and A. Muller, Appl. Phys. Lett. 83, 4698 (2003)

[13] L. R. Wilson, D. A.Carder, J. W. Cockburn, R. P. Green, D. G. Revin, M. J. Steer, M. Hopkinson, G. Hill, and R. Airey, Appl. Phys. Lett. 81, 1378 (2002)

[14] M. P. Semtsiv, M. Ziegler, S. Dressler, T.W. Masselink, N. Georgiev, T. Dekorsky, and M. Helm, Appl. Phys. Lett. 85, 1478 (2004)

[15] W. Schrenk, N. Finger, S. Gianordoli, E. Gornik, and G. Strasser, Appl. Phys. Lett. 77, 3328 (2000)

[16] C. Pflügl, M. Austerer, W. Schrenk, and G. Strasser, Electron. Lett. 41, 1331 (2005)

Doping in Terahertz Quantum-Cascade Lasers

A. Benz, G. Fasching, A.M. Andrews, Ch. Deutsch, and K. Unterrainer

Photonics Institute and Center for Micro- and Nanostructures
Vienna University of Technology, Gusshausstrasse 29/387, A-1040 Vienna

P. Klang, W. Schrenk, and G. Strasser

Institute of Solid-State Electronics and Center for Micro- and Nanostructures, Vienna University of Technology,
Floragasse 7/1, A-1040 Vienna

We present the effects of the doping concentration on a set of terahertz quantum-cascade-lasers emitting around 2.75 THz. The threshold current density decreases linearly with the doping. The output power drops monotonically.

Introduction

Since the first reported quantum-cascade-laser (QCL) in the terahertz (THz) spectral region by Köhler et. al. [1] there has been significant progress. The available frequencies are as low as 1.39 THz [2], also extremely low threshold current densities of 1 A/cm^2 can be achieved [3]. Single-mode emission at well defined frequencies is available [4]. Also the non-radiative scattering processes are well understood, mainly due to measurements performed in a magnetic field [2], [3], [5]. Three different designs for the active region are competing each other, the chirped superlattice [1], the bound-to-continuum [4] and the longitudinal-optical (LO) phonon depopulation scheme [6]. We have chosen the last one for our studies as it shows the best temperature performance.

Sample	(a)	(b)	(c)	(d)
Doping of the widest well [cm^{-3}]	1.25e16	8e15	5.3e15	3.5e15
Sheet density [cm^{-2}]	1.9e10	1.2e10	8.2e9	5.4e9
Threshold current density J_{Th} [A/cm^2]	510	305	216	142
Maximum working temperature [K]	145	147	133	140
Growth deviation [%]	+1.3	+2.6	+1.9	+5.5

Tab. 1: The doping concentration, threshold current density, maximum working temperature and growth deviation obtained by X-ray-diffraction analysis for all samples. The X-ray diffraction results show a splitting for sample (c).

We present here a systematical study on the effects of the doping concentration on the performance of THz-QCLs. The design is nearly identical to the one published by Kumar *et al*. [7], it consist of a MBE grown GaAs/$Al_{0.15}Ga_{0.85}As$-superlattice. One cascade is built up by four wells. A simulation of the structure at lasing field is shown in Fig. 1(a). Only the widest well of the structure is homogeneously doped. The rest of the cascade remains undoped, thereby minimizing the scattering inside the optically active part of the cascade. To be able to change the doping concentration in a wide range, four identical structures have been grown. To guarantee that all samples have a comparable quality, all of them have been analyzed by X-ray-diffraction measurements.

The doping concentrations and other characteristics of the samples are given in Tab. 1. The active region is 15 µm thick; it consists of 271 identical cascades, and is processed into a high-confinement double-metal waveguide using an Au-Au thermocompression bonding [8]. The top-gold is used as a self-aligned etch mask for reactive-ion-etching (RIE). The sidewalls and the facets are etched, thereby ensuring a comparable quality and dimension for all devices. This processing and the waveguide used results in devices with high-Q resonators [9], [10].

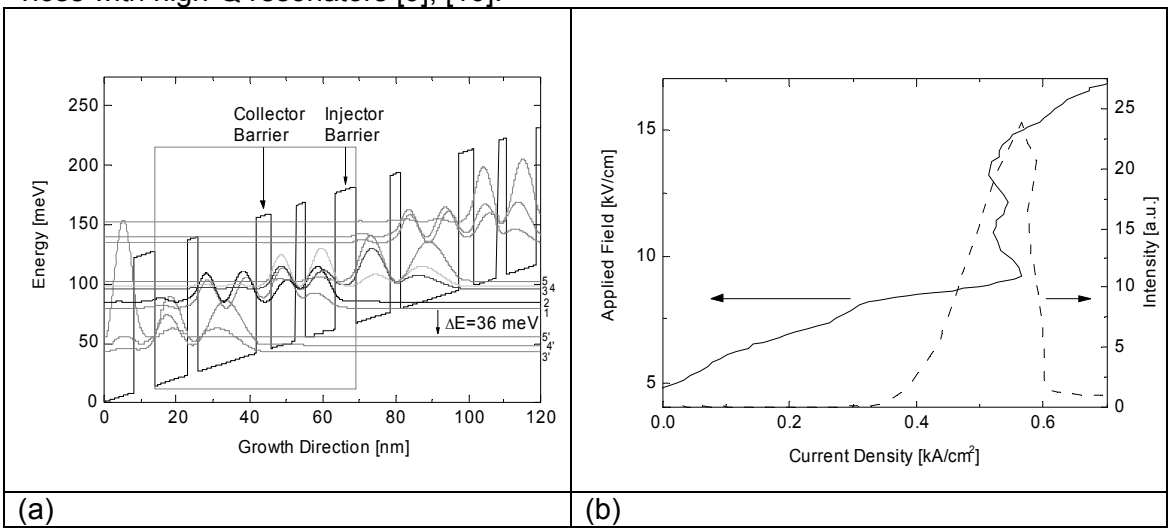

Fig. 1: A calculated bandstructure at a field of 9.8 kV/cm of the samples and an LV/IV-curve. (a) One cascade is marked with a box. The growth sequence in nm starting from the left is 9.2/**3.0**/15.5/**4.1**/6.6/**2.7**/8.0/**5.5**, where the barriers are marked with bold letters and the doped well is underlined. The optical transition happens between the wavefunctions marked with 3, 4 (upper lasers states) and 2 (lower laser state). (b) The IV shows two kinks, the first one when the structure aligns, the lasing starts, and the second one when the structure misaligns, the lasing ceases.

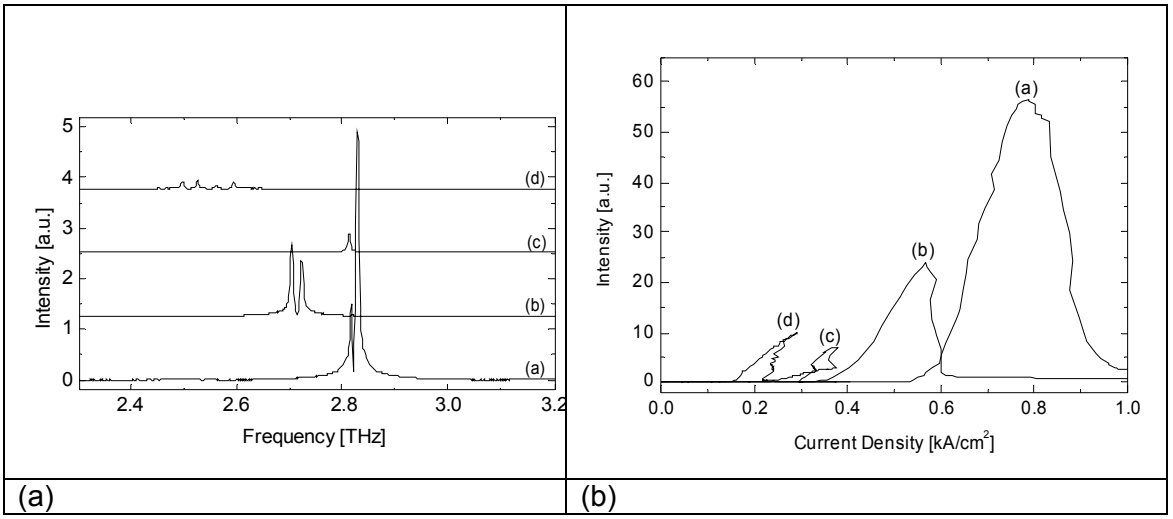

Fig. 2: Spectra of all samples at a comparable electric field and LI-measurements for the 4 samples. (a) The emission of sample (d) is slightly shifted due to a growth deviation of +5.5%. (b) The threshold and J_{max} drops linearly with a lowered doping. The peak output power decreases monotonically with the reduced doping, except for sample (c), which shows a splitting in the X-ray diffraction analysis.

Experimental Results

The first characterization of a QCL are the measurements light-versus-current (LI) and field-versus-current (IV), the results for sample (b) are shown in Fig. 1(b). A comparison of the LI and the IV reveals that the IV shows the first kink when the QCL starts to lase and the second one at maximum emission. The first one corresponds to the alignment of the cascades and therefore to an efficient transport, the second one to the misalignment of the cascades. All samples emit around 2.75 THz; the spectra are shown in Fig. 2(a). The emission of sample (d) is slightly shifted due to a growth deviation of +5.5%.

The doping concentration is a crucial factor for a working QCL as it determines the number of available carriers inside the active region. A high number of carriers in the upper laser state allows for a strong population inversion and thereby to a high gain, which scales with the doping density n. At the same time also the free-carrier absorption is increased, which scales with n^2. All our QCLs show a linear dependence of the threshold current density J_{Th} on the doping concentration. A lower doping leads to a lower threshold. Also J_{max}, the current density where maximum emission happens, drops linearly with the doping. The LIs of all samples are shown in Fig. 2(b). Beside the changes in J_{Th} and J_{max} also a drop in peak output power with a lowered doping is observable.

The relationship between the threshold current density and the temperature is an exponential one for all samples. It can be approximated with the phenomenological expression:

$$J_{Th} = J_0 + J_1 \cdot \exp\left(\frac{T}{T_0}\right). \qquad (1)$$

The parameter J_{max} on the other hand is independent of the temperature. The QCLs work up to a temperature where J_{Th} and J_{max} become equal. Unlike other publications [11] we don't see a connection between the doping and the maximum working temperature. All samples are lasing up to approx. 140 K; at this temperature the thermal energy k_BT is equal to the energy of the laser transition of 12 meV. The best results so far show a slightly higher T_{max} of 164 K [12].

A monotonical and a linear relationship between the threshold current density and the doping concentration has already been reported for THz-QCLs [11], [13]. It has been explained with the reduced waveguide losses due to the reduced free-carrier absorption in the active region. Measurements for a 10 µm thick double-metal waveguide and a sheet density for the active region of 3.2e10 cm^{-2} show a waveguide loss of 5 cm^{-1} [14]. This doping concentration is still a factor of 1.5 higher than our highest doped sample. Our simulations show a waveguide loss of 5 cm^{-1} for an undoped active region. At the extremely low doping concentration in a THz-QCL, the losses are dominated by the two gold layers and the thin n^+-contact layers and not by the free-carrier absorption in the active region. Therefore we don't attribute the increase of the threshold with a higher doping to the increased waveguide losses but to the fact that QCLs are designed to lase at a certain field and not at a certain current. Before a QCL can lase, the cascades have to be aligned properly. Therefore a higher number of available carriers, determined by the doping, leads to a higher current to establish the required field. All our samples lase strongly in a field region between 8 and 9 kV/cm independently of the doping. According to our simulations that is the field region where the coupling between the upper and the lower laser state is strong and the lower laser state is separated from the ground state by 36 meV, which corresponds to the energy of an LO-phonon in GaAs. Thereby an efficient depopulation of the lower laser level is ensured.

Conclusion

We have varied the doping concentration of a THz-QCL emitting at 2.75 THz from 5.4e9 to 1.9e10 cm^{-2}. There was no effect on the maximum working temperature observable. All samples lased up to approx. 140 K in pulsed mode operation. The threshold current density and J_{max} scaled linearly with the doping concentration. That was attributed to the fact that a QCL needs a certain field for lasing. If the doping is higher also the current has to be higher to establish that field. The output power raised monotonically with a higher doping.

Acknowledgements

This work was partly supported by the Austrian Scientific Fund FWF (SFB-ADLIS), the Austrian nanoinitative project PLATON, the EC (TERANOVA, POISE) and the Society for Microelectronics (GME, Austria).

References

[1] R. Köhler, A. Tredicucci. H. Beere, E. Lienfield, A. Davis, D. Ritchie, R. Iotti, and F. Rossi, Nature (London) **417**, 156 (2002)

[2] G. Scalari, C.Walther, J. Faist, H. Beere, and D. Ritchie, Appl. Phys. Lett. **88**, 141102 (2006)

[3] G. Scalari, S. Blaser, J. Faist, H. Beere, E. Linfield, and D. Ritchie, Phys. Rev. Lett. **93**, 237403 (2003)

[4] L. Mahler, A. Tredicucci, R. Köhler, F. Beltram, H. Beere, E. Linfield, and D. Ritchie, Appl. Phys. Lett. **87** 181101 (2005)

[5] J. Alton, S. Barbieri, J. Fowler, H. Beere, J. Muscat, E. Linfield, D. Ritchie, G. Davies, R. Köhler, and A. Tredicucci, Phys. Rev. B **68**, 081303 (2003)

[6] G. Scalari, L. Ajili, J. Faist, H. Beere, E. Linfield, D. Ritchie, and G. Davies, Appl. Phys. Lett. **82**, 3165 (2003)

[7] S. Kumar, B. Williams, S. Kohen, Q. Hu, and J. Reno, Appl. Phys. Lett. **84**, 2494 (2004)

[8] G. Fasching, A. Benz, K. Unterrainer, R. Zobl, A.M. Andrews, T. Roch, W. Schrenk, and G. Strasser, Appl. Phys. Lett. **87**,211112 (2005)

[9] G. Fasching, V. Tamosiunas, A. Benz, A. M. Andrews, K. Unterrainer, R. Zobl, T. Roch, W. Schrenk and G. Strasser, IEEE J. Quantum. Elect. **43**, 687 (2007)

[10] A. Benz, G. Fasching, Ch. Deutsch, A. M. Andrews, K. Unterrainer, P. Klang, W. Schrenk and G. Strasser, Opt. Exp. **15**, 12418 (2007)

[11] H.C. Liu, M. Wächter, D. Ban, Z. Wasilewski, M. Buchanan, G. Aers, J. Cao, S. Feng, B. Williams, and Q. Hu, Appl. Phys. Lett. **87**, 141102 (2005)

[12] B. Williams, S. Kumar, Q. Hu, and J. Reno, Opt. Exp. **13**, 3331 (2005)

[13] L. Ajili, G. Scalari, M. Giovannini, N. Hoyler, and G. Faist, J. Appl. Phys. **100**, 043102 (2006)

[14] D. Ban, M. Wächter, H.C. Liu, R. Wasilewski, M. Buchanan, and G. Aers, J. Vac. Sci. Technol. **24**, 778 (2006)

Mode Degeneracy of "Single-Mode" Whispering-Gallery Terahertz Quantum Cascade Lasers

G. Fasching[1,2], V. Tamošiūnas[4], A. Benz[1], A. M. Andrews[1,2,3], Ch. Deutsch[1], R. Zobl[3], W. Schrenk[2,3], G. Strasser[2,3], and K. Unterrainer[1,2]

[1] Photonics Institute, Vienna University of Technology, Gusshausstrasse 27-29, 1040 Vienna, Austria

[2] Centre for Micro- and Nanostructures, Vienna University of Technology, Floragasse 7, 1040 Vienna, Austria

[3] Solid-State Electronics Institute, Vienna University of Technology, Floragasse 7, 1040 Vienna, Austria

[4] Semiconductor Physics Institute, A.Gostauto 11, 01108 Vilnius, Lithuania

We present whispering-gallery terahertz quantum-cascade lasers with either "single-mode" or "double-mode" emission depending on the rotational symmetry of such resonators. Strong mode confinement in the growth and in-plane directions are provided by a double-plasmon waveguide and due to the strong impedance mismatch between the gain material and air. These ultra-compact devices exhibit increased temperature performance up to 95 K in continuous-wave mode operation and threshold currents as low as 13.5 mA. Finite-difference time-domain calculations were performed to obtain the emission spectra from such microdisk terahertz quantum-cascade lasers.

Introduction

Optical microcavities allow to confine light to extremely small mode volumes by resonant recirculation. The terahertz (THz) frequency range is very attractive to study cavity effects, as standard fabrication processes allow to realize chip based cavities on the micrometer scale with a surface roughness well below λ/30.

In recent years a great deal of research has been dedicated to realize quantum-cascade lasers (QCLs) based on Fabry-Pérot resonators emitting in the historically underdeveloped frequency region of 1 – 10 THz (30 – 300 μm) [1] – [4]. THz QCLs can be used in a wide field of applications including imaging, spectroscopy and sensing. Beside the proper design of the intersubband states waveguiding plays an important role to achieve lasing in the THz frequency range. We have recently demonstrated the first double-metal microdisk and microring QCLs operating in the THz frequency region [5] and also very recently the first single-mode emitting microdisk lasers [6].

In this contribution we present the results of our investigations on ultra-small mode volume THz QCLs based on whispering-gallery modes (WGMs) showing high temperature performance and "single"- as well as double-mode emission.

Sample Design and Fabrication

The band structure design of the $Al_{0.15}Ga_{0.85}As$/GaAs laser structure is based on the four-quantum-well THz QCL scheme introduced by Williams [4]. It combines resonant tunneling and fast depopulation of the lower laser level by the use of resonant longitudinal-optical (LO) phonons. Although the lasing transition is spatially vertical a long upper laser level lifetime of more than 5 ps is achieved.

The heterostructure was grown by molecular-beam epitaxy on a semi-insulating GaAs substrate with 271 cascaded modules resulting in a thickness of the grown laser structure of 15 µm. The QCL devices were processed into a double-metal configuration, which causes a high modal confinement in vertical direction as well as a high lateral confinement due to the semiconductor-air impedance mismatch and drastically reduces the free carrier losses compared to single-plasmon THz QCLs. Wafer pieces of the MBE-grown material and of a n^+ GaAs substrate were covered with Ti/Au. After aligning each GaAs substrate piece upside down on the metallized surface of the laser material, the samples were bonded at 330 °C for 30 min under constant pressure in a commercial wafer bonder. After removing the substrate and the $Al_{0.55}Ga_{0.45}As$ etch stop layer of the MBE-grown material, the Ti/Au top contact layers were deposited by sputtering. The contact layers as a self-aligned etch mask and an inductively coupled $SiCl_4/N_2$ plasma (ICP) were used to etch down the active region to the wafer-bonded Ti/Au layers. This resulted in perpendicular and smooth resonator boundaries with metal confinement over the whole gain medium as shown in Fig. 1. After soldering the chip onto a copper plate and wire bonding, the devices were mounted on the cold finger of a helium-flow cryostat.

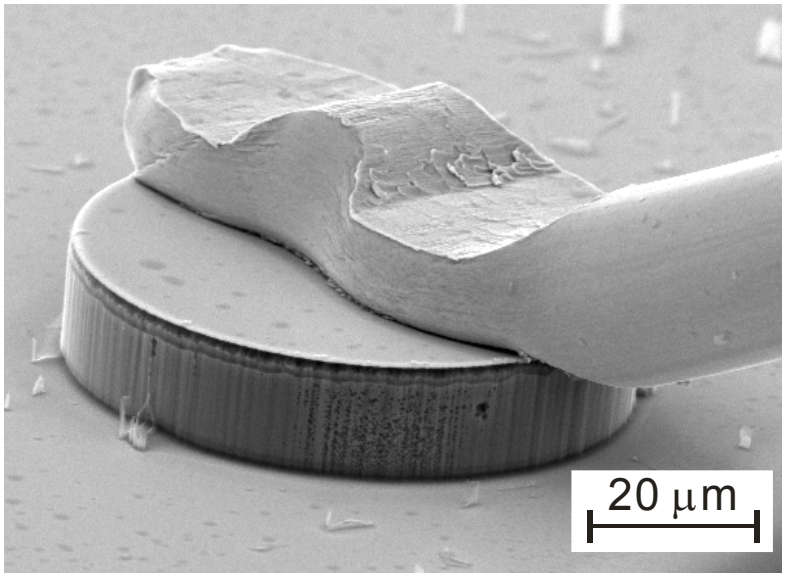

Fig. 1: Scanning electron micrograph (SEM) image of a bonded double-metal microcavity with a radius R_{out} = 35 µm and a height H = 15 µm.

Results

Simulations

A finite-difference time-domain (FDTD) method [8] is widely used to simulate the interaction of electromagnetic waves and semiconductor devices and can be efficiently em-

ployed to simulate QCLs. In this contribution, we present results of 3-D FDTD simulations of disk-shaped THz QCLs with a diameter of R = 35 µm and a height h = 15 µm. FDTD simulations of multi-mode emitting microcavities can be found in [9], [10]. Full 3-D simulations are employed to obtain the expected spectrum of the device. 350 ps of wave propagation within the resonator is simulated. The Yee cell size is set to 1.4 µm and the Courant number to 0.5 during the simulation. The average relative dielectric constant of the $Al_{0.15}Ga_{0.85}As/GaAs$ material was set to ε = 13 during the FDTD simulations. The obtained time-domain data from the last 233 ps is reprocessed using an integrated discrete Fourier-transform (DFT) algorithm. Only the amplitude values of the electric field component $|E_z|$ parallel to the growth direction near the bottom contact of the resonator are recorded in order to reduce the amount of computations and taking into account the selection rules. The maximum values of the amplitude are collected at each frequency to obtain the spectrum depicted in Fig. 2(a). The calculated mode spectrum exhibits a single cavity mode at 2.767 THz which is very close to the experimentally observed “single-mode” emission at 2.806 THz.

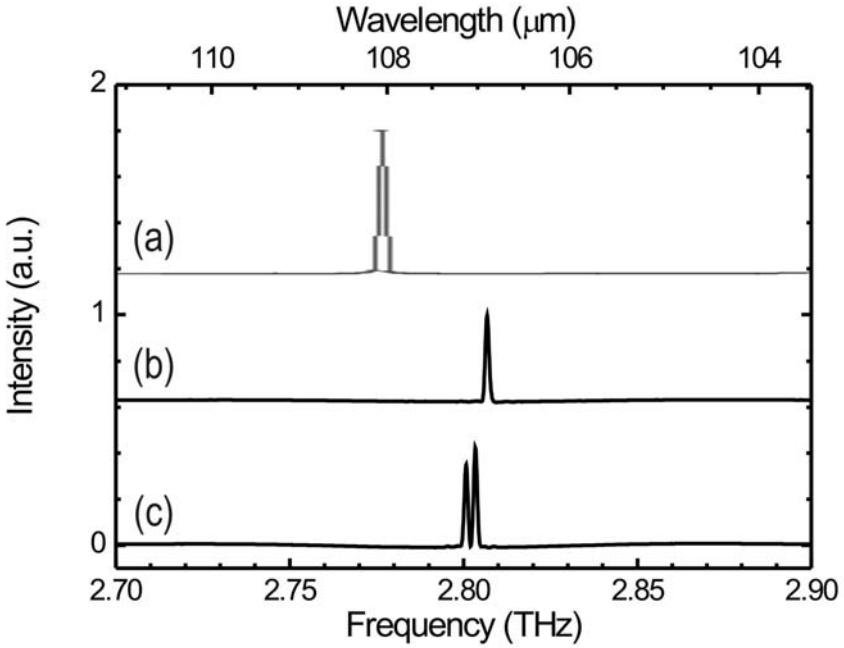

Fig. 2: (a) Simulated WGM and (b), (c) measured “single”- and double-mode emission of a microcavity THz QCL as shown in Fig. 1.

Measurements

The emission spectra were recorded using a nitrogen-purged Fourier transform infrared (FTIR) spectrometer. The spectra were measured in linear scan mode with a resolution of 0.03 cm^{-1} (0.9 GHz). The spectrometer is equipped with a 4.2 K Si bolometer. The emission spectra were measured using 3 ms long pulses with a repetition rate set to 3.33 kHz. The continuous-wave (cw) spectra of the microcavity lasers were recorded with a resolution of 0.125 cm^{-1} (3.75 GHz) using a standard DC source.

The THz QCL microcavities provide a stable “single-mode” in pulsed-mode operation as shown in Fig. 2(b) with a threshold current of 13,5 mA as well as cw operation which is highly desirable for certain applications like local oscillators. The metallic waveguide is superior to the pure dielectric waveguides with respect to heat transfer and loss for increasing wavelengths. Although the maximum achieved temperature in pulsed-mode operation is quite comparable for microdisks with different device radii, the maximum

temperature in cw operation strongly increases with decreasing device radius up to a maximum heat-sink temperature of 95 K [10]. This fact can be clearly attributed to a better thermal management for smaller devices which have the same dynamical current range as the larger ones. This demonstrates that circular-shaped microcavities give the opportunity to create ultrasmall devices with extremely low operational current and therefore low electrical power dissipation which enhances the cw performance.

In addition we have observed a closely spaced double-mode emission with a spacing below 4 GHz as shown in Fig. 2(c) from other microcavities with the same cavity dimensions under the same measurement conditions. WGMs possess a natural two-fold degeneracy due to the two possible directions of propagation (clockwise and counterclockwise). Imperfections inside or at the surface of high quality factor *Q* resonators can yield to scattering causing mode coupling of the two counterpropagating modes resulting in a mode-doublet [11]. For our cavities we broke the rotational symmetry of some of the resonators due to not perfectly centered bond wires at the top contact. This influences the phase conditions of the modes leading to a lifting of the natural two-fold degeneracy of the WGMs causing this double-mode emission [10]. In general, the ability to controllably change the field distribution inside the microcavity would lead to a controllable change of the emission frequency as well as the cavity *Q*.

References

[1] J. Faist, et al.: “Quantum cascade laser,” *Science*, vol. 264, pp. 553–556, 1994.

[2] R. Köhler, et al.: “Terahertz semiconductor heterostructure laser,” *Nature* (London), vol. 417, pp. 156-159, 2002.

[3] G. Scalari, et al.: “Far-infrared (λ ~ 87 μm) bound-to-continuum quantum cascade lasers operating up to 90 K,” *Appl. Phys. Lett*., vol. 82, pp. 3165-3167, 2003.

[4] B. S. Williams, et al.: “3.4-THz quantum cascade laser based on scattering for depopulation,” *Appl. Phys. Lett.*, vol. 82, pp. 1015-1017, 2003.

[5] G. Fasching, et al.: “Terahertz microcavity quantum-cascade lasers,” *Appl. Phys. Lett*., vol. 87, p. 211112, 2005.

[6] G. Fasching, et al.: “Sub-Wavelength Terahertz Quantum-Cascade Laser Resonators (Presented Conference Paper Style), *presented at CLEO06, Los Angeles, CA, May 21-26, 2006, Paper CTuT3*.

[7] A. Benz, et al.: “The influence of doping on the performance of terahertz quantum-cascade lasers,” *Appl. Phys. Lett.*, vol. 90, p. 101107, 2007.

[8] A. Taflove, Computational Electrodynamics: The Finite-Difference Time-Domain Method, Boston, USA: Artech House, 1995 (and references within).

[9] G. Fasching, *et al.*: “Microcavity terahertz quantum-cascade laser,” *SPIE-Int. Soc. Opt. Eng, vol. 6010, p. 601006, 2005.*

[10] G. Fasching, et al.: “Sub-Wavelength Microdisk and Microring Terahertz Quantum-Cascade Lasers,” *IEEE J. Quantum Electron.*, vol. 43, pp. 687-697, 2007.

[11] D. S. Weiss, et al.: “Splitting of high-Q Mie modes induced by light backscattering in silica microspheres,” *Opt. Lett.*, vol. 20, pp. 1835-1837, 1995.

Polarization Dependence of Photocurrent in Quantum-Dot Infrared Photodetectors

T. Gebhard[1], P.L. Souza[1,2], F.F. Schrey[1], G. Strasser[1], K. Unterrainer[1], M.P. Pires[3], S.M. Landi[2], J.M. Villas-Boas[4], N. Studart[5]

[1]Photonics Institute and Center for Micro- and Nanostructures, TU-Wien, A-1040 Vienna, Austria

[2]LabSem, CETUC, PUC-Rio,Rua Marquês de Sao Vicente 225, Rio de Janeiro, 22451-900, Brazil

[3]Instituto de Física, Universidade Federal do Rio de Janeiro, Rio de Janeiro, Brazil

[4]Ohio University, USA

[5]Instituto de Física, Universidade Federal de São Carlos, São Carlos, Brazil

Through polarization dependence measurements of photocurrent together with theoretical calculations we were able to identify different intersubband transitions in InAs/InGaAs/InP quantum dot structures for infrared photodetectors and observe 2D/0D hybrid behavior of the dot structures.

Introduction

The technology to detect infrared photons is dominated by HgCdTe (MCT) photodetectors since about four decades. The major advantage of this material system is the tunability over a large detection range. Their high optical conversion efficiency and the wide-band response are hard to compete with. Despite that, there is still a need to improve handling, reliability, speed and reproducibility of state of the art infrared photodetectors. They are bulky due to cryogenic temperature operation, and the lack of uniformity of the grown material makes them only partially suitable for large focal plain arrays. The ripening process of the MCT technology was accompanied by intensive research efforts for alternative detector concepts for increased temperature operation, reliability and reproducibility. As a consequence of the highly advanced epitaxial growth techniques for III-V semiconductor materials, intersubband photo-detection via quantum wells (QW) showed great potential as a viable alternative. However, theoretical predictions show that quantum well infrared photo-detectors (QWIP) have problems as candidates to rival the MCT technology at higher temperatures, as the dark current in QWIP increases significantly due to inherent thermoionic emission. In addition, selection rules in QW prohibit light incoming parallel to the growth-direction to be absorbed in intersubband transitions. Gratings and random reflectors are needed to circumvent this physical limit. The evolution of quantum devices led to a further reduction of the confinement dimensionality and today self organized growth techniques made the growth of quantum dots (QD) possible for a variety of material systems. Quantum dot infrared photo-detectors (QDIP) are not only able to outperform QWIP [1], but they are also potential candidates to rival or outperform MCT photo-detectors [2]. The reduced phonon-electron interaction in QD results in a long lifetime of excited carriers. The photoconductive gain increases by magnitudes compared to QWIP and also the dark

current is theoretically reduced significantly due to suppressed thermoionic emission. The absorption coefficient is also much higher than in QW. QD show the inherent feature to absorb normal incident light [3].

The features of QDIP are very sensitively connected to the degree of control during the growth process, where many different uncertainties lead to reduced reproducibility. The self-organized growth process spreads the dots size inhomogenously, and this decreases the detectivity of the devices. This effect cannot be eliminated, but only minimized technologically. QDIP without blocking layer have still a much higher dark current than QWIP caused by interlayer-dot-tunneling through defects and thermally excited carriers from upper excited states and are therefore far away from theoretically predicted limits.

Hence, real QDs are quite different from ideal. The intraband absorption and the consequently generated photocurrent (PC) in these devices should be fully understood. In particular, there has been some controversy in the literature on the polarization dependence of the PC for QDIP structures [4] – [7]. In this work we investigate the photocurrent (PC) as a function of temperature and polarization produced by QD structures where InAs dots are nucleated on top of an InGaAs QW. The dots are covered with an InP barrier. The observed PC peaks are attributed to different intraband transitions based on the PC data together with theoretical calculations.

Experimental

A doped sample with 20 and an undoped one with 10 dot layers were grown by metalorganic vapor phase epitaxy on semiinsulating (100) InP substrate. The InAs dots were grown on a 8.5 nm thick InGaAs layer lattice matched with InP and capped by 18 nm InP layer. The Si doping density of the 0.4 µm thick InP contact layers is n = 4×10^{18} cm^{-3} for both samples. The nominal doping level of the QD in the doped sample provides 2 electrons in the ground state per dot. The dot sheet density of about 9×10^{9} cm^{-2} and the median dot height of 9 nm were estimated by atomic force microscopy.

The PC polarization QD samples were investigated by a Fourier transform spectrometer for normal and 45° light incidence. Choosing the TE polarization implies that the electric field is totally in the plane of the layers. However, for the TM polarization, the electric field will have a component perpendicular to the layers.

The measured spectra were corrected by the system response and by the Fresnel refraction coefficients for both polarizations.

Results

A PC signal was detected up to 50 K and 90 K for the doped and undoped sample, respectively. Polarization dependent PC measurements of the undoped sample show a signal around 5.3 µm. Figure 1 shows the PC spectra at 6 K for the undoped sample for different experimental configurations: normal incidence, 45 degrees incidence with TE polarization, 45 degrees incidence with TM polarization, and unpolarized light. Choosing the TE polarization implies that the electric field is totally in the plane of the layers. On the other hand, for the TM polarization, the electric field will have a component perpendicular to them. The same peak is observed for all configurations. However, for the TE polarization the PC signal was expected to be of the same order of magnitude as for the TM polarization, indicating that the energy levels involved have a 0D character.

For the undoped sample the transition around 5.3 µm should depart from the ground state, because only this state is populated due to non-intentional doping. The simple 1D calculation estimate the transition energy from the ground state to the first excited state of about 184 meV; this is a underestimation of about 20% in comparison to the experimental results. Electrons in the first excited state can contribute to the photocurrent due to sequential tunneling, as it has been already observed for these samples [10]. This transition has the highest oscillator strength, so other transitions to the excited states can be excluded.

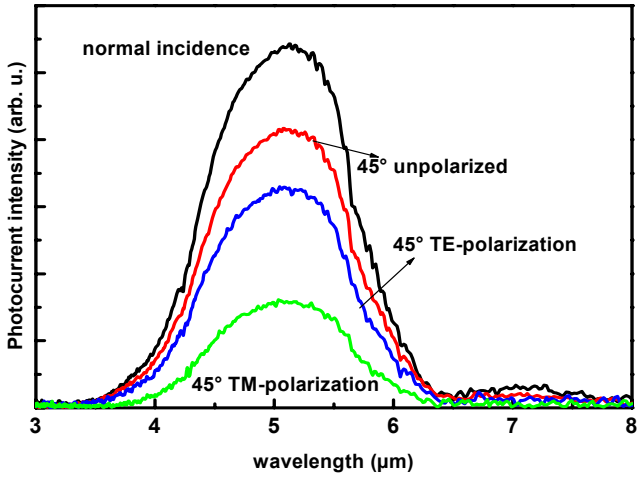

Fig. 1: Polarization dependence of the photocurrent at 6 K for the undoped sample.

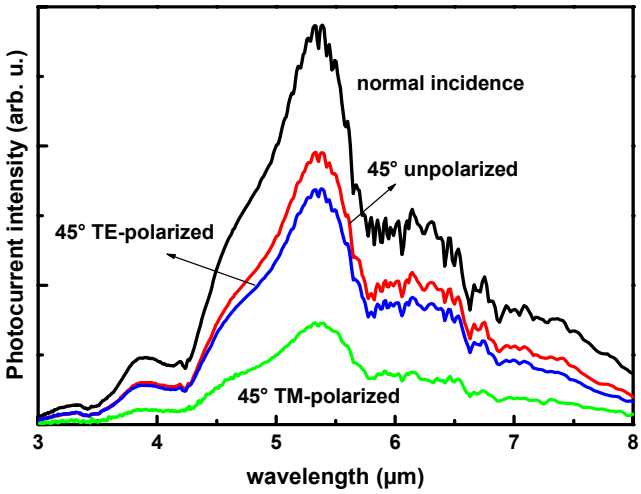

Fig. 2: Polarization dependence of the photocurrent at 6 K for the doped sample.

Equivalent polarization behavior, but noisier signal, is observed for the doped sample, as shown in Fig. 2. The doped sample contains twice as many layers as the undoped does. Even though one would expect a stronger signal, strain builds up more in such a thicker structure leading to more noise in the detected PC. Carefully looking in the spectra one observes that there are three peaks at 4 µm, 5.3 µm and 6.2 µm, corresponding to 310, 234 and 200 meV, in addition to a couple of shoulders. Using a simple 1D effective-mass model [8] for the InP/InGaAs/InAs/InP structure the band- con-

figuration shown in Fig. 3 is obtained assuming a dot height of 9 nm and an InGaAs QW thickness of 10 nm.

For the doped sample additional transitions can also occur from the first and second excited states to the third excited state or to the continuum. The oscillator strength to the continuum is small compared to these to the third excited state. The transitions E_1 – E_3 and E_2 – E_3 correspond to 5.8 and 8.9 μm, respectively. The theoretical and experimental transition energies are in fairly good agreement, considering that such a simple 1D model was used; the theoretical values being overestimated by about 15%. Results of photoluminescence give further support to these peak assignments [10].

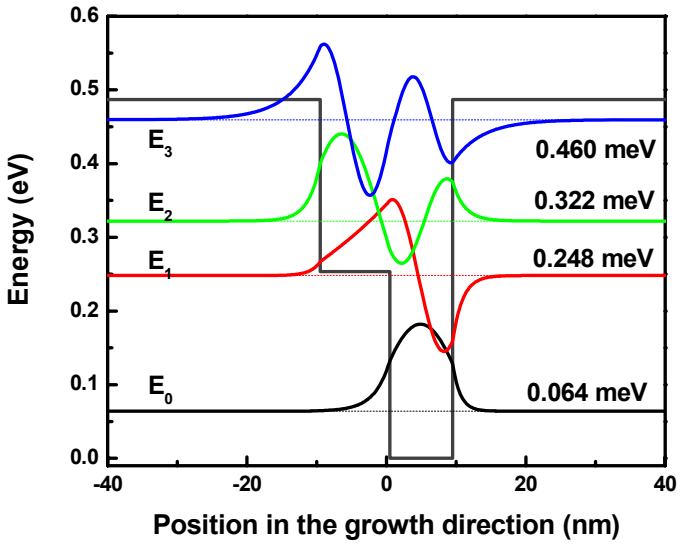

Fig. 3: Band configuration of the investigated samples.

Conclusion

We have performed polarization dependence measurements in InAs/InGaAs/InP quantum dot structures. Based on the difference between doped and undoped sample and the simple theoretical calculations, different transitions were identified. A strong PC-signal for s-polarization was observed as expected due to the 0D character of the QD. But surprisingly the PC for the p-polarization was rather weak showing little evidence 2D/0D hybrid behavior.

Acknowledgements

We acknowledge the financial support from CAPES, CNPq, FAPERJ, FINEP, Wolfgang Pauli Institute, FWF SFB IR-ON and ANSWER.

References

[1] E. T. Kim et al, 84, 3277 (2004)

[2] J. Phillips, J. Appl. Phys., 91, 4590 (2002)

[3] A. Rogalsky, Progress in Quantum Electronics, 27, 59-210 (2003)

[4] L. Chu et al, Appl. Phys. Lett., 75, 3599 (1999).

[5] L. Chu et al, Appl. Phys. Lett., 76, 1944 (2000).

[6] S. Sauvage et al, Appl. Phys. Lett., 78, 2327 (2001).

[7] B. Aslan et al, Appl. Phys. Lett., 82, 630 (2003).

[8] J. Mendoza-Alvarez et al, Physica E, 32, 85 (2006).

[9] A. G. Silva, et al, ICPS2006.

[10] T. Gebhard, et al, ICSNN2006.

Y-coupled Quantum Cascade Lasers

L.K. Hoffmann, C. A. Hurni, S. Schartner, M. Austerer, E. Mujagić, M. Nobile, A.M. Andrews, W. Schrenk, G. Strasser

ZMNS, TU Wien, Floragasse 7, A-1040 Vienna, Austria

Y-coupled cavity quantum cascade lasers have been processed from GaAs/AlGaAs and InP/InGaAs/AlAs/AlInAs wafers. Farfields of these samples were investigated. A phase coherence between the two coupled ridges was observed which results in the farfield pattern of a double slit experiment. Coherent coupling gives perspectives for high power laser arrays.

Introduction

Quantum cascade lasers (QCLs) have been intensively investigated since their first demonstration in 1994 by J. Faist *et al.* [1]. QCLs are now able to cover a broad spectrum from a few microns wavelength to the THZ regime. As mid-infrared sensing applications require high power coherent light sources, coherently coupled QCL arrays are desirable.

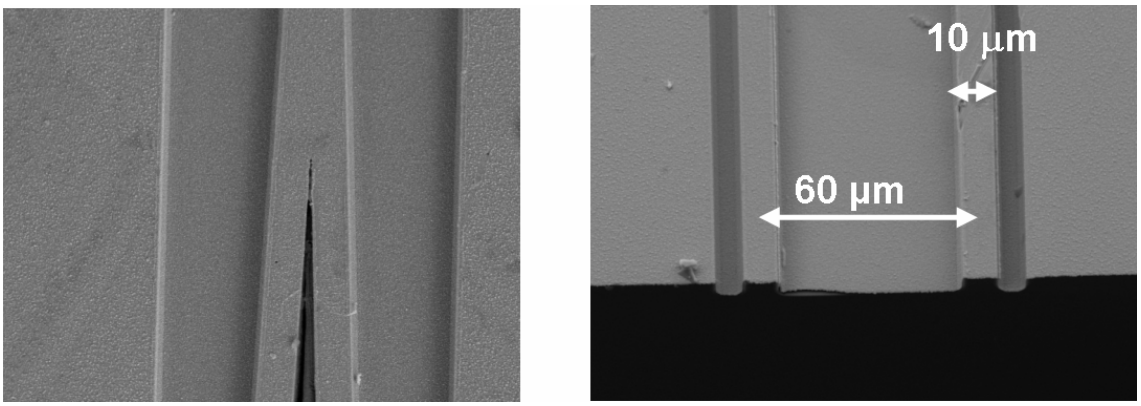

Fig. 1: SEM pictures of the InP based sample. Merging of two 10 μm ridges into one single 10 μm ridge (left). Double facet side of the sample (right).

Processing

Two QCL structures were used for the experiments. The first one is a GaAs/AlGaAs active region structure with a double plasmon waveguide [2]. Its emission spectrum peaks at about 10.5 μm at room temperature (RT). The second structure is a strain-compensated InGaAs/AlAs active region structure with an InP based waveguide [3] and an emission wavelength of about 4.3 μm at RT.

Y-coupled ridges were etched using reactive ion etching (RIE). Thereafter, a 300 nm thick SiN_x insulating layer was deposited by plasma enhanced chemical vapor deposition (PECVD). Windows were opened on top of the ridges, followed by evaporated Ge/Au/Ni/Au (150/300/140/1500 nm) top contacts. 500 nm Ti/Au extended contact

pads finished the top side processing. For the back side contact again Ge/Au/Ni/Au (150/300/140/1500 nm) was deposited. The samples were then installed into an N_2 flow cryostat, where they were analyzed at 78 K.

Figure 1 shows SEM pictures of the processed samples. The left picture illustrates the merging point, where the two 10 µm wide ridges meet and overlap to form a single 10 µm ridge. A cleaved facet of the adjacent coupled ridges is shown on the right hand side. All measurements were operated in pulsed mode with a pulse length of 100 ns at 5 kHz repetition rate.

Results

An infrared MCT detector was mounted on a 2-dimensional driving stage for lateral farfield measurements. On the left Fig. 2 shows a 2D farfield of a GaAs based laser, where a sharp interference pattern is observed in lateral direction. Due to a high level of coherence the data reveal angles of constructive and destructive interference between the two coherent sources. Experimental data were nicely fitted with theoretical values [4], where the propagation of the calculated nearfield was summed for each point of the far screen.

The right hand side of Fig. 2 shows the farfield of an InP based device. InP based samples show reduced coherence. As the wavelength is shorter, the interference pattern shows a qualitatively different behavior. Fitting the results was possible by considering more degrees of freedom than for the GaAs based samples. For GaAs devices, only the fundamental lateral mode in the coupled ridges had to be considered. However, at least the fundamental and the first harmonic mode are present in the InP devices to yield the observed farfield profiles. Additionally, the intensity of each ridge was found out to be slightly different.

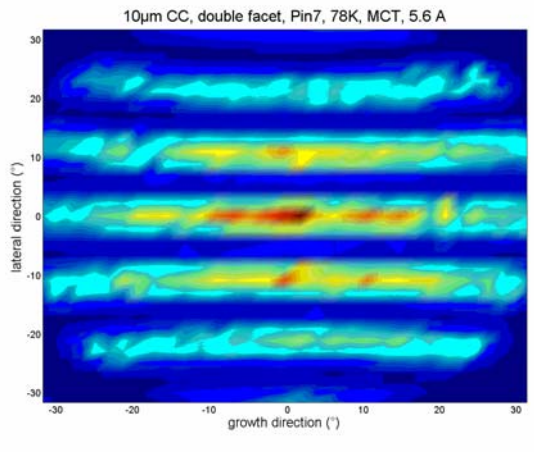

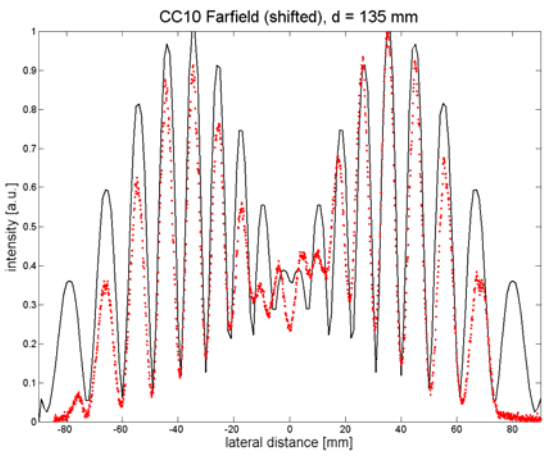

GaAs	InP

Fig. 2: 2-dimensional farfield measurement at the double facet side of a GaAs sample (left) and 1-dimensional farfield data of an InP sample (right) with simulated profile (solid line).

Conclusion

In conclusion, coherent Y-coupled QCLs have been demonstrated for InP/AlGaAs and InP/InGaAs/AlAs/AlInAs materials. Farfield measurements of the GaAs based devices show a sharp interference pattern, which can be theoretically derived. In the InP based coupled cavities, lateral modes of higher order are present in the waveguide, which results in a reduction of coherence observed in the farfields.

References

[1] Faist, F.Capasso *et al.*: 'Quantum cascade laser', Science **264**, 553-556 (1994)

[2] C. Pflügl *et al.*: 'High-temperature performance of GaAs-based bound-to-continuum quantum-cascade laser', Appl. Phys. Lett. **83**, 23 (2003)

[3] M. P. Semtsiv *et al.*: 'Circular-beam cross section quantum-cascade laser' (to be published)

[4] L. K. Hoffmann, C. A. Hurni *et al.* : ‘Coherence in Y-Coupled quantum cascade lasers’ (to be published)

THz Time-Domain Spectroscopy of Surface Plasmon Polaritons on Periodic Metal Arrays

M. Martl[1], J. Darmo[1], K. Unterrainer[1,2], E. Gornik[2,3]

[1] Photonics Institute, Vienna University of Technology, Gusshausstrasse 27-29, 1040 Vienna, Austria

[2] Centre for Micro- and Nanostructures, Vienna University of Technology, Floragasse 7, 1040 Vienna, Austria

[3] Solid-State Electronics Institute, Vienna University of Technology, Floragasse 7, 1040 Vienna, Austria

The coupling of electromagnetic radiation to surface plasmon polaritons (SPPs) by the use of periodic metal arrays is studied. Periodic metal arrays with different structures and distinct dimensions are investigated using a terahertz (THz) time-domain spectroscopy system. Transmission and reflection measurements on such metal arrays were performed. Good correlation between theory and experiment has been observed.

Introduction

The study of electromagnetic radiation interacting with periodic metallic arrays has experienced great interest in recent years [1]. In the case where radiation and pattern parameters are of the same scale the coupling to surface plasmon polaritons (SPP) offers a broad spectrum of research. For example, effects as extraordinary optical transmission [2] and photonic gaps are investigated [3]. Future applications such as optical sources and detectors or optical elements can be improved by these advances.

Coupling to two-dimensional photonic crystals in the terahertz (THz) region has been presented by several groups, showing the existence of SPPs on metals [4] as well as on semiconductors [5]. Mainly transmission measurements were presented while there are only few reflection measurements [6].

There has been work done on propagating SPPs through periodic structures in the visible [7] and more recently in the THz region [8]. To our knowledge, for two-dimensional photonic crystals there has been only research in the visible [9]. In this manuscript we present the study of surface plasmon polaritons on two-dimensional photonic crystals in transmission and reflection measurements by use of terahertz time-domain spectroscopy (THz-TDS).

Surface Plasmons and Their Coupling Techniques

The SPPs are electromagnetic waves coupled to the interface of two media, for example an air/gold interface or an air/semiconductor interface in the THz frequency region. The challenge when coupling to them is to overcome the k-vector mismatch between free propagating radiation and SPP.

Grating coupling uses the effect of scattering at the periodic array. Then, coupled SPP modes are given by

$$k_{SP} = k_0 \pm lk_x \pm mk_y$$

with k_0 the in-plane component of incident wave vector, k_x and k_y the reciprocal lattice vectors and l and m the mode defining integers. By varying the in-plane component k_0 the resonances get shifted, observable in a splitting of resonance frequency. Therefore grating coupling only allows to couple to certain given frequencies.

There are further coupling methods as it is attenuated total reflection (ATR). ATR in the THz region has been reported in [10]. Later, instead of finding ATR-coupling, the coupling by scattering on a prism has been observed [11]. Coupling by use of scattering is also applied at a technique referred as aperture coupling [12]. Further, waveguide coupling has been presented [13].

Results

Sample Fabrication and Measurement Setup

For measurements samples were prepared using standard microfabrication techniques. The metallic grid array has been deposited on highly resistive gallium arsenide plates. This material provides convenient mechanical support for the metal film and almost does not contribute to absorption and to dispersion of terahertz waves. The material used for the metallic grid array has been a 260 nm thick gold film. The SPPs were generated on the gallium-arsenide/gold and on air/gold interface. Different structures such as square, triangular and hexagonal have been prepared. Both, gold patches on GaAs and inverted structures with holes in gold on GaAs were used for measurements.

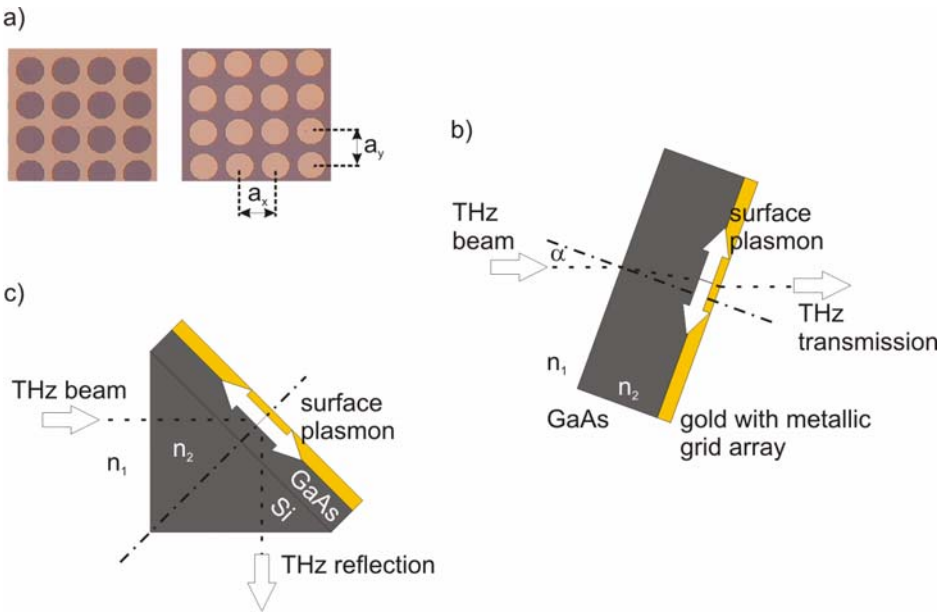

Fig. 1: Measurement Setup: (a) photograph of square samples with gold patches on GaAs and inverted structures with holes in the gold film; (b) transmission measurement configuration for varying angles of incidence; (c) reflection measurement configuration by use of a silicon prism attached to the perforated GaAs slab.

The samples were measured in transmission and reflection measurements using a THz time-domain spectroscopy (THz-TDS) system. An image of a square sample and the principle of transmission and reflection measurement are shown in Fig. 1.

Transmission Measurements

By use of transmission measurements on periodic metal arrays a study of coupling to SPPs has been performed. In transmission measurements a coupling to SPP is observed as an absorption in frequency. As can be seen in Fig. 2(a), the observed resonance frequencies for golden patches correspond to the frequencies calculated by the k-vector-matching condition given above. By tilting the axis a shift of resonance frequencies can be observed due to the increasing in-plane wave vector. Equivalent results could be observed from the inverted structures, i.e. holes in gold.

Reflection Measurements

Reflection measurements at an angle of incidence α=45° on the same samples were supposed to complete the picture of coupling to SPP. Additionally to the expected distinct resonance frequencies a coupling of SPPs to difference frequencies of calculated resonance frequencies for both interfaces, i.e. air/gold and GaAs/gold were observed. This can be seen in Fig. 2(b).

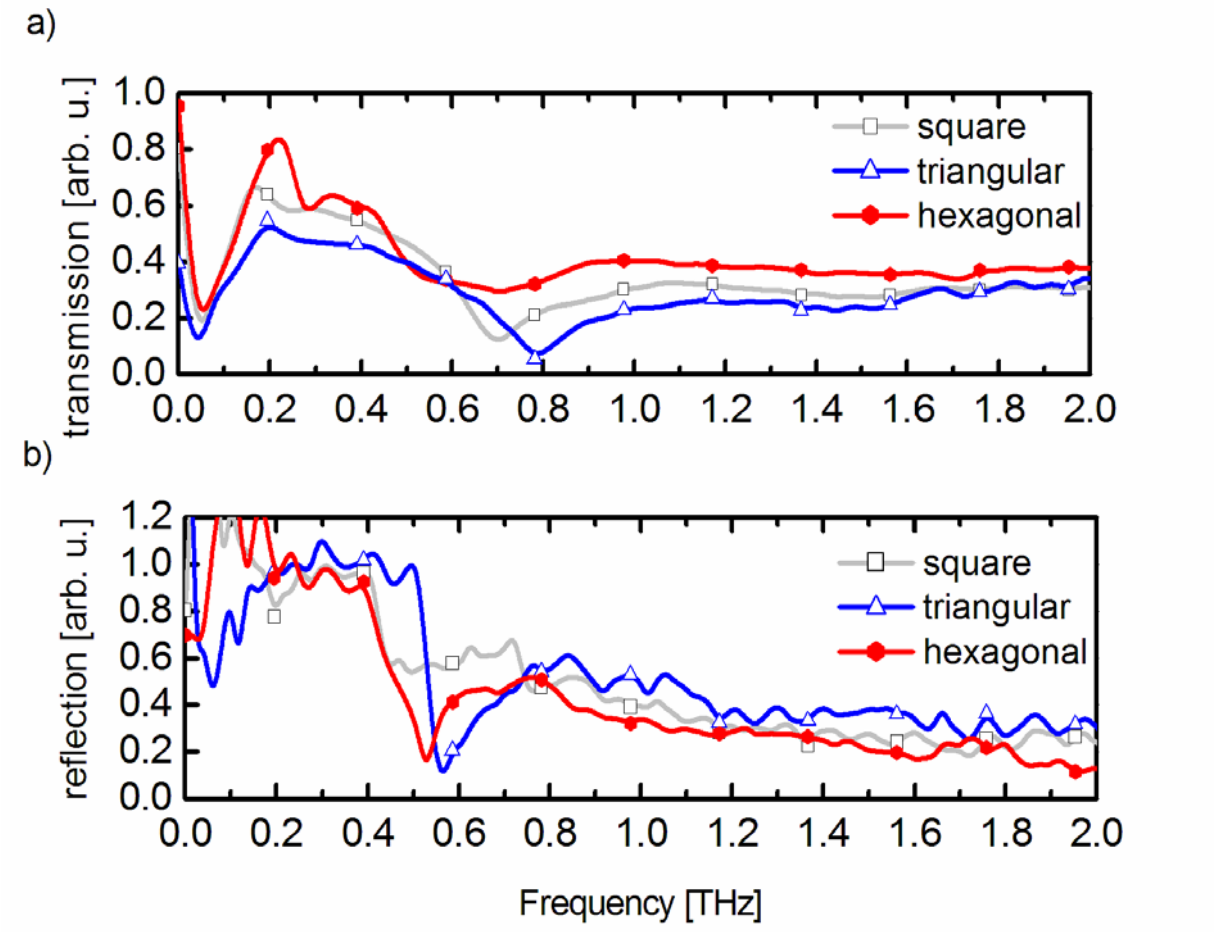

Fig. 2: Transmission at normal incidence (a) and reflection at 45° (b) for samples with golden patches on highly resistive GaAs, ordered in square, triangular and hexagonal structures.

Conclusion

In conclusion we were investigating SPPs using a THz-TDS system. We found good correlation between transmission and reflection measurements mapping the spectral response of SPPs.

References

[1] W. L. Barnes, W. A. Murray, J. Dintinger, E. Deveaux, and T. W. Ebbesen, "Surface Plasmon Polaritons and Their Role in the Enhanced Transmission of Light through Periodic Arrays of Subwavelength Holes in a Metal Film," Phys. Rev. Lett. vol. 92, no. 10, 107401, March 2004.

[3] T. W. Ebbesen, H. J. Lezec, H. F. Ghaemi, T. Thio, and P. A. Wolff, "Extraordinary optical transmission through sub-wavelength hole arrays," Nature, vol. 391, pp. 667-669, Feb. 1998.

[4] W. L. Barnes, T. W. Preist, S. C. Kitson, and J. R. Sambles, "Physical origin of photonic energy gaps in the propagation of surface plasmons on gratings," Phys. Rev. B, vol. 54, no. 9, pp. 6227-6244, 1996.

[5] D. Qu, D. Grischkowsky, and W. Zhang, "Terahertz transmission properties of thin, subwavelength metallic hole arrays," Opt. Lett., vol. 29, no. 8, pp.896-898, 2004.

[6] J. Gómez Rivas, C. Schotsch, P. Haring Bolivar, and H. Kurz, "Enhanced transmission of THz radiation through subwavelength holes," Phys. Rev. B, vol. 68, 201306, Nov. 2003.

[7] J. F. O'Hara, R. D. Averitt, and A. J. Taylor, "Terahertz surface plasmon polariton coupling on metallic gratings," Opt. Expr. vol. 12, issue 25, pp.6397-6402, Dec. 2004.

[8] J.-C. Weeber, J. R. Krenn, A. Dereux, B. Lamprecht, Y. Lacroute, and J. P. Goudonnet, "Near-field observation of surface plasmon polariton propagation on thin metal stripes," Phys. Rev. B, vol. 64, 045411, July 2001.

[9] J. Gómez Rivas, M. Kuttge, P. Haring Bolivar, and H. Kurz, "Propagation of Surface Plasmon Polaritons on Semiconductor Gratings," Phys. Rev. Lett. 93, pp. 256804, Dec. 2004.

[10] J.-Y. Laluet, E. Devaux, C. Genet, T. W. Ebbesen, J.-C. Weeber, and A. Dereux, "Optimization of surface plasmons launching from subwavelength hole arrays: modeling and experiments," Opt. Expr., vol. 15, no. 6, pp. 3488-3495, March 2007.

[11] H. Hirori, K. Yamashita, M. Nagai, and K. Tanaka, "Attenuated total reflection spectroscopy in time domain using terahertz coherent pulses," Jpn. J. Appl. Phys. 43, pp. 1287-1289, 2004.

[12] J. O'Hara, R. Averitt, and A. J. Taylor, "Prism coupling to terahertz surface plasmon polaritons," Opt. Expr., vol. 13, no. 16, pp. 6117-6126, 2005.

[13] J. Saxler, J. Gómez Rivas, C. Janke, H. P. M. Pellemans, P. Haring Bolívar, and H. Kurz, "Time-domain measurements of surface plasmon polaritons in the terahertz frequency range," Phys. Rev. B, vol. 69, 155427, Apr. 2004.

[14] T. Jeon, and D. Grischkowsky, "THz Zenneck surface wave (Thz surface plasmon) propagation on a metal sheet," Appl. Phys. Lett., vol. 88, 061113, Feb. 2006.

Time Domain Spectroscopy of Mid Infrared Quantum Cascade Lasers

W. Parz[1], T. Müller[1], M. Austerer[3], G. Strasser[2], K. Unterrainer[1,3], L. R. Wilson[4], J. W. Cockburn[4], A. B. Krysa[5], J. S. Roberts[5]

[1]Institute of Photonics, Vienna University of Technology, Gußhausstraße 27-29, 1040 Vienna, Austria

[2]Institute of Solid State Electronics, Vienna University of Technology, Floragasse 7, 1040 Vienna, Austria

[3]Centre for Micro & Nano Structures, Vienna University of Technology, Floragasse 7, 1040 Vienna, Austria

[4]Department of Physics and Astronomie, University of Sheffield, Hounsfield Road, Sheffield, S3 7RH, UK

[5]EPSRC National Centre for III-V Technologies, University of Sheffield, Mappin Street, Sheffield, S1 3JD, UK

Time domain spectroscopy measurements on quantum cascade mid-infrared laser structures are performed. From these measurements we deduce parameters like wavelength depending losses, modal gain or the gain bandwidth in the spectral domain. Parameters like group refractive index or dispersion can be inferred in the time domain. We also observe thermo optic effects.

Introduction

Mid infrared quantum cascade lasers (QCLs) have been under investigation since their invention in 1994 with the aim of increasing their overall performance [1] – [3]. For a deeper understanding of the underlying physics standard device characterization like voltage, current and output power measurements are mostly not sufficient. Quantum Cascade Laser are physical systems composed of a very complex matter structure together with high light field intensities and very high current densities. First results of the dynamics below threshold where observed by Eickemeyer *et al.*. He deduced the gain coefficient in an electrically pumped quantum cascade structure without resonator by measuring the transmission change of a tunable mid-infrared light source [4]. Later, light of a thermal source was coupled directly through the waveguide of a mid-infrared QCL showing broadband data of gain and losses under current bias close to threshold [5]. The scheme of incoherent detection hinders the exploration of operating conditions above threshold because of detector saturation due to the emitting laser light.

Electro Optic Sampling

Instead of a thermal source we use broadband mid-infrared pulses generated by phase matched difference frequency mixing in a 30 µm thick GaSe crystal. This allows us to detect the transmitted light by coherent detection facilitating the electro optic effect in a 7 µm thick ZnTe crystal. The setup we are using is shown in Fig. 1(a). This has the great advantage that the detection is invariant to the strong light fields of the QCL above threshold. With this technique we are able to achieve a time resolution of 12 fs

which allows us detection of frequencies up to 45 THz directly in the time domain. Spectroscopy is done by Fourier transformation of the time domain signal which has the advantage of conserving the phase information besides the amplitude spectrum. As can be seen in Fig. 1(b) the signal to noise ratio is 1000 for the electric field which corresponds to a SNR of 10^6 for the corresponding power.

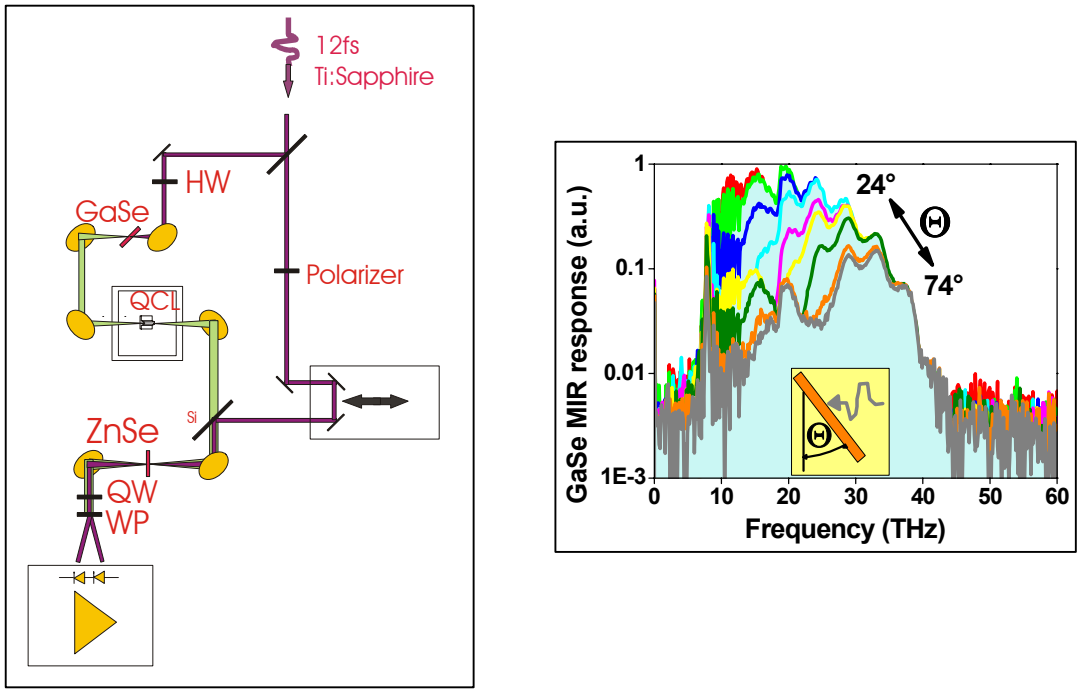

(a) (b)

Fig. 1: (a) Sketch of the electro optic sampling setup we are facilitating for measurements on quantum cascade structures; (b) shows the accessible frequency range depending on the phase matching condition

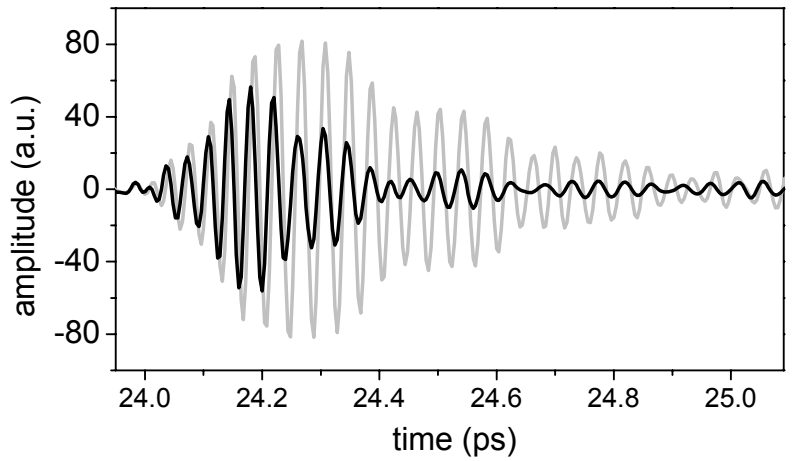

Fig. 2: Pulse response of a mid-infrared pulse coupled through the waveguide of the cold resonator (black), and through the resonator at lasing threshold in cw - operation (grey).

Experimental

For our first studies we used an InGaAs/AlInAs/InP quantum cascade laser cleaved into 495 µm long and 21 – 23 µm broad ridges emitting at 25.5 THz. The laser was mounted on the cold finger of a continuous helium flow cryostat in a way that we can access both facets with a beam of 45° divergence. Figure 2 shows the time response of a broadband 100 fs long pulse coupled through the cavity of the QCL. We clearly see the long lasting oscillations in the case of a bias current at lasing threshold (grey) compared to the response of the cold resonator (black). This corresponds to an enhancement due to gain. The phase shift between these two signals is attributed to the change of refractive index due to heating inside the cavity under cw-operation and to the phase shift according to induced gain. The effect of change in refractive index due to changing carrier concentration is much smaller in this case.

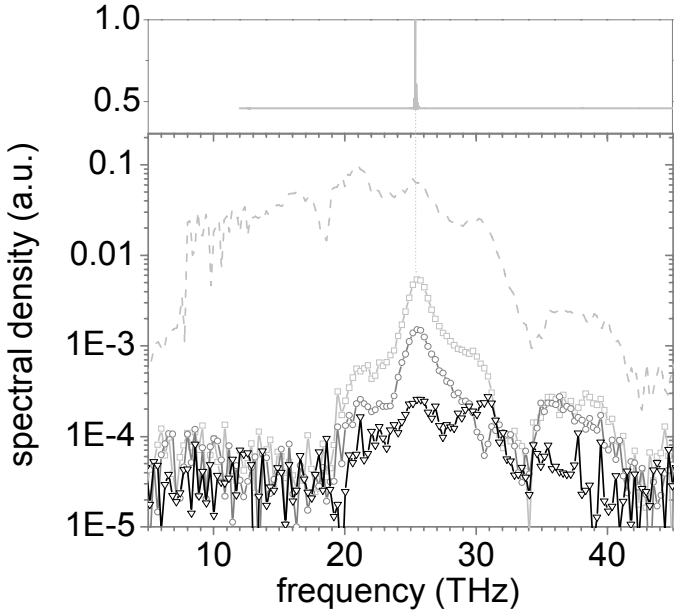

Fig. 3: The lower graph shows the spectral response of the pulse passing through the resonator under conditions of 1% threshold current density (black), 57% (grey), and 120% (light grey). The dashed curve corresponds to the spectrum of the initial mid-infrared pulse. The upper graph shows the emission spectra of the QCL at 110% of the threshold current density.

In the frequency domain shown in Fig. 3 we can see three curves corresponding to the spectral response at bias currents of 1%, 57%, and 120% of the threshold current density.

The cut off at 19 THz is attributed to the cut off of the lowest TM mode in the resonator due to the surface plasmon confining the light inside the cavity. With increasing current density a peak around 25.5 THz is forming reaching its maximum height and staying constant above threshold current density. The gain peaks at the same frequency where emission takes place. We note that this laser emits in multiple Fabry-Perot modes. This might be a reason why we do not observe any sings of spectral-hole burning at the emission frequency which we would expect from inhomogeneous broadening.

The gain bandwidth is 1.75 THz. Above the cut off frequency a broadband replica of the initial spectral pulse shape overlaps the gain peak, which is an artifact due to the phase shift caused by heating. The difference in transmission between the operation at

zero bias current and at threshold current at the emission frequency leads to a modal gain of 9.04 dB or 42 cm^{-1}. Using a reflectivity of 0.3 we deduct the waveguide losses to 17.7 cm^{-1}, which is in good agreement with the number of 17.1 cm^{-1}, deducted from the threshold current densities of different resonator lengths. The calculated value for this waveguide with a Drude absorption model leads to 16.4 cm^{-1}.

Conclusion

In conclusion we showed feedback of spectrally resolved broadband parameters like gain, waveguide- and mirror losses, over the whole range of operating conditions, together with additional time domain information we can provide essential information to characterize and to understanding the physics in a quantum cascade structure.

Acknowledgements

We acknowledge the financial support from FWF SFB ADLIS.

References

[1] J. Faist, F. Capasso, D. L. Sivco, C. Sirtori, A. L. Hutchinson, and A. Y. Cho: “Quantum Cascade Laser”, Science 264, 553 (1994)

[2] M. Beck, D. Hofstetter, T. Aellen, J. Faist, U. Oesterle, M. Ilegems, E. Gini, and H. Melchior: “Continuous Wave Operation of a Mid-Infrared Semiconductor Laser at Room Temperature”, Science 295, 301 (2002)

[3] M. Troccoli, S. Corzine, D. Bour, J. Zhu, O. Assayag, L. Diehl, B. G. Lee, G. Höfler, and F. Capasso: ” Room temperature continuous-wave operation of quantum-cascade lasers grown by metal organic vapour phase epitaxy”, Electron. Lett. 41, 1059 (2005).

[4] F. Eickemeyer, R. A. Kaindl, M. Woerner, and T. Elsaesser, “Large electrically induced transmission changes of GaAs/AlGaAs quantum-cascade structures”, APL 76, 3254 (2000)

[5] D.G. Revin, L. R. Wilson, J.W. Cockburn, A.B. Krya, J.S. Roberts and R.J Airey, “ Intersubband spectroscopy of quantum cascade lasers under operating conditions”, APL 88, 131105 (2006)

Far Field Investigations on Quantum Cascade Lasers

S. Schartner, M. Austerer, M. Nobile, S. Golka A. M. Andrews, W. Schrenk, G. Strasser

Zentrum für Mikro- und Nanostrukturen, TU Wien, Floragasse 7, A-1040 Wien

Introduction

Quantum cascade lasers (QCLs) are unipolar semiconductor lasers operating in the mid infrared region. Their emitted wavelength is defined by the separation of intersubband levels which can be tailored by band structure engineering. Due to the fact that the maximum conduction band offset in the GaAs/AlGaAs material system is 380 meV, the lowest directly accessible wavelength is roughly 7 µm. One way to reach lower wavelengths is to use intracavity nonlinearities. With sum frequency (SF) generation or second harmonic (SH) generation respectively it is possible to cover the spectroscopically important band between 3.5 µm and 7 µm. Unlike conventional interband semiconductor lasers QCLs do not suffer from the problem of strong absorption of the frequency doubled light because the emission energies (100 – 300 meV) are well below the band gap of the hosting GaAs (E_{Gap} = 1.4 eV).

Although GaAs has a nonzero second-order susceptibility, there is no resulting second-order polarization for standard QCLs. This is due to the selection rules for intersubband transitions which allow gain only for TM polarized light, which in turn due to crystal symmetry together with the typical <100> growth direction cannot excite nonlinear polarization in the host material. However it was shown that QCLs grown on <111> substrates show sum-frequency generation due to bulk nonlinearity [1]. In our approach we instead use active region designs that include a nonlinear cascade [2], [3]. These artificial nonlinear susceptibilities can reach values comparable to those for the bulk material. The principle of nonlinear light generation in QCLs was actually firstly demonstrated using this intersubband approach in 2003 with the InP material system [4].

Another very interesting topic is intracavity difference-frequency generation in QCLs. It could eventually be used to generate coherent THz radiation in a semiconductor laser at room temperature. Recently THz sideband generation from a THz QCL and a near-infrared diode laser has been shown [5].

An important issue with intracavity SH generation is the optimization of the waveguide for both fundamental and SH frequencies. We show how a double AlGaAs waveguide helps to improve the conversion efficiency compared to a conventional double-plasmon waveguide as used in GaAs based QCLs. We present farfield measurements of the fundamental laser mode and the SH emission that will help investigating modal phase-matching conditions.

Waveguide Design

The nonlinear susceptibility itself is optimized by means of band structure engineering. The external linear to nonlinear conversion efficiency however depends additionally on the waveguide used. Issues like losses, modal overlap and phase-matching have to be

considered. Originally the nonlinear active regions were all embedded in a symmetric double-plasmon waveguide that consists of a low-doped core region (GaAs, n_{Si} = $3x10^{16}$ cm^{-3}) and highly-doped cladding layers (GaAs, n_{Si} = $4x10^{18}$ cm^{-3}) (compare Fig. 1(a)). This waveguide is optimized for fundamental laser action using the dramatic drop in refractive index near the plasma frequency for confinement. However, the strong dispersion near the plasma frequency cannot provide satisfactory confinement for the fundamental and SH radiation at the same time. Figure 1(b) is illustrating this fact: a doping level leading to a refractive index sufficient to confine the fundamental mode does not yield in a sufficiently low refractive index for the SH mode. The calculated refractive index for the ~ 5 µm light in the active region is 3.24, whereas it is only 3.14 in the cladding layers. This results in low confinement of the frequency doubled light. Hence, the losses are high, the overlap to the active region is poor and so is the overlap with the fundamental mode. Additionally the refractive indices of the fundamental and the SH light differ strongly and phase-matching cannot be achieved using this kind of waveguide.

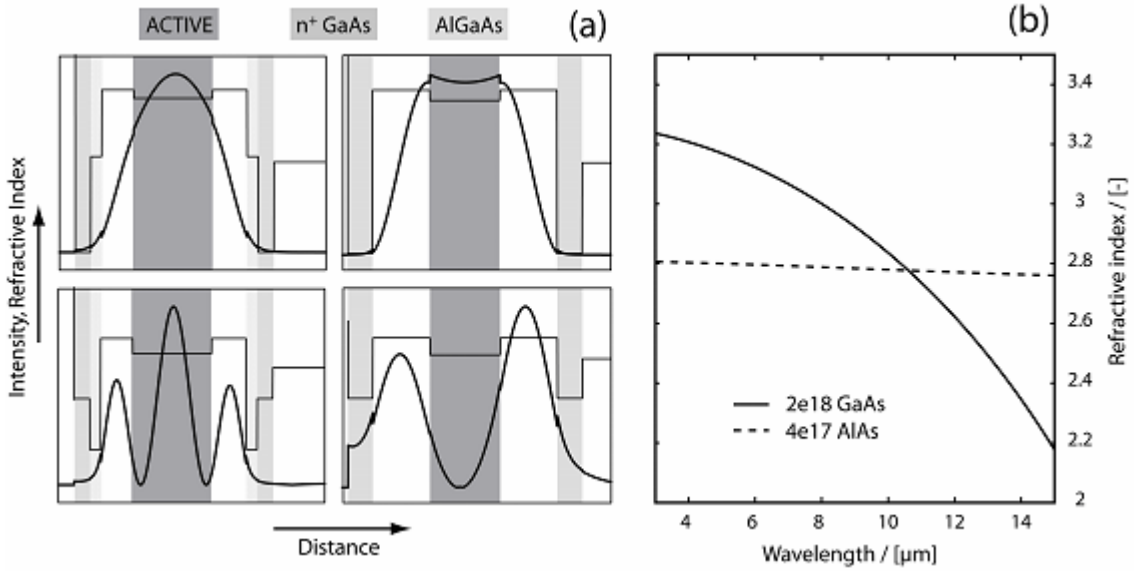

Fig. 1: (a) Mode profiles of the fundamental (upper) and SH (lower) and the line up of the real part of the refractive index are shown for a double-plasmon (right) and a double-AlGaAs (left) waveguide. The combination of a medium doped AlGaAs and a highly doped GaAs layer provides good confinement for both frequencies. (b) The real part of the refractive index calculated with the Drude model for n^+ GaAs and n AlAs.

A waveguide design which substitutes part of the plasmonic cladding with highly Al containing layers can help with these problems. As shown in Fig. 1(a) the fundamental mode is still confined by the thinner n^+ GaAs layer but with support from the AlGaAs spacers. This can even decrease the losses due to the reduced free carrier absorption. However, for the SH mode the AlGaAs actually plays the role of a cladding layer.

Two devices were grown and processed to Fabry-Perot lasers. A bound-to-continuum active region design was embedded in a double $Al_{0.9}Ga_{0.1}As$ waveguide ($n_{(5µm)}$ = 2.86). The layer sequences are 0.3 µm GaAs (n_{Si} = $4x10^{18}$ cm^{-3}), 0.7 µm $Al_{0.9}Ga_{0.1}As$ (n_S = $2.4x10^{17}$ cm^{-3}), 2 µm GaAs (n_{Si} = $4x10^{16}$ cm^{-3}), 60 cascades of bound-to-continuum active cells, 2.2 µm GaAs (n_{Si} = $4x10^{16}$ cm^{-3}), 0.7 µm $Al_{0.9}Ga_{0.1}As$ (n_{Si} = $2.4x10^{17}$ cm^{-3}), 1 µm GaAs (n_{Si} = $4x10^{18}$ cm^{-3}) and n-type GaAs substrate. For this structure we calculate refractive effective indices of 3.185 (fundamental, TM_{00}) and 3.181 (nonlinear light,

TM_{02}). This was calculated for an infinitely wide laser ridge. Using a SiN_x insulation and gold at the side walls, a ridge width dependent fine tuning of the refractive index is possible and phase matching is calculated to occur for laser ridges around 25 µm thickness. This structure further strongly increases the confinement factor, especially for the nonlinear light, where it is increased from 17% to 65%. Besides the improvement in confinement, this waveguide also enhances the overlap of fundamental and nonlinear light.

Results

Depending on the ridge width we were able to increase the conversion efficiency from approximately 15 to 100 µW/W^2 and achieve nonlinear peak powers exceeding 100 µW. This improved performance is due to a higher confinement and lower losses for the SH light. According to our calculations the overall refractive index difference between the fundamental and SH is also reduced, and it might be possible to achieve modal phase matching in such a waveguide. As shown in Fig. 2 we observe a maximum conversion efficiency of 120 µW/W² for 30 µm wide devices.

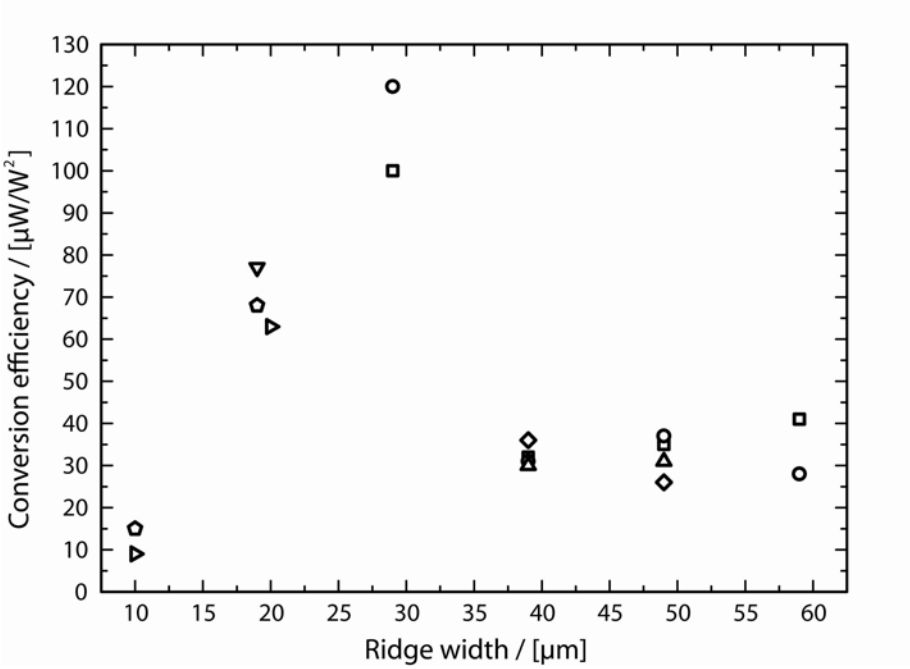

Fig. 2: Conversion efficiencies for lasers of different ridge widths. The conversion efficiency increases starting from thin ridges and falls again after it reaches a maximum around 30 µm. Modal phase matching is calculated to occur for 25 µm wide laser cavities.

To investigate the mode profiles in the laser waveguide we were analyzing their farfields. Fig. 3(a) shows a typical farfield profile of a TM_{00} mode which we observed up to ridge widths of 60 µm for the fundamental light. We attribute this to the lossy SiN_x insulation layer which suppresses higher-order lateral modes. This in turn is not the case for the SH radiation as the waveguide dimensions are roughly scaled by a factor of two, and the SiN_x losses are lower. The two-fold pattern of the SH farfield (Fig. 3(b)) in lateral direction can therefore be explained by a higher-order lateral mode. In growth direction the farfield is split in three lobes of comparable intensity. This pattern cannot be

explained by solely one TM_{02} mode, but rather suggests a superposition of at least two modes (TM_{00} and TM_{02}).

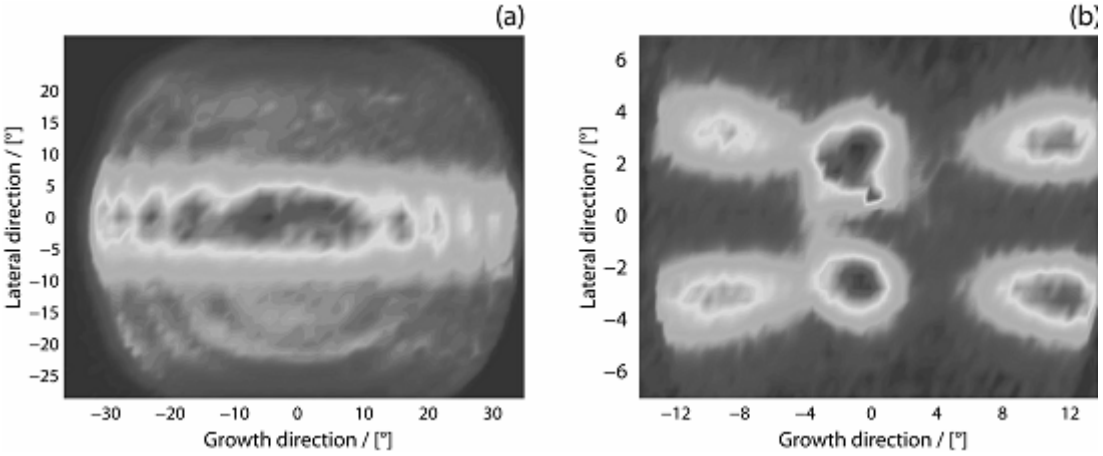

Fig. 3: Farfield profiles of the fundamental (a) and SH (b) modes for a 40 µm wide Fabry-Perot device with double AlGaAs waveguide. The plots were recorded at distances of 100 mm and 50 mm respectively.

Conclusion

We have shown that second-harmonic and sum-frequency emission in GaAs based QCLs grown on <100> substrates can be significantly enhanced with a double AlGaAs waveguide. In order to fully exploit the nonlinear properties of GaAs based QCL structures, appropriate waveguide designs that enable phase matching have to be developed. To reach this goal we performed farfield measurements that allow us insight into the SH modal behavior. Future goals include further enhancement of SH generation and the demonstration of difference-frequency generation.

References

[1] J.-Y. Bengloan et al., Appl. Phys. Lett. 84, 2019 (2004)

[2] C. Pflügl et al., Electron. Lett. 41, 1331 (2005)

[3] C. Pflügl et al., Appl. Phys. B 85, 231 (2006)

[4] N. Owschimikow et al., Phys. Rev. Lett. 90, 043902 (2003)

[5] S.S. Dhillon et al., Appl. Phys. Lett 87, 071101 (2005)

Force and Bias Dependent Contrast in Atomic Force Microscopy Based Photocurrent Imaging on GaAs-AlAs Heterostructures

W. Brezna, G. Strasser, J. Smoliner

**Institut für Festkörperelektronik, TU Wien,
Floragasse 7, A-1040 Wien, Austria**

In this work, photocurrent images of lithographically processed GaAs/AlAs heterostructures are recorded by an atomic force microscope. It is found that the AFM tip-sample contact is strongly dependent on the thickness of the native oxide layer on the sample surface. Therefore the photocurrents increase if a successively increasing tip-sample force is applied, which leads to a gradual penetration of the surface oxide layer. Due to the complex behavior of the photocurrent as a function of tip-bias and tip-force, the contrast in photocurrent images is non-monotonic and can be reversed under appropriate bias and force conditions.

Introduction

Photocurrent spectroscopy is a very versatile tool to investigate a wide range of effects in solids. The fact that electric currents can easily be measured down to the fA regime and the possibility to use very high power light sources to excite the sample leads to an exceptional high sensitivity. Due to this high sensitivity, one can even gain information about optically “forbidden” transitions [1] – [3]. Photocurrent spectroscopy applications range from investigations of interband [3], intraband, intersubband [4], [5] and intrasubband [6] transitions in heterostructures and quantum dot systems [7] – [9] to investigations of organic films [10], organic devices [11] and the analysis of dielectric materials [12]. Some efforts have been made to increase the spatial resolution of photocurrent measurements by either using shadow masks to define the illuminated sample areas [13] or by using a carefully focused and collimated beam of light [14]. One can also find some scanning near field optical microscopy (SNOM) approaches to increase the spatial resolution into the nm-regime [15].

For the characterization of materials in the nanometer regime, Scanning Probe Microscopy (SPM) based methods are the prime choice beside Scanning Electron Microscopy and Transmission Electron Microscopy. Spatially resolved optical absorption measurements have already been performed with a scanning tunneling microscope (STM) to investigate the influence of the laser irradiation on the differential conductance on an InAs covered GaAs sample surface [16]. Other groups where using the STM tip as a local Schottky contact to perform photocurrent measurements [17]. Only recently conductive Atomic Force Microscopy (cAFM) was applied to study InAs wires on GaAs [18]. However, these investigations were all performed either at low temperatures and / or under high vacuum conditions. Although this is leading to much more idealized experimental conditions, the experiments are much more demanding and time consuming.

In this work we present Atomic Force Microscopy (AFM) based photocurrent imaging experiments, which were performed under ambient conditions. We want to investigate

the details of the photocurrent contrast generation on a lithographically patterned GaAs-AlAs reference sample, e.g. how the locally collected photocurrent depends on the applied tip sample voltage and tip sample contact force beside the obvious local variations of the sample. For the AFM based photocurrent experiments the AFM feedback laser was chosen as a light source and the photocurrent is collected locally via the electrically conducting tip of an AFM.

Experimental

Figure 1 shows the assumed band profile of the AFM-tip–sample system used for photocurrent imaging under zero bias. The sample has a photodiode design as it is frequently used for the investigation of InAs quantum dots [19]. The sample consists of n+-GaAs followed by an intrinsic layer of GaAs for charge separation. On top of the intrinsic region a 10 nm AlAs barrier layer was grown and a cap layer of 10 nm GaAs was introduced to avoid oxidation. For plotting the band diagram in Fig. 1, we assumed the Fermi level at the GaAs surface to be pinned at a position near midgap about 0.6 eV to 0.8 eV lower than the conduction band edge of GaAs [20], [21].

Standard photolithography was used to remove the GaAs cap layer and the AlAs barrier on one part of the sample to define sample regions with properties. The sample structuring was done by applying selective etch solutions to remove the GaAs cap layer selective to AlAs (citric acid : H_2O_2 = 2.4 mol/l : 1 mol/l for 20s). In a second etching step, the AlAs was removed selectively to GaAs using 0.02 mol/l NaOH for 9 minutes.

To guarantee good electrical contact, InSn pellets were diffused into the sample surface at 450 °C for 5 minutes. Conductive silver was used to contact the InSn pellets on the sample surface and to glue the sample on a gold covered nickel sample plate. A gold wire was then used between the sample plate and the magnetic plate holder of the AFM to ensure a reliable electrical contact.

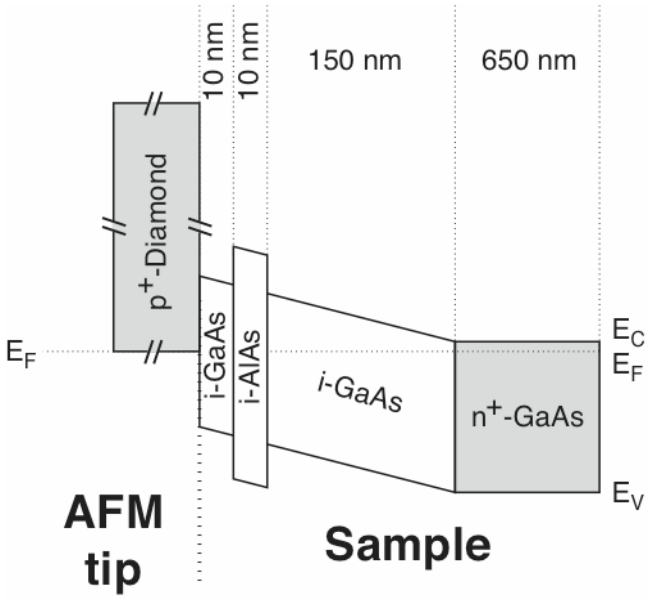

Fig. 1: Band profile of the AFM-tip–sample system under zero bias condition and ideal AFM-tip–sample contact (layer thickness not to scale). The intrinsic substrate is omitted. E_F is the Fermi level, E_C and E_V mark the conduction and valence band edges.

The AFM used in this work was a Molecular Imaging, PicoPlus system with closed loop scanner and PicoScan 3000 controller. The photocurrent measurements were performed using the built-in current-voltage preamplifier with an amplification of 10^8 V/A. The preamplifier was located in direct vicinity to the tip to minimize parasitic wire capacitance and to ensure the bandwidth of approximately 300 Hz in the fA – nA regime required for photocurrent imaging applications. As AFM tips we used highly doped (p-type 1×10^{20} cm^{-3}) conductive diamond tips (NanoWorld) which show superior resistance against abrasion. The tips' high spring constant of 40 N/m (as it is normally used for scanning spreading resistance measurements) ensures a good electrical contact to the sample, but care must be taken not to scratch the sample surface by using too high forces. As light source, the AFM feedback laser (1mW @ 670nm) was used in the present experiments. The laser diameter was approximately 60 µm leading to a nominal laser intensity of 28 W/cm^2. Note that the actual laser intensity hitting the investigated sample spot will be lower, due to shadowing effects caused by the AFM tip.

Measurements

Figure 2(a) shows a topographic AFM image of the sample after removing the AlAs barrier on one part of the sample by using photolithography. The non-etched area is labeled A and the area where the 10 nm GaAs cap-layer and the 10 nm AlAs barrier were removed is labeled with B. The measured edge height was 24 nm, which agrees quite well with the nominal 20 nm thickness of these layers.

Figure 2(b) shows two current vs. voltage (IV) curves recorded on areas A and B without any incident light (complete darkness). During the measurement, the AFM camera illumination as well as the AFM feedback laser was switched off and the AFM system was shielded from ambient light. The sweep duration for a single IV curve was only 5s, therefore the frozen AFM feedback during that time led to no issues concerning tip drifts or changes in contact force. Due to the AlAs barrier present in area A, the forward current onset occurs at higher bias values than in area B. In the reverse biased range between 0 V and –2 V no significant dark current could be detected both in area A as well as in area B.

Figure 2(c) shows typical IV spectra recorded under illumination. Under illumination, a distinct photocurrent under reverse bias is observed in areas A and B. The voltage dependence of the photocurrent, however, differs significantly in both areas.

The photocurrent in area B first shows a strong increase with reverse bias. At higher reverse voltages, however, the photocurrent saturates. This behavior can be attributed to the fact that ideally, the photocurrent is only limited by the carrier generation rate, which is proportional to the incident light power. In contrast to that, however, the reverse current in area A shows an *exponential* increase with the reverse voltage. In addition, the current in area A is lower than in area B at low applied reverse bias values, which is most likely due to the influence of the AlAs blocking layer. At higher reverse voltage, however, the current in area A even exceeds the current in area B although the power of the incident light is the same. A possible explanation for this astonishing fact can be found in a publication by Capasso *et al.* [22], who showed that the electron impact ionization and the corresponding carrier multiplication factor in a AlGaAs/GaAs heterostructure is strongly enhanced. If we also assume an enhancement of avalanche carrier generation in area A, this would explain both that the current in area A exceeds the saturation current in area B (due to avalanche generation) and the exponential current characteristics in A (due to the exponential increase of the multiplication factor with voltage).

The photocurrent vs. voltage measurements were also performed for 3 different tip–sample forces (0.17 µN, 0.5 µN and 3.3 µN). As one can see in Figure 2(c), an in-

crease in force leads to an increase of the photocurrent in both areas A and B. It must be pointed out that the increase of force has a much larger effect on the photocurrent in area A than in area B. Obviously, this behavior must be related to the presence of the AlAs layer in this area.

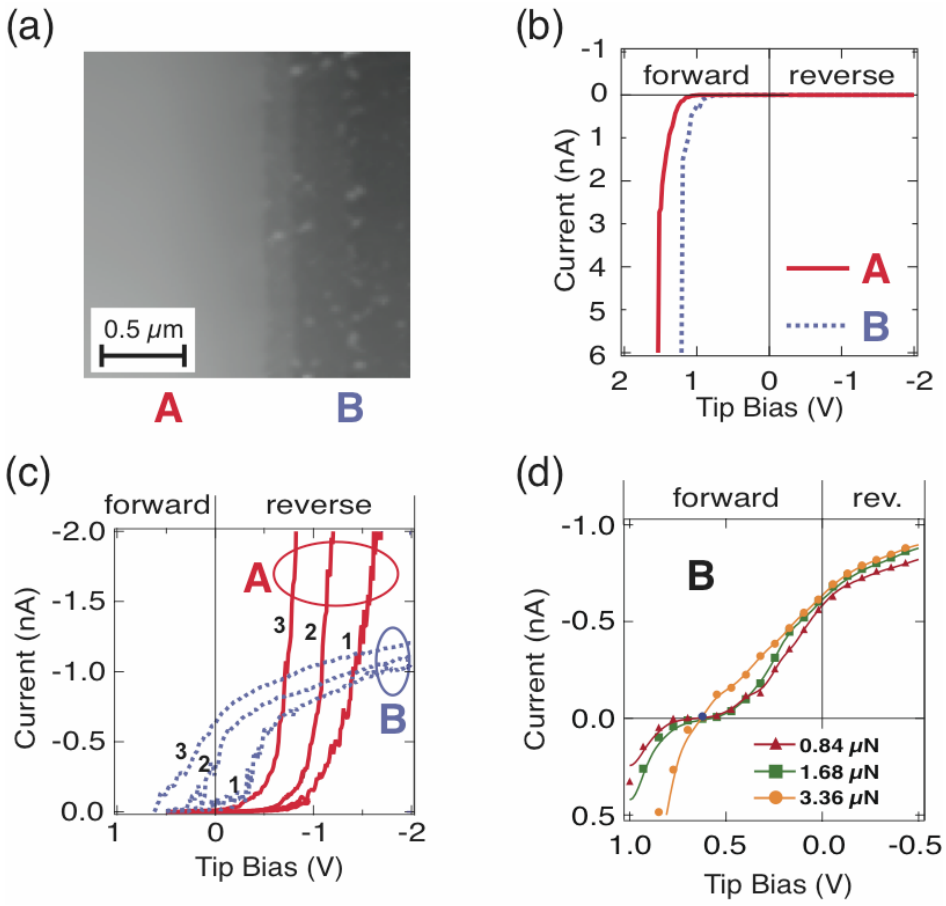

Fig. 2: (a) Topographic AFM image of the sample after etching away the AlAs barrier and GaAs cap layer on part B of the sample. (b) I-V characteristics of area A (straight line) and area B (dotted line) without illumination at tip sample force of 0.17 μN. (c) I-V characteristics of area A (straight lines) and area B (dotted lines) under illumination (1mW @ 670nm) and at different applied tip sample forces (curves (1): 0.17 μN, (2): 0.5 μN and (3): 3.3 μN). (d) I-V characteristic of area B under illumination at different applied tip forces for different voltage and current ranges.

As an explanation for the tip force dependence of the IV curves, we assume the existence of a layer of native oxide on the sample surface. Under the ambient conditions where the measurements were performed, all samples are usually covered with such a thin layer of native oxide. Even after the routinely applied HCl dips to remove the oxide layer from the GaAs sample, only a few minutes under ambient air conditions again lead to the formation of a significant amount of native oxide on the sample surface. This oxide layer acts as an additional barrier for the photo generated carriers, which can be overcome by applying higher negative tip bias values. Another possibility to overcome the barrier is to successively penetrate the native oxide by increasing the tip force, which successively decreases the thickness of the oxide barrier. The consequences of this procedure are illustrated in Fig. 2(c), where a set of force dependent IV-curves are shown.

At a low force of 0.17 µN (figure 2 (c), curve 1, area B) a significant photocurrent only occurs below -0.3 V. At higher forces of 0.5 µN (curve 2) and 3.3 µN (curve 3), the onset of the photocurrent in area B is shifted to the left by the reduced oxide barrier thickness. In contrast to that, the voltage required for zero current flow (the open circuit voltage V_{oc}) does *not* change with increasing force. This can be seen in Fig. 2(d), where the force dependent IV curves clearly intersect at the same tip voltage position of $V_{tip} = V_{oc} = +0.62$ V for all tip forces in the shown range.

The oxide layer does also influence the electrical behavior above V_{oc} (forward biased region). Here the oxide layer acts as an additional energetic barrier in series to the Schottky barrier which becomes thinner with increasing tip force. As a consequence, the forward current increases with tip force, and the observed characteristic approaches the well known IV characteristic of solar cells for higher tip forces.

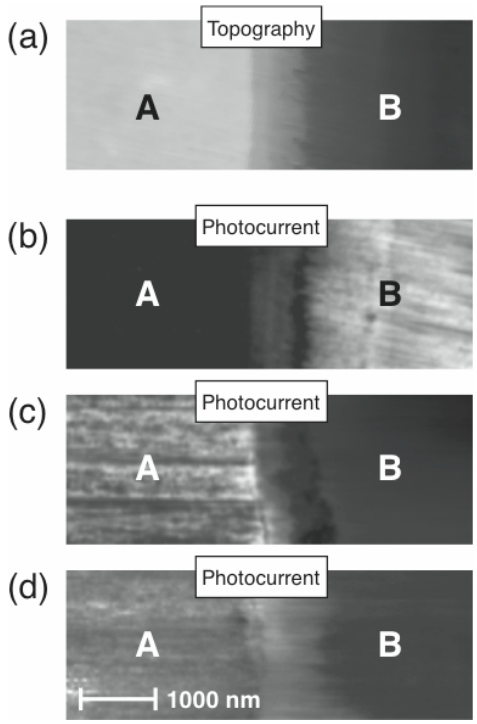

Fig. 3: (a) Topographic AFM image of the sample. (b) – (d): Corresponding photocurrent images recorded for different voltage and force value combinations. (b): low voltage, low force (–0.8 V, 0.17 µN), (c): high voltage, low force (–1.8 V, 0.17 µN), (d) low voltage, high force (–0.8 V, 3.3 µN).

The photocurrent's complex dependence on the applied bias and on the applied tip sample force has a severe impact on the contrast in photocurrent imaging. Figure 3 (a) again shows the topographic AFM image of the etch step on the sample surface together with the simultaneously recorded photocurrent data for different applied bias voltages and tip sample forces (Fig. 3(b) – (d)). As light source for the photocurrent imaging again the AFM feedback laser was used. For a low applied reverse voltage and force (–0.8 V, 0.17 µN see Fig. 3(b)) one can see good photocurrent contrast between area A and area B. However, increasing the applied (reverse) bias voltage leads to a complete contrast reversal in Fig. 3(c), where an image recorded at *high* reverse voltage and low force (–1.8 V, 0.17 µN) is shown. Leaving the applied voltage at low values but increasing the tip sample force also leads to a photocurrent contrast reversal, which can seen in Fig. 3(d). These imaging results are in good agreement with the discussion of the plot displayed in Fig. 2(c).

Summary

In summary, we have shown that photocurrents measured by AFM techniques are highly dependent on the applied bias voltage and tip sample force. The force dependence of the electrical tip-sample contact was explained by the presence of a native oxide layer on the sample. The AFM tip can successively penetrate this oxide layer with increasing applied tip force which gives rise to an increasing photocurrent. The photocurrent contrast turned out to be non monotonic. Depending on the force and the tip bias, complete contrast reversal can be obtained. Finally, the photocurrent in areas where the AlAs barrier was present showed an exponential increase as a function of reverse bias, which can be related to electron avalanche multiplication in AlAs/GaAs heterostructures. These findings demonstrate the importance of well defined experimental parameters, especially tip-sample force and tip-sample bias, for reproducible photocurrent measurements with an AFM.

Acknowledgements

This work was sponsored by FWF project SFB-025 TP08.

References

[1] R.T. Collins, L.Viña, W. I. Wang, L.L. Chang, L. Esaki, K.v.Klitzing, K. Ploog, Phys. Rev. B 36, Vol. 3, 1531 (1987)

[2] K. Yamanaka, T. Kukunaga, N. Tsukada, K. L. I. Kobayashi, M. Ishii, Appl. Phys. Lett. 48, 840 (1986)

[3] K. Tanaka, N. Kotera, H. Nakamura, J. Appl. Phys. 85 (8), 4071-4075 (1999)

[4] R. P. Leavitt, J. W. Little, Appl. Phys. Lett. 79, 2091 (2001)

[5] X. L. Huang, Y. G. Shin, E. K. Suh, H. J. Lee, Y. G. Hwang, Q. Huang, J. Appl. Phys. 82, 4394 (1997)

[6] R. J. Stone, J. G. Michels, S. L. Wong, C. T. Foxon, R. J. Nicholas, A. M. Fox, Appl. Phys. Lett. 69, 3569 (1996)

[7] L. Chu, A. Zrenner, G. Böhm, G. Abstreiter, Appl. Phys. Lett. 76(14), 1944 (2000)

[8] S. Sauvage, P. Boucaud, T. Brunhes, V. Immer, E. Finkman, J. M. Gérard, Appl. Phys. Lett. 78, 2327 (2001)

[9] L. Höglund, C. Asplund, Q. Wang, S. Almqvist, H. Malm, E. Petrini, J. Y. Andersson, P. O. Holtz, H. Pettersson, Appl. Phys. Lett. 88, 213510 (2006)

[10] C. L. Yang, Z. K. Tang, W. K. Ge, J. N. Wang, Z. L. Zhang, X. Y. Jian, Appl. Phys. Lett. 83(9), 1737 (2003)

[11] M. Breban, D. B. Romero, S. Mezhenny, V. W. Ballarotto, E. D. Williams, Appl. Phys. Lett. 87, 203503 (2005)

[12] V. J. Kapoor, F. J. Feigl, S. R. Butler, Phys. Rev. Lett. 39, 1219 (1977)

[13] G. Fasching, F. F. Schrey, W. Brezna, J. Smoliner, G. Strasser, K. Unterrainer, Phys. Stat. Sol. C 2(8), 3114 (2005)

[14] A. V. Andrianov, S. R. A. Dods, J. Morgan, J. W. Orton, T. M. Benson, I. Harrison, E.C. Larkins, F.X.Daiminger, E.Vassilakis, J.P.Hirtz, J. Appl. Phys. 87(7), 3227 (2000)

[15] A. Richter, J. W. Tomm, Ch. Lienau, J. Luft, Appl. Phys. Lett. 69(26), 3981 (1996)

[16] T. Takahashi, M. Yoshita, I. Kamiya, H. Sakaki; Appl. Phys. A 66, S1055 (1998)

[17] E. Beham, A. Zrenner, G. Böhm; Physica E 7, 359 (2000)

[18] H. Masuda, M. Takeuchi, T. Takahashi; Ultramicroscopy 105, 137 (2005)

[19] M. Kroutvar, Y. Ducommun, J. J. Finley, M. Bichler, G. Abstreiter, A. Zrenner; Appl. Phys. Lett. 83, 443 (2003)

[20] T. Sugino, T. Itagaki, J. Shirafuji; Diam. Rel. Mat. 5, 714 (1996)

[21] W.E. Spicer, P.W. Chye, P.R. Skeath, C.Y. Su, I. Lindau; J. Vac. Sci. Technol. 16, 1422 (1979)

[22] F.Capasso, W.T.Tsang, A.L.Hutchinson, G.F.Williams, Appl. Phys. Lett. 40, 38 (1982)

MBE Growth of GaAs Whiskers on LPCVD Si Nanowire Trunks

A.M. Andrews[1], A. Lugstein[2], M. Schramböck[1], M. Steinmair[2], Y.-J. Hyun[2], E. Bertagnolli[2], T. Müller[3], C. Zauner[3], K. Unterrainer[3], and G. Strasser[1]

[1]Center for Micro- and Nanostructures, Technical University of Vienna, Floragasse 7/392, A-1040 Vienna, Austria

[2]Institute for Solid State Electronics, Technical University of Vienna, Floragasse 7/362, A-1040 Vienna, Austria

[3]Institute for Photonics, Technical University of Vienna, Gusshausstrasse 27/387, A-1040 Vienna, Austria

We present the growth of III-V GaAs whiskers on group IV Si nanowire trunks. This merging of III-V and IV technology is accomplished by a combination of low pressure chemical vapor deposition and molecular-beam epitaxy. The resulting single GaAs whiskers have a 6-fold symmetry perpendicular to the {112} facets of the Si nanowire trunks and grow in a wurtzite crystal structure. The hetero-epitaxial growth shows strong luminescence, blue-shifted from zinc-blende GaAs.

Introduction

Nanowires are quickly bridging the gap from fundamental growth research to realized electronic and photonic devices. They present an excellent opportunity to combine materials when the differences in lattice mismatch, thermal expansion coefficients, or polarity prevent layer-by-layer 2D growth. We present the hetero-epitaxial growth of single crystalline GaAs whiskers on Si-nanowire (Si-NW) trunks forming hierarchical structures with a 6-fold symmetry [1]. The hetero-epitaxial growth and the good crystal quality of the Si-NWs and GaAs whiskers were confirmed by high-resolution transmission electron microscopy (HRTEM), powder x-ray diffraction (XRD), photoluminescence (PL), and energy dependent micro-PL measurements.

Experimental

The [111] oriented Si-NWs are grown on a (111) Si substrate utilizing vapor-liquid-solid (VLS) growth with Au colloids, 80 nm in diameter, by low pressure chemical vapor deposition (LPCVD), Fig. 1. HRTEM studies reveal the [111] growth direction of the core Si nanowires (Si-NWs) and cross-sectional HRTEM of the Si-NWs shows that the circumference of the Si-NW is composed of six {112} facet planes. The NW templates are removed from LPCVD and loaded into the molecular-beam epitaxy (MBE) for the GaAs deposition. The sequentially grown branches are single crystalline GaAs nanowhiskers which grow without a catalyst and are perpendicular to the {112} facets of the Si-NW backbone. Powder XRD has revealed that the GaAs whiskers are wurtzite and HRTEM of the NWs shows a [0001] orientation of the wires. The single crystal whiskers grow without observable defects on the SiO_x on the facets of the Si-NW trunk. Various GaAs deposition amounts and temperatures were investigated. Deposition amount (20 – 200 nm) and temperature (450 – 550 °C) were studied. Whisker growth first initiates at the Si-NW tip and whisker length and diameter were found to scale with

the GaAs deposition while the temperature influenced the tapering of the whisker. PL measurements on template areas without NWs show no luminescence after GaAs deposition while areas with GaAs whiskers show a peak with a blue-shift of about 30 meV compared to bulk zinc-blende GaAs, Fig. 2. Micro-PL was done on GaAs/AlAs "superlattice" whiskers and shows very bright luminescence from the whiskers and no luminescence from the other areas of the sample.

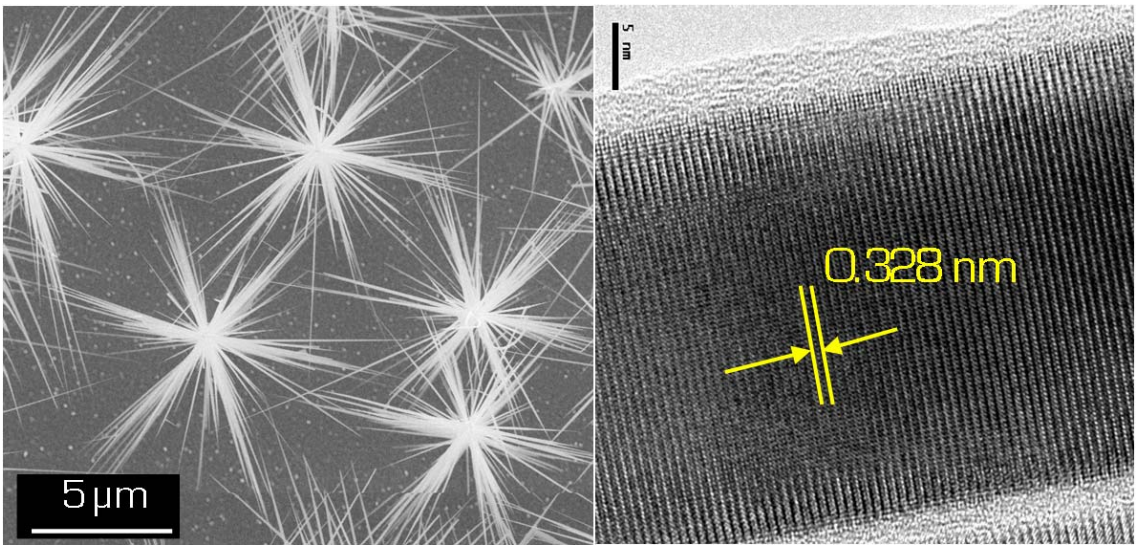

Fig. 1: Scanning electron micrograph of GaAs whiskers grown on Si nanowire trunks. The GaAs forms [0001] wurtzite whiskers on the 80 nm diameter Si-nanowires.

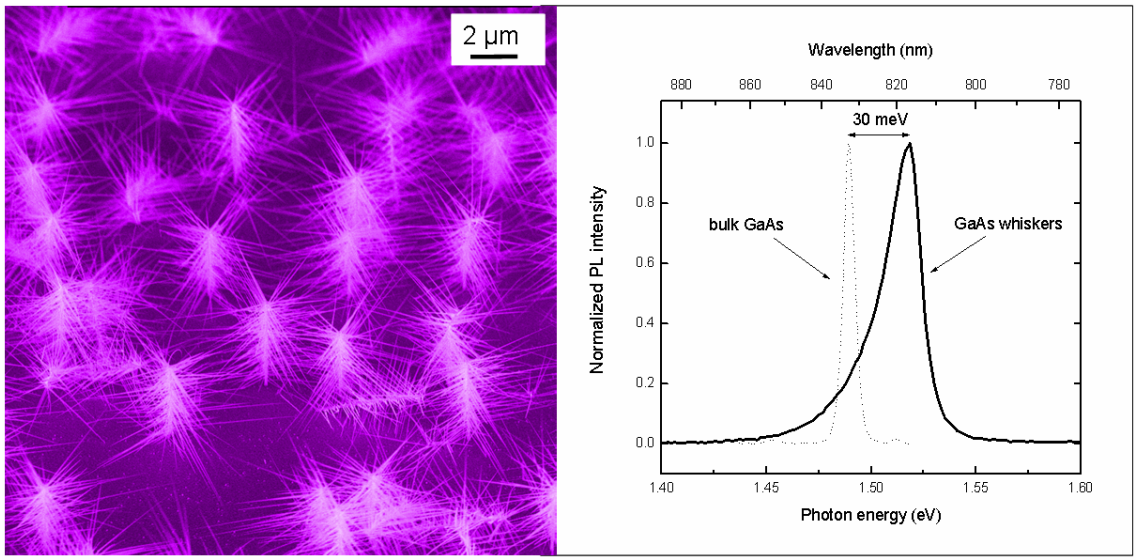

Fig. 2: Scanning electron micrograph of GaAs whiskers grown on Si nanowire trunks with the corresponding photoluminescence spectra. The wurtzite GaAs whiskers show a blue shift of 30 meV compared to bulk zinc-blende GaAs.

Conclusion

The ability to prepare rotationally branched NW structures should open new opportunities for both fundamental research and applications including monolithic 3-dim nanoelectronics and -photonics.

Acknowledgements

This work is supported partly by the Austrian Science Fund under grant P-18080-N07, partly by the Sixth EU Framework Program (NoE) SANDiE, and partly by the Austrian SFB project IR-ON; the financial support from the Austrian Society for Micro- and Nanoelectronics (GMe) is gratefully acknowledged.

References

[1] A. Lugstein, A.M. Andrews, M. Steinmair, Y.-J. Hyun, E. Bertagnolli, M. Weil, P. Pongratz, M. Schramböck, T. Roch, and G. Strasser: “Growth of branched single-crystalline GaAs whiskers on Si nanowire trunks”, Nanotechnology, Vol. 18, 2007, pp. 355306-10.

Ultrafast Spectral Hole Burning Spectroscopy of Exciton Spin Relaxation in Quantum Dots

T. Müller, T. Moldaschl, G. Strasser and K. Unterrainer

Institute of Photonics & Center for Micro- and Nano Structures, Vienna University of Technology, Floragasse 7, A-1040 Vienna, Austria

The exciton spin relaxation within the radiative doublet of the exciton ground state in InAs/GaAs selfassembled quantum dots is studied via an ultrafast spectral hole burning technique. In the case of cross-polarized pump and probe pulses a spectral "anti-hole" emerges due to relaxation of the exciton spin. The measured relaxation time decreases rapidly from 1.15 ns at T = 5 K to 90 ps at 90 K, suggesting exciton-acoustic phonon interaction as the underlying spin relaxation mechanism.

Introduction

The carrier spin couples much weaker to the environment than the carrier wavefunction. Thus, spin states in semiconductor quantum dots (QDs) are a promising candidate for the implementation of future quantum logic devices. Indeed, very long (~ns) spin relaxation times have been found in III-V [1] – [3] and II-VI [4] self-assembled QDs. Studies of spin-polarized carriers confined in QDs have so far mainly been performed by time-resolved photoluminescence measurements on QD ensembles where spin populations are created using circularly polarized light excitation. In this contribution we report measurements of the spin relaxation in an ensemble of InAs/GaAs self-assembled QDs using an ultrafast spectral hole burning (SHB) technique [5].

Experimental

Sample Preparation

The investigated sample consists of 30 layers of InAs QDs with a dot density of approximately $2x10^{10}$ per cm^2 per layer. In order to be accessible to our Ti:sapphire laser system, the exciton transitions were shifted to higher energies by rapid thermal annealing. Excitonic ground state luminescence from the dots at T = 5 K is observed at 1.281 eV with an inhomogeneous broadening of the transitions of ~45 meV (FWHM).

Measurements

SHB measurements were performed using a modelocked Ti: sapphire laser that delivers 80-fs pulses with a center frequency of 1.285 eV and a spectral width of ~14 meV (FWHM). A grating pulse shaper was used to produce 1.4 meV (FWHM) broad pump pulses and the change in the transmission induced by the pump was measured with a weaker 80-fs probe pulse. The probe was spectrally dispersed with a monochromator which allowed the determination of the changes induced at photon energies different from that of the pump. A motorized translation stage controlled the delay between the

pump and probe pulses. In addition, half-wave-plates were used to independently adjust the linear polarizations of both, pump and probe.

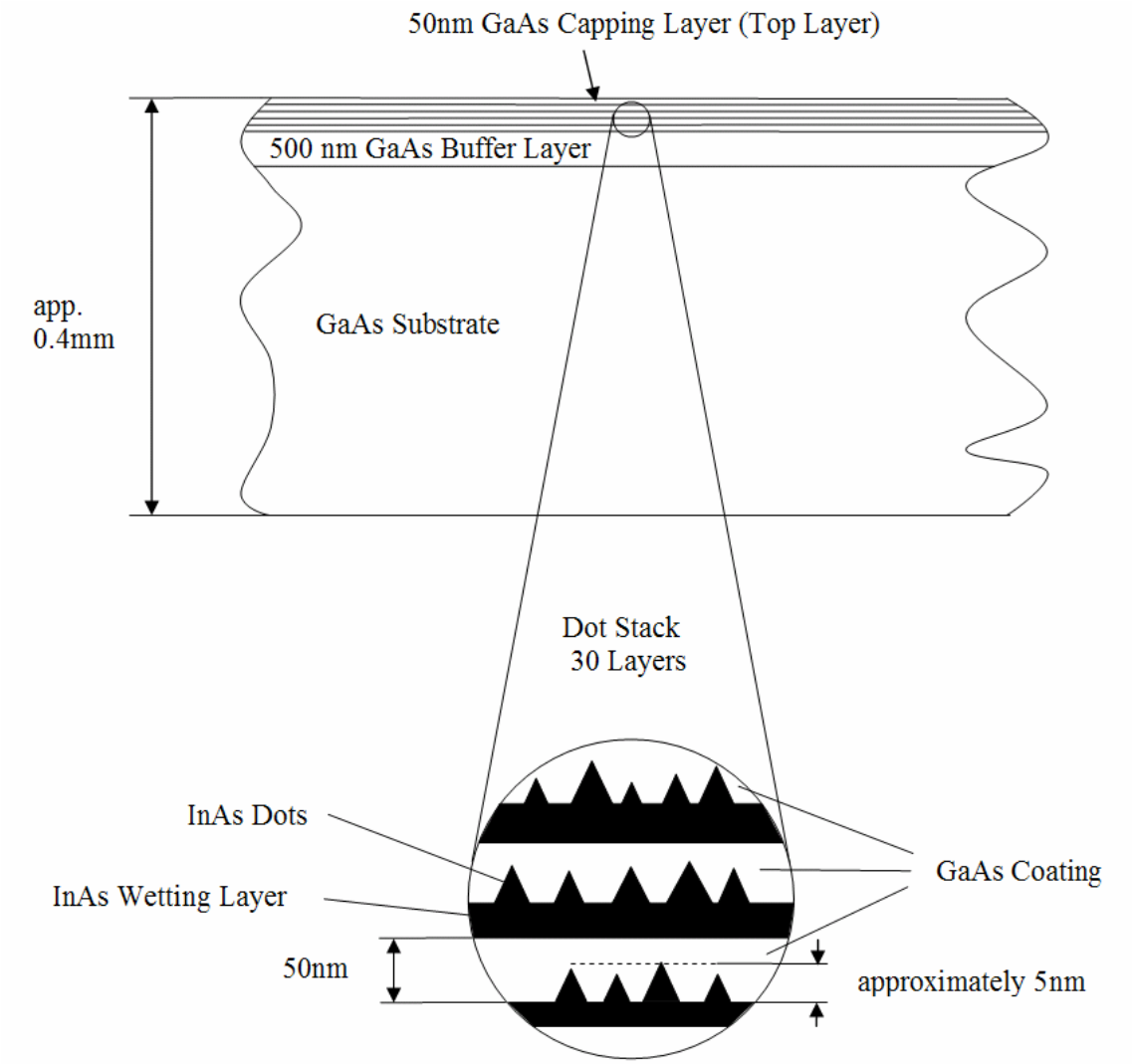

Fig. 1: Sample of self-assembled InAs / GaAs quantum dots

Figure 2 shows SHB signals recorded at T = 5 K. In these measurements a linear Πy-polarized pump pulse is tuned to the maximum of the excitonic ground state transition. The polarization of the broadband probe pulse is tuned either perpendicular (upper trace) or parallel (lower trace) to the pump and the differential transmission change of the probe is measured at a temporal delay of 10 ps after excitation. In the first case, the SHB signal shows enhanced transmission at the pump photon energy, corresponding to a bleaching of the |00> ground state population. In the case of parallel polarizations of the two pulses, we observe (i) enhanced transmission at the pump photon energy, and (ii) reduced transmission, i.e., an “antihole”, at energies below the pump photon energy [6]. The antihole arises from the population of the |01> exciton state which gives rise to absorption to the biexciton state |11> at an energy of ΔE_1 below the exciton peak. We determine a biexciton binding energy of 4.2 meV.

Results

The SHB signals strongly broaden at T = 90 K, and after deconvolution of the pump pulse we find a FWHM line width of 2.1 meV. Temperature dependent measurements show that the linewidth is determined by acoustic phonon-exciton interaction in the dots. The temporal evolution of the antihole at T = 90 K is shown in Fig. 2 (a). With increasing pump-probe delay, the ratio of cross-polarized signal to copolarized signal increases and reaches one for long delay times, as shown in the inset. It is obvious that the development of an antihole in the cross-polarized case is due to spin relaxation: As |01> excitons flip their spin, the |10> exciton state gets populated, giving rise to absorption to the biexciton state |11>. The spin relaxation rate r can be found from the equation $(A_{//} - A_{\_/\_})/(A_{//} + A_{\_/\_}) \sim \exp(-2\Gamma\tau)$, where $A_{//}$ and $A_{\_/\_}$ denote the antihole amplitudes for co- and crosspolarized probe light, and τ is the pump-probe delay time. A fit yields $1/\Gamma$ = 90 ps. Figure 3 (b) presents the temperature dependence of the relaxation time. It increases rapidly from 90 ps to 1.15 ns as the temperature is reduced from 90 K to 5 K. At 5 K the spin relaxation time is more than two times longer than the exciton lifetime which remains approximately constant (~0.5 ns) over the investigated temperature range. The large change of the spin relaxation time suggests that phonon scattering related mechanisms become significant at high temperature. The observed temperature dependence is characterized by a small activation energy which strongly points to an acoustic phonon mediated spin flip process.

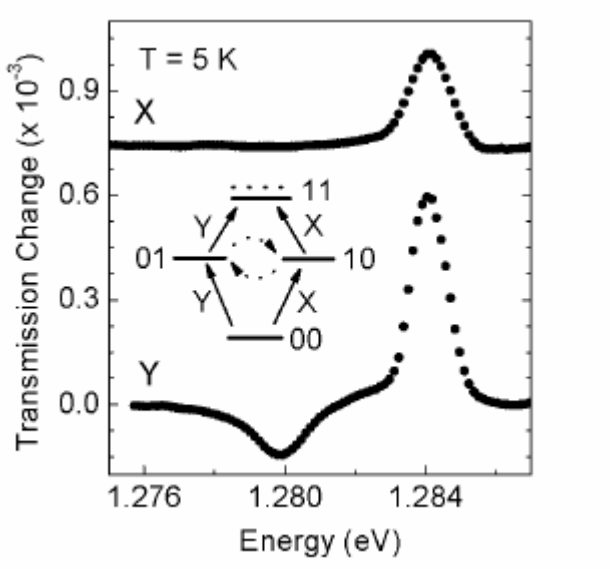

Fig. 2: SHB signals for Πx (upper trace) and Πy - polarized probe pulses. The polarization of the pump is in both cases Πy. Inset: Schematic drawing of the energy levels in a QD. |00> is the ground state; |10> and |01> correspond to the exciton states, which can be excited by Πx - and Πy - polarized light, respectively; and |11> denotes the biexciton state. The biexciton energy is less than twice the bare exciton energy, the difference between them being the biexciton binding energy ΔE.

Acknowledgements

This work was supported by the Austrian Fond zur Förderung der Wissenschaftlichen Forschung (SFBADLIS, SFB-IRON) and the ECNoE program SANDiE.

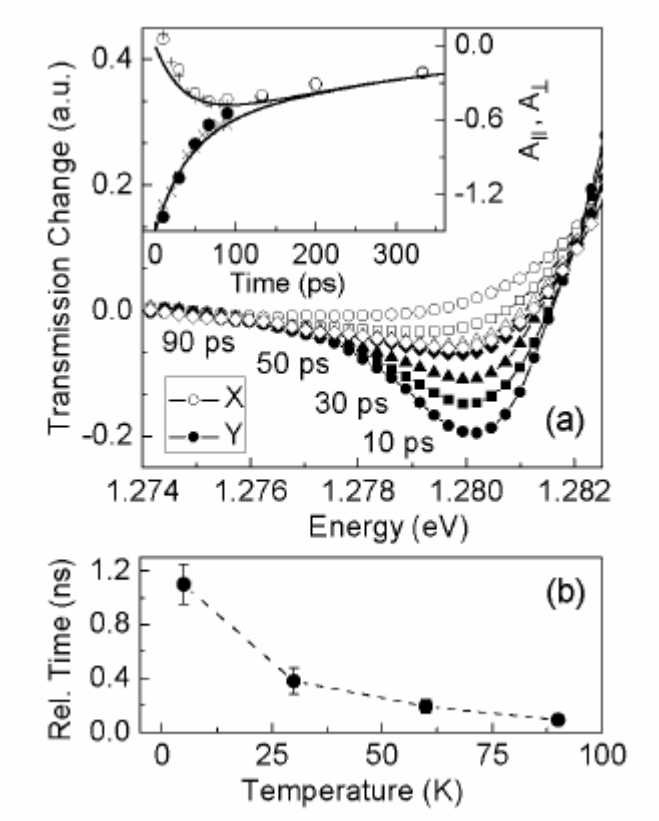

Fig. 3: (a) Temporal evolution of the antihole at T = 90 K. Inset: Antihole amplitudes for co- and cross-polarized pump and probe pulses (symbols: experimental data; lines: results from a simple rate equation model), (b) Temperature dependence of the spin relaxation time.

References

[1] M. Paillard, X. Marie, P. Renucci, T. Amand, A. Jbeli, and J. M. Gerard, *Phys. Rev. Lett.* 86, 1634 (2001).

[2] A. S. Lenihan, M. V. Gurudev Dutt, D. G. Steel, S. Ghosh, and P. K. Bhattacharya, *Phys. Rev. Lett.* 88, 223601 (2002).

[3] H. Gotoh, H. Ando, H. Kamada, A. Chavez-Pirson, and J. Temmyo, *Appl. Phys. Lett.* 72, 1341 (1998).

[4] M. Scheibner, G. Bacher, S. Weber, A. Forchel, Th. Passow, and D. Hommel, *Phys. Rev. B* 67, 153302 (2003).

[5] T. Müller, G. Strasser, and K. Unterrainer, *Appl. Phys. Lett.* 88,192105 (2006).

[6] A. S. Lenihan, M. V. Gurudev Dutt, D. G. Steel, S. Ghosh, and P. Bhattacharya, *Phys. Rev. B* 69, 045306 (2004).

Polarization Dependence of Photocurrent in Quantum-Dot Infrared Photodetectors

T. Gebhard[1], P.L. Souza[1,2], F.F. Schrey[1], G. Strasser[1], K. Unterrainer[1], M.P. Pires[3], S.M. Landi[2], J.M. Villas-Boas[4], N. Studart[5]

[1]Photonics Institute and Center for Micro- and Nanostructures, TU-Wien, A-1040 Vienna, Austria

[2]LabSem, CETUC, PUC-Rio,Rua Marquês de Sao Vicente 225, Rio de Janeiro, 22451-900, Brazil

[3]Instituto de Física, Universidade Federal do Rio de Janeiro, Rio de Janeiro, Brazil

[4]Ohio University, USA

[5]Instituto de Física, Universidade Federal de São Carlos, São Carlos, Brazil

Through polarization dependence measurements of photocurrent together with theoretical calculations we were able to identify different intersubband transitions in InAs/InGaAs/InP quantum dot structures for infrared photodetectors and observe 2D/0D hybrid behavior of the dot structures.

Introduction

The technology to detect infrared photons is dominated by HgCdTe (MCT) photodetectors since about four decades. The major advantage of this material system is the tunability over a large detection range. Their high optical conversion efficiency and the wide-band response are hard to compete with. Despite that, there is still a need to improve handling, reliability, speed and reproducibility of state of the art infrared photodetectors. They are bulky due to cryogenic temperature operation, and the lack of uniformity of the grown material makes them only partially suitable for large focal plain arrays. The ripening process of the MCT technology was accompanied by intensive research efforts for alternative detector concepts for increased temperature operation, reliability and reproducibility. As a consequence of the highly advanced epitaxial growth techniques for III-V semiconductor materials, intersubband photo-detection via quantum wells (QW) showed great potential as a viable alternative. However, theoretical predictions show that quantum well infrared photo-detectors (QWIP) have problems as candidates to rival the MCT technology at higher temperatures, as the dark current in QWIP increases significantly due to inherent thermoionic emission. In addition, selection rules in QW prohibit light incoming parallel to the growth-direction to be absorbed in intersubband transitions. Gratings and random reflectors are needed to circumvent this physical limit. The evolution of quantum devices led to a further reduction of the confinement dimensionality and today self organized growth techniques made the growth of quantum dots (QD) possible for a variety of material systems. Quantum dot infrared photo-detectors (QDIP) are not only able to outperform QWIP [1], but they are also potential candidates to rival or outperform MCT photo-detectors [2]. The reduced phonon-electron interaction in QD results in a long lifetime of excited carriers. The photoconductive gain increases by magnitudes compared to QWIP and also the dark

current is theoretically reduced significantly due to suppressed thermoionic emission. The absorption coefficient is also much higher than in QW. QD show the inherent feature to absorb normal incident light [3].

The features of QDIP are very sensitively connected to the degree of control during the growth process, where many different uncertainties lead to reduced reproducibility. The self-organized growth process spreads the dots size inhomogenously, and this decreases the detectivity of the devices. This effect cannot be eliminated, but only minimized technologically. QDIP without blocking layer have still a much higher dark current than QWIP caused by interlayer-dot-tunneling through defects and thermally excited carriers from upper excited states and are therefore far away from theoretically predicted limits.

Hence, real QDs are quite different from ideal. The intraband absorption and the consequently generated photocurrent (PC) in these devices should be fully understood. In particular, there has been some controversy in the literature on the polarization dependence of the PC for QDIP structures [4] – [7]. In this work we investigate the photocurrent (PC) as a function of temperature and polarization produced by QD structures where InAs dots are nucleated on top of an InGaAs QW. The dots are covered with an InP barrier. The observed PC peaks are attributed to different intraband transitions based on the PC data together with theoretical calculations.

Experimental

A doped sample with 20 and an undoped one with 10 dot layers were grown by metalorganic vapor phase epitaxy on semiinsulating (100) InP substrate. The InAs dots were grown on a 8.5 nm thick InGaAs layer lattice matched with InP and capped by 18 nm InP layer. The Si doping density of the 0.4 µm thick InP contact layers is n = 4×10^{18} cm^{-3} for both samples. The nominal doping level of the QD in the doped sample provides 2 electrons in the ground state per dot. The dot sheet density of about 9×10^{9} cm^{-2} and the median dot height of 9 nm were estimated by atomic force microscopy.

The PC polarization QD samples were investigated by a Fourier transform spectrometer for normal and 45° light incidence. Choosing the TE polarization implies that the electric field is totally in the plane of the layers. However, for the TM polarization, the electric field will have a component perpendicular to the layers.

The measured spectra were corrected by the system response and by the Fresnel refraction coefficients for both polarizations.

Results

A PC signal was detected up to 50 K and 90 K for the doped and undoped sample, respectively. Polarization dependent PC measurements of the undoped sample show a signal around 5.3 µm. Figure 1 shows the PC spectra at 6 K for the undoped sample for different experimental configurations: normal incidence, 45 degrees incidence with TE polarization, 45 degrees incidence with TM polarization, and unpolarized light. Choosing the TE polarization implies that the electric field is totally in the plane of the layers. On the other hand, for the TM polarization, the electric field will have a component perpendicular to them. The same peak is observed for all configurations. However, for the TE polarization the PC signal was expected to be of the same order of magnitude as for the TM polarization, indicating that the energy levels involved have a 0D character.

For the undoped sample the transition around 5.3 µm should depart from the ground state, because only this state is populated due to non-intentional doping. The simple 1D calculation estimate the transition energy from the ground state to the first excited state of about 184 meV; this is a underestimation of about 20% in comparison to the experimental results. Electrons in the first excited state can contribute to the photocurrent due to sequential tunneling, as it has been already observed for these samples [10]. This transition has the highest oscillator strength, so other transitions to the excited states can be excluded.

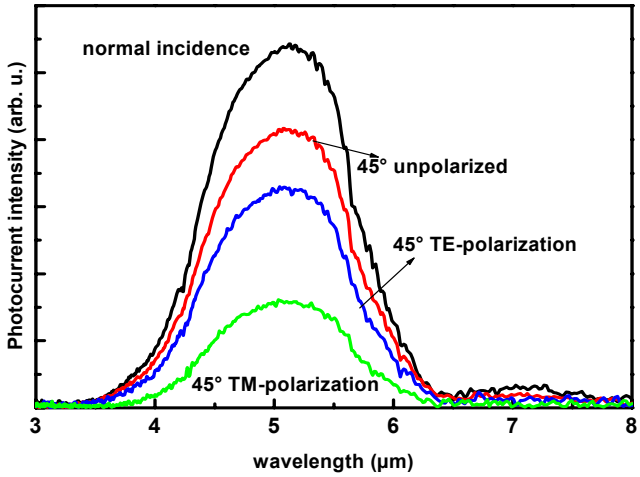

Fig. 1: Polarization dependence of the photocurrent at 6 K for the undoped sample.

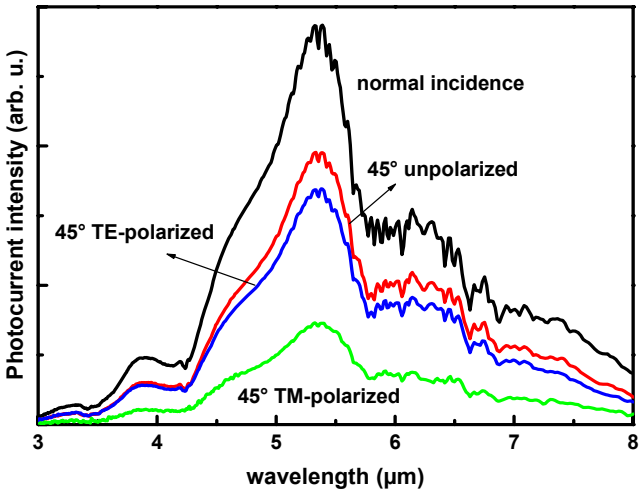

Fig. 2: Polarization dependence of the photocurrent at 6 K for the doped sample.

Equivalent polarization behavior, but noisier signal, is observed for the doped sample, as shown in Fig. 2. The doped sample contains twice as many layers as the undoped does. Even though one would expect a stronger signal, strain builds up more in such a thicker structure leading to more noise in the detected PC. Carefully looking in the spectra one observes that there are three peaks at 4 µm, 5.3 µm and 6.2 µm, corresponding to 310, 234 and 200 meV, in addition to a couple of shoulders. Using a simple 1D effective-mass model [8] for the InP/InGaAs/InAs/InP structure the band- con-

figuration shown in Fig. 3 is obtained assuming a dot height of 9 nm and an InGaAs QW thickness of 10 nm.

For the doped sample additional transitions can also occur from the first and second excited states to the third excited state or to the continuum. The oscillator strength to the continuum is small compared to these to the third excited state. The transitions E_1 – E_3 and E_2 – E_3 correspond to 5.8 and 8.9 µm, respectively. The theoretical and experimental transition energies are in fairly good agreement, considering that such a simple 1D model was used; the theoretical values being overestimated by about 15%. Results of photoluminescence give further support to these peak assignments [10].

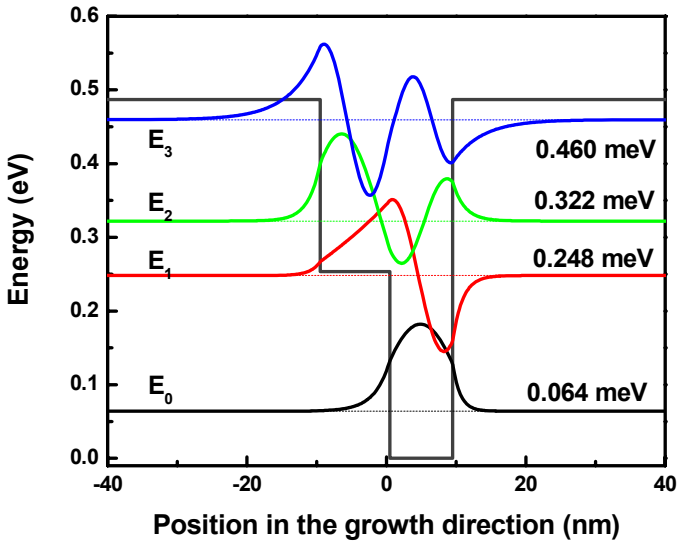

Fig. 3: Band configuration of the investigated samples.

Conclusion

We have performed polarization dependence measurements in InAs/InGaAs/InP quantum dot structures. Based on the difference between doped and undoped sample and the simple theoretical calculations, different transitions were identified. A strong PC-signal for s-polarization was observed as expected due to the 0D character of the QD. But surprisingly the PC for the p-polarization was rather weak showing little evidence 2D/0D hybrid behavior.

Acknowledgements

We acknowledge the financial support from CAPES, CNPq, FAPERJ, FINEP, Wolfgang Pauli Institute, FWF SFB IR-ON and ANSWER.

References

[1] E. T. Kim et al, 84, 3277 (2004)

[2] J. Phillips, J. Appl. Phys., 91, 4590 (2002)

[3] A. Rogalsky, Progress in Quantum Electronics, 27, 59-210 (2003)

[4] L. Chu et al, Appl. Phys. Lett., 75, 3599 (1999).

[5] L. Chu et al, Appl. Phys. Lett., 76, 1944 (2000).

[6] S. Sauvage et al, Appl. Phys. Lett., 78, 2327 (2001).

[7] B. Aslan et al, Appl. Phys. Lett., 82, 630 (2003).

[8] J. Mendoza-Alvarez et al, Physica E, 32, 85 (2006).

[9] A. G. Silva, et al, ICPS2006.

[10] T. Gebhard, et al, ICSNN2006.

Growth of Branched Single Crystalline GaAs Whiskers on Si Nanowire Trunks

A. Lugstein[1], A.M. Andrews[1], M. Steinmair[1], Y.J. Hyun[1], E. Bertagnolli[1], M. Schramböck[2], and G. Strasser[2]

[1] Institute for Solid State Electronics
[2] Center for Micro- and Nanostructures

TU Wien, Floragasse 7, A-1040 Vienna

Introduction

Any successful method to integrate GaAs on Si by means of combining silicon integrated circuits with the optical and electronic opportunities of GaAs offers a significant impact to semiconductor technology. However, there are fundamental difficulties involved with the growth of a polar compound semiconductor on a nonpolar substrate such as GaAs on Si, leading to the problem of inversion domains and boundaries at the interface. Moreover, the lattice mismatch and the difference in thermal expansion coefficients have to be dealt with to obtain high-quality hybrid substrates of crystalline GaAs on silicon substrates. Much work has been done on planar growth of III-V materials on Si using different approaches such as buffer layers, growth on patterned Si surfaces, and selected area growth from small openings. Most of the problems can be avoided by reducing the contact area of the compound semiconductor and silicon, by means of a NW approach. The crystal lattice of the compound semiconductor will be elastically deformed and the strain could be relieved near the NW interface.

In most cases, nanowire growth has been performed by using a catalyst in the so called vapor-liquid-solid (VLS) or vapor-solid-solid (VSS) growth mechanism. We developed an approach for producing III-V (GaAs) nanowhiskers, on group IV (Si) NWs. For the first time, we show that single crystalline hexagonal GaAs whiskers can be grown hetero-epitaxially on the side facets of single crystalline Si-NWs by combining VLS and MBE growth techniques [1]. This addresses both, the long-time challenge of integrating high performance III-V semiconductors with mainstream Si technology, and the possibility of 3-dimensional nanoelectronic and -photonic devices.

Experimental

Si-NWs were grown in a hot wall LPCVD reactor by the VLS growth mechanism, and a 2 nm thick Au film was used as a catalyst. Alternatively, Au colloids with a mean diameter of 80 nm were spin-coated on the cleaned and etched Si (111) substrates. The VLS growth was performed at 823 K with 2% SiH_4 in He as a precursor gas; typical growth times in this study were 30 min. For the subsequent growth of GaAs whiskers the Si-NW/Si(111) samples were indium bonded to a molybdenum carrier wafer for growth in a Mod-Gen II MBE. After loading into the vacuum chamber the samples were baked at 773 K heater temperature before transfer into the growth chamber. The samples were grown between 723 and 823 K by increasing the substrate temperature to the desired growth temperature in an As_4 flux. The GaAs branches were grown at a 2-D equivalent growth rate of 0.55 µm/h under an As_4 beam equivalent pressure of 1.5×10^{-5} mbar.

Results

Most of the Si-NWs synthesized via the VLS process on Si (111) substrates with a thin 2 nm Au layer as the catalyst grew upwards from the substrate in the <111> directions. To achieve individual and freestanding Si-NW trunks we used 80 nm gold colloids as catalyst for the VLS growth. The typical dimensions are about 104 nm for the diameter and 3 µm for the length, which appear to be uniform. The HRTEM and diffraction image in Fig. 1 (a) confirms the [111] growth direction and the single crystalline nature of the Si-NWs. Such images clearly show the Si (111) atomic planes (separation 3.14 Å) perpendicular to the NW axis. The Si-NWs are usually free of dislocations and stacking faults and are covered by a very thin amorphous oxide layer.

The SEM image in Fig. 1 (b) shows the typical morphology of the samples after the MBE growth with branched GaAs whiskers grown on Si-NW/Si(111) samples. The GaAs branches, which were grown perpendicular to the Si (111) NW trunks, appear as perfectly aligned star-like structures with a 6-fold symmetry. The low magnification image shows the large quantity of these star-like structures, which densely cover a 1x1 cm2 sample. Fig.1 (c) shows the top view SEM image of individual freestanding Si-NWs with hetero-epitaxially grown GaAs whiskers, which in the tilted view of Fig. 1 (d) appear as vertically oriented nanotrees with Si-NW trunks and GaAs branches.

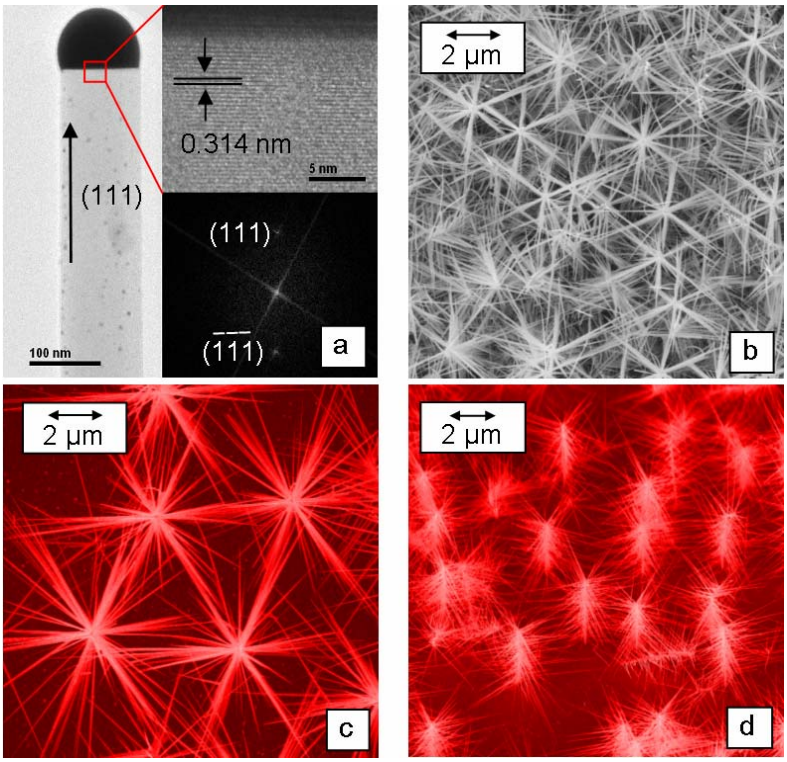

Fig. 1: (a) TEM, HRTEM and diffraction image of a single crystalline Si-NW with the catalytic Au nanoparticle on top. (b) low magnification SEM image showing the large quantity of GaAs nanowhiskers on Si-NWs; MBE growth of the GaAs nanowhiskers was performed at 723 K. (c) Top view SEM image of individual structures comprising GaAs branches with a 6-fold symmetry on the freestanding Si-NW trunks and (d) a 45° tilt SEM micrograph of GaAs branches growing perpendicular to the core Si (111)-NW trunks.

The Fig. 2 (a) shows the top view SEM image of a single nanotree with a 6-fold symmetry. TEM tilting experiments showed that the cross-section of each core Si-NW is a

trigonal hexagon with three long and three short edges. The GaAs nanowhiskers grow on each of the six facets perpendicular to the core Si-NWs like branches on the trunks of a tree. The cross-sectional HRTEM image of such a nanotree in Fig. 2(b) shows these hexagon of the Si-NW trunk with alternating wider and narrower vertical {112} facets normal to the [111] growth direction. The angle between each of these adjacent facets of the Si-NWs is 120°, leading to the 6-fold symmetry as observed. In a few cases the GaAs whiskers grew preferably on the long facets of the hexagon leading to nanotrees with a quasi 3-fold symmetry (see Fig. 2 (c)), suggesting a minimal facet size for whisker nucleation. For long MBE growth times the core Si NW is covered by an unintentionally deposited GaAs layer (see Fig 2(b)) and some of the GaAs whisker growing later on this core-shell structure lose the crystallographic relation to the core Si-NWs.

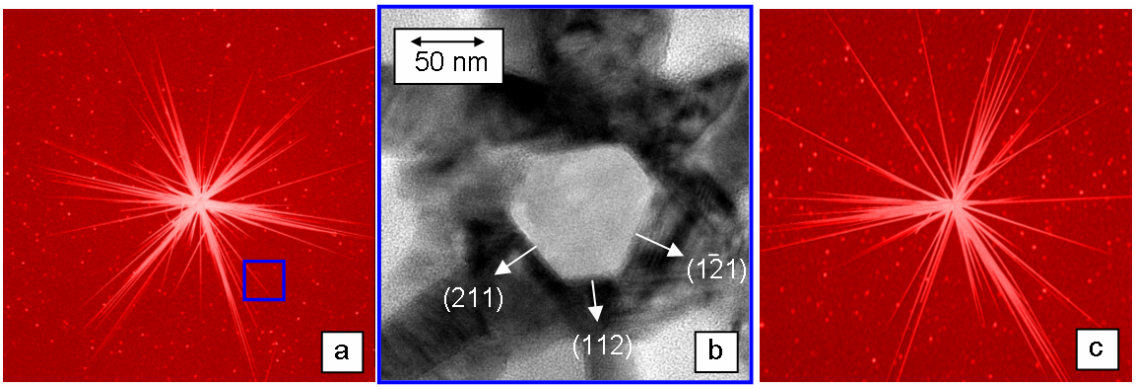

Fig. 2: (a) Top view SEM image of GaAs branches grown perpendicular to the free-standing Si-NW showing a 6-fold symmetry. (b) TEM image showing the cross-sectional hexagon of the Si-NW trunk with alternating wider and narrower vertical {112} facets normal to the [111] growth direction. (c) GaAs nanowhisker which grew preferably on the long facets of the Si-NW trunk with a quasi 3-fold symmetry.

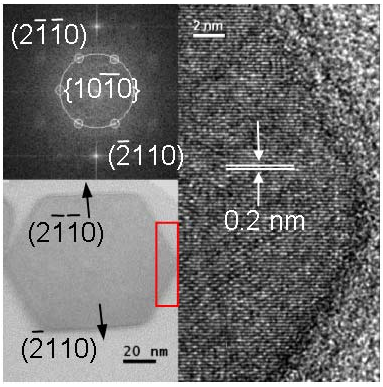

Fig. 3: Cross-sectional TEM and HRTEM image of a GaAs whisker and the respective diffraction pattern recorded along the nanowhisker axis.

The morphology and highly crystalline nature of the GaAs nanowhiskers were characterized by HRTEM and selected area electron diffraction (SAED) measurements (Fig. 3(a)). The TEM image shows the hexagonal cross-section of the GaAs whisker. The upper right SAED pattern was recorded along the nanowhisker axis and has been in-

dexed as the diffraction along the [0001] zone axis of crystalline GaAs and the facets as {2110} atomic planes. The HRTEM micrograph shows a closer view on the area marked with the red rectangle in the TEM image with the (2110) atomic planes of the GaAs whiskers separated by 0.2 nm, consistent with the tabulated value (0.199 nm).

Figure 4 shows the SEM image of GaAs whiskers on Si-NWs for a short MBE growth time. Nucleation starts at the upper part of the Si-NW trunks and the first nanowhiskers grew perfectly aligned according to the Si-NW {112} facets. For longer growth times there is no significant length difference observed for the GaAs whisker as a function of their position along the Si-NW trunks, but GaAs whiskers deviating from the 6-fold symmetry appear to be shorter (see Fig. 2 (a)). These GaAs whiskers nucleate later on pre-existing GaAs precipitations formed on the Si-NW trunks ((see Fig. 2 (b)) and thereby lose the crystallographic relation to the core Si-NWs. The thickness of the unintentionally deposited polycrystalline GaAs shell on the Si-NW trunk increases with MBE growth time according to a 2-D equivalent GaAs growth rate of 0.55 µm/h.

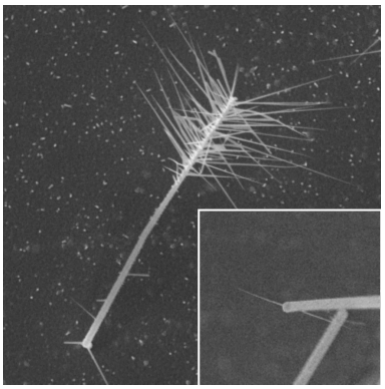

Fig. 4: GaAs nanowhiskers grown on a freestanding Si-NW trunk; MBE growth at 723 K for 524 s. The inset shows two GaAs whisker grown on opposite facets of a Si-NW; MBE growth at 723 K for 262 s.

Conclusion

Taken together, we showed hetero-epitaxial growth of branched III-V nanowhiskers on epitaxially grown group IV NWs realized by combined VLS and MBE methods. We demonstrate this for GaAs whiskers, a direct bandgap semiconductor with high electron mobility predestined for nanophotonics, grown on Si (111) nanowires. The hetero-epitaxial growth and the good crystallinity of the Si-NWs and GaAs whiskers were confirmed by HRTEM.

This work is far from complete in the aspects of synthesizing and the growth mechanism; however, we feel that the nanostructures reported here will have a high potential to be combined with Si for high-speed electronic and photonic applications.

References

[1] Alois Lugstein, Aaron Maxwell Andrews, Mathias Steinmair, Youn-Joo Hyun, Emmerich Bertagnolli, Matthias Weil, Peter Pongratz, Matthias Schramböck, Tomas Roch, Gottfried Strasser, “Growth of branched single crystalline GaAs whiskers on Si nanowire trunks”, Nanotechnology 18, 355306 (2007).

Ga/Au Alloy Catalyst for Single Crystal Silicon-Nanowire Epitaxy

A. Lugstein, M. Steinmair, Y.J. Hyun, and E. Bertagnolli

Solid State Electronics Institute, Vienna University of Technology
Floragasse 7, A-1040 Vienna

Introduction

One dimensional nanostructures, such as semiconductor nanowires or carbon nanotubes, are attractive components for future applications ranging from nanoelectronics to catalysis. In particular, Si-NWs have been suggested to be used for developing high-speed field effect transistors, bio/chemical sensors, and light emitting devices with extremely low power consumption. Many of the silicon investigations have employed the vapor-liquid-solid (VLS) growth mechanism. A metal droplet catalyzes the decomposition of a Si-containing source gas, to function as a Si reservoir by eutectic liquid formation, and finally to precipitate Si-NWs due to supersaturation. Gold has been the metal catalyst of choice and is mostly used due to its favorable physical and chemical properties. We developed a method for the epitaxial growth of Si-NWs by a metal compound gallium/gold (Ga/Au) – nanoparticle-catalyzed chemical vapor deposition (CVD) from SiH_4 on Si (111) and Si (100) surfaces. In addition shape control of the NWs is shown to be possible [1].

Experimental

The growth apparatus is a hot wall low pressure CVD reactor. After carefully cleaning the Si (111) and Si (100) substrates with acetone and isopropanol the samples were dipped in a buffered HF solution to remove any native oxide. Thin Ga and Au metal layers (nominally 1 – 4 nm thick) were deposited on the substrates by thermal evaporation, with the Ga layer always below the Au layer. As a reference sample, a similar 2 to 4 nm thick Au film was deposited on Si substrates pretreated in the same way. After evacuating the CVD-chamber down to 10^{-7} mbar the substrates were heated up in vacuum to 873 K in order to form metal droplets. The Si-NWs growth was done at a total pressure of 3 mbar using a 100 sccm flow of SiH_4 (2% in a He mixture) in the temperature range from 773 to 923 K.

Results

The scanning electron microscope (SEM) image in Fig. 1 (a) shows the typical morphology of NWs grown on Si (111) substrates at 873 K for 15 min with an optimized alloy catalyst of a 2 nm thick Au layer above a 2 nm thick Ga layer. Size and length of the Si-NWs within the grass like array are very homogeneous and most of the wires are oriented along the four ⟨111⟩ directions. The wires growing perpendicularly from the substrate (top inset in Fig. 1 (a)) appear as light spots in the top-view image. Most of the remaining nanowires grow in directions such that their top-view projections correspond to the other three ⟨111⟩ directions. A closer view in the lower inset of Fig. 1 (a) shows that the NWs are highly tapered and exhibit six fold symmetry for the vertical (110) facets.

For comparison, the Si-NWs on the reference sample with the pure Au catalyst (Fig. 1 (b)) nucleate and grow in a much less controlled way, whereby the length and diameter of the NWs appears to be randomly distributed. It is also evident, that the Au droplets solidify and appear as bright spots on the tip of every nanowire. All orientations of the NWs along the four ⟨111⟩ directions could be observed. But in comparison the proportion of the NWs growing perpendicular to the substrate is much lower for the Au catalyzed growth. The NWs show a lot of kinks but have a rod-like shape (inset in Fig. 1(b)) in contrast to the tapered NWs on the Ga/Au catalyzed samples.

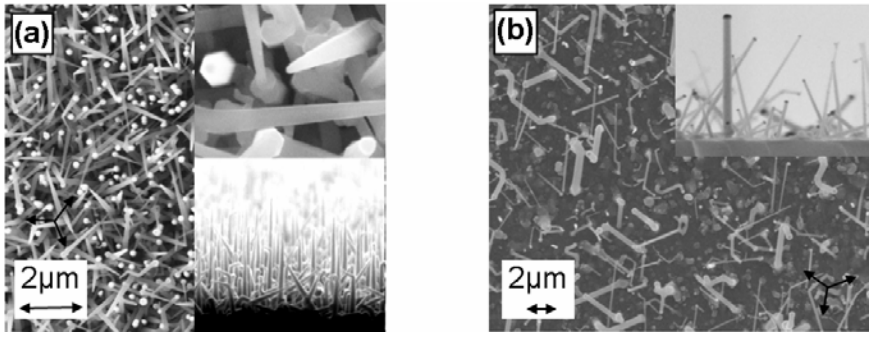

Fig. 1 (a) Top-view SEM image of Si-NWs grown at 873 K for 15 min on Si (111) with the Ga/Au catalyst. The top inset shows tapered Si-NWs exhibiting a hexagonal cross-section with six fold-symmetry and vertical {110} facets normal to the (111) direction. The inset below shows a cross-sectional view of the tapered NWs grown along ⟨111⟩ directions (b) Si-NWs grown on the reference sample with a 2 nm thick pure Au layer and identical process parameters. The cross-sectional view in the inset shows the rod-like shape of typical NWs with solidified Au droplets on top.

In order to identify the mechanism causing the tapering we grew NWs for different times and growth temperatures. Up to a growth time of 240 min, the length of the NWs was found to depend directly on the growth time. While the tip diameters of the NWs grown for a long time are the same as those grown for a short time and are determined by the catalyst diameter, the foot prints of the NWs increased during the course of the growth. This fact indicates that the NW tapering is caused primarily by sidewall deposition (radial growth) of silicon. For the longest NWs the diameter at the foot print was 1500 nm, while the diameter of the tip was less than 70 nm over a length of 15 µm. The experiments carried out for different growth temperatures clearly indicated that radial growth dominated at high growth temperatures.

The assumption that “unanalyzed” deposition of Si on the sidewalls of the NWs causes the tapering can not be sustained as NWs on the reference samples (Au catalyzed) show no tapering (see Fig. 1). Therefore, we suppose that this growth morphology results from a Ga enhanced deposition at the (110) facets of the Si-NWs. Fig. 2 (a) shows the temperature dependences of the axial NWs growth rates (R_{ax}) and the radial growth rate (R_r) for the tapered NWs. The growth rate data in the Arrhenius plot falls on straight lines, showing that all of the growth processes were done in reaction limited regimes. The value of the calculated activation energy for the Ga enhanced deposition at the (110) facets of the Si-NWs of 266 kJ/mol is close to the activation energy of the decomposition of a SiH_4 gas, which is about 234 kJ/mol. The activation energy for the axial growth on the samples with the pure Au film was found to be 89 kJ/mol. Remarkably, for 773 K no NW growth was observed for these reference samples under the given experimental conditions.

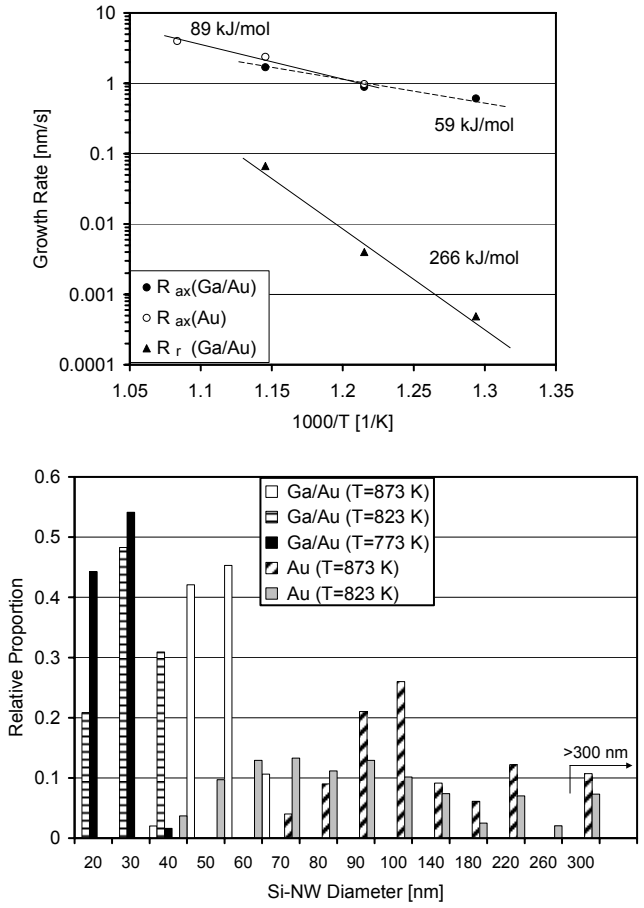

Fig. 2 (a) Temperature dependence of the axial (R_{ax}) and radial (R_r) growth rate for the Ga/Au and Au catalyzed samples at SiH4 partial pressure of 3 mbar and 30 min growth time. (b) Histogram, showing the relative proportion of the Si-NW diameters for the Ga/Au and Au catalyzed growth process as a function of the growth temperature.

This activation energy is much smaller than the one found for Si-CVD from SiH_4 sources (144 – 167 kJ/mol), which is attributed to the catalytic decomposition of SiH_4 at the surface of the Au droplets and explains the higher growth rate of Si-NWs by VLS growth. The even lower activation energy on the Ga/Au catalyzed sample of 59 kJ/mol indicates that the addition of Ga influences the SiH_4 decomposition and/or the crystallization at the liquid-solid interface. The NW grow very dense and show a much higher proportion of epitaxially oriented NWs and in case of Si (111) substrates, even perpendicular grown nanowires. Because of the lower melting point of Ga/Au alloys the addition of Gallium is already active for the formation of the catalytic droplet. Despite the fact that the Ga/Au film has two times the thickness of the pure Au film on the reference sample, the average diameter of the grown NWs is smaller, and the diameter and length distribution is narrowly dispersed at any growth stages and growth temperatures. The relative proportions of the NWs diameter obtained at different temperatures are plotted in Fig. 2 (b). The average diameter of NWs grown with the Ga/Au catalyst at 873 K is about 60 nm and decreases with temperature down to about 30 nm for 773 K. The dispersion of the diameters becomes significantly narrower for 773 K. The histograms of the NW diameter obtained on the Au catalyzed reference samples at 873 K and 823 K show a much broader dispersion with an accumulation cluster at about 70 nm and 100 nm respectively. As shown in Fig. 1, NWs with diameters of more than

300 nm were also observed on these samples. The addition of Ga might change the de-wetting behavior of the deposited metal film during the annealing. This results in smaller catalytic alloy particles with a much narrower distribution of the diameters.

Si-NWs of uniform diameter and length while preserving epitaxy were obtained by adding an additional annealing step at 873 K for 30 min in vacuum. The SEM image in Fig. 3 shows the top-view of self oriented rod-like Si-NWs grown for 15 min at 823 K on Si (100) and Si (111) substrates.

NWs with their orientation controlled by the crystal orientation of the substrate grow along any one of the four ⟨111⟩ directions, thus the visible orthographic projections forms either rectangular or triangular networks. For the (111) substrate the NWs which grow vertically from the substrate appear as light spots in the top-view image.

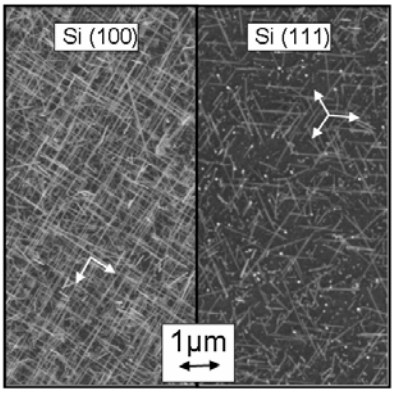

Fig. 3: Plane-view SEM images of Si-NWs forming regular networks on Si (100) and Si (111) substrates.

Conclusion

The effect of reaction conditions on the growth of Si-NWs via well defined Ga/Au nanoclusters as catalysts for VLS growth from SiH_4 source was investigated. HRTEM demonstrates that these high quality NWs grow mainly along the (111) direction with a large proportion of them even perpendicular to the substrate. The diameter and length distribution are narrowly dispersed at any growth stages and growth temperatures. The Si-NWs growth rate follows an Arrhenius law within the temperature range of 723 – 873 K with an activation energy of 59 kJ/mol. For our materials system, the tapering observed at higher temperatures is caused by a Ga catalyzed two-dimensional deposition of Si on (110) facets as the NWs continue to grow along the axial direction. By making a particular choice of growth conditions, it is possible to realize either rod-like or tapered silicon nanowires, which may be desirable for applications as field emitters.

References

[1] A. Lugstein, M. Steinmair, Y. J. Hyun, E. Bertagnolli, and P. Pongratz, “Ga/Au alloy catalyst for single crystal silicon-nanowire epitaxy”, Appl. Phys. Lett. 90, 023109 (2007).

Self-Assembled InAs QDs Grown on AlGaAs Surfaces

M. Schramboeck, A.M. Andrews, P. Klang, W. Schrenk, A. Lugstein, G. Strasser

ZMNS, Technische Universität Wien, A-1040 Wien

Introduction

Quantum dots (QDs) have been under intense investigation during the last years due to their appealing electronic and optical properties. As they offer the ultimate limit in carrier confinement, they gave rise to novel opto-electronic device applications such as QD lasers. To implement the QDs into such devices it is vital to have control over the QD density and size which are in turn determined by the growth parameters. Furthermore, it is desirable to have control over the lateral position of the QDs on the substrate. To achieve this placement, the growth of QDs on substrates pre-patterned with nano-scale structures can be exploited to laterally align the QDs [1], [2]. In this work, we demonstrate the growth of self-assembled InAs QDs on patterned and unpatterned surfaces. The growth of QDs on $Al_xGa_{1-x}As$ surfaces with different Al concentrations was studied in detail.

QDs on $Al_xGa_{1-x}As$ Surfaces

QD Growth

The QDs were grown using a solid-source molecular beam epitaxy (MBE) system. For the surface QD samples the $Al_xGa_{1-x}As$ was grown at 590 °C while subsequent InAs QDs were grown 490 – 520 °C. The sample surface, QD size, shape, volume, and density were analyzed by atomic force microscopy (AFM) with a Digital Instruments 3100 operated in tapping mode. How critical the QD density depends on the growth surface and temperature can be seen in Fig. 1.

All data points are for 0.556 nm (1.83 ML) of InAs at a growth rate of 0.01 µm/h. As can be seen, on GaAs surfaces, temperatures 500 °C – 520 °C produce a QD density variation up to two orders of magnitude. For substrate temperatures above 520 °C the In amount incorporated into the epilayer is reduced significantly. Furthermore, a rise in the Al concentration at the same growth temperature will also increase the dot density dramatically, while reducing the dot size. This is due to the reduced In surface diffusion compared to a GaAs surface. How the amount of InAs incorporated into the QDs depends on the growth temperature is shown in Fig. 2. 0.556 nm (1.83 ML) of InAs were deposited for the growth of self-assembled surface QDs as the substrate temperature was varied from 490 °C to 520 °C. Because of the reduced surface mobility there is an increase in QD volume for surfaces with a higher Al concentration. At growth temperatures of 510 °C and above there is a sharp decline of the dot volume as less InAs can be incorporated into the epilayer at high temperatures. Also at highest Al concentrations there appears to be a sharp decline in QD volume.

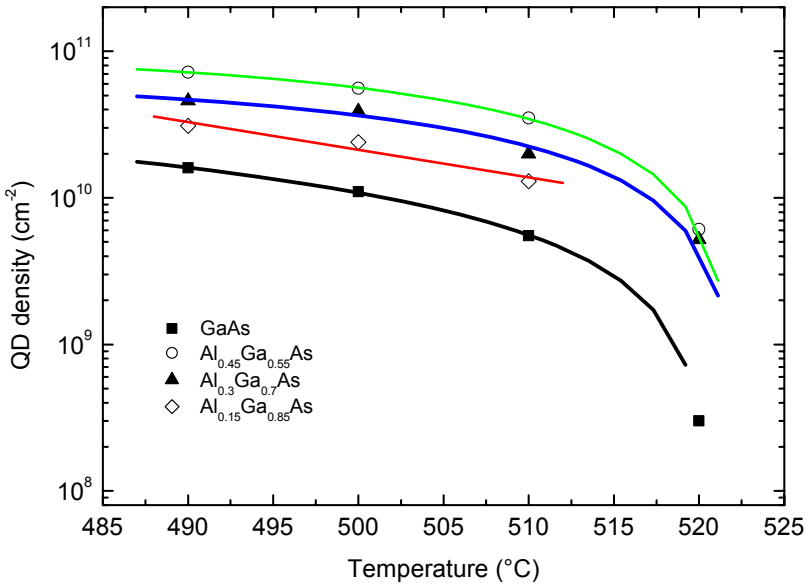

Fig. 1: QD density dependence on growth temperature and Al concentration. The fits are guides to the eye.

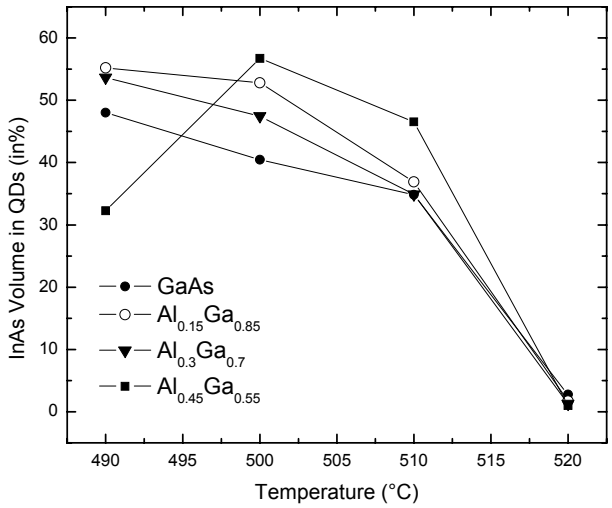

Fig. 2: InAs volume in QDs for different substrate temperatures and surfaces for 0.556 nm of InAs.

Photoluminescence Measurements

To probe the optical properties of the QDs, the buried dots were characterized by photo luminescence (PL) measurements. For the PL measurements a diode pumped solid state laser operating at a wavelength of 532 nm is used. The emission of radiation from the photo-excited carriers via interband optical transitions is measured with a cooled photomultiplier tube and a lock-in amplifier. The measurements were performed at room temperature. The samples consist of 30 layers of self-assembled QDs grown at a surface temperature of 490 °C. Figure 3 shows the measured luminescence for dots grown on surfaces with varying Al concentrations. As the Al concentration increases, the center of the emission peak is shifted to higher energies. This blue-shift can be attributed mainly to the decrease in QD size and the increase in barrier height sur-

rounding the dots. This allows tuning the wavelength of the QD emission within a certain range. Also the luminescence peaks become noticeably broader as the Al content of the growth surface increases. Because surfaces with a high Al concentration show a reduced In diffusion compared to a GaAs surface, the size distribution of the QDs is also broader. This appears in the PL signal as an increased full width at half maximum (FWHM) of the emission peak. The exact values for the FWHM are displayed next to the luminescence peaks in Figure 3.

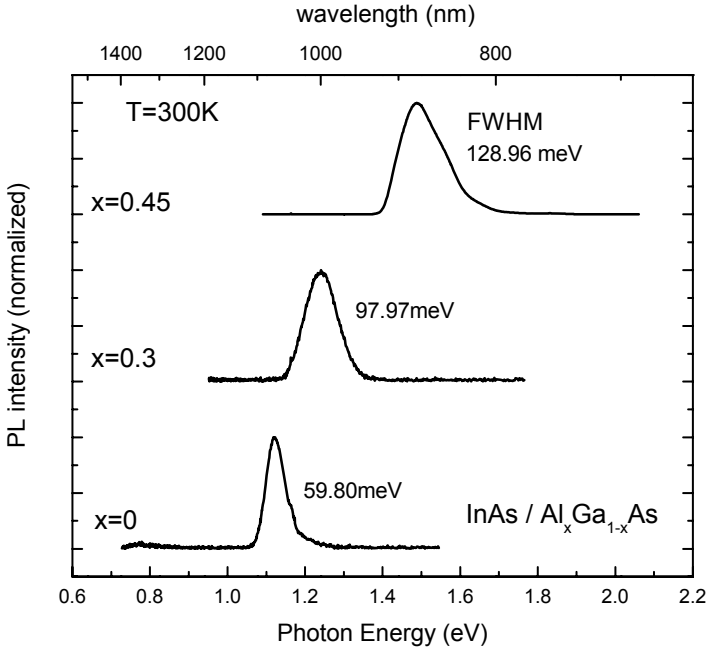

Fig. 3: PL intensity of QDs grown on surfaces with varying Al contents.

Growth on Patterned Substrates

As mentioned previously an ensemble of self-assembled QDs usually shows a broad size distribution. Therefore, the emission from the dots shows a broad spectral broadening. Also, the lateral position of the dots on the substrate can not be controlled. There have already been different approaches to seed the dots on predefined positions on the surface. The most promising approach is the growth of QDs on patterned substrates. In our work we prepared substrates patterned with focused ion beam (FIB) sputtering and laser holography.

Pattern Preparation

For the seeding of QDs, the substrates were patterned using laser holography. With this technique large areas can be exposed in a short time compared to other methods like e-beam lithography. However, in laser holography the resolution that can be achieved is limited by the wavelength of the laser. In our setup we used a He-Cd laser with a wavelength of 325 nm. With this setup patterns with a period as small as 180 nm could be realized. Using subsequent wet chemical or dry etching, the pattern is then transferred into the substrate.

With e-beam lithography, patterns as small as 40 nm in diameter were created. Figure 4 shows a patterned substrate with a period of 100 nm. For the dry etching an Ar sputter process has been employed with an RIE Plasmalab 100. The etch depth is 20 nm.

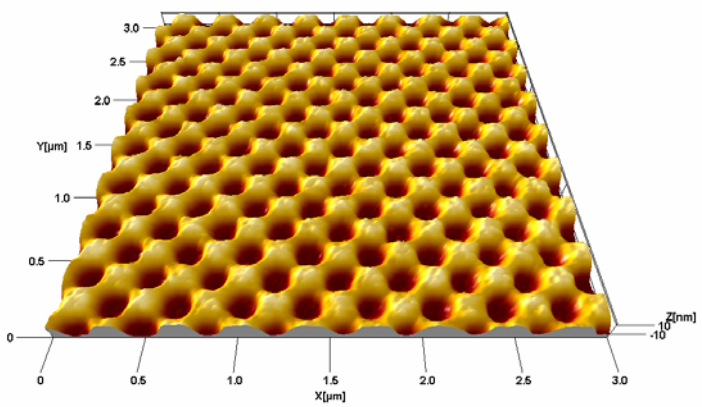

Fig. 4: AFM scan of a patterned GaAs substrate, where the pattern was created using e-beam lithography and Ar sputtering.

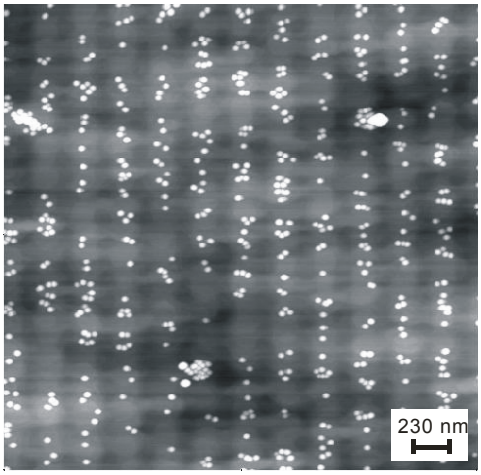

Fig. 5: AFM scan of a patterned substrate with a period of 230 nm overgrown with 20 nm $In_{0.2}Ga_{0.8}As$, 10 nm GaAs and 0.495 nm InAs. Due to preferential nucleation spots created by the template and the InGaAs layer, the dots align according to the pattern.

Overgrowth

Before inserting the samples into the molecular beam epitaxy (MBE) growth chamber, they were carefully cleaned using solvents. Afterwards, they were exposed to an oxygen plasma to remove any residual resist. Finally, an HCl etch was performed to remove the oxide on top. The cleaning process was completed with a rinse under DI water to grow a fresh layer of oxide. Inside the MBE the oxide was thermally removed under an As_4 overpressure. *In situ* reflection high energy electron diffraction (RHEED) was used to monitor the substrate surface. Directly on the pattern 20 nm of $In_{0.2}Ga_{0.8}As$ was grown followed by a 10 nm GaAs buffer layer. The QDs were grown at 510°C with an InAs deposition of 0.495 nm (1.63 ML). Figure 5 shows a typical result with a QD density of 6.8×10^9 cm^{-2} and an average dot height of 3.9 nm. After overgrowth the original depth of the pattern is reduced as the holes are covered with the strained $In_{0.2}Ga_{0.8}As$ layer and the GaAs buffer layer. The pattern together with the layer of InGaAs forms preferential nucleation spots for the QDs and therefore the dots align according to the pattern. Compared to dot densities that can be achieved on unpat-

terned substrates under the same growth conditions, the patterned substrates also show higher dot densities. It is also visible that the size of the template is not small enough to achieve an alignment of one QD per hole. Therefore, other methods like e-beam lithography have to be employed to realize smaller pattern sizes to achieve the ultimate goal of aligning one QD per hole.

FIB Patterning

Maskless patterning of GaAs substrates with ion beams focused to nanometer diameters for subsequent MBE overgrowth has been investigated. Using a focused ion beam offers the advantage that the patterns can be written directly onto the substrate and no lithographic processing is needed. The focused ion beam experiments were performed with a Micrion twin lens FIB system (model 2500) equipped with a Ga liquid metal ion source. The system was operated at an acceleration voltage of 50 kV with a selectable 50 µm beam-limiting aperture corresponding to a beam current of 45 pA. The diameter of the ion beam is 52 nm. The exposure of the holes to the ion beam was varied to achieve different diameters and sputter depths. Patterns with a pitch as small as 200 nm and a depth of the sputtered holes of 30 nm are demonstrated. Shown in Fig. 6 is the cross-section of the FIB sputtered holes. On the bottom of the holes small peaks are visible. As has been shown previously, FIB micro-patterning results in selective sputtering of arsenic, causing Ga-rich precipitations on the surface. For single dot milling these, in principle, mobile precipitations are fixed in the center of the crater. Regarding overgrowth, these precipitations can prevent the growth of crystalline In(Ga)As on the bottom of the holes. Post-exposure annealing followed by wet chemical etching to remove Ga contamination due to ion beam exposure has already shown promising results on silicon substrates and will be further investigated.

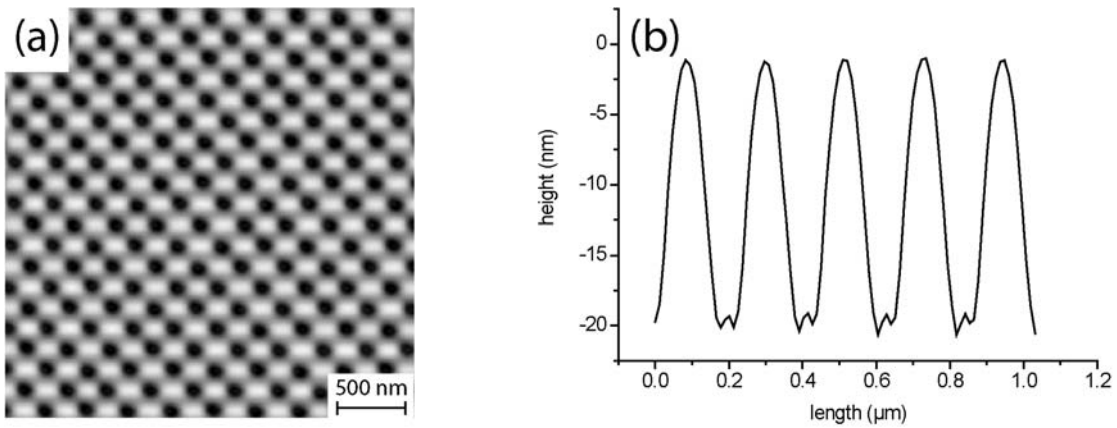

Fig. 6: AFM image (a) and cross-section (b) of a patterned substrate created by FIB sputtering, with a period of 200 nm.

References

[1] G. S. Kar, S. Kiravittaya, M. Stoffel, and O.G. Schmidt, *PRL* **93,** 246103 (2004)

[2] M. Schramboeck, W. Schrenk, T. Roch, A.M. Andrews, M. Austerer, G. Strasser, *Microelectron. Eng.***83***,* 1573 (2006)

Ultrafast Spectroscopy of QD Structures for Mid-Infrared Applications

F.F. Schrey, G. Fasching, T. Müller, G. Strasser, K. Unterrainer

Institut für Photonik und Zentrum für Mikro- und Nanostrukturen
Technische Universität Wien, Gusshausstrasse 25-29, A-1040 Wien

Introduction

The capture and relaxation of carriers in semiconductor quantum dots (QDs) has attracted much attention during the last decade, since a profound understanding of these processes is essential for the development of novel optoelectronic devices. A drastic slow-down of the relaxation compared to higher-dimensional structures has been predicted because of the so-called phonon bottleneck effect. However, it has turned out that a number of scattering processes, including multiphonon emission, electron-electron scattering, and electron-hole scattering can circumvent the phonon bottleneck, leading to very different capture and relaxation times from approximately one to above hundred of picoseconds. This discrepancy is still a major problem when the suitability of QDs for optoelectronic applications as well as for applications in quantum information processing has to be evaluated. Therefore it is essential to study fundamental optical properties of self-assembled InAs quantum dots within a GaAs host matrix or within a GaAs/AlAs quantum well superlattice in all relevant spectral regions from the NIR to the THz.

Experiments

For this purpose, we developed a multi-purpose spectroscopy system that can fulfill the special requirements for ultrafast time-domain spectroscopy in the near- and mid-infrared, while considering the dispersion properties of the short laser pulses as well as highly sensitive detection schemes in order to allow the study of isolated, single quantum dots. Further, this system offers all standard characterization methods for single quantum dot investigations and ensemble experiments such as micro-photoluminescence, photoluminescence excitation and photocurrent spectroscopy.

QD Ensembles

The necessary fundamental studies on QDs are always accompanied by the investigation of quantum dot based mid-infrared photodetectors with and without additional AlAs quantum wells in the GaAs host matrix. Here we developed a suitable model to describe the effects of vertical dot alignment within these structures. From this model, we can correctly predict the spectral photoresponse of such devices based on the growth parameters of the GaAs/AlAs quantum well system and some basic quantum dot parameters such as its exciton ground state energy. Further, it allows predicting and optimizing the polarization characteristics of these devices and explaining the emission spectra of a quantum cascade structure with embedded quantum dots in its active region [1]. As expected, comparison between the model and the experiments indicated a strong influence of the quantum dot potential onto the superlattice structure and vice

versa, the dots energetic spectrum is modified due to the presence of the GaAs/AlAs superlattice [2].

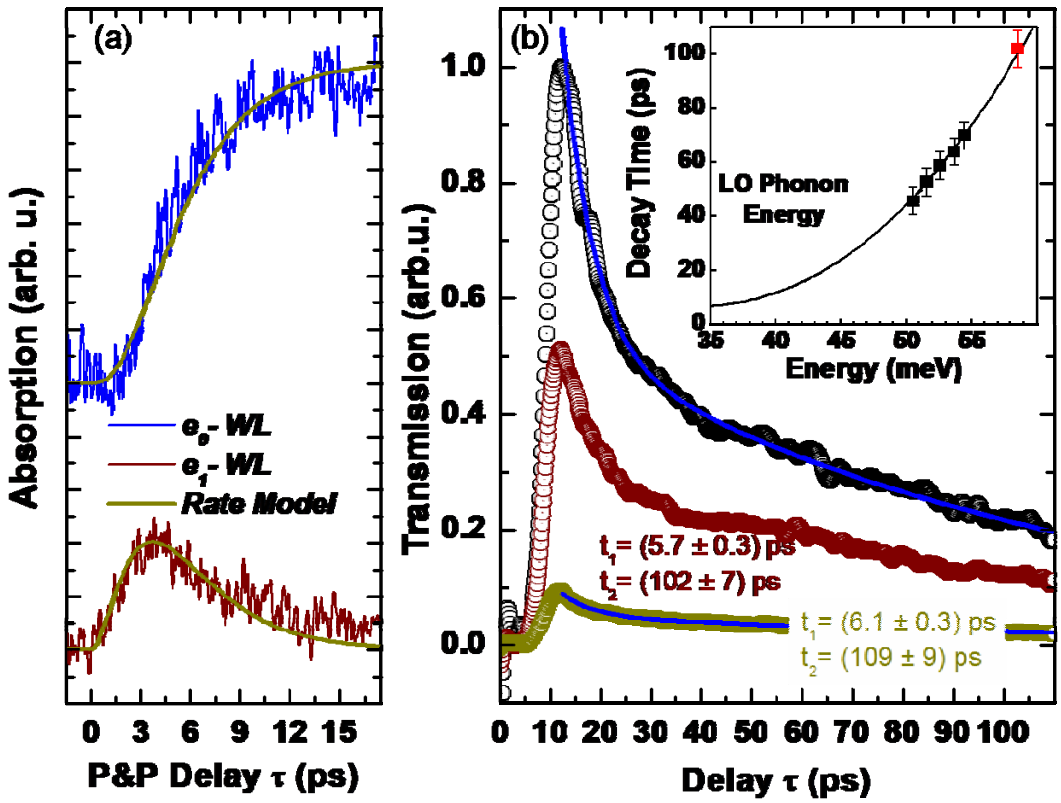

Fig. 1: Time-resolved differential transmission spectroscopy in a NIR pump, THz-probe configuration (a) and in a THz-pump, THz-probe configuration. Method (a) requires optical carrier injection into the QD via the NIR pump pulse, while method (b) traces the decay of excited doping electrons inside the dot. The inset in (b) relates the measured intersublevel decay to a polaronic decay mechanisms as described in [3].

In a parallel approach, we studied the depopulation dynamics of the excited quantum dot exciton and electron states by means of ultrafast interband pump and intersubband probe spectroscopy [4], or by single-color mid-infrared differential transmission spectroscopy on quantum dot ensembles. The related relaxation times vary between only a few and more than hundred picoseconds and strongly suggest extending our investigations to single quantum dots in order to exclude ensemble related effects such as Coulomb interactions within and between different dots [5]. Nevertheless, the obtained excited state lifetimes already point towards a significant influence of phonon related relaxation mechanisms within the quantum dots. Consequently, single quantum dot spectroscopy will also serve as a tool to further characterize these mechanisms. Within these experiments under resonant and non-resonant continuous wave laser excitation, we obtain important information about the energy level redistribution for multi-carrier complexes within a single quantum dot. Photoluminescence excitation studies further reveal and underline possible coupling mechanisms between the discrete quantum dot states and the surrounding matrix via phonons. Therefore, the quantum dot cannot be considered as isolated subsystem within the host matrix, but the variation of the coupling efficiency to different phonon modes for given intersublevel transition within the different dots suggests to further investigate those quantum dots by means of time-resolved spectroscopy for which longer relaxation times might be expected.

QD Ensembles

In a first step we had to evaluate the influence of higher filling states of the single quantum dot intersublevel dynamics. Therefore, we performed emission saturation pump and probe spectroscopy (ESS) for intense pulsed excitation into the wetting layer region of the single quantum dot as shown in Fig. 2 (a) and (b). From a corresponding rate equation model (Fig.2 (c)) we deduced that the main effect of a high carriers density in and around the quantum dot is the shortening of the carrier capture time into the highest discrete quantum dot states, but no significant acceleration of the relaxation process from the excited dot states into the exciton ground state can be observed for these highly excited multi-carrier complexes.

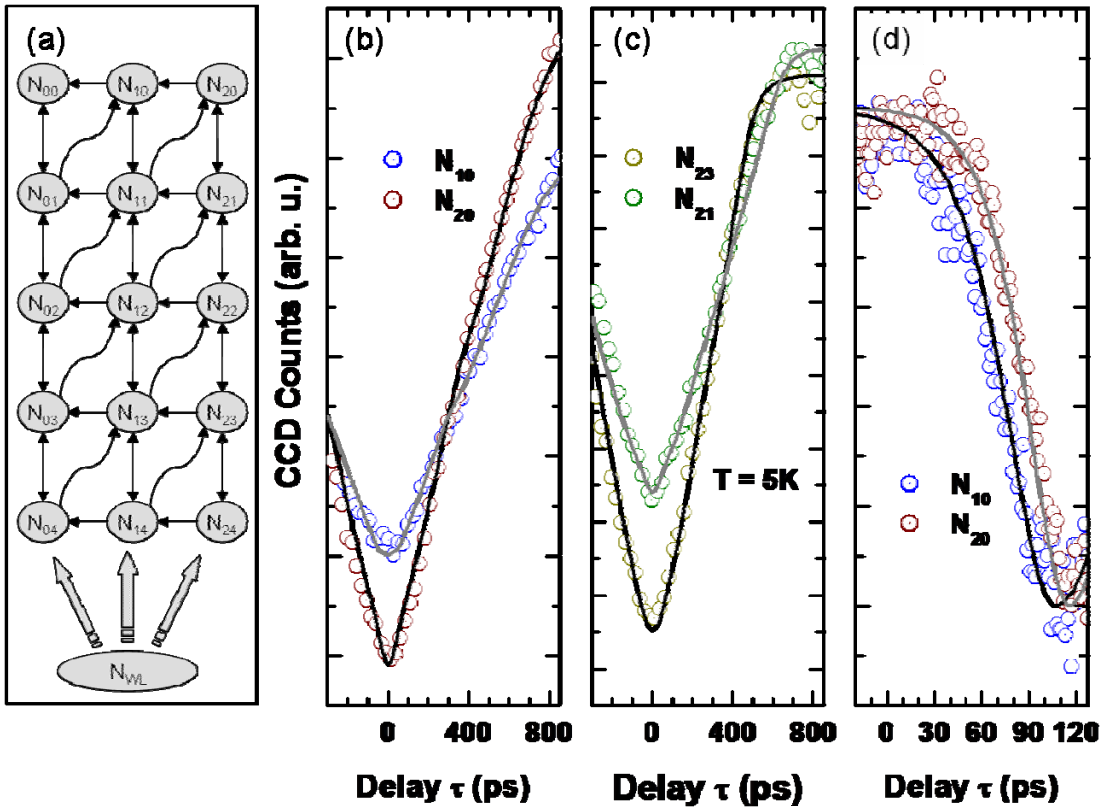

Fig. 2: (a) Scheme of the rate equation system describing the geminate capture and decay of excitons in a single QD. (b) and (c) show the ESS trace of the indicated S-states (N_{10}, N_{20}) and P-states (N_{21}, N_{23}) of a single QD. (d) Interband pump and intersubband probe spectroscopy on the same QD. All experiments lead to intersublevel relaxation times in the range of 60 to 80 ps.

Then we measured the relaxation time from the wetting layer into the exciton ground state by interband pump and intersubband probe spectroscopy, while monitoring the population of the exciton ground state via its electron-hole-pair recombination radiation. The result is shown in Fig. 2 (d). Again we can determine the intersublevel relaxation time between the S- and P-states of the QD to be in the range of several tens of picoseconds. Additionally, to our knowledge, this is also the first time that the influence of ultrafast mid-infrared excitation on the population state of a single self-assembled quantum dot is observed in the time-domain.

Conclusion

As shown in the previous paragraphs, these experiments directly confirm the intersublevel relaxation time to be in the range of several tens of picoseconds, a period that is sufficiently long to use InAs quantum dots in THz related optoelectronic as well as in quantum information processing related applications. Further, the results underline the importance of considering ensemble related effects into the design of QD based devices, since these effects can affect the relaxation times inside the dots strongly. It has to be noted here that until today mostly interband and intraband properties of QDs have been exploited. Our results now strongly motivate to focus also on intersublevel related applications in QDs and QD molecules.

Acknowledgements

This work was supported by the Austrian FWF (SFB ADLIS, SFB IR-ON) and the Austrian Gesellschaft für Mikro- und Nanoelektronik (GMe).

References

[1] F.F. Schrey, T. Müller, G. Fasching, S. Anders, C. Pflügl, W. Schrenk, G. Strasser, and K. Unterrainer, *Physica E* **25**, 271 (2004)

[2] F.F. Schrey, L. Rebohle, T. Müller, G. Strasser, K. Unterrainer, D. Nguyen, N. Regnault, I. Ferreira, and G. Bastard; *Phys. Rev. B* **72**, 155310 (2005).

[3] S. Sauvage, P. Boucaud, R.P.S.M. Lobo, F. Bras G. Fishman, R. Prazeres, F. Glotin, J.M. Ortega, and J.-M. Gérard, *Phys. Rev. Lett.* **88**, 177402 (2002).

[4] T. Müller, F.F. Schrey, G. Strasser, and K. Unterrainer, *Appl. Phys. Lett.* **83**, 3572 (2003)

[5] T. Müller, G. Strasser, and K. Unterrainer, *Appl. Phys. Lett.* **88**, 192105 (2006)

Dislocation-Free GaN/AlGaN Double-Barrier Diodes Grown on Bulk GaN

S. Golka, G. Pozzovivo, W. Schrenk, G. Strasser, C. Skierbiszewski, M. Siekacz, I. Grzegory, S. Porowski

Zentrum für Mikro- und Nanostrukturen, TU Wien, Floragasse 7, A-1040 Vienna, Austria

Introduction

Integrated resonant tunneling diodes (RTDs) are interesting devices for a number of applications, such as ultrafast switches or as components in HF oscillators. The last might be particularly interesting in the GaN/AlGaN system due to its high power handling capability and availability of well performing GaN HEMTs at elevated temperature.

While AlGaN quantum cascade electro-optic devices recently received particular interest, the behavior of such vertical devices is not well understood and their performance greatly lags behind that of horizontal devices. The RTD is a benchmark for any such quantum cascade/intersubband (ISB) device. While epitaxial quality of InGaN/AlGaN could be improved so far that blue laser diodes became possible, the fabrication of RTDs still suffers from instabilities that relate to the large defect density near such heterostructures.

Other ISB devices such as detectors could be realized already. A clear relationship between energetic levels of QW states and the continuum was established by ISB absorption and photovoltage [1] experiments. At the same time results obtained for resonant tunneling [2] are still very scarce and controversial [3]. The observed current-voltage (IV) characteristics exhibited a negative differential resistance (NDR), but only on one-sided and not reproducible. This is likely to be at least partly due to conduction over dislocations [4]. However the recent availability of high pressure grown bulk samples [5] makes fabrication of dislocation free RTDs possible [6].

Experimental

Dislocation free mesas were achieved with the low dislocation density (10^2 cm^{-2}) of bulk substrates and fabrication of single diodes of 6 µm diameter, which is much smaller than in previous studies (40 µm Ref. [2] and 100 µm Ref. [3])

The epitaxial structure was grown by plasma assisted molecular beam epitaxy (PAMBE). On top of a template overgrown by 1 µm of a metal organic chemical vapor deposition (MOVPE) GaN:Si layer the following structure was deposited (starting at substrate): GaN:Si – $Al_{0.7}Ga_{0.3}N$ – GaN - $Al_{0.7}Ga_{0.3}N$ –GaN:Si. Layer thicknesses were 150 – 2 – 2 – 2 – 100 nm respectively. Calculating this structure with a self-consistent Schrödinger-Poisson solver, not taking into account transport, the QW ground state is 0.6 eV above the Fermi level.

Mesas (Fig. 1) were defined by standard UV contact lithography. The irregular and small shape of the bulk samples was overcome by spray coating of 2 µm photoresist. Mesas were then etched in an inductively coupled plasma reactive ion etcher (ICP-RIE) with $SiCl_4$ chemistry. SiN_x (300 nm) was deposited with 300°C plasma enhanced chemical vapor deposition (PECVD) and opened with SF_6 RIE. Evaporated Ti – Al – Ni

– Au (10 – 150 – 35 – 200 nm) annealed at 580°C for 30 s serves as the top contact. Annealing was limited by the thermal resistance/adhesion of the SiN_x.

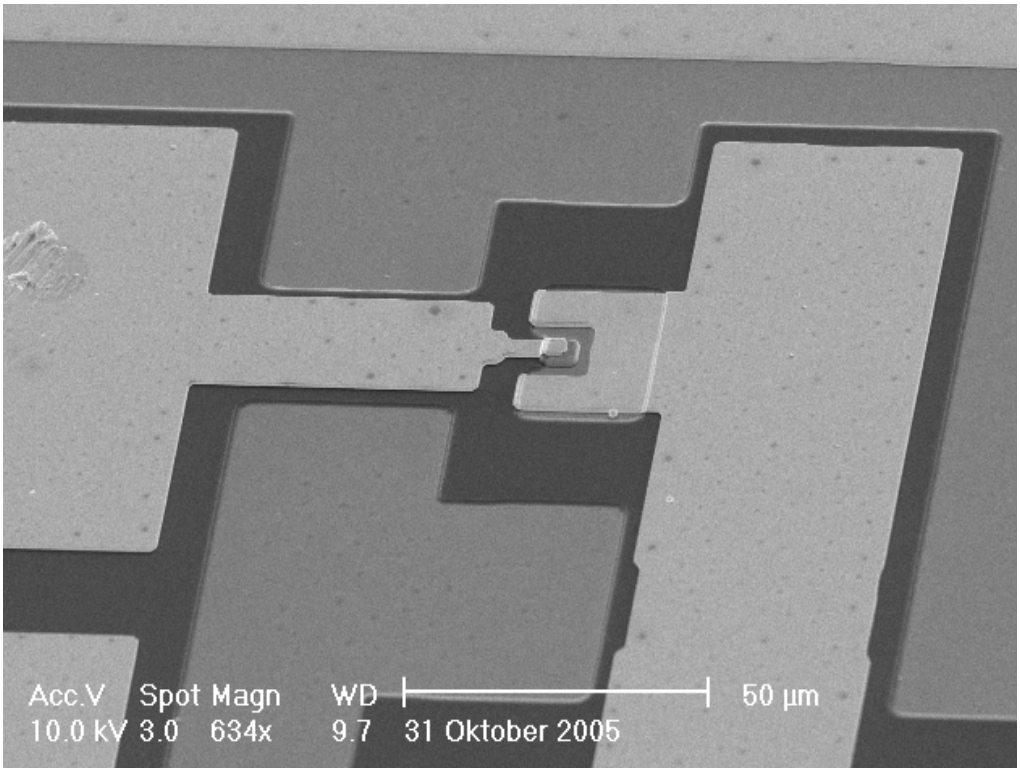

Fig. 1: SEM image of fully processed device with 6 µm diameter and separate bottom contact

Results

Like in studies published earlier [2] we see a fundamental and abrupt change in the IV curve between the first trace on a virgin mesa and the subsequent retrace or any further trace leaving only the exponential background. Contrary, the NDR (seen in 20% of all devices) our IVs consist of multiple data points. The asymmetry in the IVs (voltage applied to top contact) stems partially from the internal polarization fields and partly from the difference between a good ohmic back contact and a Schottky-like top contact. No direct relationship between measurement conditions and shape/position of the NDR has been observed. However, position of the NDR varies randomly between different devices within limits (Fig. 2). The 'hysteresis' that causes this decay is described in more detail in [6].

While in principle a degradation or breakdown of the material could be responsible for such decay, especially concerning the high peak current density in the 10 kA/cm2 range, the same observations in pulsed mode with low duty cycle contradict that assumption.

The position and magnitude of NDR depends mainly on the greatest (previously) applied voltage. After decay the NDR can be restored partly (Fig. 3) by thermal treatment. Such behavior can be explained by a combination of tunneling and electron trapping effects.

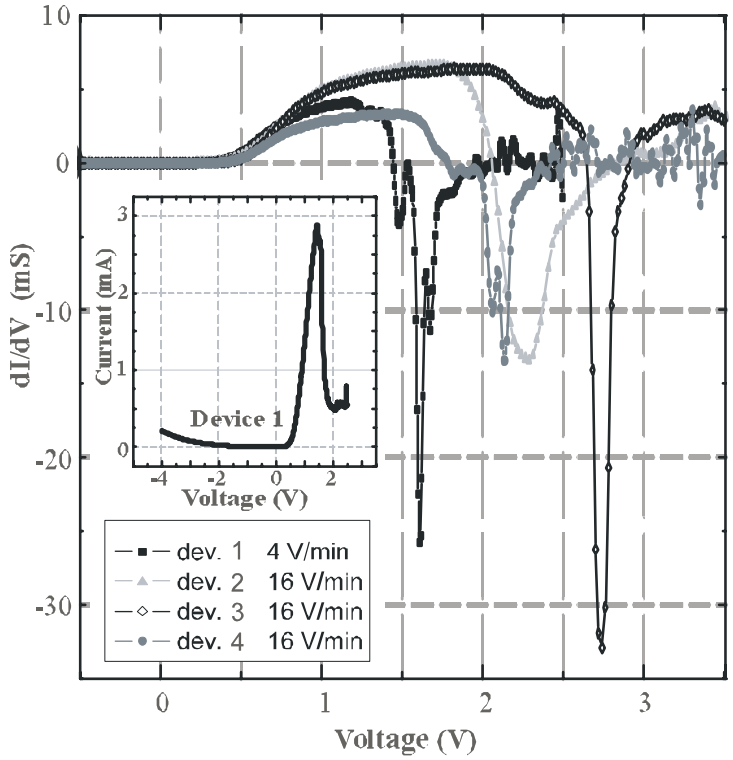

Fig. 2: Differential conductivity dI/dV of four devices all with 6 µm diameter measured at RT. *Inset:* Original IV of device 1.

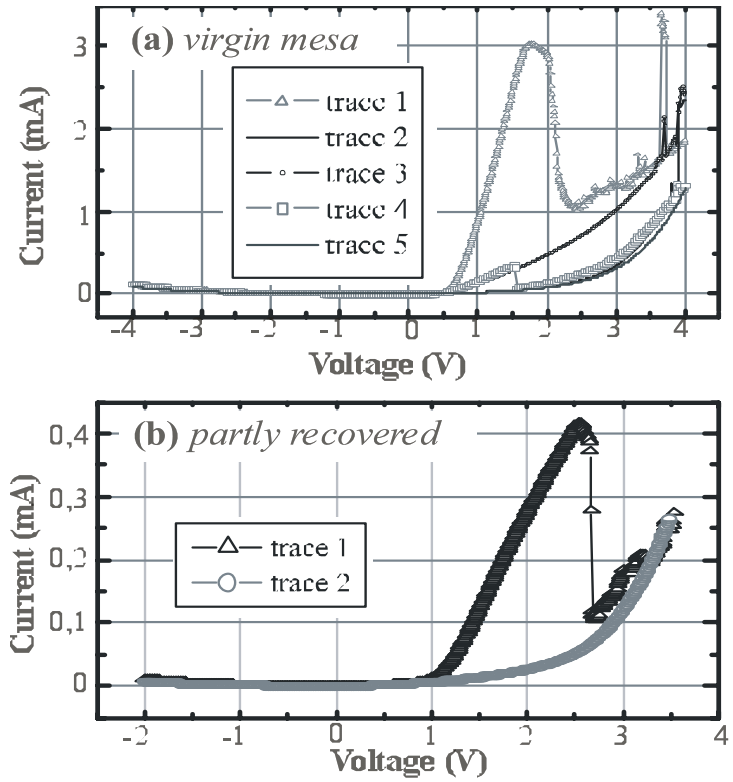

Fig. 3: IV characteristic of a device with d = 6 µm (a) before and (b) after annealing at 350°C in a RTA oven under N_2 atmosphere.

Conclusion

We have shown smooth IVs exhibiting NDR in a voltage interval of ~0.3 V, located in the range 1.2…2.8 V of a GaN based RTD. Decay of this NDR feature after a first measurement and possible recovery by thermal treatment were related to deep electron traps and consequent deformation of the conduction band profile in the double barrier region.

We acknowledge the support by the EU STREP project NITWAVE, the “Gesellschaft für Mikro- und Nanoelektronik” (GMe), and the MNA network.

References

[1] E. Baumann, F. R. Giorgetta, D. Hofstetter, H. Lu, X. Chen, W. J. Scha, L. F. Eastman, S. Golka, W. Schrenk, and G. Strasser, Appl. Phys. Lett. 87, 191102 (2005)

[2] Kikuchi, R. Bannai, K. Kishino, C.-M. Lee, and J.-I. Chyi, Appl. Phys. Lett. 81, 1729 (2002)

[3] E. Belyaev, C.T. Foxon, S.V. Novikov, O. Makarovsky, L. Eaves, M.J. Kappers, and C.J. Humphreys, Appl. Phys. Lett. 83, 3626 (2003)

[4] J.W.P. Hsu, M.J. Manfra, R.J. Molnar, B. Heying, and J.S. Speck, Appl. Phys. Lett. 81, 79 (2002)

[5] C. Skierbiszewski, K. Dybko, W. Knap, M. Siekacz, W. Krupczynski, G. Nowak, M. Bockowski, J. Lusakowski, Z. R. Wasilewski, D. Maude, T. Suski, and S. Porowski, Appl. Phys. Lett. 86, 102106 (2005)

[6] S. Golka, C. Pflügl, W. Schrenk, G. Strasser, C. Skierbiszewski, M. Siekacz, I. Grzegory, and S. Porowski, Appl. Phys. Lett. 88, 172106 (2006)

InAlN/GaN HEMTs: A First Insight into Technological Optimization

J. Kuzmik, D. Pogany

**Institute for Solid-State Electronics, TU Vienna,
Floragasse 7, A-1040 Vienna**

Introduction

AlGaN/GaN HEMTs have been studied extensively as ideal candidates for high frequency and high power applications. However, according to theoretical predictions [1], [2], $In_xAl_{(1-x)}N$/(In)GaN HEMT performance may be superior in respect to AlGaN/GaN HEMTs, primarily because of expected higher two-dimensional electron gas (2DEG) density n_S. That brings high expectations for HEMT drain current (I_{DS}) capabilities. There are no data published on optimization of ohmic and/or Schottky barrier contacts on InAlN, nor any analyses of the relation of material (like μ) and contact parameters to InAlN/GaN HEMT performance. In this paper the role of HEMT parameters on device performance is analysed using an analytical model [2]. The model considers 2DEG channel parameters like n_S, μ and electron saturation velocity v_S, device geometry-dimensions and contact parameters like R_C and φ_B. It is concluded that the increase of the 2DEG mobility is very critical prerequisite for achieving high performance InAlN/GaN HEMT devices.

Experimental

InAlN/GaN lattice-matched layers were grown by MOCVD on sapphire substrates. Free carrier concentration and mobility values were determined at room temperature by Hall technique to be 2 x 10^{13} cm^{-2} and 260 $cm^2V^{-1}s^{-1}$, respectively. HEMT gate length was 1 µm, width 200 µm.

Results

In Fig. 1 we show output characteristics of the processed InAlN/GaN HEMT. The maximal I_{DS} was 0.64 A/mm at V_{GS} = 3 V. The output characteristic show signs of self-heating. This trend is initially visible at V_{GS} = 0 V, as the output resistance starts to increase (with increasing gate bias), and is underlined by a negative differential output resistance at V_{GS} = 2 V. At V_{GS} = 3 V the HEMT dissipated power reaches 7 W/mm with possible temperature of ~ 400 °C [3]. Further channel opening may cause thermal run-away and we terminated the measurement at this power level.

The output and transfer characteristics of the InAlN/GaN HEMT were modeled using the material and geometrical parameter values listed in Table 1. The calculations were performed for increasing V_{GS} until the HEMT open channel condition is reached, i.e. V_{GS} - I_{DS} x R_S = φ_B. At this gate bias, the HEMT open channel drain current I_{DSO} can be considered as the maximal reachable current. As seen on Figs. 2 and 3, good agreement between the experiment and the model is obtained until V_{GS} ~ 0 V. The discrepancy for higher V_{GS} can be explained by self-heating effects, as the model neglects these phenomena. We measured the maximal g_m = 122 mS/mm. The model indicates

that if the self-heating was reduced (such as for SiC substrates), then we may anticipate g_m ~ 165 mS/mm and I_{DSO} ~ 1.35 A/mm.

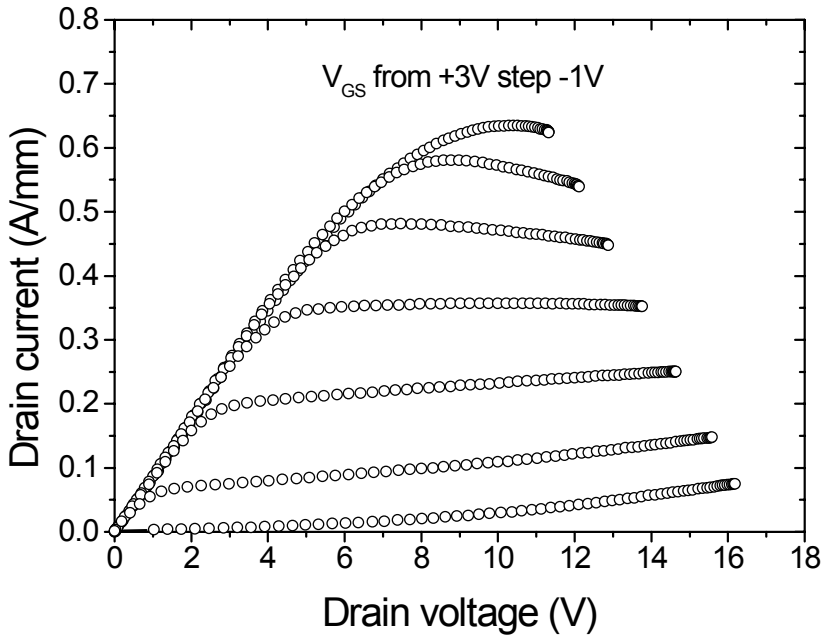

Fig. 1: Output characteristics of 1 μm gate-length InAlN/GaN HEMT. After ref. [5].

Next, using an analytical model, we analyzed three alternative ways of enhancing the InAlN/GaN HEMT capabilities: (i) The source contact resistances is improved by decreasing the source-gate distance to 0.5 μm and by decreasing R_C to 1 Ωmm, (ii) the gate length is shortened to 200 nm, or (iii) the electron mobility is increased to 1000 $cm^2V^{-1}s^{-1}$. Our analytical model does not cover all aspects of complex HEMT performance, nevertheless it can be used as an illustrative tool to describe problems of the state-of-the-art InAlN/GaN HEMTs and suggest future technological improvements. We take I_{DSO} ~ 1.35 A/mm and g_m = 165 mS/mm as reference values for comparisons. Calculated and experimental characteristics are shown in Figs. 2 and 3.

The option (i) brings the enhancement in g_m = 315 mS/mm (up from 165 mS/mm), but no improvement in I_{DSO}. The gate length shortening, option (ii), brings only small improvement in the g_m, but clear improvement in I_{DSO} (2.9 A/mm, up from 1.35 A/mm). The characteristics of 200 nm gate length HEMT (option (ii)) indicate high V_{GS} (in excess of 13 V) needed for the channel to be opened. This was because of the high R_S (caused by the low electron mobility in the source-gate region) coupled with the high I_{DS}. As shown further, the simultaneous and clear improvements of both of investigated DC parameters can be expected only if the electron mobility is increased, option (iii). In this way we may expect g_m = 275 mS/mm and I_{DSO} = 2.8 A/mm. These dramatic improvements can be understood by realizing changes in the character of the electron transport in the HEMT channel if μ is improved. The best HEMT results can be expected if μ fulfils the condition $V_{PO} >> 3\ L_g \times v_{sat}/\mu$ [4], where V_{PO} is the HEMT pinch-off voltage. Only then electrons easily reach the velocity saturation in the channel. Electron mobility values of the state-of-the-art InAlN/GaN 2DEG do not fulfill this condition and thus the InAlN/GaN HEMTs' potential capabilities are not fully exploited. We also calculated estimation for the best device with all improvements (i), (ii) and (iii) simultaneously realized (not shown). For that case we get g_m = 470 mS/mm and I_{DSO} = 3.6 A/mm at V_{GS} = 4.4 V.

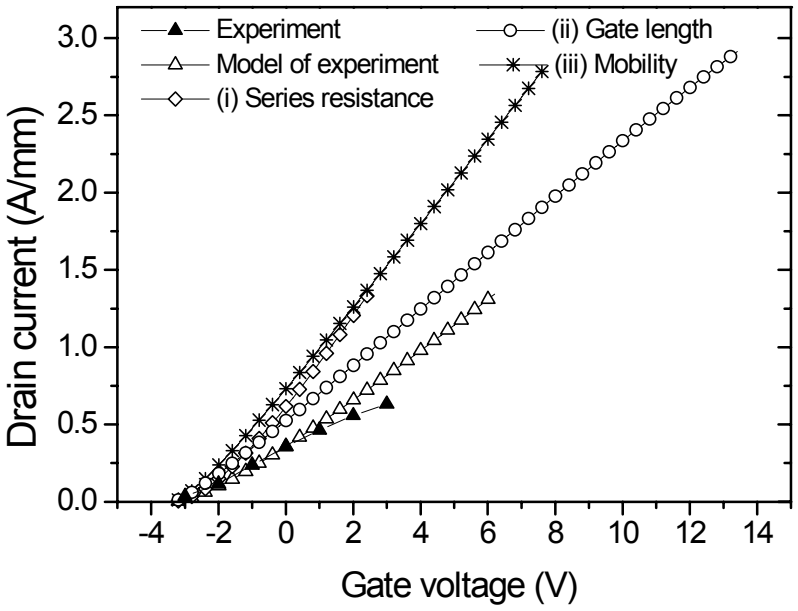

Fig. 2: Experimental and calculated output of InAlN/GaN HEMTs. “Model to experiment” curve is calculated from measured material parameters. Curves (i)-(iii) demonstrate possible enhancement of HEMT characteristics with improvement of (i) series resistance, (ii) gate dimension, and (iii) electron mobility. After ref. [5].

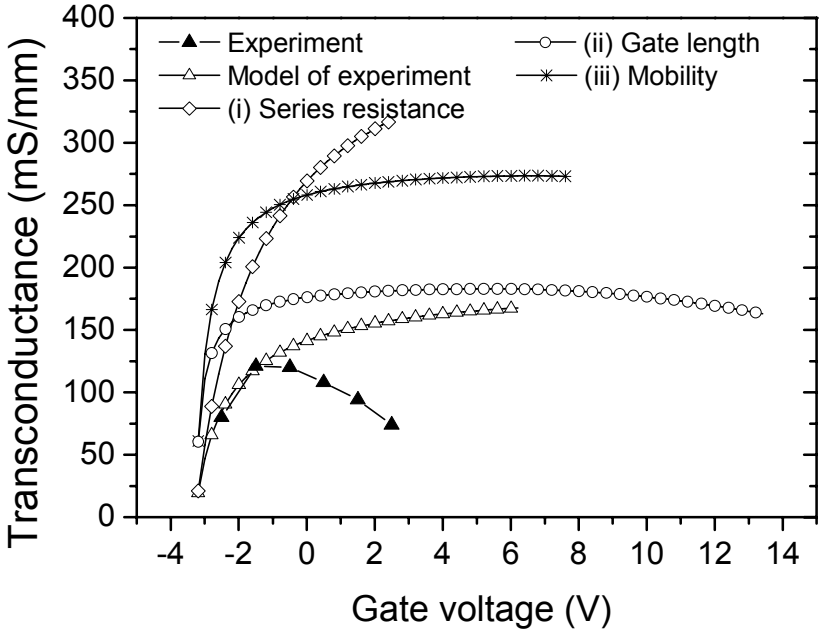

Fig. 3: Experimental and calculated transfer characteristics of InAlN/GaN HEMTs. “Model to experiment” curve is calculated from measured material parameters. Curves (i)-(iii) demonstrate possible enhancement of HEMT characteristics with improvement of (i) series resistance, (ii) gate dimension, and (iii) electron mobility. After ref. [5].

	M. to E.	*(a)*	*(b)*	*(c)*
InAlN thickness (nm)	10			
InAlN permittivity	9.8			
GaN/InAlN cond. band discontinuity (eV)	0.3			
n_S (10^{13} cm^{-2})	2			
φ_{BN}(eV)	0.63			
L_G (μm)	1		0.2	
S-G and G-D distance (μm)	2.5	0.5		
R_C (Ωmm)	1.3	1		
μ (cm^2/Vs)	260			1000
El. saturation velocity v_{sat} (10^5 m/s)	1.2			

Tab. 1 Structural and material parameters used for HEMT modelling. Model of the processed HEMT (Model of experiment) curve was calculated using parameters of the processed HEMT. Improved technological parameters listed in rows (a)-(c) represent changes used for calculating hypothetical devices.

Conclusion

The 1 μm gate-length InAlN/GaN HEMTs exhibited I_{DS} = 0.64 A/mm and g_m = 122 mS/mm. Using an analytical model we demonstrate that the most effective way of improving the state-of-the art InAlN/GaN HEMTs is to enhance the electron mobility in the InAlN/GaN 2DEG channel. Only then the capabilities of InAlN/GaN systems can be fully exploited.

Acknowledgement

This work was supported by EU IST project TARGET (IST 1-507893-NoE) and performed in collaboration with FORTH in Crete (Greece) and EPFL in Switzerland.

References

[1] J. Kuzmík, IEEE Electron Device Lett., Vol. 22, No. 11, pp. 510-512, November 2001.

[2] J. Kuzmík, Semicond. Sci. Technol. Vol. 17, No. 6, pp. 540-544, June 2002.

[3] J. Kuzmík, P. Javorka, A. Alam, M. Marso, M. Heuken, and P. Kordoš, IEEE Trans. On Electron Devices, Vol. 49, No. 8, pp. 1496-1498, August 2002.

[4] M. Shur, “GaAs Devices and Circuits”, Plenum Press, New York and London 1987, p. 319.

[5] Kuzmík, J., Kostopoulos, T., Konstantinidis, G., Carlin, J.-F., Georgakilas, A., and Pogany, D., IEEE Trans. Electron Dev. **53** (2006) 422-426.

Influence of Surface Trapping on Determination of Electron Saturation Velocity in AlGaN/GaN Heterostructures

J. Kuzmik, S. Bychikhin, D. Pogany

Institute for Solid-State Electronics, TU Vienna, Floragasse 7, A-1040 Vienna

Introduction

Investigation of the electron drift and saturation velocity (v_{dr}, v_{sat} respectively) in the AlGaN/GaN high electron mobility transistors (HEMTs) channel is of primary importance. In an *ungated* transfer length method (TLM) test structure, provided that the carrier concentration N is constant along the AlGaN/GaN quantum well (QW) channel and the critical electric field E_{cr} for the electron velocity saturation is not reached (i. e. linear regime), the current I flowing between two TLM contacts can be calculated as:

$$I = e\,N\,W\,\mu\,V / L \qquad (1)$$

where e is the electron charge, W is the channel width, μ is the low field electron mobility, V is the applied voltage and L the TLM contact distance. Monte Carlo simulations [1] have predicted that electrons in GaN at 300 K reach v_{sat} of about 3 x 10^7 cm/s at E_{cr} of about 150 kV/cm. Consequently at high electric fields $E \geq E_{cr} = v_{sat}/\mu$ the current saturates at I_{sat}:

$$I_{sat} = e\,N\,W\,\mu\,E_{cr} = e\,N\,W\,v_{sat} \qquad (2)$$

and v_{sat} can be determined as:

$$v_{sat} = I_{sat} / eNW \qquad (3)$$

Equations (2) and (3) imply that I_{sat} value and v_{sat} determination should be independent on the TLM contacts spacing L. Up to now I-V characterization of ungated AlGaN/GaN QW lead to ambiguous results. In this work we analyze mechanisms of current saturation in AlGaN/GaN TLM structures combining DC and pulsed I-V characterization with Transient Interferometric Mapping (TIM) optical method [2], [3]. We assume that similarly as suggested by Hasegawa *et al.* [4] for semi-insulating GaAs substrate, a charge injection from contacts and charge trapping on the surface may be present in AlGaN/GaN TLM structures. Consequently, the potential of AlGaN surface is not floating as expected for the ungated structure, and we suggest a different current saturation mechanism resembling the operation of gated structures. We show that TIM results also provide explanation of the current saturation mechanism and directly support conclusions of the I-V characterization.

Experimental

AlGaN/GaN structures grown on SiC are used in the experiments. The TLM structure has a width of 100 μm, contact-to-contact distance is L = 2, 4, 8, 16 and 32 μm, and each L is characterized by pulsed (50 ns duration) and DC current-voltage characteristics. In the TIM method the device is scanned from the backside using an infrared laser beam and synchronized with TLP pulses. The phase shift $\Delta\varphi$ of the beam reflected

from the top side is caused by a temperature-induced change in the material refractive index *n* along the beam path and is proportional to dissipated energy in the device [3]. The TIM method allows also to extract the *instantaneous* two-dimensional power density P_{2D} distribution [3]. The P_{2D} map serves to localize the position of the heating source.

Results

Figure 1 shows *I-V* characteristics of the TLM structure under (a) pulsed (t = 50 ns) and (b) DC conditions. DC characteristics show (i) a clear dependence of I_{sat_DC} on L, with the highest I_{sat_DC} values for the shortest L, and (ii) a practically constant V_{sat_DC} ~ 3 V for L = 8 – 32 μm. On the other hand the pulsed characteristics show (iii) higher currents and less pronounced I_{sat_pulse} dependence on L in comparison to DC *I-V*, and (iv) a clear V_{sat_pulse} dependence on L with an almost constant E_{cr} ~5 kV/cm. Provided that (3) is applicable we obtain v_{sat} ~ 1 x 10^7 cm/s at E_{cr} ~10 kV/cm for L = 2 μm in the pulsed regime, down to v_{sat} ~ 1 x 10^6 cm/s at E_{cr} ~ 1 kV/cm for L = 32 μm under DC conditions. Those values are well below values predicted theoretically [1] and observed I_{sat} vs. L dependencies contradict the current saturation mechanism represented by (2) and (3).

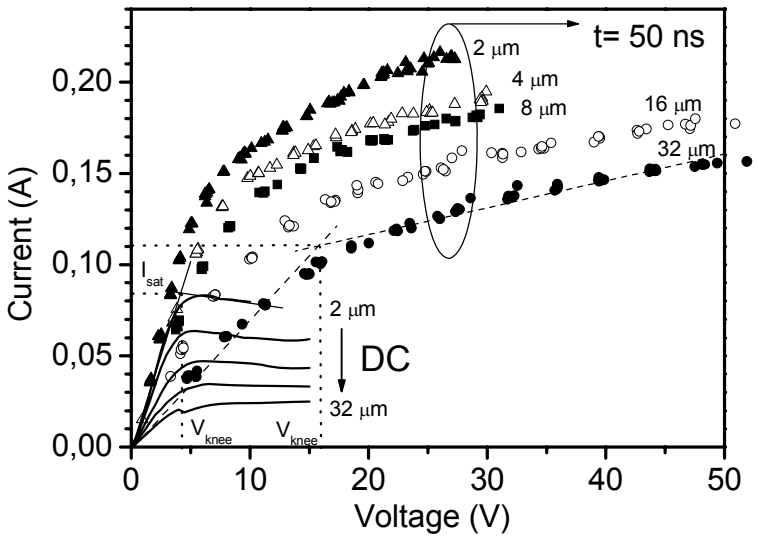

Fig. 1: *I-V* characteristics of the TLM structure with different contact distances in (a) pulsed (t = 50 ns) and (b) DC conditions.

Model

As shown above, none of Equations (1) – (3) describes the current conduction and saturation mechanism in AlGaN/GaN TLM structures properly even if the self-heating effect is considered. We assume that the main reason of that is the wrong assumption of a constant N along the channel. We suggest that the AlGaN surface potential is not floating (i.e. following the channel potential) as expected for the ungated structure, but is biased by a charge injected from contacts. For GaAs it was reported that electrons can be injected from the cathode and subsequently trapped on the surface [4]. Consequently, the potential profile along the semiconductor surface $V_{surface}(x)$ is not linearly increased from the cathode to anode, but is influenced by the presence of the surface charge. If a similar mechanism is assumed for AlGaN/GaN, then $N(x)$ varies along the

channel following changes in the channel-to-surface potential difference $V_{channel}(x)$ - $V_{surface}(x)$. This effect is schematically depicted in Fig. 2, where AlGaN/GaN TLM structures with corresponding distributions of $V_{channel}(x)$, $V_{surface}(x)$ and $N(x)$ are given for the case of (a) floating surface potential and (b) charged surface.

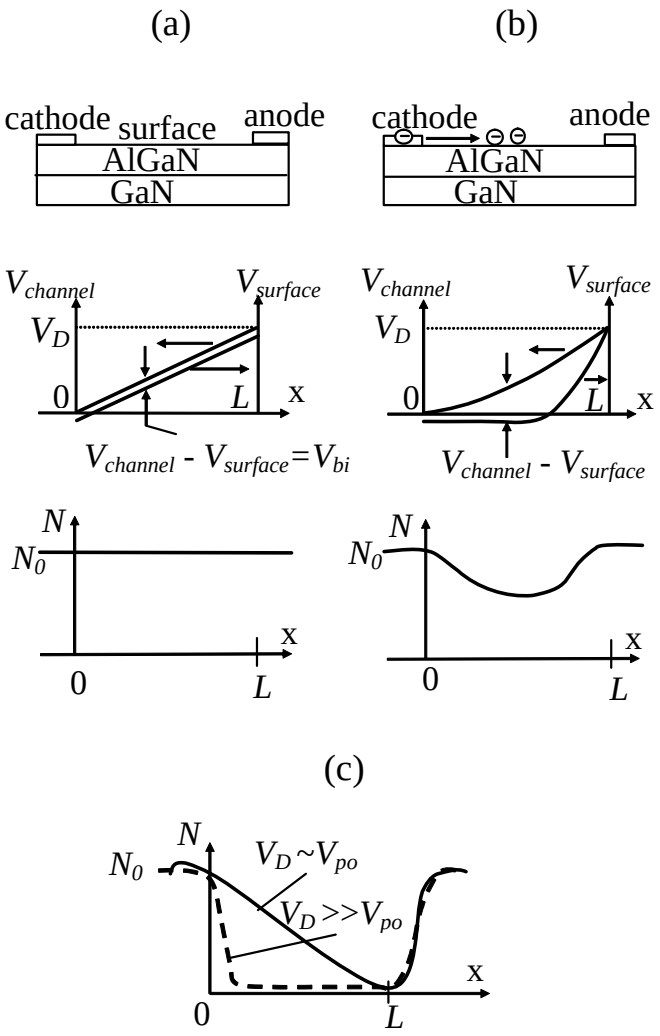

Fig. 2: Model of AlGaN/GaN TLM structures with distributions of $V_{channel}(x)$, $V_{surface}(x)$ and $N(x)$ for (a) floating surface potential, (b) charged surface with a moderate surface depletion and (c) charged surface in the "pinch-off" state. After ref. [5].

As it was shown the surface charge trapping effect seems to be dominant in explaining the differences between the pulsed and DC characteristics, while the thermal effect is marginal. It was reported elsewhere that the time constant of the AlGaN/GaN HEMT thermal transients is in the range of 10^{-7} – 10^{-6} s, while our $I(t)$ transients (not shown) indicate much longer time constants, up to seconds, similarly as reported for the trap-related current collapse.

Figure 3 shows P_{2D} obtained by TIM for structure L = 2 μm, which indicates that the heat is dissipated (and the current flow is located) also below the contacts, i.e. L_H overlaps L by transfer length L_T where the current is crowded. On the other hand, that was not observed by TIM for L = 32 μm. This can be explained by a substantial depletion of the channel in the L = 32 μm structure below the charged free surface, as illustrated by

a dash line in Fig. 2(c) and by restoration of N_0 under the contacts. Thus our TIM observations fully support the proposed model.

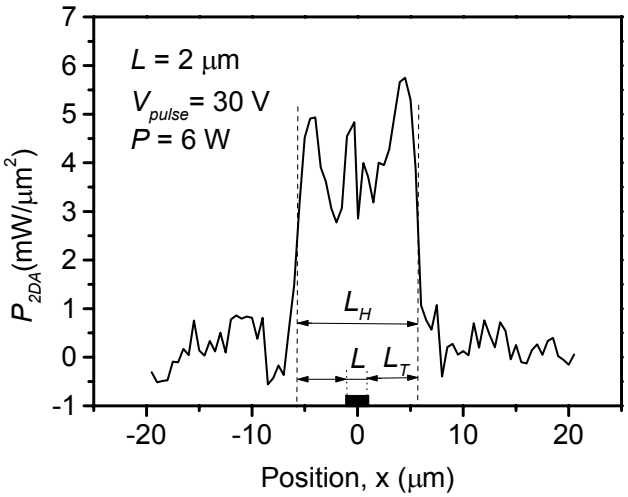

Figure 3 Apparent two-dimensional power density P_{2D} determined by TIM for L = 2 μm. After ref. [5].

Conclusion

We have investigated current conduction and saturation mechanism in AlGaN/GaN ungated TLM structures using electrical and optical mapping methods. We have suggested that the early saturation in TLM *I-V* characteristics and the determined low apparent electron saturation velocity is the consequence of the injection of charges from contacts, surface charging and channel depletion from the side of the surface. A model has been proposed explaining the potential and carrier distribution in the channel and on the AlGaN surface. This model is strongly supported by the TIM measurements, which allow to identify the channel depletion effects.

Acknowledgement

This work was supported by EU IST projects ULTRAGAN (006903) and TARGET (IST 1-507893-NoE) and done in collaboration with IEMN and Thales in France.

References

[1] U. Bhapkar, M. S. Shur, J. Appl. Phys. **82**, 1649 (1997).

[2] D. Pogany, S. Bychikhin, Ch. Fürböck, M. Litzenberger, E. Gornik, G. Groos, K. Esmark, and M. Stecher, IEEE Trans. Electron Dev. **49**, 2070 (2002).

[3] D. Pogany, S. Bychikhin, M. Litzenberger, G. Groos, M. Stecher, Appl. Phys. Lett. **81**, 2881 (2002).

[4] H. Hasegawa, T. Kitagawa, T. Sawada, H. Ohno, Electron. Lett. **20**, 561 (1984).

[5] Kuzmík, J., Bychikhin, S., Pogany, D., Gaquiere, C., and Morvan, E., J. Appl. Phys. **99** (2006) 123720.

Ballistic Electron Emission Microscopy/Spectroscopy on Au/Titanylphthalocyanine/GaAs Heterostructures

S. Özcan[1], T. Roch[1], G. Strasser[1], J. Smoliner[1], R. Franke[2] ,T. Fritz[2]

[1]Institut für Festkörperelektronik, TU Wien, A-1040 Vienna

[2]Institut für Festkörperphysik, TU Wien, A-1040 Vienna

In this article Au/titanylphthalocyanine/GaAs diodes incorporating ultra smooth thin films of the archetypal organic semiconductor titanylphthalocyanine (TiOPc) were investigated by Ballistic Electron Emission Microscopy/Spectroscopy (BEEM/S). Analyzing the BEEM spectra, we find that the TiOPc increases the BEEM threshold voltage compared to reference Au/GaAs diodes. From BEEM images taken we conclude that our molecular beam epitaxial (MBE) grown samples show very homogeneous transmission, compared to wet chemically manufactured organic films. The barrier height measured on the Au- TiOPc-GaAs is $Vb \sim 1.2$eV, which is in good agreement with the data found in reference [1]. The results indicate that TiOPc functions as a p-type semiconductor, which is plausible since the measurements were carried out in air [2].

Introduction

In recent years, organic semiconductors have attracted much interest due to their variety of interesting optical, electrical and photoelectric properties. Photo- and electroactive organic materials have been the subject of recent attention including organic semiconductors, organic light emitting diodes [3], [4], organic field effect transistors [5], [6], or photovoltaic devices [7], [8]. In addition, organic semiconductors are already widely used in xerography, plate making printings and laser printers. Physicists and chemists have focused on the charge transfer phenomena of organic molecules and polymer organic semiconductors in the field of organic solar cells during the past decade. Besides these applied aspects there are important features motivating basic research, namely the interface properties between semiconductors and organic films, e.g. the deformation of the bandstructure at the interface.

Experimental

Ballistic-electron-emission microscopy (BEEM) [9], [10] is a three terminal extension of scanning tunneling microscopy (STM) [11], [12], where electrons tunnel between the STM tip and a thin Au film evaporated on a semiconductor surface such as Si or GaAs. If the electron energy is high enough to overcome the Schottky barrier height at the metal-semiconductor interface the electrons can penetrate ballistically into the semiconductor. This causes a current, which is measured with the third electrode on the backside of the sample. By sweeping the applied tip voltage BEEM current spectra can be obtained. By mapping the BEEM current for a constant tip bias while scanning the sample surface, images can be taken with a spatial resolution of about 1 nm. Over the last two decades BEEM became a well-established technique to determine Schottky

barrier heights (SBH) and subsurface band offsets. An overview of this technique can be found in detail [13] – [15]. To guarantee good internal sample resistance and optimized BEEM signals, molecular beam epitaxial (MBE) grown GaAs samples were used as substrates. In detail, low doped (ND ~ 1 x 10^{16} cm^{-3}) GaAs layers (d ~ 1µm) were grown on an n+-wafer. On these substrates, TiOPc-films (d ~ 6 monolayers) were grown with organic MBE. Finally, a 7 nm Au layer was evaporated on top of it.

Results and Discussion

Figure 1(a) shows the topographic STM image and Fig. 1(b) the corresponding BEEM image of our Au/TiOPc/GaAs sample. The BEEM image was obtained simultaneously at a tip bias (V_t) of 1.4 V and a tip current (I_t) of 5 nA, with a scan area of 500 nm x 500 nm. The STM constant current image shows the typical or characteristic granular structure of Au. In the corresponding BEEM image, brighter areas indicate an enhanced electron transmission. Features visible in the BEEM image correlate exclusively with the granular structure and the topographic features of the Au-film and can not be correlated to the organic film underneath.

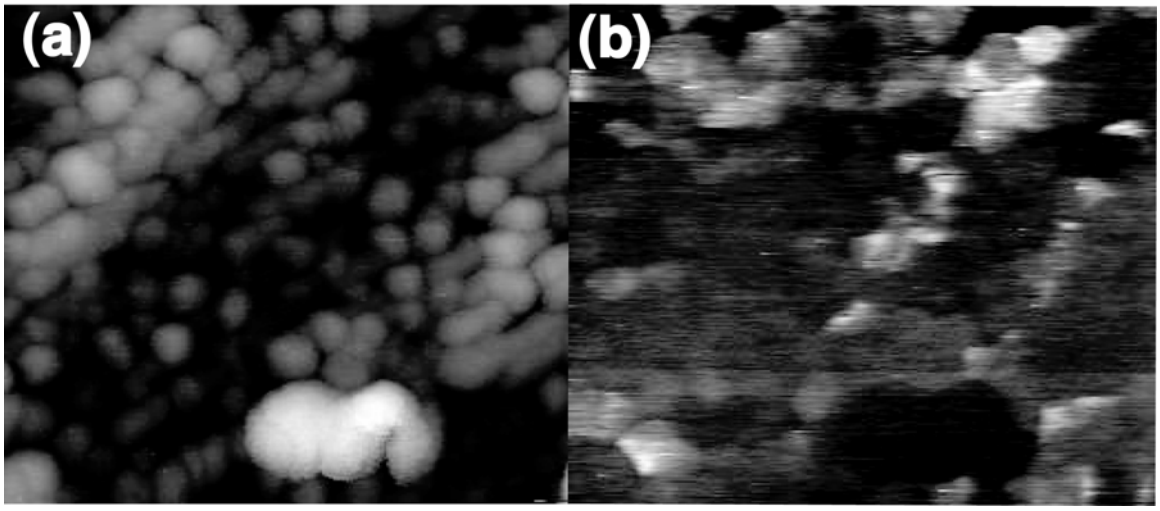

Fig. 1: (a) STM topographic image of Au/TiOPc/GaAs heterostructure, recorded at T = 300 K, I_t = 5 nA, V_t = 1.4 V. (b) Corresponding BEEM image (recorded simultaneously with the STM image, color scale corresponds to 0 . . . 1 pA .

To investigate the transmission behavior of TiOPc, we systematically measured ballistic electron spectra on various positions of our sample.

To extract the barrier height, i.e. the onset voltage, from the measured data, we use a quadratic power law fit (see, e.g. [13]). The Bell-Kaiser model was not used because already the straightforward power law, despite of its simplicity, fits our data very well and is completely sufficient for our purposes. The barrier height values gained from the power fit are 1.24 eV and 1.18 eV for sample A and B. The histograms of the two samples are in Fig. 2 and 3. We measured an effective barrier height of Au/TiOPc/GaAs. It must be pointed out that at present, we can not decide if the measured barrier height is the barrier of the Au-TiOPc interface or the barrier of the TiOPc-GaAs interface or a combination of both. It is clear that is not the Schottky barrier height of Au/GaAs interface, because the onset we measured is significantly higher then 0.9 eV.

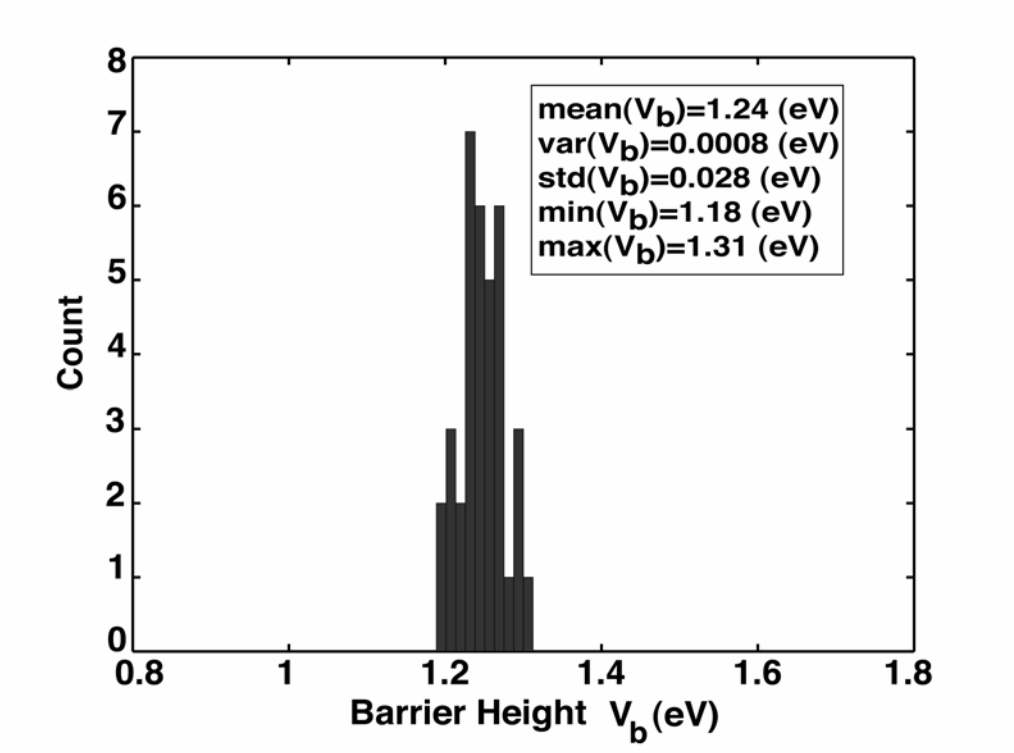

Fig. 2: Histogram of the measured barrier height of Au/TiOPc/GaAs (sample A).

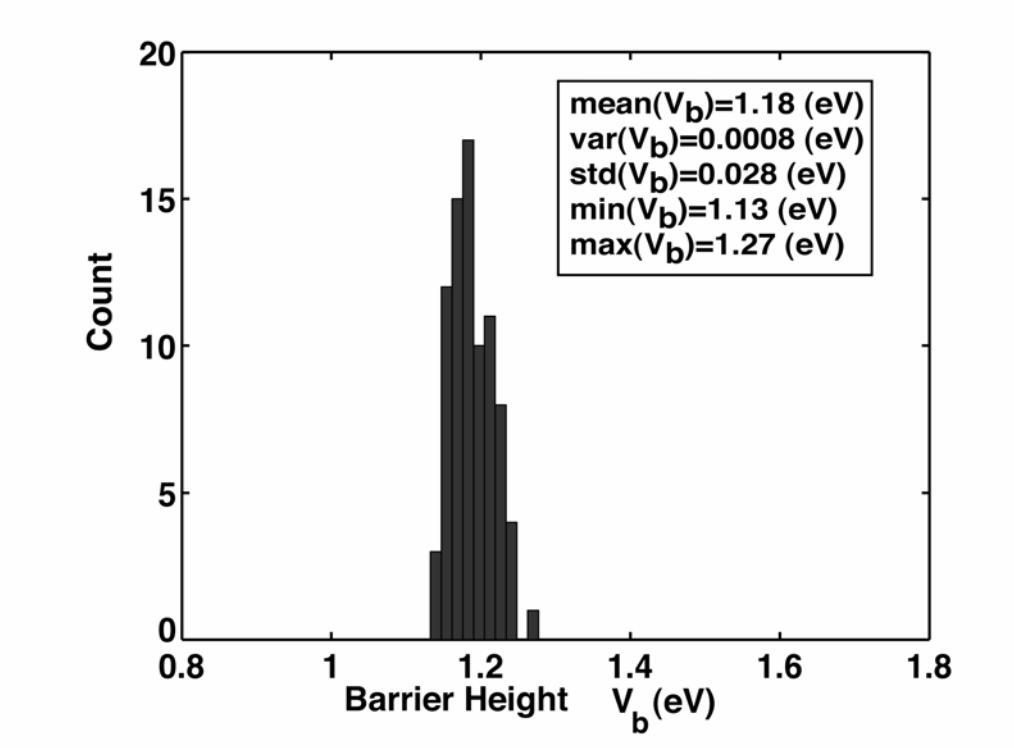

Fig. 3: Histogram of the measured barrier height of Au/TiOPc/GaAs (sample B).

The solid line in Fig. 4 shows averaged BEEM spectra (I_t = 5 nA, T = 300 K) and the dashed line is its first derivative taken of over 100 individual BEEM spectra. The spec-

tra are taken over a voltage-range of 0.8 to 2.3 V. Above the onset several features are visible, three steps at the points: 1.34, 1.52 and 1.61 V. The same behavior of metal-organic interfaces was also found in [16] – [18]. Besides these features there are two significant peaks at 1.7 and 1.85 V. Above 2.3 V the data were not reliable, because of the increased signal to noise ratio.

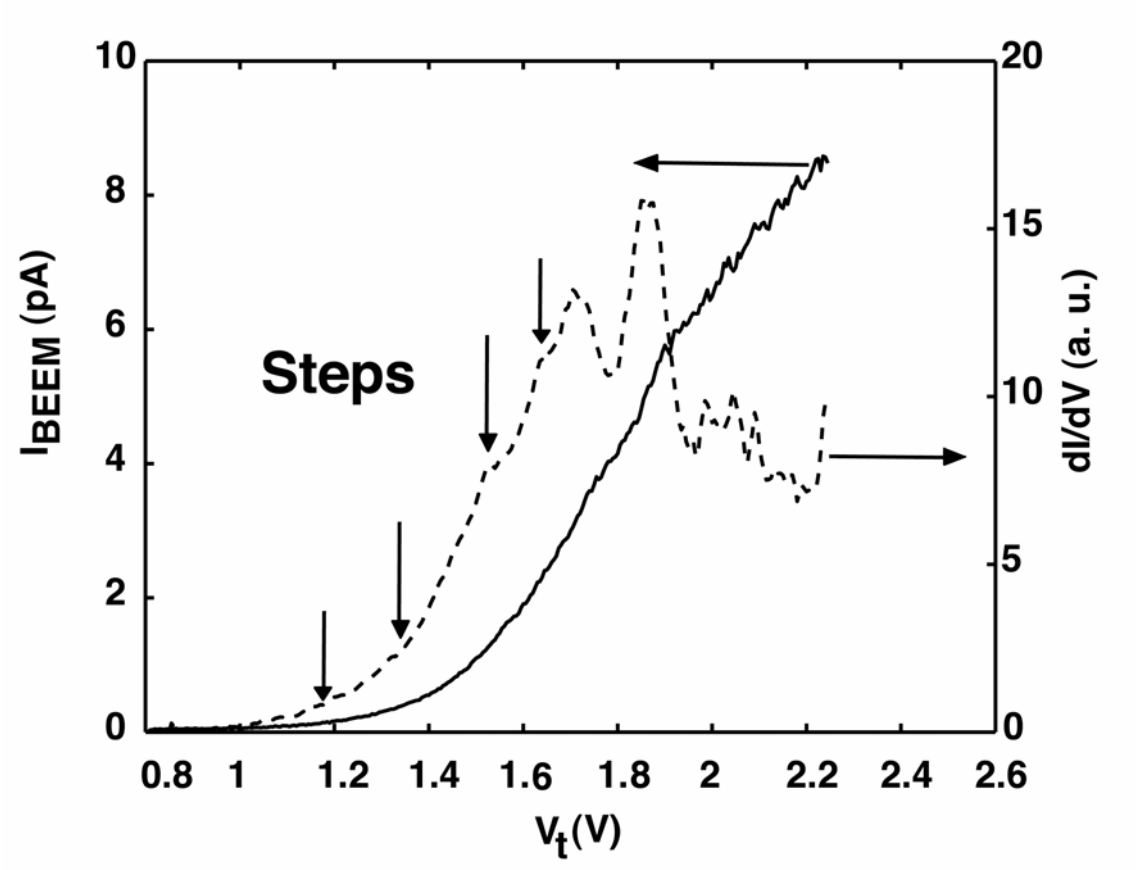

Fig. 4: Averaged BEEM spectra (solid line) and its first derivative (dashed line) from Au/TiOPc/GaAs. Multiple features are clearly visible in the first derivative.

Conclusion

Due to the BEEM images, it can be concluded that the samples are very homogeneous, in comparison to wet chemically manufactured organic films. All features visible in the BEEM images of our samples correlate exclusively with the granular structure and the topographic features of the Au-film and cannot be correlated to the organic film underneath. Analyzing the BEEM spectra we find that the TiOPc increases the BEEM threshold voltage compared to reference Au/GaAs diodes, which was also found in [19], where a BEEM study on a Au/Molecule/n-GaAs diode was done. The barrier height measured on the Au-TiOPc-GaAs is V_b ~ 1.2eV, which is in good agreement with the data found in references [1]. The results indicate that TiOPc functions as a p-type semiconductor, which is plausible since the measurements were carried out in air [2]. In addition, the derivative of the BEEM spectra shows multiple features in the energy regime above the LUMO level [2]. Possible origins of these features are currently under investigation.

Acknowledgments

The work presented here was financially supported by ”Fonds zur Förderung der wissentschaftlichen Forschung” (FWF), Project No. P16337N08 and the ”Gesellschaft für Mikro- and Nanoelektronik” (GME).

References

[1] T. Nishi, K. Tanai, Y. Cuchi, M. R. Willis, and K. Seki *Chem. Phys. Lett.*, vol. 414, pp. 479–482, 2005.

[2] K. Walzer, T. Toccoli, A. Pallaori, R. Verucchi, T. Fritz, K. Leo, A. Boschetti, and S. Iannotte *Surf. Scie.*, vol. 573, pp. 346–358, 2004.

[3] S. A. Jenckhe and J. A. Osaheni *Science*, vol. 265, p. 765, 1994.

[4] G. Yu, J. Gao, J. C. Hummelen, and A. J. Heeger *Science*, vol. 270, p. 1789, 1995.

[5] A. Dodabalapur, Z. Bao, A. Makhija, G. Laquindanum, V. R. Raju, Y. Feng, E. Katz, and J. Rogers *Appl. Phys. Lett.*, vol. 73, p. 142, 1998.

[6] C. J. Drury, C. M. L. Mutsaers, C. M. Hart, and D. M. Leeuw *Appl. Phys. Lett.*, vol. 73, p. 108, 1998.

[7] C. W. Tang *Appl. Phys. Lett.*, vol. 48, p. 183, 1986.

[8] T. Tsuzuki, Y. Kuwabara, W. Noma, Y. Shirota, and M. R. Willis *Jpn. J. Appl. Phys.*, vol. 35, p. 4, 1996.

[9] W. J. Kaiser and L. D. Bell *Phys. Rev. Lett.*, vol. 60, p. 1408, 1988.

[10] L. D. Bell and W. J. Kaiser *Phys. Rev. Lett.*, vol. 61, p. 2368, 1988.

[11] G. Binning, G. Rohrer, C. Gerber, and E. Weibel *Phys. Rev. Lett.*, vol. 49, p. 57, 1982.

[12] G. Binning, G. Rohrer, C. Gerber, and E. Weibel *Phys. Rev. Lett.*, vol. 50, p. 120, 1983.

[13] M. Prietsch *Phys. Rep.*, vol. 253, p. 163, 1995.

[14] V. Narayanamurti and M. Kozhevnikov *Phys. Rep.*, vol. 349, p. 447, 2001.

[15] J. Smoliner, D. Rakoczy, and M. Kast *Rep Prog. Phys.*, vol. 67, p. 1863, 2004.

[16] C. Troadec, D. Jie, L. Kunardi, S. J. O’Shea, and N. Chandrasekhar *Nanotech.*, vol. 15, p. 1818, 2004.

[17] C. Troadec, L. Kunardi, and N. Chandrasekhar *Appl. Phys. Lett.*, vol. 86, p. 072101, 2005.

[18] L. Kunardi and C. Troadec *J. Chem. Phys.*, vol. 122, p. 204702, 2005.

[19] W. Li, K. L. Kavanagh, C. M. Matzke, A. A. Talin, F. L´eonard, S-Faleev, and J. W. P. Hsu *J. Phys. Chem. B*, vol. 109, p. 6252, 2005.

Technology of InAlN/(In)GaN-Based HEMTs

G. Pozzovivo[1], S. Golka[1], K. Cico[3], J. Kuzmík[1], W. Schrenk[1], G. Strasser[1], D. Pogany[1], J.F. Carlin[2], M.M.Gonschorek[1], N. Grandjean[1] and K. Flohlich[1]

[1] Institute for Solid-State Electronics
TU Vienna, Floragasse 7, 1040 Vienna, Austria

[2] Institute of Quantum Electronic and Photonics,
Swiss Federal Institute of Technology/Ecole Polytechnique Federale,
Lausanne EPFL, CH 1015 Switzerland

[3] Institute of Electrical Engineering Slovak Academy of Science,
842 39, Bratislava, Slovakia

Introduction

InAlN/GaN-based HEMTs are excellent candidates for high power and high frequency applications, primarily because of the very high polarization-induced two-dimensional electron gas (n_{2DEG}) in the channel [1]. Therefore $In_xAl_{(1-x)}N$/(In)GaN performance is predicted to be superior in respect to AlGaN/GaN HEMTs. That allows obtaining higher drain saturation current and higher power. One of the most important factors that limits the performance and reliability of III-Nitride high electron mobility transistors (HEMTs) is a high gate leakage current. One way to overcome it is an introduction of an oxide layer under the gate contact. On the other hand AlGaN/GaN-based HEMTs are known to suffer from the trapping effects related to the surface states.

In this work we fabricate and investigate InAlN/GaN HEMTs with and without Al_2O_3 oxide under the gate.

Experimental

$In_xAl_{(1-x)}N$/AlN/GaN (x=0.17) heterostructures were grown by Metal Organic Chemical Vapor Deposition (MOCVD) on sapphire substrates. Free carrier concentration and mobility values of the 2D electron gas (2DEGs) were determined at room temperature by Hall measurements to be $3.0e^{13}$ cm^{-2} and 815 $cm^2V^{-1}s^{-1}$, respectively.

Standard photolithographic and lift-off techniques were used for processing the HEMT structure. Initially, the mesa region had been defined by reactive-ion etching (RIE) using a photoresist mask. $SiCl_4$ had been used as gas to etch 120 nm. The ohmic contact metallization [1] consisted of Ti/30 nm, Al/200 nm, Ni/40 nm, Au/50 nm. Just before deposition, samples were dipped into diluted HCl. Rapid thermal annealing (RTA) was performed in N_2 atmosphere for 120s at the annealing temperature. Various temperatures from 500 °C to 900 °C were tested and an optimized annealing temperature for device processing at 700 °C has been found. For the Schottky barrier contact we used Ni/30nm, Au/150 nm [1]. Prior to deposition the sample was etched in HF:HCl:H_2O 1:1:10 solution for 20 s. Furthermore, to reduce the leakage current, we are investigating the growth of Al_2O_3 and the performance of Al_2O_3/GaN MOS contacts. Al_2O_3 was grown in an AIXTRON triJet liquid precursor system at 600 °C using precursors of aluminium acetylacetonate dissolved in toluene. Various surface pre-treatments prior to

Al_2O_3 deposition will be discussed in terms of device performance. Al_2O_3 has been etched using Ar. The pressure and the V_{bias} were set at 15 mTorr and 300 V, respectively. Principal schemes of investigated structures are shown in Figure 1.

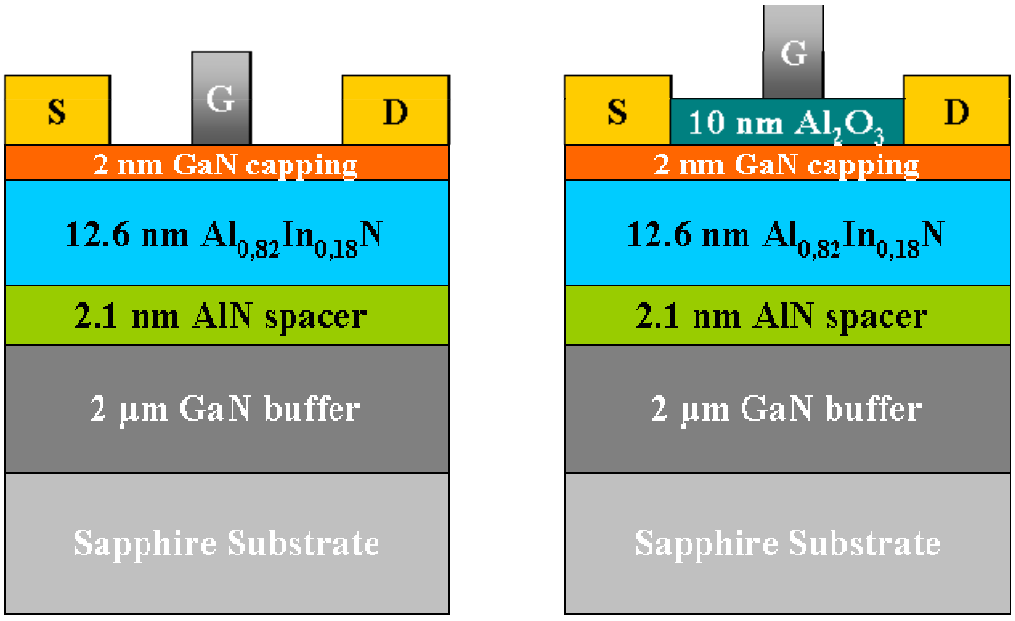

Fig. 1: Schematic cross section of GaN/InAlN/AlN/GaN with and without 10 nm AlO_2

Results

Significant leakage current reduction (2 orders of magnitude less) on MOS (Al_2O_3/Ar) was observed when compared with a reference Schottky barrier contact (Fig. 2). A comparable leakage current was found for MOS with different pre-treatment.

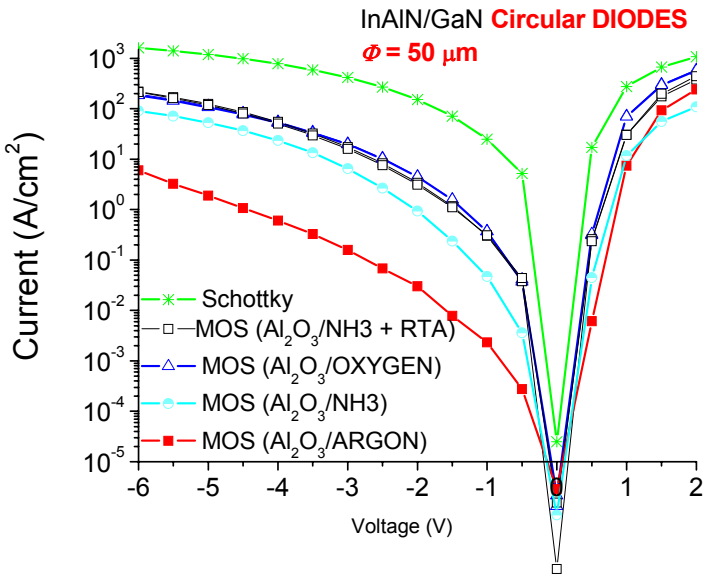

Fig. 2: Gate leakage current of MOS compared with the Schottky structure.

In Fig. 3 we show DC and Gate Lag (GL) pulsed (200 ns length) output characteristics of the InAlN/AlN/GaN HEMT. Clearly no Gate Lag effect can be seen. We assume that AlN insertion may decrease or even revert the electric field in the InAlN without affecting the n_{2DEG}. We prevent the potential energy from rising and thus our approach may eliminate surface state generation *during* InAlN growth. That may explain the reduction of the current collapse for InAlN/AlN/GaN HEMTs.

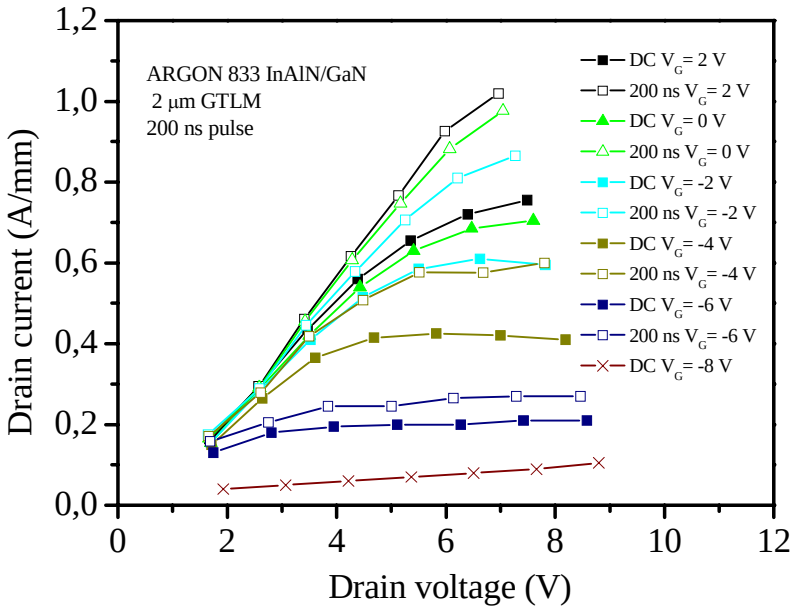

Fig. 3: DC and Gate Lag pulsed characteristics of InAlN/AlN/GaN HEMT.

I-V characterization techniques were used to determine the intensity of the electrical field at oxide breakdown which was found to be 5,5 MV/cm. 1.5 A/mm drain current at V_{GS} = 2V has been measured for 2 µm gate length MOSHEMTs (Fig. 4), and 1.4 A/mm for Schottky HEMTs (Fig. 5).

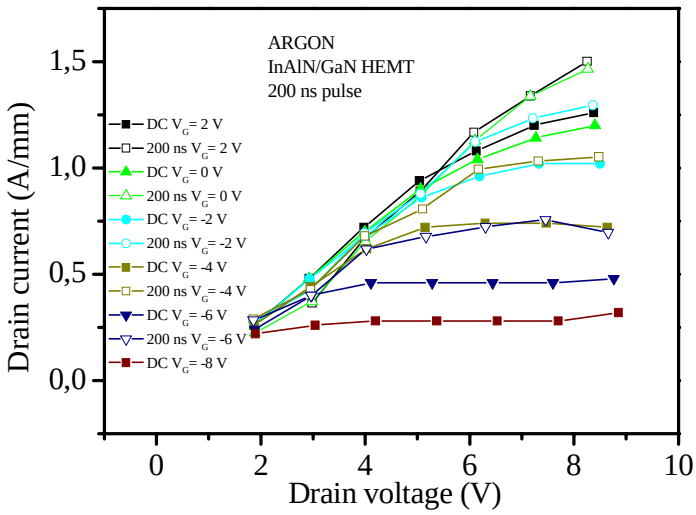

Fig. 4: I_D-V_{DS} characteristics of 2µm gate length InAlN/GaN MOSHEMT with Ar pre-treatment. V_{GS} swept from -8 to 2 V with -2 V step.

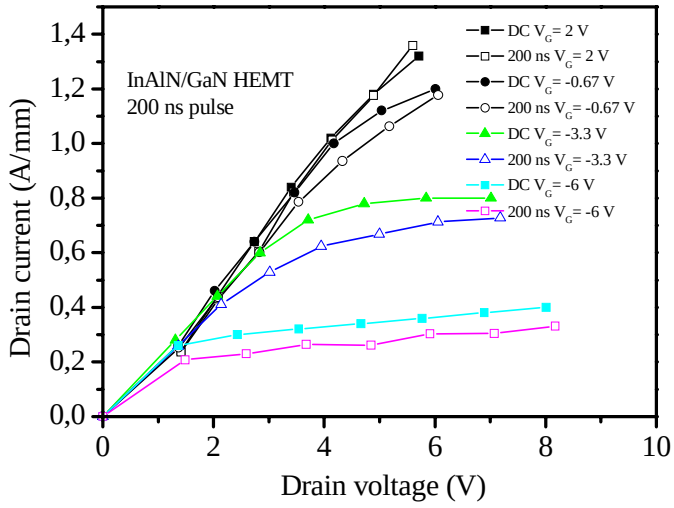

Fig. 5: I_D-V_{DS} characteristics of 2 µm gate length InAlN/GaN HEMT. V_{GS} swept from -8 to 2 V with -2 V step.

Conclusion

In conclusion we described technology and performance of InAlN/GaN MOS HEMT. We show that GaN-based MOS HEMTs (Al_2O_3/Ar) show a reduction of the gate leakage current of two orders of magnitude. For practical application point of view it is necessary to reduce this value further. The important result is that in these devices there is not gate lag effect.

Acknowledgement

This project was supported by EU IST project ULTRAGAN (006903).

References

[1] J.Kuzmík, A. Kostopoulos, G. Konstantinidis, J.F. Carlin, A. Georgakilas, D. Pogany, “InAlN/GaN HEMTs: a first insight into technological Optimization,” *IEEE Transaction on electron devices.,* vol.53, no. 3, pp. 422-426, March 2006.

Comparative Study on the Impact of TiN and Mo Metal Gates on MOCVD-Grown HfO_2 and ZrO_2 High-κ Dielectrics for CMOS Technology

S. Abermann[1], G. Sjoblom[2], J. Efavi[3], M. Lemme[3], J. Olsson[2], E. Bertagnolli[1]

[1] Institut für Festkörperelektronik, Technische Universität Wien, A-1040 Wien, Austria

[2] Solid State Electronics Division, Uppsala University, SE-752 37 Uppsala, Sweden

[3] Advanced Microelectronic Center, Aachen, AMO GmbH, 52074 Aachen, Germany

Introduction

The reduction of the equivalent oxide thickness (EOT) of the gate oxide has emerged as one of the most difficult tasks addressing future CMOS technology. In order to overcome gate tunneling, the introduction of so-called high-κ materials will be necessary [1]. Hafnium dioxide, HfO_2 [2], zirconium dioxide, ZrO_2 [3], and their silicates are assumed to be the most promising candidates to fulfil the crucial demands necessary for a successful integration of high-ķ dielectrics into CMOS devices.

Along with the introduction of high-κ dielectrics, metal gates are anticipated to be introduced [1] to circumvent polysilicon-gate depletion [4] and high gate-resistance. *Mid-gap-metal* and *dual-work-function gate technology* are the two main concepts addressing the implementation of metal gates. Whereas TiN is a promising candidate to be applied as mid-gap metal gate [5], Mo is a suitable candidate for a single-metal, tunable dual-work-function technology [6].

By this work, we present a comprehensive study on Mo- and TiN MOS capacitors, including MOCVD-deposited ZrO_2 or HfO_2 as gate isolator, and the impact of annealing on slow and fast interface traps.

Experimental

As substrates we used boron-doped (100)-silicon wafers with a resistivity of 0.04 – 2.0 Ωcm. The substrates were subjected to a modified RCA-clean and a finalizing HF-dip immediately prior to deposition. ZrO_2 and HfO_2 thin films were deposited by MOCVD in a horizontal hot-wall reactor equipped with a bubbler system. Post-deposition annealing (PDA) of the samples was done in forming gas atmosphere (FGA) at 650°C. Subsequently, ~100 nm thick gate metals – in which the gate metal patterning was done by a lift-off process – were deposited on the high-κ dielectrics without capping to complete metal-oxide-semiconductor (MOS) capacitors. Finally, post-metallization annealing (PMA) in FGA and in some cases additionally high temperature annealing (RTA) in N_2 atmosphere has been applied.

Capacitance-Voltage (C-V) and Current-Voltage (I-V) characterizations have been performed, prior and after to the different annealing steps to evaluate electrical characteristics, respectively. To eliminate any parasitic series resistance in accumulation, all C-V curves have been corrected [7], and consequently EOT and Flatband voltage V_{FB} were deduced from quasistatic C-V measurements.

Results

Results for HfO_2 or ZrO_2 as gate dielectric are in general similar and comparable to each other. They revealed that PMA in FGA is effective in annealing out interface traps located in the Si bandgap in all investigated devices. Additionally, oxide charges are neutralized, as can be concluded from a shift of V_{FB} to more positive values in the C-V characteristics. The leakage current slightly rises due to PMA and we suppose thermodynamical reactions within the dielectrics during the thermal treatment to be responsible for this behavior.

The RTA treated samples exhibit a clearly decreased oxide charge density, but also an increase of C_{oxide} in accumulation, as well as an undesirable high leakage current. We therefore assume a crystallization process of the gate oxide that takes place during RTA and changes the bulk characteristics. High resolution-Transmission electron microscopy (HR-TEM) measurements, which reveal interfacial SiO_2 that might form already during PDA, support this assumption.

Titanium-Nitride Gate

Figure 1 shows C-V and I-V (inset) measurements for various frequencies for a TiN/ZrO_2/p-Si capacitor after PMA at 450°C in FGA. Only a small hump around ~0.25 V due to interface traps in the silicon bandgap can be seen. Up to at least 450°C, this gate stack shows thermodynamical stability.

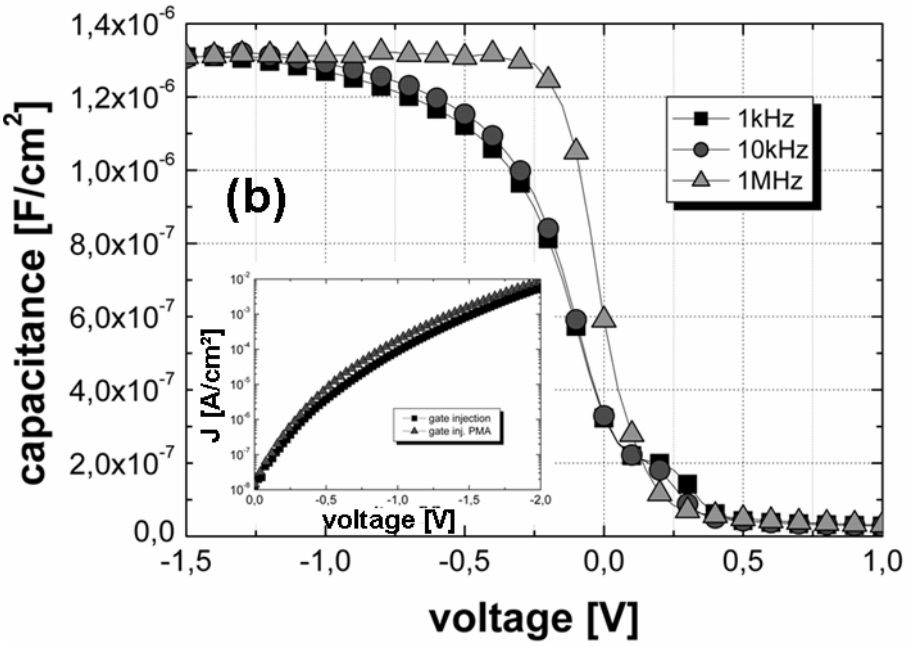

Fig. 1: C-V and I-V (inset) measurements of a TiN/ZrO_2/p-Si capacitor after PMA in FGA.

Molybdenum Gate

C-V and I-V (inset) measurements for various frequencies for a Mo/HfO_2/p-Si capacitor are shown in Fig. 2. Thermal treatment included PMA at 450°C in FGA and RTA at 950°C in N_2. A hump around ~0.0 V due to interface traps in the silicon bandgap can be seen. Leakage current after RTA is undesirably high, probably due to crystallization of the gate oxide during annealing.

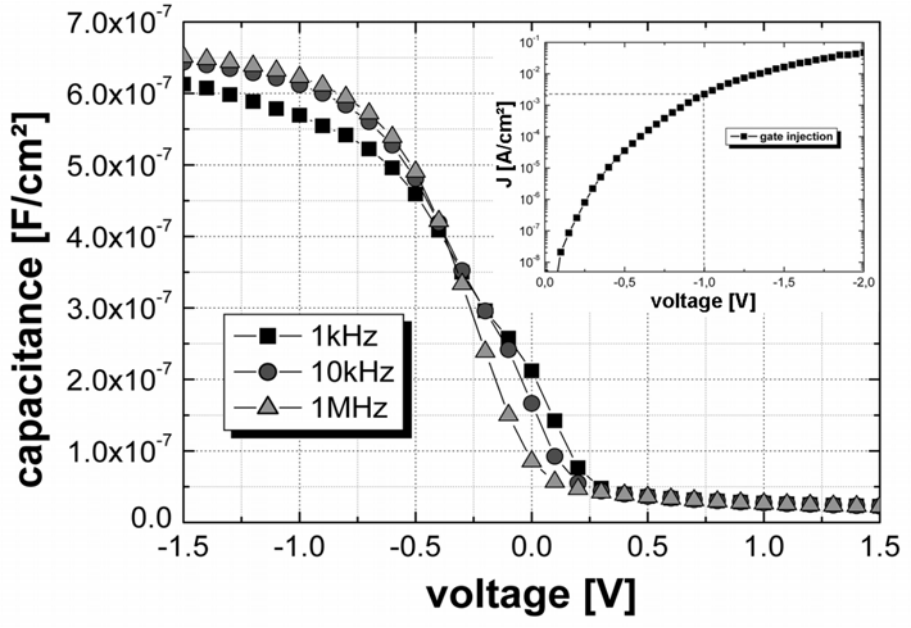

Fig. 2: C-V and I-V (inset) measurements of a Mo/HfO_2/p-Si capacitor after PMA in FGA and RTA in N_2.

Summary

A summary of the investigated gate stacks is shown in table 1. The V_{FB} values for the TiN- and Mo-capacitors indicate mid-gap pinning of the metal gates. One can see that the values of κ do not correlate with the corresponding EOT; a trade-off between EOT and κ is observed. This might be due to different contributions of an unintentional interfacial SiO_2 layer forming during the growth process and its further increase during post deposition annealing treatments.

Gate material:	TiN (PMA)	Mo (PMA+RTA)
EOT [nm]:	2.0	3.4
Diel. constant κ [1]:	12	23
Flatb. Volt. V_{FB} [V]	-0.05	-0.16
Ox. Dens. Q_0 [cm^{-2}]	1.1E+12	1.2E+10

Table 1: Summary of TiN- and Mo/ZrO_2/Si stacks.

Acknowledgements

This work is supported by the *Network of Excellence SINANO*. The *Gesellschaft für Mikro- und Nanoelektronik*, *GMe*, as well as the *Zentrum für Mikro- und Nanostrukturen*, *ZMNS*, are gratefully acknowledged for support.

References

[1] *International Technology Roadmap for Semiconductors*, 2005 Edition, http://public.itrs.net/.

[2] Y.-S. Lin, et al., *Appl. Phys. Lett*. 81, 2041 (2002).

[3] S. Lysaght, et al., *J. Non-Crystal. Solids* 303, 54 (2002).

[4] S. Youn, et al., *Vac. Sci. Technol. A* 19(4), 1591 (2001).

[5] M. Lemme et al., *Microel. Reliability* 45, 953 (2005)

[6] Q. Lu et al., *Symp. on VLSI Technology* 72-73 (2000)

[7] K. Kwa,et al., *Semic. Sci. & Tech.* 18, 82 (2003).

Synthesis of Nanowires in Room Temperature Ambient with Focused Ion Beams

A. Lugstein, C. Schöndorfer, E. Bertagnolli

Institut für Festkörperelektronik, TU Wien,
Floragasse 7, A-1040 Wien

Introduction

Exciting discoveries of essentially new nanostructures, particularly nanowires, have been sparked by a desire to tune the fundamental optical, electronic, mechanical and magnetic properties of materials through rational control of their physical size. Possible applications range from new-generation nanoelectronics [1] to catalysis [2].

Several techniques for the production of various types of nanowires have been reported, such as thermal gas decomposition or laser ablation of powder targets. Most of them are based on the Vapor-Liquid-Solid (VLS) mechanism, in which metal droplets catalytically enhance the growth of nanowires [3]. The liquid alloy cluster serves as a preferential site for adsorption of reactant from the vapor phase and – when supersaturated – as the nucleation site for crystallization. However, there is still an on-going effort in developing synthesis methods with the main goal to grow nanowires at moderate temperatures not to damage preexisting modules and to grow them at a prespecified location while eliminating the requirement of a later assembly process.

Our study differs from all of the previous reports in that an intense focused ion beam initiates the nanowire growth in room temperature ambient without using any additional materials source.

Experimental

All machining experiments were carried out using the Micrion twin lens FIB system (model 2500) equipped with a Ga liquid metal ion source. For patterning, the 50 keV Ga^+ ion beam is scanned in discrete steps across the sample surface at normal incidence. If not mentioned in particular, the processing was done in the single scan mode, thereby each pixel is irradiated only once and the fluence is adjusted by the dwell time the beam remained on each single spot.

The pattern evolution was observed by top-view and cross-sectional Secondary Electron Microscopy (SEM) of cleaved samples, High Resolution Transmission Electron Microscopy (HRTEM) and Electron Dispersive X-ray (EDX) analysis. The chemical composition of the pattern was evaluated by Auger Electron Spectroscopy (AES) using a VG Microlab 310F system enabling a lateral resolution of 20 nm for elemental analysis.

Results

In our approach, we milled holes from the back side through antimony samples, with sufficient initial smoothness, as schematically shown in Fig. 1(a). Remarkably nanowire formation was observed on both sides of the sample, i.e. at the site of the impinging

beam as well as at the plane where the FIB leaves the sample. As FIB milling is done close to the edge of the sample some nanowires extend over the rim of the sample as shown in the SEM image in Fig. 1(b). Thus, enabling HRTEM investigations and Energy Disperse X-ray EDX analysis, of undisturbed nanowires as illustrated in Fig. 1. EDX analysis performed in such a way on individual nanowires proved that the wires consist of pure antimony (left inset in Fig. 1(b)). The Cu signal is an artifact originating from the TEM copper grid. The HRTEM image revealed that the as grown nanowires are amorphous with remarkably uniform diameters in the range of about 25 nm along their entire length (right inset in Fig. 1(b)). Particularly we have investigated the tips of the wires. Neither compositional variations nor solidified catalytic particles, which are characteristic features of a VLS controlled growth mechanism, have been observed on any of the Sb nanowires.

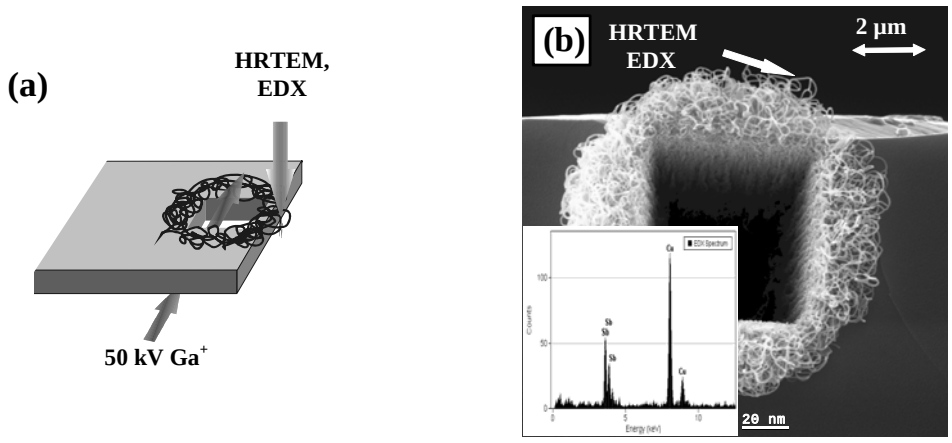

Fig. 1: (a) Schematic illustration of FIB based approach used to synthesize nanowires drilling a hole from the back side through the sample. (b) SEM image of a 5x5 µm^2 wide hole milled trough the sample. The insets show a typical EDX spectrum from an individual nanowire and the HRTEM image of such synthesized wires.

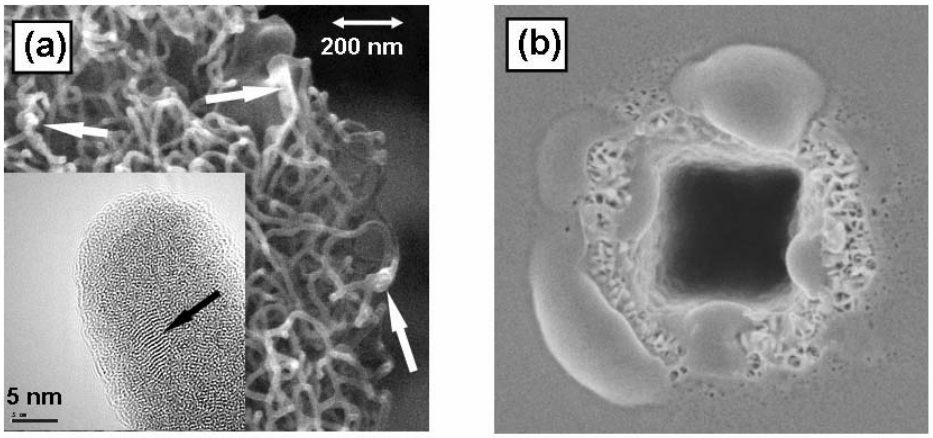

Fig. 2: (a) Low magnified SEM image of the nanowires observed on GaSb after FIB hole milling through the sample. The inset shows a high resolution TEM image of the tip of an isolated GaSb wire with a diameter around 25 nm. (b) SEM image of a hole milled in GaSb with a 30 kV focused Ga^+ ion beam.

For GaSb as substrate material FIB exposure leads to the formation of a cellular structure of columnar tangled rods and precipitations embedded within the porous network of nanowires (see SEM image in Fig. 2(a)). AES measurements revealed that the precipitations marked by the white arrows in Fig. 2(a) appear to be pure Ga. HRTEM investigations (inset of Fig. 2(a)) proved that the roughly 25 nm thick wires show mostly an amorphous structure. For some wires a few regions with a diameter up to 5 nm with crystallographic ordering are visible, indicated by the black arrow. The lattice fringes distance observed in the region marked by the black arrow is 0.35 nm and corresponds with the {111} planes in bulk GaSb with cubic Zinkblende structure. The elemental composition of the nanowires investigated using EDX revealed an almost ideal 1:1 stoichiometry of Ga and Sb independent of the morphology. For beam energies of 30 keV or lower, formation of nanowires could be observed neither for GaSb nor Sb substrates. Fig. 2(b) shows the SEM image of the GaSb surface after 30 kV FIB exposure. The droplet-like features surrounding the FIB milled hole are Ga droplets as determined by AES measurements.

In accordance with the catalytic VLS approach we suppose that the formation of GaSb nanowires necessitates a catalytic particle, mostly a eutectic alloy, with a low melting point. In our approach we suppose that Ga droplets are formed in situ during FIB exposure (Fig. 3(a) - process step 1). As we have recently reported, FIB milling of GaAs leads to the formation of Ga droplets on the surface [4]. For FIB exposure with the 30 keV beam we have also observed in-situ migration of Ga precipitations on the GaSb surface. We assume that exposing the substrate to the 50 keV Ga+ ion beam leads to material decomposition due to physical sputtering. The excess Ga atoms because of enhanced diffusion agglomerate into Ga-rich precipitations (process step 1). Due to the low melting point of Ga and high energy injection during FIB milling with the 50 keV beam, these precipitations behave like a liquid. Decomposed material from the substrate – diffusing on the surface – is adsorbed and dissolved by the Ga containing clusters (process step 2). Finally, when the concentration of the solved materials exceeds supersaturation, nucleation sites will be formed and initiate the growth of the coexisting solid GaSb phase (process step 3). Nanowire growth from the base continues as long as the droplet remains in a liquid state and reactant is available. In accordance with the phase diagram shown in Fig. 3(b) precipitation of GaSb continues at the liquid-solid as long as the catalytic particle remains in a liquid state and reactant is available.

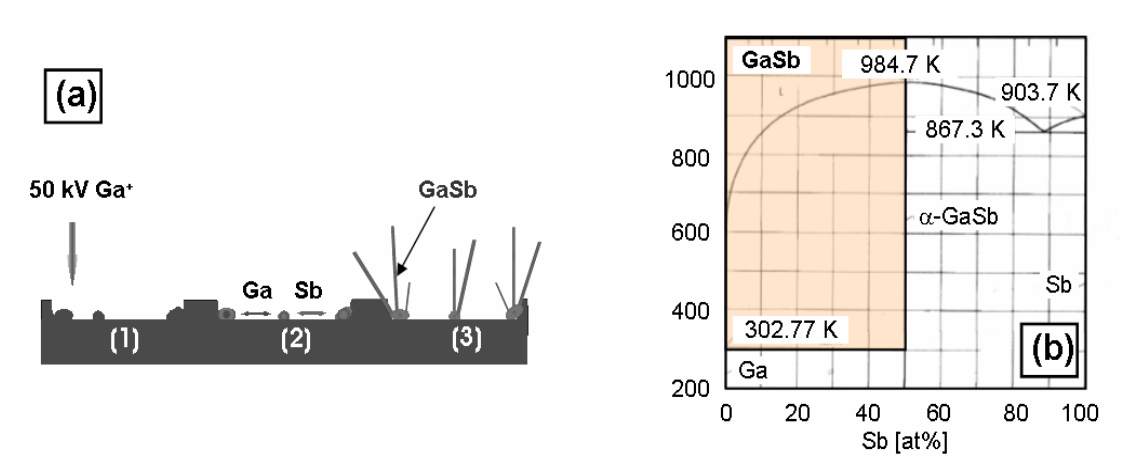

Fig. 3: (a) The proposed growth model; (b) The phase diagram (after Landolt-Börnstein, New Series IV/5) of the binary Ga-Sb system illustrates the thermodynamics of the nanowire growth.

The formation of pure Sb nanowires could be discussed straightforward by examining the Sb rich part of the binary Ga-Sb phase diagram (Fig. 3(b)). Within the framework of our approach, FIB processing of the Sb substrate produces mobile Ga and Sb species on the surface that rapidly agglomerate forming Sb-rich nanoclusters. In case of the Sb substrate Ga is introduced only by the FIB and the concentration of these clusters is somewhere in the right-most part, i.e. the Sb-rich region, of the phase diagram. Again due to supersaturation of the nanocluster, the coexisting pure Sb phase precipitates as nanowires.

At present, we do not understand the origin of the tangling of the nanowires although we note that extensive tangling has been observed previously in Ga based VLS processes [5]. The authors stated also that Ga droplets could simultaneously catalyze the growth of hundreds of thousands of nanowires. Additionally we want to mention that in contrast to the conventional VLS mechanism the growth rate for our approach is extremely high. As the whole FIB processing takes only a few seconds, growth rate must be in the range of a few 100 nm/s.

Conclusion

According to our experimental results, we assume that at least two key parameters are required to induce nanowire formation by an intense FIB. One should use an equilibrium phase diagram to choose a substrate that can form a liquid alloy with Ga. Even when FIB-induced nanowire growth occurs far-off the thermodynamic equilibrium, known phase diagrams can be used to choose a specific composition (catalyst – nanowire material) so that there is coexistence of liquid alloy and solid material. Second, a sufficiently high beam energy to ensure that the liquid alloy is formed during the FIB processing.

The above studies illustrate the potential of our approach for synthesis of nanowires in room temperature ambient without using a gas-type source. We suppose that our approach should not be limited solely to the materials discussed here – other substrates or sources of the ion beam should extend this method to other materials.

Acknowledgements

This work is partly funded by the Austrian Science Fund (Project No. 18080-N07). The authors would like to thank the Center for Micro- and Nanostructures (ZMNS) for providing the clean-room facilities. The financial support from the Austrian Society for Micro- and Nanoelectronics (GMe) is gratefully acknowledged.

References

[1] A. O. Orlov, I. Amlani, G. H. Bernstein, C. S. Lent, G. L. Snider, *Science* 277, 928 (1997); A. B. Greytak, L. J. Lauhon, M. S. Gudiksen and C. M. Lieber, *Appl. Phys. Lett*. 84, 4176 (2004); A. P. Alivisatos, *Science* 271, 933 (1996); S. Sun, C. B. Murray, D. Weller, L. Folks, A. Moser, *Science* 287, 1998 (2000).

[2] M. Valden, X. Lai, D. W. Goodman, *Science* 281, 1647 (1998).

[3] R. S. Wagner, W. C. Ellis, *Appl. Phys. Lett.* 4, 89 (1964).

[4] A. Lugstein, B. Basnar, E. Bertagnolli, *J. Vac. Sci. Technol*. B 22, 888 (2004).

[5] Z. W: Pan, Z. R: Dai, C. Ma, Z. L. Wang, *J. Am. Chem. Soc.* 124, 1817 (2002).

Focused Ion Beam Induced Synthesis of a Porous Antimony Nanowires Network

C. Schoendorfer, A. Lugstein, Y.-J. Hyun and E. Bertagnolli

Solid State Electronics Institute, Vienna University of Technology
Floragasse 7, A-1040 Vienna

Introduction

While the generation of 0-D nanostructures such as quantum dots with defined properties can be managed since a while, there is a remarkable increasing scientific and technological interest in 1-D nanostructures. During the last decade significant progress has been made in the realization of appropriate 1-D nanostructures, either by top down approaches issuing lithography and dry etching techniques, as well as bottom-up growth techniques such as electrochemical deposition within porous templates, e.g. anodic alumina membranes, or catalyst assisted chemical vapor deposition. Very recently nanowires of different types of material have been grown by the vapor-liquid-solid (VLS) mechanism, in which various metals such as Au, Fe, Ti or Ga catalytically enhance the growth of nanowires. Thereby a liquid alloy cluster serves as a preferential site for catalytic adsorption of reactants from the vapor phase and – when supersaturated – as the nucleation site for crystallization. The supersaturation of the eutectic melt acts as the driving force for the growth in a highly anisotropic manner. However, there is still an on-going effort in developing synthesis methods with the main goal to grow nanowires at moderate temperatures in order not to damage preexisting modules and to grow them at a specified location while eliminating the requirement of a later assembly process.

Experimental

Thin lamellas of antimony samples with purity > 99.999% were prepared and cleaned by rinsing with acetone and isopropyl alcohol followed by blow-drying with pure nitrogen. The used focused ion beam (FIB) system was equipped with a liquid Ga metal ion source. For the purpose of patterning the FIB is scanned over a predefined area in discrete steps with well-defined step size and dwell time, i.e. the time the beam remains on each single spot. Each scan across the selected area deposits an ion fluence which is correlated to the above mentioned parameters. Single pass milling denotes a scanning strategy where the desired fluence is deposited within one single scan. For multi pass milling, the beam is scanned several times across the predefined area and the total ion fluence is dependent on the number of scan repetitions of the FIB. The topographical and compositional evolution of the Sb surfaces irradiated by focused Ga beam is investigated by means of scanning electron microscopy (SEM), Auger electron spectroscopy (AES), high resolution transmission electron microscopy (HRTEM), selected area diffraction (SAD), and energy dispersive X-ray diffraction (EDX) measurements.

Results

Figure 1(a) shows a secondary electron microscopy (SEM) image of the Sb surface after multi pass milling of a (2x2) μm^2 wide box with a 100 times higher ion fluence of

$6.2x10^{18}$ Ga ions/cm^2. As expected, FIB exposure leads to effective sputtering of the substrate material with a high sputter yield of approximately 14.3 sputtered Sb atoms per incident Ga ion. The rim of the several micrometer deep hole is surrounded by a dense network of nanofibers which show very uniform diameters in the range of 25 nm. Milling the same box with the same ion fluence in single pass mode leads to the formation of a pattern shown in Fig. 1(b). Thereby the FIB scan starts in the upper left of the box and moves along in serpentines with a pixel and line spacing both of 10nm, which guarantees a nearly uniform ion fluence distribution. The whole FIB modified area is covered by nanofibers with the exception of the last line scan routed from the lower right to the lower left edge. Nanofibers reach even 2 µm beyond the rim of the FIB milled area. Fig. 1(c) shows the Sb surface after single pass milling viewed under a tilt angle of 75°. The FIB generated nanowire extrusions do not form a plane porous disc as one could assume from the top view SEM image in Fig. 1(b). As shown in the schematic of Fig. 1d, the nanofibers appear on a ramp-like base normal to the plane rising along the scan direction of the FIB.

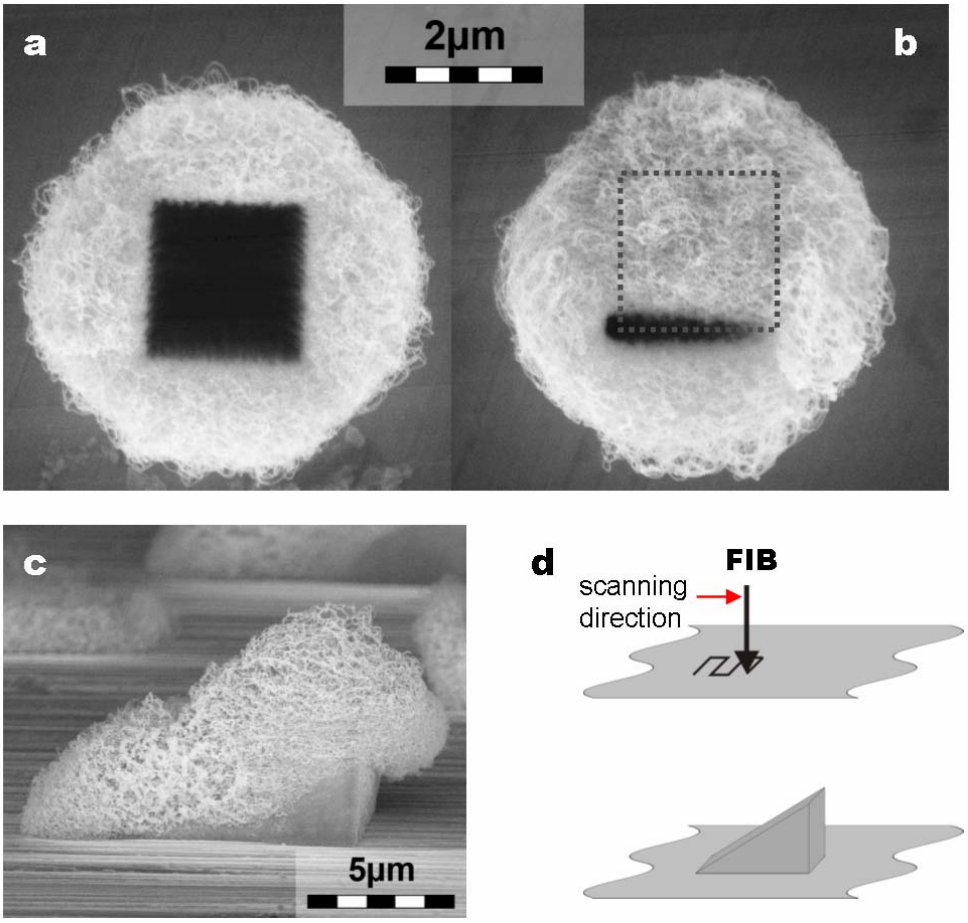

Fig. 1: Sb surface processed using a 50keV Ga FIB with an ion current of 200pA. (2x2) µm^2 milling areas irradiated by an ion fluence of $6.2x10^{18}$ ions/cm² in (a) multi pass mode and (b) single pass mode, tilted view SEM image of a (10x10) µm^2 milling area (c) exposed to an ion fluence of $3.1x10^{18}$ ions/cm² processed in single pass mode, schematic sketch (d) visualizing the FIB scanning strategy and the resulting uplifted nanofiber network.

The formation of this ramp-like structure is a result of the pixel-by-pixel and accordingly of the line-by-line scanning strategy. Scanning the first line of the predefined milling

area leads to nanofiber growth even beyond the ion irradiated region. By the guidance of the FIB through the subsequent lines, nanofibers which were grown on the not yet exposed part in the forefront of the scanning beam are removed by sputtering. Nanofibers in already irradiated zones, i.e. behind the scanning beam, remain unaffected. These nanofibers form a network which is further densified by redeposited Sb. Due to the ongoing FIB scanning this nanofiber network reduces the escape angle for the sputtered Sb and more and more of them are picked up by the network which leads to an upraising of the structures.

The cross sectional SEM image of a (10x10) μm^2 milling box in Fig. 2 shows the porous material covering the surface and the FIB milled box. The range of the porous nanofibers network generated by the impact of the FIB reaches some microns beneath the surface level.

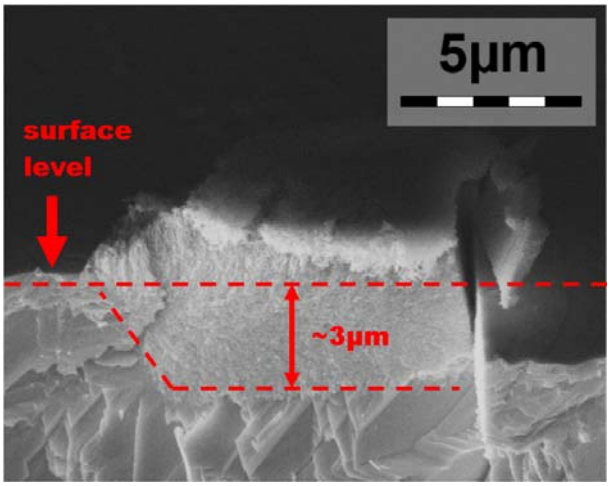

Fig. 2. SEM image of the cross sectional view of a FIB milled (10x10) μm^2 area accomplished by cleaving the sample. The porous network at the FIB exposed area using an ion fluence of $3.1x10^{18}$ ions/cm^2 reaches several micrometers in depth.

Extensive transmission electron microscopy (TEM), selected area diffraction (SAD), Auger electron spectroscopy (AES), and energy dispersive X-ray spectroscopy (EDX) of individual nanofibers prove that they are completely amorphous even in the nanometer scale and consist of pure antimony. The TEM image in Fig. 3(a) shows the exceptionally uniform diameters of the nanofibers of about 25 nm along their entire length.

The FIB modified samples covered by the nanofibers were annealed in a special furnace setup which allows processing at well-controlled temperature profiles in He atmosphere. Several experiments showed that the temperature ramp is a crucial parameter for the grain size of the resulting re-crystallized structure whereby the diameter and shape of the nanowires remain unaffected by the annealing. The high resolution TEM (HRTEM) image in Fig. 3(b) displays a Sb nanowire after moderate thermal annealing at 453 K for 30 min. The diffraction pattern in Fig. 3(c) shows the most prominent (110) and (120) reflections for Sb with its trigonal crystal structure, and the lattice parameter of 0,354 nm is consistent with the tabulated value for bulk Sb.

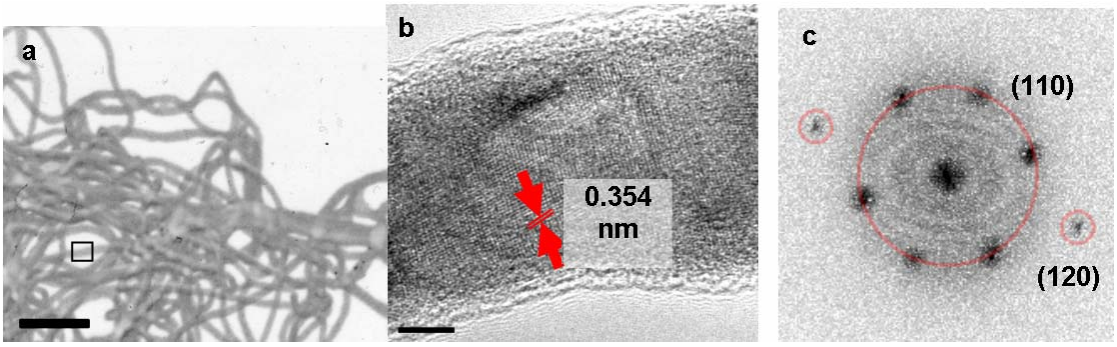

Fig. 3. The low magnified TEM image (a) gives an overview of the nanofibers network. The scale bar corresponds to 200 nm. The HRTEM micrograph in (b) shows the part of a Sb nanofiber (marked by the rectangle in Fig. 4(a)) after moderate thermal annealing at 453 K. The lattice planes as highlighted in the HRTEM image show a distance of 0.354 nm which corresponds to Sb (110) direction. The scale bar denotes 5 nm. The diffraction pattern (c) clearly shows the single crystalline nature ((110) and (120) reflections) of the nanowires after the post growth annealing at 453 K for 30 min in He atmosphere.

We assume that FIB processing with the Ga beam produces mobile Ga species on the surface which rapidly agglomerate forming catalytic nanoclusters. Sputtered Sb diffuses on the surface and acts as a quasi-vapor phase source. When the solved Sb concentration exceeds saturation, nucleation sites will be formed which initiate the precipitation of the Sb. Nanowire growth from the base continues as long as the droplet remains in a liquid state and supersaturation is maintained. At present, we do not understand the origin of the tangling of the nanowires although we note that extensive tangling has been observed previously in Ga based VLS processes [1]. The authors also stated that Ga droplets could simultaneously catalyze the growth of hundreds of thousands of nanowires.

Conclusion

In summary, the FIB irradiation of Sb with 50keV Ga ions at room temperature leads to the formation of a porous network of pure Sb nanofibers. The as-grown nanofibers are amorphous with remarkably uniform diameters in the range of about 25 nm along their entire length. The resulting porous network is uplifted several microns above the sample surface. In accordance with the catalytic VLS approach we suppose that the formation of Sb nanowires necessitates a catalytic particle, mostly a eutectic alloy, with a low melting point. Re-crystallization of the Sb nanofibers could be achieved by moderate thermal annealing at temperatures of about 473 K. Depending on the temperature ramp and heating duration finely grained crystallites as well as single crystalline regions along the nanowires can be obtained.

References

[1] Z. W. Pan, Z. R. Dai, C. Ma, Z. L. Wang, J. Am. Chem. Soc. 124, 1817 (2002).

Focused Ion Beam Induced Nanodot, Nanocrystal and Nanofiber Growth

C. Schoendorfer, A. Lugstein, E. Bertagnolli

Vienna University of Technology, Department for Solid State Electronics, Floragasse 7, A-1040 Vienna, Austria

Introduction

Ion beams focused to diameters in the range of several tens of nanometers offer an interesting opportunity for maskless processing in the nanoscale regime. Under certain sputter conditions a periodic height modulation in the form of ripples and dots on a submicron length scale develops during broad beam ion exposure as observed for semiconductor materials [1] – [4], metals [5], [6], insulator surfaces [7], and semimetals (e.g., graphite [8]). To gain full use of FIB techniques a fundamental understanding of the interaction of ion beams with the substrate material is required.

In this paper, we investigate the impact of FIB irradiation on GaAs, InAs, GaSb and Sb substrates and discuss the surface evolution. We will show, that under proper FIB adjustment of beam energy, beam diameter and beam current dots, crystals and fibers form due to selective etching and catalytic growth processes.

Experimental

Sample Preparation

In a twin lens FIB system Ga^+ ions are extracted from a liquid Ga source, followed by acceleration up to 50 keV. The beam scanning in discrete steps across the sample surface leads to an ion bombardment of a defined area. Controlled FIB exposure of the sample is achieved by variation of some basic parameters such as the beam diameter, the beam current, the distance between two discrete steps along the scanning path and the dwell time which is the time the beam remains on each spot. The experiments are carried out with various ion fluences at normal incidence and at room temperature.

Our setup offers the possibility to image the focal plane during FIB processing. Therefore the surface evolution can be observed in-situ by FIB-SEM imaging. Furthermore, the nanopatterns are investigated by atomic force microscopy (AFM), Auger electron spectroscopy (AES), high resolution transmission electron microscopy (HRTEM) and X-ray diffraction.

GaAs Substrates

The exposure of GaAs to the FIB leads to an excess of Ga on the substrate surface due to preferential sputtering of As [9]. Because of the surface tension the Ga agglomerates dots. Therefore, a formation of Ga-rich liquid droplets in the ion exposed area as shown in the SEM image in Fig. 1(a) can be observed. *In-situ* monitoring shows that these dots move around on the surface as long as this area is exposed to the FIB. Topography investigations by AFM have shown agglomeration of the droplets due to gathering at lower levels of the roughened surface which is displayed in Fig. 1(b). The

chemical composition of the dots has been analyzed by AES which confirmed that the droplets consist of nearly pure Ga.

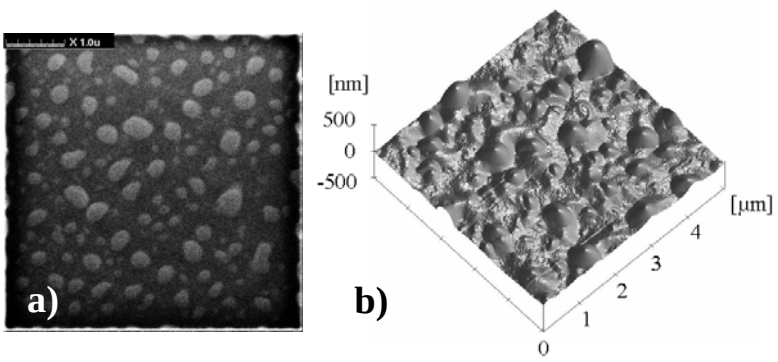

Fig. 1: (a) FIB-SEM image of a GaAs surface after FIB exposure of a 5 µm x 5 µm box with 50 keV Ga ions, (b) AFM topography of the GaAs sample after milling.

InAs Substrates

Figure 2 shows SEM images of the InAs surface after 50 keV FIB exposure with different ion fluences. For an ion fluence of 1.25×10^{16} ions/cm^2 randomly distributed nanograins are formed on the InAs surface (Fig. 2(a)). The extension size of these grains ranges from 30 to 120 nm and their typical number density is in the order of about 2×10^9 cm^{-2}. For an ion fluence of 2.5×10^{16} ions/cm^2 the size of the protrusions increases while the surface density decreases (Fig. 2(b)). For the highest investigated ion fluence of 5×10^{16} ions/cm^2 the grains grow further and emerge as well separated crystallites with obvious facets (Fig. 2(c)).

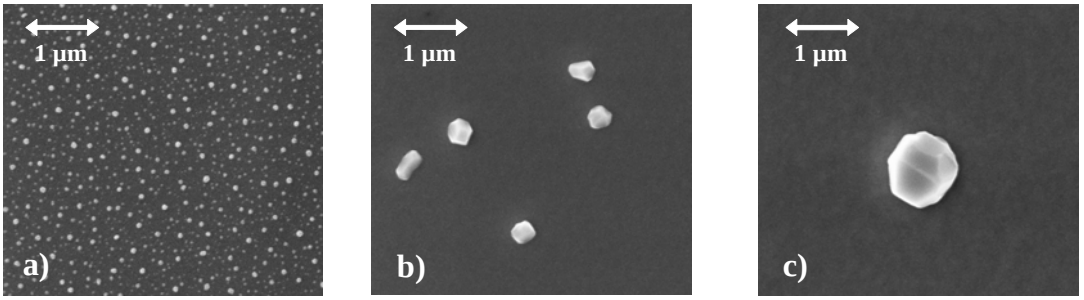

Fig. 2: Ion fluence dependency of pattern evolution on InAs exposed by the Ga FIB. The SEM images show the InAs surface after exposure fluences of (a) 1.25×10^{16} ions/cm^2, (b) 2.5×10^{16} ions/cm^2 and (c) 5×10^{16} ions/cm^2.

An explanation for this effect of an excess of In on the surface can be found in the different sputter rates of In and As. The mass difference implies that indium is sputter ejected at a much lower rate than arsenic which in addition to that is highly volatile when being in an atomic state. Due to this preferential sputtering of arsenic during FIB bombardment an excess of indium is formed on the exposed InAs surface. We assume that these excess indium atoms presumably diffuse on the ion-impacted surface, coalescing into islands or crystallites somewhere on the surface. To prove the assumption of In crystallite formation due to FIB exposure X-ray diffraction measurements are carried out, where the three most intense reflections of crystalline In are clearly visible.

Relative intensities and d spacings of these reflections are in good agreement with reference material [10].

GaSb Substrates

The impact of the Ga FIB depositing different ion fluences on GaSb substrates can be retraced by the SEM images in Fig. 3. At the beginning of the exposure process beneath a thin surface layer a structure consisting of many hollow cells like a honeycomb is built. This is a result of the conglomeration of voids in the subsurface induced by the implanted Ga ions [11]. Ongoing milling leads to a transformation of the comb structure into a sponge-like network consisting of Ga and Sb in the same ratio including some Ga-rich precipitations on top of this fiber network. We assume that a catalytic growth process similar to the vapor-liquid-solid growth process [12] occurs, whereby the Ga droplets act as the needed catalytic particles.

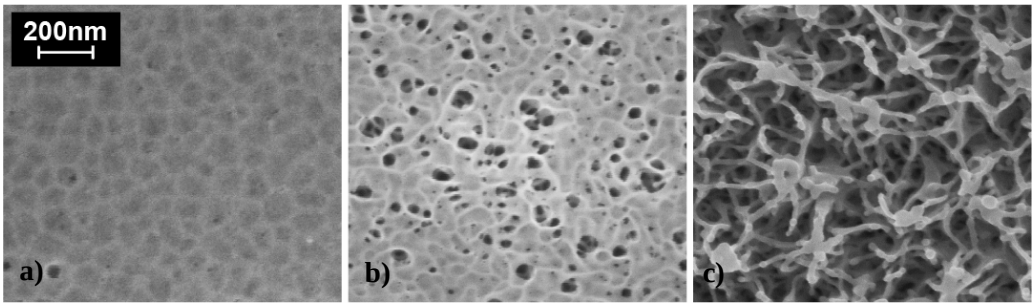

Fig. 3: GaSb surface evolution driven by ion fluence: depositing an ion fluence of $3x10^{13}$ ions/cm² (a) leads to generation of hollow combs under a thin surface layer, increasing the fluence to $6x10^{13}$ ions/cm² (b) results in a more and more porous layer and finally at an ion fluences of $3x10^{14}$ ions/cm² a transformation into a sponge-like network built up of GaSb fibers with diameter in the range of 25 nm and Ga-rich precipitations takes place.

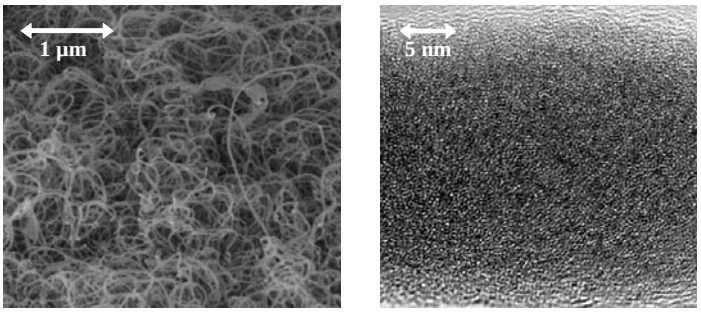

Fig. 4: The SEM image shows FIB generated Sb nanofibers with diameters in the order of 20 nm (a) and the HRTEM image of an individual Sb nanofiber proves that the as-grown nanofiber is completely amorphous even in the nanometer scale.

Sb Substrates

The results of GaSb substrates exposed to the FIB lead to the idea that fibers growth could also occur using pure Sb as substrate. The catalyst material needed for the

growth may be provided by the focused Ga beam. In Fig. 4(a) a SEM image of an FIB milled box on metallic antimony using 50 keV Ga ions at an ion fluence of $2x10^{16}$ ions/cm² is given. The Sb nanofibers similar to those found on GaSb show diameters of few tens of nanometers and seem to grow in slops beginning and ending at the substrate surface. HRTEM (Fig. 4 (b)) and AES investigations show that these fiber structures are completely amorphous and consist of pure Sb.

Summary

In summary, investigation of FIB bombardment of several substrates is done. It is demonstrated that FIB parameters and the chemical composition of the substrates show a great influence on the surface evolution. Various effects which lead to different appearance in the sample surface evolution, such as Ga droplets on GaAs, In nanocrystals on InAs and nanowires with diameters in the range of few tens of nanometers on GaSb and metallic Sb, are studied by SEM and AFM. In addition to that the resulting nanostructures are investigated in detail using HRTEM, AES and XRD techniques to gain more information about the chemical composition and crystallographic structure. Thus, e.g. the In nanostructures can be considered to be crystalline and the as-grown Sb nanowires to be completely amorphous and to consist of pure Sb.

Acknowledgements

This work is partly funded by the Austrian Science Fund (Project No. 18080-N07). The authors would like to thank the Center for Micro- and Nanostructures (ZMNS) for providing the clean-room facilities, Christian Tomastik for AES measurements and Johannes Bernardi for HRTEM investigations. The financial support from the Austrian Society for Micro- and Nanoelectronics (GMe) is gratefully acknowledged.

References

[1] E. Chason, T. M. Mayer, B. K. Kellerman, D. T. McIlroy, and A. J. Howard, Phys. Rev. Lett. 72, 3040 (1994).

[2] G. Carter and V. Vishnyakov, Phys. Rev. B 54, 17647 (1996).

[3] Z. X. Jiang and P. F. A. Alkemade, Appl. Phys. Lett. 73, 315 (1998).

[4] J. Erlebacher, M. J. Aziz, E. Chason, M. B. Sinclair, and J. A. Floro, Phys. Rev. Lett. 82, 2330 (1999).

[5] S. Rusponi, C. Boragno, and U. Valbusa, Phys. Rev. Lett. 78, 2795 (1997).

[6] S. Rusponi, G. Costantini, C. Boragno, and U. Valbusa, Phys. Rev. Lett. 81, 4184 (1998).

[7] T. M. Mayer, E. Chason, and A. J. Howard, J. Appl. Phys. 76, 1633 (1994).

[8] S. Habenicht, W. Bolse, K. P. Lieb, K. Reimann, and U. Geyer, Phys. Rev. B 60, R2200 (1999).

[9] J. G. Pellerin, D. P. Griffis, P. E. Russell, J. Vac. Sci. Technol. B 8, 1945 (1990).

[10] The Powder Diffraction File, International Centre for Diffraction Data, 12 Campus Boulevard, Newton Square, Pennsylvania 19073-3273, USA.

[11] N. Nitta, M. Taniwaki, Y. Hayashi, T. Yoshiie, J. Appl. Phys. 92, 1799 (2002).

[12] R. S. Wagner, W. C. Ellis, Appl. Phys. Lett. 4, 89 (1964).

Perpendicular Iron Nanopillars by Electron Beam Induced Deposition

H.D. Wanzenboeck, G. Hochleitner, E. Bertagnolli

Vienna University of Technology, Inst. f. Solid State Electronics
Floragasse 7/1, A-1040 Vienna, AUSTRIA

Introduction

Focused electron beam induced deposition (FEBID) is a versatile maskless method for direct fabrication of nanoscaled structures. This method allows the direct deposition of material on every surface. In contrast to conventional lithography, FEBIP is capable of fabricating 3-dimensional structures with complex geometry, which has been demonstrated by Matsui et al [1]. The method relies on the chemical vapor deposition (CVD) induced by impinging electrons from a focused beam. Using a focused electron beam FEBID allows a spatial resolution below 2 nm when using a TEM [2]

For deposition volatile metal precursors containing metalorganic compounds such as acetylacetonates [3], inorganic compounds such as trifluorophosphine metal compound and metal carbonyls [4] have been demonstrated. Due to the simplicity of the molecular structure of the complex and of the ligand metal, carbonyls of the type $Me(CO)_n$ are especially suited for study of the mechanism, and FEBID of Co, Fe, Ni, Cr, Ru has already been performed [5]. The adsorption of $Fe(CO)_5$ was studied by Cheng *et al.* [6]; also autocatalytic growth was observed [13]. Although deposition processes have been widely applied the underlying reaction mechanisms remained unclear. The *in-situ* nanodeposition of electrically conductive and of magnetic materials has been of increasing research interest, and FEBID was used to contact carbon nanotubes [7], to fabricate Hall sensors, and to generate magnetic structures [8].

This paper reports the observation of a slow vertical growth regime and a fast radial growth regime. The conditions under which these growth regimes occur and influence parameters are reported. A comparison with mechanisms proposed by literature is performed.

Experimental

As substrate silicon with a native oxide layer was used. The iron carbonyl (CAS: [13463-40-6]) was used without further purification. The actual beam current was measured before deposition using a faraday cup. The deposition setup is based on a ZEISS Leo 1530VP electron microscope with a Schottky-emitter operated at 1 to 20 keV acceleration voltage. A base pressure of 1.4E-6 mbar was achieved with an oil-free pumping system. The precursor was provided by a custom-tailored gas injection system made of steel featuring an external reservoir, a dosing valve, a vacuum gauge to measure the precursor pressure in the supply line (”pre-chamber-pressure”), and a motorized nozzle head with 3 gas nozzles made of glass tubes with an inner diameter of 600 nm. The final position of the nozzle was adjusted to be 300 nm above the sample surface and in a 500 nm distance from the deposition area.

The probe current was monitored with a 1 s time resolution as current flux from the electrically isolated sample holder. For chemical and structural studies the sample had

to be removed from the Leo 1530 VP and was exposed to ambient environment. Analysis was performed without further sample preparation and without thermal processing. The chemical composition was measured by X-ray emission spectroscopy (EDX) in a Philips XL30 electron microscope (equipped with a rotary pump).

Results

Depositions were performed in the spot mode of the electron microscope in order to avoid effects caused by the beam scan parameters. Simultaneously to all depositions the electrical current flowing from the deposition area (”specimen current”) was measured. The specimen current results from the incoming electrons of the primary beam and the outgoing electrons comprising emitted secondary electrons, backscattered electrons and Auger electrons. For an 10 keV electron beam in Si a scattering of the primary electrons over a depth of 1.3 µm and a diameter up to 2 µm has been calculated. With the deposition of pillars it has to be considered that the interaction volume of the electron beam may be larger than the dimensions of the deposited pillar. Hence, the portion of outgoing electrons will vary not only with the chosen acceleration energy of the primary electrons but also with the geometry of the deposited pillar.

During the deposition of iron pillars two different growth regimes were observed. Typical representatives of this growth process are depicted in Fig. 1. The vertical growth regime is characterized by no further radial growth occurring during ongoing length growth of the pillar. After a short tip-forming phase a constant vertical growth rate was observed for the first 45 seconds of growth time – at longer times the vertical growth rates slightly decreased as a result of a changing tip geometry. For a 1.97 nA electron beam with 10 keV and a 0.5 mbar $Fe(CO)_5$ precursor pressure in the supply line, which is equivalent to a chamber pressure of ~1E-5 mbar, vertical growth rate was in the range of 48 nm/s. The full width at half maximum of the pillars was in the range of 70 nm (+/- 5 nm) and was roughly constant over the entire length of the pillar. The constant vertical growth rate is also displayed by positive specimen current (Fig. 2) that is constant during the initial 45 seconds. Between 45 seconds and 65 seconds the broad tip cone transformed into a sharper cone, which slightly increased the specimen current. The positive specimen current indicates that more electrons (secondary electrons, backscattered electrons) are emitted than primary electrons from the focused beam are arriving at the sample. The current during the first 5 – 7 seconds is attributed to a tip-forming phase and is not representative.

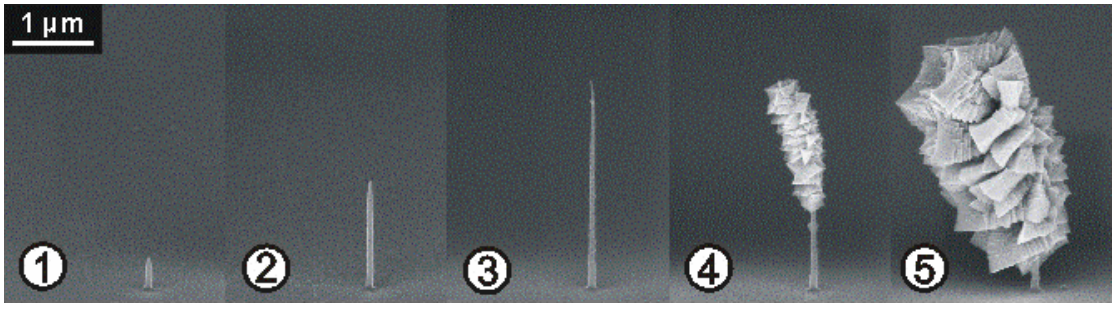

(a) (b) (c) (d) (e)

Fig. 1: Free-standing pillars deposited from $Fe(CO)_5$ with a 10 keV 1.97 nA focused electron beam. The $Fe(CO)_5$ in the supply line was 0.5 mbar resulting in a 1.0x10E-5 mbar chamber pressure. The depositions are depicted by SEM at a 75° tilt after a deposition time of (a) 10 s, (b) 30 s, (c) 60s , (d) 75 s and (e) 110s

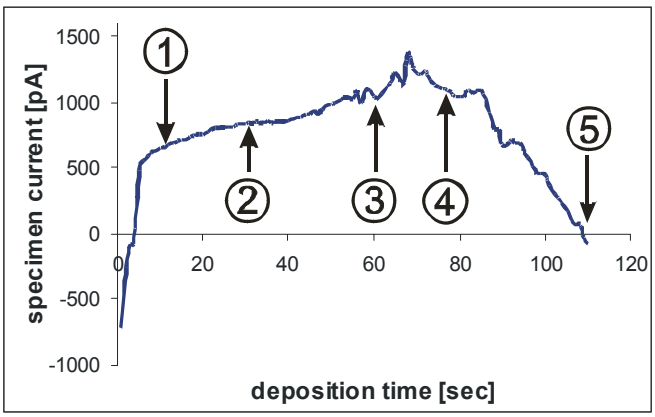

Fig. 2: Specimen current (current flowing off from the deposition area) monitored with progressing deposition time. The metal deposition was performed with a 10 keV 1.97 nA focused electron beam with a supply line pressure of 0.5 mbar $Fe(CO)_5$. This current monitoring graph relates to Fig. 1.

The radial growth regime is characterized by a fast radial growth of dendritic structures quickly increasing the diameter of the pillar. In comparison to the preceding vertical growth regime, in radial growth regime the height growth rate is significantly reduced. For a 1.97 nA electron beam with 10 keV and a 0.5 mbar precursor pressure in the supply line vertical growth rate was quenched to 15 nm/s while a radial growth rate of 19 nm/s was observed. The radial growth resulting in a strongly increased pillar diameter is also displayed as reversion of the specimen current towards negative values (Fig. 2). This change of the specimen current (Fig. 2) reproducibly occurred after 70 seconds deposition time. The negative slope of the specimen current during radial growth indicates that increasingly fewer electrons are emitted from the pillar structure. As the steadily decreasing specimen current was observed simultaneously with a growing diameter of the pillar, it is assumed that the larger volume of the pillar prevents more electrons from reaching the surface and reduces emission. The radial growth sets in autonomously and reproducibly starts at the tip of the slim pillar, but also progresses towards the bottom of the stem (Fig. 1). The self-sustained growth downward the stem supports the assumption of autocatalytic effects. That the radial growth reproducibly starts at the same pillar height may be explained by thermal heating of the pillar by the electron beam. Due to the low thermal conductivity of the slim pillar a thermal heating of the tip has been suggested by Utke *et al*. [9].

The effect of the beam current on the growth rate during the vertical growth regime was investigated with two different experiments. First different apertures with a 10 keV beam were used. Smaller apertures with a lower beam current resulted in a slower growth rate. With a 10 µm aperture (57 pA) as well as a 20 µm aperture (209 pA) no radial growth was observed during the deposition time up to 360 seconds although nanopillar heights up to 5.3 µm were achieved. This behavior supports the assumption of thermal effects as the thermal conduction of the wire may be sufficient to avoid high tip temperatures with the smaller beam currents. Radial growth never occurred with beam currents below 500 nA but was observed reproducibly with higher beam currents.

Alternatively the operation mode of the Zeiss 1530 VP was switched between “normal current” and “high current” which facilitates to change the beam current without changing the acceleration voltage or the aperture setting. For a 10 keV beam and a 60 µm aperture a beam current of either 0.97 nA (normal current mode) or alternatively 1.96 nA (high current mode) could be provided. After the same deposition time of 240 s (Fig. 3) with the 0.97 nA beam no radial growth of the 2.5 µm high pillar was observed, while with the stronger 1.97 nA beam radial growth of the 4.76 µm high pillar occurred.

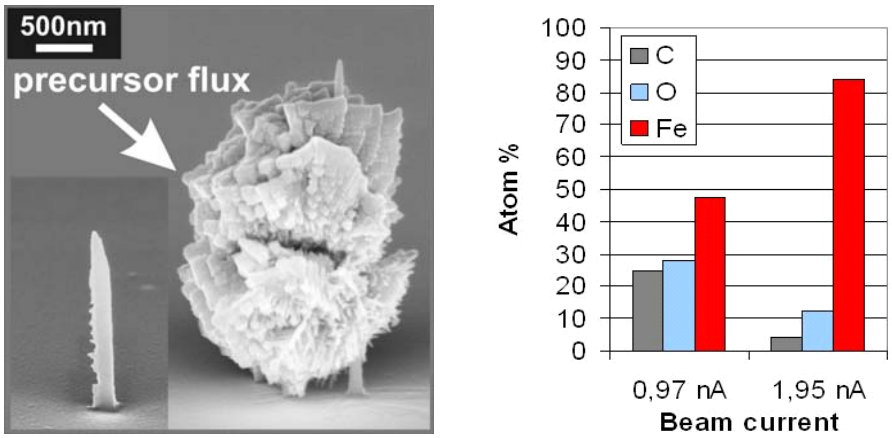

(a) (b) (c)

Fig. 3: Iron deposition at 10 kV with a 60 µm aperture after 240 s (left) in low current mode 0.97 nA and (b) in high current mode 1.97 nA (image is 75° tilted) and chemical composition of these structures as determined by x-ray emission spectroscopy

The chemical composition of the deposited structures of Fig. 3(a) and Fig. 3(b) was measured by EDX (Fig. 3(c)). For transfer to the EDX tool samples were exposed to ambient conditions. For the slim pillar deposited solely in the vertical growth regime the Fe content was 48% while 28% oxygen and 24% carbon were significant impurities. With the broad pillar mainly deposited in a self-sustained radial growth regime an 84% Fe content was measured while contaminants were strongly decreased to 10% oxygen and 6% carbon. This result suggests that material grown in the radial growth mode has a higher iron purity.

Conclusion

The deposition of iron nanopillars by focused electron beam induced deposition from iron pentacarbonyl was demonstrated. Two different growth regimes were observed. Within the vertical growth regime slim pillars with height growth rates between 25 and 55 nm/s were obtained. Within the radial growth regime fast lateral growth of dendritic structures with a low contamination level (below 20%) was observed.

References

[1] Igaki JY, Kanda K, Haruyama Y, Ishida M, Ochiai Y, Fujita J, Kaito T, Matsui S, “Comparison of FIB-CVD and EB-CVD growth characteristics”, Microelectr. Eng. 83(4-9), 1225 (2006)

[2] van Dorp WF, Hagen CW, Crozier PA, van Someren B, Kruit P, “One nanometer structure fabrication using electron beam induced deposition”, Microelect. Eng. 83(4-9), 1468 (2006)

[3] Luisier A, Utke I, Bret T, Cicoira F, Hauert R, Rhee SW, Doppelt P, Hoffmann P, “Comparative study of Cu-precursors for 3D focused electron beam induced deposition”, J. Electrochem. Soc. 151(9), C590 (2004)

[4] Hoyle PC, Cleaver JRA, Ahmed H, “Electron beam induced deposition from W(CO)(6) at 2 to 20 keV and its applications”, J. Vac. Sci Technol. B 14(2), 662 (1996)

[5] Utke T, Dwir B, Leifer K, Cicoira F, Doppelt P, Hoffmann P, Kapon E, “Electron beam induced deposition of metallic tips and wires for microelectronics applications”, Microelectron. Eng. 53(1-4), 261 (2000)

[6] Cheng HS, Reiser DB, Dean SW, Baumert K, “Structure and energetics of iron pentacarbonyl formation at an Fe(100) surface”, J Phys. Chem. B 105(50), 12547 (2001)

[7] Brintlinger T, Fuhrer MS, Melngailis J, Utke I, Bret T, Perentes A, Hoffmann P, Abourida M, Doppelt P, “Electrodes for carbon nanotube devices by focused electron beam induced deposition of gold” J. Vac. Sci. Technol. B 23 (6), 3174 (2005)

[8] Takeguchi M, Shimojo M, Furuya K, “Fabrication of magnetic nanostructures using electron beam induced chemical vapour deposition”, Nanotechnology 16(8), 1321 (2005)

[9] I. Utke, T. Bret, D. Laub, Ph. Buffat, L. Scandella, P. Hoffmann, “Thermal effects during focused electron beam induced deposition of nanocomposite magnetic-cobalt containing tips”, Microelectronic engineering 73-74, 553 (2004)

Pure Silicon Oxide by Electron Beam Induced Deposition for Nanooptical Applications

H. Wanzenboeck, M. Fischer, G. Hochleitner, E. Bertagnolli

Vienna University of Technology, Institute for Solid State Electronics
Floragasse 7/1, A-1040 Vienna, Austria

Micro- and nanostructured surfaces have increasingly been adopted for optical applications such as lithography masks, imprint masks, photonic crystals and optoelectronics. Silicon oxide takes a predominant position among transparent materials and the precise geometry and accurate position of structures if often vital.

Introduction

Optical devices for the nanoregime have to satisfy strict specifications on the material purity, on the accurate position of individual features, and on geometric tolerances of (occasionally even) 3-dimensional structures. Silicon oxide is among the most used materials for optical devices and finds applications in lens systems, photomasks and optical MEMS systems. This work reports on the progress of direct-write deposition of silicon oxide as optical-grade material.

Siloxanes such as tetramethylorthosilicate (TMOS) are frequently used as precursor for chemical vapor deposition of silicon oxide films. With plasma assisted CVD of TMOS highly transparent and adherent films with a low content of carbon residue were obtained [1]. FTIR spectra of SiO_x films deposited from TMOS are very similar to those of pure SiO_2 and had a high transmission of 90% in the wavelength range from 400 to 800 nm. Amorphous plasma enhanced chemical vapor deposited (PECVD) silicon oxide films suitable for integrated optics applications have been produced [2]. Film properties matching the corresponding properties of silicon thermal oxide were obtained by optimizing the composition of the reactant gas flow.

Focused gallium ion beams have also been used for local material deposition using tetramethoxysilane as a precursor. [3] Deposition rates of 0.33 $\mu m^3/nC$ were observed, but the material was strongly contaminated with gallium. FEB induced deposition combines the advantage of a direct write process (one exposure) with extremely high flexibility of deposit geometries (zero- to three-dimensional) at nanometer scale [4]. Due to the absence of gallium the electron beam is capable to overcome the contamination obstacle. Silicon oxide films with improved insulating properties were also deposited using an electron beam [3]. However, material purities of EBID deposited materials have not been in a satisfactory range for optical applications such as photomask repair. In this work we report on an electron beam induced deposition process for chemically pure silicon oxide. The high material qualities achieved facilitate applications as electrical insulator and for optical purposes.

Experimental

Locally confined deposition of silicon oxide is induced with a focused electron beam.

The deposition position of the silicon oxide structure could be accurately controlled by scanning the electron beam only over predefined surface areas. The deposition mechanism is based on a localized chemical vapor deposition (CVD) initiated by the energy of the focused electron beam. Electron beam induced deposition was performed with a custom-adapted Zeiss NTS "LEO 1530 VP" equipped with a 3-stage pumping system for the electron column, a high-current upgrade and a custom-tailored gas injection system for simultaneous inlet of up to 3 process gases. Beam control by a pattern generator allows fabrication of arbitrary features. The precursor gases used for silicon oxide deposition were siloxanes and oxygen. The electron beam was focused down below 10 nm diameter. At 1 kV beam voltage a 2.5 nA electron current was obtained. Substrates used for deposition of silicon oxide were silicon and gallium arsenide for chemical analysis, and quartz glass or calcium fluoride for optical characterization. For optical measurements a gold film with a 100x100 micron aperture for beam transmission was deposited by physical sputtering and structured by optical lithography. Optical transmission was performed with a microlens set-up with a UV/Vis spectroscopic detector. Chemical composition was analyzed by energy dispersive X-ray analysis (EDX). With GaAs carriers a clear distinction between deposited silicon oxide and gallium arsenide was feasible. A sample of pure quartz glass was used as reference for interpretation of EDX-results. The surface topography was determined with a "Digital Instruments 3100" atomic force microscope (AFM) utilizing a diamond-coated cantilever in tapping mode.

Results

Square area structures were deposited (Fig. 1(a)) and display well confined side faces. The surface of the deposited layer was remarkably smooth as illustrated by the AFM. The height of the 600 nm high deposition was very homogeneous; only on two opposite sides slight shoulders were observed as a result of the turnaround position in meander scan.

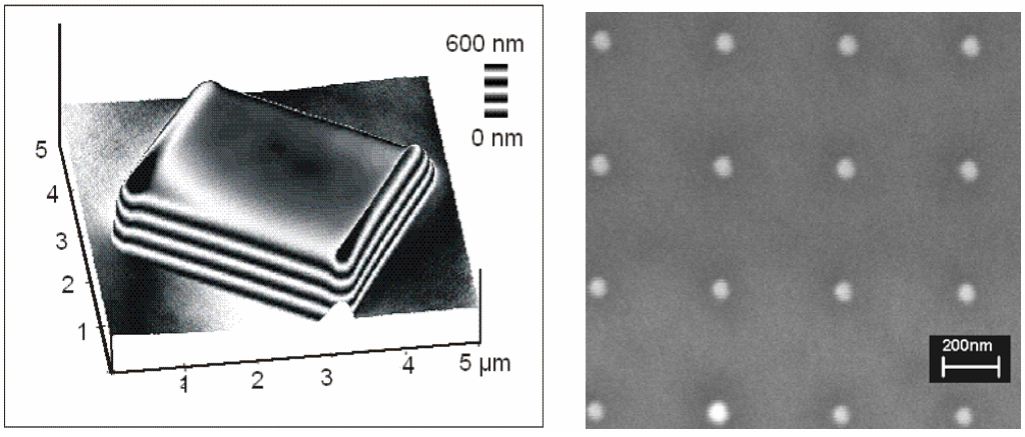

Fig. 1: Electron beam induced deposition of SiO_2 as (a) square area and (b) dot array

A dot array of silicon oxide nanoparticles (Fig. 1(b)) was deposited by deliberately setting a 500 nm wide spacing between scan pixels. Single, round-shaped nanoparticles with a diameter below 50 nm could be fabricated.

The process parameters and the gas composition had to be optimized to achieve high material quality. By oxygen addition electron induced deposition yielded contamination-free silicon oxide. The material composition as determined by energy dispersive X-ray spectroscopy (EDX) is illustrated in Fig. 2.

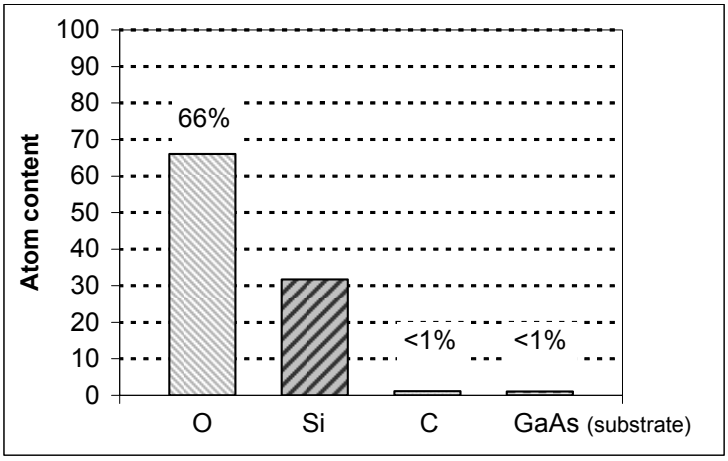

Fig. 2: Chemical composition of EBID-deposited silicon oxide measured by EDX.

Optical properties in the visual range were investigated by optical transmission in the Vis-range using a deposition made on an aperture hole (Fig. 3). With low wavelengths absorption is still considerable. In the mid visual range and with thin layers satisfactory transmission was achieved. In further investigations, thermal annealing of samples will be explored as approach to further increase the optical quality.

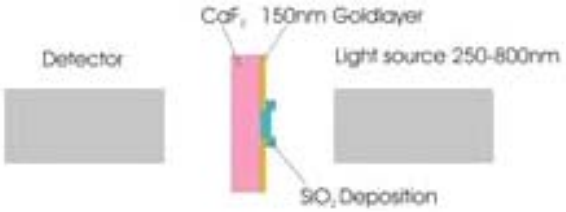

Fig. 3: Schematic illustration of setup for measurement of optical transmission of 120x120 micron deposition on 100x100 micron aperture in reflection layer.

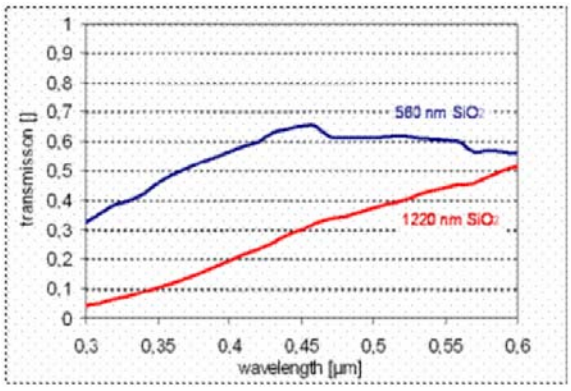

Fig. 4: Optical transmission spectrum of EBID-deposited silicon oxide.

Conclusion

With the electron beam induced deposition pure silicon oxide objects can be fabricated within a single process step. This maskless fabrication method renders a versatile prototyping and repair tool for existent and future nano optics.

References:

[1] Yang MR, Chen KS, Hsu ST, Wu TZ , Surface & Coatings Technol 123 (2-3), 204 (2000)

[2] Dominguez C, Rodriguez JA, Munoz FJ, Zine N , Vacuum 52(4), 395 (1999)

[3] Lipp S, Frey L, Lehrer C, Frank B, Demm E, Pauthner S, Ryssel H, Journal of Vacuum Science & Technology B 14(6), 3920 (1996)

[4] Bret T, Utke I, Hoffmann P, Microelectronic Engineering 78-79, 307 (2005)

Photonic Band Structure Mapping in Mid-Infrared Photodetectors

S. Schartner, M. Austerer, M. Nobile, L. Hoffmann, P. Klang, A.M. Andrews, W. Schrenk, and G. Strasser

Zentrum für Mikro- und Nanostrukturen, TU Wien, Floragasse 7, A-1040 Vienna, Austria

A periodic array of holes is etched through the light sensitive region of mid-infrared photodetectors, which therefore forms a two dimensional photonic crystal slab. This enables sensitivity to light coupled in via the surface. Moreover, since the deep etched structure provides a strong coupling between the optical mode and the photonic lattice, the detector response is enhanced whenever the incoming light matches a photonic crystal mode. This effect is visible through distinct peaks of enhancement in the spectral photocurrent. Via an angular dependent characterization it is possible to map the photonic bandstructure by tracing the energetic position of these peaks.

Introduction

Quantum well infrared photodetectors (QWIPs) are photoconductive detectors that rely on intersubband transitions in a heterostructure [1]. By means of band structure engineering the spectral response can be tailored within the mid-infrared (MIR) region and up to the THz regime [2]. Due to intersubband selection rules n-type QWIPs are only sensitive for radiation with the electric field component polarized normal to the detecting layers. To circumvent the standard detecting geometry, which couples the light via a 45° polished facet, a cavity is needed that can couple surface incident light to detectable TM modes. Surface gratings and random corrugations have been extensively studied in the past [3]. Photonic crystals (PhC) in contrast have only been used so far in combination with a quantum dot infrared detector (QDIP) [4]. The three dimensional electron confinement in a quantum dot makes QDIPs sensitive to surface incident light and the PhC was used to increase the quantum efficiency. Recently we presented a combination of a QWIP with a hexagonal PhC structure [5].

Theory

Aside from the usability as a detector (e.g. one pixel of a focal plane array) it is an ideal test object for slab PhCs. Out of the whole frequency spectrum of an incident beam from a broad band MIR source only a few frequencies are coupled into the waveguide. This happens whenever a pair of in-plane wave vector and frequency matches a mode of the photonic band structure. These modes get absorbed in the quantum wells and contribute to the photocurrent. Each mode can therefore be identified with a peak in the spectral photocurrent. With this method it is possible to map out the whole photonic band structure within the response of the QWIP by simply illuminating at different angles of incidence and crystallographic directions. A similar technique was presented earlier by Astratov *et al.* where resonant features in the reflection from a PhC slab (illuminated in the same geometry) could be related to PhC modes [6].

Experimental

Fabrication

The samples are fabricated in a mix and match processing using direct electron beam lithography for the PhC pattern and standard UV contact lithography to define the insulation openings as well as the extended contact pads for electric connections. After exposure and development of the PMMA resist the pattern is transferred into a SiN_x hard mask and subsequently into the underlying Ge/Au/NiAu contact metal. The deep etching step is performed by reactive ion etching in iCl_4/N_2 [7], which allows to fabricate ~5 µm deep air holes with the required high aspect ratio as well as smoothness of the sidewalls. Figure 1(a) shows a scanning electron picture taken from a cleaved sample directly after the deep etching process. SiN_x insulation and Ti/Au contact pads are finishing the processing (Fig. 1(b)).

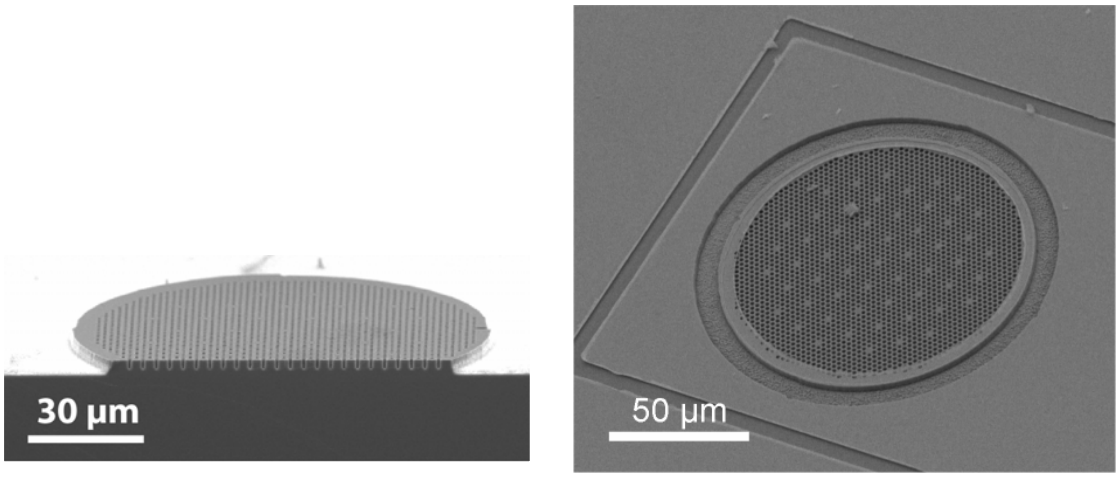

(a) (b)

Fig. 1: Scanning electron pictures taken after the deep etching process (a) and of a finished device (b).

Measurements

Band Structure Measurements

The unpolarized light of a glow bar was directed through a fourier-transform infrared spectrometer and either directly aimed on the sample or polarization filtered in order to achieve a σ (TE) or π (TM) incident wave. By tilting the cryostat around its vertical axis it is possible to collect the response spectra at varying angles of incident. The device was mounted so that either the ΓK or the ΓM direction coincided with the rotation axis. Knowing the angle θ_i and the crystallographic direction of the PhC all positions ω_i of the spectral peaks can be assigned to certain points $(\omega_i/c \cdot \sin(\theta_i), \omega_i)$ in the reduced zone scheme, and the band structure can be recorded by this method. The measurement range is limited at the low frequency end by the air light cone and at the high frequency end by the response function of QWIP used for the experiment. Figure 2(b) shows the mapping of the whole data onto the photonic band structure. The band structure was calculated with the plain wave expansion method (PWEM). Considering the uncertainty in determination of the air fill factor and the absence of the vertical waveguide in the PWEM calculation of the band structure we get very good agreement with the experimental data.

Polarization Mixing

Figure 1(a) shows a typical detector response for unpolarized, TM, and TE polarized light. Apart from the peak at ~920 cm^{-1} (which is congruent with the peak responsivity of the QWIP) there are 6 clearly displayed maxima in the spectrum taken without a polarizer. Some of the resonant peaks disappear for a TM like excitation. In Fig. 2(a) all points originating from a measurement with TM polarized light are marked as a + and can be identified as even cavity modes. This effect has been reported earlier for microwaves [8] and can be explained as free space TM wave is naturally even and can therefore not couple to odd TM PhC modes. An excitation under TE polarization in contrast leads to a detector response for the odd modes. This (even) TE to (odd) TM conversion is basically enabled through the PhC lattice and the vertical surface-plasmon waveguide which allows for polarization mixing as there is a sufficient overlap of the in plane electric fields of both polarizations [9].

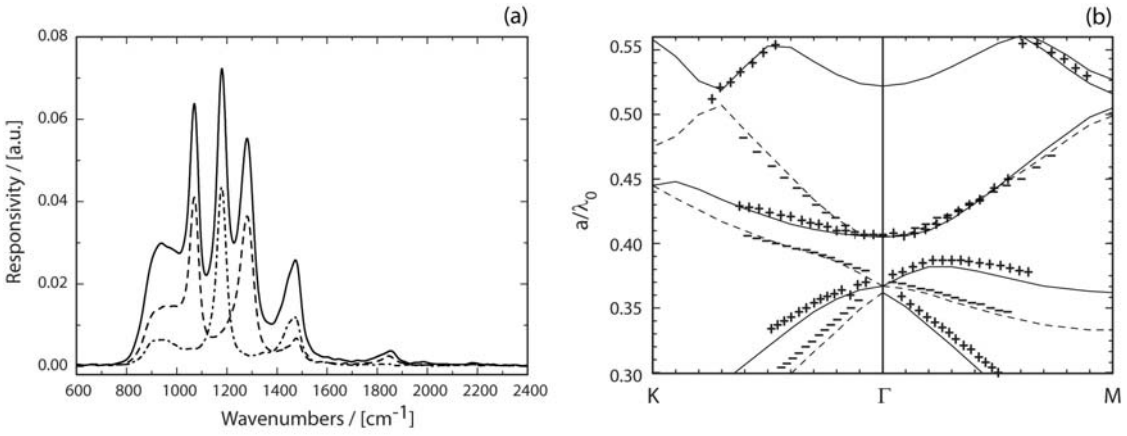

Fig. 2: (a) The response spectra were collected at 50° angle of incident and along ΓM direction. The solid line was measured without a polarizer while the dashed line refers to TM polarized excitation and the chain dotted line refers to TE polarized excitation. (b) Collecting the data points for several angles of incident adds up to the photonic band structure. The underlying lines are a 2D PWEM calculated band structure for TM like modes. The solid lines refer to modes with even symmetry, whereas the dashed lines refer to modes with odd symmetry. The measured data points are marked as + if they originate from TM excitation and are marked as – for TE excitation. Note that TM polarized light couples to even TM modes while TE polarized light couples to odd TM modes

Conclusion

The implementation of a QWIP in a planar PhC cavity makes the sensor capable to detect surface incident radiation. The angular dependence of the response spectra are a direct image of the photonic band structure above the light line and as the measurement principle directly relays on the intracavity absorption of TM polarized photonic crystal modes it represents a very realistic test object for intersubband devices. With this method we performed a polarization dependent band structure mapping which showed a strong polarization mixing for the surface-plasmon waveguide used. The detection for the bands with odd parity is realized via conversion from an incident TE polarized wave to a detectable TM polarized cavity mode.

Acknowledgements

Apart from the GMe we acknowledge partial support by the following projects and agencies: ADLIS, PLATON, and MNA.

References

[1] H. Schneider and H. C. Liu, *Quantum Well Infrared Photodetectors*, (Springer, Berlin, 2007), Vol. 126.

[2] H. C. Liu, C. Y. Song, and A. J. SpringThorpe, J. C. Cao, “THz quantum-well photodetector”, APL **84**, 4068-4070 (2004).

[3] B. F. Levine, “Quantum-well infrared photodetectors”, JAP **74**, R1-R81 (1993).

[4] K. T. Posani, V. Tripathi, S. Annamalai, N. R. Weisse-Bernstein, S. Krishna, R. Perahia, O. Crisafulli, and O. J. Painter, “Nanoscale quantum dot infrared sensors with photonic crystal cavity”, APL **88**, 151104 (2006).

[5] S. Schartner, S. Golka, C. Pflügl, W. Schrenk, A. M. Andrews, T. Roch, and G. Strasser, “Band structure mapping of photonic crystal intersubband detectors”, APL **89**, 151107 (2006).

[6] V. N. Astratov, D. M. Whittaker, I. S. Culshaw, R. M. Stevenson, M. S. Skolnick, T. F. Krauss, and R. M. De-La-Rue, “Photonic band-structure effects in the reflectivity of periodically patterned waveguides”, PRB **60**, R16255 (1999).

[7] S. Golka, S. Schartner, W. Schrenk, and G. Strasser, “Low bias reactive ion etching of GaAs with a SiCl4/N2/O2 time-multiplexed process”, JVSTB **25**(3), 839 (2007)

[8] W. M. Robertson, G. Arjavalingam, R. D. Meade, K. D. Brommer, A. M. Rappe, and J. D. Joannopoulos, “Measurement of Photonic Band Structure in a Two-Dimesional Periodic Dielectric Array” PRL. **68**, 2023 (1992).

[9] D. M. Whittaker, I. S. Culshaw, V. N. Astratov, and M. S. Skolnick, “Photonic band structure of patterned waveguides with dielectric and metallic cladding”, PRB **65**, 073102 (2002).

Microelectronics Technology — Cleanroom Linz

Contents

Micro- and Nanostructure Research: Cleanroom Linz

G. Bauer, W. Jantsch, G. Brunthaler

Institut für Halbleiter- und Festkörperphysik
Johannes Kepler Universität Linz, A-4040 Linz, Austria

The research in the class 100 cleanroom facility of the "*Institut für Halbleiter-und Festkörperphysik*" of the Johannes Kepler Universität Linz depends essentially on the basic support given by the Society for Micro- and Nanoelectronics (GMe). In 2005 and 2006, the focus of the research carried out in Linz continued to be on semiconductor hetero- and nanostructures. The support by the GMe was vital for a number of research grants, in particular for the *Spezialforschungsbereich Infrared Optical Nanostructures*, the initiative *Nanostructured Surfaces and Interfaces* (NSI) and supported within the framework of the *Austrian Nanoinitiative* and a number of other FWF, FFF, and EU supported research efforts. Our work includes nanostructure growth using molecular beam epitaxy and metal organic vapor phase epitaxy, nanostructure fabrication based on several lithography and etching techniques, structural, electronic and optical characterization, fundamental investigations and modeling of physical properties, and finally the realization of novel optoelectronic nanostructure devices, like lasers and detectors. In the Christian-Doppler Laboratory, which is also hosted in our institute, simulation and fabrication of photonic crystals for various optical applications is being performed, and furthermore novel microfluidic devices are being investigated.

The funding of the activities in the cleanroom at the University of Linz which is jointly used by the semiconductor physics group, the solid state physics group, and by the Christian Doppler laboratory is of vital importance for our micro- and nanostructure research activities. This basic funding through the GMe allows for investigations which are made possible through additional funds coming from the FWF, the FFF, the Christian-Doppler society, the European Union as well as through cooperations with industrial groups as listed in the report.

The material basis of the work at our Institute is given by the epitaxial growth of Si/SiGe, IV-VI compounds, GaN based and organic hetero-and nanostructures using growth techniques like molecular beam epitaxy and metal organic chemical vapor phase deposition as well as hot wall epitaxy. In cooperation with the University of Lund, Sweden, the Institute is also involved in the growth of III-V compound nanowires, in particular on Si. The fundamental structural, electronic, optical and magnetic properties of nanostructures and semiconducting layers are studied using a large variety of characterization techniques. These range from advanced x-ray scattering techniques using synchrotron radiation, high-resolution electron microscopy, scanning force and scanning tunneling microscopy, optical spectroscopy, magnetic Squid investigations as well as low temperature magnetotransport measurements. The focus of research is to correlate the electronic properties of nanostructures with the fabrication processes and structural properties, taking advantage of the complementarity of information gained by the different techniques and modeling tools.

As far as device related studies are concerned, vertical microcavity lasers for the mid-infrared were realized based on broad band PbEuSe/BaF_2 broad band Bragg mirrors with cw emission up to 135K. With additional support from the company Infra-Tec dual band PbTe/BaF_2 Bragg mirrors with broad stop bands grown by MBE on Si (111) sub-

strates were realized, which offer applications for sensing in the spectral range of the two atmospheric windows in the infrared. For the mid-infrared also narrow-band lead-salt based photodetectors as well as solution-processible nanocrystal photodetectors were realized, the latter ones with so far unparalleled properties. Based on colloidal nanocrystals waveguides were fabricated and optical gain studies were performed. In collaboration with Konarka, a technique for the structuring of organic semiconductors was developed based on optical lithography and oxygen etching. Within the Christian Doppler Laboratory vertical taper structures for a fiber to chip coupler were fabricated and analyzed.

In collaboration with Electronic Vision a technique for preparing microfluidic devices in a special resist (Su 8) was developed based on a low temperature wafer bonding process, which turned out to be a viable MEMS fabrication technique.

The successful MOCVD growth of GaN and Fe doped GaN was made possible by careful in-situ investigations based on optical ellipsometry and in-situ x-ray diffraction studies which led to a superior control of growth rates. Hall effect, photoluminescence in GaN:Fe and GaFeN:Mg layers were performed, the magnetic properties of these materials were investigated as a function of the co-doping, with Mg using SQUID magnetometry, magnetic resonance, electron spin resonance, having spintronic applications in mind. In the magnetic semiconductor system GeMnTe, grown by MBE in Linz, carrier-mediated ferromagnetism with Curie temperatures exceeding 200 K could be found.

In the SiGe system growth studies were focused on the realization of perfect two-dimensional lattices of SiGe islands on prepatterned Si substrates, as well as on the growth of Si islands on Ge substrates. A combination of structural characterization and photoluminescence studies was used to investigate the electron-hole recombination channels of electron-hole pairs in strained Si and SiGe islands, for which quite elaborate band-structure calculations including inhomogeneous strain fields were performed. In such structures also electron spin resonance experiments were performed and as compared to III-V compounds exceptionally long T_1 and T_2 times were observed. The transport properties of holes in undulated SiGe channels, grown on Si step-bunching templates, were studied in detail.

The study of IV-VI compound nanostructures was continued leading again to important results. A study of the overgrowth of PbSe quantum dots by PbTe and PbEuTe was performed and the shape transitions of the PbSe islands were investigated in detail using scanning tunneling microscopy, giving insight in details of the capping process. The formation of PbTe quantum dots in a zinc-blende CdTe matrix was investigated by transmission electron microscopy, bright photoluminescence was observed from these dots which are formed on the basis of a mechanism barely exploited so far for nanostructure formation.

In the electric/electronic application field, devices such as quantum dot and single electron transistors were formed in the Si/SiGe and AlGaAs/GaAs material systems and investigated in the milli-Kelvin regime.

The fabricated structures from the Institute in Linz were supplied also to external research groups in the framework of long term international collaborations. On the other hand, also materials and structures including SiGe as well as GaAs/GaAlAs based structures are supplied for studies in Linz from outside groups, in particular from the Technical University Vienna, for further processing and analysis with techniques developed at our institute.

The research activities are embedded in several large research initiatives and project clusters such as the IRON special research program, the NIS Nanostructured Surface and Interface project cluster, as well as the SANDiE European network of excellence and several other EU funded research projects. The principal investigator of a National

Research Network entitled “Interface Controlled Functionalised Organic Films”, which is funded by the FWF, is based in our Institute. In the reporting period also the PLATON project within the Austrian Nanoinitiative, in cooperation with the Technical University of Vienna and several companies, was evaluated successfully and will start in 2007.

A detailed presentation of the investigations carried out, and of the device fabrication is given below, in the individual reports.

Research Activities

Material Growth and Analysis

Mid-Infrared Optoelectronics

Microfluidics

Magnetic Semiconductors

SiGe Nanostructures

IV-VI Compound Nanostructures

Quantum Devices and Single Electron Transistors

Project Information for 2005 and 2006

Project Manager

a.Prof. Dr. Gerhard Brunthaler

Institut für Halbleiter-und Festkörperphysik,
Johannes Kepler Universität Linz,
A-4040 Linz, Austria

Project Group

Last Name	First Name	Status	Remarks
Bauer	Günther	University professor	
Jantsch	Wolfgang	University professor	
Schäffler	Friedrich	University professor	
Brunthaler	Gerhard	Associate professor	
Springholz	Gunther	Associate professor	
Sitter	Helmut	Associate professor	
Bonanni	Alberta	Assistant professor	
Heiss	Wolfgang	Assistant professor	
Fromherz	Thomas	Assistant professor	
Stangl	Julian	Assistant professor	
Binder	Fritz	Technician	
Bräuer	Stephan	Technician	
Fuchs	Othmar	Technician	
Jägermüller	Josef	Technician	
Nusko	Ekkehard	Electronics Engineer	
Teuchtmann	Michael	Technician	FWF
Vorhauer	Ernst	Electronics engineer	
Andreeva	Svetlana	Lab Technician	FWF
Halilovic	Alma	Lab Technician	
Hasenfuss	Christine	Lab Technician	CD Lab
Praus	Antonia	Lab Technician	1/2 position
Burgstaller	Elisabeth	Phys. Lab. Assistent	1/2 position
Firmberger	Johanna	Apprentice	
Hingerl	Kurt	Head of CD Lab	
Holy	Vaclav	Guest Researcher	Charles Univ. Prag
Chen	Gang	Post Doc	FWF
Egelhaaf	Hans-Joachim	Senior Post Doc	CDG
Forberich	Karen	Post Doc	CDG
Gajic	Rados	Senior Post Doc	CDG

Last Name	First Name	Status	Remarks
Kocher	Gudrun	Post Doc	CD Lab (Jan. - June)
Lechner	Rainer	Post Doc	FWF
Meduna	Mojmir	Post Doc	EC (SHINE)
Sanduijav	Bolormaa	Post Doc	FWF
Schwarzl	Thomas	Post Doc	FWF
Wolos	Agnieszka	Post Doc	FWF
Abtin	Laurel	Ph.D. student	FWF
Achleitner	Joachim	Ph.D. student	
Ameri[1]	Tayebeh	Ph.D. student	CDG
Azimi[2]	Hamed	Ph.D. student	CDG
Baumgartner	Eugen	Ph.D. student	FWF
Berer	Thomas	Ph.D. student	Uni Linz
Böberl	Michaela	Ph.D. student	FWF
Bodnarchuk	Marina	Ph.D. student	FWF
Glinsner	Thomas	Ph.D. student	EVG
Gruber	Daniel	Ph.D. student	Uni Linz
Grydlik	Martyna	Ph.D. student	FWF
Hernández Sosa	Gerardo	Ph.D. student	Scholarship from Mexico
Holly	Roman	Ph.D. student	CDG
Kaufmann	Erich	Ph.D. student	FWF
Kovalenko	Maksym	Ph.D. student	FWF
Lavchiev	Ventsislav	Ph.D. student	CDG
Lichtenberger	Herbert	Ph.D. student	FWF
Lugovyy	Dmytro	Ph.D. student	FWF
Malissa	Hans	Ph.D. student	WIMI
Matei	Dan	Ph.D. student	FWF
Mundboth	Rajivshing	Ph.D. student	FWF (Jan. - June)
Navarro-Quezada	Andrea	Ph.D. student	Scholarship from Mexico
Novak	Jiri	Ph.D. student	EC (SHINE, only 1 month)
Pachinger	Dietmar	Ph.D. student	FWF
Pillwein	Georg	Ph.D. student	FWF
Rauter	Patrick	Ph.D. student	EC (SHINE)
Rehman-Khan	Aaliya	Ph.D. student	ÖAD
Roither	Jürgen	Ph.D. student	FWF
Schmidegg	Klaus	Ph.D. student	EU ISCE-MOCVD, FWF
Simbrunner	Clemens	Ph.D. student	Projekt PANalytical
Simma	Matthias	Ph.D. student	FWF
Söllinger	Walter	Ph.D. student	FWF

[1] From April 2006 on
[2] From December 2006 on

Last Name	First Name	Status	Remarks
Wegscheider	Matthias	Ph.D. student	FWF
Wintersberger	Eugen	Ph.D. student	FWF
Zarbakhsh	Javad	Ph.D. student	CDG
Youssof	Rashid	Ph.D. student	CDG
Anzengruber	Johannes	Diploma student	
Aynul	Islam	Diploma student	
Bergmair	Michael	Diploma student	
Bergmair	Iris	Diploma student	
Brehm	Moritz	Diploma student	
Eibelhuber	Martin	Diploma student	
Groiss	Heiko	Diploma student	
Grydlik	Martyna	Diploma student	stipendiat
Huber	Martin	Diploma student	
Isfahani	Farnaz	Diploma student	CD Lab (Jan. – June)
Islam	Aynul	Diploma student	
Kirchschlager	Raimund	Diploma student	
Krimbacher	Stefan	Diploma student	
Mandl	Bernhard	Diploma student	
Niedermayr	Michael	Diploma student	
Pichler	Stefan	Diploma student	
Plochberger	Birgit	Diploma student	
Quast	Martin	Diploma student	
Suzuki	Tomoyuki	Diploma student	

Publications in Reviewed Journals

1. A. Bonanni, C.Simbrunner, M.Wegscheider, H.Przybylinska, A.Wolos, H.Sitter, W.Jantsch
Doping of GaN with Fe and Mg for spintronics applications
Phys. Stat. Sol (b) 243 (7), 1701-1705 (2006)

2. A. Kozanecki, D.Kuritsyn, W.Jantsch
On the role of Yb as an impurity in the excitation of Er3+ emission in silicon-rich silicon oxide
Optical Materials 28 (6-7), 850-854 (2006)

3. A. M. Tyryshkin, S.A.Lyon, T.Schenkel, J.Bokor, J.Chu, W.Jantsch, F.Schäffler, J.L.Truitt, S.N.Coppersmith, M.A.Eriksson
Electron spin coherence in Si
PHYSICA E-LOW-DIMENSIONAL SYSTEMS & NANOSTRUCTURES 35 (2): 257-263 DEC 2006 (2006)

4. A. Yu. Andreev, A.Montaigne, G.Hlawacek, H.Sitter, C.Teichert
Para-Sexiphenyl Thin Films Grown by Hot Wall Epitaxy on KCl(100) substrates
J. of Vac. Sci. and Technol. A, 24/4, 1660-1663 (2006)

5. B. A. Andreev, T.Gregorkiewicz, W.Jantsch, Z.F.Krasilnik, D.I.Kryzhkov, V.P.Kuznetsov

1.54μm Si:Er light-emitting diode with memory function
Appl. Phys. Lett. 88 (20), 201101/1-3 (2006)

6. B. Mandl, J. Stangl, T. Mårtensson, A. Mikkelsen, J. Eriksson, L. S. Karlsson, G. Bauer, L. Samuelson, W. Seifert, Au-free epitaxial growth of InAs nanowires, NanoLetters 6, 1817-1821 (2006).
7. C. Simbrunner, K.Schmidegg, A.Bonanni, A.Kharchenko, J.Bethke, J.Woitok, K.Lischka,H.Sitter
In-Situ Monitoring of MOCVD Growth by ellipsometry and X-ray diffraction
Phys. Stat. Sol (a), 203 (7), 1704-1707 (2006)
8. D. Gruber, D. Pachinger, H. Malissa, M. Mühlberger, H. Lichtenberger, W. Jantsch and F. Schäffler, g-Factor tuning of 2D electrons in double-gated Si/SiGe quantum wells, Physica E: Low-dimensional Systems and Nanostructures 32, 254-257 (2006)
9. E. W. Baumgartner, T. Schwarzl, G. Springholz, W. Heiss, Highly efficient epitaxial Bragg mirrors with broad omnidirectional reflectance bands in the mid-infrared, Applied Physics Letters 89, 051110-12 (2006).
10. F. Pezzoli, E. Grilli, M. Guzzi, S. Sanguinetti, H. D. Chrastina, G. Isella, H. von Känel, E. Wintersberger, J. Stangl, G. Bauer, Strain-induced shift of phonon modes in Si1-xGex alloys, Mat. Sci. Sem. Proc. 9, 541-545 (2006).
11. G. Bauer, F. Schäffler, Self-assembled Si and SiGe nanostructures: new growth concepts and structural analysis, phys. stat. sol. (a) 203, 3496-3505 (2006).
12. G. Chen, H. Lichtenberger, F. Schäffler, G. Bauer, W. Jantsch, Geometry dependent nucleation mechanism for SiGe islands grown on pit-patterned Si(001) substrates, Mat. Sci. Eng. C 26, 795-799 (2006).
13. G. Chen, H. Lichtenberger, G. Bauer, W. Jantsch, and F. Schäffler, Initial stage of the 2D-3D transition of a strained SiGe layer on a pit-patterned Si(001) template, Phys. Rev. B, 74 035302-1/8 (2006)
14. G. Chen, H.Lichtenberger, G. Bauer, W. Jantsch, F. Schäffler
Initial stage of the 2D-3D transition of a strained SiGe layer on a pit-patterned Si(001) template
Phys.Rev. B - Condensed Matter and Materials Physics 74 (3), 035302/1-8 (2006)
15. G. Grabecki, J. Wróbel, P. Zagrajek, K. Fronc, M. Aleszkiewicz, T. Dietl, E. Papis, E. Kaminska, A. Piotrowska, G. Springholz, and G. Bauer, Quantum nanostructures of paraelectric PbTe, Physica E 35, 332-337 (2006).
16. G. Grabecki, J. Wróbel, T. Dietl, E. Janik, M. Aleszkiewicz, E. Papis, E. Kaminska, A. Piotrowska, G. Springholz, G. Bauer, PbTe - A new medium for quantum ballistic devices, Physica E 34, 560-563 (2006).
17. G. Springholz, T. Schwarzl, W. Heiss, Mid-infrared Vertical Cavity Surface Emitting Lasers based on the Lead Salt Compounds, in: Mid-infrared Semiconductor Optoelectronics, ed. A. Krier (Springer-Verlag London, 2006, ISBN, 184628208X), p. 262 – 302.
18. H. Malissa, D. Gruber, D. Pachinger, F. Schäffler, W. Jantsch, Z. Wilamowski, Design and fabrication of a SiGe double quantum well structure for g-factor tuning, Superlattices and Microstructures 39, 414-420, 2006.
19. H. Malissa, W. Jantsch, G. Chen, D. Gruber, H. Lichtenberger, F. Schäffler, Z. Wilamowski, A. Tyryshkin, S. Lyon, Investigation of the spin properties of electrons in zero-dimensional SiGe structures by electron paramagnetic resonance, Mat. Sci. Eng. B 126, 172-175 (2006).

20. H. Przybylinska, A.Bonanni, A.Wolos, M.Kiecana, M.Sawicki, T.Dietl, H.Malissa, C.Simbrunner, M.Wegscheider, H.Sitter, K.Rumpf, P.Granitzer, H.Krenn, W.Jantsch
Magnetic properties of a new spintronic material - GaN:Fe
Mat. Science Engineering B 126, 222-225 (2006)

21. J. Roither, S.Pichler, M.V.Kovalenko, W.Heiß, P. Feychuk, O. Panchuk, J. Allam, B.N. Murdin
Two- and one-dimensional light propagations and gain in layer-by-layer-deposited colloidal nanocrystal waveguides
Appl. Phys. Lett. 89, 111120/1-3 (2006)

22. K. Lai, P. D. Ye, W. Pan, D. C. Tsui, S. A. Lyon, M. Mühlberger, F. Schäffler, Quantum Hall ferromagnetism in a two-valley strained Si quantum well, Physica E: Low-dimensional Systems and Nanostructures 34, 176-178 (2006)

23. K. Lai, T. M. Lu, W. Pan, C. Tsui, S. Lyon, J. Liu, Y. H. Xie, M. Mühlberger, F. Schäffler, Valley splitting of Si/Si1-xGex heterostructures in tilted magnetic fields, Phys. Rev. B 73, 161301-1/4 (2006).

24. K. Lai, W. Pan, D. C. Tsui, S. Lyon, M. Mühlberger, F. Schäffler, Intervalley gap anomaly of two-dimensional electrons in silicon, Phys. Rev. Lett. 96, 076805-1/4 (2006).

25. L. Abtin, G. Springholz, V. Holy, Surface exchange and shape transition of PbSe quantum dots during overgrowth, Phys. Rev. Lett. 97, 266103-1/4 (2006).

26. M. Böberl, T. Fromherz, J. Roither, G. Pillwein, G. Springholz, W. Heiss, Room temperature operation of epitaxial lead-telluride detectors monolithicallly integrated on midinfrared filters, Appl. Phys. Lett. 88, 041105-1/3 (2006).

27. M. Grydlik , P. Rauter T. Fromherz , G. Bauer , C. Falub , D. Gruetzmacher, G. Isella, Resonator Fabrication for Cavity Enhanced, Tunable Si/Ge Quantum Cascade Detectors, Physica E 32, 313-315 (2006).

28. M. I. Richard, T.-U. Schülli, E. Wintersberger, G. Renaud, G. Bauer, Growth mode, strain state and shape of Ge islands during their growth at different temperatures: a combined in situ GISAXS and GIXD study, Thin Solid Films 508, 213-217 (2006).

29. M. M. Rzaev, I. P. Kazakov, V. I. Kozlovski, Y. K. Skasyrsky, E. E. Onishchenko, F. Schäffler, G. Hesser, E. M. Pashaev, I. A. Soubbotin, Growth, structural and optical studies of CdSe/ZnSe nanostructures grown by MBE on GaAs and Si substrates, phys. stat. sol. (c) 3, 536-539 (2006).

30. M. Simma, D. Lugovyy, T. Fromherz, A.Raab, G. Springholz, G. Bauer, Deformation potentials and photo-response of strained PbSe quantum wells and quantum dots, Physica E 32, 123-126 (2006).

31. M. Simma, T. Fromherz, A. Raab, G. Springholz, G. Bauer, Lateral photocurrent spectroscopy on self-assembled PbSe quantum dots, Appl. Phys. Lett. 88, 201105-1/3 (2006)

32. M. Tyryshkin, S. A. Lyon, T. Schenkel, J. Bokor, J. Chu, W. Jantsch, F. Schäffler, J. L. Truitt, S. N. Coppersmith, M. A. Eriksson, Electron spin coherence in Si, Physica E: Low-dimensional Systems and Nanostructures 35, 257-263 (2006).

33. M. V. Kovalenko, E. Kaufmann, D. Pachinger, J. Roither, M. Huber, J. Stangl, G. Hesser, F. Schäffler, W. Heiss, Colloidal HgTe Nanocrystals with widely tunable narrow band gap energies: from telecommunications to molecular vibrations, J. Am. Chem. Soc. 128, 3516-3517 (2006).

34. M. Wegscheider, C.Simbrunner, H.Przybylinska, M.Kiecana, M.Sawicki, A.Navarro-Quezada, H.Sitter, W.Jantsch , T.Dietl, A.Bonanni
Photoluminescence and Hall studies of GaN:Fe and (Ga,Fe)N:Mg layers
Phys. stat. sol. (a) 204, 86-91 (2006)

35. P. Rauter, T. Fromherz, G. Bauer, N. Q. Vinh, B. N. Murdin, J. P. Phillips, C. R. Pidgeon, L. Diehl, G. Dehlinger, D. Grützmacher, Direct monitoring of the excited state population in biased SiGe valence band quantum wells by femtosecond resolved photocurrent experiments, Appl. Phys. Lett. 89, 211111-1/3 (2006).

36. R. Khan, J. Stangl, G. Bauer, D. Buca, B. Holländer, H. Trinkaus, S. Mantl, R. Loo, M. Caymax, Study of relaxation of strain in patterned Si/SiGe structures using an x-ray diffraction technique, Semicond. Sci. Technol. 21, 1-4 (2006).

37. R. Leitsmann, L. E. Ramos, F. Bechstedt, H. Groiss, F. Schäffler, W. Heiss, Kazuto Koike, Hisashi Harada, Mitsuaki Yano, Rebonding at coherent interfaces between rocksalt-PbTe / zinc-blende-CdTe, New Journal of Physics 8, 317/1-9 (2006).

38. R. T. Lechner, G. Springholz, T. U. Schülli, J. Stangl, T. Schwarzl, D. Lott, V. Leiner, A. Schreyer, H. Clemens, G. Bauer, Spin configurations in strained magnetic EuSe/PbSe1-xTex superlattices grown by molecular beam epitaxy, Physica E 32, 379-382 (2006).

39. S. D. Ganichev, S.N.Danilov, V.V.Bel'kov, S.Giglberger, S.A.Tarasenko, E.L.Ivchenko, D.Weiss, W.Jantsch, F.Schäffler, D.Gruber, W.Prettl
Pure spin currents induced by spin dependent scattering processes in SiGe quantum well structures
arXiv:cond-mat/ 0610736/1-6 v1 , 26 Oct 2006 (2006)

40. T. Berer, D. Pachinger, G. Pillwein, M. Mühlberger, H. Lichtenberger, G. Brunthaler, F. Schäffler, Lateral quantum dots in Si/SiGe realized by a Schottky split-gate technique, Appl. Phys. Lett. 88, 162112-1/3 (2006)

41. T. Berer, D. Pachinger, G. Pillwein, M. Mühlberger, H. Lichtenberger, G. Brunthaler and F. Schäffler, Single-electron transistor in strained Si/SiGe heterostructures, Physica E: Low-dimensional Systems and Nanostructures 34, 456-459 (2006).

42. T. G. Yugova, M. G. Mil'vidski, M. M. Rzaev, F. Schäffler, Thermally stimulated relaxation of misfit strains in Si1-xGex/Si(100) heterostructures with different buffer layers, Surface and Thin Films 50, 1099-1106 (2006).

43. T. Gregorkiewicz, B.A. Andreev, M.Forcales, I.Izeddin, W. Jantsch, Z.F.Krasil'nik, D.I. Kryzhkov, V.P. Kuznetsov,J.M. Zavada
Er-doped electro-optical memory element for 1.5 μm silicon photonics;
IEEE Journal of Selected Topics in Quantum Electronics, 12(6), 1539-1544 , ISSN:1077-260X; digiral object identifier:10.1109/JSTQE.2006.884062 (2006)

44. T. Schwarzl, J. Fürst, M. Böberl, E. Kaufmann, J. Roither, H. Pascher, G. Bauer, G. Springholz, W. Heiss, Mid-infrared emission from 100% spin-polarized states in IV-VI vertical-cavity surface emitting lasers, Narrow Gap Semiconductors, eds. Kono & Léotin, Institute of Physics Conference Series Number 187, Taylor & Franics 2006, 329-334 (2006).

45. T. U. Schülli, M.-I. Richard, G. Renaud, V. Favre-Nicolin, E. Wintersberger, G. Bauer, In situ investigation of the island nucleation of Ge on Si(001) using x-ray scattering methods, Appl. Phys. Lett. 89, 143114-1/3 (2006)

46. V. Glukhanyuk, H.Przybylinska, A.Kozanecki, W.Jantsch
Optical Properties of a single Er center in GaN
Optical Materials 28 (1-2), 746-749 (2006)

47. V. Glukhanyuk, H.Przybylinska, A.Kozanecki, W.Jantsch
Resonant optical spectroscopy of Er3+ centers in hexagonal GaN-analysis of symmetry
Optical Materials 28 (1-2), 111-114 (2006)

48. V. Holy, T. U. Schülli, R. T. Lechner, G. Springholz, G. Bauer, Changes in the shapes of self-organized PbSe quantum dots during PbEuTe overgrowth investigated by anomalous x-ray diffraction, Applied Surface Science 253, 177-181 (2006).

49. V. Rinnerbauer, K.Hingerl, M.Kovalenko, W.Heiß
Effect of quantum confinement on higher transitions in HgTe nanocrystals
Appl.Phys.Lett, 89, 193114 /1-3 (2006)

50. V. Rinnerbauer, M.Kovalenko, V.Lavchiev, G.Kocher, J.Roither, W.Heiß, K.Hingerl
Spectroscopic ellipsometry of layer by layer deposited colloidal HgTe nanocrystals exhibiting quantum confinement
Physica E 32, 1-2, 104 -107(2006)

51. W. Heiss, E. Kaufmann, M. Böberl, T. Schwarzl, G. Springholz, G. Hesser, F. Schäffler, K. Koike, H. Harada and M. Yano, Highly luminescent nanocrystal quantum dots fabricated by lattice-type mismatched epitaxy, Physica E: Low-dimensional Systems and Nanostructures 35, 241-245 (2006).

52. W. Heiss, H. Groiss, E. Kaufmann, G. Hesser, M. Böberl, G. Springholz, F. Schäffler, K. Koike, H. Harada, M. Yano, Centrosymmetric PbTe/CdTe quantum dots coherently embedded by epitaxial precipitation, Appl. Phys. Lett. 88, 192109-1/3 (2006).

53. Z. F. Krasilnik, B.A.Andreev, T.Gregorkiewicz, W.Jantsch, M.A.J. Klik, D.I.Kryzhkov, L.V. Krasilnikova, V.P.Kuznetsov, H.Przybylinska, D.Yu.Remizov, V.G.Shengurov, V.B.Shmagin, M.V.Stepikhova, V.Yu.Timoshenko, N.Q.Vinh, A.N.Yablonskiy, D.M.Zhigunov (invite
Erbium Doped Silicon Single- and Multilayer Structures for LED and Laser Applications
Journal of Materials Research 21 (3), 574-583 (2006)

54. Z. Wilamowski, H.Malissa, F.Schäffler,W.Jantsch
g-Factor Tuning and Manipulation of Spins by an Electric Current
arXiv:cond-mat/ 0610046/1-4 v1, 2 Oct 2006, (2006)

55. Z. Zhong, H. Lichtenberger, G. Chen, M. Mühlberger, C. Schelling, J. Myslivecek, A. Halilovic, J. Stangl, G. Bauer, W. Jantsch, F. Schäffler, Ordered SiGe islands on vicinal and pre-patterned Si(001) substrates, Microelectronic Engineering 83, 1730-1735 (2006)

56. Z. Zhong, J. Novak, J. Stangl, Th. Fromherz, F. Schäffler, and G. Bauer, Growth and characterization of two- and three-dimensionally ordered quantum dots, Journal of Physics: Conference Series 38, 69-74 (2006).

57. “Band Structure, Wiener bounds and Coupled Surface Plasmons in 1D Photonic Crystals” M. Bergmair, M Huber and K. Hingerl, Appl. Phys. Lett. 89, 081907 (2006)

58. “All-angle left-handed negative refraction in Kagomé and honeycomb lattice photonic crystals”, R. Gajic, R. Meisels, F. Kuchar, and K. Hingerl, Phys. Rev. B 73, 165310, (2006)

59. “Effect of Quantum Confinement on Higher Transitions in HgTe Nanocrystals” V. Rinnerbauer, M. Kovalenko, W. Heiss and K. Hingerl, Appl. Phys. Lett. 89, 193114, (2006)

60. “Fabrication of silicon vertical taper structures using KOH anisotropic etching”, R. Holly and K. Hingerl, Microelectronic Engineering, 83, 1430, (2006)

61. “Negative refraction and flat-lens focusing in a 2D square-lattice photonic crystal at microwave and millimeter wave frequencies” R. Meisels, R. Gajic, F. Kuchar, K. Hingerl, Opt. Expr. 14, pp. 6766-6777 (2006)

62. “Optimization of a 2D photonic crystal add/drop multiplexer based on contra-directional coupling” M. Svaluto Moreolo, F. Silvestri, M. Armellino, K. Hingerl, G. Cincotti, Photonics and Nanostructures 4, 155, (2006)

63. “Spectroscopic ellipsometry of layer by layer deposited colloidal HgTe nanocrystals exhibiting quantum confinement” V. Rinnerbauer, M. Kovalenko, V. Lavchiev, G. Kocher, J. Roither, W. Heiss, K. Hingerl, Physica E32, 1-2, 104, (2006)

64. “Strain oscillations probed with light” L. D. Sun, M. Hohage, P. Zeppenfeld, R. Balderas- Navarro and K. Hingerl, Phys. Rev. Lett. 96, 016105 (2006)

65. A. Bonanni, K. Schmidegg, H. Sitter, D. Stifter
In-situ multiple wavelength ellipsometry for real time process characterization of nitride MOCVD
Proceedings of the ICPS-27, (2005)

66. A. Bonanni, K.Schmidegg, D.Stifter, H.Sitter
Simultaneous determination of compsition and growth rate of MOCVD ternary nitride compounds by multiple wavelength spectroscopic ellipsometry
J. Cryst.Growth 275, 1763 (2005)

67. A. Borak, S. Tsujino, C. Falub, M. Scheinert, L. Diehl, E. Müller, H. Sigg, D. Grützmacher, U. Gennser, I. Sagnes, S. Blunier, T. Fromherz, Y. Campidelli, O. Kermarrec, D. Bensahel, J. Faist, “Recent results on the road to a SiGe quantum cascade laser”, Group-IV-Semiconductor-Nanostructures.-Symposium-Materials-Research-Society-Symposium-Proceedings 832, 69-80 (2005).

68. A. Kharchenko, K. Lischka, K. Schmidegg, J. Bethke, J. Wojtok, H. Sitter
In-situ and real time characterization of MOCVD growth by high resolution x-ray diffraction
Rev. Scientific Instruments 76, (2005)

69. A. Rehman Khan, K. Mundboth, J. Stangl, G. Bauer, H. von Känel, A. Fedorov, B. G. Isella, D. Colombo, “X-Ray investigation of thick epitaxial GaAs/InGaAs layers on Ge pseudosubstrates”, Proceedings of the IEEE International Conference on Emerging Technologies (ICET ‘05), pp. 323-328 (2005).

70. A. Yu. Kuntsevich, D. A. Knyazev, V. I. Kozub, V. M. Pudalov, G. Brunthaler, G. Bauer, “Nonmonotonic temperature dependence of the Hall resistance of a 2D electron system in silicon”, JETP Letters 81, 409-412 (2005).

71. A.M. Tyryshkin, S. Lyon, W. Jantsch, F. Schäffler
Spin Manipulation of free 2-dimensional electrons in Si/SiGe quantum wells
Virtual Journal of Quantum Information 4 (2005)

72. A.M. Tyryshkin, S.A. Lyon, W. Jantsch, F. Schäffler, “Spin Manipulation of Free Two-Dimensional Electrons in Si/SiGe Quantum Wells”, Phys. Rev. Lett. 94, 126802-1/4 (2005).

73. B. Henriques, A. Wierts, M. A. Manfrini, G. Springholz, P. H. O. Rappl, E. Abramof, A. Y. Ueta, “Band-edge polarized optical absorption in europium chalcogenides”, Phys. Rev. B 72, 155337-1/5 (2005).

74. C. R. Pidgeon, P. J. Phillips, D. Carder, B. N. Murdin, T. Fromherz, D. J. Paul, Wei-Xin Ni, and Ming Zhao, “Pump–probe measurement of lifetime engineering in

SiGe quantum wells below the optical phonon energy", Semicond. Sci. Technol. 20, L50-2 (2005).

75. C. V. Falub, M. Meduna, D. Grützmacher, S. Tsujino, E. Müller, H. Sigg, A. Borak, T. Fromherz, G. Bauer, "Structural studies of strain-symmetrised Si/SiGe structures grown by molecular beam epitaxy", J. Crystal Growth 278, 495-499 (2005).
76. C.P.T. Svensson, W. Seifert, M.W. Larsson, J. Stangl, G. Bauer, L. Samuelson, "Epitaxially grown GaP/GaAs1-xPx/GaP double heterostructure nanowires for optical applications", Nanotechnology 16, 936-939 (2005).
77. D. Chrastina, G. Isella, M. Bollani, B. Rössner, E. Müller, T. Hackbarth, E. Wintersberger, Z. Zhong, J. Stangl, H. von Känel, "Thin relaxed SiGe virtual substrates grown by low-energy plasma-enhanced chemical vapor deposition", J. Cryst. Growth 281, 281-289 (2005).
78. D. Gruber, H. Malissa, G. Chen, D. Pachinger, H. Lichtenberger, T. Fromherz, F. Schäffler, G. Bauer, W. Jantsch, A. M. Tyryshkin, and S. A. Lyon, High Mobility Si/SiGe Heterostructures for Spintronics Applications, in: Proceedings of the Seminar at the Vienna University of Technology, March 17-18 (ISBN: 3-901578-15-3), pp. 109-112 (2005).
79. D. Grützmacher, S. Tsujino, C. Falub, A. Borak, L. Diehl, E. Müller, H. Sigg, U. Gennser, T. Fromherz, M. Meduna, G. Bauer, J. Faist, O. Kermarrec, "Transport and absorption in strain-compensated Si/Si1-xGex multiple quantum well and cascade structures deposited on Si0.5Ge0.5 pseudosubstrates", Materials Science in Semiconductor Processing 8, 401-409 (2005).
80. E. Baumgartner, T. Schwarzl, G. Springholz, W. Heiss, "Epitaxial Bragg Mirrors with Broad Omnidirectional Stop Band in the Mid-Infrared", In: Proceedings of the Seminar at the Vienna University of Technology, March 17-18 (ISBN: 3-901578-15-3), pp. 67-70 (2005).
81. F. Pezzoli, Lucio Martinelli, E. Grilli, M. Guzzi, S. Sanguinetti, M. Bollani, H.D. Chrastina, G. Isella, H. von Känel, E. Wintersberger, J. Stangl, G. Bauer, Raman "Spectroscopy of Si1-xGex epilayers", Materials Science and Engineering B 124, 127-131 (2005).
82. G. Bauer, G. Springholz, "Lead Salts", in: Encyclopedia of Modern Optics, ed.: B. D. Guenther, Elsevier 2005, p. 385-392 (2005).
83. G. Chen, H. Lichtenberger, G. Bauer, and F. Schäffler, Self-Organization of Ripples and Islands with SiGe-MBE, in: Proceedings of the Seminar at the Vienna University of Technology, March 17-18 (ISBN: 3-901578-15-3), pp. 123-127 (2005).
84. G. Grabecki, J. Wrobel, T. Dietl, E. Janik, M. Aleszkiewicz, E. Papis, E. Kaminska, A. Piotrowska, G. Springholz, G. Bauer, "Disorder suppression and precise conductance quantization in constrictions of PbTe quantum wells", Phys. Rev. B, 125332-1/6 (2005).
85. G. Hlawacek, C. Teichert, A. Andreev, H. Sitter, S. Berkebile, G. Koller, M. Ramsey, R. Resel
Self-organization of para-sexiphenyl on crystalline substrates
Phys.Stat.Sol.(a) (2005)
86. G. Hobler, G. Otto, D. Kovac, L. Palmetshofer, K. Mayrhofer, K. Piplits
Multiscale Approach for the Analysis of Channeling Profile Measurements of Ion Implantation Damage
Nucl. Instr. Meth. B 228 (2005)

87. G. Pillwein, T. Berer, G. Brunthaler, F. Schäffler, and G. Strasser, “Lateral Quantum Dots in High Mobility Heterostructures”, in: Proceedings of the Seminar at the Vienna University of Technology, March 17-18 (ISBN: 3-901578-15-3), pp. 133-136 (2005).

88. G. Springholz, “Three-dimensional stacking of self-assembled quantum dots in multilayer structures”, Comptes Rendues de Physique 6, 89-103 (2005).

89. G. Springholz, T. Schwarzl, M. Böberl, W. Heiss, J Fürst, H. Pascher Continuous Wave Mid-Infrared IV–VI Vertical Cavity Surface Emitting Lasers GMe-Forum 2005, ed. K. Riedling, Gesellschaft für Mikroelektronik, Vienna, 51-56, (2005)

90. H. Lichtenberger, M. Mühlberger, C. Schelling, F. Schäffler, “Ordering of self-assembled Si0.55Ge0.45 islands on vicinal Si(001) substrates”, J. Crystal Growth 278, 78-82 (2005).

91. H. Lichtenberger, M. Mühlberger, F. Schäffler, “Ordering of Si0.55Ge0.45 islands on vicinal Si(001) subatrstes: the interplay between kinetic step bunching and strain-driven island growth”, Appl. Phys. Lett. 86, 131919-1/3 (2005).

92. H. Malissa, Z. Wilamowski, W. Jantsch Cyclotron resonance revisited: the effect of carrier heating AIP Conference, Phys. of Semicond., Proc. ICPS-27, ed.by J. Menendez and C. G. Van de Walle (2005)

93. H. Przybylinska, G. Kocher-Oberlehner, W. Jantsch, K. Lischka Photoconductivity study of Mg and C acceptors in cubic GaN in AIP Conference., Physics of Semiconductors, Proc. ICPS-27, ed.by J. Menendez and C. G. Van de Walle,Vol. 772, 20 (2005)

94. H. Sigg, C.V. Falub, E. Müller, A. Borak, D. Grützmacher, T. Fromherz, M. Meduna and O. Kermarrec, “Bandstructure analysis of strain compensated Si/SiGe quantum cascade structures”, Opt. Mat 27, 841 (2005).

95. I.A. Vartanyants, I.K. Robinson, J.D. Onken, M.A. Pfeifer, G.J. Williams, F. Pfeiffer, H. Metzger, Z. Zhong, G. Bauer, “Coherent x-ray diffraction from quantum dots”, Phys. Rev. B 71, 245302-1/9 (2005).

96. J. A. H. Coaquira, V. A. Chitta, N. F. Oliveira Jr., P. H. O. Rappl, A. Y. Ueta, E. Abramof, G. Bauer, “Electrical Characterization of p-Type Pb1-xEuxTe”, Journal of Superconductivity: Incorporating Novel Magnetism, Vol. 16, 115-118 (2005).

97. J. Fürst, H. Pascher, T. Schwarzl, G. Springholz, M. Böberl, G. Bauer, W. Heiss Magnetic field tunable circularly polarized stimulated emission from midinfrared VI-VI vertical emitting lasers Appl. Phys. Lett. 86, 021109 (2005)

98. J. Liday, I. Hotovy, P. Vogrincic, H. Sitter, K. Schmidegg, J. Breza, A. Bonanni NiO-based contacts for blue emitting diodes J.Electr. Engineering 56, 217-220, (2005)

99. J. Novák, V. Holý, J. Stangl, G. Bauer, E. Wintersberger, S. Kiravittaya, O.G. Schmidt, “A method for the characterisation of strain fields in buried quantum dots using x-ray standing waves”, J. Phys. D: Appl. Phys. 38, A137-A142 (2005).

100. J. Novák, V. Holý, J. Stangl, T. Fromherz, Z. Zhong, G. Chen, G. Bauer, B. Struth, “Ge/Si islands in a 3D island crystal studied by x-ray diffraction”, J. Appl. Phys. 98, 073517 (2005).

101. J. Roither, M. Kovalenko, S. Pichler, T. Schwarzl, W. Heiss Nanocrystal based microcavity light emitting devices operating in the

telecommunication wavelength range
Appl. Phys. Lett 86, 241104 (2005)

102. J. Stangl, J. Novak, E. Wintersberger, V. Holy, G. Bauer, X-Ray Diffraction from a SiGe Island Quasicrystal, in: Proceedings of the Seminar at the Vienna University of Technology, March 17-18 (ISBN: 3-901578-15-3), pp. 145-148 (2005).

103. J. Stangl, T. Schülli, A. Hesse, G. Bauer, V. Holy, "X-ray scattering methods for the study of epitaxial self-assembled quantum dots", In: "Quantum Dots: Fundamentals, Applications, and Frontiers", eds.: B.A. Joyce et al., Springer, Netherlands 2005, 183-207.

104. J.P. Leitão, A. Fonseca, N.A. Sobolev, M.C. Carmo, N. Franco, A.D. Sequeira, T.M. Burbaev, V.A. Kurbatov, M.M. Rzaev, A.O. Pogosov, N.N. Sibeldin, V.A. Tsvetkov, H. Lichtenberger, and F. Schäffler, "Low-temperature molecular beam epitaxy of Ge on Si", Materials Science in Semiconductor Processing 8, 35-39 (2005).

105. K. Lai, P. D. Ye, W. Pan, D. C. Tsui, S. A. Lyon, M. Mühlberger, F. Schäffler, "Modulation of the high mobility two-dimensional electrons in Si/SiGe using atomic-layer-deposited gate dielectric", Appl. Phys. Lett. 87, 142103-1/3 (2005).

106. K. Lai, W. Pan, D. C. Tsui, S. A. Lyon, M. Mühlberger, F. Schäffler, "Two-dimensional metal-insulator transition and in-plane magnetoresistance in a high-mobility strained Si quantum well", Phys. Rev. B 72, 081313(R)-1/4 (2005).

107. K. Schmidegg, G. Neuwirt, H. Sitter, A. Bonanni
Simultaneous determination of composition and growth rate of MOCVD-growth ternary nitride compounds by multiple wavelength spectroscopic ellipsometry
J. Cryst. Growth 275 (1-2), e1763-e1766 (2005)

108. M. A. Wilde, M. Rhode, C. Heyn, F. Schäffler, U. Zeitler, R. J. Haug, D. Heitmann, D. Grundler, "Magnetization of modulation doped Si/SiGe quantum wells in high magnetic fields", AIP Conf. Proc. 772, 467-468 (2005).

109. M. A. Wilde, M. Rhode, Ch. Heyn, D. Heitmann, D. Grundler, U. Zeitler, F. Schäffler, R. J. Haug, "Direct measurement of the spin and valley splittings in the magnetization of a Si/SiGe quantum well in tilted magnetic fields", Phys. Rev. B 72, 165429-1/12, (2005).

110. M. Draxler, M. Mühlberger, F. Schäffler and P. Bauer, Non-destructive quantitative analysis of the Ge concentration in SiGe quantum wells by means of low energy RBS, Nucl. Inst. Meth. B 240, 733-740 (2005).

111. M. Grydlik, P. Rauter, T. Fromherz, G. Bauer, L. Diehl, C. Falub, G. Dehlinger, H. Sigg, D. Grützmacher, "Resonator Fabrication for Cavity Enhanced, Tunable Si/Ge Quantum Cascade Detectors", in: Proceedings of the Seminar at the Vienna University of Technology, March 17-18 (ISBN: 3-901578-15-3), pp. 75-79 (2005).

112. M. Meduna, J. Novak, C.V. Falub, G. Chen, G. Bauer, S. Tsujino, D. Grützmacher, E. Müller, Y. Campidelli, O. Kermarrec, D. Bensahel, N. Schell, "High temperature investigations of Si/SiGe based cascade structures using x-ray scattering methods", J. Phys. D: Appl. Phys. 38, A121-A125 (2005).

113. M. Rzaev, F. Schäffler, V. Vdovin and T. Yugova, "Misfit dislocation nucleation and multiplication in fully strained SiGe/Si heterostructures under thermal annealing", Materials Science in Semiconductor Processing 8, 137-141 (2005).

114. M. Siler, I. Ohlidal, D. Franta, A. Montaigne Ramil, D. Stifter, A. Bonanni, H. Sitter
Optical characterization of double layers containing epitaxial ZnSe and ZnTe films
Journ. of Mod. Optics 52 (4), 2005

115. R. T. Lechner, G. Springholz, T. U. Schülli, J. Stangl, T. Schwarzl, G. Bauer, "Strain induced changes in the magnetic phase diagram of metamagnetic heteroepitaxial Eu/Se/PbSe1-xTex multilayers", Phys. Rev. Lett. 94, 157201-1/4 (2005).

116. R. T. Lechner, G. Springholz, T. U. Schülli, J. Stangl, T. Schwarzl, G. Bauer, "Strain induced changes in the magnetic phase diagram of EuSE/PbSeTe multilayers", ESRF Highlights 2005, p. 80-81 (2005).

117. S. Lyon, Wolfgang Jantsch, A.M. Tyryshkin, F. Schäffler, Spin Manipulation of free 2-dimensional electrons in Si/SiGe quantum wells Virt. Journ. of Nanoscale Science & Technology (2005)

118. S. Mackowski, T. Gurung, H. E. Jackson, L. M. Smith, J. Kossut, G. Karczewski, W. Heiss Sensitivity of Exciton Spin Relaxation in quantum dots to Confining Potential Appl.Phys.Lett. 86, 103101 (2005)

119. S. Tsujino, A. Borak, C. Falub, T. Fromherz, L. Diehl, H. Sigg, and D.Grützmacher, "Intra-valence-band mixing in strain-compensated SiGe quantum wells", Phys. Rev. B 72, 153315 (2005).

120. T. Berer, D. Pachinger, G. Pillwein, M. Mühlberger, H. Lichtenberger, G. Brunthaler, F. Schäffler, "Single-electron transistor in strained Si/SiGe heterostructures", cond-mat/0508260.

121. T. Fromherz, "Fourier Transform Spectroscopy", in: Encyclopedia of Modern Optics, ed.: B. D. Guenther, Elsevier 2005, p. 90-100 (2005).

122. T. Fromherz, M. Meduna, G. Bauer, A. Borak, C.V. Falub, S. Tsujino, H. Sigg, D. Grützmacher, "Intersubband absorption of strain compensated Si1-xGex valenceband quantum wells with 0.7£x£0.85", J. Appl. Phys. 98, 044501-1/7 (2005).

123. T. G. Yugova, M. G. Mil'vidski, M. M. Rzaev, F. Schäffler, "Thermally stimulated relaxation of misfit strains in Si1-xGex/Si(100) heterostructures with different buffer layers", Crystallogr. Rep. 50, 1020-1026 (2005).

124. T. Haber, A. Andreev, A. Thierry, H. Sitter, M. Oehzelt, R. Resel Para-sexiphenyl thin films on KCl(100) surfaces: Growth morphologies and their individual epitaxial order J.Chryst.Growth 284 (2005)

125. T. M. Burbaev, V. A. Kurbatov, M. M. Rzaev, A. O. Pogosov, N. N. Sibel'din, V. A. Tsvetkov, H. Lichtenberger, F. Schäffler, J. P. Leitao, N. A. Sobolev, and M. C. Carmo, "Morphological transformation of a Germanium layer grown on a Silicon surface by Molecular-Beam Epitaxy at low temperatures", Phys. Solid State 47, 71-75 (2005).

126. T. Schwarzl, G. Springholz, M. Böberl, E. Kaufmann, J. Roither, W. Heiss, J Fürst, H. Pascher, Emission properties of 6.7 mm continuous-wave PbSe-based vertical-emitting microcavity lasers operationg up to 100 K, Appl. Phys. Lett. 86, 031102 (2005)

127. T. Schwarzl, M. Böberl, G. Springholz, E. Kaufmann, J. Roither, W. Heiss, J. Fürst, H. Pascher, "Molecular beam epitaxy of vertical-emitting microcavity lasers for the 6-8 micron spectral range operating in continuous-wave mode", J. Crystal Growth 278, 723-727 (2005).

128. T.U. Schülli, M. Stoffel, A. Hesse, J. Stangl, R.T. Lechner, E. Wintersberger, M. Sztucki, T.H. Metzger, O.G. Schmidt, G. Bauer, "Influence of growth temperature on interdiffusion in uncapped SiGe-islands on Si(001) determined by anomalous x-

ray diffraction and reciprocal space mapping", Phys. Rev. B 71, 035326-1/9 (2005).

129. V. Glukhanyuk, H. Przybylinska, A. Kozanecki, W. Jantsch
High Resolution Site-Selective Studies of Erbium-Centers in GaN and GaN:Mg
Materials Research Society Symposium Proc. 866, 97-102 (2005)

130. V. Holy, T.U. Schülli, R.T. Lechner, G. Springholz, G. Bauer, "Anomalous x-ray diffraction from self-assembled PbSe/PbTe quantum dots", J. Alloys and Compounds 401, 4-10 (2005).

131. W. Jantsch, H. Malissa, Z. Wilamowski, H. Lichtenberger, G. Chen, F. Schäffler, G. Bauer,
Spin properties of electrons in low dimensional SiGe structures
J. Supercond. Inc. novel magnetism 18, 145-149 (2005)

132. Z. F. Krasilnik, B.A.Andreev, T.Gregorkiewicz, W.Jantsch, M.A.J.Klik, D.I.Kryzhov, L.V.Krasilnikova, D.M.Zhigunov
Erbium doped silicon single- and multilayer structures for LED and laser applications
Materials Research Society Symposium Proceedings 866, 13-24 (2005)

133. Z. Zhong, G. Katsaros, M. Stoffel, G. Costantini, K. Kern, O. G. Schmidet, N. Y. Jin-Phillipp, G. Bauer, "Periodic pillar structures by Si etching of multilayer GeSi/Si islands", Appl. Phys. Lett. 87, 263102-1/3 (2005).

134. Z. Zhong, O. G. Schmidt, G. Bauer, "Increase of island density via formation of secondary ordered islands on pit patterned substrates", Appl. Phys. Lett. 87, 133111-1/3 (2005).

135. "Local density of states and modes in circular photonic crystal cavities" J. Chaloupka, J. Zarbakhsh, K. Hingerl, Phys. Rev. B72, 085122, (2005)

136. "Refraction and rightness in photonic crystals" R. Gajić, R. Meisels, F. Kuchar, and K. Hingerl, Opt. Exp. 13, 8596, (2005)

Submitted 2006 / in print

1. A. Bonanni, M.Kiecana, C.Simbrunner, Tian Li, M.Sawicki, M.Wegscheider, M.Quast, H.Przybylinska, A.Navarro-Quezada, R.Jakiela, A.Wolos, W.Jantsch, T. Dietl
Paramagnetic GaN:Fe and ferromagnetic (Ga,Fe)N - relation between structural, electronic and magnetic properties
submitted to Phys. Rev. B, http://arxiv.org/abs/cond-mat/0612200 (submitted 2006)

2. A. Wolos, W.Jantsch, K.Dybko, Z.Wilamowski, C.Skierbiszewski
Plasmon-cyclotron resonance of the two-dimensional electrons confined at the GaN/AlGaN interface
submitted to PRB (sumitted 2006)

3. A. Wolos, W.Jantsch, K.Dybko, Z.Wilamowski, C.Skierbiszewski
Properties of the Two-Dimensional Electron Gas Confined in GaN/AlGaN Interface Studied by Electron Spin Resonance
Proc. of the 28th International Conference on the Physics of Semiconductors, Vienna 2006 (accepted for publication 2006)

4. C. Mocuta, J. Stangl, B. Krause, I. Vartanyants, T. Metzger, G. Bauer, X-ray micro-diffraction on single Ge islands on Si (001), ESRF Annual Report, in print.

5. C. Simbrunner, A. Navarro-Quezada, K. Schmidegg, A. Bonanni, A. Kharchenko, J. Bethke, K. Lischka, H. Sitter
In-situ x-ray diffraction during MOCVD of III-nitrides
Phys. Stat. Sol. (a) (in print 2006)

6. C. Simbrunner, H.Sitter, A.Bonanni
Fourier analysis applied to in-situ laser reflectometry during III-nitride MOCVD growth
J. Appl. Phys. (submitted 2006)

7. C. Simbrunner, K.Schmidegg, A.Kharchenko, J.Bethke, J.Woitek, K.Lischka, H.Sitter, A.Bonanni,
In-situ x-ray diffraction during MOCVD of III-nitrides: an optimized wobbling compensating evaluation algorithm
J. Cryst. Growth doi:10.1016/j.jcrysgro.2006.10.116 (in print 2006)

8. C. Simbrunner, M.Wegscheider, M.Quast, T.Li, A.Navarro-Quezada, H.Sitter, A.Bonanni, R. Jakiela, On the effect of periodic Mg distribution in GaN:-Mg
Appl. Phys. Lett. (accepted 2006)

9. E. Weschke, E. Schierl, A. Gottberg, W. Söllinger, W. Heiss, G. Springholz, G. Kaindl, Antiferromagnetism near a surface studied with atomic layer resolution, submitted to Science (submitted 2006)

10. G. Chen, H. Lichtenberger, G. Bauer, W. Jantsch, F. Schäffler, Ordering of Strained Ge Islands on Prepatterned Si(001) Substrates: Morphological Evolution and Nucleation Mechanisms, Proc. of the 28th International Conference on the Physics of Semiconductors, Vienna 2006 (accepted for publication 2006).

11. G. Springholz and V. Holy, Stacking and Ordering in Self-Organized Quantum Dot Multilayer Structures, In: “Lateral alignment of epitaxial quantum dots” (Springer Series on Nanoscience and Technology), ed. O. Schmidt, series editors: P. Avouris, K. v. Klitzing, H. Sakaki, and R. Wiesendanger, Springer, Berlin 2006, in print.

12. G. Springholz, G. Bauer, Molecular beam epitaxy of IV-VI compound hetero- and nanostructures, phys. stat. sol. (a) 195, accepted.

13. G. Springholz, L. Abtin, V. Holy, Determination of Shape and Composition of buried PbSe Quantum Dots using Scanning Tunneling Microscopy, Applied Physics Letters, submitted.

14. H. Malissa, W. Jantsch, F. Schäffler, Z. Wilamowski, Current Induced g-factor Shift in Modulation Doped Si Quantum Wells, Proc. of the Material Research Society Fall Meeting 2006, Boston (submitted 2006).

15. H. Malissa, W. Jantsch, G. Chen, H. Lichtenberger, T. Fromherz, F. Schäffler, G. Bauer, A. Tyryshkin, S. Lyon, Z. Wilamowski, Spin Relaxation in SiGe Islands, Proc.s of the Material Reseach Society Fall Meeting 2006, Boston (accepted for publication 2006).

16. H. Malissa, W. Jantsch, G. Chen, H. Lichtenberger, T.Fromherz, F.Schäffler, G.Bauer, A.Tyryshkin, S.Lyon, Z.Wilamowski, Spin Relaxation in SiGe Islands, Proceedings of the 28th Internat. Conference on the Physics of Semiconductors, Vienna 2006 (accepted for publication 2006)

17. H. Malissa, Z. Wilamowski, W. Jantsch
High mobility of photo-excited electrons in Si.
submitted to PRB (submitted 2006)

18. M. Böberl, M.N.Kovalenko, S.Gamerith, E.List, W.Heiss,
Inkjet-printed nanocrystal photodetectors operating up to 3 m wavelengths
submitted to Advanced Materials (submitted 2006)

19. M. Stoffel, A. Rastelli, J. Stangl, T. Merdzhanova, G. Bauer, O. G. Schmidt, Shape oscillations: a walk through the phase diagram of strained island, Phys. Rev. B, submitted.

20. R. T. Lechner, G. Springholz, T. U. Schülli, J. Stangl, T. Schwarzl, G. Bauer, In and ex situ characterisation of magnetic EuSe/PbSe1-xTex superlattices grown by molecular beam epitaxy, J. Crystal Growth, accepted.

21. T. Berer, D. Pachinger, M. Mühlberger, H. Lichtenberger, G. Brunthaler, F. Schäffler, Lateral Quantum Dot in Si/SiGe realized by a Schottky Split-Gate Technique, 3rd International SiGe Tachnology and Device Meeting (ISTDM) 2006, 15-17 May 2006, Princeton / New Jersey, USA, submitted.

22. T. Li, C.Simbrunner, A.Navarro-Quezada, M.Wegscheider, M.Quast, A.Bonanni
Structural analysis of Fe-rich nanocrystals in (Ga,Fe)N grown by metal organic chemical vapour deposition
Appl. Phys. Lett (submitted 2006)

23. T. Schwarzl, J. Fürst, G. Springholz, M. Böberl, E. Kaufmann, J. Roither, G. Bauer, H. Pascher, W. Heiss, Emission Properties of 6.7 Micron Vertical-Emitting Microcavity Lasers Operating in Continuous-Wave Mode, Proc. of the 28th Internation.Conference on the Physics of Semiconductors (in print 2006).

24. T. Schwarzl, M. Eibelhuber, W. Heiss, E. Kaufmann, G. Springholz, A. Winter, H. Pascher, Mid-infrared high finesse microcavities and vertical-cavity lasers based on IV-VI semiconductor/BaF2 broad band Bragg mirrors, Journ. of Applied Physics, (in print 2006).

25. W. Heiss, H. Groiss, E. Kaufmann, G. Hesser, M. Böberl, G. Springholz, F. Schäffler, R. Leitsmann, F. Bechstedt, K. Koike, H. Harada, M. Yano, Quantum dots with coherent interfaces between rocksalt-PbTe and zincblende-CdTe, submitted to J. Appl. Phys. (submitted 2006).

26. Z. Zhong, G. Bauer, O. G. Schmidt, One-, two-, and three-dimensionally ordered GeSi islands grown on prepatterned Si (001) substrates, In: “Lateral Alignment of epitaxial quantum dots”, Springer Series on Nanoscience and -technology”, ed. O. G. Schmidt, in print.

Book chapters

1. G. Springholz, T. Schwarzl, W. Heiss,
Mid-infrared Vertical Cavity Surface Emitting Lasers based on the Lead Salt Compounds
“Mid-infrared Semiconductor Optoelectronics”, ed. A. Krier, (Springer-Verlag London, 2006)

Presentations – Invited Talks:

1. G. Bauer, Structural investigations of self-assembled SiGe/Si islands, 4th International Conference on Quantum Dots, May 1-5, 2006, Chamonix-Mont Blanc, France.

2. G. Bauer, “Structural Characterization of SiGe islands based on x-ray scattering diffraction techniques”, International Conference on Epitaxial Growth of Semiconductor Nanostructures, Bonassola, Italien, 17.09. – 21.09.2006
3. G. Bauer, “2D- and 3D-ordered islands: Initial stages of growth and structural characterization”, Workshop on Positioning of Single Nanostructures, Freudenstadt, Germany, 01.11. – 03.11.2006.
4. Friedrich Schäffler, Perspective of MBE-grown SiGe quantum structures, 14th International Conference on Molecular Beam Epitaxy (MBE 2006), 3-8 September 2006, Tokyo, Japan.
5. W. Heiss, H. Groiss, E. Kaufmann, G. Hesser, M. Böberl, G. Springholz, F. Schäffler, R. Leitsmann, F. Bechstedt, K. Koike, H. Harada, M. Yano, Quantum dots with coherent interfaces between rocksalt-PbTe and zincblende-CdTe, Joint Meeting of the German Vacuum Society DVG, The Polish Vacuum Society PTP, The Swedisch Vacuum Society, Swiss Vacuum on Vacuum Based Science and Technology, Darmstadt, Germany, October 10-13 (2006).
6. W. Heiss, H. Groiss, E. Kaufmann, G. Hesser, M. Böberl, G. Springholz, F. Schäffler, R. Leitsmann, and F. Bechstedt, K. Koike, H. Harada, M. Yano, Quantum dots with coherent interfaces between rocksalt-PbTe and zincblende-CdTe, ICPS-28, Vienna, July 24-28, 2006.
7. W. Heiss, M. Kovalenko, E. Kaufmann, D. Pachinger, J. Roither, M. Huber, J. Stangl, G. Hesser, H. Groiss, F. Schäffler, M. Böberl, T. Schwarzl, G. Springholz, K. Koike, H. Harada, M. Yano, Nanocrystals for mid-infrared emission, 14th International Winterschool on New Developments in Solid State Physics, 13.-17.2.2006, Mauterndorf, Austria.
8. T. Fromherz, M. Brehm, P. Rauter, N. Q. Vinh, B. N. Murdin, J. P. Phillips, C. R. Pidgeon, Z. Zhong, G. Chen, J. Novak, J. Stangl, D. Gruetzmacher, G. Bauer, Optoelectronic Properties and Bandstructure of SiGe Quantum Dot and Cascade Structures, 2006 MRS Fall Meeting, Boston, MA, USA, Nov. 27- December 1, 2006.
9. T. Fromherz, Bandstructure of Quantum Cascades in the Valenceband: Chances and Challenges for the Si/Ge System, Colloquium SiGe Nanoclub 28.9.2006, PSI Villigen, Schweiz.
10. G. Grabecki, J. Wróbel, P. Zagrajek, K. Fronc, M. Aleszkiewicz, T. Dietl, E. Papis, E. Kaminska, A. Piotrowska, G. Springholz, and G. Bauer, Quantum nanostructures of paraelectric PbTe, 14th International Winterschool on New Developments in solid State Physics, 13.-17.2.2006, Mauterndorf, Austria.
11. G. Springholz, Introduction to Nanotechnology, ESAO Winterschool, Kitzbühel, Austria, 26.-28.1.2006.
12. G. Springholz, Photonic Structures and Devices for the Mid-Infrared Spectral Region, Colloquium at the Montanuniversität Leoben, 20.6.2006.
13. G. Springholz, Epitaxial Hetero- and Nanostructures: Properties and Applications, Colloquium at the University of Vienna, 9.6.2006.
14. J. Stangl, B. Mandl, E. Wintersberger, R.T. Lechner, C. Mocuta, W. Seifert, G.Bauer, X-ray diffraction from semiconductor nanostructures, 9th International Conference on X-ray and Neutron Scattering (SXNS 9), Taipei, Taiwan, 16.-20.07.2006
15. R. Lechner, G. Springholz, T.U. Schülli, T. Schwarzl and G. Bauer, Strain induced changes in the magnetic phase diagram of heteroepitaxial EuSe, 56.

Jahrestagung der Österreichischen Physikalischen Gesellschaft, Graz, 18.-21.9.2006.

16. A. Bonanni, Growth, Fe incorporation and properties of GaN:Fe and (Ga,Fe)N:Mg, E-MRS Fall Meeting 2006 (European Materials Research Society – Fall Meeting), 04.-09.09.2006, Warsaw, Poland
17. A. Bonanni, MOCVD of nitrides: in-situ monitoring, Montanuniversität Leoben – Physics Institute – Physikkolloquium, 15.03.2006
18. W. Jantsch, Spin manipulation and relaxation in low dimensional Si-Ge structures, International Workshop on Electron spin resonance and related phenomena in low dimensional structures, 06.-08.03.2006, Villa Nobel, Sanremo (IM), Italy
19. W. Jantsch, H. Malissa, and Z. Wilamowski, (invted), Properties and Manipulation of Spins in Low-dimensional Si-Ge Structures, E-MRS IUMRS ICEM 2006 Spring Meeting, 29.05.-02.06.2006, Nice, France
20. W. Jantsch, Spin-orbit interaction in low dimensional semiconductor structures, 11.12.2006, University Basel, Switzerland
21. W. Jantsch, Festvortrag zum 150. Geburtstag von Nicola Tesla, 28.09.2006, Institut Zeileis, Galspach
22. W. Heiss, H. Groiss, E. Kaufmann, G. Hesser, M. Böberl, G. Springholz, F. Schäffler, R. Leitsmann, F. Bechstedt, K. Koike, H. Harada, M. Yano, Quantum dots with coherent interfaces between rocksalt-PbTe and zincblende-CdTe, Joint Meeting of the German Vacuum Society DVG, The Polish Vacuum Society PTP, The Swedisch Vacuum Society, Swiss Vacuum on Vacuum Based Science and Technology, 10.-13.10.2006, Darmstadt, Germany
23. W. Heiss, H. Groiss, E. Kaufmann, G. Hesser, M. Böberl, G. Springholz, F. Schäfflr, R. Leitsmann, F. Bechstedt, K. Koike, H. Harada, M. Yano, Quantum dots with coherent interfaces between rocksalt-PbTe and zincblende-CdTe, ICPS-28, 24.-28.07.2006, Vienna, Austria
24. W. Heiss, M. Kovalenko, E. Kaufmann, D. Pachinger, J. Roither, M. Huber, J. Stangl, G. Hesser, H. Groiss, F. Schäffler, M. Böberl, T. Schwarzl, G. Springholz, K. Koike, H. Harada, M. Yano, Nanocrystals for mid-infrared emission, 14th International Winterschool on New Developments in solid State Physics, 13.-17.2.2006, Mauterndorf, Austria
25. Kurt Hingerl; “Ist Periodizität wirklich erforderlich für photonische Kristalle?”, Nano and Photonics Mauterndorf , 14.-17. März 2006,
26. Kurt Hingerl, “How necessary is periodicity for photonic crystals?, “8th International Conference on Transparent Optical Networks, June 18-22, 2006, Nottingham, United Kingdom:
27. Kurt Hingerl, “Is Periodicity a Necessity for Photonic Crystals?”, International Conference on Physics of Optical Materials and Devices , 31st August – 2nd September 2006, Herceg Novi, Montenegro
28. G. Bauer, “Structural characterization of GeSi islands on S”i , SANDiE Workshop “Growth, electronic and optical properties of semiconductor nanostructures”, Kühlungsborn, Germany, 09.06.-12.06.2005.
29. G. Bauer, “20 Jahre Wahlfachgruppe Werkstoffe der Elektronik” (Seminarvortrag), Montanuniversität Leoben, 17.06.2006.
30. G. Bauer, “Growth and characterization of 2- and 3-dimensionally ordered quantum dots”, 7th International Conference on New Phenomena in Mesoscopic

Systems and 5th International Conference on Surfaces and Interfaces of Mesoscopic Devices (NPMS6-SIMD4), Maui/Hawaii, 27.11.-02.12.2005.

31. G. Springholz, ”Lead Salt based Mid-Infrared Vertical Cavity Surface Emitting Lasers and Microcavity Devices”, VII. International Conference on Mid-Infrared Optoelectronic Materials and Devices, Lancaster, UK, 11.9. – 14.9.2005.
32. G. Springholz, ”Organization of Self-Assembled Semiconductor Nanostructures”, 12th Brazilian Workshop on Semiconductor Physics, Sao Jose dos Campos, Brazil, 4.4. –8.4.2005.
33. G. Springholz, ”Lead Salt Vertical Cavity Surface Emitting Lasers for the 3 to 8 μm Spectral Region”, Forum der Gesellschaft für Mikroelektronik, Wien, Austria 17.3. – 18.3.2005.
34. F. Schäffler, “Nanostructured Semiconductors: Top-Down and Bottom-Up Techniques”, Jahresversammlung des Mikroelektronik-Cluster, Villach, 31.03.2005.
35. F. Schäffler, Vorstellung NanoScience/Technology Center Linz, Kooperation, Nano 05, Wiener Neustadt, 19.10.05.
36. J. Stangl, “X-Day Diffraction From Semiconductor Nanostructures”, XX Congress of the International Union of Crystallography “IUCR 2005”, Florenz/Italien, 29.08.2005.
37. J. Stangl, “X-ray Investigation of Self-Assembled Nanostructures”, Workshop “Characterization and Modelling of Self-assembled Semiconductor Nanostructures”, TU Eindhoven / NL, 24.11.2005
38. W. Heiss, T. Schwarzl, M. Böberl, J. Anzengruber, G. Springholz, J. Fürst, H. Pascher, (Invited Talk), ”Novel lead-salt microcavity devices for molecule spectroscopy”, 2nd Aspect Workshop on Advanced Spectroscopy, 29.9.-2.10.2005, Kazimierz Dolny, Poland.
39. Z. Zhong, “Engineering on the positioning of GeSi nano-islands on prepatterned Si (001) substrates”, 12th International Conference on Composits/Nano Engineering, Tenerife, Spain, Auguest 1-6, 2005.
40. W. Heiss, T. Schwarzl, M. Böberl, J. Anzengruber, G. Springholz, J. Fürst, H. Pascher, Novel lead-salt microcavity devices for molecule spectroscopy, The 2nd Aspect Workshop on Advanced Spectroscopy, 29.9-2.10.2005, Kazimierz Dolny, Poland
41. E. Kaufmann, W. Heiss, M. Böberl, T. Schwarzl, G. Springholz, G. Hesser, F. Schäffler, K. Koike, H. Harada, M. Yano, Lattice type mismatched epitaxial PbTe/CdTe quantum dots giving intense mid-infrared emission, 12th Int. Conf. on Narrow Gap Semiconductors, 03-07.7.2005, Toulouse, France
42. W. Jantsch, “Spin coherence of electrons in reduced dimensions”, Int. Workshop on Spin Phenomena in Reduced Dimensions, 10.-12.03.2005, Regensburg, Germany
43. Z.F.Krasilnik, B.A.Andreev, T.Gregorkiewicz, W.Jantsch, M.A.J. Klik,D.I.Kryzhkov, L.V. Krasil’nikova, V.P.Kuznetsov, H.Przybylinska, D.Y.Remizov, V.G.Shengurov, V.B.Shmagin, M.V.Stepikhova, V.Y.Timoshenko, N.Q.Vinh, A.N. Yablonskiy, D.M.Zhigunov, “Erbium Doped Silicon Single- and Multilayer Structures for LED and Laser Applications”, MRS spring meeting, 28.03-01.04.2005, San Francisco, USA

44. W. Jantsch, “Properties and Manipulation of Electron spins in Low-dimensional Si/Ge Structures”, Ecole Thematique CNRS GdR Sesame “Le Spin dans les Semiconducteurs: Physique et Applications”, 02.-07.10.2005, La Grande-Motte, France
45. Kurt Hingerl, Univ. Roma III, Prof. Gabriella Cincotti, El. Eng. Dep. 14. + 15. 2. 2005;
46. Kurt Hingerl, Univ. Paderborn, Prof. Reinhard Noe, El. Eng. Dep. 28. 2. 2005;

Conference presentations (talks and posters):

1. A. Andreev, T. Gregorkiewicz, W. Jantsch, Z. F. Krasilnik, D. I. Kryzhkov, V. P. Kuznetsov
   Electro-optic memory effect at 1.54 μm Si:Er light-emitting diodes (Poster)
   28th International Conference on the Physics of Semiconductors, 24.-28.07.2006, Vienna, Austria
2. A. Bonanni
   Ferromagnetic behavior of GaN:Fe and (Ga,Fe)N:Mg below and above the Fe solubility limit
   IWN 2006 – International workshop on nitride semiconductors
   22.-27.10.2006, Kyoto, Japan
3. A. Bonanni
   GaN:Fe and (Ga,Fe)N:Mg - growth, characterization and magnetic properties
   XXXV international school on the physics of semiconducting compounds
   17.-26.06.2006, Jaszowiec, Poland
4. A. Bonanni, M. Kiecana, C. Simbrunner, H. Przybylinska, M. Sawicki, A. Wolos, A. Navarro-Quezada, M. Wegscheider, W. Jantsch, T. Dietl
   GaN:Fe and (Ga,Fe)N:Mg: growth, characterization and magnetic properties (Poster), 28th International Conference on the Physics of Semiconductors, 24.-28.07.2006, Vienna, Austria
5. A. Navarro-Quezada
   MOCVD of iron nanocrystals and films on (0001)Ga (Poster)
   ICPS 28 – International conference on the Physics of Semiconductors
   24.-28.07.2006, Vienna, Austria
6. A. Rehman Khan, J. Stangl, G. Bauer, D. Buca, B. Holländer, H. Trinkaus, S. Mantl, R. Loo, M. Caymax, Study of Relaxation of Strain in Patterned Structures using
   X-Ray Diffraction, Third International SiGe Technology and Device Meeting (ISTDM), Princeton, New Jersey, USA, May 15-17, 2006.
7. A. Wolos, H. Przybylińska, A. Bonanni, C. Simbrunner, W. Jantsch, M. Bockowski, I. Grzegory, and S. Porowski
   Fe as an impurity in GaN – optical and ESR studies
   E-MRS IUMRS ICEM 2006 Spring Meeting
   29.05.-02.06.2006, Nice, France
8. A. Wolos, H. Przybylinska, C. Simbrunner, A. Bonanni, Li Tian, F. Schäffler and W. Jantsch, Spin resonance investigations of the composition, shape, and orientation of ferromagnetic precipitates in GaFeN, MRS Fall Meeting, Boston, USA, Nov. 27 - Dec. 1, 2006.
9. A. Wolos, W. Jantsch, K. Dybko, Z. Wilamowski, Cz. Skierbiszewski
   Electron spin resonance investigations of the two-dimensional electron gas confined at the GaN/AlGaN interface (Poster)

28th International Conference on the Physics of Semiconductors, 24.-28.07.2006, Vienna, Austria

10. A. Wolos, W. Jantsch, K. Dybko, Z. Wilamowski, Cz. Skierbiszewski
Properties of the two-dimensional electron gas confined in GaN/AlGaN interface studied by electron spin resonance
Material Reseach Society Fall Meeting 2006, Boston.

11. B. Lindner, Georg Pillwein, Gerhard Brunthaler, Small mass enhancement near the metal-insulator transition in gated silicon inversion layers (Poster), 14th International Winterschool on New Developments in Solid State Physics, Mauterndorf, Austria, 13-17 February 2006.

12. C. Simbrunner
GaN:Fe and (Ga,Fe)N:Mg as novel materials systems for spintronics applications: growth, characterization and magnetic properties (Poster)
ICPS 28 – International conference on the Physics of Semiconductors
24.-28.07.2006, Vienna, Austria

13. C. Simbrunner
In-situ x-ray diffraction during MOCVD of III-nitrides: an optimized wobbling compensating evaluation algorithm (poster)

14. C. Simbrunner
In-situ x-ray diffraction during MOCVD of III-nitrides
XTOP 2006 – 8th Biennial Conference on High Resolution X-Ray Diffraction
19.-22.09.2006, Baden-Baden, Germany

15. D. Pachinger, H. Lichtenberger and F. Schäffler, Stranski–Krastanov growth of tensely strained Si on Ge (001) substrates, (poster), 14th International Conference on Molecular Beam Epitaxy (MBE 2006), 3-8 September 2006, Tokyo, Japan.

16. D. Pachinger, H. Lichtenberger and F. Schäffler, Stranski–Krastanov growth of tensely strained Si on Ge (001) substrates (oral), MRS Fall Meeting, Boston, USA, Nov. 27 - Dec. 1, 2006.

17. D. Pachinger, H. Lichtenberger and F. Schäffler, Stranski–Krastanov growth of tensely strained Si on Ge (001) substrates (Poster), ICPS-28, Vienna, July 24-28, 2006.

18. E. Kaufmann, W. Heiss, M. Böberl, T. Schwarzl, G. Springholz, H. Hesser, F. Schäffler, K. Koike, H. Harada, M. Yano, Intense mid-infrared emission from self-assembled PbTe/CdTe quantum dots fabricated by lattice type mismatched epitaxy, Photonics West 2006, 21.1.-26.1.2006, San Jose, USA.

19. E. Schierle, E. Weschke, A. Gottberg, G. Kaindl, W. Söllinger, G. Springholz, Layer-resolved magnetization of a Heisenberg film from magnetic Laue profiles, DPG Frühjahrstagung des AKF und Condensed Matter Devision of the Europaen Physical Society, 27.-31.3.2006, Dresden, Germany.

20. E. Schierle, E. Weschke, A. Gottberg, G. Kaindl, W. Söllinger, G. Springholz, Resonant magnetic soft x-ray scattering from thin EuTe layers, DPG Frühjahrstagung des AKF und Condensed Matter Devision of the Europaen Physical Society, 27.-31.3.2006, Dresden, Germany.

21. euSPEN 2006, Baden, Austria, 28.5. -1.6. 2006, “High Precision Alignment in Multi-Layer NanoImprint Lithography” M. Mühlberger, W. Schwinger, M. Gmainer, R. Schöftner, T. Glinsner, Ch. Hasenfuß, K. Hingerl, (Poster)

22. G. Chen, H. Lichtenberger, G. Bauer, W. Jantsch, and F. Schäffler, Initial stage of the 2D-3D transition of a strained SiGe layer on a pit-patterned Si(001) template

(Poster), 14th International Winterschool on New Developments in Solid State Physics, Mauterndorf, Austria, 13-17 February 2006.

23. G. Chen, H. Lichtenberger, Z. Zhong, G. Bauer, W. Jantsch and F. Schäffler, Ordering of strained Ge islands on prepatterned Si(001) substrates: Morphological Evolution and Nucleation Mechanisms, (poster), 14th International Conference on Molecular Beam Epitaxy (MBE 2006), 3-8 September 2006, Tokyo, Japan.
24. G. Chen, H. Lichtenberger, Z. Zhong, G. Bauer, W. Jantsch and F. Schäffler, Ordering of strained Ge islands on prepatterned Si(001) substrates: Morphological Evolution and Nucleation Mechanisms (oral), MRS Fall Meeting, Boston, USA, Nov. 27 - Dec. 1, 2006.
25. G. Chen, H. Lichtenberger, Z. Zhong, G. Bauer, W. Jantsch, F. Schäffler Ordering of strained Ge islands on prepatterned Si (001)substrates 28th International Conference on the Physics of Semiconductors, 24.-28.07.2006, Vienna, Austria
26. G. Chen, Herbert Lichtenberger, Zhenyang Zhong, Günther Bauer, Wolfgang Jantsch, Friedrich Schäffler, Initial stage of the 2D-3D transition of a strained Ge layer on a pit-patterned Si(001) template---Progress in Quantum Dot Array (QDA), (Talk), Sixth International Workshop on Epitaxial Semiconductors on Patterned Substrates and Novel Index Surfaces (ESPS-NIS 2006), April 3-5, 2006, Nottingham, UK.
27. G. Pillwein, Benjamin Lindner, Gerhard Brunthaler, Jouni Ahopelto, Mika Prunnila, Formation of quantum dots in the contact regions in the metal-insulator transition regime in high-mobility Si inversion layers (Poster), ICPS-28, Vienna, July 24-28, 2006.
28. G. Springholz, L. Abtin and V. Holy, Shape Transitions and Intermixing of Self-assembled PbSe Quantum Dots Studied by Scanning Tunneling Microscopy, Fall Meeting of the Materials Research Society, 26.11.-1.12.2006, Boston, USA.
29. G. Springholz, L. Abtin, V. Holy, Determination of Shape and Chemical Composition of Buried PbSe Quantum Dots Using Scanning Tunneling Microscopy, International Conference on Nanoscience and Technology (NANO9 and STM06), 30.7.- 4.8.2006, Basel, Switzerland.
30. H. Groiss, W.Heiss, and F. Schäffler, The coherent {100} and {110} interfaces between rocksalt-PbTe and zincblende-CdTe (oral), 14th International Conference on Molecular Beam Epitaxy (MBE 2006), 3-8 September 2006, Tokyo, Japan.
31. H. Malissa, W. Jantsch, F. Schäffler, and Z. Wilamowski, Current Induced g-factor Shift in Modulation Doped Si Quantum Wells, MRS Fall Meeting, Boston, USA, Nov. 27 - Dec. 1, 2006.
32. H. Malissa, W. Jantsch, G. Chen, H. Lichtenberger, T. Fromherz, F. Schäffler, G. Bauer, A. Tyryshkin, S. Lyon, and Z. Wilamowski, Spin Relaxation in SiGe Islands, MRS Fall Meeting, Boston, USA, Nov. 27 - Dec. 1, 2006.
33. H. Malissa, W. Jantsch, F. Schäffler, Z. Wilamowski g-factor tuning by an electric current in modulation-doped Si quantum wells 28th International Conference on the Physics of Semiconductors, 24.-28.07.2006, Vienna, Austria
34. H. Malissa, W. Jantsch, G. Chen, H. Lichtenberger, T. Fromherz, F. Schäffler, G. Bauer, A. Tyryshkin, S. Lyon, Z. Wilamowski, Spin relaxation in SiGe islands (Poster), ICPS-28, Vienna, July 24-28, 2006.
35. H. Malissa, W. Jantsch, G. Chen, D. Gruber, H. Lichtenberger, F. Schäffler, and G. Bauer, ESR investigations on low-dimensional Si-Ge structures (Poster), 14th

International Winterschool on New Developments in Solid State Physics, Mauterndorf, Austria, 13-17 February 2006.

36. H. Przybylinska, A. Wolos, C. Simbrunner, A. Bonanni, Li Tian, F. Schäffler and W. Jantsch, Magnetic resonance as a tool to investigate the omposition, shape and orientation of precipitates in ”ferromagnetic” semiconductors, 28th International Conference on the Physics of Semiconductors, Vienna, July 24-28, 2006.
37. H. Trinkaus, D. Buca, B. Holländer, S. Mantl, A. Rehman Khan, G. Bauer, Theory of X-ray Diffraction from Partially Relaxed SiGe/Si Layers Third International SiGe Technology and Device Meeting (ISTDM), Princeton, New Jersey, USA, May 15-17, 2006.
38. ICPS 2006, Vienna, Austria, 24.-28. 7. 2006, – 4 contributionsA) “High Precision Alignment in Multi-Layer NanoImprint Lithography” M. Mühlberger, W. Schwinger, M. Gmainer, R. Schöftner, T. Glinsner, Ch. Hasenfuß, K. Hingerl, H. Schmidt, E.-B. Kley, (Poster)B) “Fabrication of silicon vertical taper structures for fiber to chip coupler by KOH anisotropic etching”, Roman Holly, Kurt Hingerl, Robert Merz, Peter Hudek, Sven Neve, and Stefan Partel, (Poster)C) “Light Emission from HgTe Nanocrystals embedded in Silicon Waveguides”, Ventsislav Lavchiev, Veronika Rinnerbauer, Kurt Hingerl, Maksym Kovalenko, Wolfgang Jantsch, and Wolfgang Heiss, (Poster)D) “Negative Refraction in Aperiodic Photonic Crystals” Javad Zarbakhsh, Jozef Havran und Kurt Hingerl, (Poster)
39. J. Stangl, Kiran Mundboth, Cristian Mocuta, Till H. Metzger, Günther Bauer, Ivan Vartanyants, X-ray diffraction from single semiconductor nanostructures, (Poster), ICPS-28, Vienna, July 24-28, 2006.
40. K. Koike, H. Harada, T. Itakura, M. Yano, W. Heiss, H. Groiss, E. Kaufmann, G. Hesser, M. Böberl, G. Springholz, F. Schäffler, Growth and photoluminescence properties of coherently embedded PbTe quantum dots in crystalline CdTe host matrix, 25th Electronic Materials Symposium, Shizuoka, Japan (July 5th-7th, 2006).
41. K. Koike, H. Harada, T. Itakura, M. Yano, W. Heiss, H. Groiss, E. Kaufmann, G. Hesser, M. Bobel, G. Springholz and F. Schaffler, Photoluminescence Characterization of PbTe/CdTe Quantum Dots Grown by Lattice-Type Mismatched Epitaxy, 14th International Conference on Molecular Beam Epitaxy, 3.-9.9.2006, Tokyo, Japan.
42. K. L. Litvinenko, B.N.Murdin, C.R.Pidgeon, W Heiss, M. V. Kovalenko
Spin lifetime in chemically synthesised PbSe quantum dots
28th International Conference on the Physics of Semiconductors
24.-28.07.2006, Vienna, Austria
43. M. Böberl, J. Roither, T. Fromherz, G. Springholz, W. Heiss, Wavelength-selective lead-salt photodetectors for gas sensing in the mid-infrared, Infrared Detectors and Focal Plane Arrays VIII, Optics and Photonics, San Diego, USA (August 13-17, 2006).
44. M. Böberl, M. Kovalenko, W. Heiss,
Solution-processible photodetectors operating up to wavelength of 3 microns
Infrared Detectors and Focal Plane Arrays VIII, Optics and Photonics,
13.-17.08.2006, San Diego, USA
45. M. Böberl, T. Fromherz, T. Schwarzl, J. Roither, E. Kaufmann, G. Springholz, W. Heiss, Integrierbare epitaktische Bleisalz-Photodetektoren für Raumtemperaturbetrieb, 35. Infrarot-Kolloquium, 12.-13.4.2006, Freiburg, Germany.

46. M. Böberl, T. Schwarzl, J. Roither, T. Fromherz, G. Springholz, W. Heiss, Room temperature narrow band photodetectors for the midinfrared, Photonics West 2006, 21.1.-26.1.2006, San Jose, USA .
47. M. Eibelhuber, T. Schwarzl, G. Springholz, W. Heiss, A. Winter, H. Pascher, Mid-infrared high finesse microcavities and vertical-cavity lasers based on IV-VI semiconductor/BaF2 broad-band Bragg mirrors, 5th annual DVG Meeting together with the Polish, Swedish and Swiss Vaccuum Societies, Darmstadt, 10.-12.10.2006.
48. M. Grydlik, P. Rauter, T. Fromherz, C. Falub, D. Gruetzmacher, G. Isella, and G. Bauer, Resonator fabrication for switchable two-color MIR detectors based on p-type SiGe quantum cascade injectors, 28th International Conference on the Physics of Semiconductors (ICPS-28), Vienna, Austria, July 24-28 2006.
49. M. Grydlik, Patrick Rauter, Thomas Fromherz, Günther Bauer, Claudiu Falub, Detlev Grützmacher, Giovanni Isella, Optical properties of IR quantum dot detectors with miniband tunnel extraction (Poster), ICPS-28, Vienna, July 24-28, 2006.
50. M. Simma, Dmytro Lugovyy, Thomas Fromherz, Gunther Springholz, Günther Bauer, Strain induced modifications of optoelectronic properties of PbSe nanostructures (Poster), ICPS-28, Vienna, July 24-28, 2006.
51. M. V. Kovalenko, E. Kaufmann, J. Roither, M. Böberl, W. Heiss
Colloidal HgTe nanocrystals for near- to mid-infrared optoelectronics
Symposium on Functional Materials for Micro and Nanosystems, European Materials Research Society Spring Meeting
29.05.-02.06.2006, Nice, France
52. M. Wegscheider
Photoluminescence and Hall studies of GaN:Fe and (Ga,Fe)N:Mg layers (poster)
E-MRS Fall Meeting 2006 – European Materials Research Society – Fall Meeting
04.-09.09.2006, Warsaw, Poland
53. M.-I. Richard, Z. Zhong, G. Renaud, G. Bauer, In situ Anomalous X-ray Scattering studies during growth of Ge islands on nanopatterned Si(001) substrates: growth mode, strain, shape and composition, Sixth International Workshop on Epitaxial Semiconductors on Patterned Substrates and Novel Index Surfaces (ESPS-NIS 2006), April 3-5, 2006, Nottingham, UK.
54. M.-I. Richard, Z. Zhong, G. Renaud,T.-H. Metzger, G. Bauer, X-ray investigation of Ge islands on nanostructured and nominal Si substrates, Sixth International Workshop on Epitaxial Semiconductors on Patterned Substrates and Novel Index Surfaces (ESPS-NIS 2006), April 3-5, 2006, Nottingham, UK.
55. MNE 2006, Barcelona, – 2 contributionsA) “A Moiré Method for high Accuracy Alignment in Nanoimprint Lithography” M. Mühlberger, I. Bergmair, W. Schwinger, M. Gmainer, R. Schöftner, T. Glinsner, Ch. Hasenfuß, K. Hingerl, M. Vogler, H. Schmidt, E.B. Kley, (Poster)B) “Fabrication of silicon 3D taper structures for optical fibre to chip interface”, Roman Holly und Kurt Hingerl, (Poster)
56. NNT 2006, San Francisco, USA, 15.-17.11.2006, – 2 contributions, A) “Fabrication Process of 3D-photonic crystals via UV-Nanoimprint Lithography” T. Glinsner, P. Lindner, M.Mühlberger, I. Bergmair, R. Schöftner, K.Hingerl, (Poster), B) “High Accuracy Alignment in Nanoimprint Lithography using a Moiré Method” M. Mühlberger, I. Bergmair, W. Schwinger, M. Gmainer, R. Schöftner, T. Glinsner, Ch. Hasenfuß, K. Hingerl, H. Schmidt, E.-B. Kley, (Poster)
57. OSA, Frontiers in Optics, Rochester 8. -12. Oktober 2006 – 2 contributions, A) “Optimized photonic crystal waveguide interconnections and improved impedance

matching", Javad Zarbakhsh, Abbas Mohtashami, Michael Bergmair, Lasha Tkeshelashvili, Kurt Hingerl, and Kurt Busch, (Talk), B) "Metallic Photonic Crystals" Michael Bergmair und Kurt Hingerl (Poster)

58. P. Rauter, T. Fromherz, G. Bauer, N.Q. Vinh, P.J. Phillips, C.R. Pidgeon, B.N. Murdin, L. Diehl, G. Dehlinger, D. Grützmacher, Optical phonon limited hole lifetime in a SiGe cascade emitter structure: a direct measurement via photocurrent pump-pump measurements, POISE (Physics of Intersubband Semiconductor Emitters) Summer School, Cortona, Italy, June 25-30, 2006.

59. P. Rauter, T. Fromherz, G. Bauer, N.Q. Vinh, P.J. Phillips, C.R. Pidgeon, B.N. Murdin, L. Diehl, G. Dehlinger, D. Grützmacher, Direct measurement of optical phonon limited hole intersubband lifetimes in SiGe quantum cascade structures, 28th International Conference on the Physics of Semiconductors (ICPS-28), Vienna, Austria, July 24-28, 2006.

60. P. Rauter, T. Fromherz, G. Bauer, N.Q.Vinh, P.J. Phillips, C.R. Pidgeon, B.N. Murdin, L. Diehl, G. Dehlinger, H. Sigg, D. Grützmacher, Direct Measurement of HH2-HH1 Intersubband Lifetimes in SiGe Quantum Cascade Structures (Poster), 14th International Winterschool on New Developments in Solid State Physics, Mauterndorf, Austria, 13-17 February 2006.

61. P. Rauter, T. Fromherz, G. Bauer, N.Q.Vinh, P.J.Phillips, C.R. Pidgeon, B.N. Murdin, L. Diehl, G. Dehlinger, D. Grützmacher, Direct Measurement of HH2-HH1 Intersubband Lifetimes in SiGe Quantum Cascade Structures, ISTDM 2006 (The third International SiGe Technology and Device Meeting), Princeton, New Jersey, USA, May 15-17, 2006.

62. R. Leitsmann, F. Bechstedt, H. Groiss, F. Schäffler, W. Heiss, K. Koike, H. Harada, M.Yano
Structural and Electronic properties of PbTe(rocksalt)/CdTe(zinc blende) interfaces
13th International Conference on Solid Films and Surfaces
13-17.11.2006, San Carlos de Bariloche, Argentinia

63. R. T. Lechner, Gunther Springholz, Raimund Kirchschlager, Günther Bauer, A new superparamagnetic phase in strained and unstrainend heteroepitaxial EuSe above the critical temperature (Poster), ICPS-28, Vienna, July 24-28, 2006.

64. S. Pichler, J. Roither, M. V. Kovalenko, W. Heiss, P. Feichuk, O. Panchuk, J. Allam, B. N. Murdin
Two and one dimensional light propagation and gain in layer-by-layer deposited colloidal nanocrystal waveguides (Poster)
14th International Winterschool on New Developments in solid State Physics
13.-17.02.2006, Mauterndorf, Austria

65. S. Pichler, J. Roither, M. V. Kovalenko, W. Heiss, P. Feychuk, O. Panchuk, J. Allam and B. N. Murdin
Two and one dimensional light propagation and optical gain in colloidal nanocrystal waveguides
International Conference on Superlattices, Nano-Structures and Nano-Devices
30.07.-04.08.2006, Istanbul, Turky

66. T. Berer, Dietmar Pachinger, Georg Pillwein, Michael Mühlberger, Herbert Lichtenberger, Gerhard Brunthaler and Friedrich Schäffler, Single-electron transistor in strained Si/SiGe heterostructures (poster), 14th International Conference on Molecular Beam Epitaxy (MBE 2006), 3-8 September 2006, Tokyo, Japan.

67. T. Berer, Dietmar Pachinger, Georg Pillwein, Michael Mühlberger, Herbert Lichtenberger, Gerhard Brunthaler and Friedrich Schäffler (oral), Lateral Quantum

Dot in Si/SiGe realized by a Schottky Split-Gate Technique, ICPS-28, Vienna, July 24-28, 2006.

68. T. Berer, Dietmar Pachinger, Georg Pillwein, Michael Mühlberger, Herbert Lichtenberger, Gerhard Brunthaler and Friedrich Schäffler, Lateral Quantum Dot in Si/SiGe realized by a Schottky Split-Gate Technique (oral), ISTDM 2006, Princeton /NJ, USA, May 15-17, 2006.
69. T. Berer, Dietmar Pachinger, Georg Pillwein, Michael Mühlberger, Herbert Lichtenberger, Gerhard Brunthaler, and Friedrich Schäffler, Single-electron transistor in strained Si/SiGe heterostructures (Poster), 14th International Winterschool on New Developments in Solid State Physics, Mauterndorf, Austria, 13-17 February 2006.
70. T. Schwarzl, J. Fürst, M. Böberl, G. Springholz, E. Kaufmann, J. Roither, G Bauer, H. Pascher, W. Heiss
Emission properties of 6.7 micron vertical-emitting microcavity lasers operating in continuous-wave mod (Poster)
28th International Conference on the Physics of Semiconductors
24.-28.07.2006, Vienna, Austria
71. V. Lavchiev, V. Rinnerbauer, K. Hingerl, M. Kovalenko, W. Jantsch, W. Heiss
Light Emission from HgTe Nanocrystals embedded in Silicon Waveguides (Poster)
28th International Conference on the Physics of Semiconductors
24.-28.07.2006, Vienna, Austria
72. V. Rinnerbauer, Maksym Kovalenko, Wolfgang Heiss and Kurt Hingerl, “Effect of quantum confinement on higher transitions in HgTe nanocrystals” ICSFS-13: 13th International Conference on Solid Films and Surfaces, Bariloche (Argentina), 6 - 10 November 2006
73. W. Heiss, H. Groiss, E. Kaufmann, G. Hesser, M. Böberl, G. Springholz, F. Schäffler, K. Koike, H. Harada, M. Yano, Coherently embedded, centrosymmetric PbTe/CdTe quantum dots fabricated by epitaxial precipitation, Quantum Dots Conference, Chamonix-Mont Blanc, France (May 1 - 5, 2006).
74. W. Heiss, H. Groiss, E. Kaufmann, G. Hesser, M. Böberl, G. Springholz, F. Schäffler, Coherently Embedded Quantum Dots by Heteroepitaxy of Immiscible Semiconductors (oral), MRS Fall Meeting, Boston, USA, Nov. 27 - Dec. 1, 2006.
75. W. Jantsch, H. Malissa, F. Schäffler, Z. Wilamowski, Direct Evidence for the Bychkov-Rashba Effect in Modulation-doped Si quantum wells, 28th International Conference on the Physics of Semiconductors (ICPS-28), Vienna, Austria, July 24-28, 2006.
76. W. Söllinger, R. Kirchschlager, G. Springholz, K. Rumpf, P. Granitzer, H. Krenn, W. Heiss
Remanence and Interdiffusion in Ultrathin Antiferromagnetic Semiconductor Epilayers (Poster)
28th International Conference on the Physics of Semiconductors
24.-28.07.2006, Vienna, Austria
77. W. Söllinger, R. Kirchschlager, G. Springholz, K. Rumpf, P. Granitzer, H. Krenn, W. Heiss
Remanence and interdiffusion in ultrathin antiferromagnetic EuTe epilayers (Poster)
14th International Winterschool on New Developments in solid State Physics
13.-17.02.2006, Mauterndorf, Austria

78. A. Andreev, A.Montaigne, G.Hlawacek, H.Sitter, C.Teichert, Para-Sexiphenyl thin films on KCl(001) substrates, Workshop on two- and three-dimensional organic nanostructures, , 09. – 11.06.2005, Linz, Austria
79. A. Andreev, A.Montaigne, T.Haber, G.Hlawacek, H.Sitter, C.Teichert, R.Resel, Para-Sexiphenyl thin films on KCl(001) substrates, 55. ÖPG Jahrestagung, 27.-30.09.2005, Vienna, Austria,
80. A. Andreev, A.Montaigne, G.Hlawacek, T.Haber, R.Resel, H.Sitter, C.Teichert, Para-Sexiphenyl thin films grown by Hot Wall Epitaxy on KCl(001) substrates, 52nd Annual International Symposium of the American Vacuum Society (AVS), 31.10.-04.11.2005, Boston, USA
81. A. Bonanni, C.Simbrunner, H.Sitter, H.Przybylinska, A.Wolos, M.Sawicki, T.Dietl, W.Jantsch, (Ga, Fe) N : optical, electronix and magnetic properties, 6th International Conference on Nitride Semiconductors, 28.08-02.09.2005, Bremen, Germany
82. A. Bonanni, W.Jantsch, H.Przybylinska, A.Wolos, C.Simbrunner, H.Sitter,, M.Kiecana, M.Sawicki, T.Dietl, K.Rumpf, P.Ganitzer, H.Krenn, Electronic and magnetic properties of GaN:Fe; 6th Int. Conf. on Nitride Semiconductors, 28.08-02.09.2005, Bremen, Germany
83. A. Bonanni, W.Jantsch, H.Przybylinska, A.Wolos, C.Simbrunner, H.Sitter, A.Kiecara, A.Sawicki, T.Dietl, Electronic an magnetic properties of GaN:Fe, Spintech III, 01-05.08.2005, Awaji Island, Japan
84. B. Andreev, Z.Krasil`nik, D.Kryzhkov, V.Kuznetsov, A.Yablonskiy, W. Jantsch, Electro-Optical Memory Effect for 1.54 micron Electroluminescence of an Er doped Si diode, E-MRS 2005 Spring Meeting, Symposium C, 31.05.-03.06.2005, Strasbourg, France,
85. B. Lindner, G. Pillwein, G. Brunthaler, J. Ahopelto, and M. Prunnila, “Small mass enhancement near the metal-insulator transition in gated silicon inversion layers”, Poster, 16th Int. Conf. on Electronic Properties of Two-Dimensional Systems, 10. - 15. July 2005, Albuquerque, USA.
86. C. Simbrunner, K.Schmidegg, A.Bonanni, A.Kharchenko, J.Bethke, J.Woitok, K.Lischka, H.Sitter, In-situ and real-time monitoring of MOCVD of III-nitrides by simultaneous multiwavelength ellipsometry and X-ray diffraction, 6th International Conference on Nitride Semiconductors, 28.08-02.09.2005, Bremen, Germany
87. C. Teichert, G.Hlawacek, S.Müllegger, A.Winkler, O.Lengyel, R.Resel, S.Berkebile, G. Koller, M.Ramsey, AY.Andreev, H.Sitter , Controlling growth morphologies in crystalline oligophenelyne thin films, 5th Stransi-Kaischew Surface Science Workshop, 19.-25.02.2005, Pamporovo, Bulgaria
88. D. Gruber, Hans Malissa, Dietmar Pachinger, Michael Mühlberger, Herbert Lichtenberger, Wolfgang Jantsch, Friedrich Schäffler, “g-Factor Tuning of 2D Electrons in Double-Gated Si/SiGe Quantum wells”, MSS-12 Albuquerque, NM, July 10-15,2005.
89. D. Kuritsyn, A.Kozanecki, H.Przybylinska, W.Jantsch, A fraction of excitable Er3+ ions in Silicon-rich-silicon oxide, E-MRS 2005 Spring Meeting, Symposium C, 31.05.-03.06.2005, Strasbourg, France,
90. D. Lugovyy, G. Springholz, A.Raab, R.T .Lechner, S.G.Konnikov, O.V.Rykhova, A.A.Sitnikova (Poster), ”Vertical and lateral ordering in PbSe /PbEuTe quantum dot super-lattices as a function of Eu concentration in the spacer layers”, 13th International Symposium on Nanostructures: Physics and Technology, June 20-25, 2005, St. Petersburg, Russia.

91. Deutsche Physikalische Gesellschaft DPG Berlin, March 2005, talks from Veronika Rinnerbauer, Javad Zarbakhsh and Thomas Glinsner, poster from Roman Holly
92. E. Baumgartner, T. Schwarzl, G. Springholz, W. Heiss (poster), ”Epitaxial Bragg Mirrors with Broad Omnidirectional Stop Ban in the Mid-Infrared”, Forum der Gesellschaft für Mikroelektronik, Wien, Austria, March 17-18, 2005.
93. E. Kaufmann, W. Heiss, M. Böberl, T. Schwarzl, G. Springholz, G. Hesser, F. Schäffler, K. Koike, H. Harada, M. Yano, (invited), ”Lattice type mismatched epitaxial PbTe/CdTe quantum dots giving intense mid-infrared emission”, 12th International Conference on Narrow Gap Semiconductors, July 3-7, 2005, Toulouse, France.
94. E. Kaufmann, W. Heiss, M. Böberl, T. Schwarzl, G. Springholz, G. Hesser, F. Schäffler, K Koike, H. Harada, and M Yano (Poster), “Epitaxial quantum dots from immiscible material combinations: The case of PbTe/CdTe”, 12th International Conference on Modulated Semiconductor Structures (MSS-12), July 10-15, 2005, Albuquerque, New Mexico, USA, 2005.
95. E. Kaufmann, W. Heiss, M. Böberl, T. Schwarzl, G. Springholz, G. Hesser, F. Schäffler, K Koike, H.Harada, M.Yano (Talk), ”Intense mid-infrared emission from lattice type mismatched epitaxial PbTe/CdTe quantum dots, 7th International Conference on Mid-Infrared Optoelectronic Materials & Devices, 11.-14.9.2005, Lancaster, UK.
96. E. Kaufmann, W. Heiss, M. Böberl, T. Schwarzl, G. Springholz, G. Hesser, F. Schäffler, K. Koike, H. Harada, M. Yano, Intense mid-infrared emission from lattice type mismatched epitaxial PbTe/CdTe quantum dots, Mid-Infrared Optoelectronics: Materials and Devices, MIOMD VII, 12.-14.9.2005, Lancaster, UK
97. E. Weschke, E. Schierle, , A. Gottberg, A. Helmke, G. Kaindl, W. Söllinger, G. Springholz,, ”Layer-resolved magnetization of a Heisenberg film from magnetic Laue profiles”, Conference on X-Ray Spectroscopy of Magnetic Solids, 18.-20.10.2005, Villigen, Switzerland.
98. G. Chen, H.Lichtenberger, F.Schäffler, G.Bauer, W.Jantsch, Geometry dependence of nucleation mechanism for SiGe islands grown on pitpatterned Si(001) substrates, E-MRS 2005 Spring Meeting, Symposium A, 31.05.-03.06.2005, Strasbourg, France, ,
99. G. Grabecki, J. Wróbel, T. Dietl, E. Janik, M. Aleszkiewicz ,E. Papis, E. Kamińska, A. Piotrowska, G. Springholz, and G. Bauer, “PbTe – a new medium for quantum ballistic devices”, 16th International Conference on Electronic Properties of Two-Dimensional Systems (EP2DS), July 10-15, 2005, Albuquerque, New Mexico, USA.
100. G. Pillwein, T. Berer, G. Brunthaler, F. Schäffler, and G. Strasser, “Lateral Quantum Dots in High Mobility Heterostructures”, GME-Forum 17-18 März 2005, Wien, Poster.
101. H. Lichtenberger, M. Mühlberger, C. Schelling and F. Schäffler, “Ordering of Si0.55Ge0.45 Islands on Self-Organized Si(001) Ripple Templates”, 13th Euro-MBE Workshop, Grindelwald, Switzerland, 07. - 09. March 2005.
102. H. Lichtenberger, Z.Zhong, J.Myslivecek, M.Mühlberger, C.Schelling, G.Bauer and F.Schäffler, “Epitaxial Growth on Vicinal and Nanostructured Si(001): From Basic Growth Instabilities to Perfectly Ordered Dot Arrays”, 13. Int. Symposium on Nanostructures, St. Petersburg, Russia, 20 - 24. June 2005.
103. H. Malissa, W. Jantsch, G. Chen, D. Gruber, H. Lichtenberger, F. Schäffler, Z. Wilamowski, A. Tyryshkin and S. Lyon, Investigation of the Spin Properties of

Electrons in Zero Dimensional SiGe Structures by Electron Paramagnetic Resonance, E-MRS 2005 Spring Meeting, Symposium B, 31.05.-03.06.2005, Strasbourg, France, ,

104. H. Malissa, W.Jantsch, G.Chen, D.Gruber, H.Lichtenberger, F.Schäffler, G.Bauer, A.M. Tyryshkin, S.A.Lyon, ESR investigations on low-dimensional Si-Ge structures, SPINTECH III, 01.-05.08.2005, Awaji Yumebutai, Hyogo, Japan,

105. H. Przybylińska, A. Bonanni, A. Wolos, M. Kiecana, M. Sawicki, T. Dietl, H. Malissa, C. Simbrunner, T. Wegscheider, H. Sitter, K. Rumpf, P. Granitzer, H. Krenn, W. Jantsch,, Magnetic properties of a new spintronic material – GaN:Fe, E-MRS 2005 Spring Meeting, Symposium B, 31.05.-03.06.2005, Strasbourg, France, ,

106. J. Roither, M. V. Kovalenko, S. Pichler, T. Schwarzl, W. Heiss, Nanocrystal based microcavity light emitting devices operating in the telecommunication wavelength range, Optics and Photonics, 31.7-4.8.2005, San Diego, California USA

107. J. Roither, M. V. Kovalenko, S. Pichler, T. Schwarzl, W. Heiss, Nanocrystal based microcavity emitters operating at a wavelength of 1.54 microns, E-MRS 2005 Spring Meeting, 31.5.-3.6.2005, Strasbourg, France

108. Kozanecki, D. Kuritsyn, W. Jantsch, On the role of Yb as an impurity in the excitation of Er3+ emission in silicon-rich silicon oxide , E-MRS 2005 Spring Meeting, Symposium C, 31.05.-03.06.2005, Strasbourg, France, ,

109. L. Abtin, G Springholz, V. Holy (Poster), “Shape transitions of self-assembled PbSe quantum dots during overgrowth studied by in situ STM”, 7th International Conference on Mid-Infrared Optoelectronic Materials & Devices, 11.-14.9.2005, Lancaster, UK.

110. L. Abtin, G Springholz, V. Holy (Talk), “Shape transitions of self-assembled PbSe quantum dots during overgrowth studied by in situ STM”, Summer School on Self-Organized Nanostructures, July 17-23, 2005, Cargese, France.

111. L. Abtin, G Springholz, V. Holy (Poster), “Shape transitions of self-assembled PbSe quantum dots during overgrowth studied by in situ STM”, 12th International Conference on Narrow Gap Semiconductors, July 3-7, 2005, Toulouse, France.

112. M. Böberl, T. Fromherz, T. Schwarzl, J. Roither, E. Kaufmann, G. Springholz, W. Heiss, ”Integrierbare epitaktische Bleisalz-Photodetektoren für Raumtemperaturbetrieb “, 35. Infrarot-Kolloquium, 12.-13.4.2006, Freiburg, Germany.

113. M. Böberl, T. Fromherz, T. Schwarzl, J. Roither, E. Kaufmann, G. Springholz, W. Heiss, Integrable epitaxial lead salt photodetectors for room temperature operation , 12th Int. Conf. on Narrow Gap Semiconductors, 3.-7.7.2005, Toulouse, France

114. M. Böberl, T. Schwarzl, J. Fürst, T. Fromherz, E. Kaufmann, J. Roither, H. Pascher, G. Bauer, G. Springholz, W. Heiss, “Optoelectronic lead-salt devices for integrated mid-infrared gas spectroscopy”, 12th International Conference on Modulated Semiconductor Structures (MSS-12), 10.-15.6.2005 Albuquerque, USA.

115. M. Böberl, T. Schwarzl, J. Roither, T. Fromherz, G. Springholz and W. Heiss, (Talk), ”Narrow-band room temperature photodetectors for the midinfrared”, 7th International Conference on Mid-Infrared Optoelectronic Materials & Devices, 11.-14.9.2005, Lancaster, UK.

116. M. Boeberl, T. Fromherz, T. Schwarzl, J. Roither, E. Kaufmann, G. Springholz, W. Heiss, (poster), ”Integrable epitaxial lead salt photodetectors for room temperature operation”, 12th International Conference on Narrow Gap Semiconductors, July 3-7, 2005, Toulouse, France.

117.M. Draxler, M. Mühlberger, H.Malissa, D.Gruber, F. Schäffler and P. Bauer, “Quantitative Analysis of the Ge Concentration in SiGe Quantum Wells by Low Energy Rutherford Backscattering”, 13th Euro-MBE Workshop, Grindelwald, Switzerland, 07. - 09. March 2005.

118.M. Simma, D. Lugovyy, T. Fromherz, A. Raab, G. Springholz, G. Bauer, ”Deformation potentials and photo-response of PbSe nanostructures”, 12th International Conference on Modulated Semiconductor Structures (MSS-12), 10.-15.6.2005 Albuquerque, USA.

119.M. V. Kovalenko, J. Roither, W. Heiss , Colloidally prepared HgTe nanocrystals emitting in the wavelength range of 1.2-2.4 □m, Optics and Photonics, 31.7-4.8.2005, San Diego, California USA

120.M. V. Kovalenko, J. Roither, W. Heiss, Chemically synthesized semiconductor nanocrystals emitting in the telecommunication wavelength region, E-MRS 2005 Spring Meeting, 31.5.-3.6.2005, Strasbourgh, France,

121.R. T. Lechner and G. Springholz (Talk), “Cationic surface exchange in binary and ternary IV-VI heterostructures: 2D intermixing and dot formation” 13th European Workshop on Molecular Beam Epitaxy, March 7-9, 2005, Grindelwald, Switzerland.

122. R. T. Lechner, G. Springholz and G. Bauer, “Dot formation and 2D intermixing driven by cationic exchange in IV-VI heterostructure” (Poster), 12th International Conference on Modulated Semiconductor Structures (MSS-12), 10.-15.6.2005 Albuquerque, New Mexico, USA.

123.R.T. Lechner, T.U. Schülli, V. Holy, J.Stangl, E. Wintersberger, G. Springholz and G. Bauer, “X-ray diffraction on a single layer of quantum dots: Magnetic, anomalous and conventional scattering”, 6th Autumn School on X-ray scattering from surfaces and thin layers, oral presentation, 18.9.-21.9. 2005 in Smolenice, Slovakia.

124.S. Soellinger, R. Kirchschlager, G. Springholz, K. Rumpf, P. Grantizer, H. Krenn, W. Heiss, Remanence and interdiffusion in ultrathin antiferromagnetic EuTe epilayers, 50th Magnetism and Magnetic Materials Conference, 30.10.-3.11.2005, San Jose, California, USA

125.T. Berer, Dietmar Pachinger, Georg Pillwein, Michael Mühlberger, Herbert Lichtenberger, Gerhard Brunthaler, and Friedrich Schäffler, “Single-electron transistor in strained Si/SiGe heterostructures”, Poster, 4th Int. Conf. on Silicon Epitaxy and Heterostructures (ICSI-4), May 23-26, 2005, Awaji Island, Hyogo, Japan.

126.T. Berer, Dietmar Pachinger, Georg Pillwein, Michael Mühlberger, Herbert Lichtenberger, Gerhard Brunthaler, Friedrich Schäffler, “Single-Electron Transistor in Strained Si/SiGe Heterostructures”, EP2DS-16 Albuquerque, NM, July 10-15,2005.

127.T. Hörmann, G. Pillwein, and G. Brunthaler, “Dipole trap model for the metal-insulator transition in gated silicon inversion layers”, Poster, 16th Int. Conf. on Electronic Properties of Two-Dimensional Systems, 10. - 15. July 2005, Albuquerque, USA.

128.T. Schwarzl, J. Fuerst, H. Pascher, M. Boeberl, G. Bauer, G. Springholz, W. Heiss (Talk), ”Mid infrared laser emission from 100% spin polarized states in IV-VI vertical-cavity surface -emitting lasers”, 7th International Conference on Mid-Infrared Optoelectronic Materials & Devices, 11.-14.9.2005, Lancaster, UK.

129.T. Schwarzl, J. Fürst, M. Böberl, E. Kaufmann, J. Roither, H. Pascher, G. Bauer, G. Springholz, W. Heiss (talk), “IV-VI vertical-cavity lasers: cw operation at 6-8

microns and emission from 100% spin-polarized states", 12th International Conference on Narrow Gap Semiconductors, July 3-7, 2005, Toulouse, France.

130. V. Glukhanyuk, H. Przybylinska, A. Kozanecki, W. Jantsch, Optical Properties of a single Er Center in GaN, E-MRS 2005 Spring Meeting, Strassbourg, Symposium C, 31.05.-03.06.2005, Strasbourg, France

131. V. Glukhanyuk, H. Przybylińska, A. Kozanecki, W. Jantsch,, High Resolution Site-Selective Studies of Erbium-Centers in GaN and GaN:Mg, MRS Spring meeting , 28.03-01.04.2005, San Francisco, USA

132. V. Rinnerbauer, M. Kovalenko, V. Lavchiev, G. Kocher, J. Roither, W. Heiss, K. Hingerl, Spectroscopic ellipsometry showing quantum confinement effects in layer by layer deposited colloidal HgTe nanocrystal films, 12th Int. Conf. on Modulated Semiconductor Structures, 10.-15.7.2005, Albuquerque, New Mexico, USA

133. W. Heiss, E. Kaufmann, M. Böberl, T. Schwarzl, G. Springholz, G. Hesser, F. Schäffler, K Koike, H. Harada, and M. Yano (Poster), "Epitaxial quantum dots from immiscible II-VI/IV-VI material combinations", 12th International Conference on II-VI Compounds, September 12 - 16, 2005, Warsaw, Poland.

134. W. Söllinger, R. Kirchschlager, G. Springholz, K. Rumpf, P. Grantizer, H. Krenn, W. Heiss, "Remanence and interdiffusion in ultrathin antiferromagnetic EuTe epilayers", 50th Magnetism and Magnetic Materials Conference, 20.10.-3.11.2005, San Jose, California, USA.

135. Z. Zhong, G. Chen, H. Lichtenberger, G. Bauer, W. Jantsch, F. Schäffler, "Ordered SiGe islands on vicinal and pre-patterned Si (001) substrates", 31th International Conference on Micro- & Nano-Engineering, Vienna, Austria, September 19-22, 2005, Poster.

136. "2D photonic crystal add/drop multiplexer based on contra-directional coupling" 7th International Conference on Transparent Optical Networks, M. Svaluto Moreolo July 2005, Barcelona

137. "Circular Photonic Crystals" 1st International Workshop on photonic Crystals, Mashad, invited, September 2005, Kurt Hingerl

138. "Curvilinear and Circular Photonic Crystals" Gesellschaft für Mikroelektronik, invited, March 2005, Kurt Hingerl

139. "Curvilinear and Circular Photonic Crystals" Invited talk, Kurt Hingerl, XVth Int. Conf. on Material Research, August 2005, Cancun

140. "Fabrication of a silicon vertical taper structure connecting fibers to high index waveguides using KOH anisotropic etching", R. Holly and K. Hingerl, Micro and Nano-Engineering Conference, MNE 2005, September 2005, Vienna

141. "Fabrication tolerance for photonic crystals", J. Zarbakhsh, V. Rinnerbauer, K. Hingerl, Proceedings of the Opt. Soc. Amer. Meeting, Tucson, October 2005

142. "Finite Difference Time Domain Simulations of Photonic Crystals" 1st International Workshop on photonic Crystals, Mashad, invited, September 2005, Javad Zarbakhsh

143. "Geometric freedom for constructing variable size photonic bandgap structures" J. Zarbakhsh, V. Rinnerbauer, K. Hingerl, Proceedings of the Eur. Conf. on Opt. Comm. ECOC September 2005, Glasgow

144. "Geometric freedom for constructing variable size photonic bandgap structures" Javad Zarbakhsh, Kurt Hingerl, PECS VI, June 2005, Crete

Patents

1. “Vorrichtung zum Umwandeln infraroter Strahlung in elektrischen Strom”, G. Matt, T. Fromherz, Patent: 27. 7. 2006, AZ 1274/2006
2. “Speicherelement für eine optische Signalausgabe”, D. I. Kryzhkov, W. Jantsch, B.A. Andreev, T. Gregorkiewicz, Z. F. Krasilnik, V.P. Kuznetsov, Patentanmelding 3A A 99/2006 am 20. Jänner 2006
3. “Verfahren zur Beeinflussung des Spinzustandes von Ladungsträgern in einem Festkörper, insbesondere in einer Quantenstruktur eines Halbleiters”, W. Jantsch, H. Malissa, Z. Wilamowski, Patentanmeldung 3A A 1582/2006 am 22. Sept. 2006
4. “Vorrichtung zur Leitung von Lichtwellen”, J. Roither, M. Böberl, S. Pichler, M.V. Kovalenko, W. Schwinger, F. Schäffler, W. Heiss, D.V. Talapin, Patentanmeldung: 19.7.2006, AZ 1227/2006
5. “Improved Optical Design of Polymer Solarcells by employing diffractive layers”: Karen Forberich, Kurt Hingerl, Christoph Brabec und Markus Scharber, transferred to Konarka USA
6. “One-dimensional Metallic Photonic Crystals” - K. Hingerl, M. Bergmaier, M. Huber, transferred to Photeon: Deutsche Anmeldung, P2006, 0816DE
7. Siemens 2005: Effizienzverbesserung von Schwarzkörper-Strahlern durch Beschichtung eines photonischen Kristalles
8. “Photeon 2005: Verfahren zum Herstellen einer Lichtkopplungseinrichtung”, beim Ö. Patentamt eingereicht

Diploma Theses

Finished in 2005:

1. Matthias Wegscheider
   “Growth and Optical Characterisation of Nitride-based Diluted Magnetic Semiconductors”

Finished in 2006:

1. Moritz Brehm
   ”Photoluminescence investigation of SiGe and InAs1-xPx nanostructures”
2. Heiko Groiss
   ”Transmission electron microscopy of self-organized PbTe/CdTe nanocrystals”
3. Martyna Grydlik
   “Low temperature process for integrating Si based infrared photodetectors into optical resonators”
4. Thomas Hörmann
   “Modellrechnungen zum Metall-Isolator-Übergang in einer zweidimensionalen Silizium-Inversionsschicht in der Dipol-Streuungsnäherung”
5. Stefan Krimbacher
   “Funktionsweise der Solarzelle mit Betonung der didaktischen Aufbereitung”
6. Bernhard Mandl
   “Au-free growth of nanowires and their characterization”

7. Pichler Stefan
   "Nanokristall basierende elektrooptische Bauteile"
   (Supervisor: W. Heiss)

Current works:

1. Elisabeth Lausecker
   "Large-area high resolution microcontact printing"
2. Oliver Majovsky
   "p-Modulationsdotierung auf verkippten Si(001) Substraten"
3. Michael Niedermayr
   "Herstellung von Einzelelektronen-Transistoren auf der Basis von Nanokristallen"
4. Tomoyuki Suzuki
   "Quantum Dots Simulation with Finite Element Method"
5. Anzengruber Johannes
   "Optische Resonatoren für die Molekülspektroskopie"
   (Supervisor: W. Heiss)
6. Kirchschlager Raimund
   "Magnetooptische Eigenschaften von Eu-Chalcogeniden"
   (Supervisor: W. Heiss)
7. Eibelhuber Martin
   "Epitaktische BaF2/Bleisalz Heterostruktur-Bauteile für das mittlere Infrarote"
   Supervisor: W. Heiss)
8. Plochberger Birgit
   "Ba doped C60 layers for organic FET's"
   (Supervisor: H. Sitter)
9. Martin Quast
   "Transport phenomena in Fe-doped GaN"
   (Supervisor: A. Bonanni)

Doctor's Theses

Finished in 2005:

1. M.Sc. Jiri Novak
   "Untersuchung der strukturellen Eigenschaften von Quantenpunkten"
2. Dipl.Ing. Klaus Schmidegg
   "Growth and optical characterisation of GaN and its ternary compounds "
3. Dipl.Ing. Gernot Fattinger
   "Acoustic Wave Phenomena in Multilayered Thin Film Layer Stacks"

Finished in 2006:

1. DI Herbert Lichtenberger
   "Kinetic and strain-induced seof-organization of SiGe heterostructures"
2. M.Sc. Jiri Novak
   "Structural investigations of nano-islands using x-ray diffraction techniques"

Current works:

1. M.Sc. Laurel Abtin
   "STM investigation on self-assembled IV-VI semiconductor nanostructures"
2. Dipl.Ing. Thomas Berer
   "Electronic and spin properties of Si/SiGe heterostructures"
3. Dipl.Ing. Daniel Gruber
   "Substitutional Carbon in Si/SiGeC Heterostructures"
4. Dipl. Phys. Anke Hesse
   "Strukturelle Untersuchungen an Halbleiternanostrukturen"
5. M.Sc. Dmytro Lugovyy
   "Investigation of vertical and lateral ordering in self-organized PbSe quantum dot superlattices"
6. M.Sc. Dan G. Matei
   "Scanning tunneling microscopy invetsigations of self-assembled semiconductor nano-structures"
7. Dipl.Ing. Dietmar Pachinger
   "High Mobility Si/SiGe Heterostructures for spintronic Applications"
8. Dipl.Ing. Georg Pillwein
   "Elektrische Untersuchungen von Quanteneffekten an Nanostrukturen"
9. Dipl.Ing. Patrick Rauter
   "SiGe nanostructures for next generation infrared detectors"
10. M.Sc. Aaliya Rehman Khan
    "Growth and structural characterisation of Si/SiGe hetero- and nanostructures"
11. Dipl.Ing. Mathias Simma
    "Photoleitungsuntersuchungen an Quantenpunkten"
12. Dipl.Ing. Eugen Wintersberger
    "Röntgenbeugung und –reflexion an Si/SiGe/GaAs Hetero- und Nanostrukturen "
13. Dipl.Ing. Joachim Achleitner
    "Simulation magnetooptischer Effekte in EuTe"
    (Supervisor: W. Heiss)
14. Dipl. Ing. Eugen Baumgartner
    "Optoelectronic devices based on nanocrystals"
    (Supervisor: W. Heiss)
15. Dipl.Ing. Michaela Böberl
    "Electro-optical IV-VI devices for the mid-infrared"
    (Supervisor: W. Heiss)
16. Mag. Erich Kaufmann
    "Lateral emitting lead-salt microlasers"
    (Supervisor: W. Heiss)
17. M.Sc. Maksym Kovalenko
    "Synthesis and characterization of nanocrystals for the mid infrared"
    (Supervisor: W. Heiss)
18. Dipl.Ing. Hans Malissa
    "Spin properties of low-dimensional systems"
    (Supervisor: W. Jantsch)

19. Dipl.Ing. Jürgen Roither
    "Light emitting nanodevices: Novel concepts and their realization"
    (Supervisor: W. Heiss)
20. Dipl.Ing. Clemens Simbrunner
    "MOCVD growth and In-situ characterization of ferromagnetic nitride semiconductors."
    (Supervisor: H. Sitter)
21. Dipl.Ing Walter Söllinger
    "Monte Carlo simulations of spin-related phenomena in magnetic semiconductor structures"
    (Supervisor: W. Heiss)
22. M.Sc. Andrea Navarro-Quezada
    "Magnetic nanostructures on nitride surfaces for spintronics applications"
    (Supervisor: A. Bonanni)
23. M.Sc. Gerardo Hernandez Sosa
    "Growth and Characterization of selforganised organic nanostructures"
    (Supervisor: H. Sitter)
24. Dipl.Ing Matthias Wegscheider
    "Optical characterization of transition metal doped ferromagnetic nitrides"
    (Supervisor: A. Bonanni)

Cooperations

Industrial Cooperations

1. AIXTRON AG, Aachen, D;
2. AMS, Unterpremstätten
3. E+E ELEKTRONIK Ges.m.b.H, Langwiesen 7, A-4209 Engerwitzdorf, www.epluse.at
4. EV Group, E. Thallner GmbH, 4780 Schaerding, www.evgroup.com
5. Lumics GmbH, Berlin, Germany
6. PANalytical B.V, Lelyweg 1, 7602 EA Almelo, Niederlande, www.panalytical.com
7. Photeon Technologies GmbH, Kirchstrasse 35, 6900 Bregenz, www.photeon.com
8. PROFACTOR Produktionsforschungs GmbH, A-4407 Steyr-Gleink, Im Stadtgut A2, www.profactor.at
9. Siemens AG, Corporate Technology, Materials and Manufacturing, Innovative Electronics, D-91050 Erlangen, Deutschland, w4.siemens.de/ct/de
10. SENTECH Instruments GmbH, 12489 Berlin, Deutschland, www.sentech.com
11. ST Microelectronics, Crolles CEDEX, France, www.st.com
12. TeraView Ltd., Cambridge, UK;
13. Thales, Paris, France, www.thalesgroup.com
14. Toshiba Research Europe Ltd, Cambridge, UK;
15. Unaxis Balzers AG, Liechtenstein;
16. Unaxis (Balzers), Trübbach, Schweiz, www.unaxis.com

17. Upper Austrian Research GmbH, TECHCENTER Linz-Winterhafen, Hafenstrasse, 47-51, A-4020 Linz, www.uar.at
18. SOITEC, Crolles, France

Cooperations with scientific places

1. Advanced Technology Institute, University of Surrey, UK
2. Charles University Prague, Czech Republic
3. Dipartimento di Fisica, Universita degli Studi di Cagliari, Monserrato, Italy
4. Experimentalphysik I, Universität Bayreuth, Germany
5. FOM-Institute for Plasma Physics, Rijnhuizen, The Netherlands.
6. Forschungszentrum Jülich, Deutschland
7. Heriott Watt University, Edinburgh
8. Inst. for Chemistry and Technology for organic materials, TU Graz
9. Inst. for computational solid state physics, Montanuniversität Leoben
10. Inst. for Physical Chemistry, University Chernivtsi, Ukraine
11. Inst. für Angewandte Physik, Univ. Linz
12. Inst. für Experimentalphysik I, Universität Bayreuth, Deutschland
13. Inst. für Experimentalphysik, Universität Graz, Graz, A
14. Inst. für Festkörperelektronik, TU Wien
15. Inst. für Festkörperphsik, TU Graz
16. Inst. für Festkörpertheorie und Theoretische Optik, Universität Jena, Germany
17. Inst. für Mikroelektronik, TU Wien
18. Inst. für Physik, Montanuniversität Leoben
19. Inst. für Physikalische Chemie, Universität Linz, A
20. Inst. of Physics, Polish Academy of Sciences, Warschau
21. Laboratorium für Festkörperphysik, Eidg. Technische Hochschule Zürich, Zürich
22. Max-Born Institut fuer Nichtlineare Optik, Berlin-Adlershof
23. Max-Plank-Institut Stuttgart, Germany
24. Osaka Institute of Technology, Osaka 535-8585, Japan
25. Paul Scherrer Institute, Switzerland
26. Princeton University, USA (Prof. Lyon, Prof. Tsui)
27. RIIC (Research Institute for Integrated Circuits), JKU Linz
28. Surface Physics Institute, Fudan University, Shanghai, China
29. Technical Univesity Delft, Dimes, Netherlands
30. Technical University Munich
31. Technical University Vienna
32. Thales Research and Technology, France
33. Universität Graz, Institut für Experimentalphysik

34. Universität Jena
35. Universität Paderborn, Prof. Lischka
36. Universität Wien
37. Universität Würzburg, Prof. L. Molenkamp
38. University of Linköping, Sweden
39. University of Lund, Sweden
40. University of Maryland, MD, USA
41. University of Milan
42. University of Neuchatel, Switzerland
43. University of Southampton, England

Structuring of Organic Semiconductors by Optical Lithography

K. Forberich[1], T. Fromherz[2], K.Hingerl[1], M. Morana[3], C.Brabec[3]

[1] CD-Labor für Oberflächenoptische Methoden, Institut für Halbleiter- und Festkörperphysik, Altenbergerstraße 69, A-4040 Linz

[2] Institut für Halbleiter- und Festkörperphysik, Altenbergerstr. 69, A-4040 Linz

[3] Konarka Austria, Konarka Austria Forschungs und Entwicklungs GmbH, Altenbergerstraße 69, A-4040 Linz

Introduction

Organic semiconductors are now in wide use for devices such as OFETs, OLEDs and organic solar cells. However, the transport properties like for example the carrier mobility of these materials are not completely understood. Carrier mobility is usually determined from the dependence of the saturation current on the applied gate voltage of a field effect transistor (FET). These results reflect the mobility under large electric fields. Information about the low field mobility can be extracted from Hall measurements, which have been done for small molecule organic semiconductors [1], but not for conjugated polymers. In order to produce the well-defined Hall bar that is necessary for these measurements, we developed a process to structure a thin layer of an organic semiconductor. In the development of this process, care was taken to protect the semiconductor from oxygen and UV-radiation. In order to monitor the residual influence of the process on the organic semiconductor, FET structures were fabricated by the same process. In addition, Structuring organic semiconductors can also be useful for other applications, for example in a FET where a well-defined structure would reduce the leakage current, or for the definition of pixels in an organic photodetector.

Experimental

Sample Preparation

We start with silicon substrates with a 230 nm oxide layer. Gold contacts are applied by lithography, evaporation and subsequent liftoff (Fig. 1). The organic semiconductor Poly(3-hexyl)thiophen (P3HT) is then spin-coated onto this structure. As the next step, three additional layers are applied on top: photoresist (~1.4 µm), gold (~50 – 100 nm) and a second layer of photoresist (~1.8 µm). The top layer of photoresist is structured by optical lithography and the gold that is not covered by the remaining photoresist is removed by wet chemical etching.

Subsequently, the samples are etched in an oxygen plasma so that all the exposed organic materials are removed. The remaining gold layer acts as an etch mask. In addition, the gold protects the semiconductor form the detrimental influence of UV radiation and oxygen during the whole process. After the etching, the photoresist and gold on top of the polymer layer are removed in a liftoff step with acetone. The smallest feature size that was demonstrated with this process is about 10 µm.

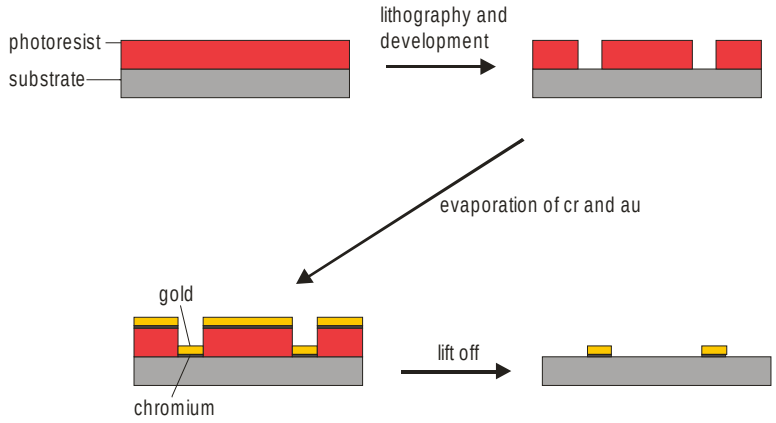

Fig. 1: Process steps for the contacts.

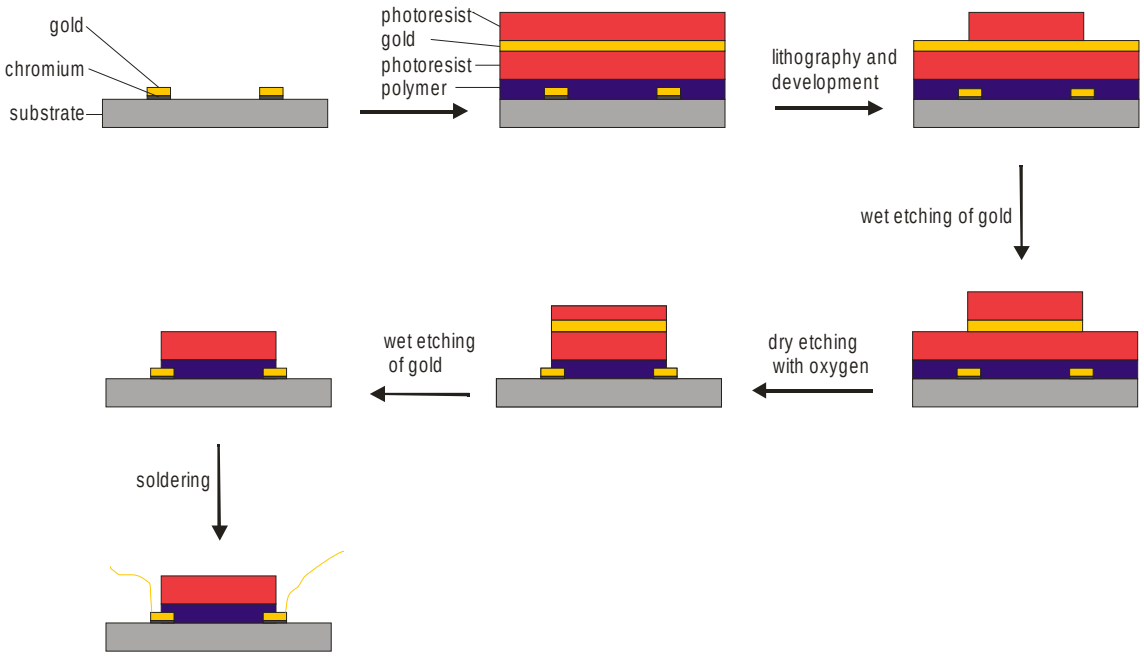

Fig. 2: Process steps for the structuring of the organic semiconductor.

Measurements

To examine the influence of the process steps on the electrical properties of the organic semiconductor, one of the structures on our samples was an OFET geometry with a channel length of 10 µm and a channel width of 1 cm. The transistor characteristics were measured before and after the structuring of the semiconductor layer, the results are shown in Figs. 3 and 4.

These measurements show that the conductivity of the P3HT-layer was increased by one to two orders of magnitude as a consequence of the process steps. The dependence of the source-drain-current on the applied gate voltage decreases accordingly. We interpret these results as being caused by unintentional doping of the P3HT during one of the process steps in spite of the protective gold layer. Up to now, it is not clear during which of the process steps sketched in Fig. 2 the oxygen doping predominantly

occurs. The identification and improvement of this step has to be the subject of future work.

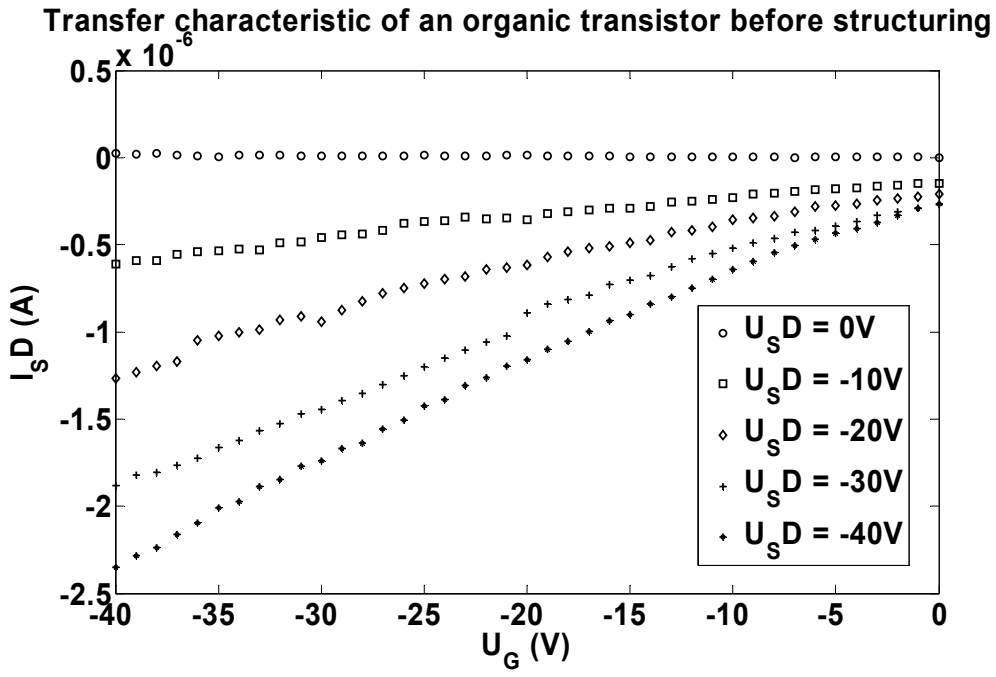

Fig. 3: Transfer characteristics of an organic field effect transistor before structuring the semiconductor.

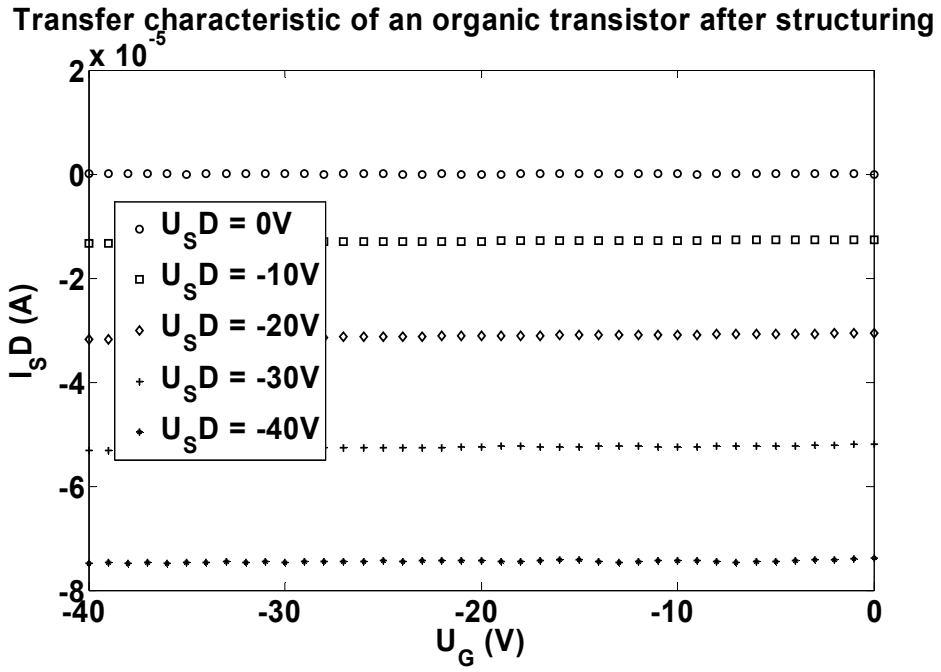

Fig. 4: Transfer characteristics of an organic field effect transistor after structuring the semiconductor.

Conclusion

We have shown that organic semiconductors can be structured by a combination of optical lithography and oxygen etching. Reference measurements on a transistor showed that the semiconductor was doped by oxygen during the process. The influence of the particular process steps has yet to be examined carefully, so that those steps can be modified in order to prevent or reduce the doping of the semiconductor. The experiments were done for P3HT. In principle, this process can be applied to any organic semiconductor, but the influence of the process on the electrical properties of the semiconductor might differ.

References

[1] V. Podzorov et al., *PRL* **95**, 226601 (2005)

Au-free Epitaxial Growth of $InAs_{1-x}P_x$ Nanowires

B. Mandl, J. Stangl, M. Brehm, T. Fromherz, G. Bauer

Institute for Semiconductor and Solid State Physics, University of Linz, A-4040 Linz

T. Mårtensson, L. Samuelson, W. Seifert

Department for Solid State Physics, S-221 00 Lund University, Sweden

InAs and $InAs_{1-x}P_x$ nanowires have been grown by the use of a metal-organic vapor phase epitaxy. The nanowire growth is initiated by a thin SiO_x layer deposited on the substrate prior to growth. The wires exhibit a non-tapered shape with a hexagonal cross section. Further the growth of InAs on Si is demonstrated as well as the growth on a pre-patterned InP (111)B substrate.

Introduction

Semiconductor nanowires as one-dimensional structures and building blocks for nano-devices have received increased attention in recent years. Controlling the one-dimensional growth on a nanometer scale offers unique opportunities for combining materials, manipulating properties, and designing novel devices. We present a general method to produce epitaxial nanowires of InAs, without using Au-particles as catalyst. It has been shown that InAs nanowires can easily be contacted and gated. With inbuilt barriers (e.g. InP), the functionality of such structures in single electron transistors [1] and resonant tunneling devices [2] has been demonstrated.

Moreover, InAs has a high potential to be used complementary in combination with Si for high-mobility applications. For this purpose, however, nanowires grown Au-assisted impose severe restrictions due to the introduction of deep-level defects into Si. We show in this report that InAs nanowires can be obtained epitaxially on various substrates without any metal catalyst when one covers the substrates by a thin layer of SiO_x ($x \approx 1$) prior to InAs growth. X-ray diffraction measurements indicate that the wires form in part in the wurtzite modification and grow spontaneously in c-direction [000.1], equivalent to the cubic [111] direction.

Experimental

For wire-growth we used low pressure metal organic vapor phase epitaxy (LP-MOVPE) at a pressure of 10 kPa, with trimethylindium (TMI), arsine (AsH_3), and phosphine (PH_3) as precursor materials, transported in a flow of 6000 ml/min of H_2 as carrier gas. For the precursors typical molar fractions of 2×10^{-6} for TMI and 2×10^{-4} for AsH_3 were used. For TMI also higher molar fractions were tested, but had no significant effect on the growth rate. The molar fractions for PH_3 were varied between 3.5 and 15×10^{-3}. As substrates we used epitaxy-ready III/V wafers and Si wafers. In case of Si substrates, the native oxide was removed by an HF dip. Before loading the substrates into the growth chamber, a thin SiO_x layer was sublimated onto the surface. The substrates were then heated to the growth temperature between 520 °C and 680 °C in H_2 atmosphere. As soon as growth temperature was reached, the precursors were switched on simultane-

ously. The growth was stopped by switching off the TMI source, and the samples were cooled under AsH_3 flow, or for $InAs_{1-x}P_x$ deposition, under additional PH_3 flow. To characterize the wires we employed scanning electron microscopy (SEM) and x-ray diffraction (XRD). SEM investigations were performed using a JEOL 6400 and a LEO 150 microscope. From SEM we obtain the length, orientation, shape, and density of the wires.

XRD experiments have been performed at beamline 10B (Troïka II) at the ESRF in Grenoble, to get information on the orientation of the wires relative to the used substrate and relative to each other, about the lattice constant and the crystalline structure of the wires. SEM images of InAs wires grown at different temperatures on InP (111)B surfaces, covered by 1.3 nm SiO_x prior to growth, are presented in Fig. 1. We observe the following trends:

(i) The wires grow spontaneously on the InP(111)-surface and appear epitaxially oriented, i.e., they are standing vertically on the surface and grow in continuation of the substrate [111]B orientation. Remarkably, the wires are homogeneously thick, i.e., in contrast to typical MOVPE wire growth [3], [4], we cannot determine any measurable tapering and also no thickening at the wire foot/substrate connection.

1. In general, the growth temperatures are much higher than for Au-assisted growth of InAs nanowires in MOVPE, where growth suddenly ceases when the temperature exceeds 500 °C. The wire length is not a linear function of time: in parallel investigations, not presented here, we have seen that the length growth rate starts with a high value and decreases then over time according a power law $R \sim t^n$ ($n \approx -0.5$). This fact can be seen as a hint on the growth mechanism.

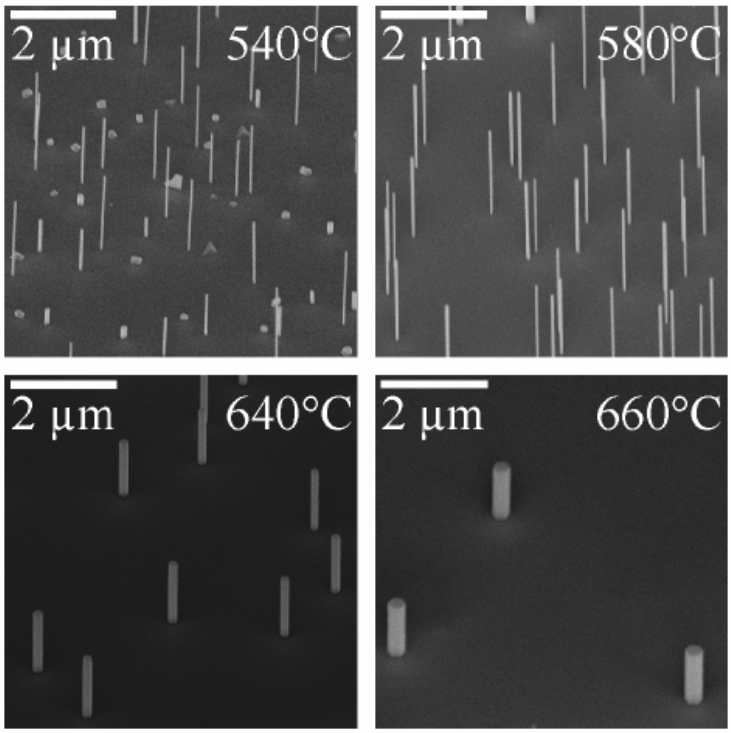

Fig. 1: SEM images (45° tilt) of InAs wires grown on InP (111)B at different temperatures, growth time was 60 s [5].

(iii) The wire density is also a function of growth temperature. In general, the density decreases with increasing temperature. This indicates that there are relations to

the general laws which govern the nucleation kinetics of clusters on surfaces, where the density ρ of critical nuclei follows the general proportionality ρ ~ R/D(T), with R the deposition rate and D(T) the temperature-dependent coefficient of surface diffusion. This result indicates that clusters may be involved in pre-stages of wire growth. At higher temperatures these clusters grow anisotropically and form one-dimensional wires. At lower temperature only a part of the clusters adopts this growth mechanism, others grow by isotropic expansion instead. In fact, we find that at low temperatures the wires compete with InAs-clusters on the surface (see the 540 °C sample in Fig. 1).

(iv) In parallel to the decreasing density, the aspect ratio length/width of the wires decreases with increasing temperature: At higher temperatures the radial growth on the side facets gets more and more important. At the highest growth temperature of 680 °C, the aspect ratio dropped down to below 1 and we obtained epitaxially grown hexagonal platelets.

(v) The morphology of the nanowires is rod-shaped with a regular hexagonal cross-section. The top of the wires is flat, visible at least in case of the thicker wires grown at higher temperatures. From x-ray diffraction experiments performed at ID01 at the ESRF Grenoble it follows that the structure of the wires is in part wurtzite, which is the thermodynamically metastable modification of InAs.

By using different materials as substrate, the influence of the lattice mismatch on the wire growth was investigated. For this study different epiready III-V (111)B substrates (InAs, InP, GaAs, and GaP) as well as Si (001) substrate are used. With these substrates, a range of lattice mismatches up to 12% (InAs/Si) is covered, with all substrates, epitaxial wire growth along [111]B could be demonstrated, indicating that the lattice mismatch poses no restriction for the wire growth.

Position controlled nucleation of InAs nanowire is demonstrated when using a pre-patterned InP (111)B substrate. The pattern is defined by electron beam lithography, SiO_x and a subsequent e-beam resist lift-off. For structured substrates, a slightly different growth sequence was used, in that the precursors are activated at 500 °C during the heating of the samples to 580 °C, wires are growing on the positions defined by the SiO_x patches. Such a patterned nucleation can be seen in Fig. 2(a). It has to be mentioned that the wires are nucleated by patches remaining on the substrate surface, in difference to processes where openings in a SiO_2 layer are used to control the growth position of III-V nanowires [7].

Another result of this study is the successful growth of InAs nanowires on Si (001) and Si (111), nucleated using a 1.3 nm thick SiO_x layer instead of Au as nucleation centers [8]. Before the deposition of the SiO_x layer, the native oxide is removed by a HF etch. The wires grow in the four incline [111] directions on the Si (001) substrate. For the growth on such substrates, the exposure of the substrate to Oxygen prior to the growth is critical. Such a growth mechanism opens the possibility to use InAs as high mobility semiconductor on Si, without making use of Au particles that are detrimental for the performance of Si based electronics.

Further, the growth of $InAs_{1-x}P_{x,}$ as a III-V alloy is demonstrated. The growth is done similar to InAs, on a InP (111)B substrate with a 1.3 nm thick SiO_x layer. As precursor material Phosphine is used in addition to TMI and Arsine. The growth results in wires very similar to those of InAs, with a constant diameter, showing no tapering and no thickening at the wire foot/substrate interface and show a hexagonal cross-section, again the wires grow in the <111>B direction, continuing the substrate orientation. The wires are shown in Fig. 2(a). In photoluminescence and XRD measurements a change of the energy gap and the lattice constant as a function of the Phosphine flux is found, demonstrating a significant phosphorus incorporation into the wires [9]. The maximum concentration of P in the wires so far achieved is estimated to be x = 0.17.

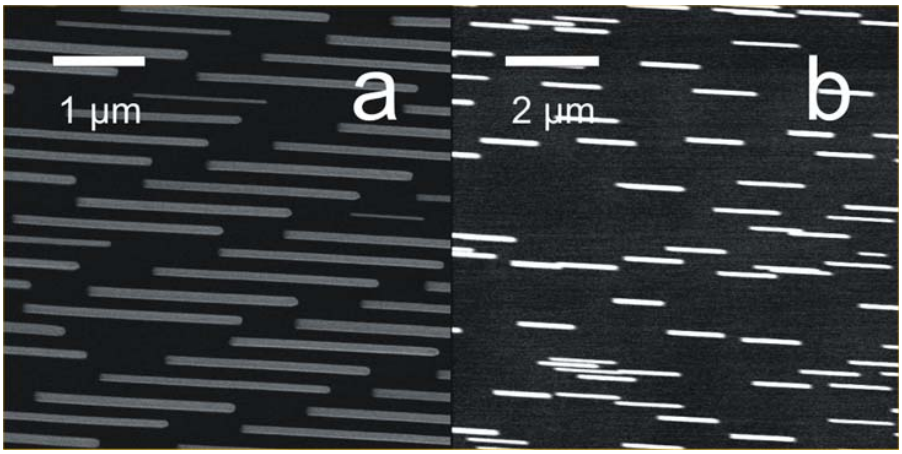

Fig. 2: 45° tilt SEM images of a) InAs nanowires grown using a pre-patterned SiO_x layer on an InP (111)B substrate. b) SEM image of $InAs_{1-x}P_x$ nanowires (45° tilt) grown at InP (111)B at 620 °C for 60 s [9].

Conclusion

We demonstrate a novel mechanism for the growth of InAs and $InAs_{1-x}P_x$ nanowires which relies on a SiO_x layer deposited at the substrate surface. This growth mechanism shows epitaxial grown wires with homogeneous shape. The wire growth rate is depending on the growth temperature and growth time. Also, the density of the wire nucleation is depending on the growth temperature indicating a growth initialized by clusters formed on the substrate prior to wire formation. In addition the wire length to width ratio is found to be temperature dependent. From XRD measurements the existence of a wurtzite phase together with the zinkblende phase is found for the wire crystal structure. Additional to the growth on InP, various III-V and even Si substrates were used, showing no influence of strain on the wire growth. The demonstrated growth of InAs wires on Si substrates in the absence of metal catalysts opens a promising route for integrating III-V high mobility devices with standard Si based electronics. In addition, the growth of wires on a pre-patterned substrate is demonstrated with a high yield for the wire nucleation on pre defined positions. Also, the growth of $InAs_{1-x}P_x$ wires is demonstrated, opening the possibility to grow additional III-V materials and heterostructures by this method.

References

[1] M. T. Björk *et al.*, Nano Letters **2**, 87 (2002)

[2] C. Thelander *et al.*, Appl. Phys. Lett. **83**, 2052 (2002)

[3] K. Hiruma *et al.*, J. Appl. Phys. **77**, 447 (1997)

[4] W. Seifert *et al.*, J. Cryst. Growth **272**, 211 (2004)

[5] K. A. Dick *et al.*, Nano Letters **5**, 761 (2005)

[6] B. Mandl *et al.*, Nano Letters **6**, 1817 (2006)

[7] M. Inari *et al.*, Physica E **21**, 620 (2004)

[8] T. Mårtensson *et al.*, Nano Letters **4**, 1987 (2004)

[9] B. Mandl *et al.*, ICPS conference proceedings (in press)

Fabrication of Narrow Split Contacts for Nanocrystal Investigations

M. Niedermayr, G. Pillwein, W. Heiss, G. Brunthaler

Institut für Halbleiter- und Festkörperphysik, Johannes-Kepler-Universität, A-4040 Linz

A simple method for producing metallic electrodes with gaps below 10 nm is presented. The fabrication of these electrodes is achieved by electron beam (e-beam) lithography and shadow evaporation. Thereby the gap width can be adjusted directly by the exposure time in the lithography process. At the moment we can create gaps as small as 4 nm. In later investigations such electrodes will be used for electrical transport studies of nanocrystals made of different materials and sizes.

Introduction

Using colloidal techniques, nanocrystals can be made of different materials [1]. The size of these nanocrystals can be easily changed via the fabrication conditions. The size is e.g. ranging from 5 to 15 nm for IV-VI semiconductors. For investigation of electrical transport properties it is necessary to have electrodes with different gap sizes fitting to the size of the nanocrystals. One way of producing them is by e-beam lithography using a scanning electron microscope (SEM) combined with shadow evaporation.

A single electron transistor can be fabricated with a nanocrystal in between two electrodes and in combination with an additional gate [2] (see Fig. 1). Such a device has the same behavior as common quantum dots produced by lithography processes [3]. In this case, the electrons tunnel one by one from the source electrode to the nanocrystal and from the nanocrystal to the drain electrode. This current is switched on and off by the applied gate voltage from the conducting p-Si substrate which is isolated with the oxide layer from the contacts.

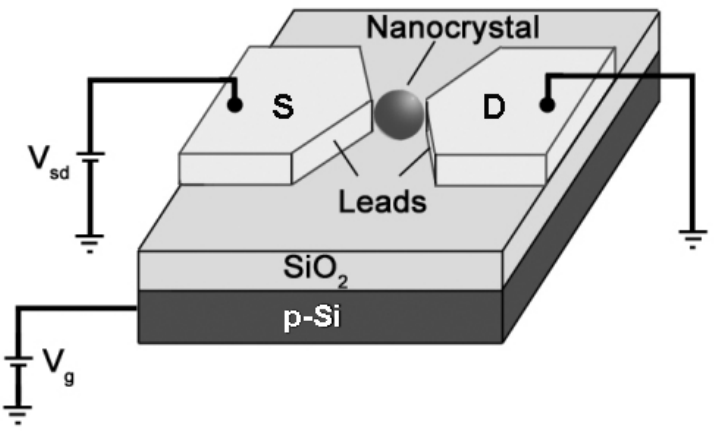

Fig. 1: Schematic picture of a nanocrystal single electron device consisting of two side contacts and an underlying conducting substrate as a plunger gate.

Experimental

The used high-doped Si substrates have a 100 nm thick SiO_2 cover layer. First they are consecutively cleaned in acetone, trichloroethylene, acetone and methanol in an ultrasonic bath for 5 minutes each. The positive photoresist Allresist AR-P 671.04 950K is spun onto the substrates at 6000 rpm for 1 minute. The photoresist is made of a solution of 4% 950K PMMA in chlorobenzene. Therewith a uniform layer with a thickness of 250 nm is achieved. The coated substrates were annealed at 160 °C for 60 minutes. Afterwards the samples are exposed with a Leo 35 scanning electron microscope. The required mask was designed with the ELPHY Plus software. In order to find the ideal mask design, different contact tip shapes were tested. We get the best results with obtuse tip shapes.

After exposure the contact electrode shape is created in the photoresist layer by putting it into a developer and a stopper for 2 minutes and 30 seconds, respectively. The samples are evaporated with an 8 nm Cr layer and a 50 nm Au layer, where the Cr layer ensures a good mechanical contact between SiO_2 and gold. In a lift-off process, the residual photoresist together with the metallic layers on top of it is removed at 75°C for 2 hours.

To apply an external voltage to the contact electrodes bonding pads are required. These pads are produced by optical lithography using the photoresist Shipley S1813 at 4000 rpm for 1 minute, baking at 90°C for 10 minutes and UV-exposure through a mask. After resist development, a 300 nm Al layer is deposited and the remaining resist is removed again. We could produce electrodes with gaps as small as 10 nm with this method.

Because of electron scattering an undercut is formed into the photoresist. Between the two electrodes the resist is so small that the undercuts are overlapping and we get a kind of bridge (Fig. 2(a)).

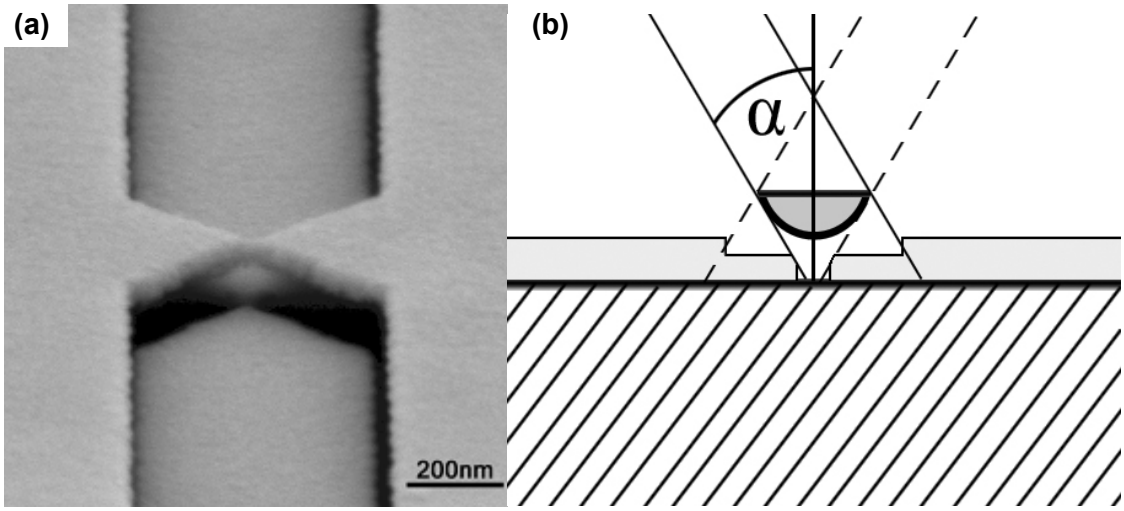

Fig. 2: (a) SEM picture of two electrodes after evaporation and before lift off; you can see the photoresist bridge covered by the Cr and Au layer; (b) schematic picture of cross section of the photoresist bridge during shadow evaporation; the first layer is deposited from right at angle of -α, the second one is deposited from left at angle α

By using shadow evaporation we can reduce the width of the gap. For this we deposited two gold layers with a thickness of 25 nm at α = +/- 6.67° instead of one 50 nm

layer at normal incidence (Fig. 2(b)). With this technique gaps up to 4 nm are possible (Fig. 3).

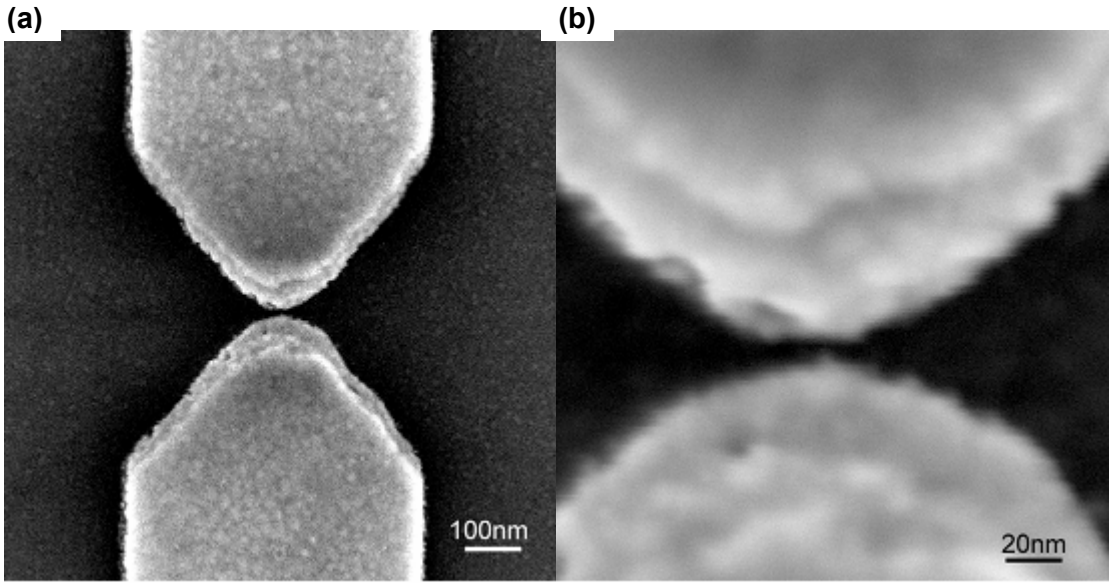

Fig. 3: SEM pictures of a pair of electrodes with different magnifications; gap width: 5.5 nm

To get the nanocrystal onto the substrate, the drop casting method is used (Fig. 4). You can see in picture Fig. 4(b), there are a lot of crystals between the electrodes. However, for general transport studies, and especially studies on the nanocrystal-SET, we just want charge transport through one single nanocrystal. However the tunneling exponential decay length is very small. A simple estimation determines this length to 1 Å. Thus, the electrons can only tunnel into well placed nanocrystals.

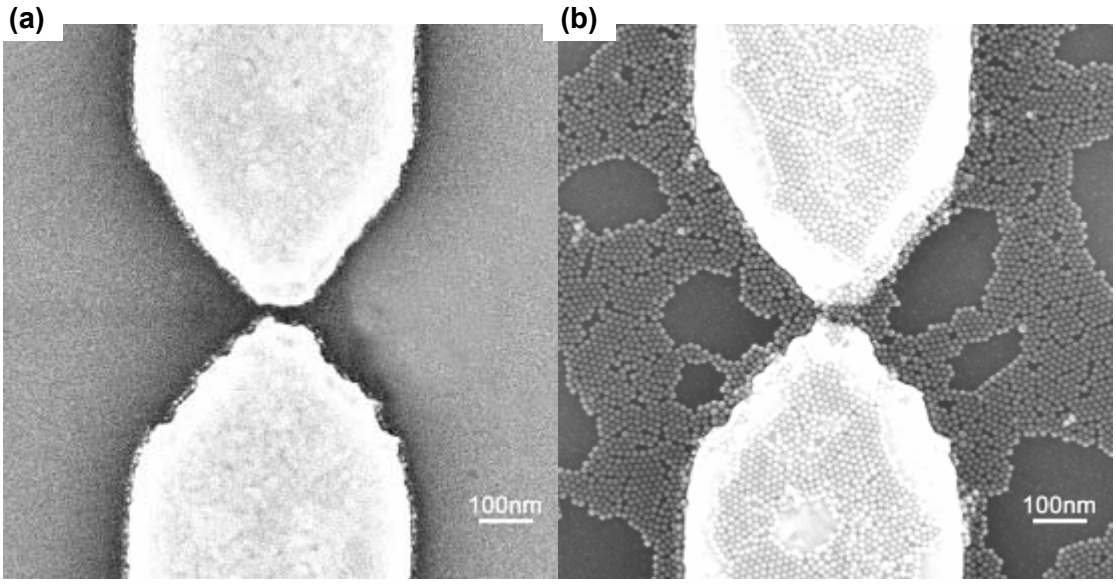

Fig. 4: SEM picture of a pair of electrodes; (a) before drop casting (b) after drop casting FeO nanocrystal (d = 12nm)

Conclusion

A simple technique has been developed to fabricate electrodes with sub-10 nm gaps. In future experiments these electrodes will be used to investigate electrical transport through nanocrystals and SET made of nanocrystals with Si substrate as back gate.

Acknowledgements

Work was supported by “Fonds zur Förderung der wissenschaftlichen Forschung” (Austrian Science Fonds) Project P16160.

References

[1] M. Kovalenko, E. Kaufmann, D. Pachinger, J. Roither, M. Huber, J. Stangl, G. Hesser, F. Schäffler, W. Heiss : “Colloidal HgTe Nanocrystals with Widely Tunable Narrow Band Gap Energies: From Telecommunications to Molecular Vibrations”, J.Am.Chem.Soc., 128, 3516-3517 (2006)

[2] D. L. Klein, R. Roth, A.K.L. Lim, A.P. Alivisatos, P.L. McEuen : “A single-electron transistor made from cadmium selenide nanocrystal”, Nature, 389, 699-701 (1997)

[3] U. Meirav E.B. Foxman, “Single-Electron Phenomena in Semiconductors”, Semicond. Sci. Technol. 10, 255 (1995).

Structure of Single InAs Nanowires

J. Stangl[1], B. Mandl[1], R.T. Lechner[1], G. Bauer[1], T. Mårtensson[2], W. Seifert[2]

[1] Institute for Semiconductor Physics, Univ. Linz, Austria

[2] Solid State Physics, Lund University, Box 118, S-221 00 Lund, Sweden

A method for the Au-free growth of InAs nanowires on (111) oriented Si substrates is presented which is based on a thin SiO_x layer apparently catalyzing wire growth. Structural investigations carried out by TEM and by high resolution x-ray diffraction reveal that these InAs wires contain stacking faults, i.e. regions with a wurtzite instead of a zinc-blende stacking. In order to assess the amount of the hexagonal phase, intensities from hexagonal and zinc-blende allowed x-ray reflections were measured and compared with each other.

Introduction

Semiconductor nanowires attract attention due to their potential to integrate optical functionality with mainstream Si technology. The main problem here is the fabrication of mainly III-V devices, i.e., polar semiconductor structures, on top of the unpolar Si surface. Usually the starting point are epitaxial layers, which suffer in addition to the polarity issue also from lattice mismatch values up to about 12%. The introduction of SiGe layers helps to reduce the mismatch and hence limit the dislocation densities, but a problem not easy to avoid are antiphase boundaries between regions where growth started with the group III or group V element, respectively.

Au-Free InAs Nanowire Growth on (111) Si

All these problems are greatly relieved when instead of 2D layers wires with a small diameter and a large aspect ratio are grown: with diameters around 100 nm, heights of several µm are commonly achieved. Due to the small contact region between the wires and the substrate, strain relief is easily achieved. Although it is not clear so far whether relaxation takes place purely elastically or partially plastically, no dislocations penetrating the wires are observed. Also antiphase boundaries are no big problem with nanowires.

The growth processes leading to nanowires are still under development, and the underlying growth mechanisms are not completely known. Relatively well understood are vapor-liquid-solid or vapor-solid-solid growth schemes: here, small catalytic particles, in most cases gold spheres with several 10 nm diameter, are deposited onto the substrate. Precursor gases such as trimethylgallium and arsine (just as one example) are taken up by the Au spheres, and a solid or liquid solution of Au with GaAs is formed. Once the critical concentration is reached, GaAs crystallizes, and as the energy barrier is slightly lower at the boundary from the droplet to the substrate, material starts to grow there and lift the Au-GaAs droplet up. In this way, a large number of semiconductors can be grown on various substrates. For growth on Si, however, a very unfavorable background doping with Au, which acts as a recombination centre in Si, makes the use of this growth mechanism problematic.

Recently, a different scheme was developed in collaboration between our institute and the University of Lund: it was found that instead of Au spheres, a thin SiO_x ($x \approx 1$) can

be used to “catalyze” wire growth. The details of the mechanism are still under debate: catalytic action as in the case of Au is discussed as one possibility, the formation of a growth-inhibiting SiO_2 layer with “holes” that serve as nucleation centers another [1], [2]. So far, the hard facts are as follows: using the growth scheme, wires always grow in ⟨111⟩ direction, they exhibit a hexagonal cross-section with $\{1\bar{1}2\}$ side facets, and their thickness is constant from bottom to top. No “foot” region and no “catalytic particle” at the top are observed in SEM or TEM. However, TEM reveals stacking faults of the {111} planes, where the stacking switches from an ABCABC sequence (i.e., zincblende lattice structure ZB) to ABAB (wurtzite lattice structure WZ). This indicates that the energetic difference of both lattices might be rather similar, although in bulk only ZB is stable. This could be either due to growth kinetics or be a consequence of hydrogen termination during CVD growth [3].

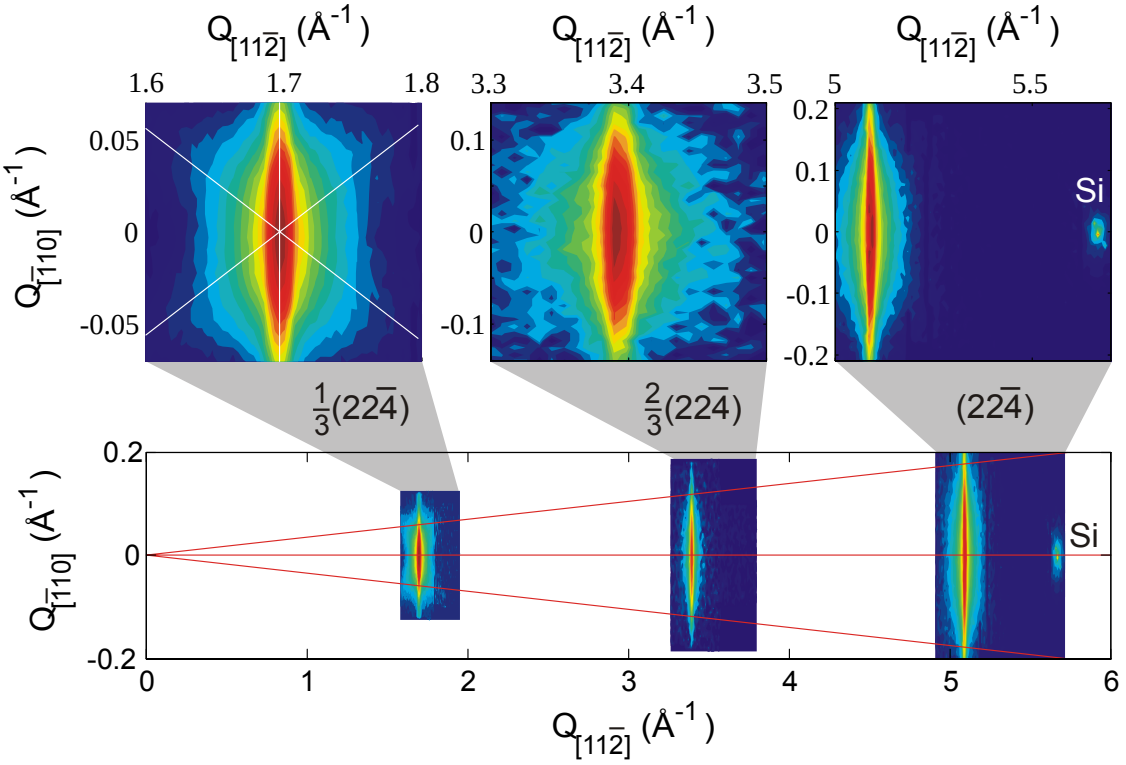

Fig. 1: Reciprocal space maps in the $[1\bar{1}2]$ substrate direction. Only the $(22\bar{4})$ is allowed in the ZB substrate, the intensity around the 1/3 and 2/3 order reflection from the InAs wires are due to stacking faults in the wires with a local transition to WZ structure.

Structural investigations are hence required in order to understand the wire structure and the growth process. We used x-ray diffraction in order to assess the crystal quality, the crystal orientation, and the amount of stacking faults in the wires for different growth parameters. In order to asses the overall amount of WZ in the wires, measurements with a “large” beam diameter of 200 µm were used. The intensity distribution was measured around several reciprocal lattice point to obtain the lattice parameters of InAs wires on Si(111) in the [111] growth direction as well as parallel to the substrate surface. Figure 1 shows reciprocal space maps recorded in the $[1\bar{1}2]$ direction of the substrate, i.e., in grazing incidence geometry. Clearly the peaks from the InAs wire material are aligned with the Si reciprocal lattice, confirming epitaxial growth. From the peak positions, the lattice parameters are determined, and it is found that InAs is com-

pletely relaxed. The $(22\bar{4})$ reflection is allowed in the ZB lattice of the Si substrate and the InAs wires. However, for the wires intensity is found also around the $1/3(22\bar{4})$ and $2/3(22\bar{4})$ reflections. These do not exist in ZB, but correspond to the $(10\bar{1}.0)_{WZ}$ and $(20\bar{2}.0)_{WZ}$ reflection of the WZ lattice, i.e., the intensity reflects the amount of InAs grown in the WZ structure. From the figure, a broadening of the peaks by a constant angle can be observed, which is due to a random rotation of the wires around their axis (mosaicity) with a magnitude of several tenths of a degree, depending on the growth conditions. For the lowest order reflection, streaks perpendicular to the wire side facets are observed due to the hexagonal wire shape. For the higher order reflections, these streaks are smeared due to the peak broadening.

Discrimination between Cubic and Hexagonal Phase

In order to quantify the WZ amount, we integrated the intensity of the three in-plane reflections as shown in Fig. 1 for each sample. Knowing the structure factors for the reflections as well as the amount of illuminated wires (which changes due to the changing Bragg angle from reflection to reflection), we can calculate the intensity decay as a function of peak order. This is plotted in Fig. 2 as dashed line. The experimental data are plotted as symbols, the intensities are normalized to the $(10\bar{1}.0)_{WZ}$ reflection. The excess intensity for the $(30\bar{3}.0)_{WZ}$, which is equivalent to the cubic $(22\bar{4})$ reflection, is due to the ZB part of the wires. Evaluating these data reveals that only 10 – 20% of the wire volume grows in the WZ lattice.

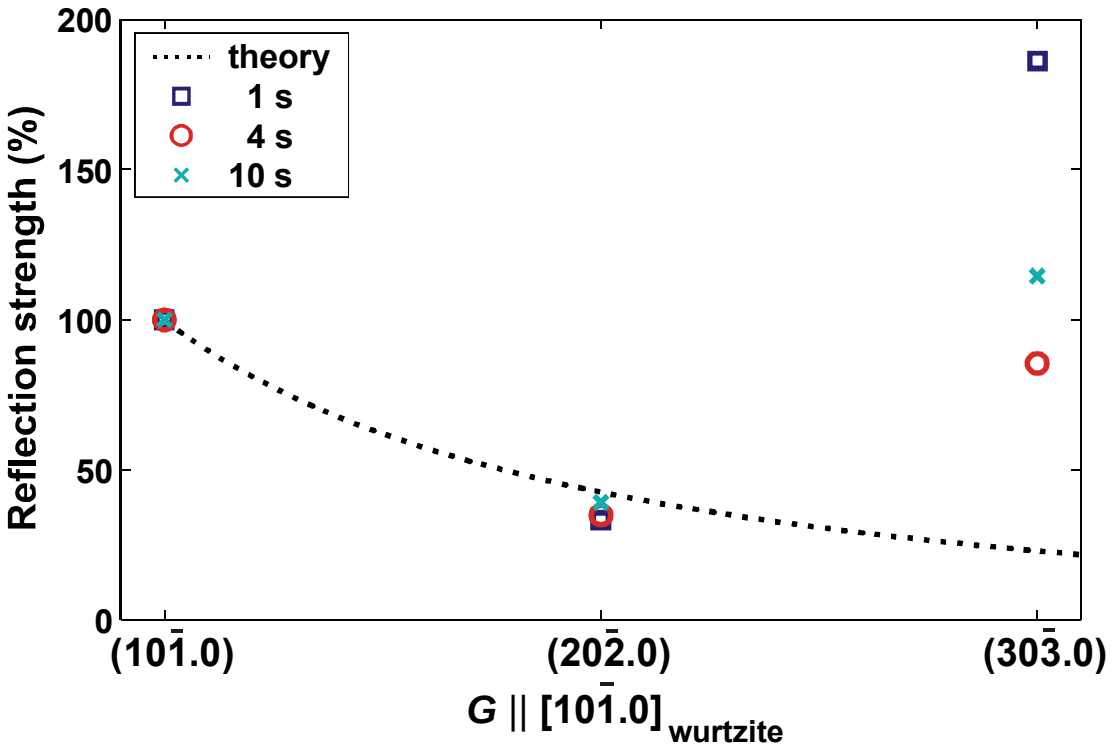

Fig. 2: Intensity from InAs wires as a function of reflection. Dashed line shows the theoretical behavior for pure WZ lattice. The experimental points show the measured intensity normalized to the $(10\text{-}1.0)_{WZ}$ reflection. The excess intensity for the $(30\text{-}3.0)_{WZ}$ is due to the ZB part of the wires.

Summary

From the data, no information is obtained concerning the length of the WZ and ZB segments in the wires. If the energies of both configurations are almost equal, longer WZ segments can be expected, whereas shorter segments indicate that ZB is still the more stable lattice, and WZ is only introduced as a defect. Recent measurements using coherent diffraction, where the interference between the radiation scattered from different WZ segments of one and the same wire are observed, rather hint on the latter, but the data analysis is not yet conclusive enough.

Acknowledgements

Funding was supported by FWF, EU, GME, and BMWV Austria.

References

[1] B. Mandl, J. Stangl, Th. Mårtensson, A. Mikkelsen, J. Eriksson, L.S. Karlsson, G. Bauer, L. Samuelson, and W. Seifert, “Au-Free Epitaxial Growth of InAs Nanowires”, Nano Letters 6, 1817-1821 (2006).

[2] Th. Mårtensson, J.B. Wagner, E. Hilner, A. Mikkelsen, C. Thelander, J. Stangl, B.J. Ohlsson, A. Gustafsson, E. Lundgren, L. Samuelson, W. Seifert, “Epitaxial Growth of Indium Arsenide Nanowires on Silicon Using Nucleation Templates Formed by Self-Assembled Organic Coatings”, Advanced Materials, submitted.

[3] P. Leitsmann and F. Bechstedt, to be published.

Narrow-Band Lead Salt Photodetectors and Solution-Processible Nanocrystal Photodetectors for the Midinfrared

M. Böberl, M. Kovalenko, J. Roither, T. Fromherz, G. Springholz, W. Heiss

Institut für Halbleiter- und Festkörperphysik, Universität Linz, Altenbergerstrasse 69, A-4040 Linz

Introduction

Molecular absorption line strengths are much stronger in the midinfrared spectral range than in the near infrared and the visible. Thus, for sensitive gas analysis and atmospheric pollution monitoring highly efficient optoelectronic devices for the midinfrared are required. For portable gas detection systems, infrared spectrometers and other applications, one obvious requirement is to avoid the need for cryogenic cooling of the system components, including also the detectors. To achieve room temperature photodetectors we show two different approaches. One is the use of epitaxial PbTe detectors which we integrated monolithically on optical filter structure like λ/2 microcavities. The second is the development of photodetectors based on solution-processible nanocrystals.

Narrow-Band PbTe Photodetectors

The integrated PbTe detector consists of a 500-nm-thick PbTe photosensitive layer deposited on top of a microcavity filter, designed for a target wavelength of λ = 3.6 µm. The microcavity filter consists of two EuTe/$Pb_{0.94}Eu_{0.06}Te$ Bragg interference mirrors separated by a λ/2 $Pb_{0.94}Eu_{0.06}Te$ cavity layer [1]. For the bottom mirror, a single EuTe/PbEuTe layer pair is chosen, which is sufficient to obtain a reflectivity of 83%, whereas for the top mirror an odd number of layers (3) has to be used in order to obtain similar reflectivities in respect to PbTe. The samples were grown with excess Te flux resulting in a p-type doping of the PbTe layers with a hole concentration of 10^{17} cm^{-3} and a mobility of 1700 cm^2/Vs at room temperature. By adjusting the substrate temperature and the Te to Eu flux ratio during growth, n-type conductivity is obtained in the EuTe films. Mesas were fabricated by standard photolithography and chemical wet etching. Pt/Ti/Au pads are used as ohmic contacts for p-type PbTe whereas In contacts serve as n-type contacts for EuTe.

A cross sectional scanning electron microscope (SEM) image of the complete structure is shown in Fig. 1(a), where the chemical contrast between the layers was enhanced by selective plasma etching. In the SEM image, the PbEuTe and EuTe layers of the Bragg mirrors and of the cavity region as well as the photosensitive PbTe film on top of the structure can be clearly distinguished.

The high optical quality of the microcavity filter is demonstrated by the FTIR transmission spectrum depicted in Fig. 1(a). Within the wide stop band from 2.7 µm to 5 µm a narrow cavity resonance peak at 3.66 µm is observed, corresponding to the first order cavity resonance mode. The full width at half maximum (FWHM) of the peak is 100 nm, which corresponds to a cavity finesse of 27. The photovoltage spectrum of the device under backside illumination in Fig. 1(b) exhibits a single peak at 3.67 µm, which is just

above the PbTe band gap at room temperature. This resonance peak position coincides exactly with the strong O=C-H stretching bond absorption line characteristic for non-aromatic aldehydes. This is indicated in Fig. 1(b) by the characteristic absorption spectrum of acetaldehyde used e.g. in the production of perfumes, polyester resins, and basic dyes. Obviously the relative width of the photoresponse peak of $\Delta\lambda/\lambda = 2.7\%$ corresponds very well with the width of the acetaldehyde absorption peak. The single photovoltage peak of the detector coincides in position and line width with the peak found in transmission measurements. Therefore, the photovoltaic response of the detector is directly correlated to the filter transmittance. The broadband feature shown in Fig. 1(b) at shorter wavelengths (< 3 µm) is due to the transmission of the filter structure above the Bragg mirror stop band. This signal can be eliminated by adding a PbEuTe absorber layer underneath the microcavity filter structure, acting as long pass filter and blocking all radiation above the band gap energy. This would allow to obtain detectors with only a narrow-band photoresponse, which can be easily tuned to the molecular vibration-rotation lines of other gases just by adjusting the filter design. Such monolithically integrated detectors would perfectly meet the demands given by compact gas detection systems.

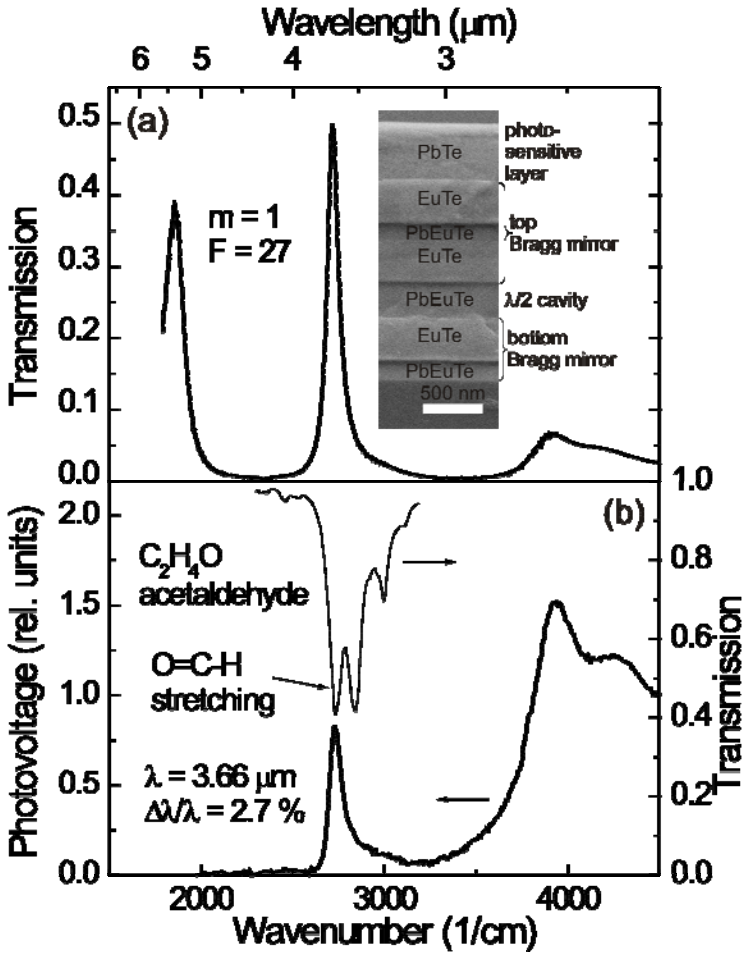

Fig. 1: (a) Transmission spectrum of the integrated PbTe photovoltaic detector on a λ/2 microcavity filter. The inset shows a SEM image of the device cross section. (b) Room temperature photovoltage spectrum of the integrated PbTe photovoltaic detector, compared to the absorption spectrum of acetaldehyde.

Nanocrystal Photodetectors for the Midinfrared

For the solution-processible photodetectors we used HgTe nanocrystals (NC), whose photoluminescence peak can be tuned between 1.2 and 3.5 µm by increasing the NC average size from 3 to 12 nm [2]. The HgTe NCs were prepared in aqueous solutions with hydrophilic thiols as stabilizers. A post-synthetic heat treatment increased the sizes of the NCs and pushed their bandgap to longer wavelength. Subsequently, a ligand exchange with dodecanethiol was carried out making the NCs soluble in commonly used organic solvents. The photoluminescence peak of the NCs can be tuned between 1.2 and 3.5 µm by increasing the NC average size from 3 to 12 nm [2].

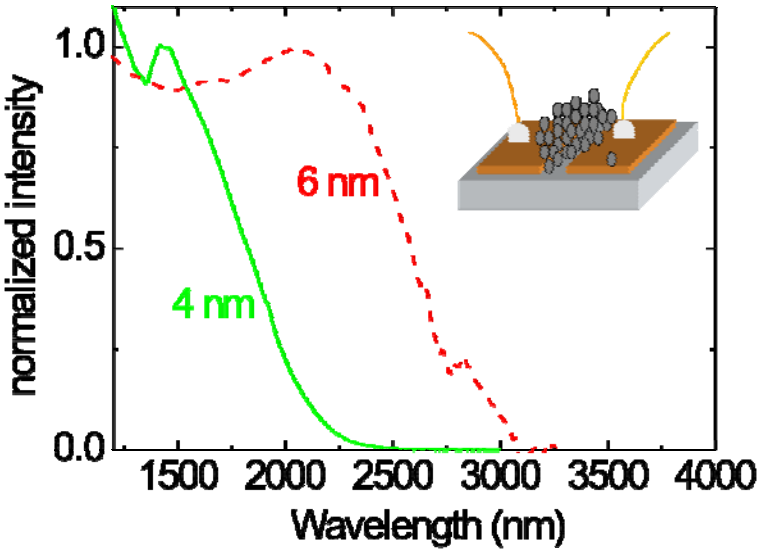

Fig. 2: Sensitivity spectra of HgTe NC photodetectors different in the NC size. The inset shows schematically the device structure.

For photoconductive devices NCs in solution were drop-casted on glass substrates and dried to form solid films. Cr/Au pads with a spacing of 50 µm serve as lateral contacts to the films. The sketch of the device structure is depicted in the inset of Fig. 2. The NC detectors were measured at room temperature and under ambient conditions. The normalized sensitivity spectra of the samples with different HgTe NC sizes are shown in Fig. 2. The onset of the photoresponse for 4 nm-big NCs is around 2.3 µm, whereas the onset for 6 nm-big NCs is shifted to longer wavelength due to the reduced confinement effect and is at 3 µm. The dark current of the NC detectors is about 10 nA. Illumination with a power of only 20 µW increases the current to 300 nA, thus the increase is more than a factor of 10. Measurements of the time behavior show that the time constant of the HgTe NC detectors is less than 20 µs, which is fast compared to organic semiconductor devices. The device structure is not yet optimized; nevertheless the sensitivity obtained from the HgTe NC detectors is 30 mA/W. A big advantage of the HgTe NCs in contrast to conjugated polymers is that they are photostable even under ambient conditions.

The ability to use solution-processible HgTe NCs gives future prospects for infrared devices on flexible or porous substrates and for highly integrated detector arrays.

Conclusion

In conclusion, we demonstrate monolithically integrated PbTe detectors, where the photosensitive PbTe layer is grown on top of a microcavity filter. The detectors show a single resonance in the photoresponse spectrum with a relative width of 2.7%. By adjusting the filter design, the peak wavelength and line width of the photoresponse can be matched to the characteristic absorption lines for various gases, as demonstrated for acetaldehyde. This makes these detectors ideal for molecule identification and quantification purposes in low-cost integrated systems.

Furthermore, we present solution-processible photodetectors based on HgTe NCs. With the size of the NCs the onset of the photoresponse can be tuned. We obtained an onset wavelength of 3 µm which is the longest wavelength demonstrated so far for NC photodetectors. These detectors offer a low-cost possibility to conventional photodetectors for the midinfrared due to the easy process handling.

Acknowledgements

Financial support from bm:bwk, FWF (Project START Y179 and SFB IR-ON) is gratefully acknowledged.

References

[1] M. Böberl, T. Fromherz, J. Roither, G. Pillwein, G. Springholz, W. Heiss: “Room temperature operation of epitaxial lead-telluride detectors monolithically integrated on midinfrared filters” Appl. Phys. Lett. **88**, 041104 (2006)

[2] M. V. Kovalenko, E. Kaufmann, D. Pachinger, J. Roither, M. Huber, J. Stangl, G. Hesser, F. Schäffler, W. Heiss: “Colloidal HgTe Nanocrystals with Widely Tunable Narrow Band Gap Energies: From Telecommunications to Molecular Vibrations” J. Am. Chem Soc., **128**, 3516-3517 (2006)

High-Reflectivity Dual-Band Bragg Mirrors Grown by MBE on Si(111) Substrates for the Atmospheric Transmission Windows Between 4 – 5 μm and 6 – 12 μm

M. Eibelhuber, G. Springholz, T. Schwarzl, W. Heiss

Institut für Halbleiter- und Festkörperphysik, Johannes Kepler Universität, A-4040 Linz, Austria

We show dual-band Bragg mirrors for the mid-infrared consisting of BaF_2 and PbTe grown by molecular beam epitaxy (MBE) on Si(111) substrates. The mirrors exhibit broad stop bands near the atmospheric windows between 4 – 5 μm and 6 – 12 μm with reflectivities of at least 95 %. The Si substrate easily enables device processing of the mirrors in order to fabricate tunable narrow band pass Fabry-Perot filters for the mid-infrared. The measured spectra are in good agreement to transfer matrix simulations of the whole structures indicating the high quality of the dual-band Bragg mirrors.

Introduction

The mid-infrared (MIR) spectral region covering the wavelength range between 2 and 30 μm is of enormous importance as it contains the fundamental fingerprint absorption bands of almost all poly-atomic molecular species of interest. Consequently, the MIR is very attractive for the development of optoelectronic devices such as lasers, detectors and filters for gas sensing applications. Such devices enable, e. g., dynamic exhaust gas analysis in automotive industry by detecting NO, CO and CH_4. They are also used for medical diagnostics by analyzing C isotopes in exhaled air or by detecting endogenous NO and CO in breath as an indicator of diseases (for a review see, e. g., Ref. [1]). In addition, there are atmospheric transmission windows between 3 and 5 μm as well as between 8 and 14 μm enabling free space optical communications and thermal imaging.

For such applications, high-reflectivity Bragg interference mirrors are important tools for fabrication of, e. g., narrow band pass filters. However, to access the whole wavelength range of the atmospheric windows, the stop bands of such mirrors have to be very broad. Therefore, we employed the material combination of PbTe and BaF_2 being transparent in this spectral region and exhibiting an exceedingly large difference in refractive index. As a consequence, not only a much smaller number of Bragg mirror pairs is required to obtain high reflectivities, but also the required very large stop band width can be achieved.

Here, we show PbTe/BaF_2 dual-band Bragg mirrors grown by molecular beam epitaxy (MBE) on Si(111) substrates exhibiting broad stop bands near the atmospheric windows between 4 - 5 μm and 6 - 12 μm. The Si substrate easily enables device processing of the mirrors in order to fabricate tunable narrow band pass Fabry-Perot filters for the mid-infrared.

Experimental

Structure and Design

The combination of PbTe and BaF_2 yields a very high refractive index ratio of 3.8 at a wavelength of 6 µm. This index contrast is about a factor of 3 larger than what can be achieved with the typically used III-V semiconductors (see, e. g., Ref. [2]) and leads to a large relative stop band width $\Delta\lambda/\lambda$ of 79 % for a standard Bragg mirror. However, it is still not possible to cover the whole spectral range of the two atmospheric windows.

Therefore, we employed the concept of dual-band mirrors with additional $\lambda/4$ phase shifting layers (for details see Ref. [3]). The mirrors were designed by transfer matrix calculations using the exact dispersion of the optical constants of PbTe as determined by Fourier-transform infrared (FTIR) spectroscopy of reference layers. Several dual-band mirror structures were fabricated in a IV-VI semiconductor molecular beam epitaxy (MBE) system on Si(111) substrates. Due to the mismatch in lattice-type, lattice constant (19 %) and thermal expansion coefficients (a factor of 10) between PbTe and Si, the total growth thickness is rather limited in order to achieve a reasonable quality of the mirrors. Thus, the number of mirror periods has to be kept as low as possible.

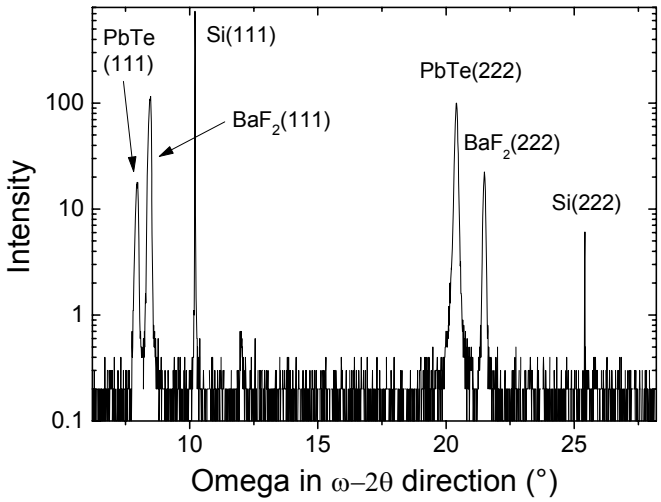

Fig. 1: X-ray ω–2Θ scan of a dual-band Bragg mirror consisting of BaF_2 and PbTe grown by MBE on Si(111) substrates .

Results

As is seen by the x-ray ω–2Θ scan in Fig. 1, the growth on Si(111) substrates of the PbTe/BaF_2 dual-band mirror structures yields fully strain-relaxed layers only with (111) orientation, as desired. The Fourier-transform infrared (FTIR) reflectivity spectra of two different structures both optimized for a minimum total thickness (3.1 µm and 3.6 µm, respectively) are shown in Fig. 2. The dual-band 1 structure (top) exhibits stop bands from 4.2 to 5.6 µm and 6.3 to 10.9 µm both with reflectivities in excess of 95 % despite its low number of layers. A slightly thicker structure (dual-band 2) (bottom) also results in two high reflectivity bands, this time even broader (3.8 – 4.6 µm and 6.4 – 12.3 µm). The spectra of both samples show a very good agreement to transfer matrix simulations of the whole structure indicating the high quality of the mirror structures.

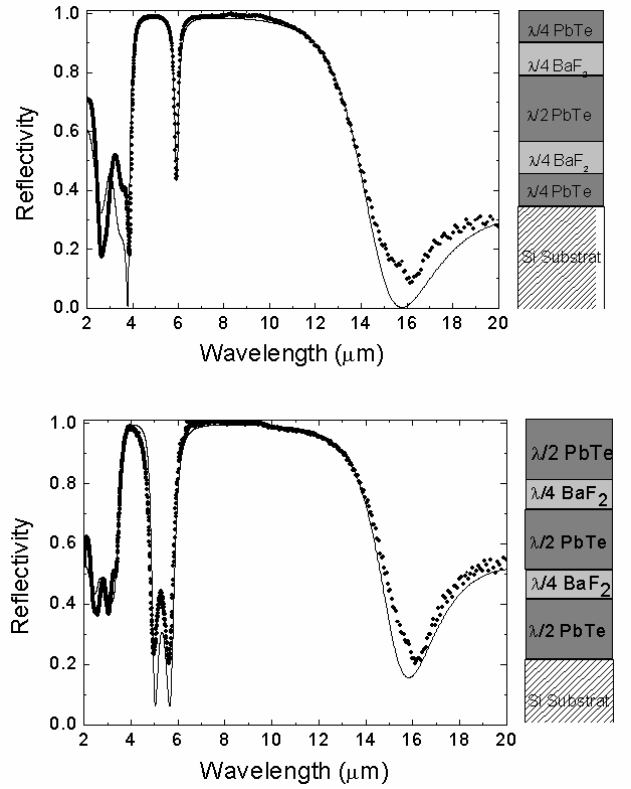

Fig. 2: FTIR reflectivity spectra (dots) of two types of dual-band Bragg mirrors consisting of BaF_2 and PbTe grown by MBE on Si(111) substrates (top: dual-band 1, bottom: dual-band 2). Both structures are sketched on the right-hand side of the spectra. The measured spectra are in good agreement to transfer matrix simulations of the whole structure shown as a line.

Conclusion

Our work demonstrates that dual-band PbTe/BaF_2 Bragg mirrors with broad stop bands in the mid-infrared spectral region can be grown by MBE in high quality on Si(111) substrates for use in tunable Fabry-Perot narrow-band filters. Such filters can be used for various sensing applications in the spectral range of the two atmospheric windows.

Acknowledgements

Financial support from the InfraTec GmbH, Germany and the Austrian Science Fund FWF, Austria is gratefully acknowledged.

References

[1] M. Tacke: Infrared Phys. Technol., Vol. 36, 1995, pp. 447 - 463.

[2] G. Springholz, T. Schwarzl, and W. Heiss: “Mid-infrared Vertical Cavity Surface Emitting Lasers based on the Lead Salt Compounds”, in Mid-infrared Semiconductor Optoelectronics, ed. A. Krier (Springer, London, 2006), pp. 265 – 301.

[3] W. Heiss, T. Schwarzl, et al.: “Epitaxial Bragg Mirrors for the Mid-infrared and their Applications”, Prog. Quantum Electron., Vol. 25, 2001, pp. 193 - 228.

Vertical-Emitting Microcavity Lasers for the Mid-Infrared based on PbEuSe/BaF_2 Broad Band Bragg Mirrors

M. Eibelhuber[1], T. Schwarzl[1], A. Winter[2], H. Pascher[2], E. Kaufmann[1], W. Heiss[1], G. Springholz[1]

[1]Institut für Halbleiter- und Festkörperphysik, Johannes Kepler Universität, A-4040 Linz, Austria

[2]Experimentalphysik I, Universität Bayreuth, Universitätsstr. 30, D-95447 Bayreuth, Germany

We report on molecular beam epitaxially grown mid-infrared surface-emitting microcavity lasers operating in continuous wave (cw) mode. The devices are based on high-reflectivity broad band Bragg mirrors consisting of three periods of PbEuSe and BaF_2 λ/4 layers. This material combination exhibits a high ratio between the refractive indices of 2.9, leading to a broad mirror stop band with a relative width of 65%. Optical excitation of the laser structures with a PbSe active region results in cw stimulated emission at various cavity modes between 7.3 µm and 5.9 µm at temperatures between 54 K and 135 K. Laser emission is evidenced by a strong line width narrowing with respect to the line width of the cavity mode and a clear laser threshold at a pump power of 130 mW at 95 K.

Introduction

Mid-infrared lasers are of great importance for high-resolution gas spectroscopy due to the numerous absorption lines of almost all molecular gases in this spectral region. Thus, these lasers have a wide range of applications, including pollution monitoring, trace gas sensing, medical diagnostics, time resolved exhaust gas analysis, as well as free space communication. Lead salt diode lasers have long been used in these applications because they cover the whole 3 to 30 µm wavelength region and feature the highest operation temperatures of conventional infrared band gap lasers. This is due to their favorable electronic band structure as well as the two orders of magnitude lower non-radiative Auger recombination rates as compared to those of III-V or II-VI narrow band gap semiconductors. As a consequence, also the first vertical-cavity surface-emitting lasers (VCSELs) for the mid-infrared were developed using the IV-VI semiconductors [1]. VCSELs offer a variety of advantages such as a small beam divergence, single mode operation and the possibility of monolithic integration. The lead salt mid-infrared VCSELs show optically pumped pulsed operation up to a temperature of 340 K and continuous-wave (cw) operation up to 100 K [2]. Here, we present optically pumped cw PbSe VCSELs with PbEuSe/BaF_2 broad band Bragg mirrors exhibiting a high ratio between the refractive indices of 2.9. These cw lasers operate at different microcavity modes at temperatures between 54 K and 135 K.

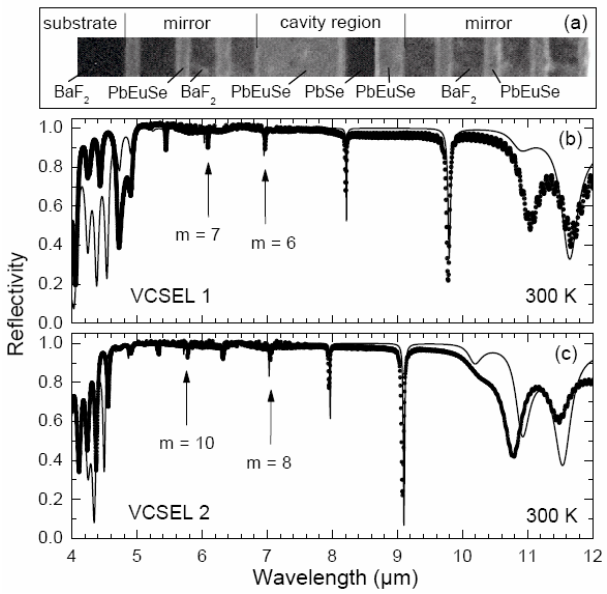

Fig. 1: (a) Cross sectional SEM micrograph of a PbSe VCSEL with PbEuSe/BaF_2 Bragg mirrors. (b), (c) FTIR reflectivity spectra of two PbSe VCSEL structures ((b) VCSEL 1, (c) VCSEL 2) measured at 300 K (dots). The corresponding transfer matrix simulation is depicted as solid line. The resonances intended for lasing are indicated by arrows and their order m is given.

Experimental

Structure, Design and Experimental Set-up

The laser structures were designed by transfer matrix calculations using the exact dispersion of the optical constants of the individual layer materials as determined by Fourier-transform infrared (FTIR) spectroscopy of reference layers. The structures were all grown by MBE onto (111) BaF_2 substrates. The growth temperature was 380 °C and the growth rate was 1.1 µm/h for all layers. The PbEuSe/BaF_2 high reflectivity laser mirrors exhibit a very large refractive index ratio n_1/n_2 of 2.9 and relative stop band widths $\Delta\lambda/\lambda_c$ of 65 %. Both the refractive index ratio and the stop band width are not only among the largest for MBE grown Bragg mirrors, but also for Bragg mirrors fabricated by other methods with less limitation on the material choice [3]. Compared to the most common III-V semiconductor Bragg mirrors, the refractive index ratio and the stop band width is a factor of 3 and 7 larger, respectively. Such a high index contrast leads to a reflectivity in excess of 99 % for only three layer pairs, thus being suitable for a VCSEL mirror. The laser cavity region is comprised of a PbEuSe buffer layer followed by the PbSe active region. The complete laser structure can be seen in the cross-sectional scanning electron microscopy (SEM) image of VCSEL 1 in Fig. 1(a). The individual parts of the multilayer structure and the materials are indicated in the image. Due to the strong temperature dependence of the IV-VI band gap energy, lead salt VCSELs have to be tailored for a certain operation temperature [1] at which the maximum of the gain has to coincide with the cavity resonance. Here, we have chosen for our structures temperatures between 50 K and 140 K. This temperature range corresponds to the spontaneous emission of PbSe between 7.5 µm and 5.8 µm which therefore, is the design wavelength range for the cavity resonances intended as lasing modes. All samples were characterized by room temperature FTIR reflectivity measurements. The laser samples were optically excited by a CO laser operated in cw mode

at a wavelength of 5.2 µm. The emitted light was measured by a liquid-nitrogen-cooled HgCdTe photoconductive detector through a grating spectrometer using lock-in technique.

Results

The reflectivity spectra of the two VCSEL samples measured at room temperature are shown in Fig. 1(b) and (c) (dots). A very broad mirror stop band with almost 100 % reflectivity and pronounced interference fringes outside the stop band are found. Due to the several micron thick cavity region, many cavity resonances appear inside the mirror stop bands. The cavity modes near the center of the stop bands are the intended laser modes because they benefit from the highest mirror reflectivities. These resonances are indicated by arrows in Fig. 1(b) and (c). The line widths of the central cavity modes are very narrow with values of about 7 nm demonstrating the high quality of the laser structures.

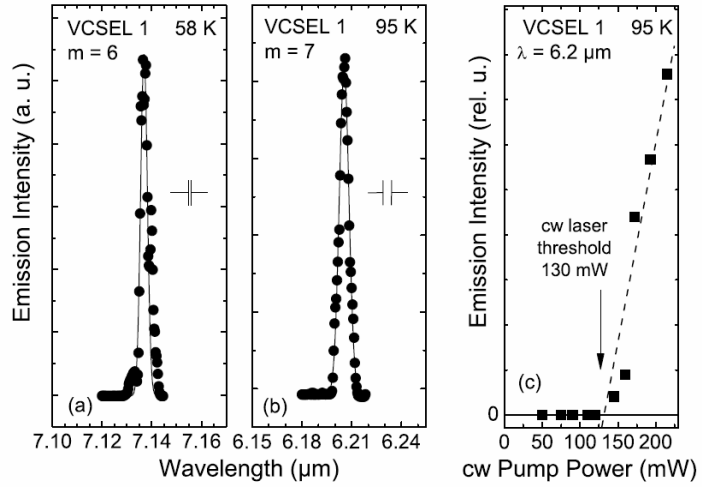

Fig. 2: Laser emission spectra of sample VCSEL 1: (a) mode m = 6 at 58 K, (b) mode m = 7 at 95 K. The lines are Gaussian fits. The spectrometer resolution for each spectrum is denoted by -||-. (c) Emission intensity as a function of the cw pump power for the m = 7 mode at 6.2 µm at 95 K (squares). The laser threshold is indicated. The dashed line is a linear fit to the measured data above threshold.

The optically pumped cw laser emission spectra of VCSEL 1 are shown in Fig. 2(a) and (b). Each of the two central cavity modes gives rise to laser emission at the given design temperatures at which the PbSe spontaneous emission overlaps with the cavity mode [1]. The resonance m = 6 yields its strongest emission at a temperature of 58 K and a wavelength of 7.14 µm, whereas the m = 7 mode emits best at 95 K with a wavelength of 6.2 µm. Both emission lines are fitted with a Gaussian line (solid line), yielding a laser line width of only 2.3 nm and 2.6 nm for the lower and higher temperature mode, respectively. Compared to the line width of the cavity resonances of around 7 nm deduced from the reflectivity spectra, a significant line width narrowing is observed. This is the first strong indication for stimulated emission from the VCSEL structure. One can estimate the expected laser line width by the Schawlow-Townes and Henry formula [4]. Using the measured cavity mode line width of 7 nm, this results in an emission line width (m = 6 mode) of only 0.14 nm at an output power of 0.1 mW [4]. This is a factor of about 20 lower than the measured one, and therefore an indication for additional line width broadening mechanisms present in our VCSEL. However, the Schaw-

low-Townes formula underestimates the actual laser line width of VCSELs by about one order of magnitude [4]. One such additional broadening effect in our VCSEL could be the interface roughness in the multilayer mirrors, which also broadened the cavity line width. Figure 2(c) depicts the pump power dependence of the emission of the m = 7 mode at 95 K. Obviously, a clear laser threshold at about 130 mW cw excitation power is found with an almost linear intensity increase above threshold and almost no emission below threshold. Therefore, we conclude that the observed spectra represent stimulated laser emission and not just spontaneous emission filtered out of the cavity at the resonance wavelength, which would be not only very weak emission but would display the same line width as the cavity mode and would not show a threshold behavior. The second laser sample VCSEL 2 is similar to the one already described, but is designed for having a laser resonance at a shorter wavelength, thus leading to emission at higher temperatures up to 135 K [4]. The line width of the two measured laser modes are 2 nm and 3 nm, thus showing again the strong line width narrowing as compared to the cavity resonance line width of 7 nm. Furthermore, to our knowledge, 135 K is the highest operation temperature for cw-emission for long wavelength VCSELs with $\lambda >$ 3 µm, which in turn indicates the high quality of our PbEuSe/BaF_2 high-reflectivity broad band Bragg mirrors.

Conclusion

We demonstrated molecular beam epitaxially grown mid-infrared mirocavity lasers operating in continuous wave (cw) mode. The devices are based on high-reflectivity broad band Bragg mirrors consisting of three periods of PbEuSe/BaF_2 layers. Optical excitation of laser structures with a PbSe active region results in cw stimulated emission at various cavity modes between 7.3 µm and 5.9 µm at temperatures between 54 K and 135 K. We evidenced the laser emission by a strong line width narrowing with respect to the line width of the cold cavity mode and a clear laser threshold at a pump power of 130 mW at 95 K.

Acknowledgements

Financial support from the Austrian Science Fund FWF, Austria is gratefully acknowledged.

References

[1] G. Springholz, T. Schwarzl, and W. Heiss: “Mid-infrared Vertical Cavity Surface Emitting Lasers based on the Lead Salt Compounds”, in Mid-infrared Semiconductor Optoelectronics, edited by A. Krier (Springer, London, 2006), pp. 265 – 301.

[2] T. Schwarzl, G. Springholz, M. Böberl, E. Kaufmann, J. Roither, W. Heiss, J. Fürst, H. Pascher, “Emission properties of 6.7 µm continuous-wave PbSe-based vertical-emitting microcavity lasers operating up to 100 K”, Appl. Phys. Lett. 86, 031102 (2005)

[3] W. Heiss, T. Schwarzl, J. Roither, G. Springholz, M. Aigle, H. Pascher, K. Biermann, and K. Reimann: “Epitaxial Bragg Mirrors for the Mid-infrared and their Applications”, Prog. Quantum Electron., Vol. 25, 2001, pp. 193 - 228.

[4] T. Schwarzl, M. Eibelhuber, W. Heiss, E. Kaufmann, G. Springholz, A. Winter, H. Pascher, “Mid-infrared high finesse microcavities and vertical-cavity lasers based on IV-VI semiconductor/BaF_2 broad band Bragg mirrors”, J. Appl. Phys., in print

Fabrication of Silicon Vertical Taper Structures for Fiber to Chip Coupler by KOH Anisotropic Etching

R. Holly, K. Hingerl

Christian Doppler Laboratory of Surface Optics, Institute of Semiconductor and Solid State Physics, Johannes Kepler University, Altenbergerstrasse 69, A-4040 Linz

R. Merz, P. Hudek, S. Neve, S. Partel, T. Auer

Forschungszentrum Mikrotechnik, FH Vorarlberg, Dornbirn, Austria

In order to exploit the full potential of silicon photonic devices we require an efficient way of coupling light from fibers to integrated photonic circuits. One of the most common solutions to this problem is the use of tapered silicon waveguides. We present a method of vertical silicon taper fabrication using KOH anisotropic etching. The main advantage of this method is the low roughness of the tilted surface, which should lead to a good optical transmission of the tapered waveguide. We successfully created vertical silicon tapers with heights more than sufficient for the use in fiber to chip light couplers.

Introduction

The use of high index contrast waveguides and devices is the key to successful development and fabrication of photonic integrated circuits. Considering the widespread use of silicon technologies and the suitable optical properties of silicon in the infrared range, this material is one of the best candidates for such devices [1]. In order to exploit the full potential of silicon photonic devices we require an efficient way of coupling light from fibers to integrated photonic circuits. One of the most common solutions to this problem is the use of tapered silicon waveguides [2]. However this approach is connected with the problem of creating a vertical taper. The efforts to fabricate such a taper are currently concentrated mainly on various lithography techniques used to create a taper shaped structure in photoresist. The pattern is then transferred to silicon by reactive ion etching. Although silicon taper structures have been already successfully fabricated using grayscale lithography methods [3], this approach introduces an additional non-standard lithography step and may also lead to the increase of the surface roughness, which is critical for the proper function of photonic devices [2].

One of the possibilities to fabricate a vertical taper structure is the use of a silicon substrate with a tilted <111> crystallographic orientation. Such wafers are produced by changing the cutting angle in the silicon wafer production process. In order to fabricate the desired vertical taper structure a very small angle (2 – 5 degrees) between the <111> orientation and the wafer surface is needed.

These substrates can then be used for the creation of a taper by means of anisotropic etching (i.e. etching along preferred crystallographic direction). One of the most suitable chemicals for anisotropic etching of silicon is potassium hydroxide (KOH) water solution. Under suitable process conditions (temperature, KOH concentration) we can achieve a big etching speed difference resulting in the uncovering of <111> planes.

Therefore using a substrate with tilted <111> plane should lead to the formation of vertically tilted surfaces which could be used for the fabrication of vertical taper structures.

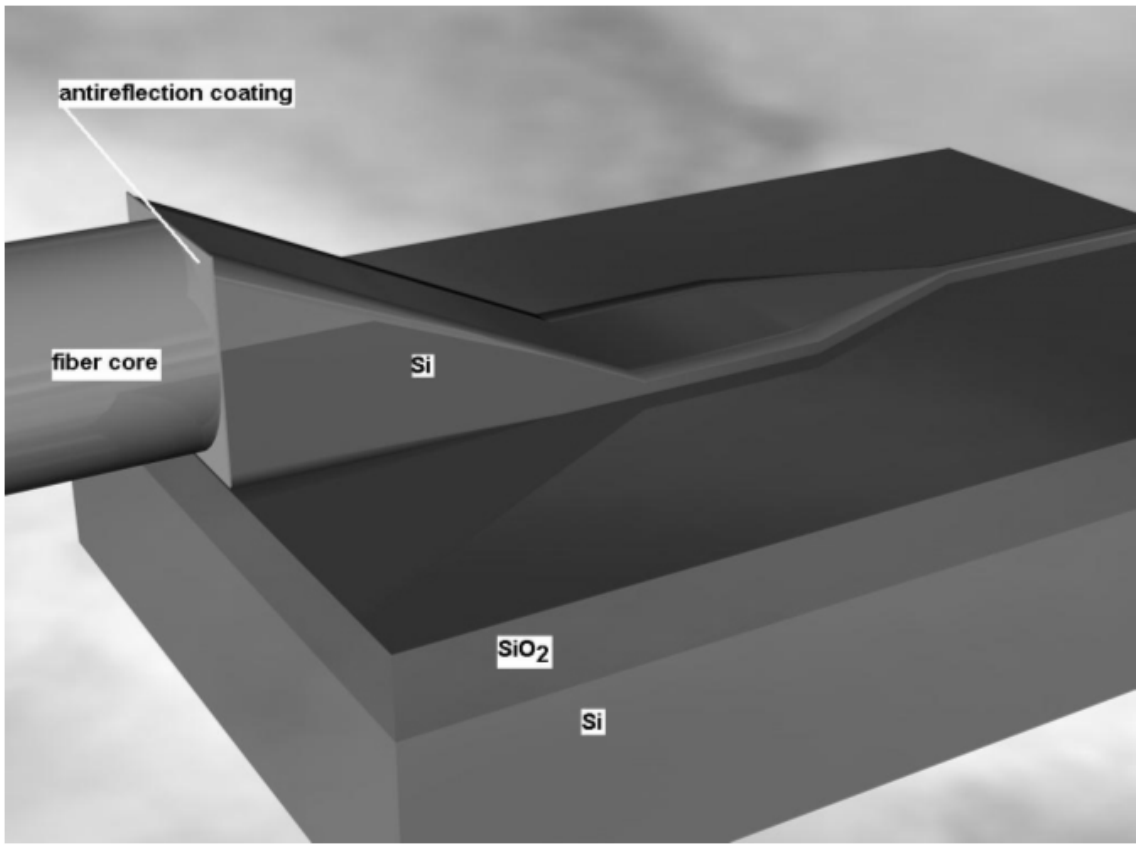

Fig. 1: Fiber to chip interface consisting of two silicon structures - one with vertical and one with horizontal tapering. The optical signal from a fiber core is led to the first taper via an antireflection coating to compensate the refractive index difference. The light propagates through both tapers and finally ends in a single mode silicon waveguide. Dimensions – Start: fiber core 6 µm in diameter; End: Si waveguide 300 x 300 nm; Length = 200 – 400 µm.

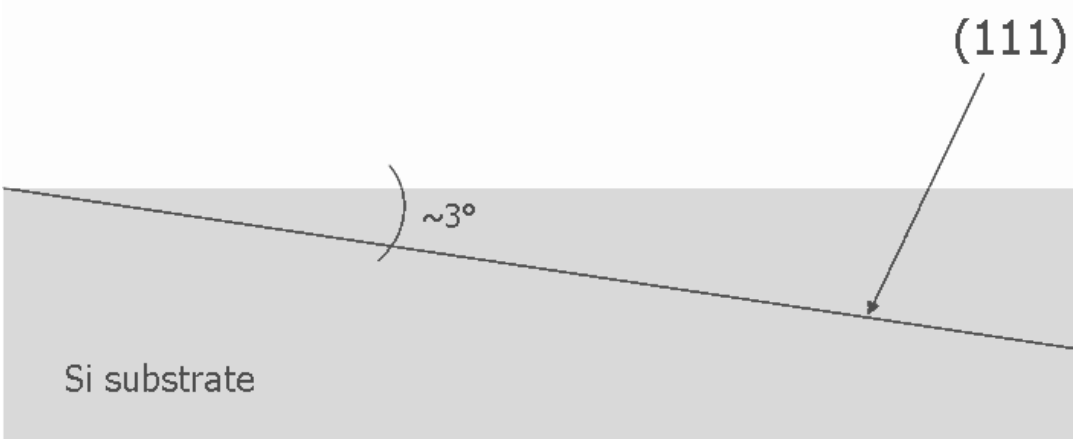

Fig. 2: Silicon substrate with tilted <111> plane.

The main advantages of this process are:

1. Simplicity (KOH wet chemical etching is well known and often used process)
2. Set tilt angle and shape (the angle only depends on the substrate and is not influenced by the process parameters and the shape is always linear)
3. Low roughness of the tilted surface

Experimental

The process of anisotropic silicon etching is influenced by several parameters. Besides etching solution parameters (KOH concentration, temperature), the etching process also depends on the roughness of the silicon substrate. This influence is becoming stronger with the decreasing angle between the <111> orientation and the wafer surface. The main reason for this behavior is the low etching speed of such substrate surfaces caused by the very small tilt angle – the surface plane orientation is very close to <111>. The presence of the surface roughness increases the etching speed, because it offers a possibility of directly etching the silicon in directions much different from the <111> plane. However this process continues only until the <111> planes are revealed and the surface consists of triangle shapes of random sizes. The average size of these triangles is determined by the initial surface roughness of the silicon substrate. Further etching results only in low etching speeds because the surface consists of <111> planes. Because of these obstacles, the fabrication of larger taper structures by simple etching of an unstructured silicon substrate is very difficult.

In order to obtain a larger structure, we can no longer depend on the surface roughness influence or the low etching speed in the vertical direction. Instead of this, we have to take advantage of much faster etching in the direction parallel to the substrate. This can be achieved by structuring the surface before the actual anisotropic etching takes place. One of the possibilities how to do this is to etch trenches or steps to the substrate and thus reveal planes perpendicular to the surface – Fig. 3.

With the structured substrate, we are able to achieve high etching speeds and reveal the <111> planes much faster than in the case of unstructured substrate. The size of the tilted surface obtained from the structured surface is dependent on the structuring depth – the depth of the etched steps / trenches.

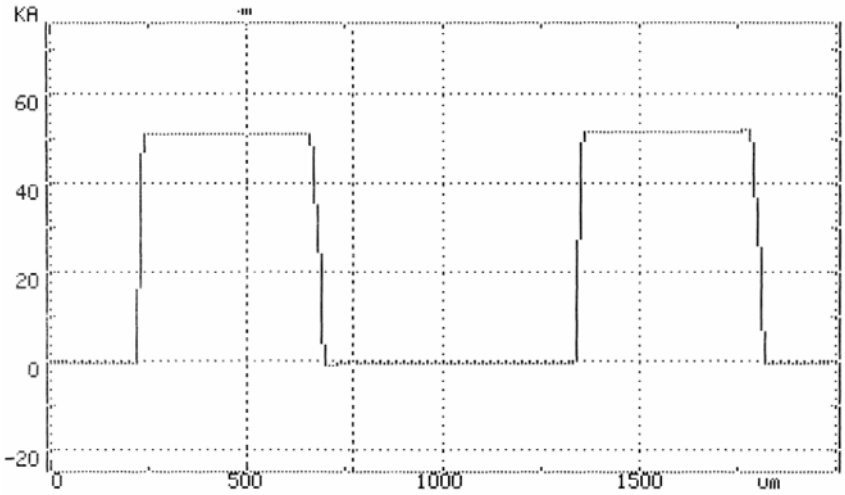

Fig. 3: Structured silicon profile – 5 µm deep trenches etched in silicon by reactive ion etching process.

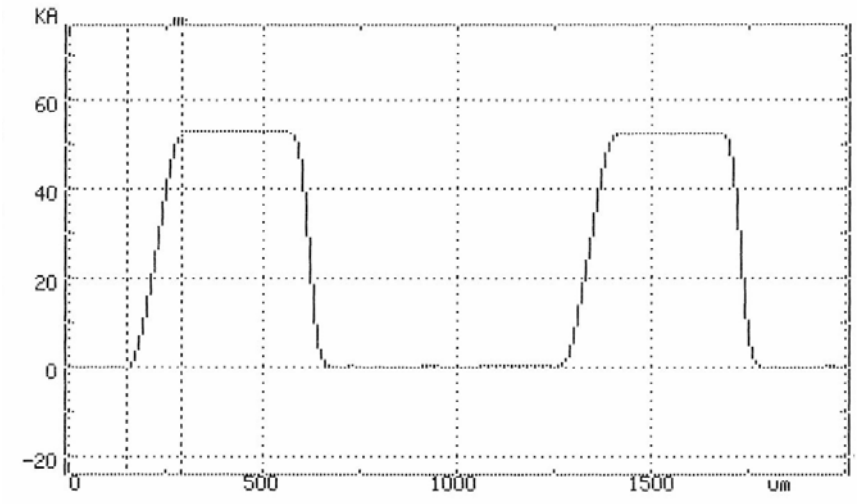

Fig. 4: The profile of the structured silicon after 30 min KOH etching, 47% KOH solution, 80ºC.

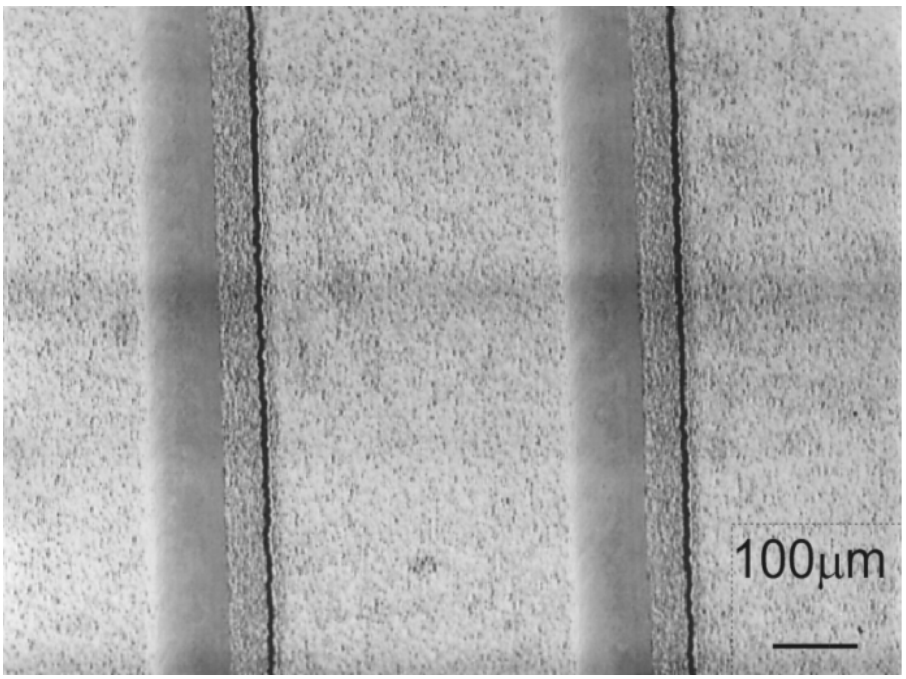

Fig. 5: Structured silicon surface after 30 min KOH etching, 47% KOH solution, 80ºC.

The KOH etching of the Si trenches can be described by two processes:

1. Etching in the direction parallel to the surface. Taper structures are formed mainly by fast etching parallel to the surface (~100 µm/hour). Taper height depends on the initial trench/edge depth or roughness – in the case of unstructured substrate. This process continues only until the <111> planes are revealed.
2. Etching in the direction perpendicular to the surface. This process is slow, results in further increase of the taper height but also increases the surface roughness.

In order to create a vertical taper structure with small surface roughness we need therefore to keep the KOH etching time as short as possible (the etching perpendicular to the surface will be in this case negligible).

Conclusions

Using the anisotropic etching of silicon with tilted <111> plane, we successfully created vertical silicon tapers with heights up to 35 µm and lengths up to 500 µm, which is more than sufficient for them to be used for fiber to chip light coupling.

We furthermore investigated the etching process of structured as well as unstructured silicon substrates and found out, that only the use of reactive ion etching prior to the KOH etching can ensure a well defined shape of the silicon vertical taper. Our experiments indicate a significant time dependence of the etched taper profile. In order to create a structure for the purpose of optical fiber to chip coupling, we need to keep the surface roughness minimal and therefore we have to reduce the time of the anisotropic etching to a minimum.

Basing on our experimental results, we are now able to design a fiber to chip optical interface with low scattering losses and high transmission.

References

[1] Mike Salib, Ling Liao, Richard Jones, Mike Morse, Ansheng Liu, Dean Samara-Rubio, Drew Alduino, Mario Paniccia, "*Silicon Photonics*", Intel Technology Journal Volume 08 Issue 02 (2004).

[2] Roel Baets, Wim Bogaerts, Dirk Taillaert, Pieter Dumon, Peter Bienstman, Dries Van Thourhout, Joris Van Campenhout, Vincent Wiaux, Johan Wouters, Stephan Beckx, "*Low Loss Nanophotonic Waveguides and Ring Resonators in Silicon-on-Insulator*" in *Proceedings of the International School of Quantum Electronics*, 39th course "*Microresonators as building blocks for VLSI photonics*", 709, Italy, p.308-327 (2003).

[3] Anita Sure, Thomas Dillon, Janusz Murakowski, Chunchen Lin, David Pustai and Dennis W. Prather, "*Fabrication and characterization of three-dimensional silicon tapers*", Optics Express Vol. 11, No. 26 (2003).

Two and One Dimensional Light Propagation in Layer-by-Layer Deposited Colloidal Nanocrystal Waveguides

S. Pichler, J. Roither, M. V. Kovalenko, W. Heiss

Institute of Semiconductor and Solid State Physics, University Linz, A-4040 Linz

P. Feychuk, O. Panchuk

Institute of Organic Chemistry, University of Chernivtsi, Chernivtsi 58012, Ukraine

Optical waveguides containing high concentrations of colloidal nanocrystals have been fabricated by layer-by-layer deposition on planar and patterned glass substrates. The two- and one dimensional waveguiding in these structures is demonstrated by propagation loss experiments. The experimental results obtained for various film thicknesses and widths of the waveguide stripes indicate that the losses are dominated by surface roughness. The deposition on the structured samples does not lead to any additional losses. This fact and the exceptionally high content of nanocrystals make these structures highly suitable for photonic applications like laser or optical amplifiers.

Introduction

Colloidal semiconductor nanocrystals (NCs) [1] – [3] give a widely size tunable room temperature luminescence [4], [5] with quantum efficiencies close to unity [6], and they are soluble in various organic and inorganic solvents [7]. All these characteristics provide a flexible platform for the development of integrated photonic devices like optical amplifiers and lasers operating at room temperature and over a broad spectral range. The main difficulty in achieving NC-based lasing is the very efficient nonradiative Auger recombination [8], so that laser operation is achieved so far only with pulsed excitation [9] – [11]. Strategies to improve the laser performance are (a), to increase the NC concentration in the active layer in order to increase the gain [12], (b), the use of high-finesse optical feedback structures [9] – [11], and (c), the optimization of the quality of the optical waveguides. Therefore, here we present a systematic investigation of the optical properties of two (2D) and one dimensional (1D) waveguides (WGs) optically activated by strongly luminescent colloidal CdTe NCs. To obtain structures with smooth surfaces and high NC volume fractions the layer-by-layer deposition technique [13] is applied. The waveguiding properties are investigated by propagation loss measurements. These measurements are done for waveguides with different parameters (width, thickness).

Sample Preparation

The NC WGs are fabricated by controlled deposition of CdTe NC/polymer films onto glass substrates by the layer-by-layer assembly method. This makes use of the alternating adsorption of (sub)monolayers of positively charged poly(diallyldimethylammonium chloride) (PDDA) molecules and negatively surface-charged CdTe NCs,

each provided in aqueous solutions. The total film thickness is controlled by the number of PDDA/CdTe NC bilayers and by the deposition time for each monolayer. For a film with 40 bilayers we obtain a typical thickness of 120 nm. Since the effective thickness of a PDDA molecule (approx. 1 nm) is several times smaller than that of the used CdTe NCs with a diameter of approximately 3.2 nm [14], the layer-by-layer technique allows to obtain exceptionally high NC concentrations (close to 60% in volume as determined from the optical film density).

For the fabrication of 1D WGs, the NC/polymer bilayer films were deposited on substrates which were patterned with grooves, with a width of 5, 10, 20 and 40 µm and a length of 2 cm. The grooves with a depth of 450 nm were wet chemically etched by a buffered HF solution whereby a 30 nm thick Cr layer was used as etch mask (see inset of Fig 1(g)).

Results and Discussion

The waveguiding properties of the NC/polymer films are studied by propagation loss measurements, making use of the NC luminescence. In particular, an Ar-ion laser was used to excite the NCs from a direction perpendicular to the sample surface while the photoluminescence (PL) emitted in lateral direction is collected from the sample edge by a microscope objective. The PL spectra are recorded as a function of the distance z, measured between the excitation spot, which is moved by a mirror, and the edge of the sample (see inset in Fig 1(c))

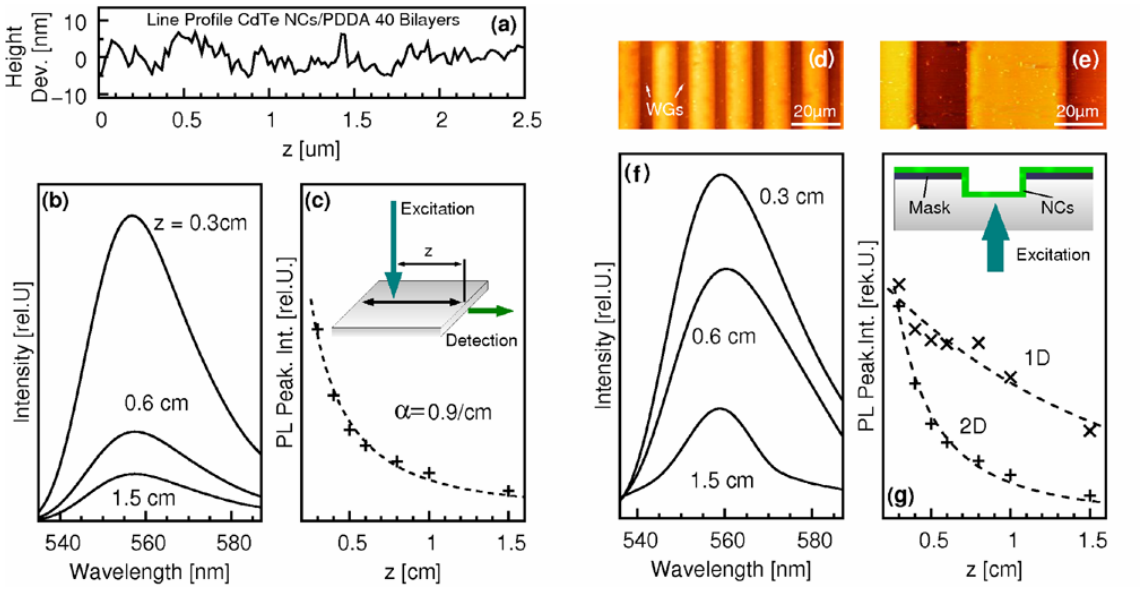

Fig. 1: (a) Surface scan of 2D 40 BL sample, (b) spectra recorded at different excitation distances (2D), (c) PL Intensity over several distances (2D), (d) and (e) AFM micrographs of 1d samples, (f) spectra recorded at different excitation distances (1D), (g) PL Intensity over several distances (1D)

Figure 1(b) shows the PL spectra for various distances z between excitation point and sample edge, revealing that increasing z results in a decrease of the PL intensity, regardless of the emission wavelength. Therefore, it is sufficient to examine the dependence of the peak intensity, as is given in Fig. 1(c). There, the experimental data are fitted by a function which is proportional to $(1/z)e^{-\alpha z}$ (solid line). Here the factor 1/z accounts for the intensity drop of a radial wave, originating from a point source, within a

2D slab. The exponentially decaying part is ascribed to the intensity drop caused by losses in the WG.

The luminescence spectra observed for the NCs in the grooves (Fig. 1(f)) exhibit a very similar shape than those for the planar films. The decay of the PL intensity with increasing propagation distance z, however, is by far smaller as in the 2D case. This is shown in detail in Fig 1(g), where the dependence of the peak PL intensities on z for the 1D and the 2D case are compared. For the 1D in particular, the decay can be fitted by a single exponential one, without the 1/z prefactor, which we quote as an indication for the truly 1D waveguiding of the light in the NC/PMMA film deposited on the patterned substrates. The resulting loss coefficients are the same for 1D and 2D samples, evidencing that purely 1D waveguiding occurs in the patterned samples.

To show that the WG losses are dominated by the surface roughness, we investigated 1D WGs with various layer thicknesses and widths. Reducing the thickness from 40 to 10 NC/PDDA bilayers results in an increase of the loss coefficient by a factor of 2. This is almost independent on the width of the substrate grooves, varied between 5 and 40 µm.

Conclusion

In summary the high potential of layer-by-layer deposited NC/PDDA films for applications in optical devices is demonstrated. In these films, deposited on planar as well as on patterned glass substrates two and one dimensional waveguiding is observed with penetration length of several centimeters.

Acknowledgements

Financial support from the Austrian Science Foundation FWF (Project START Y179 and SFB 25-IRON) is gratefully acknowledged.

References

[1] C. B. Murray, D. J. Norris, and M. G. Bawendi: "*Synthesis and characterization of nearly monodisperse CdE (E=S, Se, Te) semiconductor nanocrystallites*", J. Am. Chem. Soc. 115, 1993, p. 8706

[2] M. A. Hines and P. Guyot-Sionnest: "*Synthesis and characterization of strongly luminescing ZnS-capped CdSe nanocrystals*", J. Phys. Chem. 100, 1996, p. 468

[3] A. P. Alivisatos, "*Semiconductor clusters nanocrystals, and quantum dots*", Science 271, 1996, p. 933

[4] J. M. Pietryga, R. D. Schaller, D. Werder, M. H. Stewart, V. I. Klimov, and J. A. Hollingsworth: "*Pushing the Band Gap Envelope: Mid-Infrared Emitting Colloidal PbSe Quantum Dots*" J. Am. Chem. Soc. 126, 2004, p. 11752

[5] L. Qu and X. Peng: "*Control of photoluminescence properties of CdSe nanocrystals in growth*" J. Am. Chem. Soc. 124, 2002, p. 2049

[6] I. Mekis, D. V. Talapin, A. Kornowski, M. Haase, and H. Weller: "*One-pot synthesis of highly luminescent CdSe/CdS core-shell nanocrystals via organometallic and "greener" chemical approaches*" J. Phys. Chem. B 107, 2003, p. 7454.

[7] M. A. Petruska, A. V. Malko, P. M. Voyles, and V. I. Klimov: "*High-Performance, Quantum Dot Nanocomposites for Nonlinear Optical and Optical Gain Applications*", Adv. Mater. 15, 2003, p. 610 and Refs. therein.

[8] V. I. Klimov, A. A. Mikhailovsky, D. W. McBranch, C. A. Leatherdale, and M. G. Bawendi: "*Quantization of multiparticle auger rates in semiconductor quantum dots*", Science 287, 2000, p. 1011,

[9] H.-J. Eisler, V. C. Sundar, M. G. Bawendi, M. Walsh, H. I. Smith, and V. I. Klimov: "*Color-selective semiconductor nanocrystal laser*" Appl. Phys. Lett. 80, 2002, p. 4614,

[10] A. V. Malko, A. A. Mikhailovsky, M. A. Petruska, J. A. Hollingsworth, H. Htoon, M. G. Bawendi, and V. I. Klimov: "*From amplified spontaneous emission to microring lasing using nanocrystal quantum dot solids*", Appl. Phys. Lett. 81, 2002, p. 1303,

[11] P. T. Snee, Y. Chan, D. G. Nocera, and M. G. Bawendi: "*Whispering-Gallery-Mode Lasing from a Semiconductor Nanocrystal/Microsphere Resonator Composite*", Adv. Mater. 17, 2005, p. 1131,

[12] V. I. Klimov, A. A. Mikhailovsky, S. Xu, A. Malko, J. A. Hollingsworth, C. A. Leatherdale, H.-J. Eisler, and M. G. Bawendi: "*Optical gain and stimulated emission in nanocrystal quantum dots*" Science 290, 2000, p. 314

[13] G. Decher: "*Fuzzy Nanoassemblies: Towards Layered Polymeric Multicomposites*", Science 277, 1997, p. 1232 (1997)

[14] W. W. Yu, L. Qu, W. Guo, and X. Peng: "*Experimental Determination of the Extinction Coefficient of CdTe, CdSe, and CdS Nanocrystals*", Chem. Mater. 15, 2003, p. 2854

Mid-Infrared High Finesse Microcavities based on IV-VI Semiconductor/BaF_2 Broad Band Bragg Mirrors

T. Schwarzl, M. Eibelhuber, W. Heiss and G. Springholz

Institut für Halbleiter- und Festkörperphysik, Johannes Kepler Universität, A-4040 Linz, Austria

We report on molecular beam epitaxially grown high-reflectivity broad band Bragg mirrors for mid-infrared devices using IV-VI semiconductors and BaF_2. This material combination exhibits a high ratio between the refractive indices of up to 3.5, leading to a broad mirror stop band with a relative width of 75%. To verify the high quality of the PbEuTe/BaF_2 Bragg mirrors, we study a half-wavelength microcavity formed by mirrors with only three periods. The resonance of the microcavity has a narrow line width of 5.2 nm corresponding to a very high finesse of 750. From this, a mirror reflectivity higher than 99.7% is deduced, in good agreement to transfer matrix simulations.

Introduction

High-reflectivity Bragg interference mirrors with almost zero absorptive losses are of great importance for advanced optoelectronic devices such as vertical-cavity surface-emitting lasers. These interference mirrors consist of pairs of dielectric layers with quarter wavelength thicknesses and different refractive indices. Epitaxial Bragg mirrors grown by molecular beam epitaxy (MBE) generally exhibit a much higher quality compared to those produced by conventional evaporation. This is due to the excellent control of the growth process and layer thicknesses, the smooth and abrupt heterointerfaces and the extremely low levels of unintentional impurities, resulting in negligible stop-band absorption [1]. However, to achieve very high mirror reflectivities with a reasonable number of layer pairs, Bragg mirror materials with as large as possible refractive index contrasts are required [1], [2]. On the other hand, for MBE the crystal structure as well as lattice parameters of the involved materials should be as close as possible in order to obtain a good structural and electronic quality of the layers, which is of crucial importance, e. g., for subsequent growth of the active material of laser structures.

In the present work, we have employed MBE grown high reflectivity broad band Bragg mirrors for infrared device applications, combining the narrow band gap IV-VI semiconductors with the dielectric material BaF_2. This material combination exhibits an exceedingly large difference in refractive index, with corresponding index ratio about a factor of 3 larger than that achievable with III-V semiconductors [3]. As a consequence, not only a much smaller number of Bragg mirror pairs is required to gain reflectivities above 99%, but also a very large stop band width can be achieved.

We successfully demonstrate PbEuTe/BaF_2 Bragg microcavities for the mid-infrared with very high finesse values, thus evidencing the very high reflectivity of the three-period Bragg mirrors of at least 99.7%. The mirrors with a very high refractive index ratio of 3.5 exhibit a very broad stop band with a relative width of 75%. The mid-infrared region is particularly important for gas spectroscopy applications, as most molecular gases have strong absorption lines in this spectral region [4].

Experimental

Structure and Design

The Bragg mirrors and microcavities were designed by transfer matrix calculations using the exact dispersion of the optical constants of the individual layer materials as determined by Fourier-transform infrared (FTIR) spectroscopy of reference layers. The structures were all grown by MBE onto (111) BaF_2 substrates. The growth temperature was 380 °C and the growth rate was 1.1 µm/h for all layers. The Bragg mirrors forming the microcavity consist of three periods of $Pb_{0.92}Eu_{0.08}Te/BaF_2$ quarter-wave layers designed for a wavelength of 3.9 µm. The half-wavelength cavity layer between the mirrors also consists of $Pb_{0.92}Eu_{0.08}Te/BaF_2$, thus being optically transparent at the design wavelength. All samples were characterized by room temperature FTIR reflectivity and transmission measurements.

Results

To verify the high quality of our $PbEuTe/BaF_2$ Bragg mirrors, first we study a half-wavelength microcavity formed by these mirrors. From the finesse or quality factor of the cavity, we can accurately evaluate the mirror reflectivity. Figure 1 shows the reflectivity spectrum of the cavity sample measured at room temperature (dots). One can see the very broad mirror stop band with almost 100 % reflectivity between 3 µm and 6 µm. On both sides of the stop band pronounced interference fringes from the total thickness of the structure appear. The relative mirror band width $\Delta\lambda/\lambda_0$ is about 75 %, where λ_0 is the central wavelength of the mirror stop band. This is due to the very large refractive index ratio n_1/n_2 between the used mirror materials $Pb_{0.92}Eu_{0.08}Te$ and BaF_2 of 3.5. Both the refractive index ratio and the stop band width are not only among the largest for MBE grown Bragg mirrors, but also for Bragg mirrors fabricated by other methods with less limitation on the material choice [1]. Compared to the most common III-V semiconductor Bragg mirrors [3], the refractive index ratio and the stop band width are a factor of 3 and 7 larger, respectively.

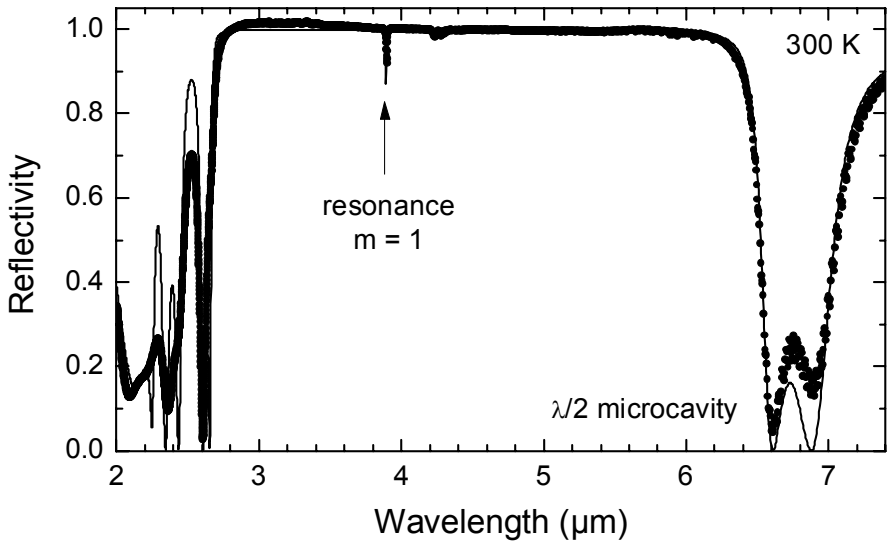

Fig. 1: FTIR reflectivity spectrum of a half-wavelength microcavity consisting of two three-period $PbEuTe/BaF_2$ Bragg mirrors measured at 300 K (dots). The corresponding transfer matrix simulation is depicted as solid line. The resonance (order m = 1) is indicated by the arrow.

Near the center of the stop band, one narrow cavity resonance line at 3.9 µm is found. This is the first order resonance mode (m = 1) of the half-wavelength cavity. As shown by the solid line in Fig. 1, the whole experimental spectrum, in particular the stop band width and the cavity resonance position, is in very good agreement with simulations based on the transfer matrix method. In order to evaluate the finesse of the microcavity, the line width of the cavity mode has to be analyzed. For that, a high-resolution FTIR transmission spectrum of the resonance was recorded. The measured data is depicted as dots in Fig. 2. From a Lorentzian line fit, a line width δλ of only 5.2 nm is deduced. This corresponds to a very high finesse of the microcavity structure of $F = \lambda/(m\,\delta\lambda) = 750$ for the m = 1 order mode. Using $F = (\pi R^{0.5})/(1 - R)$, this in turn corresponds to a mirror reflectivity R of 99.7%. Such a high reflectivity mirror with only few layer pairs is well suited for realization of laser devices.

The solid line in Fig. 2 represents the transfer matrix simulation which is in perfect agreement to the experiment when cavity losses corresponding to an extinction coefficient κ of 0.0028 are included. These losses are very low because they are on the order of magnitude of the residual absorption of PbEuTe *below* the band gap energy. They may arise from background absorption in the cavity material or from interface roughness between the layers in the multilayer cavity structure. These results demonstrate that our Bragg mirrors not only exhibit one of the largest refractive index contrasts and broadest stop bands, but also provide very high reflectivity values well above 99 % for only three Bragg layer pairs. To our knowledge, only one other such mirror with comparable index ratio and band width has been reported in the literature up to now. However, for this mirror consisting of BaF_2 and PbEuSe grown on (111) Si substrates, the measured reflectivity was only 95 % for three layer pairs [5].

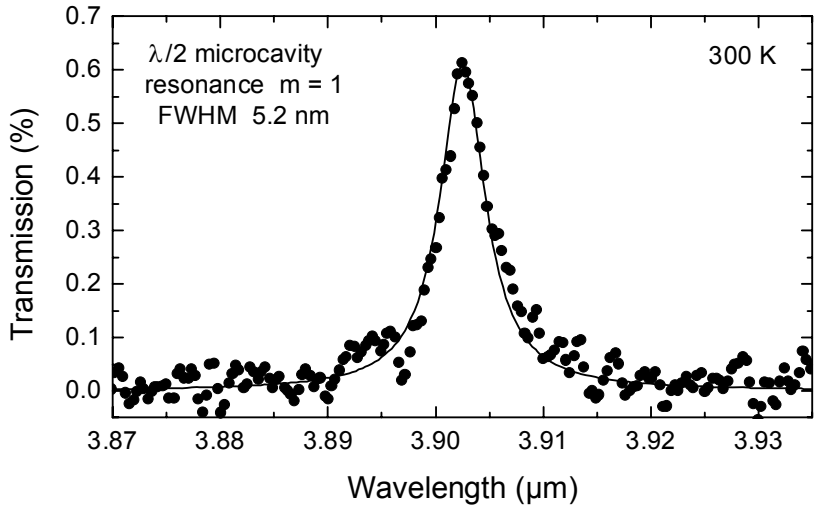

Fig. 2: High-resolution FTIR transmission spectrum around the cavity mode of the half-wavelength cavity at 300 K (dots). The corresponding transfer matrix simulation is shown as solid line.

Conclusion

To summarize, we have demonstrated MBE grown high-reflectivity broad band Bragg mirrors for mid-infrared device applications, using IV-VI semiconductors and BaF_2 as mirror materials. This material combination exhibits an exceedingly large difference in refractive index, with a corresponding index contrast ratio n_1/n_2 of up to 3.5. As a con-

sequence, we have observed a very broad mirror stop band with a relative band width of 75% for $Pb_{0.92}Eu_{0.08}Te/BaF_2$ Bragg mirrors, in good agreement with our simulations based on the transfer matrix method. Both the index contrast and the stop band width are not only among the largest for MBE grown Bragg mirrors, but also for Bragg mirrors fabricated by other methods with less limitation on the material choice. As a decisive characteristic for the mirror quality, the finesse of cavity structures produced on basis of these Bragg mirrors has been shown to be 750 for a half-wavelength microcavity which exhibits a narrow resonance line width of only 5.2 nm. From that, a mirror reflectivity higher than 99.7% is obtained for only three layer pairs. This evidences the high quality and efficiency of MBE grown IV-VI/BaF_2 Bragg mirror structures, and underlines their high potential for practical device applications.

Acknowledgements

Financial support from the Austrian Science Fund FWF, Austria is gratefully acknowledged.

References

[1] W. Heiss, T. Schwarzl, J. Roither, G. Springholz, M. Aigle, H. Pascher, K. Biermann, and K. Reimann: “Epitaxial Bragg Mirrors for the Mid-infrared and their Applications”, Prog. Quantum Electron., Vol. 25, 2001, pp. 193 - 228.

[2] G. Springholz, T. Schwarzl, and W. Heiss: “Mid-infrared Vertical Cavity Surface Emitting Lasers based on the Lead Salt Compounds”, in Mid-infrared Semiconductor Optoelectronics, edited by A. Krier (Springer, London, 2006), pp. 265 – 301.

[3] J. L. Jewell, J. P. Harbison, A. Scherer, Y. H. Lee and L. T. Florez: “Vertical-cavity Surface-emitting Lasers: Design, Growth, Fabrication, Characterization”, IEEE J. Quantum Electron., Vol. 27, 1991, pp. 1332 - 1346.

[4] M. Tacke: “New Developments and Applications of Tunable IR Lead Salt Lasers”, Infrared Phys. Technol., Vol. 36, 1995, pp. 447 - 463.

[5] X. M. Fang, H. Z. Wu, Z. Shi, and P. J. McCann: “Molecular Beam Epitaxy of periodic BaF_2/PbEuSe Layers on Si(111)”, J. Vac. Sci. Technol., Vol. B 17, 1999, pp. 1297 - 1300.

Fabrication of Su 8 Microfluidic Devices using Low Temperature Bonding

M. Mikolasek[1], R. Holly[1], M. Wimplinger[2], G. Mittendorfer[2], Ch. Thanner[2], K. Hingerl[1]

[1]Christian Doppler Laboratory for Surface Optics, Johannes-Kepler-Universität Linz, A-4040 Linz

[2]EV Group, A-4782 St.Florian/Inn

Introduction

Microfluidic devices have enjoyed attention of many researchers and technological institutes due to their enormous potential applications including pharmaceuticals, biotechnology, the life sciences, defense and public health [1], [2]. Many microfluidic devices are currently fabricated in silicon or glass [3]. Both of these materials are suitable as substrates for microchemical reactors. Moreover, well developed processing techniques for silicon offer opportunity to produce fully integrated structures. However, fabrication of these kinds of devices is still very expensive [2].

A promising material for preparing microfluidics devices is the photo-resist Su 8 developed by IBM. It is a negative, photo definable epoxy-based resist that is compatible with standard silicon processing conditions and can be patterned using a standard lithography technique [4]. The use of Su 8 material for the fabrication of microfluidic devices by photolithographic techniques presents an advantage for easy and low-cost manufacturing of high-aspect-ratio microstructures. Furthermore, Su 8 has good mechanical properties, chemical resistance and it is also a biologically compatible material [5]. Su 8 can be partially pre-baked and bonded with a companion wafer by applying pressure and heat.

This paper describes a method for fabricating microfluidic devices using low-temperature wafer-level adhesive bonding. The fabrication is based on a 4 inches wafer polymer bonding process, using Su 8 polymer epoxy photoresist as a structural material. The uniformity and crosslinking level of the Su 8 in the photolithography process have been optimized to obtain a strong bond without defects and sealed channels.

Adhesive Wafer Bonding

In adhesive bonding, an intermediate adhesive layer (in our case resist Su 8) is used to create a bond between two surfaces to hold them together. The main advantages of adhesive wafer bonding are the insensitivity to surface topography, the low bonding temperatures, the compatibility with standard integrated circuit wafer processing, and the ability to join different types of wafers [6]. This technique is simply and low cost, so suitable for commercial usage.

Fabrication Process for Microfluidic Devices in Su 8

The critical parameter for high-quality bonding is a good thickness uniformity as well as suitable crosslinking level of the Su 8 layer. These two parameters determined our de-

velopment of a technology for preparing microfluidic devices. Our task was to prepare 100 μm thick Su 8 microfluidic structures on a 4 inch Si wafer, which was afterwards bonded to a glass wafer with an approximately 4 μm thick non-exposed Su 8 layer.

Thickness uniformity can by affected mainly be spincoating and soft bake. Our developed recipe for the spincoater allows fabricating a 100 μm thick Su 8 layer with a thickness uniformity of ±4%. After spincoating, wafers are left to relax on a flat surface approximately for 1 day. During this time the wafers are covered with a glass cover. This technique leads to reflow of the resist and results in final thickness uniformity of ±2.5 – 3.5% across the wafer.

After softbake, edge beads of 40 – 50 μm height are present. These edge beads are removed with acetone. Our experiments show that new edge beads of 6 – 8 μm height arise after drying on a hotplate (temperature above 50°C). For this case all future heating treatment after edge beads removal has to be omitted.

The second critical parameter is the crosslinking level of Su 8 layer. There are two parameters which can affect the crosslinking level of the Su 8 resist; exposure dose and post-exposure bake. Both were optimized in order to obtain suitable crosslinking level. A high crosslinking level leads to bad bond strength and large unbonded areas. On the other hand, a low crosslinking level results in sealing of the channels. Optimized parameters are: exposure dose 400mJ/cm^2 and post-exposure bake 12 min on a hotplate at 95°C.

The crosslinking of Su 8 occurs also during the bake at temperatures above 160°C [7]. This feature of Su 8 was used to obtain a suitable crosslinking level for a 4 μm thick Su 8 layer deposited on glass wafer. Optimized data for baking are: temperature 170 °C and 28 – 30 minutes time.

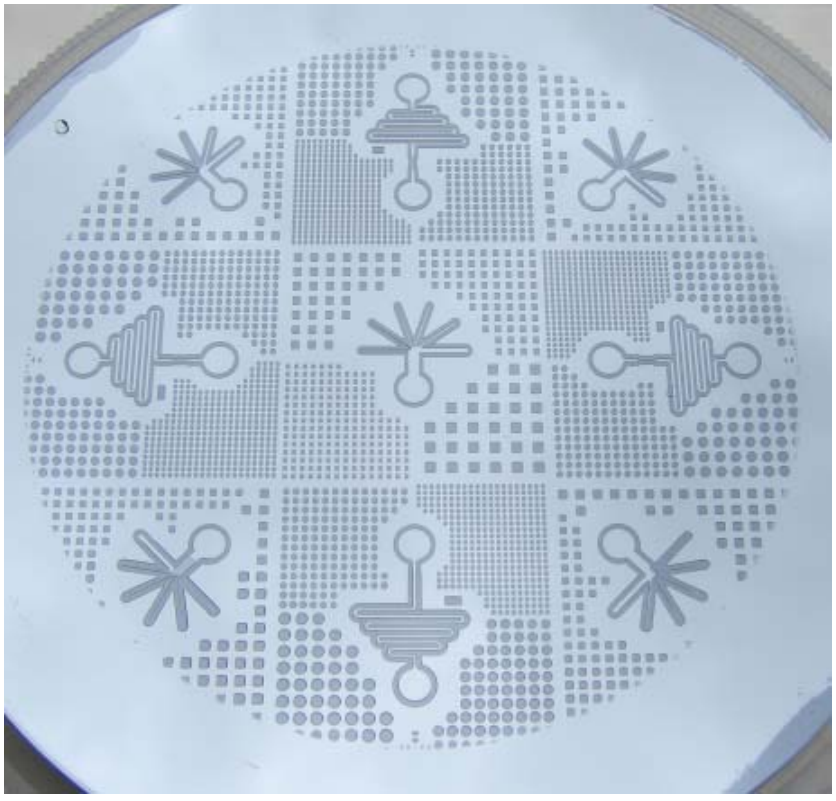

Fig. 1: Bonded 100 μm thick microfluidic structures on a 4 inch wafer without defects and deformation of channels.

Bonding Experiments

Our bonding experiments were realized with an EVG 501 bonder. Wafers were inserted into the bonder chamber on an elastic base holder of approximately 3 inch diameter. This wafer base improves the distribution of the applied bonding force across the wafer. The bonding chamber is evacuated in order to avoid trapping air bubbles in the bond area. Wafers are brought into contact, pressed together and heated to a temperature of 180°C. Heating was realized in 3 steps in order to obtain a uniform heating ramp. A pressure of 1200 N is applied for 10 min. During this time full crosslinking of the Su 8 resist takes place, and permanent contact between the exposed and non-exposed layers is created. Bonding with these parameters results in bonding on all places across the 4 inch wafer without defects and closed channels (Fig.1). Details on bonded structures with channels with widths in the range of 25 µm to 500 µm are presented in the Fig. 2. The bond interface is directly inspected through the transparent glass wafer to identify the status of sealed and unbonded areas.

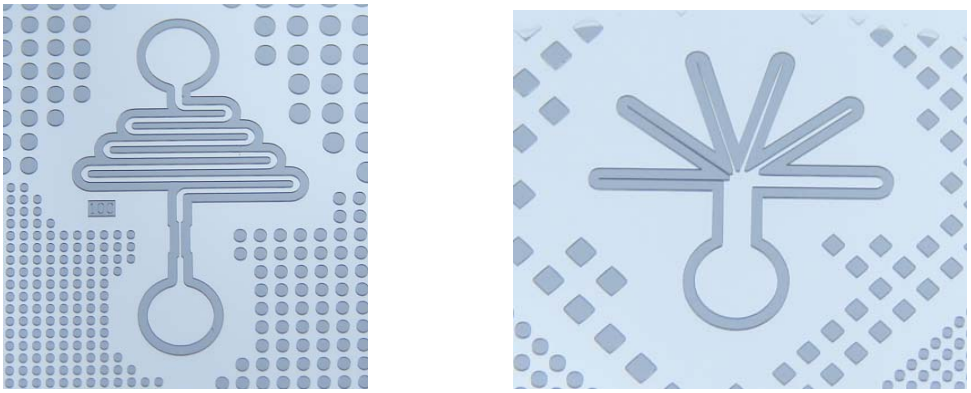

Fig. 2: Detail on bonded structures with channels of 25 – 500 µm width. Structures are bonded without deformation and without sealing of the channels.

Conclusion

We developed a technique for preparing microfluidic devices in Su 8 resist. The final bonding recipe can be used for low-cost mass-production of microfluidic devices. Bond strength was inspected be inserting tweezers between wafers. The bond was strong enough to allow the dicing of devices without detachment or partial release of them. Leakage test results show that this low-temperature wafer bonding process is a viable MEMS fabrication technique for microfluidic applications.

References

[1] R.H. Liu, P. Grodzinski; J. Microlith. Microfab. Microsyst. 2 (2003) 340.

[2] S. Rajaraman, H.Noh, P. J. Hesketh, D.S. Gottfried; Sensors and Actuators B 114 (2006) 392–401.

[3] L.C. Waters, S.C. Jacobson, N. Kroutchinina, J. Khandurina, R.S. Foote, J.M. Rasey; Anal. Chem. 70 (1998) 158.

[4] J. M. Shaw, J. D. Gelorme, N. C. LaBianca, W. E. Conley, S. J. Holmes; IBM J. res. develop. vol. 41 no. 112 january-march 1997.

[5] L. Yu, E.H. Tay, G. Xu, B. Chen, M. Avram and C. Iliescu; Journal of Physics Conference Series 34 (2006) 776–781.

[6] F. Niklaus, G. Stemme, J. -Q. Lu and R. J. Gutmann; Journal of Applied Physics 99, 031101 (2006).

[7] P. Svasek, E. Svasek, B. Lendl, M. Vellekoop; Sensors and Actuators A 115 (2004) 591–599.

Paramagnetic GaN:Fe and Ferromagnetic (Ga,Fe)N: Relation between Structural, Electronic and Magnetic Properties

A. Bonanni[1], C. Simbrunner[1], M. Kiecana[2], Tian Li[1], M. Wegscheider[1], A. Navarro-Quezada[1], M. Quast[1], H. Przybylinska[2], T. Dietl[2]

[1]Institut für Halbleiter- und Festkörperphysik, Johannes Kepler Universität Linz, A-4040 Linz,

[2]Institute of Physics, Polish Academy of Sciences, Warsaw, Poland

GaN:Fe and (Ga,Fe)N layers have been grown by means of metalorganic chemical vapor deposition on c-sapphire substrates and thoroughly characterized via high-resolution x-ray diffraction, transmission electron microscopy (TEM), spatially-resolved energy dispersive X-ray spectroscopy (EDS), secondary-ion mass spectroscopy, photoluminescence, Hall-effect and SQUID magnetometry. A combination of TEM and EDS reveals the presence of coherent nanocrystals, presumably Fe_xN with the composition and lattice parameter imposed by the host. In layers with iron content $x > 0.4\%$ the presence of ferromagnetic signatures, such as magnetization hysteresis and spontaneous magnetization, have been detected. The ferromagnetic-like response is shown to arise from the (Ga,Fe)N epilayers, it increases with the iron concentration, it persists up to room temperature, and it is anisotropic.

In recent years, it has become more and more clear that wide band-gap semiconductors and oxides doped with transition metals (TM) constitute a new class of materials system exhibiting magnetic properties whose origin and methods of control are still not understood [1]. While extensive studies have been conducted on (Ga,Mn)N as promising workbench for future applications in spintronics, only little is known about (Ga,Fe)N. In the attempt to compensate this gap, we have carried out a comprehensive study [2] of the GaN:Fe (below the solubility limit of Fe into GaN at our growth conditions) and (Ga,Fe)N materials systems, beginning with a careful on-line control of the metalorganic chemical vapor deposition (MOCVD) process and proceeding with a possibly thorough investigation of the structural, electrical, optical and magnetic properties in order to shed new light into the mechanisms responsible for the paramagnetic and high-temperature ferromagnetic response of these novel material.

The studied epilayers have been fabricated in an AIXTRON 200RF horizontal-tube MOCVD reactor. All structures have been deposited on c-plane sapphire substrates according to a well established growth procedure [3]. The employed reactor offers the unique possibility of controlling in real time the deposition process via simultaneous on-line spectroscopic ellipsometry and X-ray diffraction [4]. A combination of transmission electron microscopy (TEM) and spatially resolved energy dispersive X-ray spectroscopy (EDS) analysis reveals the presence of coherent nanocrystals, presumably Fe_xN with the composition imposed by the host, like the one reported in Fig. 1. From both TEM and secondary ion mass spectroscopy (SIMS) studies, it is stated that the density of nanocrystals, and thus the Fe concentration increases towards the sample surface.

According to Hall effect measurements, electrons from residual donors are trapped by mid-gap Fe acceptor states in the limit of iron content $x < 0.4\%$, indicating that the concentration of Fe^{2+} ions increases at the expense of Fe ions in the 3+ charge state. This effect is witnessed by photoluminescence measurements as changes in the intensity of

the Fe^{3+}-related intra-ionic transition, which can be controlled by co-doping with Si donors and Mg acceptors. In this regime, EPR of Fe^{3+} ions and Curie-like magnetic susceptibility are observed. As a result of the spin-orbit interaction, Fe^{2+} does not produce any EPR response. However, the presence of Fe ions in the 2+ charge state may account for a temperature-independent Van Vleck-type paramagnetic signal that we observe by SQUID magnetometry.

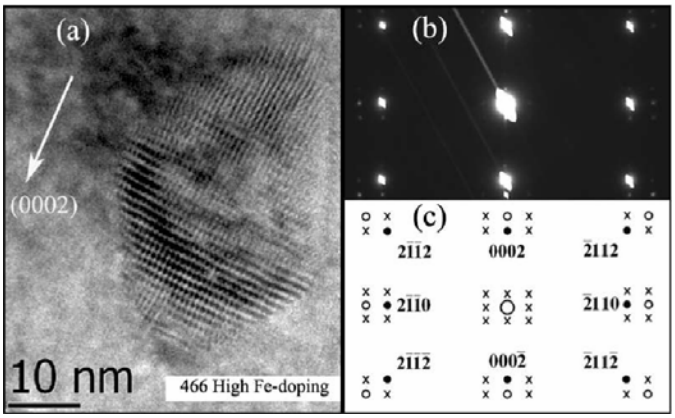

Fig. 1: (a) Elongated nanocrystal observed in an HRTEM image of Moiré fringes contrast. (b) SADP pattern acquired in the region around the precipitate along the (1010) zone axis; (c) the corresponding schematic graph for indexing of the diffraction spots.

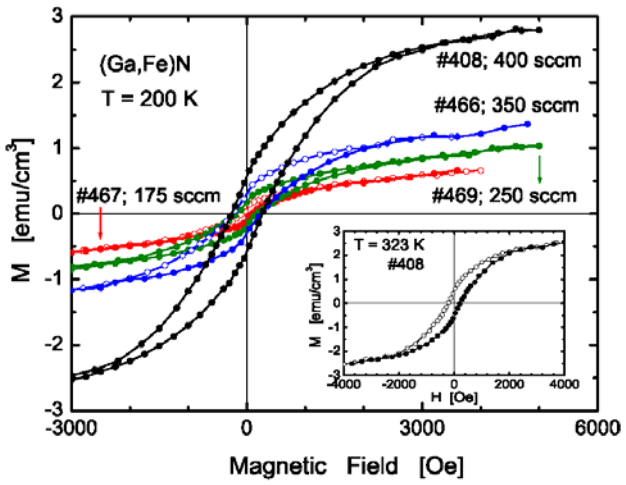

Fig. 2: Magnetization at 200 K for a series of (Ga,Fe)N samples with various Fe content (solid symbols). Inset: above room temperature M(H) for a sample with 3% Fe content.

Surprisingly, at higher Fe concentrations, the electron density is found to increase substantially with the Fe content. The co-existence of electrons in the conduction band and Fe in the 3+ charge state is linked to the gradient in the Fe concentration. In layers with iron content x > 0.4% the presence of ferromagnetic signatures, such as magnetization hysteresis and spontaneous magnetization, have been detected. A set of precautions has been undertaken in order to rule out possible sources of spurious ferromagnetic contributions. Under these conditions, a ferromagnetic-like response is shown to arise from the (Ga,Fe)N epilayers, it increases with the iron concentration, it persists up to

room temperature, and it is anisotropic – i.e., the saturation value of the magnetization is higher for in-plane magnetic field.

According to the findings summarized in Fig. 2, the ferromagnetic signal does not diminish remarkably when the temperature is increased to 200 K, and it persists up to above room temperature, as shown in the inset. The set of magnetization curves obtained in the full available temperature and field range allows to establish the temperature variation of spontaneous magnetization MS, determined from the Arrot plot, as depicted in Fig. 3. If the ideal Brillouin MS(T) dependence is assumed, the data displayed in the inset point to an apparent Curie temperature T_C of ~ 500 K.

We link the presence of ferromagnetic signatures to the formation of Fe-rich nanocrystals, as evidenced by TEM and EDS studies. This interpretation is supported by magnetization measurements after cooling in- and without an external magnetic field, pointing to superparamagnetic properties of the system.

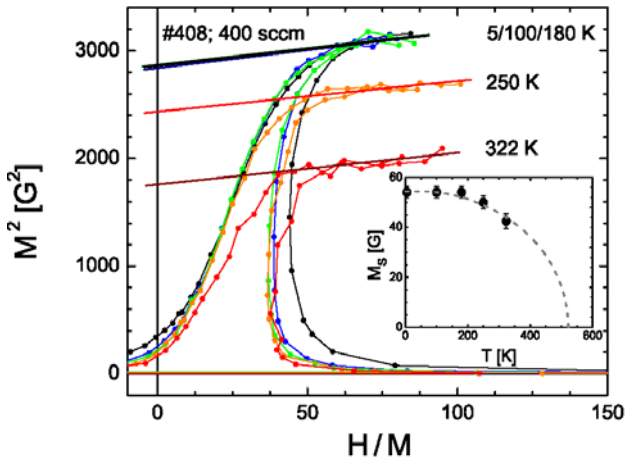

Fig. 3: Determination of the spontaneous magnetization at various temperatures obtained by plotting the square of the magnetization vs. the ratio of the magnetic field to the magnetization (Arrot plot). The inset shows the established spontaneous magnetization as a function of temperature. The extrapolation leads to an apparent Curie temperature of 500 K.

From our findings, we can argue that the high temperature ferromagnetic response due to spinodal decomposition into regions with small and large concentration of the magnetic component is a generic property of diluted magnetic semiconductors and diluted magnetic oxides showing high apparent Curie temperature.

References

[1] T. Dietl, MRS Bulletin **714** (2003).

[2] A. Bonanni et al., Phys. Rev B (to be published).

[3] A. Bonanni et al., J. Cryst. Growth **248**, 211 (2001).

[4] C. Simbrunner et al., J. Cryst. Growth **298**, 243 (2007).

Magnetic Resonance Studies of GaN:Fe

W. Jantsch[1], A. Wołoś[1,2], A. Bonanni[1], C. Simbrunner[1], H. Przybylińska[1,2]

[1] Institute of Semiconductor and Solid State Physics, Johannes Kepler Universität Linz, Austria

[2] Institute of Physics, Polish Academy of Sciences, Warsaw, Poland

We investigate one of the candidates for room temperature ferromagnetism, GaN:Fe grown by MOCVD, by means of electron spin resonance. In heavily Fe doped material we observe in addition to the signal due to isolated, substitutional Fe^{3+} ferromagnetic resonances with outstanding sensitivity. The anisotropy of the spectra allows to conclude on the crystal structure of the precipitates and we identify three different kinds. One of them most likely is Fe_4N.

Introduction

Following the prediction of carrier mediated, room-temperature ferromagnetism in wide-band-gap, diluted magnetic semiconductors substantial effort has been devoted to fabrication and investigation of transition-metal doped oxides and nitrides (GaMnN, GaFeN, AlCrN, ZnVO, ZnCoO). Numerous papers report ferromagnetic signatures of such materials, with Curie temperatures ranging from a few up to several hundred Kelvin. The highest apparent Curie temperatures are found, however, in samples in which the carrier mediated mechanism is not operative, so the origin of the ferromagnetism is not really understood. Here we report on magnetic resonance studies performed on a series of GaN:Fe samples grown by MOCVD at identical conditions but with the iron precursor flow rates differing in a wide range. These studies allowed us to determine the solid solubility limit of substitutional Fe in GaN as well as to demonstrate the presence of ferromagnetic precipitates of three different phases.

Experiments and Results

In all studied structures, independent of the iron concentration, a paramagnetic resonance signal of isolated, substitutional Fe^{3+} ions is observed. Figure 1(a) shows the concentration of Fe^{3+} estimated from the EPR signal intensity (circles) compared to the total Fe concentration measured by SIMS (triangles) as a function of the iron source flow rate for two series of samples (full and open symbols). With increasing iron precursor flow rate – up to about 200 sccm – the concentration of substitutional Fe^{3+} ions increases continuously, but at a lower rate than the total iron concentration in the sample. Above 200 sccm the Fe^{3+} content is reduced and considerable fluctuations are observed from sample to sample. We relate this effect to the change of the Fermi level position and, hence, greater occupancy of the Fe^{2+} charge state. In the high doping regime a drastic increase of the oxygen donor concentration, by about two orders of magnitude as compared to that of GaN:Fe grown at low Cp_2Fe flow rates, is detected by SIMS. The oxygen accumulation seems to be correlated with the enhanced sample roughness.

The algorithm used so far is based on peak maxima detection and the maximum intensity is interpreted as the peak center defining the relative correction shift. In this paper we present a novel algorithm which takes into account also the surrounding of the peak

maxima and results in more precise information on growth rate, composition and crystal quality.

The presence of Fe^{2+} ions cannot be determined directly by magnetic resonance since the ground state is a spin singlet state and there is no resonance transition observed in the X-band. We have detected a 20% increase of the EPR signal intensity of Fe^{3+} under illumination with light of energies above 1.2 eV, confirming the presence of Fe in the 2+ charge state, but no estimations of the actual concentration can be made from such experiments. Therefore, in order to estimate the total concentration of substitutional Fe ions in the sample, we have analyzed the width of the EPR absorption line of Fe^{3+}. At very low concentrations, the linewidth, σ, should be mainly governed by interactions with nuclear magnetic moments of the Ga and N isotopes, however, with increasing Fe concentration dipole-dipole interactions between iron ions should lead to line broadening. The broadening consists of two contributions: one due to the interaction with other 3+ ions and one related to the interaction with Fe ions in the 2+ charge state. Both contributions depend on the i^{th} to j^{th} ion distance, r_{ij}, as r_{ij}^{-3}. Assuming that the ions as well as their charges are uniformly distributed in the lattice, one can expect a linear correspondence between the dipolar broadening σ-σ_0 and the Fe concentration. Figure 1(b) gives the linewidth broadening as a function of iron precursor flow rate for the -1/2 → 1/2 transition of Fe^{3+} at B || [0001] for the same samples shown already in Fig. 1(a). As it can be seen, the linewidth increases continuously with the Cp_2Fe flow rate up to 250 sccm and saturates above this value. In the low doping regime we obtain exactly the same slope for the dipolar line broadening versus Cp_2Fe flow rate as that for the SIMS concentration. This allows us to set the solubility limit for substitutional iron in GaN at our growth conditions to 1.8×10^{20} cm^{-3}, *i.e.*, 0.4% [1].

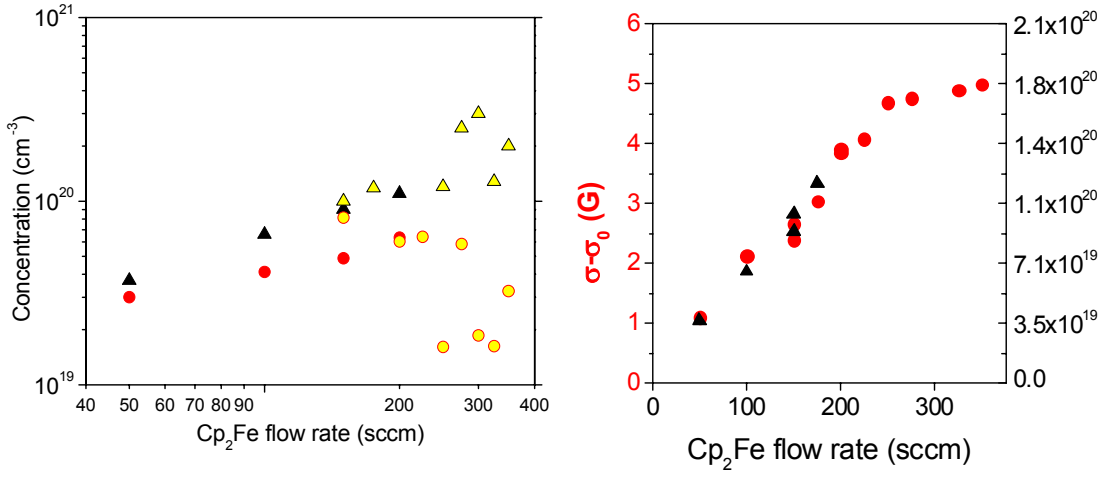

Fig. 1: (a) Fe^{3+} concentration estimated from the EPR signal intensity (circles) as compared to the total Fe concentration measured by SIMS (triangles) vs. the iron precursor flow rate. Full and open symbols identify two different sample series, grown at the same conditions. (b) EPR line broadening (left y-axis) as a function of the iron precursor flow rate (circles) for σ_0 = 12 G. The SIMS concentration (right y-axis, in units of cm^{-3}) at low flow rates, denoted by triangles, is shown for comparison.

In highly Fe doped samples additional resonance transitions are observed. In contrast to the Gaussian shaped paramagnetic resonance signals of Fe^{3+} the line shape of the new signals is Lorentzian. The signal amplitudes are almost temperature independent, as expected of a ferromagnet well below the Curie temperature. However, the angular dependence of the ferromagnetic resonance (FMR) peak positions, shown in Fig. 2,

reveals neither the sample shape anisotropy nor the hexagonal crystalline anisotropy of GaN. In contrast, the peak positions are very well described assuming cubic crystalline anisotropy only. This indicates that we deal with almost spherically shaped ferromagnetic precipitates of a cubic phase.

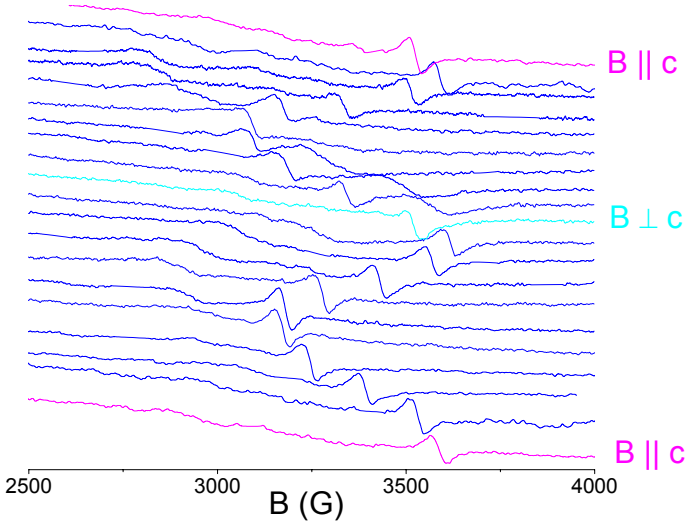

Fig. 2: As measured ferromagnetic resonance spectra at room temperature. The magnetic field is rotated in the $(1\bar{1}00)$ plane of GaN.

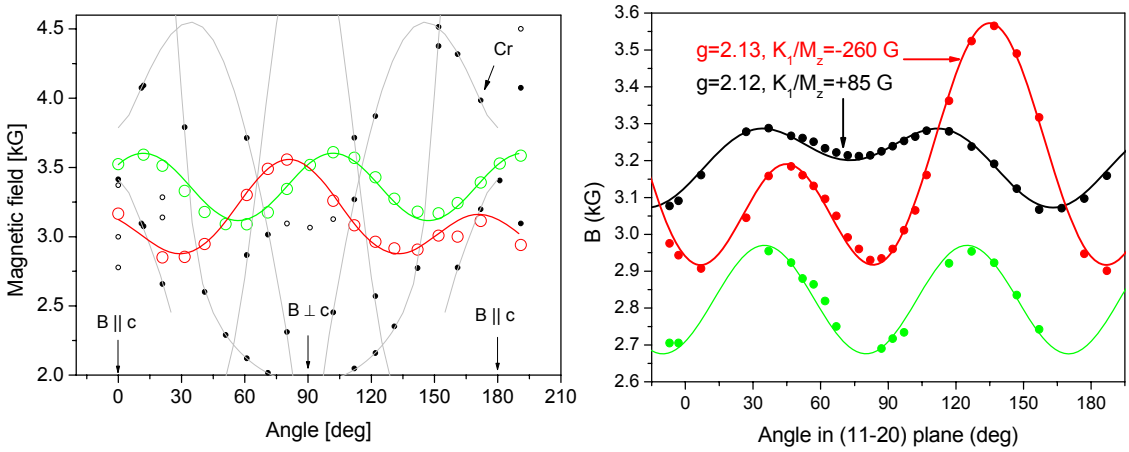

Fig. 3: Angular dependencies of FMR signals in two samples grown at the same conditions.

Conclusions

Altogether, we have identified three different kinds of ferromagnetic precipitates in GaN:Fe. The first kind has a negative first order cubic anisotropy constant, K_1, with the easy magnetization, M, direction along [111]. This is expected for ferromagnetically ordered ions occupying *fcc* lattice sites. In addition, the value of K_1/M=-260 G, determined from the fit of the angular dependence of the FMR peak positions (red lines in

Fig. 3) is consistent with that of *fcc* Fe_4N. The Fe_4N precipitates grow preferentially with a [100] axis along one of the in-plane crystallographic axes of GaN. The second kind of precipitate has a positive cubic anisotropy constant and an easy magnetization axis along [100], like bcc Fe. However, the determined value of K_1/M=85 G (black line in Fig. 3) is considerably smaller than 270 G observed in bulk Fe. This may be due to possible size effects. We also detected ferromagnetic precipitates growing with one of the [100] directions along the in-plane crystallographic axes of GaN. Here (green line in Fig. 3) we can only estimate the absolute value of $|K_1/M|$=200 G and, hence, cannot determine the exact crystallographic structure. This value, however, is very close to that expected for magnetite, Fe_3O, which has a stable cubic phase at room temperature. Moreover, the FMR peak positions were found to depend strongly on temperature in the region close to 200 K and disappear at lower temperatures, consistent with the transition of magnetite to a tetragonal symmetry phase.

The magnetic moment of each kind of precipitate estimated from the FMR signal amplitude is of the order of 10^{12} Bohr magnetons, which is well below the SQUID detection limit.

Acknowledgements

This work was supported by the Austrian Science Fund (FWF), ÖAD and Gesellschaft für Mikroelektronik (GMe).

References

[1] A. Bonanni, M. Kiecana, C. Simbrunner, Tian Li, M. Sawicki, M. Wegscheider, M. Quast, H. Przybylinska, A. Navarro-Quezada, R. Jakiela, A. Wolos, W. Jantsch, and T. Dietl, cond-mat/ 0612200

Ferromagnetic GeMnTe Epilayers and Heterostructures with T_c Values above 200 K

R.T. Lechner, G. Springholz, R. Kirchschlager, T. Schwarzl and G. Bauer

Institut für Halbleiter- und Festkörperphysik, Johannes-Kepler-Universität Linz, A-4040 Linz

Introduction

Magnetic semiconductors have attracted great interest as possible key elements for realization of spintronic devices. For such applications, ferromagnetic (FM) semiconductors with high Curie temperatures T_C are required that can be integrated in heteroepitaxial multilayer structures. A promising material is the IV-VI ferromagnetic semiconductor $Ge_{1-x}Mn_xTe$, which has been reported to have a T_C ~ 150 K for bulk material and of 130 K for thin films grown by molecular beam epitaxy (MBE) techniques [1], respectively. In contrast to the Mn-based III-V compounds, in the IV-VI materials the carrier density can be controlled independently of the concentration of the magnetic ions, and the ternary solid solutions are thermally stable and exist over a very wide composition region.

In this work, the magnetic and structural properties of $Ge_{1-x}Mn_xTe$ epilayers as well $Ge_{1-x}Mn_xTe$ heterostructures with MnTe and PbSe spacer layers were studied. The aim is to investigate the influence of the non-magnetic spacer layers on the magnetic properties of the FM semiconductor layer, as it was shown for other IV-VI superlattice (SL) structures [2], [3].

Sample Preparation

The samples were grown by MBE using compound GeTe and elemental Mn and Te_2 sources. The Mn concentration x_{Mn} was varied from 0.23 to 0.65, whereas the hole concentration was varied by excess Te_2 flux from 5 ×10^{18}cm^{-3} to 1 × 10^{21}cm^{-3} to find the optimum value for the highest T_C. The 1 µm epilayers were grown directly on (111) BaF_2 substrates or on 2 µm thick PbSe buffer layers. Under appropriate growth conditions single crystalline epilayers are obtained as proven by *in situ* reflection high energy electron diffraction (RHEED) studies. *Ex situ* x-ray diffraction investigation (XRD) revealed that the $Ge_{1-x}Mn_xTe$ epilayers show a cubic NaCl structure with (111) orientation.

Experiments

Magnetization measurements were performed with a super conducting quantum interference device (SQUID) magnetometer to determine the magnetic properties of the samples.

In Fig. 1 we compare the magnetization data of 3 samples with the same x_{Mn} value: Of one $Ge_{0.66}Mn_{0.34}Te$ single layer sample, as well as of two superlattice (SL) samples consisting of 20 × [3 nm $Ge_{0.66}Mn_{0.34}Te$ / 27 nm PbSe] and 40 × [86 nm $Ge_{0.68}Mn_{0.32}Te$ /

3.5 nm MnTe], respectively. The epilayer sample and the $Ge_{1-x}Mn_xTe$ / MnTe SL show clear ferromagnetic (FM) hysteresis loops and T_C values of above 200 K derived from magnetization vs. temperature curves (see Fig. 1). In strong contrast to the pronounced FM behavior of these two samples, the $Ge_{0.66}Mn_{0.34}Te$ / PbSe SL depicts only paramagnetic behavior (see Fig. 1).

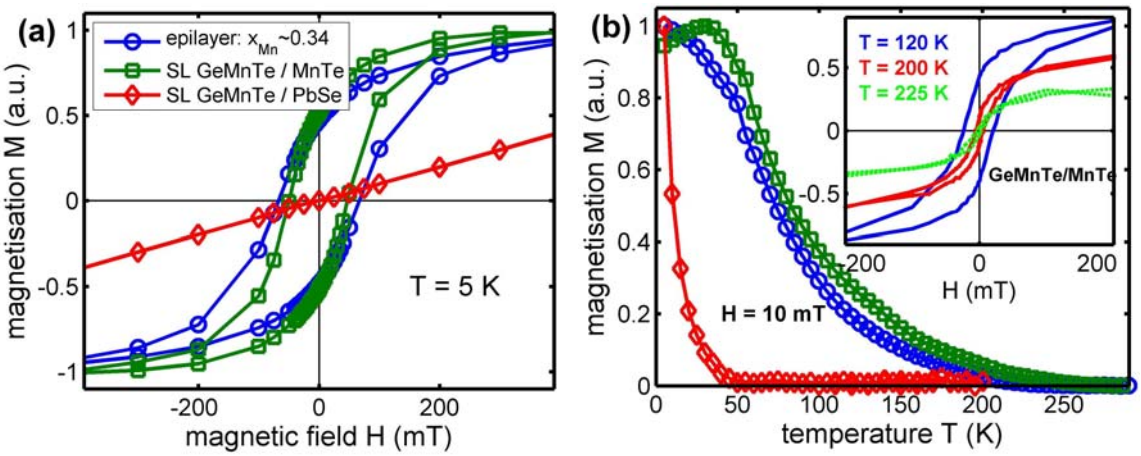

Fig. 1: (a) Magnetization M vs. magnetic field H of a GeMnTe epilayer, a GeMnTe/MnTe and a GeMnTe/PbSe superlattice at T = 5 K. (b) M vs. temperature T of the samples in (a) at magnetic field H = 10 mT. inset: Ferromagnetic hysteresis loops of the GeMnTe/MnTe SL at temperatures T = 120 K, 200 K and 225 K.

Conclusion

We suggest that this is due to a smaller band gap of the non-magnetic spacer layer PbSe with respect to GeMnTe, which forms wells in the GeMnTe/PbSe heterostructures. From FTIR spectroscopy we derive an effective band gap value of around 280 meV for PbSe and 1800 meV for MnTe compared to 700 meV for $Ge_{0.66}Mn_{0.34}Te$. Hence, for the PbSe SL the conducting holes in the FM layer are transferred to the non-magnetic layer and the ferromagnetic ordering caused by the carrier induced RKKY interaction breaks down. In contrast, MnTe has a higher band gap value and thus in the GeMnTe/MnTe SL the holes remain in the GeMnTe layer.

References

[1] W.Q. Chen, et al., J.Appl.Phys. 99, 08D515 (2006)

[2] R.T. Lechner, G. Springholz, T.U. Schülli, J.Stangl, T.Schwarzl, D.Lott, V.Leiner, A. Schreyer,H. Clemens, and G. Bauer, Physica E 32, 379-382 (2006).

[3] R.T. Lechner, G. Springholz, T. U. Schülli, J. Stangl, T. Schwarzl and G. Bauer Phys. Rev. Lett. 94, 157201 (2005)

Iron Nanoparticles in Fe/GaN

A. Navarro-Quezada[1], T. Li[1], C. Simbrunner[1], M. Kiecana[2], G. Hernandez-Sosa[1], T. Dietl[2], H. Sitter[1] and A. Bonanni[1]

[1] Institute of Semiconductor and Solid State Physics, University Linz, Austria

[2] Institute of Physics, Polish Academy of Sciences, Warsaw, Poland

In this work we present the formation of Fe-alloy nanoparticles upon the deposition of Fe onto GaN(0001) surfaces *via* metalorganic chemical vapor deposition. The growth has been monitored *in-situ* by means of spectroscopic ellipsometry and the samples have been characterized *ex-situ* by means of high-resolution x-ray diffraction, high resolution transmission electron miscroscopy, atomic force microscopy and SQUID.

Introduction

In the last years physical processes governed by spin-dependent phenomena have been intensively studied. Ferromagnetic metals such as iron are natural sources of spin-polarized electrons, and semiconductors have shown to be an ideal host for the transport and manipulation of spins. Therefore, structures like Fe/GaAs, Fe/AlGaAs and Fe/GaN are of high interest. Recently spin injection efficiencies up to 50% in heterostructures like Fe/GaAs [1] have been demonstrated. Theoretical calculations have predicted the spin relaxation lifetime in GaN as being three orders of magnitude longer than in GaAs, arising great interest on the hybrid Fe/GaN system for future quantum information processing.

So far the Fe/GaN heterostructure has been achieved by depositing Fe and GaN separately in two different steps. In this work we report the first attempts of fabrication of Fe films on (0001)GaN fully accomplished via metalorganic chemical vapor deposition (MOCVD). Special attention has been devoted to the Fe nucleation on the nitride surface and the growth has been monitored in-situ via spectroscopic ellipsometry (SE) and ex-situ via high-resolution x-ray diffraction (HRXRD), atomic force microscopy (AFM), high resolution transmission electron microscopy (HRTEM) and SQUID magnetrometry for the structural and magnetic characterization of the structures respectively.

A systematic study of the effect of Fe deposition onto the (0001)GaN templates has been performed, with particular attention to the early stages of Fe nucleation. Several series of samples were fabricated at different Fe source flux (50 – 400 sccm) and different substrate temperature (150 – 1020 °C). Insights into the surface roughness and its evolution with Fe deposition could be gained by routinely performing in-situ SE upon growth. SIMS studies gave information on the diffusion of Fe into the GaN buffer and a considerable effort has been devoted to the identification of a suitable window of growth parameters allowing a compromise between the substrate temperature required to ensure an efficient performance of the metallorganic ferrocene source and the unwanted diffusion of Fe into the buffer.

Experimental Procedure

All samples have been grown in an AIXTRON 200RF horizontal reactor MOCVD system using Trimethylgallium (TMGa), ammonia (NH_3) and Ferrocene (Cp_2Fe) as precur-

sors. The GaN(0001) samples were fabricated using a standard procedure of substrate nitridation, GaN nucleation layer deposition at 540 °C and 1 µm GaN Buffer deposition at a constant pressure of 200 mbar and 1020 °C in N_2 atmosphere. Afterwards, Fe was directly deposited on top at 200 °C under N_2 atmosphere.

Results

Surface roughening became evident after studying the samples with atomic force microscopy. These measurements clearly show the changes in the GaN surface morphology with Fe deposition. As can bee seen in the images reported in Fig. 1, there is a significant increment in surface roughness with increasing deposition time, and after 60 minutes of Fe growth we can observe the presence on the sample surface of hexagonal structures, which disappear for longer deposition time.

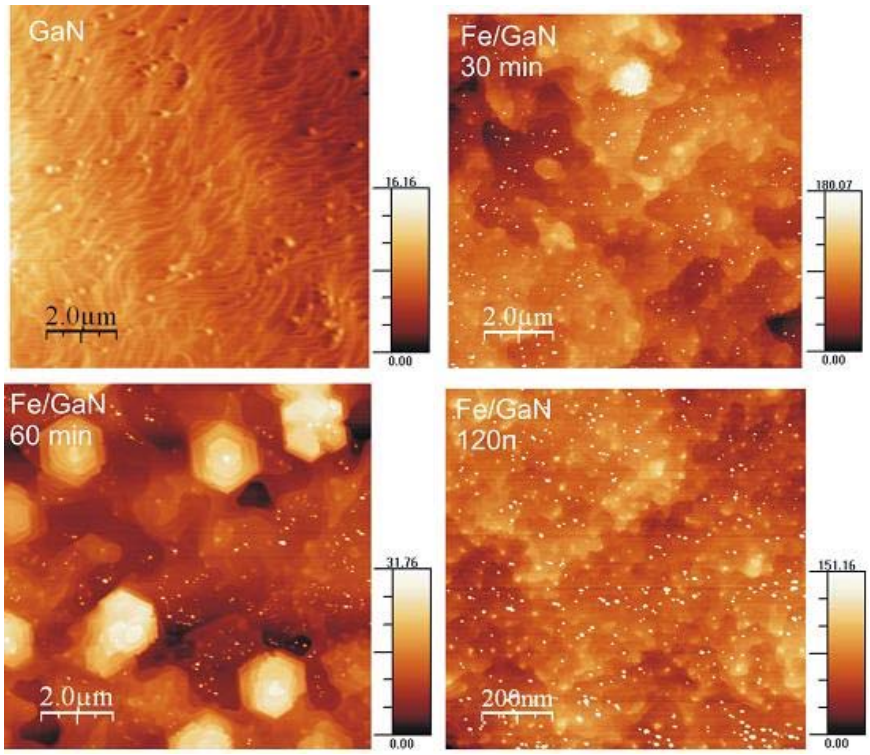

Fig. 1: AFM images of GaN, and Fe/GaN samples with Fe deposition times of 30 min (top right), 60 min (bottom left), and 120 min (bottom right).

TEM studies carried out on the samples presenting the hexagonal reconstructions on the surface revealed the presence of nanoparticles distributed few nanometers below the surface as reported in Fig. 2. The nanoparticles size is of several nanometers and energy dispersive spectra (EDS) confirmed the presence of Fe inside the particles.

Previous HRTEM studies on (Ga,Fe)N samples uncovered the presence of Fe-rich nanocrystals embedded into the GaN matrix for samples with Fe concentrations above the solubility limit at the given growth conditions [2]. The comparison of these Fe-rich nanocrystals with the nanoparticles found in the Fe/GaN samples will contribute in shading new light on the origin of the magnetic response of the Fe/GaN samples.

Figure 3 summarizes the SQUID magnetization curves, measured at 200 K for a Fe/GaN structure (where Fe has been deposited for 60 minutes onto the GaN surface) compared with a (Ga,Fe)N sample. The magnetic response of (Ga,Fe)N shows a pro-

nounced hysteresis loop – generally assigned to a ferromagnetic behavior –, while the Fe/GaN structure only shows two paramagnetic contributions: a temperature-dependent Curie component at low temperatures and a temperature-independent one above 30 K.

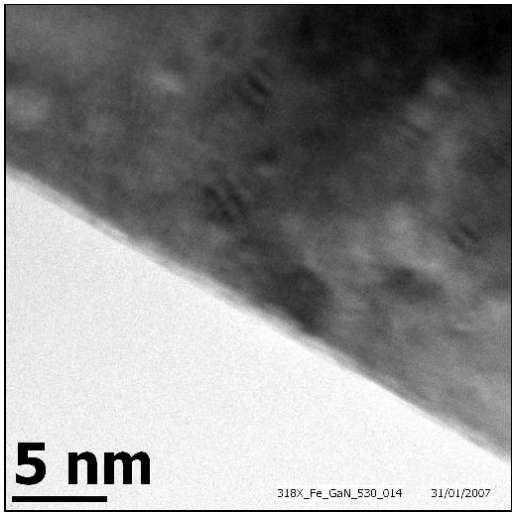

Fig. 2: HRTEM image of sample with 60 minutes Fe deposition, showing the presence of Fe-rich nanoparticles close to the surface.

The paramagnetic signal coming from the Fe/GaN sample suggests the formation of antiferromagnetic clusters (non metallic nanoparticles) close to the surface, tentatively identified as FeN clusters. This result can be supported by the HRTEM images, from where we can state that the nanoparticles are located *below* the surface rather than on the surface.

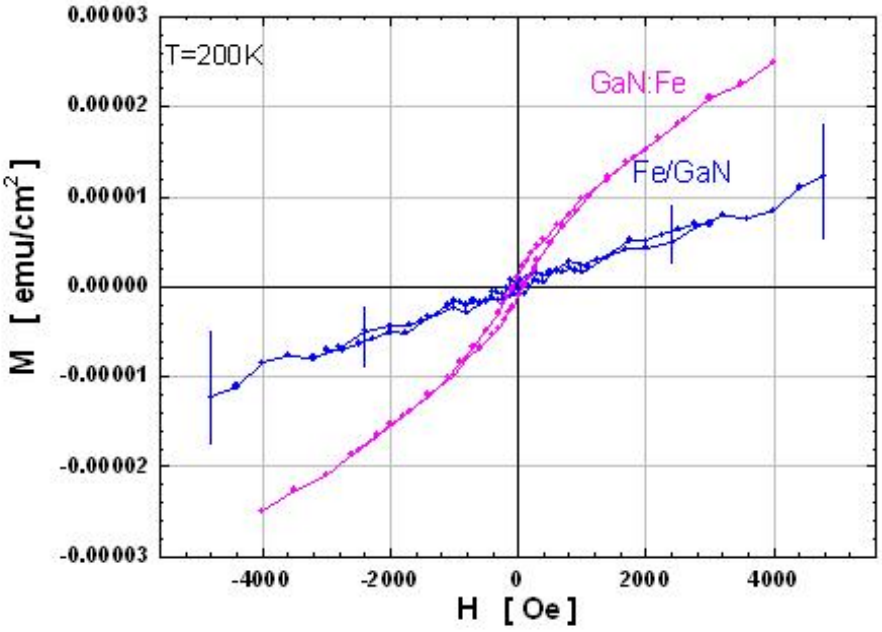

Fig. 3. Comparison of magnetic response vs. magnetic field at 200 K for (Ga,Fe)N and Fe/GaN.

References

[1] C.Adelmann et. al, Phys. Rev. B 71 (2005) 121301.

[2] A. Bonanni et al., Phys. Rev. B (to be published).

Fourier Transformation Applied on *in-situ* Laser Reflectometry during MOCVD Growth

C. Simbrunner, H. Sitter, A. Bonanni

Institut für Halbleiter- und Festkörperphysik, Johannes-Kepler-Universität Linz, A-4040 Linz

We present an additional aspect of laser reflectometry by introducing Fourier transformation in order to analyze the kinetic reflectometry spectra taken during metal organic chemical vapor deposition. We can show that offset errors due to background radiation can be completely removed by the method itself without using filters or lock-in amplifiers. Additionally calibration of the reflected intensity is needed as long as the response of the detector is linear to the reflected intensity of the sample. By analyzing the time dependent part of the signal growth rate, layer thickness and the refractive index of the growing layer can be deduced.

Introduction

In-situ monitoring with high accuracy and real time feedback are important requirements for the reproducibility of the deposition steps. The possible spectrum of *in-situ* diagnostic tools is quite narrow, since the metalorganic chemical vapor deposition (MOCVD) procedure, being carried out at almost ambient pressure, excludes all techniques requiring ultra high vacuum, like reflection high electron diffraction. Only optical methods like spectroscopic ellipsometry (SE) [1], laser reflectometry [2] – [4] and x-ray diffraction [5] are successfully applied to gain information on layer thickness, layer composition and crystalline quality. Laser reflectometry represents nowadays one of the standard methods for optical *in-situ* investigations and is delivered with most of the MOCVD reactors. In this article we report on the Fourier analysis of *in-situ* reflectometry data leading to dramatic simplifications of the hardware and of the calibration processes.

Theory

Fresnel's equations and the applied transfer matrix formalism [2] are the roots of the reflectometry analysis of multi layer structures containing n different layers, assuming each of them to be homogeneous and isotropic. By mathematical considerations it can be shown that the time dependent reflectivity Rp,n(t) of a growing layer can always be described as an Airy function if we assume a static history of layers 1..(n-1) and real refractive indices for the growing layer n which can be expanded in a Fourier series as shown in [6]:

$$\omega_{g,n} = \frac{4\pi v_{g,n}}{\lambda}\sqrt{\varepsilon_n - \varepsilon_0 \sin^2\varphi}$$

$$R_{p,n}(t) = R_c + (2R_c - 1)\sum_{k=1}^{\infty}(-\rho_n)^k \cos(k\omega_{g,n}t - k\Phi_{n,0}) \qquad (1)$$

where ρ_n, $\Phi_{n,0}$ and R_c represent time invariant material constants recursively defined by the dielectric function of the growing layer ε_n, the ambient ε_{amb} and the material constant of the previous grown layer structure ρ_{n-1} [6]. The time invariant parameter $\omega_{g,n}$ represents the angular growth speed which is connected to the optical properties of the growing layer ε_n, the wavelength λ and angle of incidence φ of the reflectometer as defined in equ. (1).

Thus, the experimental signal can be described as a constant offset R_c and a sum of cosine functions where the argument is linearly dependent on the growth time t. Therefore, fast Fourier transformation (FFT) of the kinetic signal gives direct access to the angular growth velocity including high frequency noise reduction by the method itself. Higher harmonics of $\omega_{g,n}$ are damped by a factor of $(-\rho_n)^k$ as $\rho_n \leq 1$ [6] and allow to conclude that for the analysis the absolute scale of the detector is not important, as long as the response is linear with the intensity of the signal, since the relation between the intensity of two harmonics can be defined as:

$$I_{k+1} = -\rho_n I_k \tag{2}$$

Experimental results

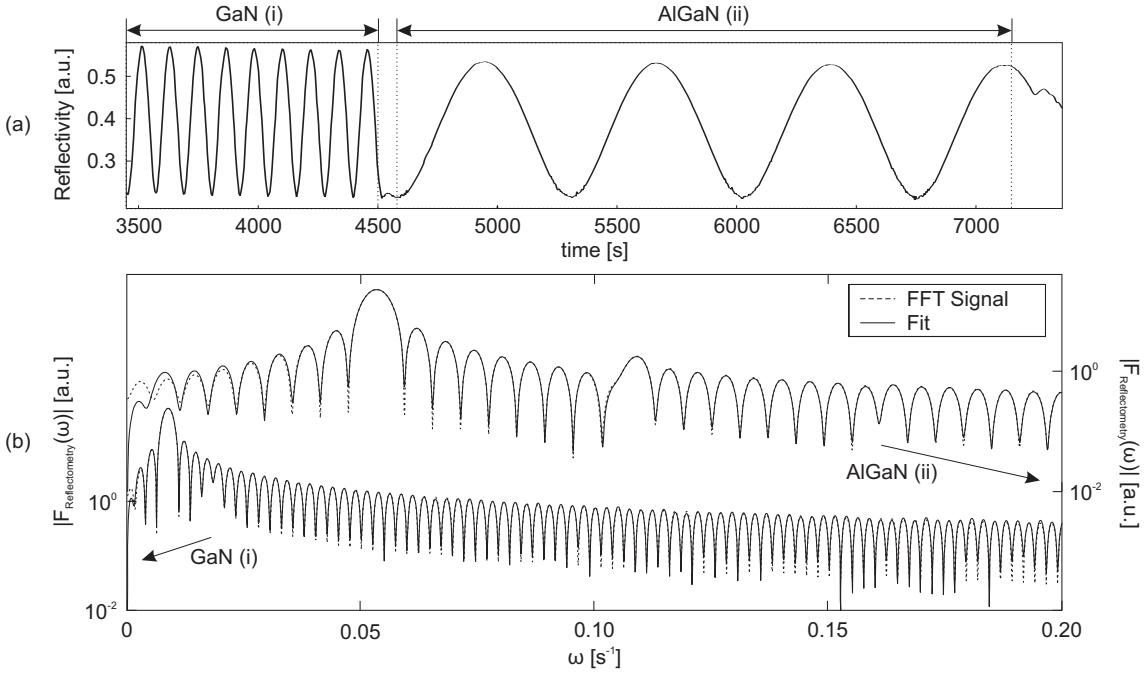

Fig. 1: (a) reflectometry spectrum as a function of time acquired during GaN and AlGaN growth. The time scale is taken relative to the start of the growth procedure including the thermal cleaning process of the substrate. (b) The FFT signal (dashed line) and the fit to the data (solid line)

Figure 1(a) shows a typical reflectometry spectrum taken during the deposition of a GaN layer followed by AlGaN. A GaN buffer is grown on sapphire substrate (i) with a growth rate of 3.6 µm/h. On the GaN buffer layer AlGaN is deposited using a lower growth rate, as evidenced by the onset of a longer period of the thickness oscillations (ii). After the removal of the offset part of the signal, the data are transformed into frequency domain by using FFT plotted in Fig. 1(b) as a power spectrum. The time range of the transformation is indicated by vertical dotted lines in the reflectometry spectrum.

For fitting the data, a sum of four harmonics has been employed and is in agreement with the measured data, due to a strong damping of the higher harmonics as expected from equ. (2). The fit is indicated by solid lines in the Fourier spectra.

In Table I we summarize the results for the fitted angular growth velocity ω_k and the damping factor $|\rho_k|$ together with the calculated values for the refractive indices n_k and the growth rates v_k. The refractive index for sapphire has been taken from literature [7] and the nitrogen and hydrogen atmosphere in the growth chamber has been assumed to be comparable to ambient. A comparison with previous works [8], [9] leads to a very good agreement of the measured refractive indices for GaN.

	k	ω_k [s^{-1}]	$\|\rho_k\|$	V_k [nm s^{-1}]	n_k
Al_2O_3	0	-	0	-	1.78
GaN	1	0.0533	0.0614	1.094	2.403
AlGaN	2	8.68 10^{-3}	0.0557	0.182	2.351
Ambient	3	-	-	-	1

Tab. I: Experimental results of $|\rho_k|$, the angular growth velocity, the growth rate and the resulting refractive indices for GaN and AlGaN layer at 1050°C.

The refractive index of $Al_xGa_{1-x}N$ shows a strong dependence on the achieved Al concentration x which was determined to be x=20.7% in the considered sample as proven by x-ray diffraction. The relative change at the GaN/AlGaN interface of $\Delta n = -0.052$ is comparable with literature data [10] for similar Al concentrations at room temperature.

Conclusion and Outlook

We have demonstrated that Fourier analysis of kinetic reflectometry measurements acquired during a MOCVD process leads to fast and accurate information about the deposited layers, including optical properties, growth rate and layer thickness. The method eliminates offset errors resulting from thermal radiation from the reactor chamber and does not need careful calibration. Furthermore the measured signal is independent on an absolute scale. Further potential of applied Fourier transformation on kinetic reflectometry data is expected for periodic grown structures as shown in ref. [6].

References

[1] A. Bonanni et. al., J. Cryst. Growth **275**, 1763 (2005)

[2] N. Dietz, Mat. Sci. Eng. B **87**, 1 (2001)

[3] B. Beaumont et. al., J. Cryst. Growth **170**, 316 (1997)

[4] H. Protzmann et. al., J. Cryst. Growth **221**, 629 (2000)

[5] C. Simbrunner et. al., phys. stat. sol. (a) **203**, 1704 (2006)

[6] C. Simbrunner et. al., J. Appl. Phys., submitted

[7] I. H. Malitson, J. Opt. Soc. Am. **52**, 1377 (1962)

[8] C. Liu et. al., phys. stat. sol. (c) **3**, 1884 (2006)

[9] U. Tisch et. al., J. Appl. Phys. **89**, 2676 (2001)

[10] N. A. Sanford et. al., J. Appl. Phys. **94**, 2980 (2003)

In-situ Growth Observation of GaN/AlGaN Superlattice Structures by Simultaneous x-Ray Diffraction and Ellipsometry

C. Simbrunner[1], Tian Li[1], M. Wegscheider[1], A. Navarro-Quezada[1], M. Quast[1], A. Bonanni[1], A. Kharchenko[2], J. Bethke[2], K. Lischka[3], H. Sitter[1]

[1] Institut für Halbleiter- und Festkörperphysik, Johannes-Kepler-Universität Linz, A-4040 Linz

[2] PANalytical B.V., Almelo, The Netherlands

[3] Department of Physics, University of Paderborn, Germany

A considerable effort has been lately invested in the improvement of optical-based *in-situ* methods for the real-time control of metallorganic chemical vapor deposition (MOCVD) processes. In this report we present a novel approach combining *in-situ* x-ray diffraction and spectroscopic ellipsometry applied during the MOCVD of GaN/AlGAN superlattices.

Introduction

During the last years III-nitride semiconductors established for the production of opto- and high power electronic devices [1]. The optimization of superlattice structures (SL) is the key to increase the efficiency of several devices, *e.g.* nitride based vertical cavity surface emitting lasers. Furthermore, low dimensional structures improve the electrical properties of semiconducting materials [2]. Metal organic chemical vapor deposition (MOCVD) of epitaxial layers works at non-ultra high vacuum conditions and consequently electron based methods like reflection high energy electron diffraction are excluded from the possible spectrum of *in-situ* characterization techniques, narrowing the window to optical based ones like spectroscopic ellipsometry (SE) [3], [4], laser reflectometry [5], [6] and in-situ x-ray diffraction (IXRD) [7], [8]. Recently, complementary techniques have been combined, leading to consistent and extended information, as it was shown for SE combined with laser reflectometry [9] and micromechanical cantilever-based sensing [10]. In this article we focus on the *in-situ* and on-line monitoring of the MOCVD of GaN/AlGaN superlattice structures, accomplished through a novel approach based on the simultaneous use of SE and IXRD. The combination of surface- and bulk-sensitivity yields complementary and consistent information on the growing layers.

Experimental Procedure

All experiments were performed in an AIXTRON 200 RF-S horizontal flow reactor whose geometry allows simultaneous SE and IXRD *in-situ* measurements. Further details on the IXRD setup and data acquisition can be found elsewhere [11], [12]. Two optical windows allow *in-situ* SE in the energy range 1.5 – 5.5 eV. By applying the common pseudosubstrate approximation (CPA) to kinetic ellipsometry data layer-thickness, -composition and growth rate can be determined [9], [13]. For epitaxial layers, a complex pseudo-dielectric function $\langle\varepsilon_p\rangle$, summarizing the whole sample structure, can be

obtained [13] and consists of an imaginary ε_i and a real ε_r part. In the case of an optically thick material, ε_r considered as a function of ε_i, generates in the complex plane logarithmic spirals, whose converging points represent the dielectric function of the growing layer at the given energy and temperature. Therefore, by choosing the ellipsometer wavelength above the energy gap of the growing material and by applying the CPA, $\langle\varepsilon_p\rangle$ and consequently the composition and growth rate of the growing layer can be determined in real time.

All samples have been fabricated using trimethylgallium (TMGa), trimethylaluminum (TMAl) and ammonia as precursors. Upon deposition of a low temperature GaN nucleation layer on the (0001) sapphire substrate, a GaN buffer layer of 1 µm was deposited using standard procedures [9]. In order to prove the complementarity of the two techniques, a 500 nm thick AlGaN layer was grown onto the GaN buffer and kinetic ellipsometry measurements at photon energy of 3.815 eV have been performed. The resulting values for ε_i are reported in Fig. 1(a) as a function of time. Fig. 1(b) outlines the acquired SE data in the complex plane by plotting ε_r as a function ε_i. By applying the CPA, data points have been fitted and are indicated by solid lines in the plots. The increasing time scale is indicated by arrows. Simultaneously measured IXRD spectra are given in Fig. 1(c) as a contour plot illustrating the spectral intensity as a function of time and of the detection angle Δε relative to GaN buffer peak. The time scale is taken relative to the start of the SL structure, grown onto the AlGaN intermediate layer, and has been synchronized for IXRD and SE measurements.

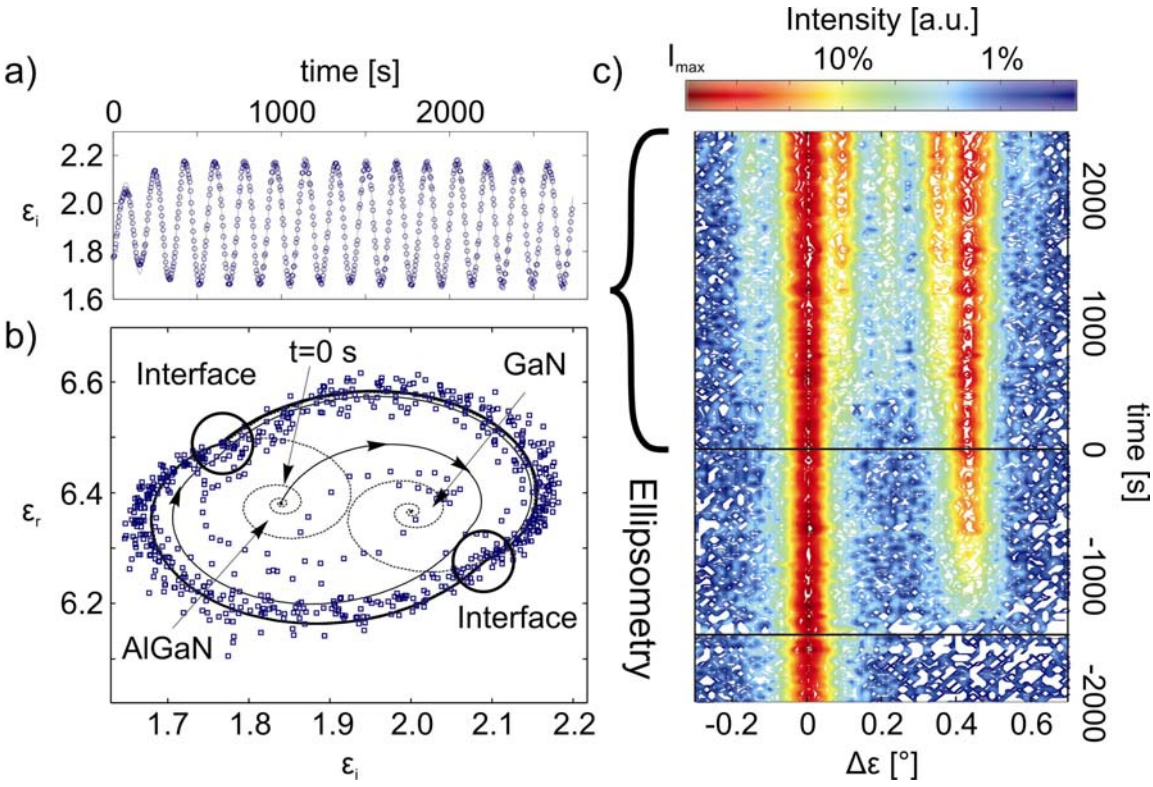

Fig. 1: (a) ε_i as a function of time. (b) ε_r as a function of ε_i acquired by SE during SL growth (blue rectangles). Solid lines represent the fit to the data. (c) Contour plot of IXRD spectra acquired simultaneously during GaN buffer, AlGaN and SL growth as a function of time and diffraction angle Δε relative to GaN buffer peak.

With the increase of the AlGaN layer thickness and due to the constant alloy composition, the value of ε_r as a function of ε_i converges on the complex plane. At t = 0 s the value corresponds to the pseudo-dielectric function of a growing layer with a well defined Al content. SE measured in the absorbing region of the growing compound ceases to provide information as soon as the layer becomes optically thick. On the other hand, at this thickness the layer is still transparent to the x-rays and a peak originating from the GaN buffer situated 500 nm below the surface is detectable. More detailed studies of the growing AlGaN layers show a dynamic behavior of the integrated peak intensity which increases linear with the layer thickness [7] and can be assigned to the increasing number of lattice planes contributing to the diffracted signal. By turning off the TMAl source at t = 0 s the deposition of the SL is accomplished by periodically switching the TMAl source every 90 s. As an effect of the change to GaN growth $\varepsilon_i(\varepsilon_r)$ follows a different logarithmic spiral converging at the center of the GaN helix, as shown in Fig. 1(b). The oscillations of ε_i as a function of time reported in Fig. 1(a) result from the periodic change of the growth conditions generating a competing behavior between GaN and AlGaN spirals. After 2 – 3 grown SL periods the SE response is balanced and results in two spiral tails in the complex plane indicated by solid lines in Fig. 1(b). Interfaces in the grown SL structure are characterized by discontinuity points of the spirals and underline the sensitivity of SE to surface effects.

The fitted SL periodicity and layer composition determined by SE are listed in Tab. I indicated by footnotes. The calculations are based on calibration curves relating the Al concentration to the corresponding dielectric function [9]. In contrast to the surface sensitive and fast responding SE, the SL peaks become visible in IXRD after 2 – 3 grown periods. By choosing for the SL the same Al concentration as for the AlGaN intermediate layer and with an identical period thickness for the GaN and AlGaN layers, the SL-0 peak is centered between the GaN buffer and the AlGaN intermediate layer peaks. By fitting the IXRD spectra the SL periodicity and concentration can be evaluated. The detected peak positions determine the achieved Al concentration by applying the Vegard's law and the periodicity can be easily deduced from the distances between the single SL peaks. The resulting values for GaN and AlGaN layer thickness and Al concentrations are listed in tab. I and are in excellent agreement with the values originating from SE measurements.

	d_{GaN} [nm]	d_{AlGaN} [nm[	Al conc.
AlGaN	-	-	15.02% (15.49%[a])
SL	36.07 (36.96[a])	36.29 (36.89[a])	14.05% (15.49%[a])

Tab. I: Fitted IXRD SL layer thickness and composition compared with values obtained by SE indicated by the footnote.

References

[1] O. Ambacher, J. Phys. D: Appl. Phys. **31**, 2653 (1998)

[2] A. Y. Polyakov, et. al., Appl. Phys. Lett. **79**, 4372 (2001)

[3] A. Bonanni, et. al., J. Cryst. Growth **275**, e1763 (2005)

[4] M. Drago, P. Vogt and W. Richter, phys. stat. sol. (a) **203**, 116 (2006)

[5] N. Dietz, Mat. Sci. Eng. B **87**, 1 (2001)

[6] B. Beaumont, et. al., J. Cryst. Growth **170**, 316 (1997)

[7] C. Simbrunner, et. al., phys. stat. sol. (a) **203**, 1704 (2006)

[8] P. Fuoss, et. al., Phys. Rev. Lett. **69**, 2791 (1992)

[9] A. Bonanni, et. al., J. Cryst. Growth **248**, 211 (2003)

[10] M. Godin, et. al., Rev. Sci. Instr. **74**, 4902 (2003)

[11] C. Simbrunner, et. al., J. Cryst. Growth **298**, 243 (2007)

[12] A. Kharchenko, et. al., Rev. Sci. Instr. **76**, 033101 (2005)

[13] D. E. Aspnes and N. Dietz, Appl. Surf. Sci. **130-132**, 367 (1998)

In-situ X-Ray Diffraction during MOCVD of III-Nitrides: an Optimized Evaluation Algorithm

C. Simbrunner[1], K. Schmidegg[1], A. Bonanni[1], A. Kharchenko[2], J. Bethke[2], K. Lischka[3], H. Sitter[1]

[1] Institute of Semiconductor and Solid State Physics, University Linz, A-4040 Linz

[2] PANalytical B. V., Almelo, The Netherlands

[3] Department of Physics, University of Paderborn, Germany

Presently, we are able to measure in situ x-ray diffraction and spectroscopic ellipsometry simultaneously on rotating samples during the deposition process in our MOCVD reactor using a commercial available PANalytical Cu ceramic tube as x-ray source. Due to the natural wobbling of the rotating sample a compensation algorithm is used before adding up single spectra in order to improve signal to noise ratio before fitting procedure. In this paper we present an improved compensation algorithm based on a symmetric peak shape enabling the calculation of the peak symmetry axes from the centre of weight.

Introduction

Gallium nitride (GaN) and its alloys promise to be key materials for future heterojunction semiconductors devices aimed at high frequency, high power electronic applications [1]. However, manufacturing of such high performance products is challenged by reproducibility and material quality constraints that are notably higher than those required for optoelectronic applications. To meet this challenge, we already implemented, to our knowledge the first time, in situ x-ray diffraction (IXRD) for the metalorganic chemical vapor deposition (MOCVD) of III-nitrides as a real-time process tool using a standard x-ray source [2].

Presently, we are able to measure IXRD on rotating samples during the deposition process and in order to improve the signal to noise ratio a summation of single spectra is done. Because of the natural wobbling effects in MOCVD, all the single spectra are shifted with respect to each other. Therefore, a correction has to be done before adding up the channel intensities.

The algorithm used so far is based on peak maxima detection and the maximum intensity is interpreted as the peak centre defining the relative correction shift. In this paper we present a novel algorithm which takes into account also the surrounding of the peak maxima and results in more precise information on growth rate, composition and crystal quality.

Experimental Procedure

GaN and AlGaN layers are grown on c-plane sapphire substrates in an AIXTRON AIX 200~RF-S horizontal flow MOCVD reactor using standard techniques [3]. The sub-

strate is rotating in the gas flow (about 15 rotations per minute) in order to improve the homogeneity of the growing layer.

On the reactor shell two Be windows enable the incidence of the x-rays focused by a Johansson monochromator and the detection of the diffracted beam. The x-ray setup consists of a PANalytical Cu x-ray source and a commercially available multichannel detector of the type X'Celerator [4]. Furthermore, an in-situ multi-wavelength spectroscopic ellipsometer (SE) provides additional information during growth.

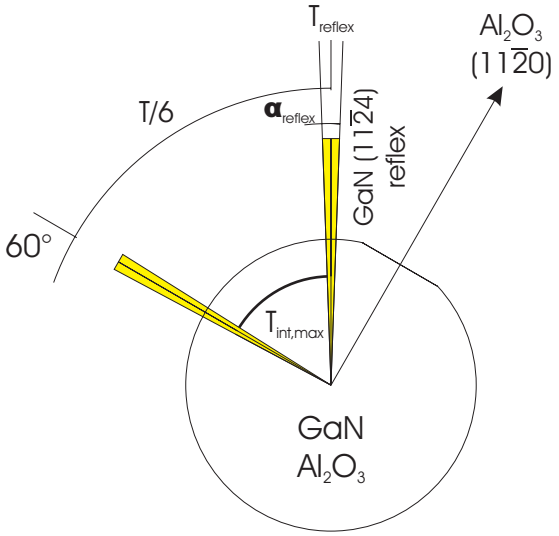

Fig. 1: Principal geometry of detected GaN (11-24) reflex (top view on the substrate).

The hexagonal GaN layer grows in the (0001) direction. The incident beam and the detector are adjusted in order to be sensitive to the (11-24) reflection of hexagonal GaN. Due to the hexagonal symmetry, the detector is illuminated six times per rotation period by a reflex which has an angular size defined by the angle α_{refl}. In connection with the rotation time of the sample (T) the time during which the reflex is visible for the detector (T_{refl}) is calculated by equation 1. To avoid a blur of the acquired spectrum only one GaN reflex must be included and this situation can be guaranteed by choosing a lower integration time than the critical integration time ($T_{int,max}$) which is defined by equation 1.

$$T_{int,max} = \frac{T}{6}\left(1 - T_{reflex}\right) = \frac{T}{6}\left(1 - \frac{\alpha_{refl}}{60}\right) \qquad (1)$$

On the one hand the use of integration times (T_{int}) below the critical time $T_{int,\,max}$ ensures that never more than one reflex is included in the resulting spectrum. On the other hand the reduction of the integration time leads to an increase of the probability (p_{empty}) to get empty spectra, decreasing in this way the efficiency of the system. Equation (2) defines p_{empty} as being proportional to T_{reflex} and the chosen integration time T_{int}.

$$p_{empty} = 1 - \left(T_{reflex} + T_{int}\right)\frac{6}{T} \qquad (2)$$

For the growth experiments, a constant integration time of about 90% of $T_{int,max}$ was used in order to ensure that only one reflex is included in the acquired spectrum, even if an increase of the rotation speed due to pressure or temperature changes in the growth chamber would take place.

In order to increase the signal to noise ratio, the single spectra have to be added up because of the unavoidable wobbling of the sample and due to the rotation during growth the spectra are shifted by an unknown angle in respect to each other. Previous works [2] report on an algorithm based on finding the maximum peak position (Pos_M) interpreted as the peak center and the point of reference. The results could be reasonable fitted at high enough spectral intensity expected at large layer thickness. An improved algorithm, working also at lower intensities, would represent a direct step toward an improved thickness resolution of the IXRD system.

For the results presented in this paper, we made use of a novel algorithm based on the fact that the reference peak has a symmetric shape. With this assumption the symmetry centre (Pos_{cw}) can be calculated from equation (3) by using the centre of weight of the reference peak. The detected maximum intensity of the spectrum (Pos_M) is taken as a first estimation of the centre of weight. The region around the maximum which should be included in the calculation can be defined by a constant (dk).

$$Pos_{cw} = \left(\sum_{k=Pos_M-dk}^{Pos_M+dk} I_k . x \right) \Big/ \left(\sum_{k=Pos_M-dk}^{Pos_M+dk} I_k \right) \qquad (3)$$

After compensation, the spectra are summed up and fitted by standard procedures [2].

Results and discussion

By using the data acquired during a standard AlGaN growth process typical spectra are analyzed by both rotation compensating algorithms. After growing a GaN buffer on Al_2O_3 an $Al_{0.21}Ga_{0.79}N$ layer of about 500 nm is deposited and an IXRD spectrum is taken every 1.6 s. In order to improve the fitting results, 20 single spectra have been added after wobbling compensation and analyzed with both algorithms.

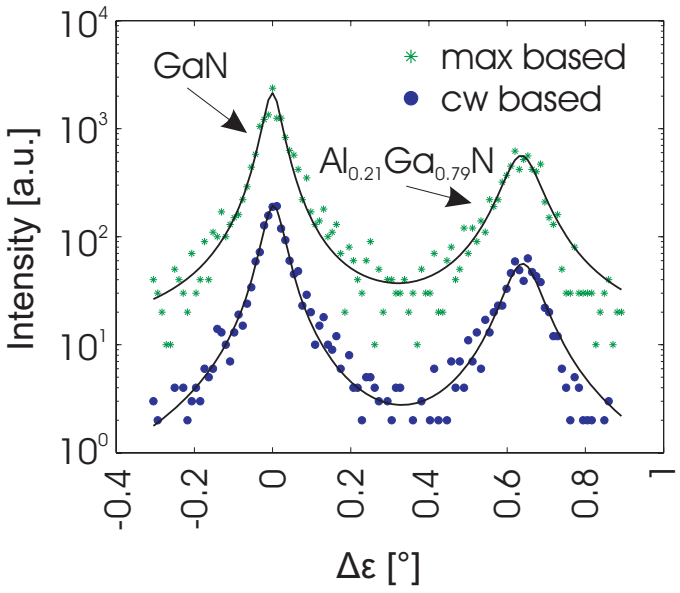

Fig. 2: 20 single spectra added up and fitted using the maximum based algorithm (star) and center of weight based algorithm (circles) as a function of angle Δε.

Figure 2 shows the intensity as a function of the diffraction angle of the scattered beam Δε relative to the GaN reference peak. A fit of the experimental points has been carried out by employing Pseudovoigt functions (solid lines).

For the top spectrum which is shifted for clarity by one order of magnitude represents the result by using the maximum based compensation algorithm. The fact that the channel with the maximum intensity is always shifted to $\Delta\varepsilon = 0$ results in a clearly visible overestimated peak intensity at this point. The lower spectrum (full dots) is the result of using the novel center of weight based algorithm which is not dominated by the previous described anomalous peak shape.

Summary

During MOCVD growth *in-situ* XRD spectra are acquired on rotating samples. In order to improve the signal to noise ratio the single spectra have to be added up before fitting procedure. Due to natural wobbling of the samples all single spectra are shifted in respect to each other which has to be compensated by an algorithm to avoid a blur of the added up spectra. We presented a new rotation compensation algorithm which is based on the symmetry of the peak all spectra are relatively shifted to. As a consequence the novel algorithm, taking into account also the surrounding of the peak maxima, results in a more precise information on growth rate, composition and crystal quality. Furthermore, the algorithm is more sensitive to small peak intensities, yielding an improved thickness resolution. The actual composition of the AlGaN layers could be determined already on a thickness of about 20 nm.

The obtained accuracy and the improved performance of the in-situ XRD setup represent a substantial step forward in the perspective of an effective closed-loop control of the MOCVD growth process.

Acknowledgements

The research was supported by the Austrian Foundation for Advancement of Scientific Research project P17169, and by PANalytical, Almelo, Netherlands. Part of the laboratory infrastructure was funded by the Austrian Gesellschaft für Mikroelektronik (GMe).

References

[1] S. C. Jain, M. Willander, J. Narayan, R. Van Overstraeten, J. Appl. Phys. 87 (3), 965-1006 (2000)

[2] C. Simbrunner, K. Schmidegg, A. Bonanni, A. Kharchenko, J. Bethke, J. Woitok, K. Lischka, H. Sitter, Phys. stat. sol. (a), (2006)

[3] A. Bonanni, D. Stifter, A. Montaigne-Ramil, K. Schmidegg, K. Hingerl, H. Sitter, J. Cryst. Growth 248, 211-215 (2003)

[4] A. Kharchenko, K. Lischka, K. Schmidegg, H. Sitter, J. Bethke, J. Woitok, Rev. Sci. Instrum. 76, 033101 (2005)

Photoluminescence and Hall Studies of GaN:Fe and (Ga,Fe)N:Mg Layers

M. Wegscheider[1], C. Simbrunner[1], H. Przybylińska[2], Tian Li[1], M. Kiecana[2], M. Sawicki[3], A. Navarro-Quezada[1], H. Sitter[1], W. Jantsch[1] , T. Dietl[2,4] and A. Bonanni[1]

[1] Institut für Halbleiter- und Festkörperphysik, Johannes Kepler University, Altenbergerstr. 69 4040 Linz, Austria

[2] Institute of Physics, Polish Academy of Sciences, al. Lotników 32/46, 02-668 Warsaw, Poland

[3] Institute of Physics and ERATO Semiconductor Spintronics Project, Polish Academy of Sciences, al. Lotników 32/46, 02-668 Warsaw, Poland

[4] Japan Science and Technology Agency

Temperature dependent photoluminescence (PL) in the ultraviolet regime and Hall measurements at room temperature have been performed on Metal-Organic-Chemical-Vapor-Deposition grown GaN:Fe and (Ga,Fe)N:Mg layers. PL measurements were employed in order to study the dopants' influence on the near-band edge excitonic emission and their tendency to provoke the formation and suppression of defects or incorporation of impurities. For their identification and for the understanding of the PL spectra the evaluation of the free carrier concentrations via Hall measurements was necessary. Depending on the iron concentration of the (Ga,Fe)N layers, the near-band edge emission goes through two different stages: at low Fe-concentration no excitonic emission can be seen whereas with higher doping levels, excitonic features develop. The (Ga,Fe)N films exhibit n-type behavior. The Mg codoped samples show strong Mg and defect related luminescence bands, whose occurrence and intensity also strongly depends on whether high or low Fe concentration is present. The (Ga,Fe)N:Mg layers were semi insulating.

Introduction

Transition metal doped GaN has been predicted theoretically to be an apt candidate for the realization of novel Diluted Magnetic Semiconductors (DMS) for spintronic applications. Employing Zener's model of ferromagnetism, Dietl et al. [1] calculated a Curie temperature TC exceeding room temperature (RT) for p-type Mn doped GaN. These layers have a Mn concentration of 5% and $3.5x10^{20}$ holes/cm^3, which is necessary for carrier-mediated exchange coupling between localized spins and thus ferromagnetic spin alignment. The localized spins are provided by the transition metal incorporated substitutionally on Ga lattice sites. The Zener type ferromagnetism for GaN:Mn could not be realized due to the presence of a Mn^{3+} level decreasing the free hole concentration [2]. Thus, our research has switched to the promising material system GaN:Fe and (Ga,Fe)N:Mg.

Experiments

Temperature dependent PL in the ultraviolet (UV) regime and Hall measurements at RT have been performed on Metal-Organic-Chemical-Vapor-Deposition (MOCVD) grown GaN:Fe and (Ga,Fe)N:Mg layers. Two different doping procedures have been

employed: bulk and delta doping. In the bulk-doping, the doping precursor-line valve was opened during the whole layer growth. This procedure was employed for the GaN:Fe samples presented in this work. In the case of the delta-doping, the doping elements have been brought into the films layer by layer, separated by a pure GaN intermediate layer of about 25 nm. Thus the growing sequence is …GaN/Fe/GaN/Mg… etc.

PL measurements were employed in order to study the dopants' influence on the near-band edge excitonic emission (NBEE) and their tendency to provoke the formation and suppression of defects or incorporation of impurities. For their identification and for the understanding of the PL spectra the evaluation of the free carrier concentrations via Hall measurements was necessary.

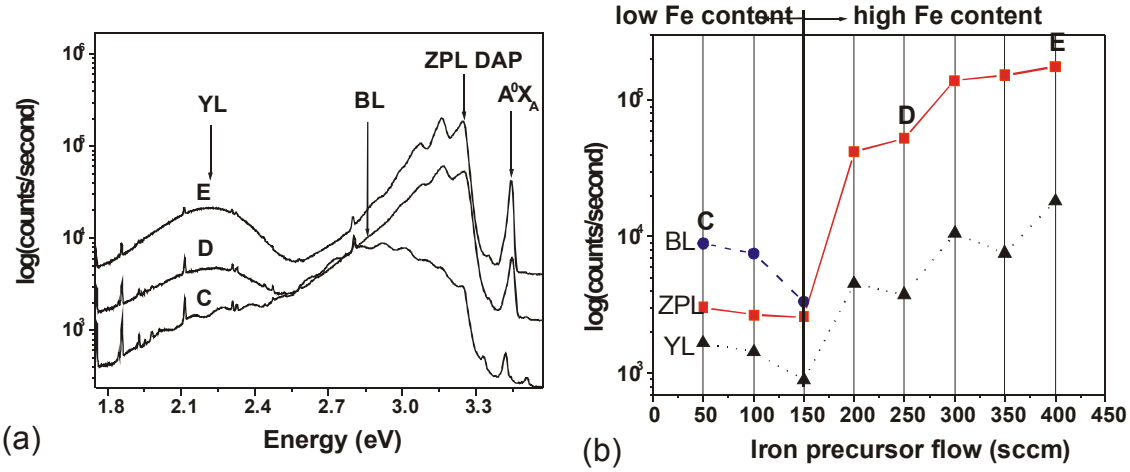

Fig. 1 (a) PL spectrum of samples A and C at 10K. The inset shows the excitonic region of sample C with its donor-bound-exciton (D^0X_A), two-electron-satellite ($D^0X_{A,n=2}$) and phonon replicas of bound (D^0X_A +LO) and free exciton (FX_A+LO). (b) shows in logarithmic scale the evolution of the NBEE as a function of the iron precursor flux for a whole series of samples.

Results and Discussion

1. GaN:Fe:

Sample A was grown with an iron precursor flow of 50 sccm and sample C with a flow of 350 sccm. The spectrum of sample A exhibits a defect-related yellow luminescence (YL) band which centers at 2.2 eV and a second weakly developed blue luminescence band (BL) peaked at 2.8 eV. On the spectrum of the highly iron doped sample C, these bands can be seen as well. In addition, the spectrum exhibits a fairly strong NBEE, whose intensity turned out to scale strongly with the iron precursor flux. Figure 1(b) shows the development of the intensity of the NBEE as a function of the iron content of a whole series of differently doped GaN:Fe samples. At low fluxes, practically no NBEE is formed, whereas between a flux of 150 sccm (sample B) and 350 sccm (sample C) the intensity rises by about three orders of magnitude. The peak broadening of the NBEE is, with a FWHM of 4.65 meV, quite large. It differs from sample to sample only slightly and could not be correlated with the Fe-content. Hall measurements at RT revealed n-type character of these samples and resulted in electron concentrations between $6.7x10^{16}$ for sample B and $9.1x10^{17}$ electrons/cm³ for sample C rising with in-

creasing iron flux. The exact origin of the increased electron concentration in the Fe-doped samples compared to the GaN ones is unknown at present due to difficulties in distinguishing between the contributions from nucleation, buffer and doped layer. Comparison of the determined positions and thermal activation energies with PL studies on MOCVD grown nominally undoped GaN [3] allows to attribute the NBEE to a neutral-donor-bound exciton D^0X_A that is related to the upper valence subband of hexagonal GaN. The low intensity emission at 3.4609 eV (see inset in Fig 1(a)) is assigned to a two electron satellite $D^0X_{A,n=2}$, where the dissociation of the D^0X_A leaves the donor in its excited n=2 state [4] – [6]. From the distance of the principal D^0X_A line and the $D^0X_{A,n=2}$ times 4/3 the donor-ionization energy can be obtained. In our case it results in E_D ~ 30 meV and is comparable to the value determined before. The values of E_D point to oxygen or silicon as principal binding site for the D^0X_A [7] as confirmed by an increase in the oxygen and silicon concentration from SIMS data, but interstitially incorporated iron acting as a double donor can not be excluded. The inset in Fig. 1(a) also presents the longitudinal phonon (LO) replica of the D^0X_A and FX_A. The comparison of the intensities of the phonon replica illustrates a weaker phonon coupling of the bound than of the free exciton. From the results presented above, it seems likely that depending on the iron doping level, two types of spectra are measured: with low Fe concentration, the excitonic luminescence measured on nominally undoped GaN reference sample vanishes. The reason could be that due to the introduction of a donor $Fe^{3+/4+}$ and an acceptor $Fe^{2+/3+}$ state [8], the free carriers forming excitons are trapped immediately after excitation. At high doping fluxes the dominating excitonic emission of pure GaN appears again. From AFM, MFM and TEM studies it can be argued that the growth mode is changed when reaching the saturation limit of Fe in GaN [3], [9] leading to regions of pure GaN in the (Ga,Fe)N films. The saturation limit seems to be related to an iron content of about 1– $3x10^{20}$ iron atoms/cm³ corresponding to a precursor flux of 150 sccm. Another explanation is that due to the elevated electron concentration the Fe charge state is shifted towards a higher Fe^{2+}(d6) state resulting in a lower suppression of the exciton formation since the $Fe^{3+/4+}$ donor state can not be active any more.

2. (Ga,Fe)N:Mg:

As mentioned above, the Mg-Fe codoped samples have been grown following a delta-doping procedure at 950 °C. The single iron or magnesium delta layers are separated by about 25 nm of pure GaN. The Mg flux was kept at 350 sccm whereas the iron flux was varied between 50 and 400 sccm. Hall measurements revealed a semi insulating character of this series. Fig. 2(a) shows PL spectra of samples D, E and F at 10 K. The iron fluxes of the three samples were 50, 250 and 400 sccm. The spectra exhibit three luminescence bands, a YL band peaked at 2.2 eV, a blue luminescence band (BL) centered at 2.8 eV and the third band which has its zero-phonon-line (ZPL) at 3.25 eV. The development of the intensities of these three bands over the iron flux is presented in Fig 2(b). The intensities of the YL and the 3.25 eV ZPL emissions rise, whereas the BL quenches with increasing Fe-concentration. The intensity of the 3.25 eV ZPL rises two orders of magnitude between 150 and 400 sccm. The calculation of the activation energy from its thermal behavior leads to a value of 58.6±17.6 meV. The authors of Ref. [10] and Ref. [11], respectively, report on the formation of similar band at 3.27 eV particularly in n-type silicon codoped GaN:Mg and slightly doped GaN:Mg. They assign this emission to a shallow donor-shallow acceptor pair transition, but report on an activation energy of 210 meV and 160 meV attributed to the thermal release of trapped holes from the Mg acceptor state. However, as we can not consider the effect of band-benching and potential-fluctuations introduced by the delta doping procedure at the moment, an interpretation of the measured values remains difficult. The BL intensity lowers with increasing iron content. The free holes of GaN:Mg are most likely compensated with the introduction of iron raising the Fermi level and thus the formation energy [12] of the deep defect-related donor complex that is responsible for the 2.8 eV transi-

tion. The YL band quenches with iron contents between 50 and 150 sccm, followed by a strong increase between 150 and 400 sccm. This is probably due to a change in the defect states leading to the YL due to iron doping to be confirmed by the evaluation of activation energies on low and high Fe doped (Ga,Fe)N:Mg layers from further temperature-dependent PL studies. The narrow emission at 3.445 eV labeled A^0X_A is commonly attributed to an acceptor-bound exciton whose binding sites are Mg acceptors [13].

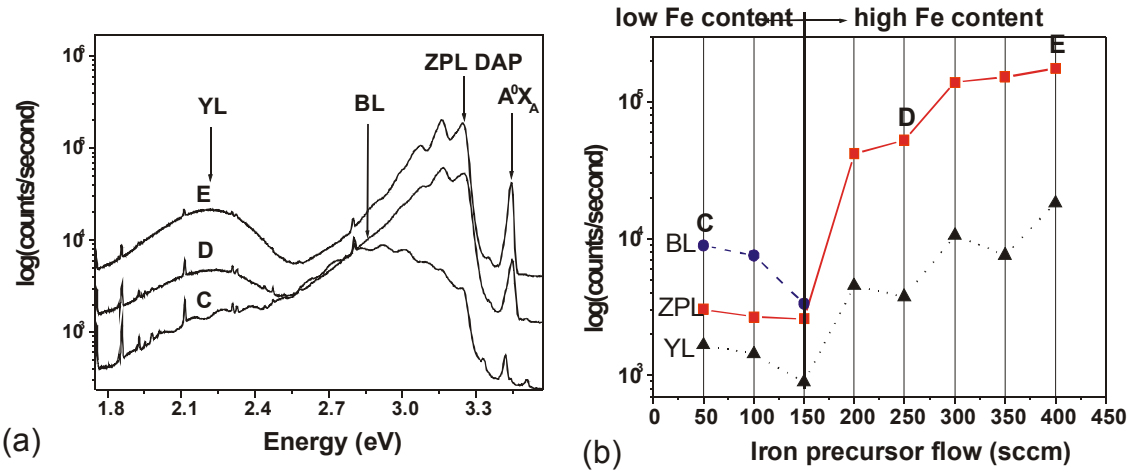

Fig 2: (a) PL spectra of samples D, E and F at 10 K. (b) Evolution of the intensity of the three luminescence bands over iron precursor flux for a whole (Ga;Fe)N:Mg series.

Conclusion

Temperature dependent PL and Hall measurements have been made on MOCVD grown GaN:Fe and delta doped (Ga,Fe)N:Mg samples. The spectra of both material systems exhibit a dependence on the iron precursor flux in the MOCVD process and thus on the overall iron concentration. Different PL transitions can be measured, for high and low iron concentrations. GaN:Fe spectra show a donor-bound exciton whose intensity scales with the iron flux. In contrast, the codoping of Fe and Mg leads to the formation of defect bands, especially to the formation of DAP transition at 3.25 eV as well as an acceptor-bound exciton. In both materials, a threshold for the formation of the iron-related emissions of 150 sccm iron precursor flux can be stated. We attribute this behavior to the saturation concentration of iron on Ga sites, where new, secondary phases are formed and interstitial iron incorporated. Hall measurements reveal n-type behavior of the GaN:Fe layers and a semi insulating character of the codoped samples.

References

[1] T. Dietl, H. Ohno, F. Matsukura, J. Cibert and D. Ferrand, Science 287, 1019 (2000)

[2] H. Przybylińska, A. Bonanni, A. Wolos, M. Kiecana, M. Sawicki, T. Dietl, H. Malissa, C. Simbrunner, M. Wegscheider, H. Sitter, K. Rumpf, P. Granitzer, H. Krenn, W. Jantsch, Marterials Science and Engineering B 126, 222 (2006)

[3] M. Wegscheider, unpublished data

[4] A. Wysmolek, K. P. Korona, R. Stępniewski, J. M. Baranowski, J. Błoniarz, M. Potemski, R. L. Jones, D. C. Look, J. Kuhl, S. S. Park, S. K. Lee, Phys. Rev. B 66, 245317 (2002)

[5] K. P. Korona, Phys. Rev. B 65, 235312 (2002)

[6] B. Monemar, J. Phys.: Condens. Matter 13, 7011 (2001)

[7] J. K. Sheun, G. C. Shi, J. Phys.: Condens. Matter 14, R657 (2002)

[8] U. Gerstmann, A. T. Blumenau, and H. Overhof, Phys. Rev. B 63, 075204 (2001)

[9] H. Przybylińska et al., unpublished work

[10] B. Han, J. M. Gregie, B. W. Wessels, Phys. Rev. B 68, 045205 (2003)

[11] M. A. Reshchikov, G.-C. Yi, B. W. Wessels, Phys. Rev. B 59, 13176 (1999)

[12] J. Neugebauer and C. G. Van der Walle, Phys. Rev. B 50, 11, 8067 (1994)

[13] S. Hess, R. A. Taylor, J. F. Ryan, N. J. Cain, V. Roberts and J. Roberts, phys. stat. sol. (b) 210, 465 (1998)

Lateral Quantum Dot in Si/SiGe Realized by a Schottky Split-Gate Technique

T. Berer, D. Pachinger, G. Pillwein, M. Mühlberger, H. Lichtenberger, G. Brunthaler, F. Schäffler

Institut für Halbleiter- und Festkörperphysik, Johannes-Kepler-Universität Linz, A-4040 Linz

Introduction

Single electron transistors (SET) in silicon/silicon-germanium heterostructures are of great current interest because of their envisaged use as elements for quantum computation [1]. Recently, several SETs in silicon/silicon-germanium have been reported [2] – [5]. However, none of these were achieved by the classical split-gate technique that is necessary for the coupling of quantum dots and for high integration. Furthermore, it was argued that a SET realized only with Schottky gates is not feasible because of excessive gate leakage currents which were attributed to threading dislocations. We report on the first Coulomb blockade measurements of a SET formed by the split gate technique on a modulation doped SiGe heterostructure.

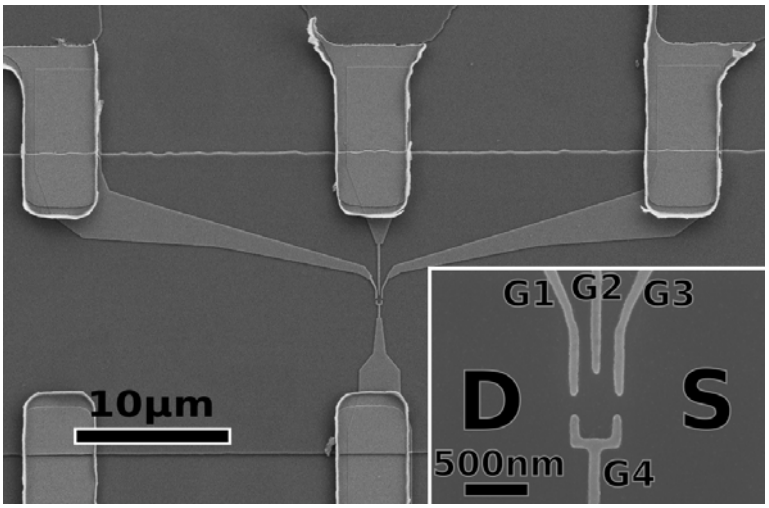

Fig. 1: Scanning electron micrographs of the palladium split gate arrangement on a mesa-etched Hall bar. The main image shows the complete area of the Pd gates including the leads to the bond pads. Insert shows the active SET region defined by the four split gates G1 – G4. The half-pitch of the upper gates is 90 nm.

Sample Preparation

The sample was grown in a Riber SIVA 45 Si molecular beam epitaxy (MBE) apparatus. The 2DEG is formed at the upper interface of a 150 Å thick strained Si channel grown on a 3 µm relaxed step graded buffer ($Si_{0.95}Ge_{0.05}$ to $Si_{0.75}Ge_{0.25}$). A 150 Å thick

$Si_{0.75}Ge_{0.25}$ spacer layer separates the channel from a 150 Å thick antimony doped $Si_{0.75}Ge_{0.25}$ layer. Finally a 450 Å thick layer $Si_{0.75}Ge_{0.25}$ and a 100 Å Si cap were grown. Electrical measurements at 1.5 K showed an electron mobility of 150000 cm^2/Vs at an electron density of 3.2 x 10^{11} cm^{-2}.

Ohmic contacts were formed by deposition of Au/Sb and subsequent annealing at 350 ºC for 60 sec. A Hall bar structure was prepared by reactive ion etching (RIE) with SF_6. Subsequently the split gate structures were written by e-beam lithography with a LEO Supra 35 SEM in PMMA. Finally the split gates were fabricated by using a lift-off technique after depositing a layer of Pd. The final structure is shown in Fig. 1. The pitch between the upper gates is 185 nm.

Experiments

As the feasibility of a Schottky-gate approach for SET applications on Si/SiGe heterostructures was generally questioned [2], [3], [6], we carefully characterized the I-V characteristics of the Schottky gates. For testing the worst-case condition, all four gates were connected in parallel to maximize possible leakage currents. The total gate area for the connected gates was about 150 μm^2. Down to a voltage of about –3 V the total leakage current is below 20 pA (Fig. 2), which is on the lower limit of our experimental setup [7]. Since the measurements we report below are observed at gate voltages between –1.6 V and –1.46 V, we stay safely within the non-conducting part of the diode characteristics.

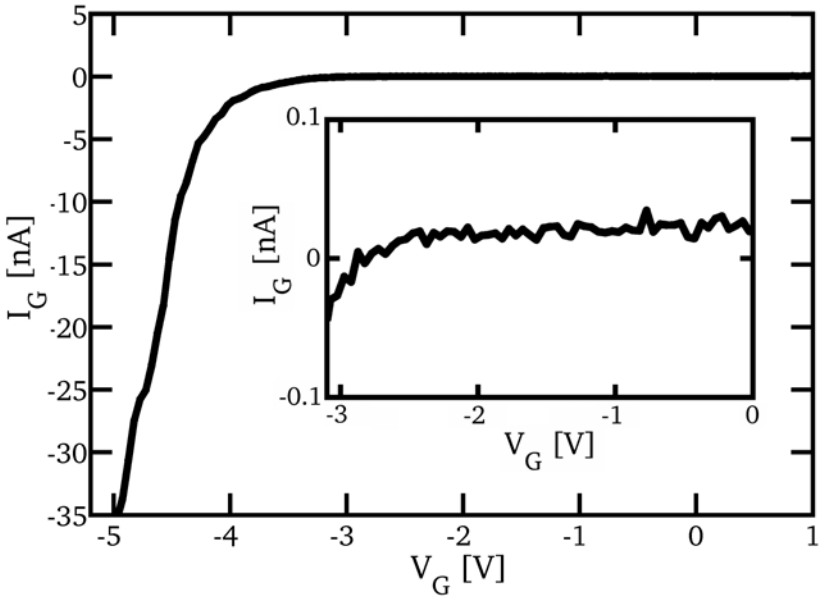

Fig. 2: I-V-characteristics of all gates connected in parallel to maximize possible leakage currents. Down to about –3 V the leaking currents are below the measurement accuracy. The insert shows a zoom-in of the non-conducting range of the diode characteristics.

By applying negative voltages to the gates the underlying 2DEG can be depleted and a quantum dot (QD) is formed. Negative voltages applied to gates G1 and G4, and G3 and G4 define the tunnel barriers, on the drain, and source side, respectively. The QD is controlled by the voltage applied to the plunger gate G2, and the voltage on G4. In the SET operation mode conductance between source and drain is measured as a function of the plunger gate voltage. For this purpose, we utilized a standard low fre-

quency lock-in technique [8]. The experiments were performed in a 3He/4He dilution refrigerator at a temperature of 30 mK. By scanning the voltage V_G, which was here applied to both gates G1 and G2 typical conductance oscillations where recorded (Fig. 3).

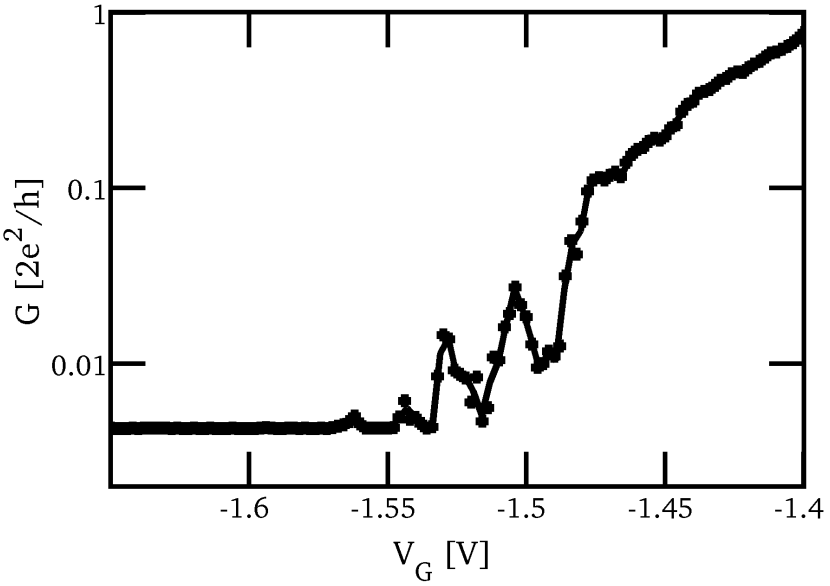

Fig. 3: Conductance oscillations measured at 30 mK by changing the gate voltages of gates G1 and G2 with fixed gate voltage at G3 and G4. One can distinguish different conductance peaks separated by vanishing conductance in the Coulomb-blockade regions. Lines are guides to the eye.

By measuring the conductance as a function of the plunger gate voltage and an additional DC voltage VDS applied between source and drain contacts, one can obtain the quantum dot spectrum, resulting in Coulomb blockade ''diamonds''. Figure 4 shows well resolved Coulomb blockade diamonds. Such experiments reveal the stability of the SET with regard to the number of electrons on the dot [8]. During the measurement time of about 70 h no indication for any transient in the number of electrons was found. Well-behaved Coulomb blockade diamonds were measured up to a temperature of 1.5 K, which was the maximum reachable temperature in the measurement apparatus.

By analyzing the distance between neighboring Coulomb diamonds and their confining slopes we estimated the gate and drain capacity to be C_G = 6.5 aF and C_D = 18 aF, respectively, and the total dot capacity to be C = 40 aF which results in a Coulomb charging energy of about 4 meV. Assuming the dot to be a metallic disc with radius R we estimated the dot radius to be about 50 nm, which corresponds to a maximum number of about 25 electrons on the dot and an estimated single particle energy spacing of 0.16 meV.

Conclusion

Our experiments demonstrate that Schottky-barrier reducing mechanisms can be overcome by adequately designed Si/SiGe heterostructures and that SET functionality can be achieved in modulation-doped Si/SiGe heterostructures with a standard split-gate approach that can easily be integrated into an array of coupled SETs as suggested in Ref. 1.

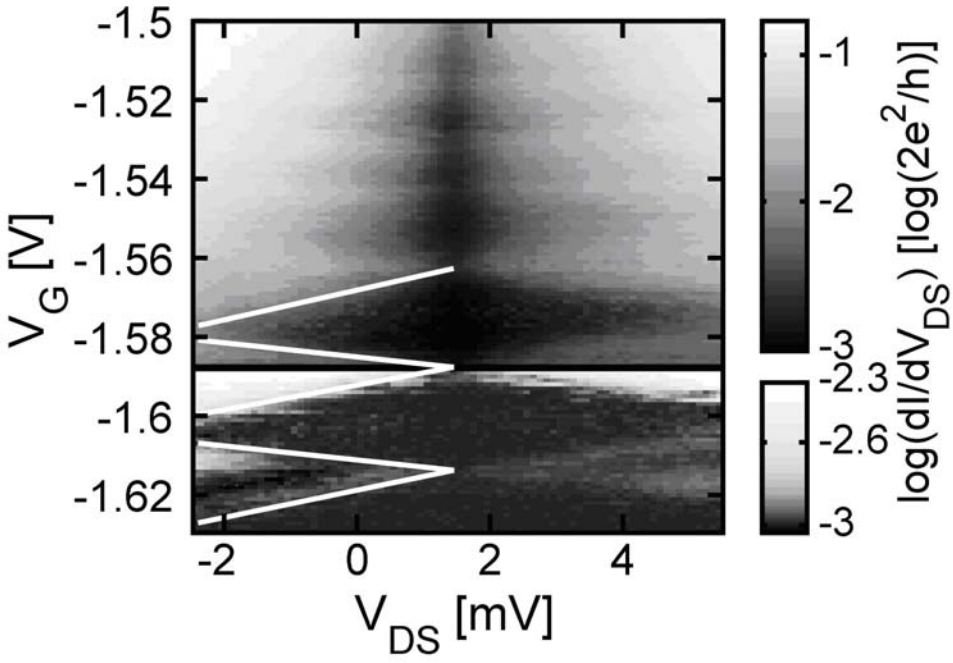

Fig. 4: Stability plot at 30 mK of the differential conductance through the dot as a function of the dc voltage V_{DS} between drain and source, and the gate voltage V_G applied to gates G1 and G2. Seven stability diamonds are clear visible.

References

[1] M. Friesen, P. Rugheimer, D. E. Savage, M. G. Lagally, D. W. van der Weide, R. Joynt, and M. A. Eriksson, Phys. Rev. **B 67**, 1213010 (2003)

[2] A. Notargiacomo, L. Di Gaspare, G. Scappucci,G. Mariottini, F. Evangelisti, E. Giovine and R. Leoni, Appl. Phys. Lett. **83**, 302 (2003)

[3] L. J. Klein, K. A. Slinker, J. L. Truitt, S. Goswami, K.L. M. Lewis, S. N. Coppersmith, D. W. van der Weide, M. Friesen, R. H.Blick, D. E. Savage, M. G. Lagally, Charlie Tahan, R. Joynt, M. A.Eriksson, J. O. Chu, J. A. Ott, and P. M. Mooney, Appl. Phys. Lett. **84**, 4047 (2004)

[4] P. W. Li, W. M. Liao, D. M Kuo, S. W. Lin, P. S. Chen, S. C. Lu, and M.-J. Tsai., Appl. Phys. Lett. **85**, 1532 (2004).

[5] K. A. Slinker, K .L. M.Lewis, C. C. Haselby, S. Goswami, L. J. Klein, J. O. Chu, S. N. Coppersmith, R. Joynt, R. H. Blick, M. Friesen, and M. A. Eriksson, New J. Phys. **7**, 246 (2005)

[6] S. Kanjanachuchai, T.J. Thornton, J.M. Fernandez, and H. Ahmed, Semic. Sci. Technol. **13**, 1215 (1998)

[7] T. Berer, D. Pachinger, G. Pillwein, M. Mühlberger, H. Lichtenberger, G. Brunthaler, and F. Schäffler, Appl. Phys. Lett. **88**, 162112 (2006)

[8] J.Weis, R.J.Haug, K.v.Klitzing, and K.Ploog, Phys. Rev. **B 46**, 12837 (1992), and Phys. Rev. Lett. **71**, 4019 (1993)

Bandstructure and Photoluminescence of SiGe Islands with Controlled Ge Concentration

M. Brehm, T. Suzuki, Z. Zhong, T. Fromherz, J. Stangl, G. Bauer

Institut for Semiconductor and Solid State Physics, University Linz, Austria

The dependence of the photoluminescence (PL) emission wavelength of SiGe islands embedded into a Si matrix on their Ge concentration and gradient was investigated. Intense PL signals at wavelengths that can be shifted over most of the telecom wavelength range (1.38 – 1.77 µm) by varying the Ge concentration were observed. Using the structural island parameters determined by AFM, TEM and a careful analysis of x-ray reciprocal space maps, good agreement between calculated and measured PL emission wavelength was achieved, indicating that by combining PL and x-ray experiments, an accurate determination of the Ge concentration and a quantitative modeling of the bandstructure of the SiGe islands is possible.

Introduction

Due to its indirect fundamental bandgap in k-space, bulk silicon – the dominating material for microelectronics – is not suitable for optoelectronic applications. Nevertheless, the demand for processing and transmitting a large amount of data in very short times is steadily increasing and intra-chip optical communication links will become more and more important in the near future [1]. Evidently, a Si based optoelectronic platform compatible with modern CMOS technology is highly desirable. Promising sources for light emission in the SiGe system are quantum dots (QDs). It is well known [2] that due to the strain field originating from the QDs, not only holes, but also electrons are bound to the QDs. Due to this confinement, the k-space selection rules are relaxed in all three dimensions. However, while the holes are bound to the Ge-rich region in the interior of the QDs, the electrons are localized in the Si matrix along the surface of the QDs. Thus a spatial indirect (type II) band alignment results and optical interband matrix elements are expected to be small. For optimizing the emission efficiency, a detailed understanding of the bandstructure and its dependence on the structural parameters of the SiGe dots is a prerequisite. In this work, we focused on the influence of the Ge content and its gradient along the growth axis on the emission wavelength and efficiency. Samples containing a single layer of SiGe QD were grown by solid source MBE in the cleanroom of the University Linz. For the Si buffer and QD layer, a growth temperature (rate) of 650 °C (1 Å/s) was used. On top of the buffer, a SiGe alloy layer with the target Ge concentration x_b for the base of the QD was deposited. The Ge flux was kept constant until 3D island nucleation was observed in the RHEED pattern and then ramped up/down in order to reach the desired Ge concentration x_t at the top of the QD. After QD growth, part of the wafer was covered by a shutter during the growth of the 150 nm Si capping layer. The capping layer growth started with a growth temperature (rate) of 450 °C (0.5 Å/s) and was ramped up after 10 nm to 650 °C (1 Å/s). TEM, AFM, and x-ray diffraction were used to investigate the structural parameters of the SiGe islands. These parameters served as input for calculating the bandstructure of the islands by the next**nano** code [3]. From the bandstructure, the emission energy of the islands is calculated and compared to the photoluminescence (PL) spectrum measured at 10 K

under excitation with an Ar-ion laser at a wavelength of 514 nm and an intensity of 5 W/cm^2.

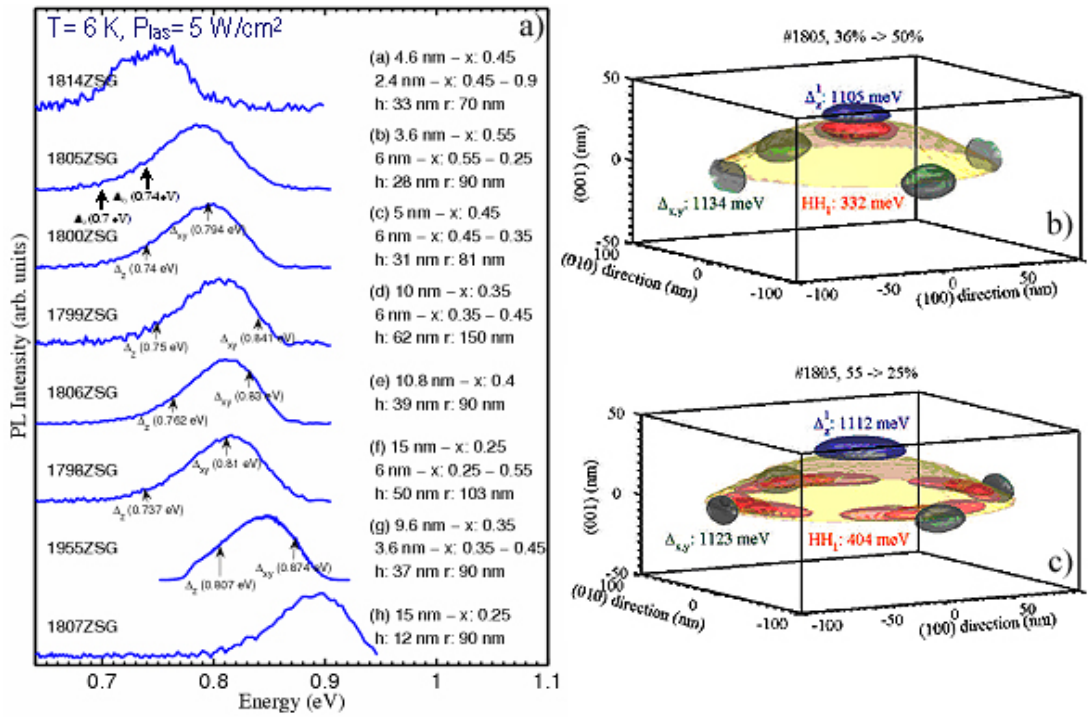

Fig. 1: (a) Measured PL spectra for SiGe islands with nominal structural parameters indicated in the plot. In b), c) the bandstructures for paraboloidal island (r: 90 nm, h: 28 nm) are compared for two different linear Ge gradients ((b) 36→50%; (c) 55→25%). The island surface is shown in yellow, the blue, green and red surfaces confine the regions in which $|\psi_{\Delta z}|^2$,$|\psi_{\Delta xy}|^2$,$|\psi_{HH}|^2$ are larger than 3% of their maximum. The holes are concentrated in the regions of the islands with maximum Ge concentration. The ring-like shape of the HH wavefunction in c) is caused by the strain in the island.

Results and Discussion

The part of the sample covered with a shutter during capping layer growth was used for measuring the dimensions of the QDs by AFM. Paraboloidal islands with base radii and heights between 70 –150 nm and 12 – 60 nm, respectively, as indicated in Fig. 1(a) are observed depending on x_b and x_t. The inter-island distance is typically a few nm in these samples. In Fig. 1(a), the measured PL spectra are shown. For all samples, an intense PL band is observed, the spectral position of which can be adjusted within the telecom range from 0.7 eV (1.77 µm) to 0.9 eV (1.37 µm) by the Ge content of the islands. The samples shown in Fig. 1(a) were grown with an intentionally varied Ge concentration during the growth of the islands. By establishing this gradient we tried to investigate the influence of the position of the electrons and holes in their respective groundstates on the luminescence efficiency and energy of the samples. As an example, the dependence of the groundstate positions on the Ge gradient is shown in Figs. 1(b) and 1(c) for sample 1805. For two different Ge gradients (55 to 25% (nominal, Fig. 1(c)), 36 to 50% (Fig. 1(b))) the groundstate wavefunctions for the electrons and holes as calculated by next**nano** [3] are shown in a 3D isosurface plot. Here, the red, green and blue surfaces confine the spatial regions, within that the groundstate

$|\psi|^2$ for the heavy holes (HH), the electrons in the Δ-valleys oriented perpendicular (Δ_{xy}) and parallel (Δ_z) to the growth direction, respectively, are larger than 3% of the $|\psi|^2$ maximum. For isolated islands, the calculations show that the electron ground state with the lowest energy is the Δ_z state. A gradient with more Ge at the base than at the apex localizes the HH groundstate at the base (see Fig. 1(c)), resulting in an unfavorable configuration with vanishing overlap of the electron and hole groundstate wavefunctions. On the other hand, the overlap between the energetically higher lying Δ_{xy} states with the heavy hole (HH) groundstate is enhanced in this situation, and radiative Δ_{xy} – HH recombination seems to be more likely than Δ_z – HH recombination, given that the non-radiative lifetime in the Δ_{xy} states is large enough for a sufficiently large metastable electron population to be established there. The arrows shown in Fig. 1(a) indicate the calculated Δ_z – HH and Δ_{xy} – HH transition energies that were obtained by using the nominal structural parameters in the next**nano** [3] calculations. It is evident that for all samples shown in Fig. 1(a) the calculated energy difference between the Δ_z – HH and Δ_{xy} – HH transitions is smaller or comparable to the observed inhomogenously broadened width of the PL emission band. Thus, from comparing these data to the calculated transition energies, it is not possible to identify which transition (Δ_z – HH or Δ_{xy} – HH) is observed. Most probably, the broadening of the PL emission bands is due to a statistical variation of the island size and distance (the influence of the island distance will be discussed in the following). Also the observed shift of the PL line for the various samples is smaller than the calculations based on the nominal structural island parameters indicate. In order to determine the actual structural parameters, and to check whether the designed Ge gradient was correctly established in our growth process, extensive x-ray experiments were performed. In these experiments, we concentrated on the pair of samples with the largest gradient in opposite directions (#1805 and #1798). X-ray diffraction around the 004 and 224 reciprocal lattice points were performed at the beam line BW2 of Hasylab (Hamburg). For various assumed parameter sets for the Ge gradient and for the inter-island distance (the island dimensions were determined by AFM and TEM measurements), the strain distribution in the samples was calculated by finite element (FEM) calculations. Using the results of the FEM calculations, the x-ray intensity around the (115) reciprocal space points was calculated and compared to the measured reciprocal space maps. The best agreement between simulated and measured x-ray maps was achieved assuming that the lateral inter-island distance approaches zero. Under this assumption, for several combinations of x_b and x_t equally good agreement between simulated and measured maps can be obtained. For sample 1805, the range of x_t and x_b for that x-ray fits have been performed, is shown on the abscissa of Fig. 2 (a) together with the nominal parameters (left end of axis) that are not compatible with the x-ray data. The gradients shown at the centre of the axis result in significantly better fits than the gradients on both ends of the axis. Large deviations from the nominal parameters follow from the x-ray analysis indicating that it is difficult to control the Ge gradient during the island growth. As an example for a good fit, the result of the x-ray simulation for sample #1805 assuming a linear gradient from x_b = 40% to x_t = 38% is shown by the contour lines in Fig. 2(b) superimposed over the experimental data. For the combinations of x_b and x_t shown in Fig. 2(a), next**nano**[3] energy band calculations have been performed. The calculated Δ_{xy}–HH and Δ_z–HH PL transition energies are shown by the green and blue symbols in Fig. 2(a). For the Δ_{xy}–HH transition, the results for two assumed lateral inter-island distances (infinity, 2 nm) are shown (light and dark green symbols). The calculations show that the Δ_{xy}–HH transition energy is sensitive to the inter-dot distance. This is because the energy of the Δ_{xy}-states is determined by the compressive strain in the Si around the base of the island. This energy is lowered if the strain fields of adjacent islands start to overlap. The dependence of the Δ_{xy}-HH transition energy on the lateral dot distance is shown in the inset of Fig. 2(a) for sample #1805 with an assumed Ge gradient of 40-38%. For this sample, the Δ_{xy} states become the electron states with the lowest energy

at an inter-island distance below ~10 nm. The measured energy and FWHM of the PL line observed for sample #1805 are indicated by the full and broken red lines in Fig. 2(a). For an assumed inter-dot distance of 2 nm, good agreement between calculated and measured PL transition energies is obtained for those gradients, for which also the x-ray simulations result in the best fits (40% – 32%, 40% – 38%). The other gradients shown in Fig. 2(a), for which the next**nano** [3] results also agree reasonably with the measured PL energy, produce no reasonable correspondence between measured and simulated x-ray data.

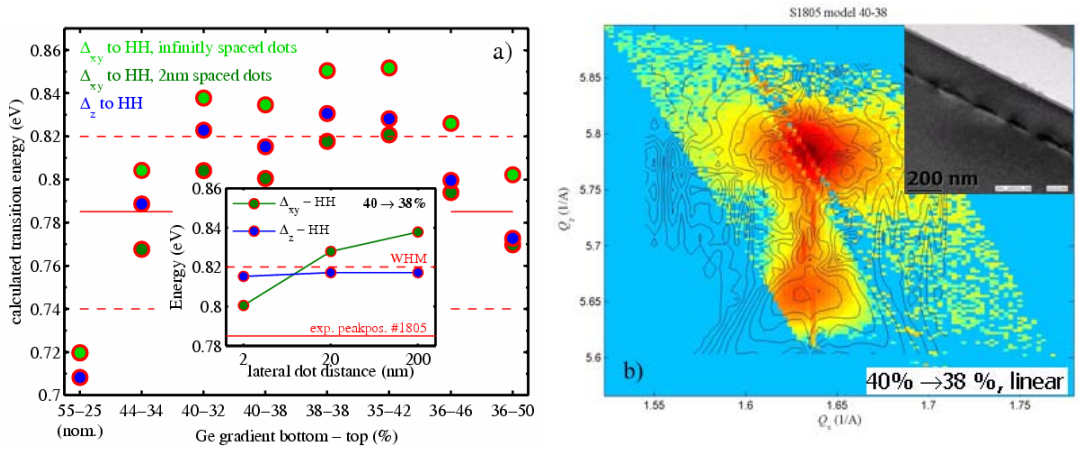

Fig. 2: (a) Calculated PL energies using the dimensions of sample 1805 and the Ge gradients indicated on the abscissa. Blue (green) symbols indicate the calculated $\Delta_z \rightarrow$HH ($\Delta_{xy} \rightarrow$HH) transition energies. Dark (light) green symbols indicate results for 2 nm (∞) spaced islands. Inset: Dependence of the calculated PL energies on the island separation for islands with 40 → 38% Ge gradient in more detail. The full (broken) red lines show the measured peak position (FWHM). (b) Measured (color) and simulated (full lines) x-ray reciprocal space map for sample 1805. The good fit shown was obtained for a Ge gradient of 40 → 38% and vanishing island spacing. Inset: TEM picture of sample 1805.

Summary

Intense PL bands are observed for single layer SiGe islands with intentionally varied Ge content grown by MBE. Depending on then Ge content, the PL emission wavelength is observed at various wavelengths covering the whole technologically important telecom wavelength range. From both the simulation of x-ray reciprocal space maps and the calculation of PL transition energies based on the next**nano** [3] code, the Ge concentration and its gradient within the islands can be determined consistently. The obtained results strongly deviate from the nominal values, indicating that a tight control of the Ge gradient in the islands is a difficult task. In addition to the variation of the island size, the statistical variation of the inter-island distance is identified as a source of inhomogenous PL line broadening.

Acknowledgements

This work was supported by the FWF (SFB IRON, Proj. Nrs. F2512-N08, F2507-N08).

References

[1] http://mph-roadmap.mit.edu/about_ctr/report2005/5_ctr2005_silicon.pdf

[2] O. Schmidt, Phys. Rev. B **62**, 16715 (2000).

[3] http://www.wsi.tu-muenchen.de/nextnano3/index.htm

Ordering of Strained Ge Islands on Prepatterned Si(001) Substrates: Morphological Evolution and Nucleation Mechanisms

G. Chen, H. Lichtenberger, G. Bauer, F. Schäffler, W. Jantsch

**Institut für Halbleiter- und Festkörperphysik,
Johannes-Kepler-Universität Linz, A-4040 Linz, Austria**

Introduction

The spontaneous formation of 3D islands during epitaxial growth of lattice-mismatched heteromaterials (Stranski-Krastanov [SK] growth) has become the most important self-organization mechanism for the fabrication of coherently embedded nanostructures. However, the randomness of island nucleation, and the broad distribution of their size severely restrict the application potential of this approach: Most electronic and spintronic device applications require the individual addressability of such nanostructures, and thus a means for the precise control of their nucleation sites.

We realized perfectly ordered SiGe and Ge islands in two (2D) and three dimensions (3D) by providing preferential nucleation sites through nanostructuring for the SK growth mode [1]. The islands nucleate preferentially at the bottom of reactively ion etched pits, which assume the shape of truncated inverted pyramids, after overgrowth with a thin Si buffer layer. This nucleation site is at first sight rather surprising, because it appears to be the least favorable site for strain relaxation within the pit template. To gain a better understanding of the mechanisms that lead to the preferential nucleation of the Ge dots there, we studied the very early stages of Ge coverage in detail [2].

Experimental

The samples were grown by solid source molecular beam epitaxy (MBE) in a Riber SIVA 45 reactor. Pit-patterned templates on Si(001) substrates were obtained by electron beam lithography and reactive ion etching (RIE) in SF_6. The pits form a regular two-dimensional grid ordered along two orthogonal <110> directions with a periodicity between 260 and 380 nm. After etching, the samples were chemically cleaned to remove RIE deposits and residues from the e-beam resist. Immediately before introduction into the MBE reactor the samples were treated in diluted HF to create a hydrogen terminated surface that stabilizes the nanostructures against transient enhanced diffusion during the following *in situ* thermal treatment at 900°C for 5 minutes. Since we wanted to characterize the very early stages of ordered Stranski-Krastanov growth on prepatterned substrates, we employed growth conditions that were optimized for this purpose over the last few years. MBE growth always commenced with a 100 nm thick Si buffer layer that was grown at a rate of 0.5 Å/s while ramping the substrate temperature from 450°C to 520°C. This procedure eliminates surface roughness and damage induced by RIE, but, most importantly, modifies the morphology and improves the homogeneity of the pattern. Subsequently, 0 (reference for the effect of the Si buffer alone), 2.6, 4, and 5 monolayers (ML) of Ge were deposited at 620°C and at a fixed

rate of 0.03 Å/s on samples A, B, C, and D, respectively. An additional series of samples (E, F, G) was grown to investigate the stability of the observed features. Under otherwise identical conditions, 5 ML of Ge were deposited at 670 and 570°C on samples E and F, respectively, and 9 ML at 570°C on sample G. The denoted substrate temperatures were calibrated with a thermocouple embedded into a Si reference wafer to an estimated accuracy of ±15°C. Since the rate for Ge deposition is at the lower limit of our flux controller, we further enhanced the migration of the deposited Ge atoms or dimers by growth interruption for 10 s after each deposited ML. Afterwards, the substrate temperature was quickly decreased, and the surface morphology was characterized *ex-situ* with a Digital Instruments atomic force microscope (AFM) in the tapping mode.

Results

Sample	A	B	C	D
Ge Coverage (ML)	0	2.6	4	5
Morphology	Faceted Inverted Pyramid	Corrugations Without Pyramid[1]	Corrugations With Pyramid[2]	Corrugations With Dome[3]

Tab. 1: Shows the morphological evolution in the samples with different Ge coverage.

[1]As exhibited in the AFM images in Fig. 1(a) and (b);
[2]As exhibited in the 3D model in Fig. 2;
[3]As exhibited in the AFM images Fig. 1(c) and (d);

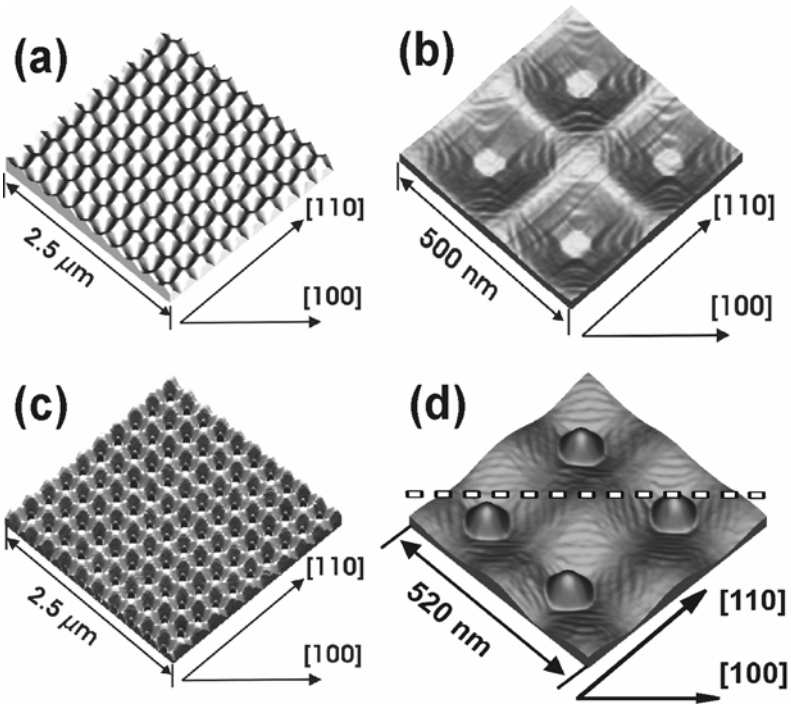

Fig. 1: AFM images in different scale for the pits after 2.6 ML Ge deposition [(a) and (b)]; after 5 ML Ge deposition [(c) and (d)], respectively..

The experiments showed that the initially forming Ge wetting layer develops a complex, but highly symmetric morphology on the inclined sidewalls of the pits [as described in Table 1].

This pattern is driven by strain- and surface energy minimization, and leads after the deposition of typically three monolayers of Ge to a conversion of the pit sidewalls into a pattern that consists exclusively of {105} and (001) facets. We attribute the subsequent islands nucleation to Ge accumulation at the bottom of the pits, which is driven by capillarity and the enhanced surface diffusion on the by now {105} faceted sidewalls of the pits. This complex interplay of mechanism in the confined geometry of the pits leads to preferential dot nucleation at the bottom of the pits despite the disadvantages of this site in terms of strain relaxation.

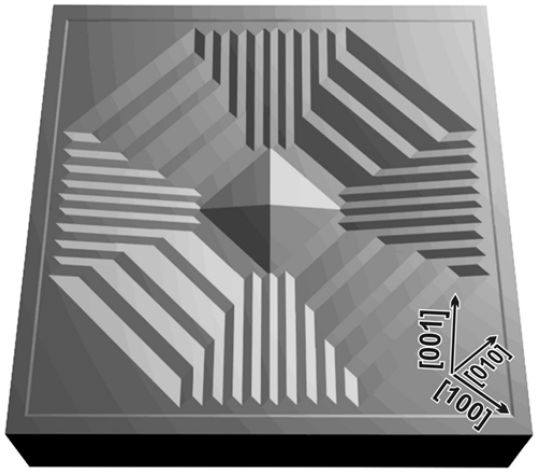

Fig. 2: Schematic 3D representation of the pit structure after the surface is converted into {105} and (001) facets. The central pyramid is pointing outwards. The 3D effect is seen best in the upper right corner.

Conclusion

The results show that SK growth in combination with nanostructured surfaces can be exploited for the implementation of perfectly ordered SiGe and Ge nanostructures that fulfill basic preconditions for meaningful device applications, namely addressability.

Acknowledgements

Valuable discussions with Z. Zhong are gratefully acknowledged. We thank H. Hoppe and G. Springholz for help with the AFM measurements. This work was financially supported by GMe (Vienna), FWF (Vienna) via Projects No.14684, No. 16631, No. 16223, and SFB 025, INTAS via Project No. 03-51-5015, as well as by EC Projects SANDIE, and D-DOTFET (EC012150).

References

[1] Z.Zhong et al., J. Appl. Phys. **93**, 6258 (2003).

[2] G. Chen, H. Lichtenberger, G. Bauer, W. Jantsch, and F. Schäffler, Phys. Rev. B **74**, 035302 (2006).

p-Modulation Doping on Si Step-Bunching Templates: Anisotropic Transport and Mobility Analysis for an Undulated SiGe-Channel

H. Lichtenberger, T. Berer, D. Gruber, G. Pillwein, G. Brunthaler, F. Schäffler

Institute of Semiconductor and Solid State Physics, Johannes Kepler University Linz, Austria

In this report first results on p-modulation doped Si/SiGe heterostructures grown on top of a rippled step-bunching Si-buffer are outlined. The short-scale periodic height fluctuations of the Si-buffer (Λ ~ 100 nm) are intended to form well-defined undulations in the SiGe-channel of the remotely p-doped quantum well, giving rise to increased scattering. Thus, an asymmetry in mobility, perpendicular and parallel to the undulations, is expected. This might help to uncouple the different scattering mechanisms, which are conversely discussed as predominant hole-mobility limiting factors for p-modulation doped quantum well structures (p-MODQW), namely alloy scattering and interface-roughness related scattering.

Introduction

Modulation-doped Si/SiGe heterostructures were first realized in 1984 with a SiGe quantum well sandwiched between the Si substrate and an unstrained Si-cap layer. Selective p-type doping in the Si cladding layers leads to an enhanced hole mobility for the established two-dimensional hole gas (2DHG) in the SiGe-channel which is formed according to the valence band offset. Historically later, n-doped structures featuring a two-dimensional electron gas (2DEG) were fabricated. Employing relaxed virtual $Si_{1-x}Ge_x$ substrates, an in-plane tensilely strained Si-channel is formed due to the conduction band offset. Such relaxed SiGe-buffers are nowadays also used in p-type structures with Ge-rich or even pure Ge-channels. Whereas for n-MODQW structures extremely high mobilities reaching values beyond 500 000 $cm^2V^{-1}s^{-1}$ were observed, p-MODQW structures seem to be restricted to hole mobilities around 20 000 $cm^2V^{-1}s^{-1}$ for SiGe-channels, and well below 100 000 $cm^2V^{-1}s^{-1}$ even for pure Ge-channels with a strongly reduced effective hole mass and absent alloy scattering. The origin of the vast difference in low-temperature mobilities is still not clear. Alloy scattering and interface-roughness scattering together with strain fluctuations arising from smeared-out Si/SiGe interfaces coming along with Ge-segregation and interface charges are discussed as the ultimate limitations regarding mobility. However many theoretical treatments are found in literature [1], [2] which usually adjust numerous parameters to fit the experimentally observed low-mobility results for p-modulation-doped structures. Thus, often the predictions for the dominant limiting scattering mechanism are different [3], [4].

Herein, first results on p-modulation doped Si/SiGe heterostructures grown on top of a rippled step-bunching Si-buffer are presented. The short-scale periodic height fluctuations of the Si-buffer (Λ ~ 100 nm) – which were extensively discussed in our preceding work [5] – [7] – are intended to form well-defined undulations in the SiGe-channel of the remotely p-doped quantum well, giving rise to increased scattering. Thus, an asymmetry in mobility, perpendicular and parallel to the undulations, is expected. This is in-

tended to uncouple the different scattering mechanisms, which are conversely discussed as predominant hole-mobility limiting factors for p-modulation doped structures, namely alloy scattering and interface-roughness related scattering.

Earlier experiments in this direction were published by Waltereit et al. [8] for n-modulation doped Si/SiGe heterostructures grown on vicinal Si(001) substrates on top of a compositionally graded strain-relaxed $Si_{0.72}Ge_{0.28}$ buffer. Also, by Neumann et al. [9], [10] anisotropic hole transport measurements on p-modulation doped SiGe channels on step-bunched vicinal Si(113) surfaces were reported. These however were performed on Si(113) which shows strong step-bunching but will hardly become of technical relevance. Our investigations are based on Si(001) substrates with a miscut of 4° which are also used commercially.

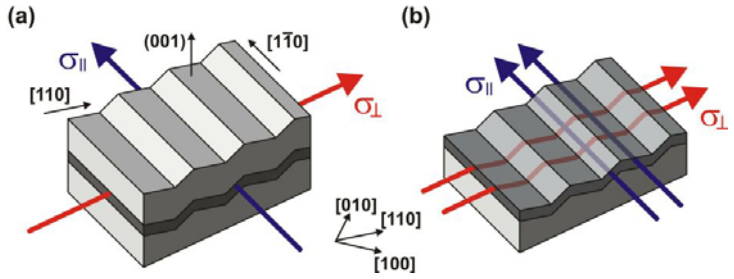

Fig. 1: Schematic drawings of a conventional p-SiGe modulation-doped structure with front-side doping. The conduction takes place at the upper interface of the SiGe-channel. The modulation of the channel yields expected differences in conductivity for measurements parallel ($\sigma_{\parallel}$) and perpendicular ($\sigma_{\perp}$) to the ripple structure.

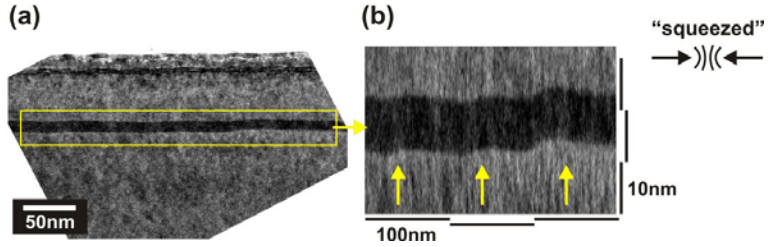

Fig. 2: (a) XTEM image of the $Si_{0.75}Ge_{0.25}$ channel of a miscut sample. The yellow box serves as guide to the eye to help resolving the periodic modulations (Λ ~ 100 nm) of the $Si_{0.75}Ge_{0.25}$ channel grown on top of the step-bunching template. (b) Representation of the same image squeezed together in lateral direction to emphasize the modulation of step-bunching for the SiGe-channel. The yellow arrows indicate the minima of the undulations with ~100 nm periodicity.

Experimental Procedure

The modulation-doped quantum well structures (MODQW) grown on a step-bunching template enable surface-roughness-dependent measurements on one and the same sample (Fig. 1) which makes the experiment and interpretation less sensitive to other growth-process- or sample processing-induced artifacts: Especially background impurity scattering is known to be hard to control and thus giving unpredictable results.

Low-temperature epitaxial growth in our solid source SiGe-MBE system is used to prepare the Si step-bunching buffer and to define a conformal 10 nm thick $Si_{0.75}Ge_{0.25}$-channel by suppressing strain-driven thickness fluctuations, which are known to occur already at moderately elevated temperatures. Cross-section transmission electron microscopy (XTEM) reveals the intended periodic modulation of the buried SiGe-channel (Fig. 2) with rather sharp interfaces.

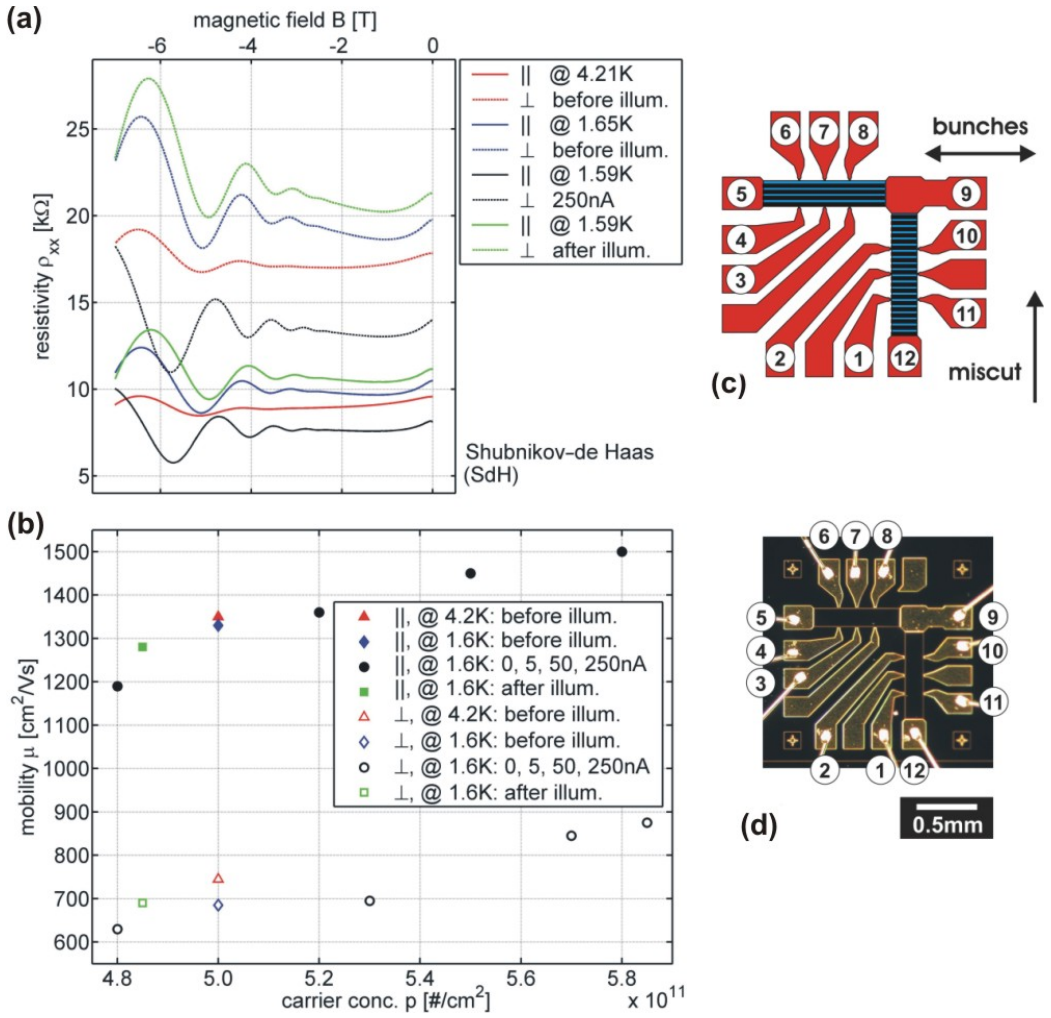

Fig. 3: (a) Plots of the longitudinal resistivity ρ_{xx} for the Hall-bars parallel (solid curves) and perpendicular (dashed curves) to the periodic modulations in the SiGe-channel due to step-bunching. (b) Evaluated data from (a) summarized in a plot showing mobility μ versus carrier concentration p_s. The data clearly prove a lower carrier mobility perpendicular to the ripples due to increased scattering. (c) Schematics of metal contact pads (red color) and etched Hall-bars (blue color). The line pattern indicates the elongation direction of step-bunching. Thus, the upper branch of the Hall-bar is used to measure the conductivity parallel to the bunches ($\sigma_{||}$), and the lower branch perpendicular to the ripple structure ($\sigma_{\perp}$). (d) Photograph of a processed Hall-bar, mounted and bonded onto a sample carrier.

The electrical characterization is performed in a ^{4}He-immersion cryostat with adjustable temperatures down to 1.6 K and magnetic fields up to B = 7 T. Magneto-transport measurements on a special two-branch Hall-bar geometry (Fig. 3(c) – (d)) are applied to extract important parameters from Shubnikov-de Haas oscillations in the longitudinal

resistivity ρ_{xx}. These are the carrier concentration p_s, the mobility parallel ($\mu_{||}$) and perpendicular ($\mu_{\perp}$) to the undulations in the SiGe-channel.

Results and Discussion

Although still at the beginning, the first measurements confirm a significant resistivity anisotropy with a decreased low-temperature mobility across the undulations by nearly a factor of two (Fig. 3). Such a remarkable effect was beyond expectations for the technologically relevant Si(001) surface.

The reported results, combined with additional modeling are expected to provide a new approach toward settling the long-lasting dispute on the limiting scattering mechanisms of the hole mobility in p-MODQW structures.

Summary

First results on p-modulation doped Si/SiGe heterostructures grown on top of a rippled step-bunching Si-buffer are reported. The short-scale periodic height fluctuations of the Si-buffer (Λ ~ 100 nm) are used to form well-defined undulations in the SiGe-channel of the remotely p-doped quantum well, giving rise to increased scattering. In fact, an asymmetry in mobility perpendicular and parallel to the undulations was found. This way the different scattering mechanisms might be uncoupled, to finally identify the predominant hole-mobility limiting factor for p-modulation doped structures.

Acknowledgements

The research was supported by GMe and FWF project P16223-N08.

References

[1] D. R. Leadley, M. J. Kearney, A. I. Horrell, H. Fischer, L. Risch, E. C. H. Parker, and T. E. Whall, Semicond. Sci. Technol. 17 (2002), 708–715.

[2] D. N. Quang, V. N. Tuoc, T. D. Huan, and P. N. Phong, Phys. Rev. B 70 (2004), 195336.

[3] F. Schäffler, Semicond. Sci. Technol. 12 (1997), 1515–1549.

[4] Y. Shiraki and A. Sakai, Surface Science Reports 59 (2005), 153–207.

[5] H. Lichtenberger, M. Mühlberger, C. Schelling and F. Schäffler, J. Cryst. Growth 278 (2005), 78–82.

[6] H. Lichtenberger, M. Mühlberger and F. Schäffler, Appl. Phys. Lett. 86 (2005), 131919.

[7] Herbert Lichtenberger, “Kinetic and Strain-Induced Self-Organization of SiGe Heterostructures”, PhD-Thesis, Institut für Halbleiterphysik, Johannes Kepler Universität Linz, August 2006.

[8] P. Waltereit, J. M. Fernandez, S. Kaya, and T. J. Thornton, Appl. Phys. Lett. 72 (1998), 2262–2264.

[9] R. Neumann, J. Zhu, K. Brunner, and G. Abstreiter, Thin Solid Films 380 (2000), 124–126.

[10] R. Neumann, K. Brunner, and G. Abstreiter, Physica E **13** (2002), 986–989.

Photo-ESR of Self-Organized SiGe Islands and High Frequency Effects on a Si 2DEG

H. Malissa[1], G. Chen[1], W. Jantsch[1], Z. Wilamowski[2]

[1]Institut für Halbleiter- und Festkörperphysik, Johannes Kepler Universität Linz, A-4040 Linz

[2]Institute of Physics, Polish Academy of Sciences, Warsaw, Poland

Photo-ESR on Self-Organized SiGe Islands

Introduction

Currently, there is much research activity on electron spins confined in zero dimensional structures [1], as they present a promising candidate for future spintronic and quantum computation applications [2] – [4]. In III-V compounds, the high degree of confinement leads to a significant increase in spin relaxation times [2], [3]. Earlier, we investigated self-organized Ge islands embedded in a Si buffer in photoluminescence (PL) and electron spin resonance (ESR) experiments in continuous wave (CW) and in time resolved mode [5] and found a single ESR line with a g-factor of g = 1.998, corresponding to electrons confined in the strained Si regions directly above the locations of the Ge islands [6]. This line appears only under the illumination with white light, which creates electron-hole pairs. The holes are localized inside the Ge islands, and the electrons in the strained Si regions nearby. Transitions between these two states are observed at 0.85 eV in PL experiments [5].

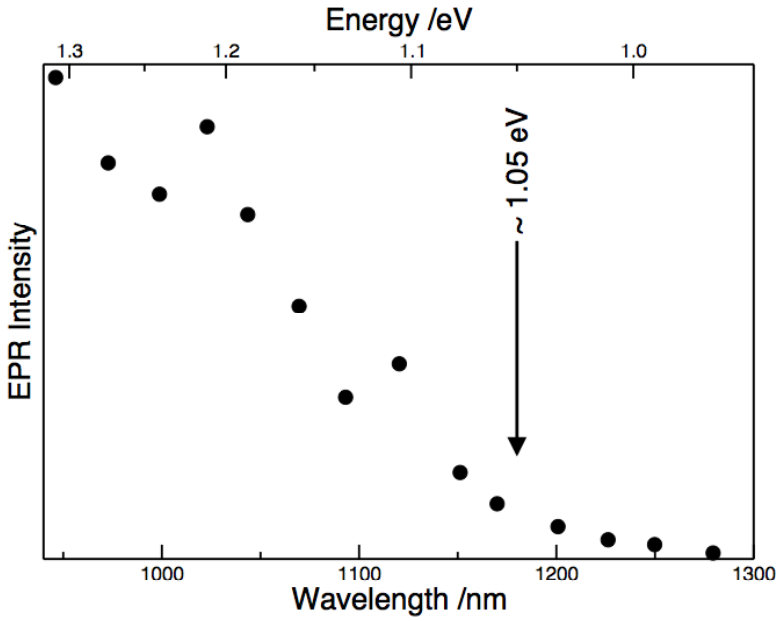

Fig. 1: ESR intensity as a function of wavelength/energy. A clear onset of ESR intensity is observed at 1.05 eV.

Experiment

During CW ESR at 2.5 K the sample is illuminated with monochromatic light from an optical parametric oscillator (OPO) source (details on the ESR experimental setup and the sample structure are found in Ref. [5]). At wavelengths around 1450 nm, corresponding to the transition energy from the Ge valence band (VB) to the strained Si conduction band (CB) states at 0.85 eV, no ESR intensity is detected. We find a strong increase of the ESR signal in the range of 1300 nm to 950 nm, with an onset at 1.05 eV, shown in Fig. 1.

Results and Discussion

The excitation from the Ge VB to the strained Si CB states at 0.85 eV in a photo-ESR experiment with monochromatic light is rather unlikely. For these transitions to occur, the OPO wavelength (energy) has to match the transition energy exactly, although there is a certain spread in transition energies due to fluctuations in Ge island sizes and locations [5].

Excitation from the Ge VB states above the band-gap, followed by relaxation into the strained Si regions, is much more probable. Such an excitation process is shown in Fig. 2. The observed onset at 1.05 eV appears quite realistic for it.

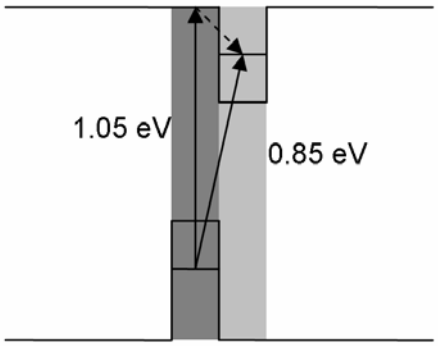

Fig. 2: Schematic sketch of the band structure variation along growth direction, through the center of a Ge island. The excitation from the Ge VB to the strained Si CB states at 0.85 eV is indicated, as well as the excitation from the Ge VB above the conduction band, followed by a relaxation into the strained Si CB (dashed arrow).

High Frequency Effects on a Si 2DEG

Introduction

Confinement of electrons in 2D structures, in particular in 2D electron gas (2DEG) in a Si/SiGe heterostructure has been extensively studied previously by us [7], [8]. We found that both the g-factor and the ESR line width are governed by the Bychkov-Rashba (BR) effect, arising from a structure inversion asymmetry introduced by the one-sided Sb modulation-doping layer in these structures. In the low field regime, the BR effect manifests itself by an effective magnetic field $\boldsymbol{B}_{BR}$ that is parallel to the 2DEG plane, perpendicular to the electron momentum. Recently, we reported on the direct observation of this BR field in the presence of an electric current that causes an additional contribution to the electron momentum vectors [9], [10]. When the sample is ori-

ented in such a way that this BR field is parallel to the external field, it can be simply observed as a shift in the ESR line. Rotating the sample around an axis perpendicular to the external field gives exactly the expected anisotropy: the effect vanishes for $\boldsymbol{B}_{BR} \perp \boldsymbol{B}_{ext}$ and is maximized for $\boldsymbol{B}_{BR} || \boldsymbol{B}_{ext}$.

A high frequency (hf) current thus is expected to produce a hf BR field, which can be utilized directly for spin excitation and spin manipulation [11]. This effect is observed as an increase in ESR signal when the sample is moved towards a position where the electric mode of the resonator has its maximum [12].

Experiments

This effect is observed indirectly in our sample structures as well [8]. The observed ESR signal is a complex superposition of three components: the antisymmetric absorption signal (AS), corresponding to magnetic dipole transitions in the sample at resonance (the traditional ESR signal), the symmetric dispersion signal (DS), arising from the frequency dependence of the electric conductivity, and the antisymmetric polarization signal (PS) which appears due to the dependence of the conductivity on spin polarization.

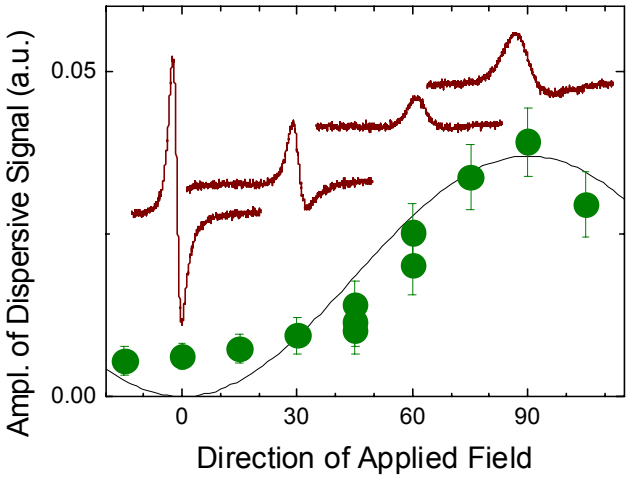

Fig. 3: Amplitude of the DS component of the ESR signal as a function of sample orientation with respect to the external field. The overall ESR line shape is shown qualitatively as insets.

When the sample is rotated around the direction of the magnetic component of the microwave (MW) radiation inside the resonator, $\boldsymbol{B}_1$, perpendicular to the external field it is found that the ESR signal is mostly antisymmetric when the external field is perpendicular to the 2DEG, and becomes more symmetric when the sample is rotated towards an orientation where the field is in-plane (see Fig. 3). This is due to the finite dimensions of the 2DEG. The electric component of the MW radiation, $\boldsymbol{E}_1$, vanishes completely exactly in the center of the resonator only. For in-plane orientation, it is parallel to the 2DEG, which gives rise to hf currents, leading to an increase in DS amplitude by a factor of ~30. When the 2DEG is oriented perpendicular to $\boldsymbol{B}_1$ ($\boldsymbol{E}_1$ in-plane), the DS amplitude is increased by a factor of ~100.

Acknowledgements

This work was supported additionally by FWF and the ÖAD, both Vienna.

References

[1] D. V. Bualev and D. Loss: “Spin relaxation and anticrossing in quantum dots: Rashba versus Dresselhaus spin-orbit coupling”, Phys. Rev. B, 71, 2005, 205324.

[2] M. Kroutvar, Y. Ducommun, D. Heiss, M. Bichler, D. Schuh, G. Abstreiter, and J. J. Finley: “Optically programmable electron spin memory using semiconductor quantum dots”, Nature, 432, 2004, 81.

[3] A. C. Johnson, J. R. Petta, J. M. Taylor, A. Yacoby, M. D. Lukin, C. M. Marcus, M. P. Hanson, and A. C. Gossard: “Triplet-singet spin relaxation via nuclei in a double quantum dot”, Nature, 435, 2005, 925.

[4] J. M. Elzerman, R. Hanson, L. H. Willems van Beveren, B. Witkamp, L. M. K. Vandersypen, and L. P. Kouwenhoven: “Single-shot read-out of an individual electron spin in a quantum dot”, Nature, 430, 2004, 431.

[5] H. Malissa, W. Jantsch, G. Chen, D. Gruber, H. Lichtenberger, F. Schäffler, Z. Wilamowski, A. Tyryshkin, and S. Lyon: “Investigation of the spin properties of electrons in zero-dimensional SiGe structures by electron paramagnetic resonance”, Mater. Sci. Eng. B, 126, 2006, 172.

[6] O. G. Schmidt, K. Eberl, and Y. Rau: “Strain and band-edge alignment in single and multiple layers of self-assembled Ge/Si and GeSi/Si islands”, Phys. Rev. B, 62, 2000, 16715.

[7] Z. Wilamowski, W. Jantsch, H. Malissa, and U. Rössler: “Evidence and evaluation of the Bychkov-Rashba effect in SiGe/Si/SiGe quantum wells”, Phys. Rev. B, 66, 2002, 195315.

[8] Z. Wilamowski and W. Jantsch: “Suppression of spin relaxation of conduction electrons by cyclotron motion”, Phys. Rev. B, 69, 2004, 035328.

[9] H. Malissa, W. Jantsch, and Z. Wilamowski: “Current induced g-factor shift in modulation doped Si quantum wells”, Proceedigs of the 2006 Fall Meeting of the Material Research Society, Boston, USA, 2006.

[10] Z. Wilamowski, H. Malissa, F. Schäffler, and W. Jantsch: “g-factor tuning and manipulation of spins by an electric current”, cond-mat/0610046, 2006.

[11] M. Duckheim and D. Loss: “Electric-dipole-induced spin resonance in disordered semiconductors”, Nature physics, 2, 2006, 195.

[12] M. Schulte, J. G. S. Lok, G. Denninger, and W. Dietsche: “Electron spin resonance on a two-dimensional electron gas in a singel AlAs quantum well”, Phys. Rev. Lett., 94, 2005, 137601.

MBE Growth Conditions for Si Island Formation on Ge(001) Substrates

D. Pachinger, H. Lichtenberger, G. Chen, J. Stangl, G. Hesser and F. Schäffler

Institute of Semiconductor and Solid State Physics, University Linz, Austria

Here, we report on MBE growth conditions for Si island formation on Ge (001) substrates. After buffer layer growth Si deposition was varied from 6 to 20 ML in the temperature range from 400 to 550 °C. AFM and HRTEM images confirmed the Stranski-Krastanov growth of Si on Ge substrates.

Introduction

In the Si/SiGe heterosystem self-organization schemes based on Stranski-Krastanov (SK) growth were mainly investigated for compressively strained Ge layers on Si substrates [1]. Because of the Type II band alignment this leads to hole confinement in the Ge islands, whereas tensely strained, Si-rich dots would be required for electron confinement. Little is known about SK growth of Si on Ge or SiGe, but there are strong indications that dot formation is kinetically hampered, if the epilayer is under tensile strain [2]. However, SK growth is driven by total energy minimization, which is independent of the sign of the lattice mismatch. And indeed, SK growth has been observed in heterosystems under tensile strain [3].

Experimental Procedure

Here, we report on MBE growth conditions for Si island formation on Ge (001) substrates. The substrates were chemically pre-cleaned, followed *in-situ* by a 30 minutes outgassing step at 300 °C and by a thermal oxide desorption step. We optimized the growth conditions for the subsequent Ge buffer to get smooth surfaces with double atomic height steps only.

Results and Discussion

On such buffers Si growth was initially investigated at 750 °C to stay close to thermal equilibrium. Under these conditions island formation was observed, which was, however, concomitant with strong alloying to average Ge compositions of up to 80% [4].

Lower growth temperatures drastically reduce alloying. We therefore investigated the formation of Si-rich islands in the temperature range from 400 to 550 °C with varying Si deposition from 6 to 20 monolayers. As an example, Fig. 1(a) – (d) shows a series of samples grown at 500 °C with Si coverages from 10 to 20 ML. In Fig. 1(e) the dot densities vs. Si deposition are plotted for four different growth temperatures. The steep increase in each curve allows for the extraction of the 2D-to-3D transition, which decreases from ≈14 ML at 550 °C to ≈8 ML at 450 °C, most likely due to more pronounced alloying at higher temperatures.

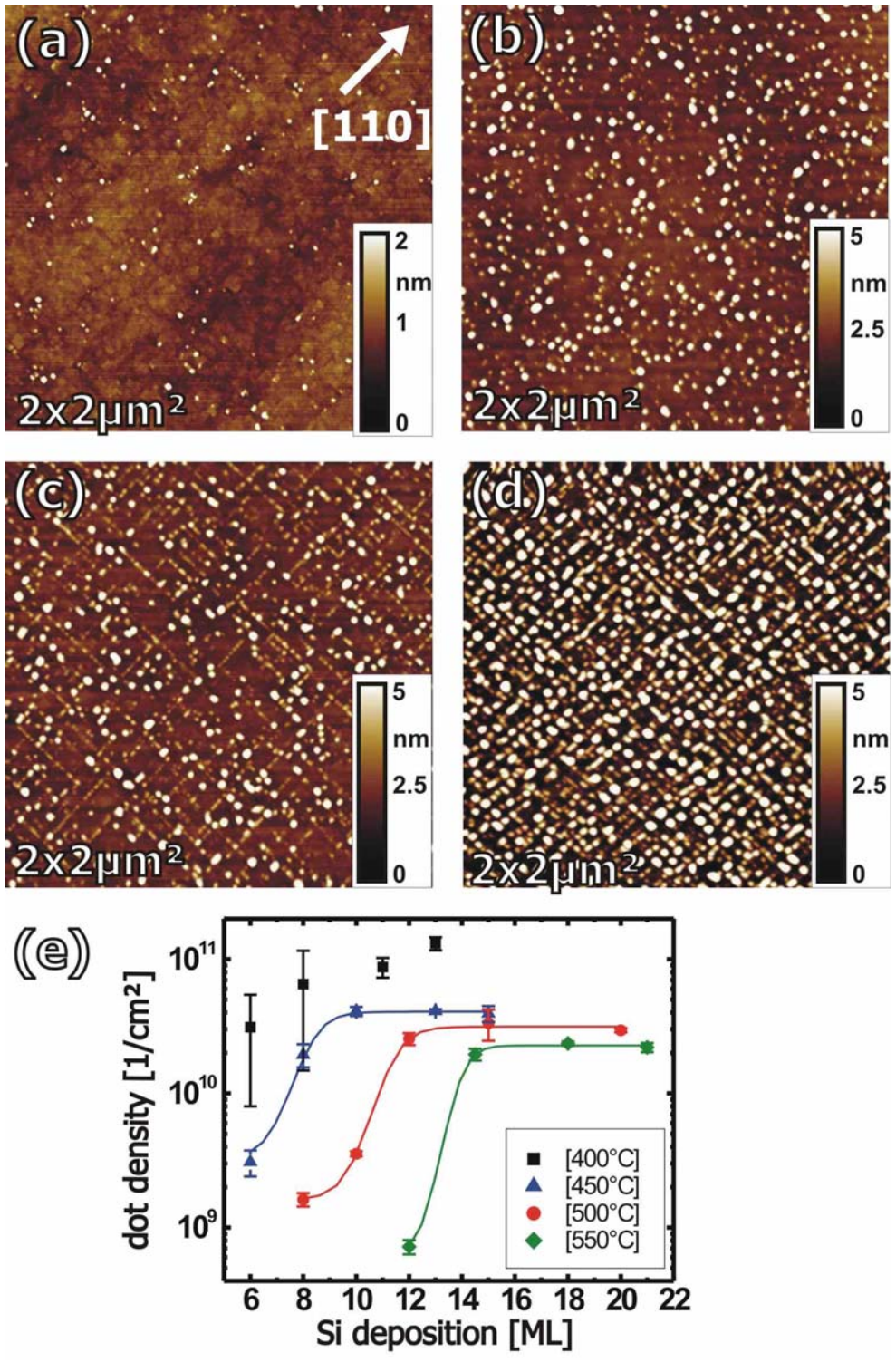

Fig. 1: AFM images of Si grown at 500°C with a varying ML deposition (a) 10 ML, (b) 12 ML, (c) 15 ML and (d) 20 ML; (e) dot density vs Si deposition as a function of growth temperature.

At 500 °C the wetting layer is about 10ML thick, a value which we also confirmed by high-resolution cross-sectional TEM (HRXTEM) images (Fig. 2). Evidently, the Si wetting layer on Ge is much thicker than the typical 3 ML found for Ge growth on Si, and, even worse, it reaches the equilibrium critical thickness for dislocation nucleation. It is therefore not too surprising that the HRXTEM images revealed dislocations already in

the wetting layer (Figs. 2(b) – (c)). Evidence for the presence of dislocations in the wetting layer can also be found in the AFM images in Figs. 1(c) – (d), which clearly show partial ordering of the Si islands along <110> oriented lines. Most likely, these islands decorate misfit dislocation segments, as has also been observed for Ge on dislocated SiGe(001) pseudosubstrates.

Surface orientation maps show that the larger islands are truncated pyramids with {113} facets, whereas the small islands consist predominantly of facets orientations between {117} and {1 1 10}. These facets have inclination angles against the (001) substrate plane between 8° and 11°, and have also been found in earlier work on pit-patterned Si substrates after overgrowth with a Si buffer layer [5]. Compared to {105} faceted Ge pyramids on Si, the small Si islands have similar inclination angles of the sidewall facets, but are rotated by 45°.

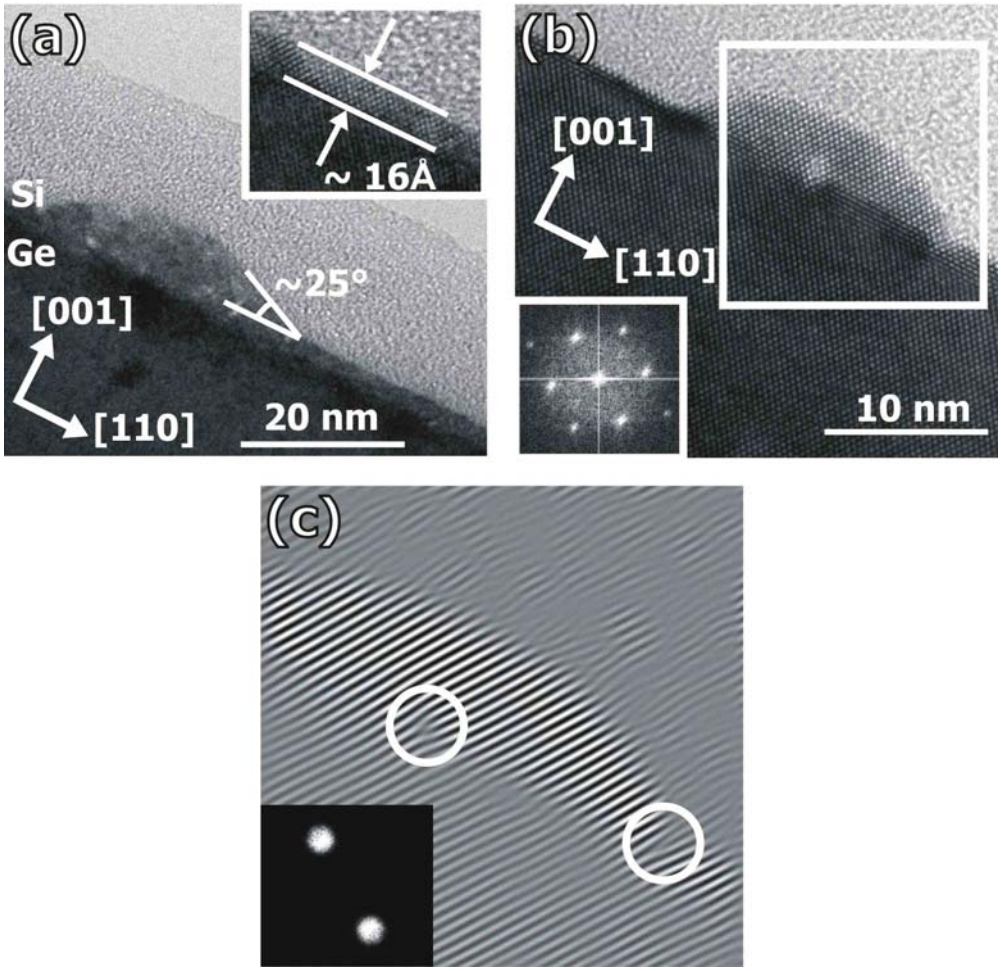

Fig. 2: Cross-sectional TEM images of 15 ML Si grown at 500°C; (a) Si dot with {113} facets and wetting layer thickness of ~ 11 ML (=16Å); (b) high resolution TEM image of a Si dot and wetting layer with dislocations; (c) filtered fast Fourier transformation (FFT) of the marked area in (b) showing two dislocations (circles).

Summary

Our experiments clearly demonstrate that SK-growth of Si on Ge is possible. Further growth optimization is still required to suppress dislocation formation in the wetting layer.

Acknowledgements

The research was supported by FWF via SFB 025: “IRON”. Part of the laboratory infrastructure was funded by the Austrian Gesellschaft für Mikroelektronik (GMe).

References

[1] Z. Zhong et al., Appl. Phys. Lett. 84, 1922 (2004)

[2] Y.H. Xie et al., Phys. Rev. Lett. **73**, 3006 (1994)

[3] G. Springholz et al., Phys. Rev. Lett. **84**, 4669 (2000)

[4] D.Pachinger et al., Proc. ICPS 28, in print

[5] G.Chen et al., Phys. Rev B **74**, 035302 (2006)

Stranski-Krastanov Growth of Tensely Strained Si on Ge (001) Substrates

D. Pachinger, H. Lichtenberger, F. Schäffler

**Institut für Halbleiter- und Festkörperphysik,
Johannes-Kepler-Universität Linz, A - 4040 Linz**

Introduction

In the Si/SiGe heterosystem self-organization schemes based on Stranski-Krastanov (SK) growth were mainly investigated for compressively strained Ge layers on Si substrates, which offer hole confinement in the islands. Due to the Type II band alignment, electron confinement requires tensely strained, Si-rich dots, which can be realized on Ge substrates or pseudosubstrates. Very little is known about SK growth of Si on Ge, but there are strong indications that dot formation is kinetically hampered, if the epilayer is under tensile strain [1]. On the other hand, SK growth is driven by total energy minimization, and since the elastic energy depends quadratically on strain, close to thermal equilibrium 3D island formation is not expected to depend on the sign of the lattice mismatch. Indeed, SK growth has already been observed in tensely strained layers, e.g. in the PbSe/$Pb_{1-x}Eu_xTe$ heterosystem [2].

Here, we report on MBE growth conditions for Si island formation on Ge(001) substrates. Buffer layer growth was optimized and Si island formation was investigated in the temperature range between 550 and 750 °C for 5 to 15 ML Si coverage. Seeded nucleation was observed after carbon pre-deposition on a Ge buffer layer. Finally, Ge substrates were pre-structured to offer suitable nucleation sites for the Si islands.

Experimental

Substrates used in this study were Ga-doped Cz-Ge(100) wafers with a resistivity of about 8 Ωcm. Pieces of 17,5 x 17,5 mm were chemically pre-cleaned [3] and loaded into our Riber SIVA45 MBE system via a load lock system, followed by an *in-situ* thermal oxide desorption step at 750 °C for 15 minutes.

AFM measurements were carried out for the characterization of buffer and island growth. Surface orientation maps extracted from these AFM images were used for facet analysis.

Pre-structuring of the Ge substrates was realized by e-beam lithography with a Leo Supra 35 FE-SEM at 20 kV and subsequent reactive ion etching in an Oxford Plasmalab 80 reactor with 100 % CF_4. (50 sccm CF_4 flow, 30 W, 50 mTorr pressure). The etch rate was about 100 nm/min for the chosen parameters.

Results

After oxide desorption a Ge buffer layer was deposited to smoothen the roughness of the substrate. By systematically varying its deposition temperature, we found that a 50 nm thick Ge buffer grown at 400 °C offers the lowest mean-root-square roughness of about 0.1 nm (Fig. 1).

A nearly ideal surface with large terraces separated by one- and two-atomic height steps is created.

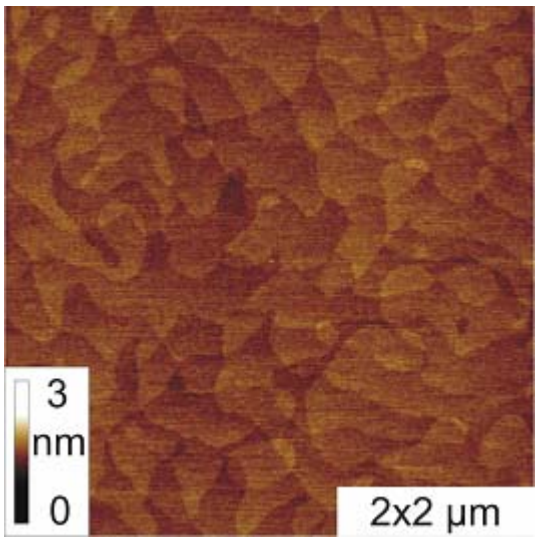

Fig. 1: AFM image of a 50 nm thick Ge buffer layer on a Ge (001) substrate grown at 400 °C providing a mean-root-square roughness of about 0.1 nm. Flat areas seen in the image are separated by one- and two-atomic height steps.

On this buffer we deposited 5 – 15 ML of Si at temperatures between 550 °C and 750 °C. Island formation was observed at the highest deposition temperature (Fig. 2(A)), but these islands were almost complete alloyed with the Ge substrate. Lowering the growth temperature to 550 °C leads to a drastic reduction of the dot density and to a pronounced trench around the islands (Fig. 2(B)).

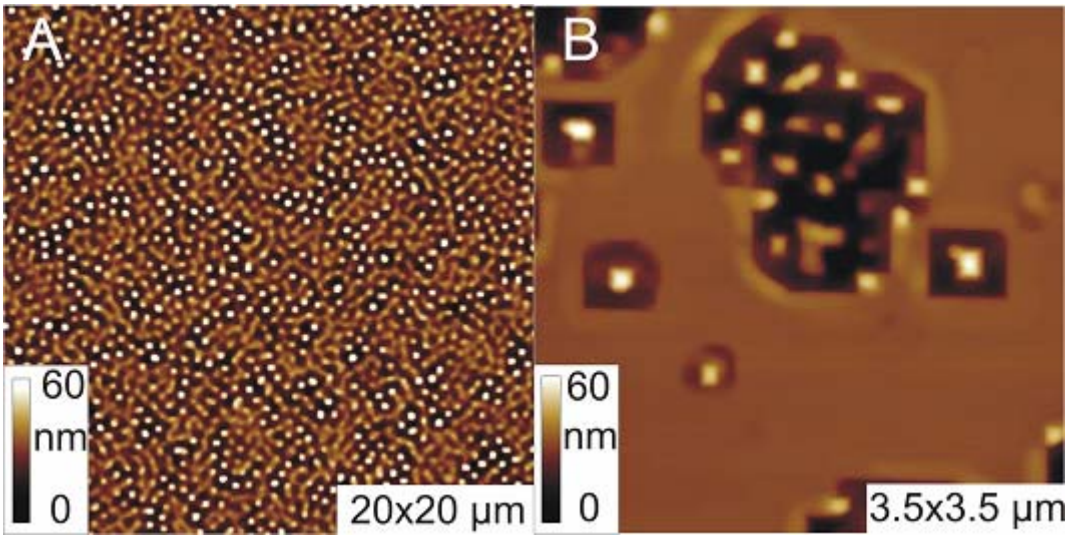

Fig. 2: (A): AFM images of 10 ML Si grown on a 50 nm Ge buffer layer at 750 °C showing a dot density of $4x10^8$ cm^{-2}; (B): AFM images of 10 ML Si grown on a 50 nm Ge buffer layer at 675 °C, showing coupled and uncoupled trenches enclosing the dots; dot density is $3x10^8$ cm^{-2}

These experiments confirm the kinetically restricted nucleation of Si islands at lower growth temperatures, which is, in our case, the only temperature range where alloying with the buffer layer can be efficiently suppressed. It is therefore essential to enhance island formation in tensile strained films by providing suitable nucleation centers. For this purpose we deposited a fraction of a ML of carbon onto the Ge buffer layer just prior to Si deposition. With carbon pre-deposition varying from 0.05 to 0.5 ML, Si island growth could be observed over the whole range of growth temperatures investigated (Fig. 3).

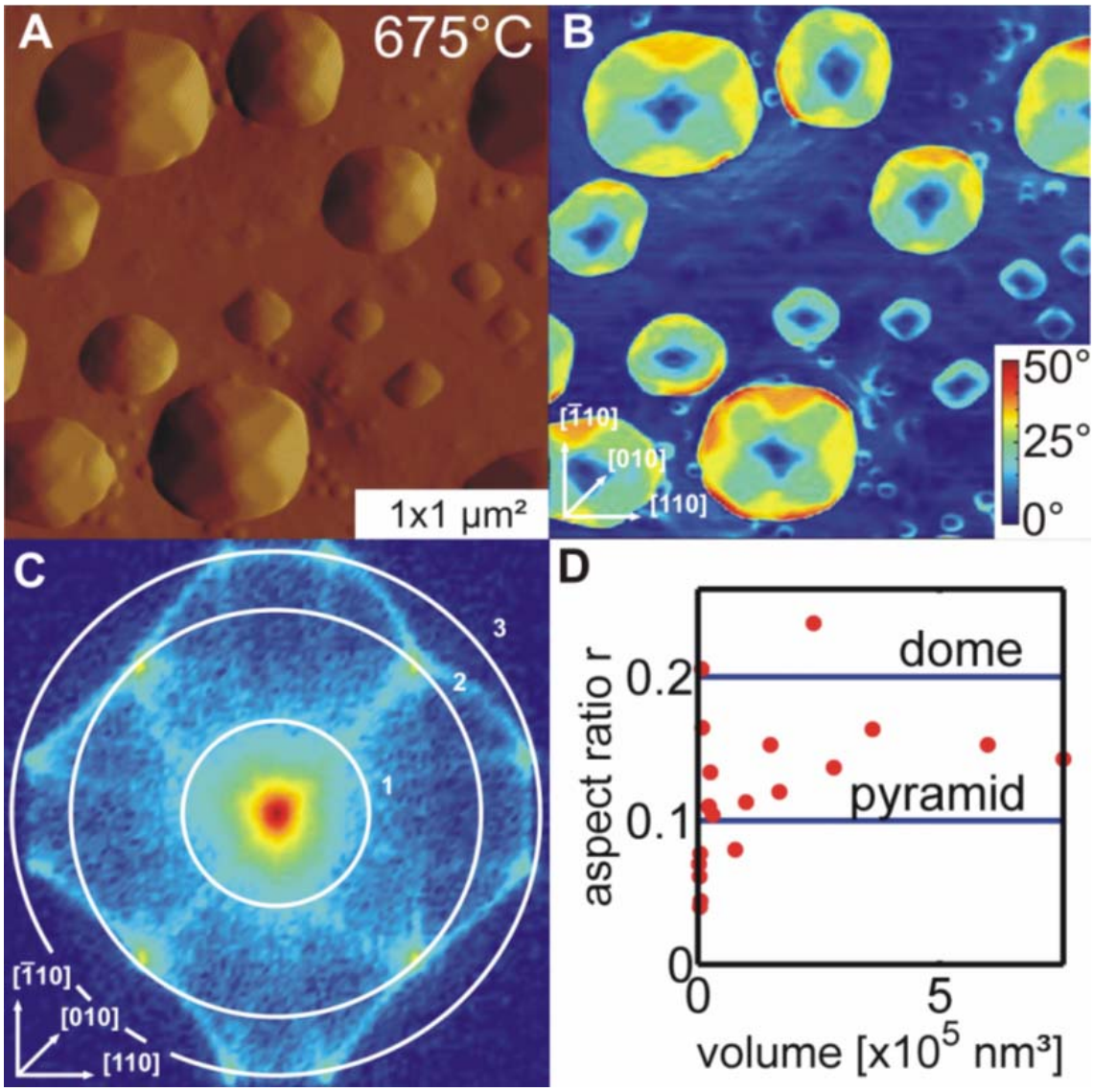

Fig. 3: (A): AFM image in the derivative mode of 15 ML Si grown on 50 nm Ge buffer layer at 675 °C after 0.1 ML carbon predepostion on the buffer layer; (B): Surface angle plot and surface orientation map extracted from figure (A) show 1: {105}, 2: {113} and {15 3 23} facets, which are the same characteristic facets found for dome-shaped and pyramidal-shaped Ge dots on Si (figure (B) and (C)). Aspect ratio distribution of the sample grown at 675°C can be seen in Fig. (D).

Extracting surface orientation maps from the AFM images we found for both growth conditions Si-rich islands with {105}, {113} and {15 3 23} facets (Fig. 3 (B)). These are

the same characteristic facets found for SiGe islands on Si, indicating that Si also forms the well-known dome-shaped and pyramid-shaped islands [4]. Especially the appearance of the {105} facet, which can clearly be seen on the topmost parts of the dome-shaped islands in Fig. 3(A), is somewhat surprising, because it is usually associated with a facet that appears only on compressively strained SiGe and Ge layers [5], [6].

As a further step to enhance island nucleation and order, pit- and trench-structures with a periodicity of 800 and 400 nm were realized by reactive ion etching with CF4. The overgrowth of the pit-structures with a 500 nm Ge buffer layer at a temperature of 400 °C leads to pits of about 80 nm depth showing {105}, {113} and {15 3 23} facets (Fig. 4(A) and (B)).

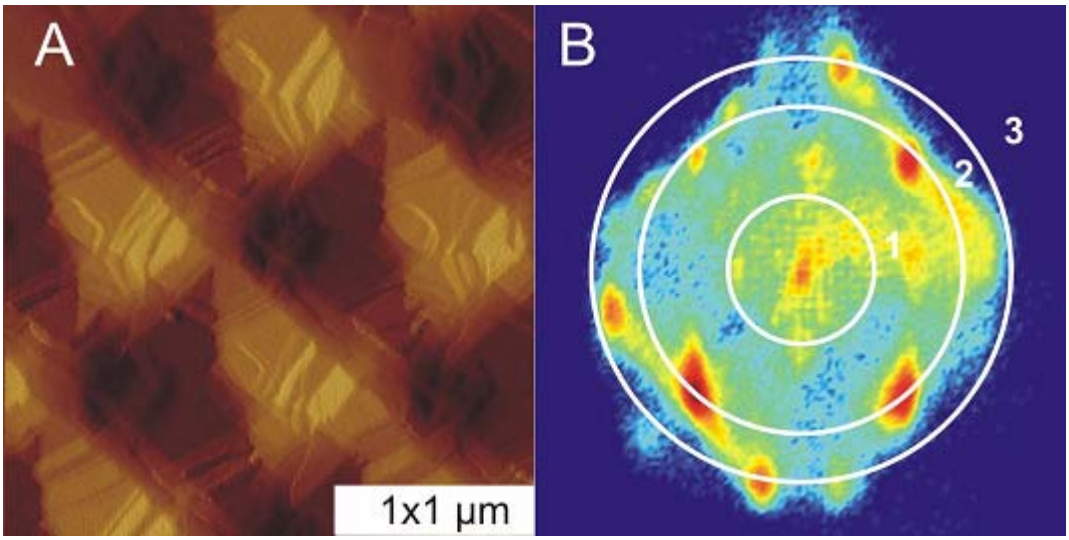

Fig. 4: (A): AFM image in the derivative mode of a 50 nm thick Germanium buffer layer on a pre-structured Ge (001) substrate grown at 400 °C; (B): Surface Orientation Map of A, showing 1:{105}, 2:{113} and 3:{15 3 23} facets.

On these templates we already observed preferential Si island formation, indicating that these structures offer suitable nucleation centers.

References

[1] Y.H. Xie et al., Phys. Rev. Lett. 73, 3006 (1994)

[2] G. Springholz et al., Phys. Rev. Lett. 84, 4669 (2000)

[3] Okumura et al., Appl. Surf. Sci. 125, 125-128 (1998)

[4] Z. Zhong et al., Appl. Phys. Lett. 84, 1922 (2004)

[5] P. Raiteri*, D. B. Migas, and Leo Miglio, A. Rastelli, H. von Känel, Phys. Rev. Lett. 88, 256103 (2002)

[6] Guang-Hong Lu, Feng Liu, Phys. Rev. Lett. 94, 176103 (2005)

Ultrafast Intersubband Relaxation in SiGe Quantum Well Structures

P. Rauter[1], T. Fromherz[1], N.Q. Vinh[2], B.N. Murdin[3], J.P. Phillips[2], C.R. Pidgeon[4], L. Diehl[5], G. Dehlinger[5], D. Grützmacher[5], Ming Zhao[6], Wei-Xin Ni[6], G. Bauer[1]

[1] Institute for Semiconductor and Solid State Physics, University Linz, Austria

[2] FOM Institute for Plasma Physics Rijnhuizen, Nieuwegein, Netherlands

[3] University of Surrey, University Linz, Austria

[4] Heriot-Watt University, Edinburgh, UK

[5] Paul Scherrer Institut, Villingen, Switzerland

[6] University of Linkoeping, Linkoeping, Sweden

We report the quantitative and direct determination of hole intersubband relaxation times in a voltage biased SiGe heterostructure using density matrix calculations applied to a four-level system in order to interpret photocurrent pump-pump experiments. One consistent set of parameters allows the simulation of two kinds of experiments, namely pump-pump photocurrent experiments at a free electron laser (wavelength 7.9 µm) and the laser-power dependence of the photocurrent signal. This strongly confirms the high reliability of these parameter values, of which the most interesting in respect to Si based quantum cascade laser development is the extracted heavy-hole relaxation time. The simulations show that this relaxation time directly determines the experimentally observed decay of the pump-pump photocurrent signal as a function of the delay time. For a heavy hole intersubband spacing of 160 meV, a value of 550 fs was obtained. The experimental method was further applied to determine the LH1-HH1 relaxation time of a second sample with a transition energy below the optical phonon energy. The observed relaxation time of 16 ps is consistent with the value found for the same structure by transmission pump-probe experiments.

Introduction

The strong need for cheap and integrable Si-based optoelectronic devices for a wide range of applications has been inducing considerable endeavor to develop structures for light emission, modulation and detection in this material system. While recent breakthroughs bring the concept of transition from electrical to optical interconnects closer to realization, the base for any silicon photonics, namely a group IV laser source, still waits to be developed. Up to now, the only lasing device demonstrated in Si is a Raman laser [2], which essentially lacks the advantages associated with the silicon system by requiring an external pump laser source. For silicon as an indirect semiconductor the concept of infrared emitters based on quantum cascade (QC) heterostructures, which is very successfully applied to III-V material systems, provides a promising approach towards a SiGe infrared laser. But despite the successful demonstration of infrared electroluminescence (EL) of various wavelengths for p-type SiGe quantum cascade structures, lasing has yet to be achieved. The build-up of population inversion in order to achieve lasing fundamentally depends on the relaxation lifetime of the excited energy level of the lasing transition. Therefore the measurement and optimization of

the intersubband relaxation time constitutes a key issue for the realization of a Si cascade laser source. The intersubband hole relaxation time for transitions *below* the optical phonon energy (Si–Si: 58 meV, Ge–Ge: 36 meV) is significantly larger than 10 ps and therefore is experimentally well accessible [3]. The lifetimes for energies *above* the optical phonon energies are smaller than 1 ps and are limited by optical deformation potential scattering [4]. So far experiments aimed at the measurement of the lifetime of hole intersubband transitions in this energy range suffered from a lack of time resolution [5] or from hole heating requiring subtraction of heating contributions in order to gain a value for the relaxation time [4].

Results and Discussion

Two samples are investigated in this work. Sample 1 for time resolved measurements at transition energies higher than the optical phonon energy was grown pseudomorphically on a Si [100] substrate at low nominal temperature (350 °C). The active region consists of five $Si_{1-x}Ge_x$ valence band QW (widths: 39, 26, 24, 23 and 35 Å; Ge content: 0.42, 0.42, 0.40, 0.37, and 0.28 respectively) and is *p*-type doped ($5x10^{17}$ cm^{-3}). This sequence is repeated ten times and separated by an undoped 500 Å Si barrier. The ten QW periods were sandwiched between 300 nm (100 nm) *p*-type ($2x10^{18}$ cm^{-3}) bottom (top) contacts. The structure was processed into mesa stripes of 7x0.5 mm and contacted with an Al:Si metallization in order to measure the vertical PC. On samples containing similar sets of undoped QW with only a thin barrier between the QW series, QC EL has been observed [6]. Self consistent k.p bandstructure calculations have been performed, providing the dipole matrix elements required for the density matrix simulations. The HH1-HH2 transition energy of the deepest well 1 (39 Å, 42 % Ge) is calculated to be 160 meV. Sample 2 with transition energies below the optical phonon energy was grown by MBE on 30% Ge pseudosubstrate. One period of the active region consists of one $Si_{0.67}Ge_{0.33}$ valence band QW with a width of 50 Å and two 16 Å wide $Si_{0.8}Ge_{0.2}$ barriers flanking the well. This *p*-type doped ($1x10^{18}$ cm^{-3}) sequence is repeated 12 times and separated by undoped 100 Å Si barriers. The 12 QW periods were sandwiched between 300 nm (100 nm) *p*-type ($2x10^{18}$ cm^{-3}) bottom (top) contacts. Sample 2 was processed analogue to sample 1. The HH1–LH1 transition energy is calculated to be 32 meV. For this sample, pump-probe transmission experiments revealed an HH1–LH1 lifetime of 20 ps [7]. The height of the PC peak induced by a free electron laser (FEL) pulse was measured as a function of the FEL micropulse energy for TM polarized radiation in order to verify that a nonlinear absorption process is responsible for the PC signal at the HH1–HH2 energy. For pulse energies smaller than $3x10^{-2}$ µJ the data presented in Fig. 1(d) show a clear superlinear dependence of the peak maximum on the pulse energy, which is typical for multi-photon processes. A saturation of the PC signal is observed for pulse energies higher than $5x10^{-2}$ µJ. In order to understand the power dependence of the PC signal over the whole range of micropulse energies as well as the dynamics of the state occupancies, the response of the system to a laser pulse resonant with the HH1–HH2 transition was simulated using a density matrix (DM) approach. The processes and states included in this model are depicted in the inset of Fig. 1(d). The HH1 and HH2 states are labeled by 0 and 1, respectively. The continuum is modeled by two states (2, 3) only. State 2 represents the continuum state that is resonantly coupled to the HH2 state by the radiation field. The relaxation from state 2 into state 3 accounts for the decay from the resonant continuum state into delocalized continuum states not coupled to the QW states by the radiation field but contributing to the measured current. In order to determine the intersubband relaxation times in our samples, the FEL wavelength was tuned into resonance with the targeted transition. Time resolved measurements were performed using the free electron laser (FEL) FELIX at FOM Rijnhuizen. FELIX provides micropulses with full widths at half maximum (FWHM) down to 280 fs and peak powers of 100 MW. The micropulse

repetition rate is 25 MHz, 5 macropulses of 7 µs duration are provided per second. The FEL pulses were split into two, where one of the pulses was delayed passing a movable mirror. The polarization of the undelayed pulse was rotated by 90° into TM. Before coupling into the sample in waveguide geometry, the pulses were made collinear again. The photocurrent through the samples was measured as a function of the pulse delay. Figure 2 compares the experimental results with the simulation. The black (a) and red (b) curves present the PC signals after subtracting a background corresponding to large delays. The green line represents the density matrix simulation results. In the simulations, the HH2–HH1 relaxation time τ_{10} was used as a fitting parameter. With τ_{10} = 550 fs an excellent agreement between measured and simulated results was obtained. Moreover, with this value for τ_{10} also the power dependence of the PC can be accurately modeled over 3 decades of micropulse powers (see Fig. 1(d)). This finding strongly suggests that all relevant processes are included in the simulation and that the extraction of the parameters, most interestingly the HH intersubband relaxation time, is performed correctly. The interpretation of the experimental data is based on the picture presented in Fig. 1. The strong asymmetry of the curves in Fig. 2(a) with respect to the sign of the delay is due to the strong polarization dependence of the transition involved. Negative delays in Fig. 2(a) present results for cases, in which the TM polarized pulse is the first to interact with the sample.

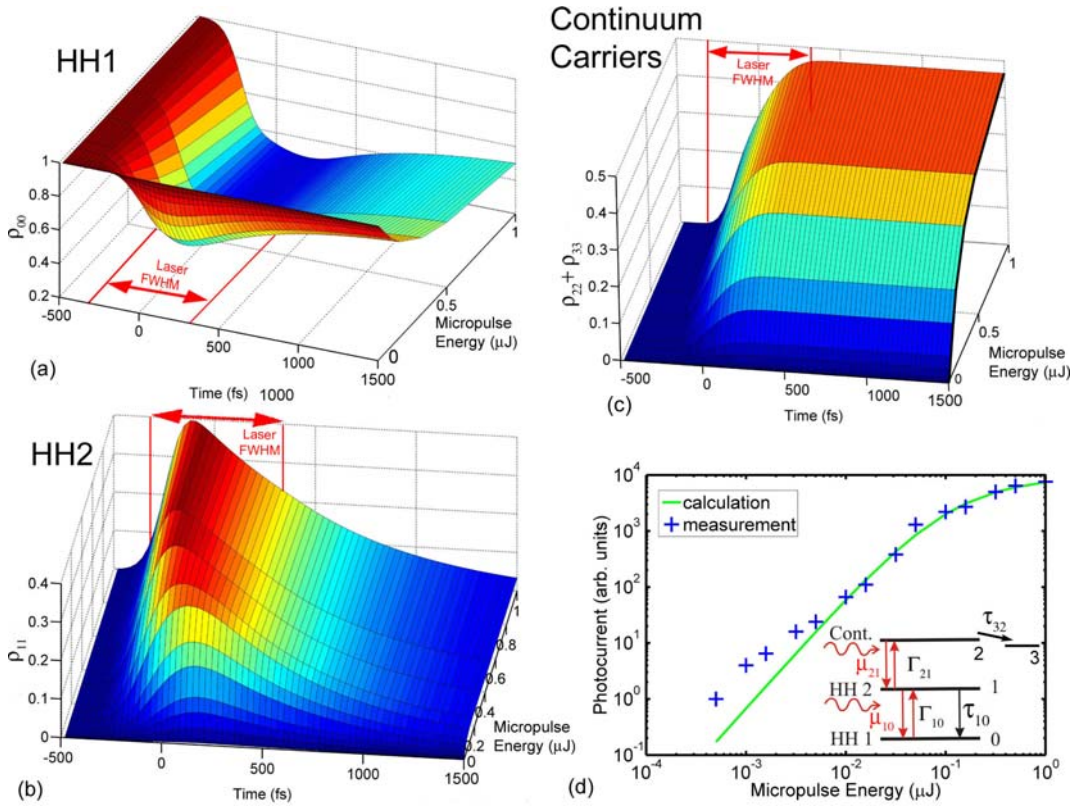

Fig. 1: Sample 1: FEL power dependence of the PC signal. Panel (d) shows a double logarithmic plot of the PC signal vs. the macropulse power of FELIX. The experimental data (crosses) were measured at a bias of 3 V and a temperature of 10 K in TM polarization. The inset sketches the processes considered in the DM calculations, while the plots (a), (b) and (c) show the calculated time evolution of the HH1, HH2 and continuum state occupancies for a TM polarized laser pulse hitting the sample at t = 0. The calculated dependence of the PC is shown as solid line in plot (d) and is proportional to the number of continuum carriers at the end of the laser pulse as shown in (c).

In TM polarization the HH1–HH2 transition is allowed, and thus a non-equilibrium population of the HH2 state will build up. This non equilibrium HH2 occupation decays exponentially with the time constant τ_{10}, as presented in Fig. 1(b). From the HH2 state, holes can be excited to the continuum also in TE polarization. Therefore, if the TE pulse hits the structure before the HH2 carriers have relaxed, the integral PC increases proportionally to the residual holes in the HH2 state. Thus the measured decay of the integral PC change as a function of the pulse delay directly monitors the HH2 lifetime, allowing the extraction of the HH2–HH1 relaxation time by performing an exponential fit for the data in Fig. 2(a) gained at negative delays. In TE polarization, HH1–HH2 transitions are forbidden at the Γ point and become only weakly allowed for HH1 vectors with finite momentum perpendicular to the growth direction. Thus only negligible HH2 populations can be excited from the HH1 ground state by a TE pulse. As a consequence, the HH2 relaxation cannot be observed if the TE pulse arrives first (positive delays in Fig. 2(a)), resulting in an asymmetry with respect to the pulse order as observed in the experiment. The fast decaying increase of the PC signal between 0 and 1.5 ps in Fig. 2(a) results from the overlap of the TE and TM pulse, and thus indicates the time-resolution of the experimental setup. The extracted HH2–HH1 relaxation time of 550 fs is significantly longer than the time resolution of the measurement setup. To further confirm experimentally that PC pump-pump experiments probe the excited state lifetime, we compare time resolved pump-pump measurements on sample 2, for which a HH1–LH1 transition time of 20 ps was reported in [7], with conventional pump-probe experiments in transmission. Figure 2(b) shows the result of PC pump-pump measurements at a FEL wavelength of 37.9 µm, a macropulse energy of 70 µJ and an attenuation of 13 dB (red line), where the FEL beams hit the sample surface normally (both beams TE polarized, but cross-polarized). The side peaks found in the experimental data at 15 ps originate from the overlap of the second beam with the fraction of the first beam reflected by the sample's back surface. The 15 ps delay are consistent with the sample thickness of 600 µm. The reflection of the first pulse is included in the fit presented in Fig. 2(b), which reveals a HH1-LH1 relaxation time of 16 ps in good agreement with the value of 20 ps in [7].

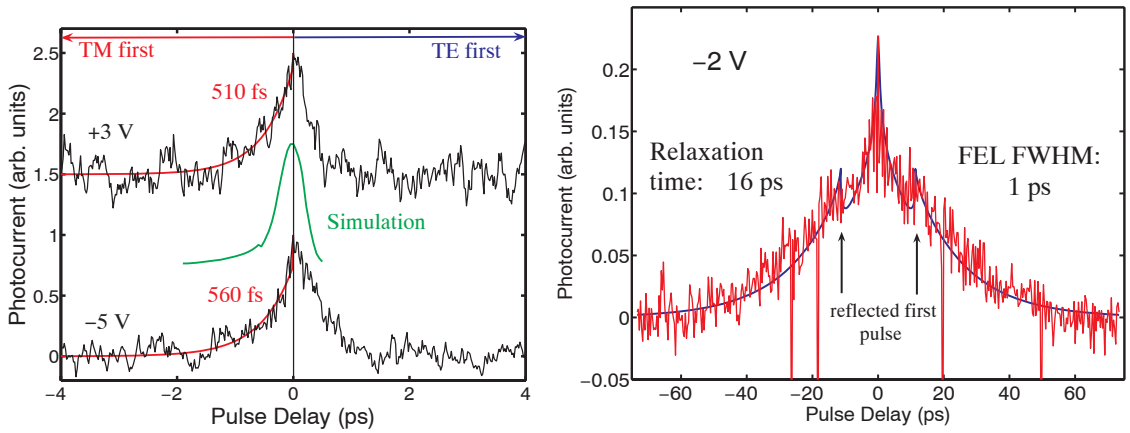

Fig. 2: Plot of the PC as a function of the delay between the TM and TE pump pulses for different bias voltages. A constant background equivalent to the current-integral over the two non-interacting pulses has been subtracted and the traces have been offset vertically for clarity. Sample 1 (a): An exponential fit results in an HH2–HH1 relaxation time of 510 fs for +3 V and 560 fs for -5 V (red lines). Sample 2 (b): The exponential fit of the decay reveals an LH1-HH1 relaxation time of 16 ps (blue line), where the FEL pulse FWHM is 1 ps.

Acknowledgements

This work was supported by the FWF (SFB IRON, Proj. Nrs. F2512-N08, F2507-N08).

References

[1] A. Liu *et al.*, Nature 427, 615 (2004)

[2] O. Boyraz *et al.*, Optics Express 12, 5269 (2004)

[3] R. Kelsall *et al.*, Phys. Rev. B 71, 115326 (2005)

[4] R. Kaindl *et al.*, Phys. Rev. Lett. 86, 1122 (2001)

[5] P. Boucaud *et al.*, Appl. Phys. Lett., 69, 3069 (1996)

[6] G. Dehlinger *et al.*, Science 290, 2277 (200)

[7] C. Pidgeon *et al.*, Semicond. Sci. Technol. 20, L50 (2005)

Formation of *Rocksalt*-PbTe Quantum Dots Embedded in *Zincblende*-CdTe

H. Groiss[1], W.Heiss[1], F. Schäffler[1], R. Leitsmann[2], F. Bechstedt[2,] K. Koike[3], H. Harada[3], M. Yano[3]

[1] Institute of Semiconductor and Solid State Physics, University Linz, Austria

[2] Institut für Festkörpertheorie und -optik, Friedrich-Schiller-Universität, Germany

[3] Osaka Institute of Technology, Japan

We recently reported the formation of highly symmetric quantum dots (QD) during annealing of a heteroepitaxial PbTe single quantum well clad between CdTe. The formation of these dots is driven by the mismatch of the lattice types of the involved materials. We investigated the QDs with conventional transmission electron microscopy (TEM), which reveals a strong influence of the layer thickness and annealing conditions on the resulting QDs. We perform high resolution TEM investigation combined with multislice simulation for the characterization of the new types of interfaces between the two cubic materials. One effect is the formation of two differently terminated {001} interfaces due to the polar properties of CdTe.

Introduction

We recently reported the formation of highly symmetric quantum dots (QD) during annealing of a heteroepitaxial PbTe single quantum well clad between CdTe layers [1], [2]. The mechanism relies on the mismatch of the two lattice types. The ionic IV-VI compound PbTe possesses *rocksalt* (*rs*) structure; the more covalently bonded II-VI compound CdTe has a *zincblende* (*zb*) crystal structure. Both tellurides show a face-centered cubic (*fcc*) translation symmetry with almost the same lattice constants. This leads to a continuous Te *fcc* sublattice throughout the heterostructure. Although the two heteromaterials are immiscible, coherent layer-by-layer growth is possible far from equilibrium at low growth temperatures around 220 °C. However, during annealing (e.g. 10 min at 320 to 350 °C) the PbTe layer disintegrates into coherent QDs terminated by the three low index {100}, {110} and {111} facets. The resulting QDs exhibit intense room-temperature mid-infrared photoluminescence due to electron-hole pair recombination in the narrow-gap PbTe QDs [1].

Conventional TEM Characterization

We investigated by conventional transmission electron microscopy (TEM) samples with various PbTe layer thicknesses. Mainly bright (BF) and dark field (DF) imaging of the structure-sensitive {002} diffraction spot under two-beam conditions was performed. The specimens were prepared along a <001> zone axis (plan-view sample) or along a <011> zone axis (cross-sectional sample). These investigations give insight into the disintegration of the 2D layer into islands, and show the strong influence of the annealing parameters on the symmetry of the QDs. They reveal also the dependence of the size and density distribution of the resulting PbTe on the epilayer thickness. Figure 1 shows several samples with epilayers of different thickness annealed under different

conditions. Figures 1(a) and 1(b) show a similar PbTe pattern (BF image, dark areas image PbTe). It has, however, to be mentioned that (a) was recorded from a 5 nm thick epilayer annealed at 320 °C for 10 min, whereas (b) is from an as-grown 3 nm thick epilayer, which started to disintegrate due to heating during the specimen preparation process. Figure 1(c) and 1(b) show a 3 nm and a 1 nm PbTe epilayer annealed under the same conditions.

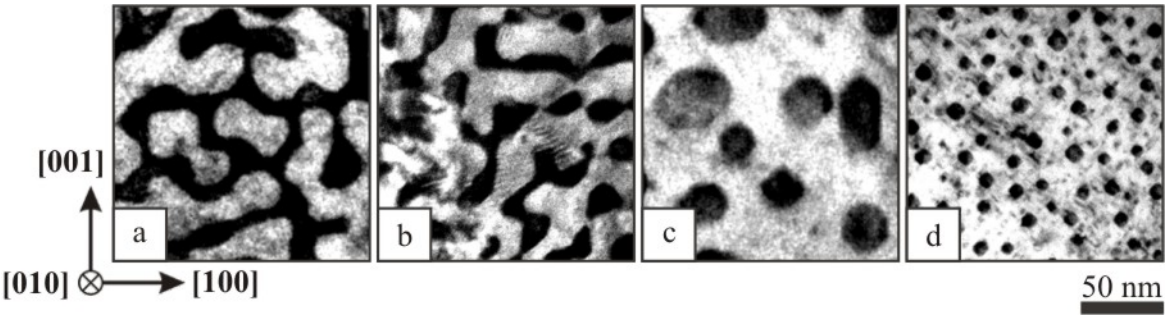

Fig. 1: Bright field (BF) plan-view images of samples with deposited PbTe layers of different thickness. (a) 5 nm PbTe epilayer, annealed at 320 °C for 10 min. (b) as-grown 3 nm thick PbTe epilayer; here the disintegration is induced by the thermal heat transferred during sample preparation. (c) 3 nm PbTe epilayer, annealed at 320 °C for 10 min. The original PbTe layer has already separated into islands with dimensions from 20 to 50 nm and the characteristic set of interface facets. (d) 1 nm PbTe epilayer, annealed at 320 °C for 10 min. The specimen contains only highly symmetric QDs in the range from 5 to 12 nm.

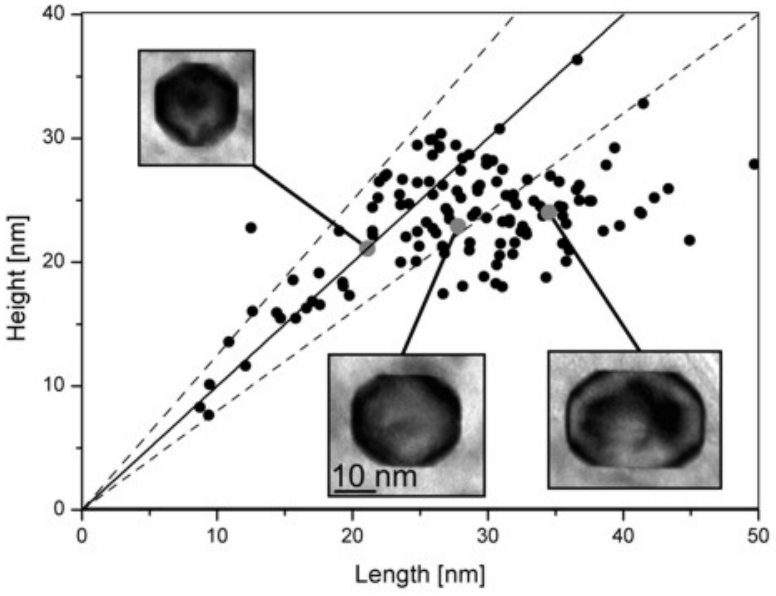

Fig. 2: Evaluation of the dot size distribution form a nominally 5 nm PbTe thick epilayer annealed at 350 °C for 10 min. The height of the dot was measured along the growth direction in a cross- sectional specimen.

Cross-sectional specimens are best suited for statistical evaluation, because both the in-plane and out-of-plane dimensions are visible. Figure 2 shows the size distribution found in a nominally 5 nm thick sample, which was annealed at 350 °C for 10 min. The BF images are from a cross sectional specimen, which means that the plotted height of the dots corresponds to the dimension in growth direction of the SQW. The height ranges form 10 to 30nm, whereas the lateral dimensions can be larger, especially for larger dots. We also evaluated the size of other samples, and found scaling with the initial epilayer thickness. For instance, the resulting QDs from a 1nm SQW are not larger than 12nm.

High Resolution TEM Characterization

HRTEM images of {001} facets prove the coherence and the continuous Te matrix at the interfaces between the two types of crystal structures. It is necessary to perform HRTEM simulations for further insight into the structure of the interfaces. This was done with the JEMS program package. The simulation employs the so-called multislice method, which uses a stack of projected potentials calculated from a thin crystal slice to determine electron transmission through the crystal in connection with the imaging conditions. Theoretical considerations result in two different atomic structures of the {001} interfaces due to the polar character of the {001} CdTe faces (Fig. 3). The figure shows a 3D model of a PbTe SQW with the two kinds of (001) interfaces on opposite sides. As the projection of the crystal structures is different for a 90° rotation of the line of sight along a <011> zone axis, both projections are also shown in Fig. 3.

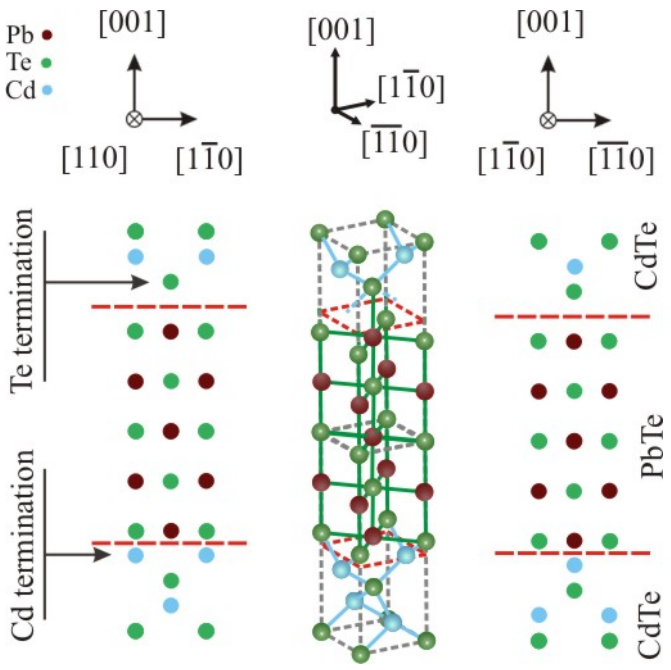

Fig. 3: Model of the {001} interfaces. According to the termination of the polar *zb* CdTe faces, two kinds of {001} interfaces are possible. The Te terminated interface has a lattice plane spacing of ½a at the interface, the Cd terminated has a smaller one of ¼a. Two possible projections of these interfaces can occur in a cross -sectional TEM specimen. The two projections are shown at the left and right hand side of the 3D model.

The identification of these interfaces requires a comparison of simulated HRTEM maps with recorded HRTEM defocus series. This allows an unambiguous allocation of the

projected crystal potentials, which are specifically different for Cd and Te terminated interfaces, to the images. The procedure is necessary, because the relation between the intensity of the recorded images and the projected potential is strongly non linear, and the thickness and defocus conditions of a HRTEM image are only poorly known. This way it was possible to identify both kinds of {001} interfaces in our specimen, as show in Fig. 4. The two HRTEM images of Fig. 4(a) are recorded at opposite interfaces of one and the same QD. Figure 4(b) shows a section of a simulated HR map.

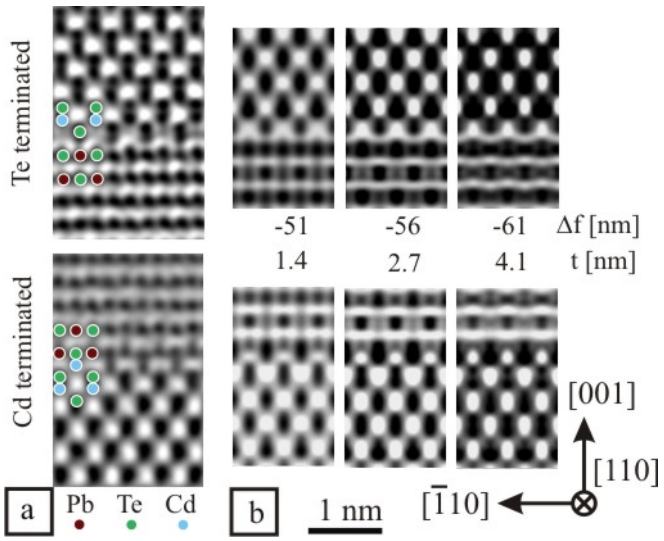

Fig. 4: (a) HRTEM images of a Cd and a Te terminated (001) interface. The respective atomic positions are indicated. (b) A selection of the simulated HR maps for the recorded TEM images. Characteristic for a large range of simulation parameters are the overlapping lattice fringes for the Cd terminated interface and separated lattice fringes for the Te terminated interface.

Acknowledgements

We gratefully acknowledge expert TEM preparation by G Hesser and valuable discussions with E Kaufmann and G. Springholz. Financial support was provided by the Fonds zur Förderung der Wissenschaftlichen Forschung (Austria) via SFB25 IR-ON.

References

[1] W. Heiss, H. Groiss, E. Kaufmann, G. Hesser, M. Böberl, G. Springholz, F. Schäffler, K. Koike, H. Harada, and M. Yano, APL **88**, 192109 (2006)

[2] R Leitsmann, L E Ramos, F Bechstedt, H Groiss, F Schäffler, W Heiss, K. Koike, H. Harada, and M. Yano, New J. Phys. **8**, 317 (2006)

Strain Induced Modifications of Optoelectronic Properties of PbSe Nanostructures

M. Simma, D. Lugovyy, T. Fromherz, G. Springholz, G. Bauer

Institut für Halbleiter- und Festkörperphysik, Universität Linz, A-4040 Linz, Austria

Deformation potentials D_u and D_d for PbSe were analyzed using transmission data of PbSe/PbEuSeTe multi-quantum wells. We use calculations based on a *kp* model to obtain the strain induced intervalley splitting in the quantum wells. For the reduction of the Fabri-Pérot interference fringes of the multilayer structures 480 Å NiCr anti-reflex coating is deposited on top of the multi-quantum wells. At low temperature we found PbSe deformation potentials D_u = -1.97 and D_u = 5.88. The results of the transmission measurements are compared with photo-current spectra measured with self-assembled PbSe/PbEuTe quantum dot superlattices.

Introduction

For the design of heterostructure optoelectronic devices the accurate knowledge of deformation potentials is of crucial importance. In the narrow gap IV-VI semiconductors due to large deformation potentials, even moderate strain values result in significant shift of the band edges. Theoretically [3], [2] and experimentally [8], [5] determined deformation potentials are spread over a wide range, especially the biaxial deformation potentials components. For example, according to Zasavitskii et al. [8] the uniaxial deformation potential component for PbSe D_u varies from -0.2 to -3.7 eV. In addition, most values do not agree with the isotropic deformation potentials, which can be measured with high accuracy from hydrostatic pressure experiments.

Experimental

IV-VI semiconductors are soft materials and therefore, it is rather difficult to produce uniaxial strains by applied external forces. In this work, the strain in PbSe layers result from the lattice mismatch between the constituting materials of epitaxial PbSe/PbEuSeTe multi-quantum well structures (MQW). The heterostructures are grown on (111) oriented BaF_2 substrates in a molecular-beam epitaxy (MBE) system. The 80 periods MQWs were grown on 1.5 µm fully relaxed buffer layers consisting of PbEuSeTe with the same composition as the barrier layers. The strain in the PbSe QWs is caused by the lattice mismatch to the PbEuSeTe buffer and barrier layers. The latter is determined mainly by the Te content in the quaternary layers, for which the lattice constant follows the same Vegards law as for PbSeTe. Thus, for the used quaternary composition of y_{Te} = 6 – 14% the strain in the PbSe QWs varies between $\varepsilon_{||}$ = 0.48 – 1.1%. The barrier height, on the other hand, is mainly determined by the Eu concentration due to the very large bandgap increase with increasing Eu content. For $x_{Eu} \approx 8\%$ used in this work, the energy band gap of the PbEuSeTe barrier layer is about 290 meV larger then that of PbSe. The thin PbSe 40 Å quantum wells (QW) are grown below the critical layer thickness and are pseudomorphically strained. Using this material

system we have the possibility to tune the energy gap in the barriers and the strain in the QWs virtually independently by the Eu and Te content of the PbEuSeTe alloy.

Samples with different strain values and similar Eu content were investigated using Fourier transform infrared spectroscopy (FTIR). Transmission spectra of the PbSe/PbEuSeTe MQWs were measured at temperatures between 6 K and 300 K in the spectral range of 500 cm^{-1} to 6000 cm^{-1} with a resolution of 8 cm^{-1} using a Bruker IFS-113v Fourier transform spectrometer.

Using two spectra measured at slightly different temperatures, we obtain the differential transmission as the logarithm of the ratio between the spectra measured at higher temperature and lower temperature. This approach takes advantage of the very strong temperature dependence of the PbSe and PbEuSeTe bandgaps and consequently, of the energy levels in the QWs, which results in pronounced peaks in the differential transmission spectra at the transition energies. Additionally, the differential spectra show much less pronounced Fabri-Pérot interference fringes caused by the layer refractive index contrast between the transparent BaF_2 substrate ($n \approx 1.5$) and the IV-VI epilayers ($n \approx 4.5$). This is due to the fact that the dielectric constants of the materials in the multilayer structure vary only weakly with temperature. For further reduction of the Fabri-Pérot interference fringes 480 Å NiCr [11] anti-reflection coating was deposited on the multilayer stack of the samples.

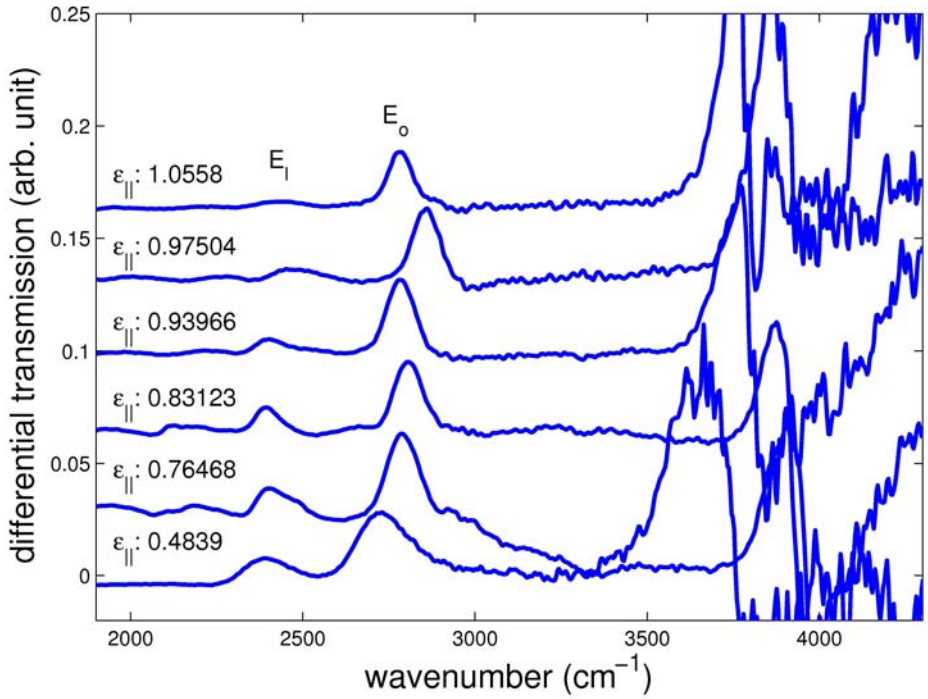

Fig 1: Differential transmission spectra of PbSe/PbEuSeTe MQWs for different strain values. As the strain increases, the L-valley splitting between the longitudinal (E_l) and the oblique valley (E_o) increases.

For each sample, the differential transmission shown in Fig. 1 exhibits three peaks caused by the optical transitions related to the longitudinal (E_l) and oblique L-valleys (E_o) in the PbSe QWs and the PbEuSeTe fundamental absorption in the barrier layers. Because of the narrow 40 Å PbSe well width no transitions to higher energy levels can be observed, indicating that higher energy levels are not confined in the QWs. The peaks related to the longitudinal valley transition show a weaker intensity compared to the peaks of the oblique valleys. This is due to the threefold degeneracy of the oblique

valleys. The clearly resolvable L-valley splitting Δ (see Fig. 1) increases with increasing strain. This intervalley splitting is caused on the one hand by the different effective electron and hole masses along the confinement direction of the oblique and longitudinal valleys, on the other hand by the different band gap shifts due to the biaxial strain in the layers. In thick epitaxial layers were the confinement shift of the optical transitions is zero the intervalley splitting is equal [8]

$$\Delta = \delta E_g^N - \delta E_g^O = \frac{8}{9} D_u (\varepsilon_\perp - \varepsilon_\parallel) \quad (1),$$

where D_u denotes the uniaxial component of the deformation potentials and $\varepsilon_\parallel$ and $\varepsilon_\square$ are the in-plane and perpendicular strains, respectively. In smaller QWs the optical transition energies as well as the intervalley splitting is increased by the quantum confinement effect. Therefore, in order to be able to apply Eq. 1 the confinement energies have to be subtracted from the measured transition energies.

The energy levels in the PbSe quantum wells can be calculated numerically with high accuracy using the envelope function method based on a *kp* model if the confinement energies in valence and conduction band are known. We estimated these confinement energies assuming that the unstrained PbSe/PbEuSeTe band-offsets in valence and conduction bands are equal ($\Delta E_c = \Delta E_v$), due to the mirror like bandstructure [7] of these materials. For the calculation of ΔE_v we used temperature dependent energy gaps of PbEuSe and PbEuTe given in [9] and [10], where the energy gap of PbEuSeTe is linearly interpolated.

The influence of the strain on the band-edge energies is given by the expression

$$\delta E = \sum D_{ij}^{c,v} \varepsilon_{ij} (2) \quad (2),$$

where $D_{ij}^{c,v}$ is the deformation potential tensor in the conduction and valence band and ε_{ij} denotes the strain tensor. In cubic systems this expression is simplified to two components $D_u^{c,v}$ and $D_d^{c,v}$ i.e., the uniaxial and dilatation deformation potentials and the $\varepsilon_\square$ and $\varepsilon_\parallel$ strain components.

The change in the bandgap is then characterized by the deformation potentials Du and Dd which are equal to the difference of the $D_u^{c,v}$, $D_d^{c,v}$ values of the conduction and valence bands. Using deformation potentials given in literature [3] we calculated from the optically measured transition energies the strain induced intervalley splitting. To derive the uniaxial deformation potential constant D_u with the help of Eq. (1) the calculated energy levels are subtracted from the measured transition data. For the 6 K measurement we get for D_u a value of -1.97 eV and at 77 K a value of D_u = -2.39 eV. Using the relation $D_{iso} = 3D_d + D_u$ and D_{iso} = 15.7 eV for the isotropic deformation potential constants [5] we calculated the dilatation deformation potential as D_d = 5.88 eV and D_d = 6.03 eV at 6 K and 77 K, respectively. The measured values for D_u agrees well with the theoretically determined values given in [3], [2].

Assuming a symmetric band offset in the unstrained case and the theoretical deformation potentials values given in Ref. [3], one obtains a rapidly increasing band offset asymmetry with increasing strain in the PbSe layers. In particular a type I - type II band alignment discontinuity transition is expected at strain values larger than about 80% for the given Eu concentration of 8%. Thus, at high strain values the PbSe valence band edge lies energetically below the barrier valence band edge. In this case, the PbSe valence band acts as barrier for the holes. For such a type II band alignment, the spatially indirect optical transitions are much weaker due to the reduced wavefunction overlap. The upper spectra in Fig. 1 resulting from the highly strained MQW structures exhibits a significantly weaker longitudinal valley peak than the spectra of the other samples.

Indications for such a type II band alignment are also obtained from photo-current (PC) measurements on highly strained PbSe/PbEuTe self-assembled quantum dot superlattices. These superlattices were grown by MBE onto (111) BaF_2 substrates [4] on 1.5 µm PbEuTe buffer layers at 340 – 420 °C. On these buffer 5 – 8 monolayers of PbSe were grown followed by a PbEuTe spacer layer with 6% Eu content and a thickness varying between 250 and 650 Å. The strain in the thin epitaxial PbSe layer resulting from the lattice misfit between PbSe and PbEuTe relaxes via island formation. This island formation starts after deposition of 3 ML PbSe [4] which compose a 2D wetting layer. By deposition of many PbSe/PbEuTe bilayers, a highly efficient 3D dot ordering takes place [4]. Using FTIR spectroscopy, we performed spectral resolved lateral photo-current measurements on these self-assembled QD structures.

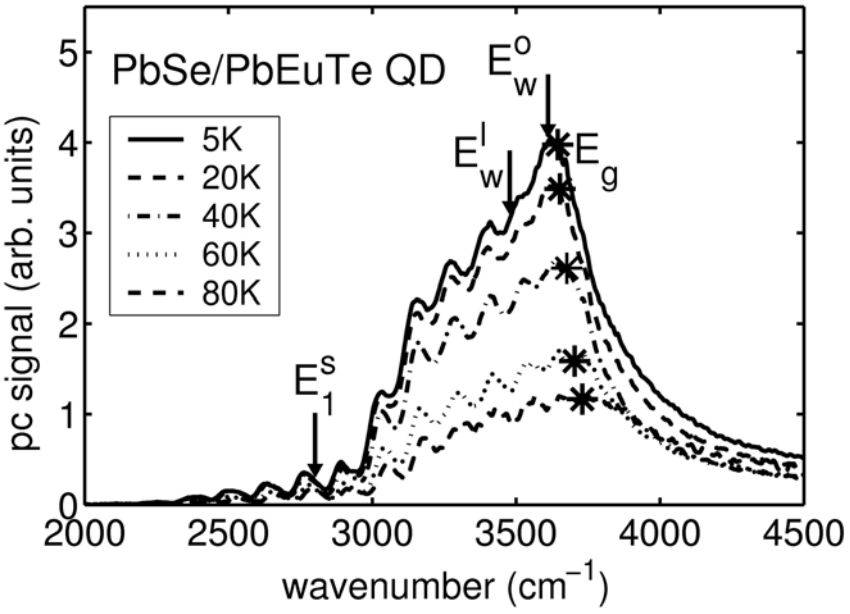

Fig 2: Photo-response of a PbSe/PbEuSeTe QD superlattice for different temperatures. Arrows indicates the optical transitions to different structures in the superlattice: E_1^s PbSe QD, E_w^l and E_w^o longitudinal and oblique wetting layer valley. The barrier bandgap E_g is marked with (*).

For a type I band alignment one would expect a freeze out of the carriers in the QD at low temperature resulting in vanishing lateral pc-signal. Figure 2 shows the photo-response measured at different temperatures performed with 50 Å high QD. The transition energies caused by various structures in the QD structures are marked by arrows. The arrow labeled as E_1^s is related to the QD ground s-state transition. The arrows labeled by E_w^l and E_w^o are the ground state transitions of the longitudinal and oblique valleys in the wetting layer. The quantum size energies in the dots and the wetting layer were calculated with the envelope function method using a *kp* model. For the QDs a simplified spherical shape [1] was assumed. The absorption edge at 3800 cm^{-1} marked by * is caused by the buffer and barrier layer fundamental transition. Clearly the pc-signal is well resolved for all temperatures, in particular, no freeze out of the carriers is observed. This indicates a type II band alignment of the PbSe QD. Assuming a band discontinuity of 120 meV between the PbSe/PbTe valence band edges [6] leads to a type I band alignment in the unstrained case. Using deformation potentials given in [3] shifts the valence band edge of PbSe below the PbEuTe valence band edge. This

assumptions result in a type II band alignment which explains the observed pc-signal at low temperatures.

Conclusion

In summary, strained PbSe multi-quantum wells and quantum dot superlattices structures were investigated by FTIR spectroscopy. We deposit a NiCr anti-reflection coating on the MQW samples in order to reduce the Fabri-Pérot interference fringes. Longitudinal and oblique valley subband transitions were observed and from the intervalley splitting the PbSe deformation potentials were determined. For increasing strain in the samples we observe a transition from type I to type II band alignment. Temperature dependent spectrally resolved photo-response of PbSe QD superlattices does not show any freeze out of the carriers. This indicates a type II band alignment of the PbSe dots.

Acknowledgments

Work supported by Öster. FWF Forschung, SFB IRON, Projekt Nr. F2504-N08.

References

[1] M. Califano and P. Harrison: J. Appl. Phys., 86, 5054, (1999).

[2] P. Enders: Phys. Status Solidi B, 129, 89, (1982); 132, 165, (1985).

[3] L. G. Ferreira: Phys. Rev., 137, 1601, (1965).

[4] G. Springholz, V. Holy, M. Pinczolits, and G. Bauer: Science, 282, 734, (1998).

[5] M. V. Valeiko, I. I. Zasavitzkii, A. V. Marveenko, B. N. Matsonashvili, and Z. A. Rukhadze: Superlattices. Microstruct, 9, 195, (1991).

[6] S. H. Wei and A. Zunger: Phys. Rev B, 55, 13605, (1997).

[7] G. Bauer: Narrow Gap Semiconductors: Physics and Applications, Vol. 133, Springer Lecture Notes in Phys., edited by W. Zawadski (Springer, Berlin, 1980), p. 427.

[8] I. I. Zasavitskii, E. A. de Andrada e Silva, E. Abramof, and P. J. McCann: Phys. Rev. B, 70, 115302–1, (2004).

[9] T. Maurice, F. Mahoukou, G. Breton, S. Charat, P. Masri, M. Averous, and R. Bisaro: Phys. Stat. Sol., (b) 209, 523, (1998).

[10] S. Yuan, H. Krenn, G. Springholz, and G. Bauer: Phys. Rev. B, 47, 7213, (1993).

[11] S. W. McKnight, K. P. Stewart. H. D. Drew, and K. Moorjani: Infrared Phys. 27, 327 (1987)

Shape Transitions of Self-Assembled PbSe Quantum Dots during Overgrowth

L. Abtin[1], G. Springholz[1] and V. Holy[2]

[1]Institut für Halbleiterphysik, Universität Linz, A-4040 Linz, Austria
[2]Charles University, Praha, Czech Republic

Epitaxial overgrowth of self-assembled pyramidal PbSe quantum dots is shown to drastically affect their shape and composition due to anion exchange reactions. As shown by scanning tunneling microscopy, for PbTe capping layers this results in a complete truncation of the dots. Introduction of EuTe into the cap layer leads to an effective suppression of the anion exchange process. This preserves the original dot pyramids and induces a large stress concentration above the buried dots.

Introduction

Self-assembled semiconductor quantum dots are of great importance for optoelectronic devices. Their synthesis is based on the Stranski-Krastanow growth mode of lattice-mismatched heteroepitaxy in which 3D surface nanoislands spontaneously nucleate on a 2D wetting layer in order to relax the elastic energy of the system [1]. For practical device applications, these dots have to be covered by a protective capping layer in order to suppress surface oxidation as well as non-radiative carrier recombination. During this capping process, however, a strong redistribution of the dot material and alloying with the surrounding matrix takes place [2]. This changes the electronic and optical properties of the dots as well. In this work, we focus on the role of the chemical composition of the capping layer on the overgrowth process of self-assembled PbSe quantum dots. Using *in situ* scanning tunneling microscopy (STM), we reveal that an intricate interplay between intermixing and shape transitions occurs. While for pure PbTe overgrowth, a rapid dot dissolution and shape transition occurs, this effect is effectively suppressed by introduction of EuTe into the capping material and thus, the pyramidal structure of the native PbSe dots is preserved.

Experimental

The samples were grown by molecular beam epitaxy onto PbTe (111) buffer layers [3], [4]. Their structure consists of 5 monolayers (ML) PbSe dots followed by $Pb_{1-x}Eu_xTe$ capping layers with composition varying between x_{Eu} = 0 and 8% and thicknesses up to 200 Å. Identical growth conditions were used for all samples with a substrate temperature of 350 °C. Due to the -5.4% lattice-mismatch, PbSe dots are formed at a critical coverage of 1.5 ML, and at 5 ML the surface is uniformly covered by dots with a density of ~250 /μm^2. Immediately after growth, the samples were quenched and transferred to an attached UHV scanning tunneling microscopy chamber. Surface imaging was performed at a sample bias of 1 – 2 V and tunneling currents of 0.5 – 1 nA.

Results

Figure 1 (a) shows the 3D surface image of the initial uncapped PbSe islands, representing the starting condition for the overgrowth experiments. The as-grown dots display an average height of 110 Å and a base width of 280 Å, with a dispersion of ±12%.

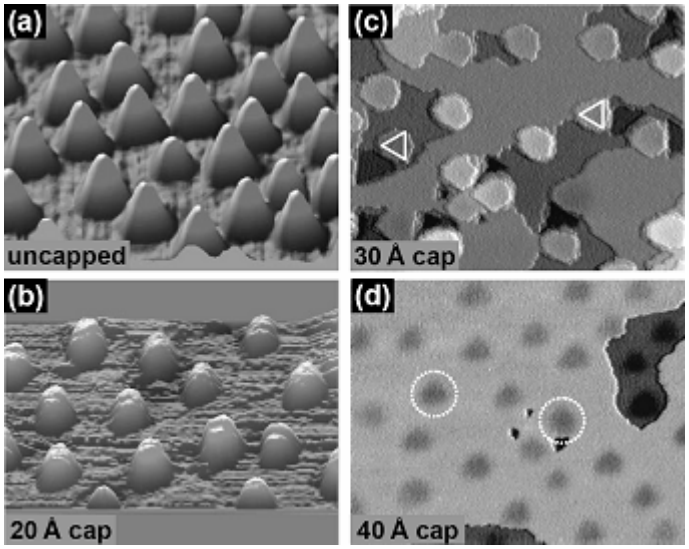

Fig. 1: STM surface images (0.3 x 0.25 μm^2) of 5 ML PbSe dots covered with different PbTe cap thicknesses of 0, 20, 30 and 40 Å from (a) to (d), respectively.

All dots exhibit an identical pyramidal shape defined by three low-energy {100} side facets [3]. In the first set of experiments, the dots were capped with PbTe layers. As revealed by Fig.1, with increasing cap thickness a rapid shrinking of dot height and a transition in island shape occurs. Already after 20 Å PbTe deposition (Fig. 1(b)), the dots are transformed into truncated pyramids and their height is reduced to *half* of the original value. At 30 Å cap thickness (Fig. 1(c)), the surface has become almost completely flat with just the top 1 – 3 ML of the pyramid trunks still sticking out through the capping layer. Thus, the whole upper part of the dots has been completely dissolved. The flat top plateaus of the dots show a substantial rounding of the corners and a notably increased width compared to the original dot pyramids. Thus, the dot material has been redistributed towards the island edges. Further incrementing the cap thickness to 40 Å (Fig. 1(d)) renders a completely planarized surface with the usual 200 nm wide monolayer terraces typical for PbTe epilayers. In addition, evenly distributed shallow triangular surface depressions appear. Their density exactly matches the density of the buried dots and thus, they stem from the local lattice distortions induced by the dots.

A strikingly different surface evolution takes place when the dots are overgrown with $Pb_{0.92}Eu_{0.08}Te$ capping layers. This is demonstrated by the series of STM images displayed in Fig. 2. At 80 Å thickness (Fig. 2(a)), the PbSe pyramids still stick out through the cap layer and their tips remain visible even at 100 Å cap thickness (Fig. 2(b)). In addition, the apices of the dots retain the triangular shape of the pristine PbSe pyramids as evidenced by the enlarged STM images shown as inserts. Thus, the native PbSe dots are completely preserved and the deposited capping material just fills up the space between the islands. In addition, however, deep trenches remain at the perimeter of the dots, i.e., cap layer growth is strongly suppressed at the pyramid edges. The structure of the trenches consists of a ~200 Å wide denuded zone around the apex of the dots and additional holes at the pyramid corners. The depth of the trenches increases from 2-3 ML at 80 Å cap thickness to 5-8 ML at 100 Å cap thickness. As a re-

sult, the apices remain visible even at 120 Å cap thickness. As growth further proceeds, just one single ~10 ML deep hole is left above each island (Fig. 2(c)). The inner structure of these holes still displays the symmetry of the original PbSe dots. Only after further PbEuTe deposition, the holes start to be filled up such that at 160 Å a completely planar surface is regained (Fig. 2(d)). On the flat monolayer terraces again the signature of the dots in form of shallow triangular surface depressions appears.

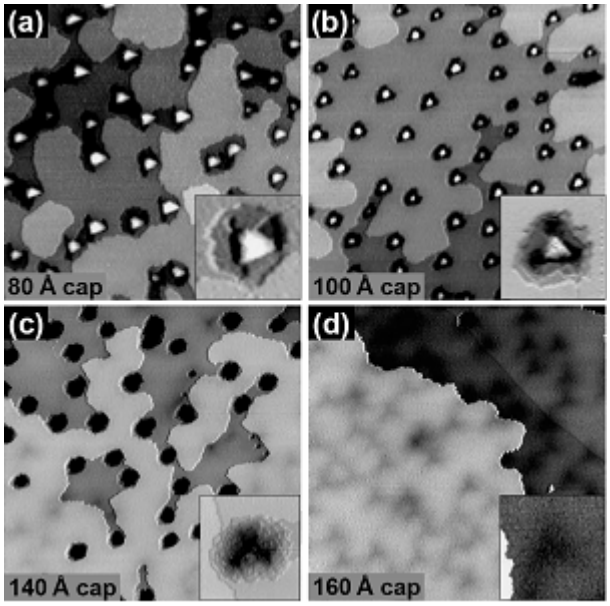

Fig. 2: STM images (0.5 x 0.5 μm^2) of 5 ML PbSe dots covered with $Pb_{0.92}Eu_{0.08}Te$ cap thicknesses of 80, 100, 140 and 160 Å from (a) to (d), respectively. The enlarged images around single dots are shown as insert.

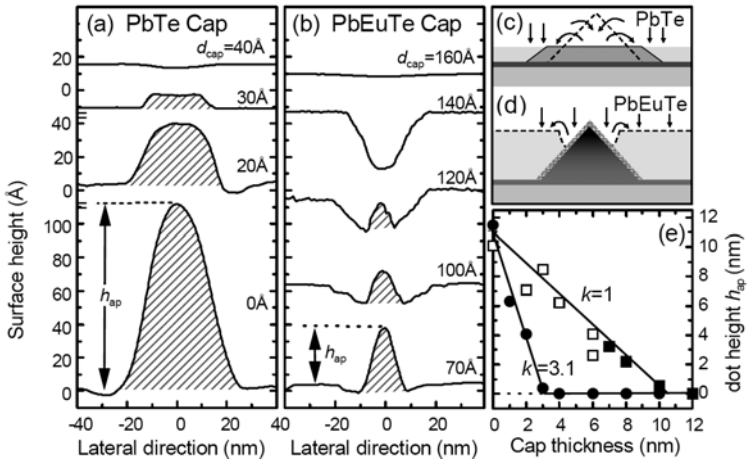

Fig. 3: STM surface profiles across PbSe dots capped with different PbTe (a) or PbEuTe (b) thicknesses d_{cap}. The shaded areas indicate the dot part extending above the cap surface. (e) Average apparent dot height h_{ap} plotted as a function of PbTe (●) and PbEuTe (■, □) cap thickness. The mechanisms determining the surface evolution are illustrated schematically in (c) and (d).

For a quantitative analysis, STM surface profiles were measured across the dots. The results are displayed in Fig. 3(a) and (b) for both sets of samples. For the PbTe case, the profiles show a rapid transition from sharp to truncated pyramids within 30 Å cap deposition. For the PbEuTe case, the island tips are preserved up to a cap thickness of 120 Å, and even at 140 Å deep holes are left on top of the islands that just reach to the bottom of the holes. The average apparent height hap of the dots indicated by arrows in Fig. 3(a) and (b) is plotted in Fig. 3(e) for PbTe (●) and PbEuTe (■) capping layers. As indicated by the solid lines, in both cases, the dot height decreases linearly with increasing cap thickness d, according to $h_{ap} = h_0 - k \times d$, where h_0 is the initial dot height and k is a scaling constant that characterizes planarization properties of the growth process. For usual thin film deposition, k is generally less than one, with the limiting case of k = 0 for conformal overgrowth. For PbEuTe capping, the fit of the experimental data yields a value of k = 1, representing the ideal case when growth takes place exclusively in between but not on top of the islands as shown schematically in Fig. 3(d). For PbTe overgrowth, k exceeds this value by as much as a factor of 3, indicating that the dissolution rate of the island tops is two times larger than the deposition rate. This dissolution is driven by strong intermixing between the dots and the capping material via anion surface exchange. Generally, intermixing is quite favorable in strained-layer heteroepitaxy because it effectively reduces the lattice-mismatch and thus, the total energy of the system. The reduced lattice mismatch, on the other hand, reduces the driving force for strain-induced coherent islanding [1]. Therefore, as the Se concentration at the top of the dots is reduced, the material starts to migrate towards the island edges to form more planar surface structures. This is illustrated schematically in Fig. 3(c).

Our model is supported by several control experiments. First of all, we find that PbSeTe ternary layers are stable against strain-induced coherent islanding when the Se concentration drops below a critical value of about 40%. Thus, intermixing indeed destabilizes the PbSe dots when the alloying is sufficiently large. Secondly, the characteristic shape transition is only observed for overgrowth but not during post growth annealing. This indicates that a direct exposure of PbSe with Te atoms is required for the dissolution process. Particular support comes from the dramatic effect of introduction of EuTe into the capping layer. This was clarified by an additional set of experiments which showed that predeposition of an intermediate EuTe layer as thin as 0.2 ML onto the PbSe islands before PbTe overgrowth is sufficient to completely inhibit the dot dissolution process. This is explained by the very large difference in binding energy of EuTe of 7.9 eV per atom pair compared to ~ 4 eV for the lead salt compounds, which drastically increases the energy barrier for surface exchange. This proves that atom exchange at the surfaces of the dots is the decisive mechanism for island dissolution.

Conclusion

In conclusion, overgrowth of self-assembled PbSe quantum dots induces pronounced shape transformations due to anion surface exchange reactions, leading to a significant shrinking of dot height and rounding of shape. This process can be suppressed by introduction of a barrier layer by which the pyramidal structure of the native dots is preserved. This demonstrates that the cap layer composition is an effective means for tailoring the structure of self-assembled quantum dots as required for device applications.

Acknowledgements

Financial support from the Austrian Science Fund (IR-ON SFB), Gesellschaft für Mikroelektronik and the EU network of excellence (SANDiE) is gratefully acknowledged.

References

[1] V. A. Shchukin and D. Bimberg, Rev. Mod. Phys. **71**, 1125 (1999).

[2] J. Stangl, V. Holý, G. Bauer, Rev. Mod. Phys. **76**, 725 (2004).

[3] G. Springholz, V. Holy, M. Pinczolits and G. Bauer, Science **282**, 734 (1998).

[4] L. Abtin, G. Springholz and V. Holy, Phys. Rev. Lett. **97**, 266103 (2006).

Coupled Split Gate Quantum Dots in GaAs Heterostructures

G. Pillwein[1], G. Strasser[2], G. Brunthaler[1]

[1]Institute for Semiconductor Physics, Univ. Linz, Austria

[2]Institute for Solid State Electronics, TU-Vienna, Austria

We report electrical investigations on a GaAs based double quantum dot structure at low temperatures. The split-gate structure forming the dots was fabricated by a combination of optical and electron beam lithography. The measurements were performed in a dilution refrigerator at temperatures down to 30 mK. We were able to observe a strong indication of a double dot with variable coupling in-between the dots.

Introduction

Split gate quantum dots are among the discussed options for realizing a split-gate quantum computer [1]. A single dot could be used as a qubit, forming a basic building block for quantum computation. However, at least two coupled dots are needed to create entanglement between electrons and perform more useful qubit operations. In the past we have successfully created single GaAs split-gate dots, followed by similar structures in the SiGe system [2]. We now have extended our design to double dots within the GaAs system with the prospect of using the gathered experience in measurements on coupled SiGe dots in the future, where the experimental situation is more difficult.

Sample Preparation

Our samples are based on a MBE grown GaAs/$Al_{0.3}Ga_{0.7}As$ heterostructure with a 2DEG situated approx. 70 nm below the sample surface. They have a carrier concentration of about 2×10^{11} cm^{-2} and a mobility of up to 1.4×10^{6} cm^2/Vs. Ohmic contacts were made from an Au/Ni/Ge alloy and Hall bar mesas were wet-etched with H_2SO_4:H_2O_2:H_2O (1:6:150). The quantum dot structure was defined by e-beam lithography and subsequent deposition of Cr/Au metal electrodes (i.e. the split gates) on top of the hall bar mesa. Figure 1 shows all important parts of the sample at different magnifications. By applying a negative voltage to the split gates the dot potential is formed in the underlying 2DEG. This double dot design consists of six gate fingers, which define a quantum dot (see Fig.1 (d)). Three tunnel barriers are formed by gate 1 in conjunction with gates 2, 4 and 6. These barriers are supposed to separate the two dots from the surrounding 2DEG and from each other. Gates 3 and 5 are designed to be used as plunger gates to be able to vary the number of electrons on the two dots independently of each other. Gates 7 and 8 form quantum point contacts together with gates 2 and 6 respectively, which are intended for use as charge detectors. The size of the whole double dot structure is less than 500 nm, leaving roughly a size of 200 nm for each of the single dots.

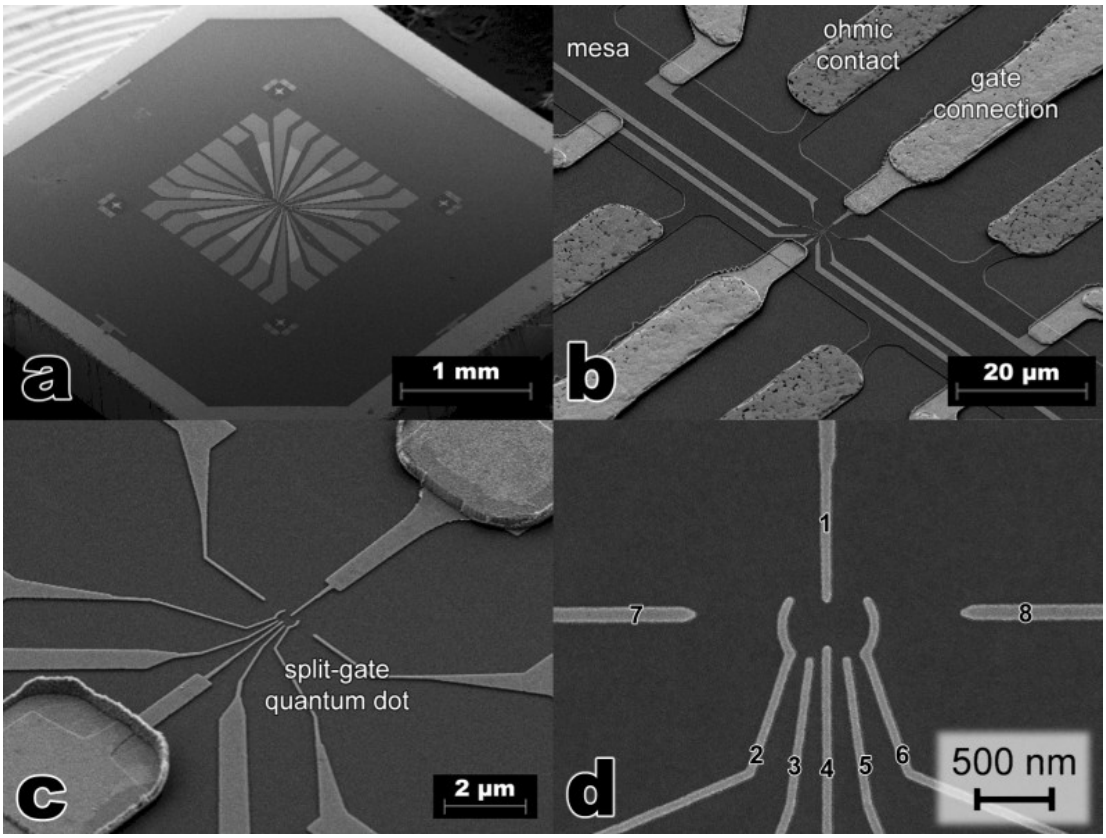

Fig. 1: SEM images of a double quantum dot split-gate structure fabricated by electron beam lithography. Pictures (a) – (d) show the sample at increasing magnifications.

Measurements

Measurements on this sample were performed in a dilution refrigerator capable of reaching temperatures of down to 30 mK. A low frequency lock-in technique was used for the measurements. A small AC voltage signal is applied on the sample and the resulting current through as well as the voltage drop across the device is measured by the lock-in amplifier. This gives the differential conductance $G=dI/dV_{SD}$. The applied voltage should not lead to additional heating of the sample, which means the condition $V_{SD} < kT/e$ should be fulfilled. At 30 mK this means the voltage should not exceed 2.5 µV. Additionally a larger DC voltage can be superimposed on the AC signal, which shifts the working point of the device, allowing to trace the nonlinear current voltage characteristics.

Single Quantum Dot

The double dot structure can of course also be used as a single dot, by adjusting the gates in corresponding fashion. Figure 2 shows a 2D plot of the differential conductance G of such a single dot depending on both the plunger gate voltage and on the source drain voltage. In the dark rhombic regions transport through the dot is blocked, whereas the lines around these regions mark transport through ground and excited states of the dot. From this plot the relevant basic data of the quantum dot can be easily extracted.

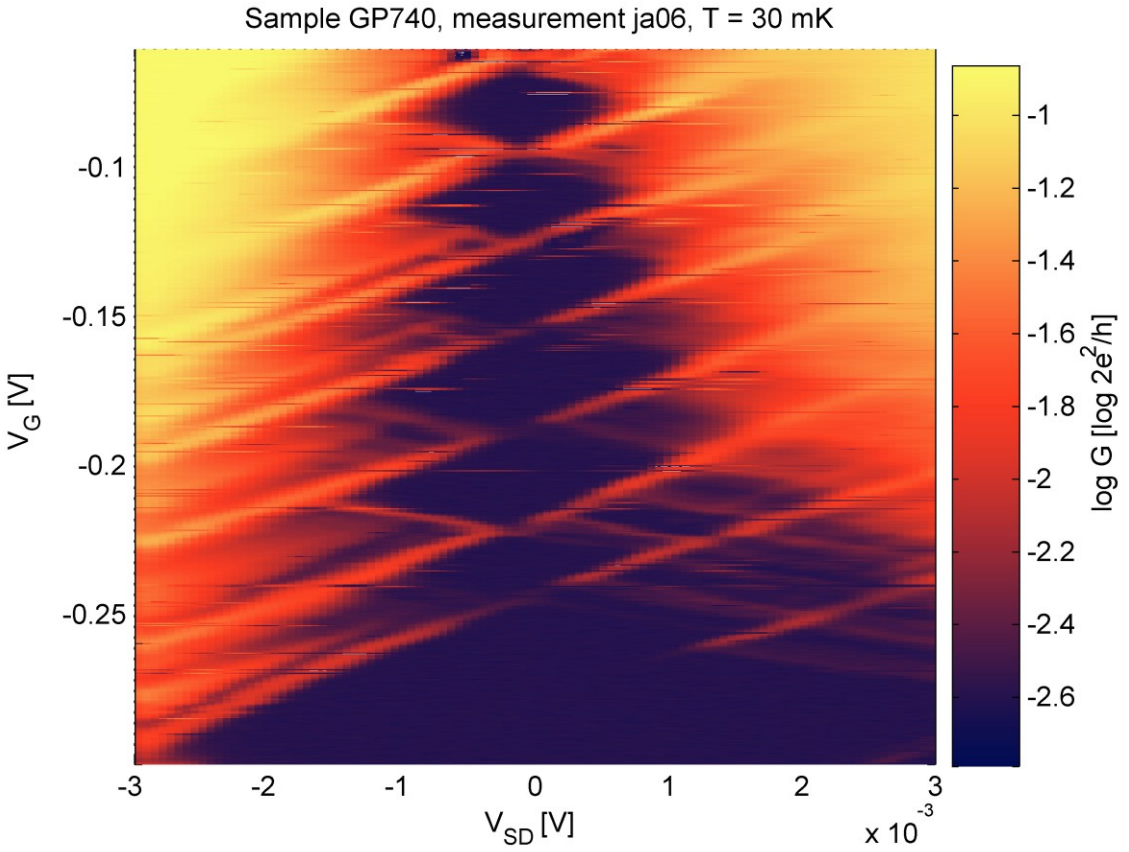

Fig. 2: Differential conductance G versus V_G and V_{SD} of a single quantum dot formed in our double dot structure. The dark rhombic regions mark where the Coulomb blockade is preventing transport through the dot. From the slope and distance of the diagonal lines we can evaluate the basic parameters of the dot.

In case of this dot we obtain a total capacitance C = 159 aF, a source capacitance C_S = 81.5 aF and a gate capacitance C_G =5.3 aF. The closely spaced lines outside the diamond regions correspond to excited states of the dot and their spacing can be used to roughly estimate the active size of the dot. In this case the average spacing ΔE is about 0.14 meV, giving an estimate of 182 nm for the diameter.

Double Quantum Dot

By varying gates 3 and 5 independently of each other one can check for the existence of coupled dots in the structure. In a single dot both gates couple to the same dot and one will observe a series of parallel lines in the conductance. For two dots each gate will mainly have an effect on its associated dot. That means the energy levels in the two dots are shifted more or less independently, leading to a pattern of crossed lines. In the extreme case of no coupling between the dots these lines would theoretically cross at right angle. The more strongly the dots are coupled the smaller the angle between the lines becomes. The extreme case of very large coupling corresponds to a single dot again. In between one observes a so-called honeycomb pattern. Figure 3 shows four such plots of the differential conductance G versus $V_{G,3}$ and $V_{G,5}$ for various settings of the other gates. In Fig. 3(a) the resulting conductance peak lines clearly cross, at a relatively small angle indicating the presence of a rather strongly coupled double dot. For the subsequent Figs. 3(b) – (d) the coupling is further increased to the extreme limit of a single dot (parallel lines) in Fig. 3(d).

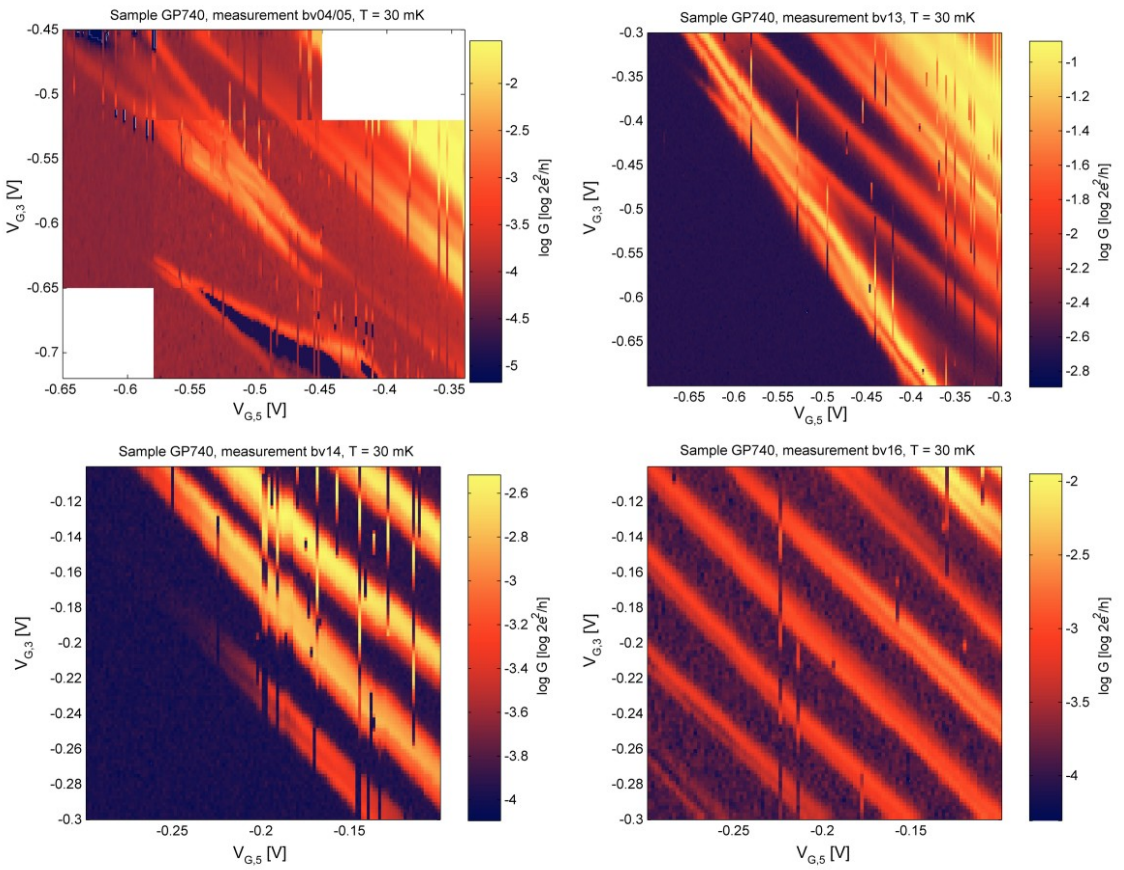

Fig. 2: 2D plots of the differential conductance G versus gate voltage on gate 3 and 5. (a) the crossed lines are a clear indication of having two rather strongly coupled dots. (b) – (d) with increasing coupling the lines become more parallel, finally indicating a large single dot in (d).

Conclusion

We have fabricated and electrically investigated a split-gate double quantum dot structure equipped with quantum point contacts for charge read-out. A single dot created in this structure had an estimated diameter of 180 nm. We could also observe the signature of variable coupling between two dots created in this structure.

Acknowledgements

FWF (P16160)

References

[1] D. Loss and D. P. DiVincenzo: “Quantum computation with quantum dots”, PRA, Vol. 57, 1998, pp. 120

[2] T. Berer, D. Pachinger, G. Pillwein, M. Mühlberger, H. Lichtenberger, G. Brunthaler and F. Schäffler: “Lateral quantum dots in Si/SiGe realized by a Schottky split-gate technique”, APL, Vol. 88, 2006, pp. 162112

Effect of Quantum Confinement on Higher Transitions in HgTe Nanocrystals

V. Rinnerbauer, K. Hingerl, M. Kovalenko, W. Heiss

Christian Doppler Labor für oberflächenoptische Methoden, Institut für Halbleiter- und Festkörperphysik, Johannes-Kepler Universität 4040 Linz

Spectroscopic ellipsometry measurements on 1-10 bilayers of HgTe nanocrystals and polymer were performed in the spectral range from 0.5 – 5 eV. The experiments show that the band model respectively band energy shifts due to quantization can be applied onto nanocrystals with as few as 5 unit cells in diameter. These nanocrystals exhibit strong transitions at higher critical points. The critical point energies shift up to 0.4 eV. It turns out that transitions between bands which are closer to the Fermi energy and have a smaller carrier mass are more strongly affected by quantum confinement.

Introduction

Recently, a number of devices based on HgTe nanocrystals (NCs) have emerged which use photoluminescence or electroluminescence to create light in the near infrared [1], [2]. Due to quantum confinement, the energy levels in the NCs are changed, and HgTe is transformed from a semiconductor with a negative bandgap of E_g = -0.15 eV to a semiconductor with a bandgap of up to 1 eV, covering the important telecommunication wavelength range at 1.5 µm. All these devices are based on the creation of the bandgap, which takes place when the radius of the NC is reduced below the Bohr exciton radius, which is r = 40 nm in bulk HgTe. The influence of the size, the preparation and deposition method on the bandgap and the emission properties of the NCs have been extensively studied [3], [4]. However, there have been no studies up to now on the effects of the quantum confinement on higher critical point energies for HgTe NCs. For other NCs like CdTe and PbSe, ellipsometric studies have been used before to determine optical properties and the effects of quantum confinement [5], [6]. In this work, we use spectroscopic ellipsometry (SE) to study quantization effects on HgTe NCs, especially the relation between the size of the NCs and the energy shift of higher transitions. These measurements clearly show the existence of critical points in the dielectric function of the NCs and their shift to higher energies compared to the bulk value caused by size quantization. Previous authors adapt concepts coming from bulk semiconductor optics like critical points (CPs) and apply these concepts to NCs, using the same lineshape models for these CPs [6], [7]. In our case, the agreement between model calculations and measurements justifies the use of these models as well.

Experimental

Sample Preparation

We use HgTe NCs prepared from colloidal solution, using an aqueous thiol-capping method [3], [8] with thioglycerol (TG) as stabilizer. The size of the NCs was controlled by post-synthetic heat treatment. We have fabricated 5 different sizes of NCs by using growth times of 0, 90, 150, 300 and 600 minutes, which corresponds [3] to approximate NC diameters of 3.5 nm, which we name “smallest”, 4.1 nm, 5.3 nm, 6.9 nm, and

10.7 nm, which we name “largest”. With these NCs, thin mono- and multilayer films were self-assembled using a layer-by-layer deposition technique driven by electrostatic interaction [1], [9]. Alternative adsorption of poly(diallyldimethylammonium chloride) (PDDA) and TG-stabilized HgTe NCs from their aqueous solution resulted in the formation of a sequence of PDDA/HgTe NCs bilayers. We use samples with 10 bilayers on a glass substrate to determine the properties of these layers by SE. For the purpose of determining the CPs of the HgTe NCs we use samples with only one layer of NCs on one layer of PDDA on a glass substrate, which minimizes the influence of layer thickness and roughness originating from deposition.

Measurements

We performed SE on these samples to determine the dependence of the CP energies on the size of the NCs. Figure 1 shows the measured pseudodielectric function of a sample with 10 bilayers with the smallest NCs on a glass substrate, as well as the fit. We determined independently the dispersion relation of PDDA and used this information to model the compound layers with effective medium approximation [10]. The surface roughness of the sample was taken into account with an additional effective medium modeled layer of polymer, HgTe and air. Due to the shift of the CPs of NCs we cannot use the bulk reference material and therefore model the dispersion of HgTe with three Lorentz oscillators for the three transitions found in the measurement range (E_0, E_1, $E_1+\Delta_1$). This model describes the measured dielectric function remarkably well, and the blueshift of the CPs of the NCs with respect to the values of HgTe bulk material found in literature can be observed. Especially the E_0 HgTe transition can only be observed in NC samples, where a bandgap exists due to quantum confinement, in contrast to bulk HgTe, which has a negative bandgap and does not exhibit this transition. The photoluminescence (PL) energy of this sample is shifted approximately by 190 meV from the E_0 CP.

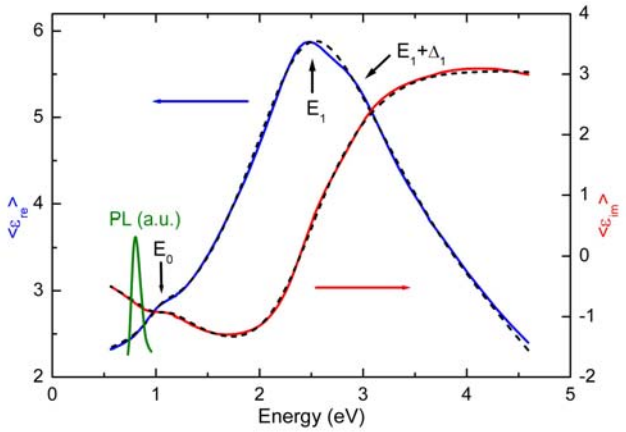

Fig. 1: SE measurement (straight line) and fit (dashed line) as well as PL measurement of a sample with 10 bilayers of HgTe NCs with a diameter of 3.5 nm on glass; inset: TEM picture of a NC with a diameter of ~9 nm

For determining the energy of the CPs, however, we follow the literature and use the second derivative of the pseudodielectric function [11], which facilitates the determination of the CP energy. With simulations we checked for our (with the exception of HgTe) almost dispersion less system (glass / 1 nm polymer / 1 layer of NCs) that the singularities which show up in the second derivative of the measured pseudodielectric function directly correspond to the CPs of the HgTe NCs. We found that the influence

of layer thickness and NC content can be neglected, which makes the thin-film approximation applicable. Figure 2 shows the second derivative of the imaginary part of ε for bulk material [12], and the second derivative of the measured pseudodielectric function for the biggest and the smallest NCs. As can be seen, the positions of the E_1, $E_1+\Delta_1$ CPs shift to higher energies with decreasing size, whereas there is almost no change in the position of the E_2 transition. One can also observe the increase of the oscillator width, which is due to the size distribution of the NCs. The oscillator strength of these transitions is much smaller for the NCs than for the bulk material. For bulk material the strength of the E_2 transition is smaller than for the other transitions, whereas in the NCs the relative strength of the CPs is comparable. The change in the type of the singularity is attributed to a different phase caused by a thin film effect, rather than another type of transition caused by a change in the band structure.

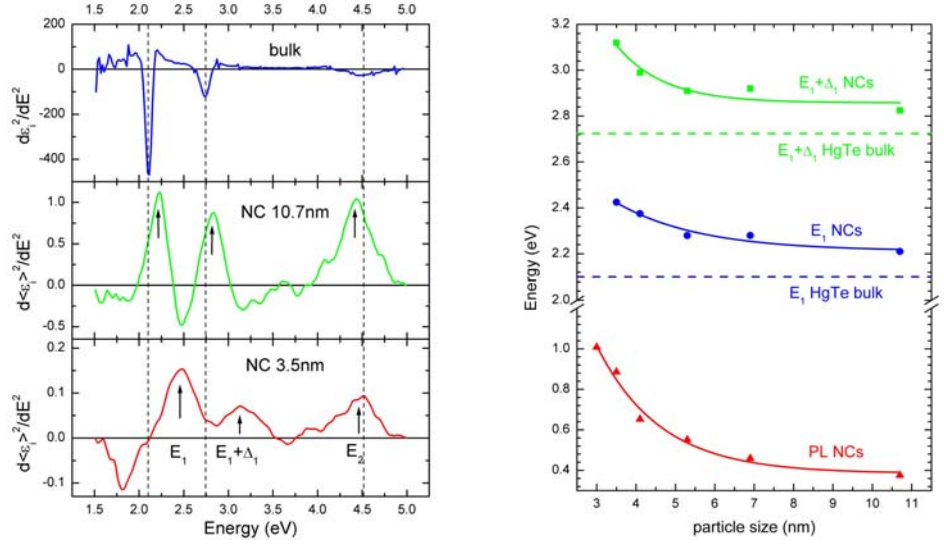

Fig. 2: (a) Second derivative of the imaginary part of the dielectric function of bulk HgTe (top) and the measured pseudodielectric function of HgTe NCs of 10.7 nm diameter (middle) and 3.5 nm diameter (bottom) (b) size dependence of PL wavelength and higher transition energies

The measured transitions were fitted with the same lineshape models used in bulk semiconductor physics. The line-shape of the CPs can be described as [10]:

$$\langle \varepsilon \rangle'' = f \cdot e^{i\Phi} \left(E - E_i + i\Gamma \right)^{-n} \tag{1}$$

with the dielectric function ε, the oscillator strength f, the oscillator energy E_i, oscillator width Γ and phase Φ. In the absence of theoretical models, the exponent n is set to 3, which is used to describe excitonic effects and the phase Φ is set to 0 [13]. In contrast to the NCs the reference data of HgTe bulk material [11] was fitted with n = 2 and Φ = 90°, which corresponds to the line-shape of a 2D Van Hove singularity with a saddle point in the energy band as it is the case for the E_1, $E_1+\Delta_1$ and E_2 transition in HgTe. As mentioned before, the change of the phase for the NC sample is caused by the small thickness of the film. However, the fit of the measured data leads to similar results of the CP energies and oscillator strength irrespective of the used values for n and Φ. The fit of the bulk material gives values of 2.10, 2.73 and 4.52 eV for E_1, $E_1+\Delta_1$ and E_2, respectively, which is in good agreement with values in literature [14]. As can be seen in Figure 2 the shift of the E_2 CP in the NCs is much smaller than the linewidth, and is thus hard to determine. It is also possible that it overlaps with the E_0' transition, which is

located at 4.14 eV [14], and has in bulk another phase angle due to the different dimensionality of the CP.

It is well known that the bandgap and consequently the PL energies of NCs increase with decreasing size due to the quantum confinement. In particular, the PL wavelength of the NCs used in this study ranges from 1.4 µm for the smallest NCs to 3.3 µm for the biggest NCs as determined in a previous study [3]. From the SE measurements we can determine that the higher order transitions E_1 and $E_1+\Delta_1$ exhibit the same behavior, even though to a lesser extent. As expected, the energy of these transitions increases with decreasing growth time, i.e. decreasing size (see Fig. 3). For the smallest NCs, the blueshift of the E_1 transition (heavy hole) is about 0.3 eV and the shift of the $E_1+\Delta_1$ (light hole) transition about 0.4 eV to higher energies compared to the bulk HgTe values. It is clear that transitions between bands which are closer to the Fermi energy (E_0) are more strongly affected by quantum confinement. The effect of the quantum confinement depends on the value of the Bohr exciton radius and therefore on the effective mass, which are different at the Γ point and at the band edge, where the higher transitions occur.

The oscillator strength of the E_1 and $E_1+\Delta_1$ transitions increases with increasing NC size, but it is still by far smaller than the values obtained from the fit for bulk HgTe (2.63 and 1.72 for the E_1 and $E_1+\Delta_1$ transitions respectively). The transition strength is given by the product of the dipole matrix element and the joint density of states (JDOS). The JDOS is lower for NCs because due to the finite periodicity in real space less k states (i.e. less unit cells) can contribute to transitions.

Conclusion

In conclusion, we have determined the effect of quantum confinement on the optical properties of HgTe by spectroscopic ellipsometry. A blueshift of the higher energy transitions E_1 and $E_1+\Delta_1$ for the nanocrystals with respect to the bulk material is observed. The blueshift decreases with increasing size and the transition energies approach the bulk value for large sizes of the NCs. There is a broadening of the CPs due to the size inhomogenity of the NCs, and the transition strength is much lower for the NCs than in bulk material and increases with increasing size of the NCs.

Acknowledgements

The authors are grateful to Dr. Thomas Wagner of LOT-Oriel for performing SE measurements in the mid-infrared region and to Dietmar Pachinger, Günther Hesser and Friedrich Schäffler for taking TEM pictures. The authors also acknowledge financial support from Photeon Technologies as well as the Fonds zur Förderung der wissenschaftlichen Forschung (FWF) and the European community.

References

[1] J. Roither, M. V. Kovalenko, S. Pichler, T. Schwarzl, and W. Heiss, Applied Physics Letters 86, 241104 (2005); S. I. Shopova, G. Farca, A. T. Rosenberger, W. M.S. Wickramanayake, and N. A. Kotov, Appl.Phys. Lett. 85, 6101 (2004).

[2] E. O'Connor et al., Applied Physics Letters **86**, 201114 (2005); D. S. Koktysh et al., ChemPysChem **5**, 1435 (2004).

[3] M. V. Kovalenko et al., J. Am. Chem. Soc. 128, 3516 (2006).

[4] M. T. Harrison et al., J. Mater. Chem. **9**, 2721 (1999).

[5] P. Babu Dayal, B. R. Mehla, and P. D. Paulson, Phys. Rev. B **72**, 115413 (2005).

[6] Z. Hens et al., Phys. Rev. Lett. **92**, 026808 (2004).

[7] D. Amans et al., J. Appl. Phys. **93**, 4173 (2003).

[8] A. Rogach et al., Adv. Mater. **11**, 552 (1999).

[9] G. Decher, Science **277**, 232 (1997).

[10] D. E. Aspnes, Am. J. Phys. **50**, 704 (1982).

[11] M. Cardona, in *Modulation Spectroscopy, Supplement 11 of Solid State Physics*, edited by F. Seitz (Academic Press, New York, 1969)

[12] H. Arwin and D. E. Aspnes, J. Vac. Sci. Technol. A **2**, 600 (1984).

[13] U. Rossow, in *Epioptics*, edited by J. F. McGilp (Springer Verlag, Berlin, 1995), Chap. 3, p.46.

[14] G. Nimtz, in *Landolt-Börnstein*, edited by K.-H. Hellwege (Springer Verlag, Berlin, 1982), Vol. **17b**, p.239.

Plasmon-Cyclotron Coupling in a High-Mobility Two-Dimensional Electron Gas in GaN/AlGaN Heterostructures

A. Wolos[1], W. Jantsch[1], K. Dybko[2], Z. Wilamowski[2], and C. Skierbiszewski[3]

[1] Institute of Semiconductor and Solid State Physics, Johannes Kepler Universität, Linz, Austria

[2] Institute of Physics, Polish Academy of Sciences, Warszawa, Poland

[3] Institute of High Pressure Physics, Polish Academy of Sciences, Warszawa, Poland

We report on the observation and theoretical modeling of sample-size dependent plasma oscillations coupled to the cyclotron motion [1] in a high-mobility two-dimensional electron gas (2DEG) confined at the GaN/AlGaN interface. We record plasmon-cyclotron features using standard microwave resonance spectrometry (electron spin resonance, ESR), which provides a convenient, contact-less method to characterize transport properties of the 2DEG.

Introduction

In this communication we report on the observation of sample-size dependent plasma oscillations coupled to the cyclotron motion in a high-mobility two-dimensional electron gas, 2DEG, confined at the GaN/AlGaN interface. We record plasmon-cyclotron features using standard microwave resonance spectrometry, which provides a convenient, contact-less method to characterize transport properties of the 2DEG.

Experimental

The heterostructures used in these studies were grown on semi-insulating GaN bulk substrates, on the Ga-polarity (0001) surface, by plasma-assisted molecular beam epitaxy (MBE). The surface of the substrates was prepared for the growth by the standard method including mechanical polishing followed by mechano-chemical polishing. The MBE-grown heterostructure consisted of a 0.9 μm GaN layer followed by the 25 nm-thick $Al_{0.09}Ga_{0.91}N$ barrier, and a 3 nm-thick GaN cap layer.

It has been observed, *e.g.* for GaAs-based 2D heterostructures, that the cyclotron motion of an electron and the plasma oscillations hybridize, when the frequency of the two modes approach each other. The two resonance frequencies for plasmon-cyclotron coupling are then given by: [1]

$$\omega_{res}^{\pm} = \pm\frac{\omega_c}{2} + \sqrt{\omega_p^2 + \left(\frac{\omega_c}{2}\right)^2}\,, \qquad (1)$$

where ω_c stands for the cyclotron frequency and ω_p is plasma frequency, which scales with plasmon wave vector, and thus with the sample size. For a disc-shaped sample with a radius *R* this dependence is given by:

$$\omega_p^2 = \frac{n_{2D}e^2}{m^*(1+\varepsilon_{GaN})\varepsilon_0 R} \quad . \tag{2}$$

Here, n_{2D} is the sheet electron concentration, $m^* = 0.2\ m_0$ the electron effective mass, ε_0 vacuum permittivity, and $\varepsilon_{GaN} = 10.4$ is a static dielectric constant of GaN.

To describe the line shape of the coupled resonance recorded by ESR in our GaN/AlGaN heterostructures, we assumed a Lorentzian shape for the absorption of circular polarized electromagnetic waves in the frequency domain, with two resonance frequencies given by Eq. (1):

$$F^{\pm}(\omega,B) = \frac{2A}{\pi}\frac{\Delta}{\Delta^2 + 4\left(\omega - \omega_{res}^{\pm}(B)\right)^2}, \tag{3}$$

for σ^+ and σ^- polarization, respectively. The final expression for the line shape has a following form, which takes into account the linear polarization of the absorbed microwaves, and the fact that we measure the first derivative of the absorption *vs*. magnetic field due to the use of modulation of $\mathbf{B_0}$ and lock-in detection:

$$f(\omega,B) = \frac{1}{2}\frac{\partial}{\partial B}\left(F^{+}(\omega,B) + F^{-}(\omega,B)\right). \tag{4}$$

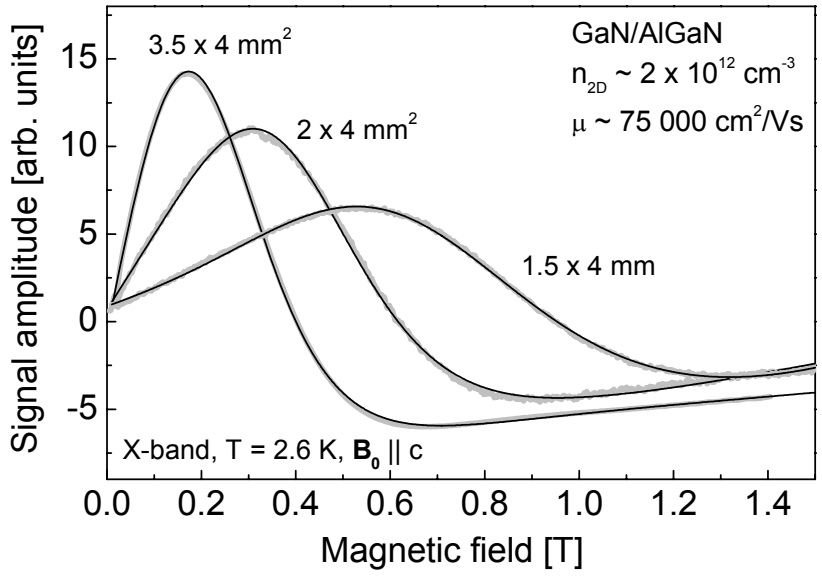

Fig. 1: Plasma-cyclotron resonance in GaN/AlGaN with different sample dimensions: 3.5 x 4 mm^2, 2 x 4 mm^2, and 1.5 x 4 mm^2 respectively ($n_{2D} = 1.95 \times 10^{12}$ cm^{-2} and $\mu_{tr} = 70\,000 - 80\,000$ cm^2/Vs for each sample). Grey lines are experimental spectra. The black lines represent least squares fits of Eq. (4).

Results

With help of Eq. (4) we can reproduce the characteristic asymmetric line shape of the recorded resonance. Figure 1 shows the ESR spectra for three GaN/AlGaN samples having the same sheet electron concentration and mobility, but different sample dimensions. Together with recorded spectra, fits using Eq. (4) are shown. Best fit parameters, plasma frequency (dependant on both sheet electron concentration and a sample di-

mension, Eq. (2)), and a line width Δ (which can be translated to the mobility using Drude relation) are listed below:

Sample size [mm^2]	$\omega_p/2\pi$ [GHz] ± 2	$\Delta/2\pi$ [GHz] ± 1	μ_t [cm^2/Vs] ± 5000
3.5 x 4	26	18.4	76 000
2.0 x 4	32	16.8	83 000
1.5 x 4	41	18.3	77 000

Conclusion

The observation of a coupled plasmon-cyclotron resonance by the ESR technique provides a contact-less method to characterize electronic properties of the 2D electron gas. Both the sheet electron concentration and the mobility may be determined with high precision from the resonance position and the line shape of coupled magneto-plasma modes, for which we have derived a simple formula basing on the theory for dimensional resonances.

Acknowledgements

Work supported by the Austrian Science Fund (FWF), ÖAD and by the Austrian Gesellschaft für Mikroelektronik (GMe).

References

[1] S. J. Allen, Jr., H. L. Stormer, and J. C. M. Hwang, Phys. Rev. B **28**, 4875 (1983).

Properties of the Two-Dimensional Electron Gas Confined at a GaN/AlGaN Interface Studied by Electron Spin Resonance

A. Wolos[1], W. Jantsch[1], K. Dybko[2], Z. Wilamowski[2], C. Skierbiszewski[3]

[1] Institut für Halbleiter- und Festkörperphysik, Johannes-Kepler-Universität Linz, A-4040 Linz

[2] Institute of Physics, PAS, Warsaw, Poland

[3] Institute of High Pressure Physics, PAS, Warsaw, Poland

We present electron spin resonance investigations of the two-dimensional electron gas confined at a GaN/AlGaN interface. On a single spectrum we observe (i) Shubnikov-de Haas oscillations, from which we determine the sheet carrier concentration of the order of $2*10^{12}$ cm^{-2}, (ii) the coupled plasmon-cyclotron resonance, from which the free electron mobility as high as about 140 000 cm^2/Vs is determined, and (iii) a narrow resonance line with a g-factor close to 2. We assign the narrow line to the conduction electron spin resonance. The g-factor close to the free electron value, small anisotropy and a narrow linewidth of the resonance indicate that the spin-orbit fields are small in the investigated heterostructure. This is in contrast to the high value of the effective Rashba parameter reported in the literature determined from transport experiments. On the other hand our result is in agreement with the weak spin-orbit interaction expected for wide band-gap materials, such as GaN.

Introduction

GaN-based heterostructures are used in blue optoelectronics and high-frequency electronics. Now, they are also considered for spintronics, which wants to exploit not only the electron's charge, but also its spin. In order to establish GaN-based heterostructures in spintronics, the spin-orbit interactions governing, *e.g.* electron spin dynamics need to be investigated. Contradictory reports regarding these issues have appeared up to now in literature. Early papers evaluating the g-factor of free electrons in GaN give a value between 1.94 ± 0.01 in bulk crystals [1] and 2.06 ± 0.04 in heterostructures [2], indicating rather weak spin-orbit interaction, which actually is expected for GaN. On the other hand, recent weak antilocalization experiments give rather large values of the Rashba spin-orbit coupling parameter in GaN, of the order of $6*10^{-13}$ eVm [3]. For comparison, in SiGe asymmetric quantum wells, conduction electrons are also characterized by a g-factor close to 2, and the Rashba parameter is about an order of magnitude lower [4].

In order to investigate spin-orbit interaction in GaN, GaN/AlGaN heterostructures have been grown by plasma assisted molecular beam epitaxy on bulk GaN substrates. The two-dimensional (2D) electron gas formed at the GaN/AlGaN interface exhibits a record-high mobility of a several thousand cm^2/Vs and above, as determined from Hall measurements and confirmed later by spin resonance experiments. The samples are of wurtzite structure with their c-axis normal to the plane of the 2D electron gas.

The electron spin resonance (ESR) experiments have been performed using a standard Bruker ELEXSYS E-580 spectrometer operating at the X-band microwave fre-

quency (9.48 GHz). The measurements have been performed at the temperatures between 2.4 K and 300 K, using an Oxford constant-flow cryostat.

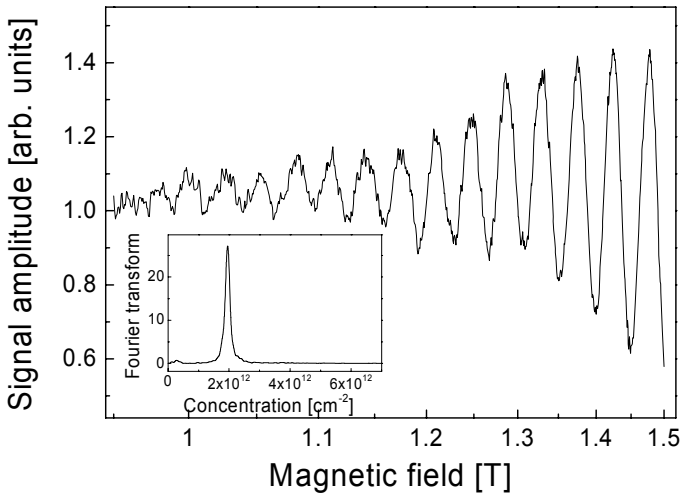

Fig. 1: Shubnikov-de Haas oscillations measured in a GaN/AlGaN sample. Inset: Fourier transform of the signal showing a dominant oscillation frequency corresponding to a sheet electron concentration of n_{2D} = 1.95 * 10^{12} cm^{-2}.

Electron Spin Resonance Experiments

An essential prerequisite to observe signals from the 2D electrons in the ESR technique is a high mobility of the electron gas. This requirement is met by our GaN/AlGaN samples, thanks to the high-quality and low dislocation density of the used substrates. On single ESR spectra we observe (i) Shubnikov – de Haas oscillations, (ii) a broad and strong resonance, which can be explained as a plasma-shifted cyclotron resonance, and (iii) a narrow line with a g-factor close to 2, which we attribute to the conduction electron spin resonance.

Figure 1 shows Shubnikov – de Haas oscillations measured by this contactless resonance technique. Fourier transform of the signal indicates only one oscillation frequency, from which a sheet carrier density n_{2D} = 1.95*10^{12} cm^{-2} can be calculated. The obtained concentration agrees well with the dc transport results.

As it was shown, *e.g.* for GaAs-based heterostructures, when the frequency of the electron cyclotron motion approaches plasma frequency of the two-dimensional electron gas, the two modes hybridize in a collective magnetoplasma excitation. The lower resonance frequency of a coupled plasmon-cyclotron mode is then given by:

$$\omega_{res} = -\frac{\omega_c}{2} + \sqrt{{\omega_p}^2 + \left(\frac{\omega_c}{2}\right)^2}\,, \qquad (1)$$

where ω_c and ω_p stand for the cyclotron- and the plasma-frequency, respectively. Figure 2 shows such a combined resonance recorded for a GaN/AlGaN sample, for different angles Θ between the external magnetic field and the direction normal to the sample plane. The resonance field shows a 1/cos(Θ) dependence, typical for the cyclotron resonance of the 2D electron gas. The resonance is shifted, however, from the cyclotron frequency, according to the Eq. (1). Assuming a Lorenzian lineshape in the frequency domain, we can fit the shape of the spectrum recorded in the magnetic field

domain. Results are shown in the inset (b) of Fig. 2. The fitted linewidth yields a record-high mobility of the 2D electron gas of 136 000 cm^2/Vs. It is worth to note, that the plasma frequency of the 2D electrons depends on the dimension of the sample what gives the possibility of tuning the coupled magnetoplasma mode in a wide range of frequencies (the examined sample is a few mm in diameter).

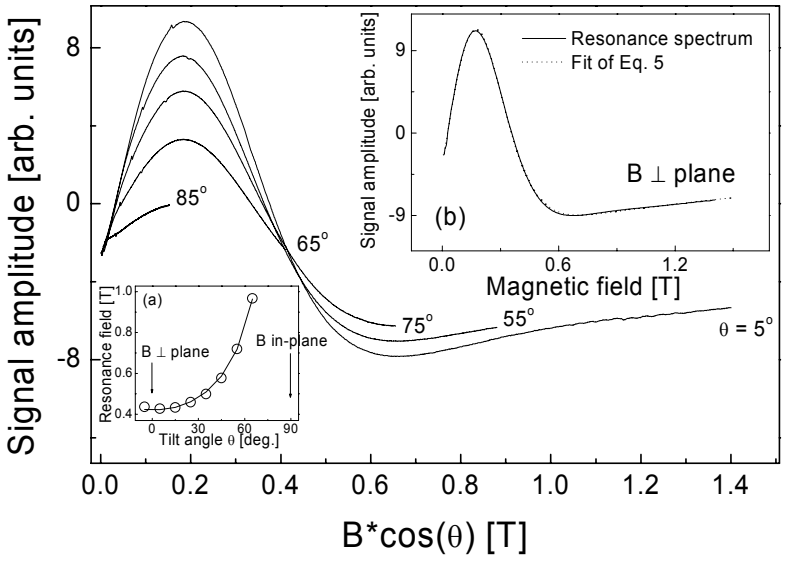

Fig. 2: Coupled plasmon-cyclotron resonance in GaN/AlGaN measured for different angles *Θ* between the external magnetic field and the direction normal to the sample plane. Inset (a): Open points – resonance magnetic field versus the tilt angle *Θ*; solid line – 1/cos(*Θ*) fit. Inset (b): Solid line – the spectrum; dotted line – theoretical fit.

Figure 3 shows the recorded narrow resonance line with $g_{||} = 2.00175$ (B || c) and $g_{\perp} = 2.00196$ (B $\perp$ c) at T = 2.4 K. The anisotropy of the g-factor slightly changes with the temperature from negative $g_{||} < g_{\perp}$ at very low temperatures to positive $g_{||} > g_{\perp}$ at the room temperature. The linewidth of this resonance is extraordinarily narrow, below 1 G, which is characteristic for the motional narrowing of the conduction electrons. The integrated amplitude of the line is practically temperature-independent, indicating Pauli-type of paramagnetism, which is also characteristic for free carriers. Thus, we attribute this line to the conduction electron spin resonance.

As it was shown, *e.g.* in Ref. [4], the conduction electron g-factor and the resonance linewidth are affected by the presence of the internal spin-orbit fields which add to the magnetic field externally applied in the experiment. These spin-orbit fields (called Rashba or Dresselhaus fields) originate from bulk- and/or structure-induced asymmetry of the investigated quantum well. A detailed quantitative analysis of the narrow resonance recorded for GaN/AlGaN is under progress. However, even now we can draw the conclusion that the spin-orbit interaction in the investigated heterostructure is very small. This is due to the fact, that the observed g-factor is very close to the free electron value, and the observed g-factor anisotropy and the resonance linewidth are small. Thus a value of the Rashba spin-orbit parameter similar to that obtained for SiGe quantum wells may be expected. In the contrary to SiGe heterostructures the negative anisotropy of the g-factor observed for GaN/AlGaN suggest also significant contribution of the cubic Dresselhaus term in the spin-orbit Hamiltonian, that should result in a Dresselhaus field perpendicular to the plane of the 2D electron gas.

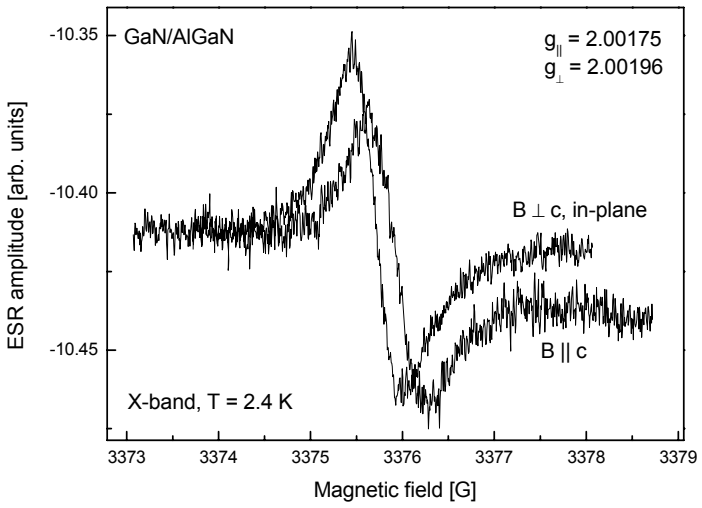

Fig. 3: Conduction electron spin resonance in GaN/AlGaN heterostructure.

Conclusion

We have investigated the properties of the high-mobility two-dimensional electron gas confined at the GaN/AlGaN interface by ESR techniques. For the first time a coupled plasmon-cyclotron excitation in GaN has been observed. As the frequency of this excitation depends on the dimension of the sample, one can predict that in micrometer-size structures the magnetoplasma frequency will fall into the THz range, making this phenomenon interesting for the field of generation or detection of THz radiation.

For the first time, the g-factor of the 2D conduction electrons in GaN has been measured with high precision in a direct experiment. The qualitative analysis of the resonance reveals weak spin-orbit interaction, in contrast to recently reported results of weak antilocalization experiments [3]. However, a weak spin-orbit coupling has been expected for GaN, and it is highly appreciated in spintronic materials as it leads to long spin lifetimes.

References

[1] B. Beschoten, E. Johnston-Halperin, D. K. Young, M. Poggio, J. E. Grimaldi, S. Keller, S. P. DenBaars, U. K. Mishra, E. L. Hu, D. D. Awschalom: “Spin coherence and dephasing in GaN”, Phys. Rev. B **63**, 121202-1/4 (2001).

[2] W. Knap, E. Frayssinet, M. L. Sadowski, C. Skierbiszewski, D. Maude, V. Falko, M. Asif Khan, M. S. Shur: “Effective g^* factor of two-dimensional electrons in GaN/AlGaN heterojunctions”, Appl. Phys. Lett. **75**, 3156-3158 (1999).

[3] S. Schmult, M. J. Manfra, A. Punnoose, A. M. Sergent, K. W. Baldwin, R. J. Molnar:”Large Bychkov-Rashba spin-orbit coupling in high-mobillity GaN/$Al_xGa_{1-x}N$ heterostructures”, Phys. Rev. B **74**, 033302-1/4 (2006).

[4] H. Malissa, W. Jantsch, M. Mühlberger, F. Schäffler, Z. Wilamowski, M. Draxler, P. Bauer: “Anisotropy of g-factor and electron spin resonance linewidth in modulation doped SiGe quantum wells’’ Appl. Phys. Lett. **85**, 1739-1741 (2004).

Sensor Systems

Contents

Sensor Systems

A. Jachimowicz

Institute of Sensor and Actuator Systems,
Vienna University of Technology, Gusshausstrasse 27/366, A-1040 Vienna

In 2005 and 2006 several new devices have been designed and realized within the ZMNS for various projects.

To be able to determine corrosive components in engine oils, a novel sensor consisting of thin-film strips (e.g. made of copper), featuring different thicknesses deposited on a glass substrate has been developed in cooperation with the AC^2T. Over 100 sensors were manufactured and successfully tested.

The thermal conductivity of insulating oil yields important information about the oil's ageing and consequently about the condition of oil-filled high-voltage power transformers. In the frame of a FFF project in cooperation with the Graf Group, thermal conductivity sensors featuring chromium heating elements and germanium thermistors both on closed membrane structures and on spatially separated micro-bridges have been fabricated. The thermal conductivity of transformer oil and several others fluids was determined. The experimental results were implemented in a doctoral thesis and presented in a couple of publications.

In cooperation with TU Delft, a new particle sensor chip has been designed for combined optical and impedance measurements on single cells. Fabrication alternatives for compensation of parasitic substrate coupling have been investigated.

In the course of a "lab-on-chip" project, a silicon-based prototype requiring an external heating for PCR (Polymerase Chain Reaction) has been realized. Further, thin film nano-scale (500 nm conductor path width and 500 nm gap) interdigital electrodes arrays composed of Cr and Au have been realized. The arrays were deposited on thermally oxidized silicon wafers. The usability of the chips for DNA detection is currently investigated in cooperation with ARC-Research.

Miniaturized rheometric devices, featuring in-plane oscillating micromachined silicon nitride bridges which are driven by the Lorentz force, have been designed and fabricated. The micro-bridges have been characterized by means of optical and electrical measurements. The devices show different modes of vibration, suitable for sensing of density and viscosity of liquids. This project is supported by FWF.

A system-capable flow sensor was developed in the course of an FWF project in cooperation with the *Forschungsstelle für Integrierte Sensorsysteme* (Austrian Academy of Sciences). Nine different sensor configurations consisting of thin film germanium thermistors and chromium heaters placed on a 1.3 µm thick silicon nitride membrane (anisotropic etching of Silicon) were designed an manufactured. The properties of the sensor devices are currently investigated.

The research has led to 44 publications in scientific journals and international conference proceedings.

Research Activities

Sensors for the Properties of Liquids

G. Fercher *et al.*: Contactless Conductivity Measurement of Ion Concentrations in Solutions (*page 373*)

A. Jachimowicz *et al.*: Bridge-Based Microsensor for Determining the Thermal Properties of Liquids (*page 379*)

C. Riesch *et al.*: Measurement of Liquid Properties with Resonant Cantilevers (*page 385*)

Particle Sensors

G. Hairer *et al.*: A Non Coaxial Sheath Flow Device for Micrometer Sample Stream Profiles (*page 391*)

S. Kostner *et al.*: On-chip Cytometric Detection of Single Biological Cells Using Integrated Photodiodes (*page 397*)

S. Kostner *et al.*: Particle and Cell Detection using a DVD Pickup Head (*page 401*)

Biosensors

G. Hairer *et al.*: PCR Microsystem for Fast Cycling (*page 405*)

Thermal Flow Sensors

F. Keplinger *et al.*: Sensitive Measurement of Flow Velocity and Flow Direction Using a Circular Thermistor Array (*page 411*)

J. Schalko *et al.*: Advanced Thermal Flow Sensors (*page 417*)

Project Information

Project Manager

Dr. Artur JACHIMOWICZ

Institute of Sensor and Actuator Systems, Gusshausstrasse 27-29, A-1040 Wien

Project Group

Last Name	First Name	Status	Remarks
Agoston	Attila	Ph.D. student	
Avian	Jürgen	student	
Beigelbeck	Roman	student	
Cerimovic	Samir	Ph.D. student	
Fercher	Georg	Ph.D. student	
Graschopf	Dieter	student	
Hairer	Gabriel	Ph.D. student	
Jachimowicz	Artur	Senior researcher	
Jakoby	Bernhard	Associate Prof	
Keplinger	Franz	assistant Prof	
Kostner	Stefan	Ph.D. student	Univ. Ass.
Kuntner	Jochen	Ph.D. student	
Pärr	Günther	student	
Pirker	Ewald	technician	
Riesch	Christian	Ph.D. student	
Rogler	Gerhard	technician	
Schalko	Johannes	postdoc	
Stangl	Günther	technician	
Svasek	Edeltraud	technician	
Svasek	Peter	technician	
Talic	Almir	Ph.D. student	
Vellekoop	Michiel J.	full professor	
Zoppel	Sandra	Ph.D. student	

Books and Contributions to Books

1. J. Nieuwenhuis:
   "*Microsystems for Particle Analysis*";
   Institute of Sensors and Actuator Systems, Vienna, Austria, 2005, ISBN: 3-85465-014-0; 103 S.

2. F. Keplinger:
   "*Disposable Ion-Selective Electrodes*";
   in: "*Encyclopedia of Sensors*", American Scientific Publishers, 2006, ISBN: 1-58883-058-6, S. 369 - 393.

Publications in Reviewed Journals

1. A. Agoston, F. Keplinger, B. Jakoby:
   "Evaluation of a vibrating micromachined cantilever sensor for measuring the viscosity of complex organic liquids";
   Sensors and Actuators A, 123-124 (2005), S. 82 - 86.
2. A. Agoston, C. Ötsch, B. Jakoby:
   "Viscosity sensors for engine oil condition monitoring - Application and interpretation of results";
   Sensors and Actuators A, 121 (2005), S. 327 - 332.
3. B. Jakoby, G. Art, J. Bastemeijer:
   "*Novel Analog Readout Electronics for Microacoustic Thickness Shear-Mode Sensors*";
   IEEE Sensors Journal, 5 (2005), 5; S. 1106 - 1111.
4. B. Jakoby, F.P. Klinger, P. Svasek:
   "*A novel microacoustic viscosity sensor providing integrated sample temperature control*";
   Sensors and Actuators A, 123-124 (2005), S. 274 - 280.
5. B. Jakoby, M. Vellekoop:
   "*Miniaturized Sensors for Monitoring and Physical Chemosensor Applications*";
   Geophysical Research Abstracts (GRA), 7 (2005), 07930.
6. F. Keplinger, R. Beigelbeck, R. Fasching, S. Kvasnica:
   "Miniaturized Cantilever Device with a Broad Measurement Area to Determine Two Orthogonal Magnetic Flux Density Components";
   Geophysical Research Abstracts (GRA), 7 (2005), 11086.
7. J. Kuntner, R. Chabicovsky, B. Jakoby:
   "*Sensing the thermal conductivity of deteriorated mineral oils using a hot-film microsensor*";
   Sensors and Actuators A, 123-124 (2005), S. 397 - 402.
8. J. Kuntner, R. Chabicovsky, F. Kohl, B. Jakoby:
   "*Applicability of Thermal Conductivity Sensing for Condition Monitoring*";
   Geophysical Research Abstracts (GRA), 7 (2005), 11087.
9. J. Kuntner, G. Stangl, B. Jakoby:
   "Characterizing the Rheological Behavior of Oil-Based Liquids: Microacoustic Sensors Versus Rotational Viscometers";
   IEEE Sensors Journal, 5 (2005), 5; S. 850 - 856.
10. S. Kvasnica, P. Adamek, P. Spatenka:
    "*Imaging of Unbalanced Magnetron DC Discharge*";
    IEEE Transactions on Plasma Science, 33 (2005), 2; S. 364 - 365.
11. M. Mannsberger, A. Kukovecz, A. Georgakilas, J. Rechthaler, J. Schalko, F. Hasi, G. Allmaier, M. Prato, H. Kuzmany:
    "*Thermal Stripping of Supramolecular Structures: C60 Nanorods*";
    Journal of Nanoscience and Nanotechnology, 5 (2005), 2; S. 198 - 203.

12.J. Nieuwenhuis, A. Jachimowicz, P. Svasek, M. Vellekoop:
"*Optimization of Microfluidic Particle Sorters Based on Dielectrophoresis*";
IEEE Sensors Journal, 5 (2005), 5; S. 810 - 816.E. Hofer, F. Keplinger, T. Thurner, T. Wiener, D. Sanchez-Quintana, v. Climent, G. Plank: "A new floating sensor array to detect electric near fields of beating heart preparations"; Biosensors & Bioelectronics, 21 (2006), S. 2232 - 2239.

13.N. Kaun, S. Kulka, J. Frank, U. Schade, M. Vellekoop, M. Harasek, B. Lendl:
"*Towards biochemical reaction monitoring using FT-IR synchrotron radiation*";
Analyst, 131 (2006), S. 489 - 494.

14.N. Kaun, M. Vellekoop, B. Lendl:
"Time-Resolved Fourier Transform Infrared Spectroscopy of Chemical Reactions in Solution Using a Focal Plane Array Detector";
Applied Spectroscopy, 60 (2006), 11; S. 1273 - 1278.

15.S. Zoppel, M. Farsari, R. Merz, J. Zehetner, G. Stangl, G.A. Reider, C. Fotakis:
"*Laser micro machining of 3C-SiC single crystals single crystals*";
Microelectronic Engineering, 83 (2006), S. 1400 - 1402.

Talks and Poster Presentations

1. A. Agoston, B. Jakoby:
"*The Monitoring of Mechanical Aging of Engine Oil Using Microacoustic Viscosity Sensors*";
EUROSENSORS XIX, Barcelona, Spain; 11.09.2005 - 14.09.2005; in: "*Proceedings - Vol. 1 (M,T)*", (2005), ISBN: 84-475-2984-3; 4 pages

2. A. Agoston, C. Ötsch, B. Jakoby:
"*Application Aspects of Viscosity Sensors for Online Oil Condition Monitoring*";
12th International Conference (Sensors 2005), Nuremberg, Germany; 10.05.2005 - 12.05.2005; in: "*Proceedings Volume I*", (2005), p. 389 - 392.

3. R. Beigelbeck, F. Kohl, J. Kuntner, B. Jakoby:
"Heat Transfer Analysis of Micromachined Thermal Conductivity Sensors";
IEEE International Conference on Emerging Technologies and Factory Automation (ETFA), Catania, Italy; 19.09.2005 - 22.09.2005; in: "*Proceedings of the ETFA 2005*", (2005), ISBN: 0-7803-9402-X; p. 977 - 983.

4. E. Hofer, F. Keplinger, T. Wiener, T. Thurner, G. Plank:
"*Neue Sensoren zur Nahfeldmessung und Ermittlung von Mikrolatenzen der Erregungsausbreitung*";
Biomedizinische Technik, UMIT/Hall; 10.11.2005 - 12.11.2005; in:
"*Wissenschaftliche Beiträge zur Jahrestagung 2005 - Biomedizinische Technik*", (2005), 2 pages

5. E. Hofer, T. Wiener, T. Thurner, F. Keplinger, P. Svasek, D. Sanchez-Quintana, v. Climent, A. Lueger, G. Plank:
"*Cardiac Near Field Sensors - Technical Requirements and Validation Procedures*";
European Medical and Biological Engineering Conference, Praque, Czech Republic; 20.11.2005 - 25.11.2005; in: "*Proceedings EMBEC '05*", Vol. 11 (2005), ISSN: 1727-1983; 5 pages

6. B. Jakoby, E. Svasek:
"*Ein miniaturisierter Viskositätssensor mit integrierter Temperierungsmöglichkeit*";
7. Dresdner Sensor-Symposium - Neue Herausforderungen und Anwendungen in der Sensortechnik, Dresden, D; 12.12.2005 - 14.12.2005; in: "*Tagungsband 7. Dresdner Sensor-Symposium*", (2005), ISBN: 3-938863-29-3; p. 77 - 80.

7. F. Keplinger, R. Beigelbeck, H. Hauser:
"*Measurement of Two Orthogonal magnetic Flux Density Components with a Single Oscillating U-Shaped Micromachined Cantilever*";
12th International Conference (Sensors 2005), Nuremberg, Germany; 10.05.2005 - 12.05.2005; in: "*Proceedings Volume I - Sensor 2005*", (2005), p. 131 - 135.

8. F. Keplinger, R. Beigelbeck, F. Kohl, S. Kvasnica, A. Jachimowicz, B. Jakoby:
"*Frequency and Transient Analysis of Micromachined U-Shaped Cantilever Devices for Magnetic Field Measurement*";
13th European Conference on Solid-State Sensors, Actuators and Microsystems, Seoul, Korea; 05.06.2005 - 09.06.2005; in: "*Digest of Technical Papers*", (2005), ISBN: 0-7803-8994-8; p. 630 - 635.

9. F. Kohl, R. Beigelbeck, J. Schalko, A. Jachimowicz:
"*Towards System-Ready Flow Sensors*";
IEEE International Conference on Emerging Technologies and Factory Automation (ETFA), Catania, Italy; 19.09.2005 - 22.09.2005; in: "*Proceedings of the ETFA 2005*", (2005), ISBN: 0-7803-9402-X; p. 959 - 966.

10. S. Kostner, J. Nieuwenhuis, M. Vellekoop:
"*DEP Particle Separator with Adaptive Sensitivity*";
12th International Conference (Sensors 2005), Nuremberg, Germany; 10.05.2005 - 12.05.2005; in: "*SENSOR 2005, 12th international Conference*", Proceedings Volume I (2005), p. 261 – 265.

11. J. Kuntner, R. Chabicovsky, F. Kohl, B. Jakoby:
"*Online Oil condition Monitoring Using Thermal Conductivity Sensing*";
12th International Conference (Sensors 2005), Nuremberg, Germany; 10.05.2005 - 12.05.2005; in: "*Proceedings Volume I*", (2005), p. 67 - 71.

12. J. Kuntner, F. Kohl, B. Jakoby:
"*Characterizing the Thermal Transport Properties of Liquids Using a Miniaturized Pulsed Hot-Film Sensor*";
EUROSENSORS XIX, Barcelona, Spain; 11.09.2005 - 14.09.2005; in: "Proceedings - Vol. 1 (M,T)", (2005), ISBN: 84-475-2984-3; 4 pages

13. J. Kuntner, F. Kohl, B. Jakoby:
"*Micromachined thermal conductivity sensor for the liquid phase*";
13th International Conference on Solid-State Sensors, Actuators and Microsystems (Transducers 05), Seoul, Korea; 05.06.2005 - 09.06.2005; in: "*Digest of Technical Papers - Volume 2*", (2005), ISBN: 0-7803-8952-2; p. 571 - 574.

14. M. Vellekoop:
"*Micro-Devices for Particle Detection and Analysis*";
Annual Workshop on Semiconductor Advances for Future Electronics and Sensors, Veldhoven, Netherlands (invited); 17.11.2005 - 18.11.2005; in: "*Proceedings SAFE 2005*", M. Vellekoop (Hrg.); Technology Foundation SAFE & ProRISC, (2005), ISBN: 90-73461-50-2; 1 page

15. M. Vellekoop, S. Kostner, J. Nieuwenhuis:
"*On-chip particle analysis*";
7. Dresdner Sensor-Symposium - Neue Herausforderungen und Anwendungen in der Sensortechnik, Dresden, D; 12.12.2005 - 14.12.2005; in: "*Tagungsband 7. Dresdner Sensor-Symposium*", (2005), ISBN: 3-938863-29-3; p. 57 - 60.

16. R. Beigelbeck, J. Kuntner, F. Kohl, B. Jakoby:
"*Sensing Thermal Material*"; EUROSENSORS XX, Göteborg, Schweden; 17.09.2006 - 20.09.2006; in: "*Proceedings EUROSENSORS 2006*", Vol. II (2006), ISBN: 91-631-9280-2; p. 242 - 243.

17.Hairer, M. Vellekoop:
"*Experiments on Hydrodynamic Focusing of Non-coaxial Sheath Flows*"; IEEE Sensors, Deagu, Korea; 22.10.2006 - 25.10.2006; in: "*Abstract Book IEEE Sensors 2006*", (2006), p. 123.

18.F. Keplinger, J. Kuntner, A. Jachimowicz, F. Kohl, B. Jakoby:
"*Highly Sensitive Sensor for Flow Velocity and Flow Direction Measure*"; IEEE Sensors, Daegu, Korea; 22.10.2006 - 25.10.2006; in: "*Abstract Book - IEEE Sensors 2006*", (2006), p. 398.

19.F. Kohl, R. Beigelbeck, P. Loschmidt, J. Kuntner, A. Jachimowicz:
"*FEM-Based Analysis of Micromachined Calorimetric Flow Sensors*"; IEEE Sensors, Daegu, Korea; 22.10.2006 - 25.10.2006; in: "*Abstract Book - IEEE Sensors 2006*", (2006), p. 337.

20.F. Kohl, F. Keplinger, R. Beigelbeck, J. Kuntner, J. Schalko, A. Jachimowicz:
"*Refined Thermal Flow Sensors by Transduction Engineering*"; EUROSENSORS XX, Göteborg, Schweden; 17.09.2006 - 20.09.2006; in: "*Proceedings EUROSENSORS 2006*", Vol. II (2006), ISBN: 91-631-9280-2; p. 186 - 187.

21.S. Kostner, M. Vellekoop:
"Optical Detection of Different Single Biological Cells in an Integrated Projection Cytometer"; IEEE Sensors, Daegu, Korea; 22.10.2006 - 25.10.2006; in: "Abstract Book IEEE Sensors 2006", (2006), p. 36.

22.J. Kuntner, A. Jachimowicz, F. Kohl, B. Jakoby:
"*Determining the thin-film thermal conductivity of low temperature PECVD silicon nitride*"; EUROSENSORS XX, Göteborg, Schweden; 17.09.2006 - 20.09.2006; in: "*Proceedings EUROSENSORS 2006*", Vol. II (2006), ISBN: 91-631-9280-2; p. 388 - 389.

23.J. Kuntner, A. Jachimowicz, F. Kohl, B. Jakoby:
"Determining thermal properties of liquids: membrane-based versus bridge-based micromachined sensors"; IEEE Sensors, Daegu, Korea; 22.10.2006 - 25.10.2006; in: "Abstract Book - IEEE Sensors 2006", (2006), p. 391.

24.E. Reichel, Ch. Riesch, A. Jachimowicz, B. Weiß, B. Jakoby:
"*A Novel Micromachined Liquid Property Sensor Utilizing a Doubly Clamped Vibrating Beam*"; EUROSENSORS XX, Göteborg, Schweden; 17.09.2006 - 20.09.2006; in: "*Proceedings EUROSENSORS 2006*", Vol. I (2006), ISBN: 91-631-9281-0; p. 114 - 115.

25.Ch. Riesch, E. Reichel, F. Keplinger, B. Jakoby:
"*Characterizing Resonating Cantilevers for Liquid Property Sensing*"; IEEE Sensors, Daegu, Korea; 22.10.2006 - 25.10.2006; in: "*Abstract Book - IEEE Sensors 2006*", (2006), p. 293.

26.C.P.L. Van Vroonhoven, D. Rocha Wiese Meneses, M. Vellekoop, C. Nöhammer:
"*A Readout Circuit for Capacitive Biosensors with Integrated SAR A/D Conversion*"; IEEE International Symposium on Circuits and Systems, Island of Kos, Greece; 21.05.2006 - 24.05.2006; in: "*Proceedings*", (2006), ISBN: 0-7803-9390-2; p. 1418 - 1421.

27.M. Vellekoop, S. Kostner:
"*On-Chip Cell Handling and Analysis*";
EUROSENSORS XX, Göteborg, Sweden (invited); 17.09.2006 - 20.09.2006; in: "*Proceedings Eurosensors 2006*", Vol. I (2006), ISBN: 91-631-9280-2; p. 28 - 29.

Patents

1. F. Keplinger, R. Beigelbeck:
   "*Elektrodeneinrichtung zur Messung eines elektrischen Potentials*";
   Patent: Österreich, Nr. A 858/2005; submitted: 19.05.2005.
2. F. Keplinger, H. Hauser, S. Kvasnica:
   "*Verfahren zur Messung starker Magnetfelder und Sensor zur Ausführung des Verfahrens*";
   Patent: Austria, Nr. AT 413 448 B; submitted: 04.10.2002, granted: 15.02.2006.

Doctor's Theses

1. J. Nieuwenhuis:
   "*Microsystems for particle analysis*";
   Reviewer: M. Vellekoop, P. Telleman; Institut für Sensor- und Aktuatorsysteme, 2005.

Diploma Theses

1. T. Lindenbauer:
   "*Seminumerische Analyse von piezoelektrischen TSM Quarzresonatoren in viskosen Flüssigkeiten*";
   Supervisor: B. Jakoby; Institut für Sensor- und Aktuatorsysteme, 2005.
2. Ch. Riesch:
   "Auswertelektronik für einen Schwingquarz-Viskositätssensor mit Kompensation der parasitären Komponenten";
   Supervisor: B. Jakoby; Institut für Sensor- und Aktuatorsysteme, 2005.

Cooperations

1. AC2T, Wiener Neustadt, F. Franek
2. AMS Unterpremstätten, M. Brandl, F. Schrank
3. ARC Seibersdorf, H. Kroath, C. Nöhammer
4. IMS, E. Fantner, H. Löschner
5. EVG, Schärding, Lind, J. Weixlberger
6. Jenbacher, Jenbach, S. Chvatal
7. OMV, Wien, F. Novotny-Farkas
8. R. Bosch, Reutlingen, Germany, O. Schatz
9. R. Bosch, Stuttgart, Germany, H. Eisenschmidt
10. Elmar Graf GmbH, Dornbirn, E. Graf
11. Applikon, the Netherlands, A. Oudshoorn
12. National Center for Scientific Research, Demokritos, Athens, Greece, D. Ithakissios
13. National Hellenic Research Foundation, Athens, Greece, I. Siotis
14. TU Wien, B. Lendl, E. Benes
15. Universität für Bodenkultur Wien, U.Sleytr, D. Pum, B. Schuster

16.Fachochschule Wiener Neustadt, H. Noll

17.Fachhochschule Vorarlberg, R. Merz, P. Hudek

18.Universität Krems, D. Falkenhagen

19.ÖAW Forschungstelle Integrated Sensor Systems, T. Sauter, F. Kohl

20.TU Delft, The Netherlands, A. Bossche, C. Dekker, P.J. French, I.T. Young

21.ETH Zürich (CH), Ch. Hierold, A. Hierlemann

22.University of Freiburg, IMTEK, Germany, G. Urban, J. Korvink, O. Paul.

23.University of Technology Berlin, Germany, E. Obermeier

24.University Leuven, Belgium, C. Kirschhock

Contactless Conductivity Measurement of Ion Concentrations in Solutions

G. Fercher[1,2] , H. Homolka[1], W. Smetana[1], M. J. Vellekoop[1]

[1] Institute of Sensor and Actuator Systems, Vienna University of Technology, Vienna, Austria

[2] IMA GmbH, Wiener Neustadt, Austria

In this work we present a device manufactured in low temperature co-fired ceramics (LTCC) technology for the contactless conductivity measurement of ion concentrations in aqueous solutions. The signal gets coupled into the microchannel across a ceramic plate of high permittivity. This allows better detection sensitivities as compared to other materials such as glass or PMMA. Finite element modeling (FEM) was carried out to underpin this advantage. First measurements with different concentrations of ion solutions were conducted.

Introduction

Contactless conductivity detection is a powerful and versatile sensing method for biochemical applications and is extensively employed for miniaturized analytical devices [1], [2]. It belongs, covering amperometric, potentiometric and contact conductivity detection, to the category of electrochemical detection. Common advantages in contrast to fluorescence- or absorbance-based systems are the relatively small dimensions of both the detector and read-out electronics. Compounds can furthermore be sensed without prior modification, and chip materials do not need to be transparent.

The working principle of contactless conductivity detection is based on capacitively coupling the excitation signal by either two or four electrodes into the microchannel [3] – [5]. Fluid and electrodes are not in direct contact with each other, thus preventing fouling processes and increasing life time of the device.

Low Temperature Co-fired Ceramics (LTCC) as a low-cost alternative for the fabrication of microanalytical devices is gaining increased interest. In its pre-fired state, LTCC is a flexible tape and can be easily structured using stamping, cutting or laser ablation techniques. Microchannel structures can so be fabricated in a multilayer arrangement [6].

Contactless conductivity detection in combination with PMMA or glass suffers from very low capacitive coupling into the channel. Employing ceramics with high values of permittivity (high-K ceramics) overcomes this drawback.

In our work a LTCC microfluidic device with a contactless conductivity detector has been fabricated. The detector consists of two planar electrodes separated from the channel by a high-K ceramics plate. Since LTCC tapes are not available with very high permittivities, a HTCC ceramic plate is used for the fabrication of the detector. Changes in the detection signal due to varying concentrations of an NaCl solution were measured. The benefit of high-K ceramics compared to low-K materials is pointed out using finite element modeling (FEM).

Device Fabrication

For realization of the device the A6-M LTCC-tape of FERRO with a thickness of 100 µm (unfired) has been applied. A stack of 7 layers of tape was laminated to provide mechanical stability. Micromachining of channels and holes has been conducted with a diode pointed NdYAG laser.

The channel cross-section is 100 µm x 100 µm, the length is 60 mm. Total thickness of the device is 700 µm. The top layer contains a detection window for inserting a planar detector after the firing process. Lamination was carried out at a pressure of 17 N/mm^2 and a temperature of 70 °C in an uniaxial press. Firing of the laminated stack has been conducted in a conventional belt furnace with a peak temperature of 850 °C and a total cycle time of 90 minutes. Figure 1 shows the fully assembled LTCC device.

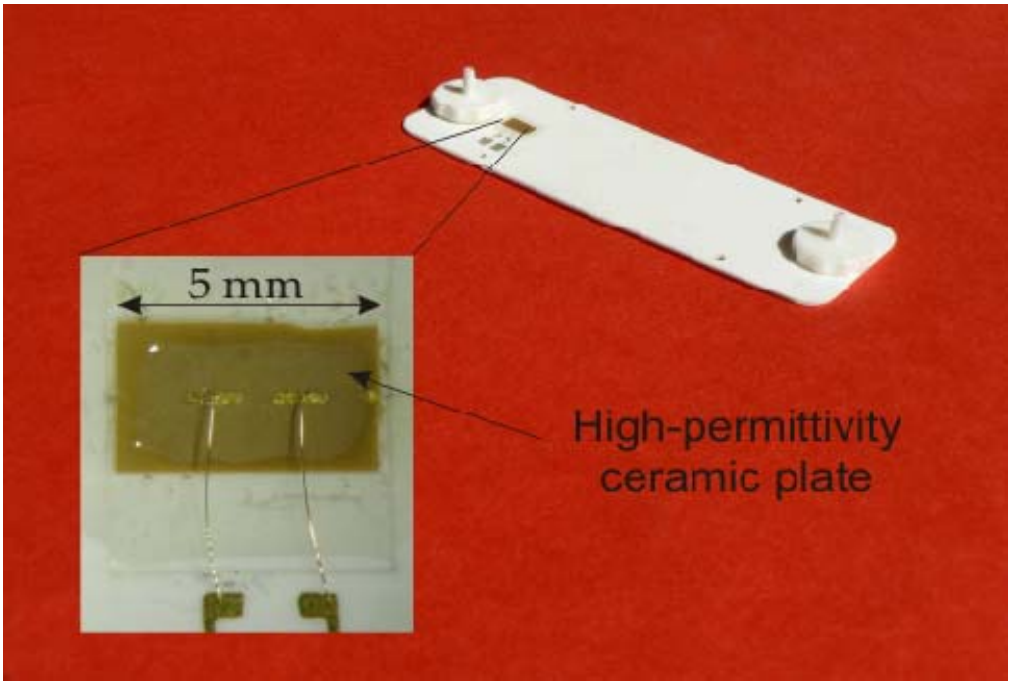

Fig. 1: LTCC device with planar detector-ceramic mounted in the recess above the channel (see inset). Electrode dimensions are 1 mm x 100 µm. Electrodes were wire-bonded to contact pads positioned on the LTCC substrate.

The planar detector was realized using a high-K HTTC ceramic plate with a permittivity of ε_r = 2000. It has a thickness of 300 µm. Gold electrodes were screen-printed on top using thick-film technology. After the firing process, the detector was glued into a cavity in the top layer of the LTCC device, enabling a direct contact between microchannel and high-K ceramic plate. The inset in Figure 1 depicts a detailed view of the detector. In order to reduce potential stray capacitance effects, the electrical connection of electrodes was not performed by conductor paths but by wirebonds.

Detector Simulation

A main benefit of the planar-detector arrangement is the ease of production, as electrodes need not be placed inside the channel. The high permittivity of the detector plate provides a better coupling of the excitation signal into the channel as compared to other low-K materials such as PMMA or glass.

Figure 2 shows FEM results of the real part of the electric current flowing into the detector at an excitation frequency of 200 kHz and a voltage of 5 V. For higher values of permittivity the inflowing current increases, indicating a higher coupling of the measurement signal with the channel. A problematic factor, however, is the increased stray capacitance across the ceramics short-circuiting the detection signal and thus lowering sensitivity. This can be tackled by optimizing electrode layout and measurement frequency.

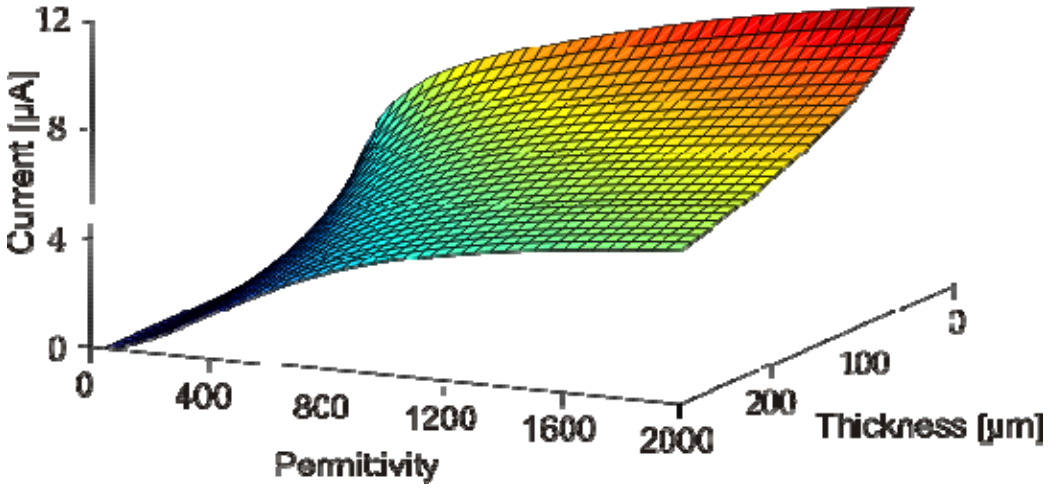

Fig. 2: FEM results of the electric current flowing into the detector for different values of ceramics permittivity and thickness. Simulation parameters for the channel were ε_r = 80 and electrical conductivity σ = 0.1 S/m. This corresponds to an ion concentration of about 10 mM for the mentioned channel dimensions.

The simulation results show that a decrease of ceramics thickness further improves detection sensitivity. In the proposed detector a plate with a thickness of 300 µm is used – a value that could not be further decreased due to mechanical stability issues. A possible workaround is the use of a thinner high-K LTCC tape instead of the HTCC plate used here. Such tapes are available at thicknesses of 100 µm in their unfired state; however, their permittivity is nevertheless much lower as compared to the HTCC plate used in this work.

Stray capacitance can be almost entirely suppressed using an opposite electrode setup as employed in [5]. Fabrication of such an arrangement, however, is somewhat more complex than that of the planar design, as stability and wiring issues have to be considered and photolithographic steps are necessary.

Results

Detector sensitivity was determined by measuring the change in impedance for different concentrations of an NaCl solution. Starting from and ideal infinite dilution (i.e. DI-water), solutions were pumped through the device with increasing concentrations (1, 2, 5 and 10 mM respectively). Figure 3 shows the resulting change in impedance and phase.

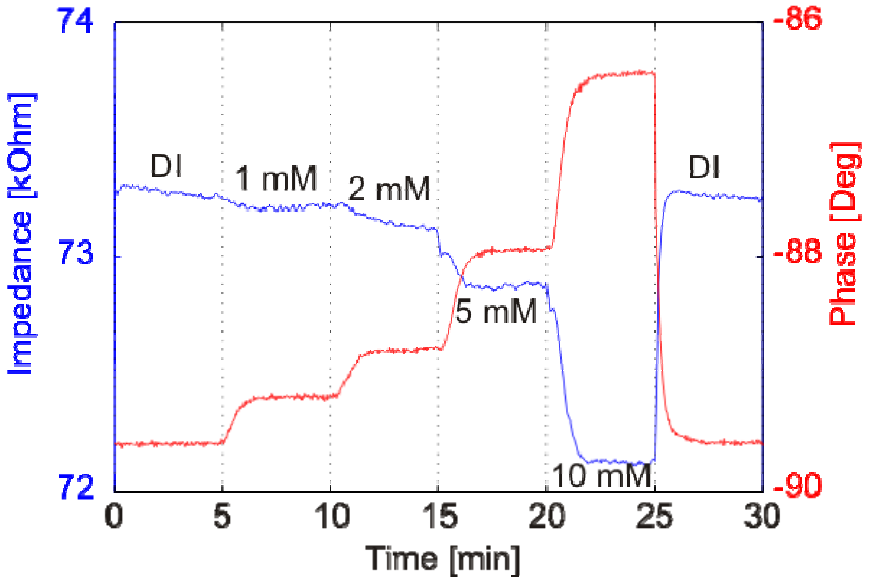

Fig. 3: Measured changes of impedance and phase over time for varying concentrations of an NaCl solution.

A Quadtech LCR-meter (Model: 7600) set to a measurement frequency of 200 kHz and a signal voltage of 5 V was used to obtain impedance and phase values.

In the case of the channel filled with DI-water, the device showed almost purely capacitive behavior. Due to resistive losses in the ceramics, however, the phase angle is somewhat bigger than the expected -90°. At intervals of 5 minutes the ion concentration was increased. The corresponding changes in impedance and phase did not happen immediately, but took place between 60 and 90 seconds to settle at a stable value. Increasing ion concentration of the solution contributes to a decrease in impedance as well as phase angle. The smallest concentration value that could be distinguished was 1 mM, with a corresponding change in impedance in the range of 1000 ppm.

Reproducibility of the measurement was confirmed by immediately changing from the 10 mM solution to DI-water and comparing the result with the value of the impedance recorded 30 minutes earlier. After a settling time of 90 seconds it reached the same value, indicating that the ceramics did not change its physical properties when in contact with the ion solution. Long-term effects such as possible changes in permittivity due to permanent contact with the fluid are being examined at the moment.

Conclusion

An LTCC microfluidic device with a contactless conductivity detector made of high-K ceramics has been introduced. Conductivity measurements were carried out with NaCl solutions ranging down to a concentration of 1 mM. The advantage of better coupling as compared to low-K materials was shown. FEM was employed to estimate the influence of different permittivities and thicknesses of the ceramic plate on detection sensitivity.

In microfluidic devices made of ceramics the material porosity is a serious matter that can influence the performance of the device. Long-term effects such as changes in permittivity due to contact with fluids in the channel are being examined at the moment and will be reported on.

References

[1] V. Solinova, V. Kasicka, “Recent applications of conductivity detection in capillary and chip electrophoresis”, *J. Sep. Sci.*, **29,** pp 1743-1762, 2006.

[2] J.G.A. Brito-Neto, J.A.F. da Silva, L. Blanes, C.L. do Lago, “Understanding Capacitively Coupled Contactless Conductivity Detection in Capillary and Microchip Electrophoresis. Part 1+2”. *Electroanalysis*, **17,** no. 13, pp 1198-1214, 2005.

[3] F. Laugere, R.M. Guijt, J. Bastemeijer, G. van der Steen, A. Berthold, E. Baltussen, P. Sarro, G.W.K. van Dedem, M.J. Vellekoop, A. Bossche, “On-Chip Contactless Four-Electrode Conductivity Detection for Capillary Electrophoresis Devices”, *Anal. Chem.*, **75,** pp 306-312, 2003.

[4] F. Laugere, G.W. Lubking, J. Bastemeijer, M.J. Vellekoop, Design of an electronic interface for capacitively coupled four-electrode conductivity detection in capillary electrophoresis microchip, *Sensors and Actuators B*, **83,** pp 104-108, 2002.

[5] J. Lichtenberg, N.F. de Rooij, E. Verpoorte, “A microchip electrophoresis system with integrated in-plane electrodes for contactless conductivity detection”, *Electrophoresis*, **23,** pp 3769-3780, 2002.

[6] W. Smetana, B. Balluch, G. Stangl, E. Gaubitzer, M. Edetsberger, G. Köhler, “A multi-sensor biological monitoring module built up in LTCC-technology”, MME, **84,** pp 1240-1243, 2007.

Bridge-Based Microsensor for Determining the Thermal Properties of Liquids

A. Jachimowicz[1], J. Schalko[1], J. Kuntner[1], F. Kohl[2], B. Jakoby[3]

[1] Institute of Sensor and Actuator Systems, Vienna University of Technology, A-1040 Vienna

[2] Research Unit of Integrated Sensor Systems, Austrian Academy of Sciences, A-2700 Wr. Neustadt

[3] Institute for Microelectronics, Johannes Kepler University Linz, A-4040 Linz

Due to unique features like small thermal masses and reduced conductivities, miniaturized thermal sensors offer properties superior to those provided by comparable macroscopic measurement setups. In this contribution a micromachined device is applied to characterize the thermal transport properties of various liquids. By means of sinusoidal excitation of a heater structure placed on a micro-bridge, and recording the resulting temperature at a specified distance using integrated germanium thermistors also located on micro-bridges, the liquid's thermal parameters can be determined. A simple two-dimensional analytical model allows to interpret the amplitude and the phase of the measured sinusoidal temperature variation, yielding both, the thermal conductivity and the diffusivity of the liquid.

Introduction

In the past decades, a number of different measurement methods for thermal material properties of liquids have been developed. Most devices comprise of a single heater or a heater in combination with a spatially separated temperature sensor [1] – [3]. In the former case the temporal evolution of the heater temperature is recorded, whereas in the latter case the temperature in some distance from the heater is measured using the additional temperature sensor. In both approaches the resulting temperature response is determined by the thermal material properties of the surrounding medium and can thus be utilized to extract these parameters. Regardless of the particular realization, all methods aim to restrict an imposed thermal flow to the liquid under test, and to avoid spurious thermal shunts. Due to the unique geometrical features that can be achieved by microtechnology, micromachined devices offer various opportunities for fulfilling this requirement. Here, thin membranes are most commonly applied to decouple the actual sensing region from the sensor substrate and thus obtain high sensitivity and a short response time. For some liquids, however, the remaining spurious heat flow in the membrane is still not negligible. These unwanted thermal shunts can be further decreased by utilizing structures, like cantilevers or micro-bridges. If, on the other hand, materials are used which prohibit exceeding a particular maximum temperature in subsequent process steps, the manufacturing of such sophisticated devices can be challenging. A prominent example is the application of amorphous materials, where high temperatures would cause recrystallization. In this contribution a bridge-based microsensor with highly sensitive amorphous germanium thermistors for determining the thermal conductivity and diffusivity of liquids is presented.

Sensor Design and Fabrication

The sensor presented in this contribution consists of three silicon nitride bridges supported by a silicon frame. On the outer bridges highly sensitive amorphous germanium thermistors (T2 and T3) are located, whereas on the central bridge a chromium heater (H) is placed. Amorphous germanium exhibits high values of both, resistivity and associated temperature coefficient. The specific resistivity is about 5 Ωm and the temperature coefficient of resistance is approximately –1.8%/K at room temperature. Additional thermistors (”substrate thermistors” T1 and T4) arranged at the silicon frame supporting the bridges provide the opportunity of determining the ambient temperature (see Fig. 1 and Fig. 2).

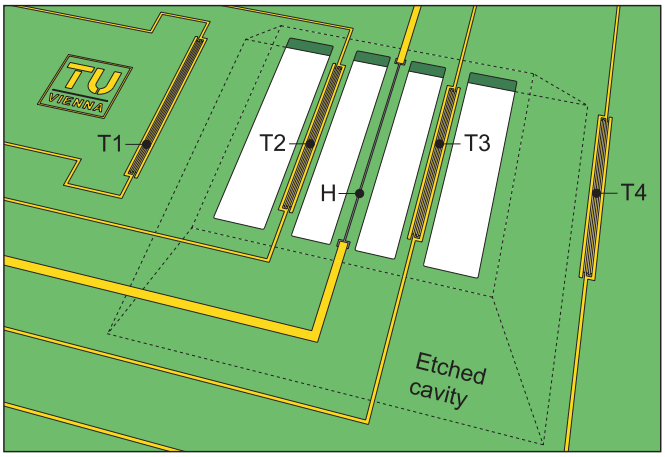

Fig. 1: Schematic picture of the device.

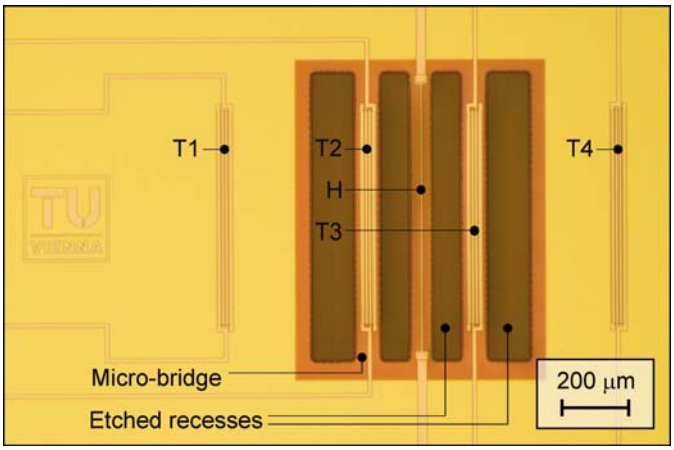

Fig. 2: Photomicrograph of the device.

To fabricate the bridge-based sensor, a 350 µm thick, (100) oriented, and double-sided polished silicon wafer was used. The wafer was coated with 250 nm of thermally grown silicon oxide (SiO_2) and 70 nm of LPCVD silicon nitride (Si_3N_4) on both sides. First, a 250 nm thick layer of germanium has been vapor-deposited and patterned using lift-off technique to form the thermistors. Next, a 130 nm thick layer of chromium has been applied and patterned to create the heater. Subsequently, a titanium-gold-chromium layer featuring a thickness of 50-100-30 nm has been deposited and lift-off patterned to obtain interdigitated electrodes for the thermistors, and connection leads to the bonding

pads for heater and thermistors. Then, a low stress silicon nitride (SiN_x) protective film with a thickness of about 1000 nm has been applied using low temperature plasma enhanced chemical vapor deposition (PECVD) at 100 °C. Here, the low deposition temperature prevents the germanium film from recrystallization. Afterwards, square apertures in the wafer backside coating were created by means of photolithography and reactive ion etching (RIE). The membranes have then been manufactured using a KOH based anisotropic wet etching process. In order to obtain the required micro-bridges, the membranes have subsequently been patterned from the topside using photolithography and a RIE process. The apertures for the bond pads were made in the same step. Finally, the chromium has been removed from the bond pad areas by means of a wet-etching. Consequently, the sensor chips feature an overall thickness of about 1.3 µm.

Measurement Principle and Setup

By applying a sinusoidal heater current, a diffusive heat wave propagates from the heater into the surrounding liquid. The steady-state amplitude ΔT_{pk}[1] and the phase Φ of the temperature oscillations measured by the thermistors are determined by the thermal properties of the liquid. The phase Φ denotes the phase lag between the applied heating power and the resulting temperature oscillation. Moreover these temperature oscillations are related to the applied heating power and thus feature twice the frequency of the applied AC heater current plus an additional DC component. Considering the geometry of the heater structure, the corresponding AC temperature field can be approximated by using the solution of the two-dimensional heat diffusion equation for a periodic line source $P(r,t)=P_0 e^{j\omega t}$ yielding

$$\Delta T(r) = \frac{P_0}{2 \cdot \pi \cdot \lambda} \cdot K_0\left(\sqrt{\frac{j\omega}{a}} \cdot r\right). \tag{1}$$

Here P_0 denotes the peak of the AC component of the heating power per unit length of the heater structure, λ the thermal conductivity, K_0 the modified Bessel function of the second kind, ω the angular frequency, a the thermal diffusivity, and r the radial distance from the line source [4]. The thermal diffusivity a is related to the heat capacity c_p by

$$a = \frac{\lambda}{\rho \cdot c_p}, \tag{2}$$

where ρ denotes the mass density. It can be seen, that the amplitude in Equation (1) is essentially determined by the thermal conductivity of the liquid under investigation whereas the corresponding phase is governed by the thermal diffusivity. Note that the model above considers heat conductance only, which means that the effects of heat radiation and convection, i.e. flows induced by the non-uniform temperature distribution, are neglected. This can be justified since the considered excess temperatures are in the range of fractions of degree Centigrade. For the measurements, the device was completely immersed into the sample liquid and a sinusoidal heater voltage was applied. In order to single out the steady-state amplitude ΔT_{pk} and the phase Φ of the temperature oscillation measured at the thermistors, a DC voltage was applied to the thermistors and the resulting current oscillations were measured. After eliminating the superposed DC-component, representing the ambient temperature plus the temperature increase associated with the DC-offset of the generated heating power, the amplitude and the phase of the exciting signal's second harmonic were determined by means of a lock-in amplifier (see Fig. 3).

[1] Here, Δ indicates the excess temperature, i.e., the difference between ambient and actual temperature.

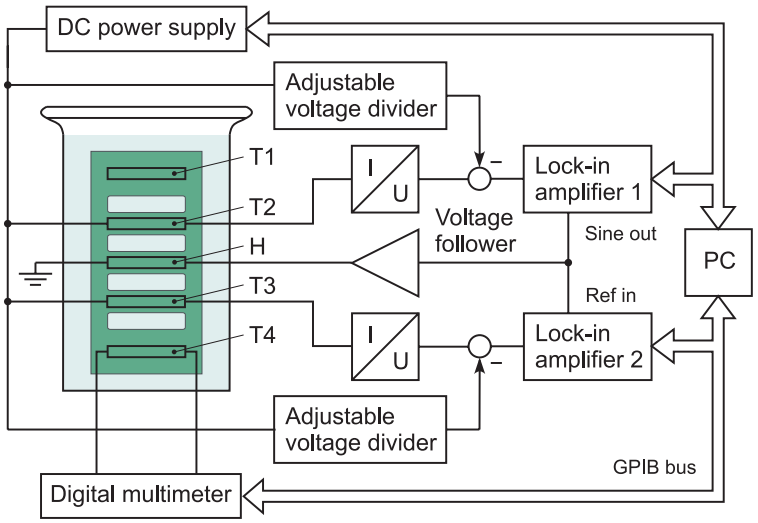

Fig. 3: Measurement setup.

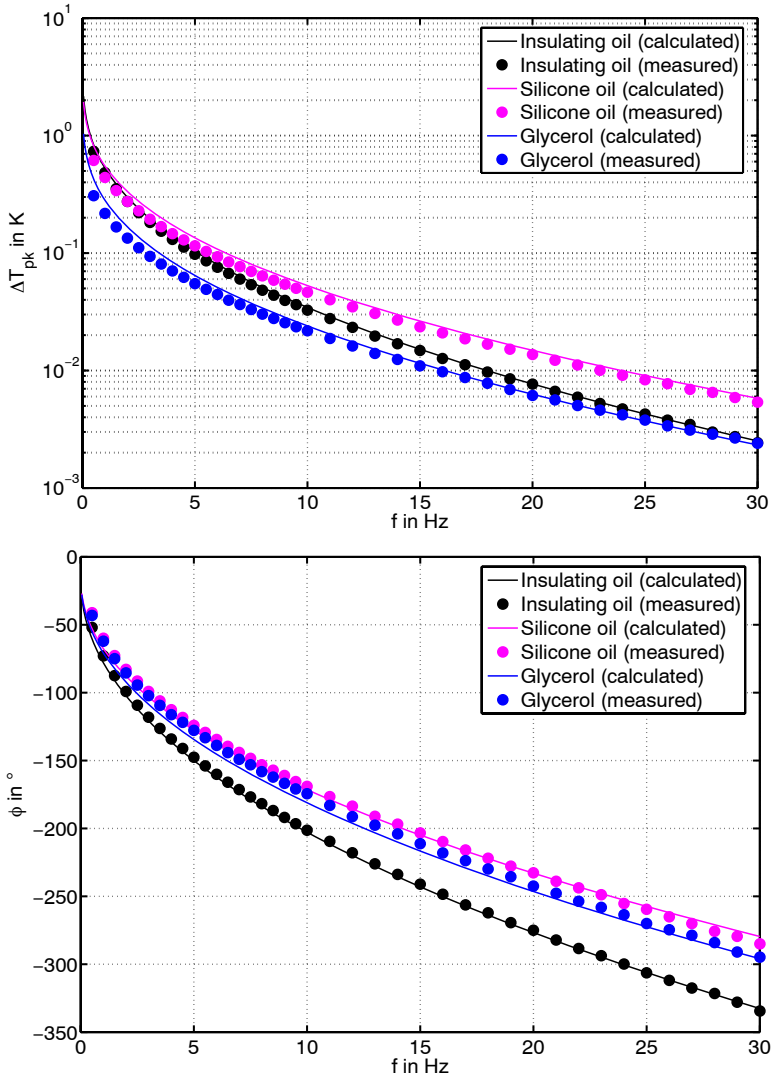

Fig. 4: Amplitude ΔT_{pk} and phase Φ measured for a heater voltage of 1 V_{rms}.

Results and Discussion

In order to investigate the performance of the developed sensor, different liquids have been analyzed. The liquids have been chosen in such a way, that a comparatively large parameter range in both, the thermal conductivity and the thermal diffusivity could be probed. Figure 4 shows the amplitude ΔT_{pk} and the phase Φ of the AC excess temperature amplitude measured at the thermistor T3 compared to the values for the model described above versus the frequency f.

It can be seen that the measurement results correspond well with those predicted by the simple two-dimensional model. Consequently the developed device enables to determine the thermal conductivity and diffusivity of liquids without the need for a complex model for data interpretation.

Conclusion

By utilizing a micromachined structure, the simultaneous measurement of the thermal conductivity and diffusivity of an adjacent liquid has been demonstrated. This was achieved by applying a sinusoidal heater signal and recording amplitude and phase of the resulting temperature increase in some distance by means of a germanium thermistor located on a micro-bridge. A simple two-dimensional analytical model was used to interpret the measurands. The presented approach is well suited for thermal liquid analysis in the laboratory and in the field. In particular, it is suited for online monitoring applications, where size and power consumption can be issues and where the determination of the absolute values is secondary compared to the detection of relative changes.

Acknowledgements

The authors would like to thank E. Svasek and P. Svasek from the Institute of Sensor and Actuator Systems, Vienna University of Technology, for dicing and bonding the devices, respectively. This work was financially supported by the Austrian Research Promotion Agency (FFG), Project 810220 which is gratefully acknowledged.

References

[1] J. J. Healy, J. J. de Groot, and J. Kestin: “The theory of the transient hot-wire method for measuring thermal conductivity”, Physica C, Vol. 82, no. 2, 1976, pp. 392-408.

[2] S. E. Gustafsson, E. Karawacki, and M. N. Khan: “Transient hot-strip method for simultaneously measuring thermal conductivity and thermal diffusivity of solids and fluids”, Journal of Physics D: Applied Physics, vol. 12, no. 9, 1979, pp. 1411-1421.

[3] D. G. Cahill: “Thermal conductivity measurements from 30 to 750 K: the 3ω method”, Review of Scientific Instruments, vol. 61, no. 2, 1990, pp. 802-808.

[4] H. S. Carslaw and J. C. Jaeger: “Conduction of Heat in Solids”, Clarendon Press, 2nd ed., 1986.

Measurement of Liquid Properties with Resonant Cantilevers

C. Riesch[1], E. Reichel[2], F. Keplinger[1], B. Jakoby[2]

[1] Institute of Sensor and Actuator Systems, Vienna University of Technology, 1040 Vienna, Austria

[2] Institute for Microelectronics, Johannes Kepler University Linz, 4040 Linz, Austria

Liquid viscosity and density sensors are essential devices in online process or condition monitoring. Microacoustic sensors combine advantages such as small size, low cost, and absence of macroscopically moving parts. However, these devices feature measurement at high shear rates and, therefore, the results may diverge from those obtained with traditional viscometers. In our contribution we investigate a PZT driven bending actuator and a micromachined doubly clamped bridge device for use as viscosity and density sensors. The presented models allow the description of the sensor's interaction with the surrounding liquid.

Introduction

In many applications like online process or condition monitoring liquid viscosity and density are of high relevance. Microacoustic sensors such as quartz crystal resonators and SAW devices have proved particularly useful alternatives to traditional viscometers [1]. However, these devices basically measure liquid viscosity at high shear rates. The results of microacoustic measurements are thus often not comparable to the readout of conventional viscosity measurement, e.g., based on the Ubbelohde method or rotational viscometers [2]. In contrast, resonating cantilevers allow for measurements at lower frequencies and higher shear amplitudes, making the measuring results more comparable to laboratory methods [3]. Furthermore they allow the determination of liquid viscosity and density separately [4].

In our contribution, we investigate two different types of resonant cantilever sensors: A PZT (lead zirconate titanate) driven bimorph bending actuator and a micromachined sensor utilizing a doubly clamped vibrating beam.

PZT Cantilever Sensor

Sensor Fabrication

Commercially available PZT bimorph bending actuators consist of two piezoelectric PZT layers polarized in the thickness direction and a carbon fiber substrate. Electrodes on both sides of the piezoelectric layers enable the excitation of the actuator. A voltage applied to the electrodes causes transversal contraction in the piezoelectric layer but not in the substrate, and, therefore, leads to flexural mode vibrations of the beam.

The bending actuators used in this work were supplied by Argillon GmbH, Redwitz, Germany. The center electrode is used as ground electrode (Fig. 1(a)), whereas a sinusoidal voltage is applied to the driving electrode to excite bending vibrations. The actual beam deflection is determined by measuring the voltage at the sensing elec-

trode. The phase shift between driving voltage and sensor voltage is measured by means of a lock-in amplifier (Stanford Research SR830). In our setup (Fig. 1(a)), the bending actuator is clamped at one end, whereas different tips of well-defined cross-sections have been attached to the free end of the cantilever (fig. 1b). The clamping fixture is mounted on a rigid frame allowing for vertical positioning of the sensor and preventing vibrations of the whole setup.

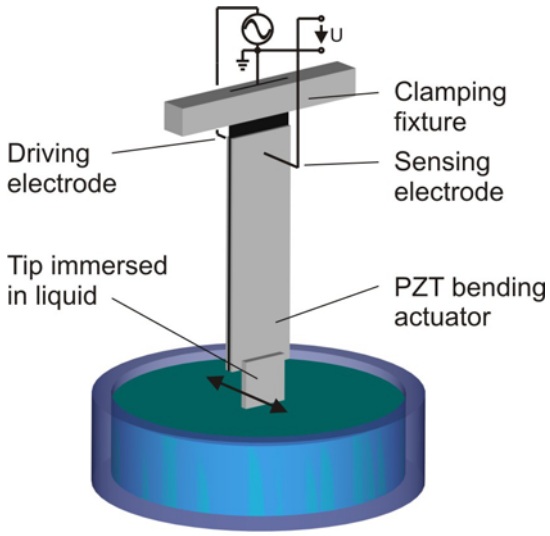

(a)

	Tip	Width [mm]	Thickness [mm]
A	Silicon	7	0.5
B	Silicon	5	0.5
C	Silicon	2	0.5
D	terminal pin, soldered on	0.7	0.7

(b)

Fig. 1: (a) Measurement setup; (b) Tip geometries investigated in this work.

Characterization of the PZT Cantilevers

From the cantilever's frequency response we obtained the resonance frequency f_n of the considered vibration mode n and the damping factor D. These parameters are influenced by the liquid's viscosity η and density ρ and the cross-section of the immersed tip. In [5] the relationships between f_n, D and η, ρ were modeled by approximating the oscillating cantilever by an oscillating sphere immersed in a liquid. The force F acting on the said sphere is given by [6]

$$F = \underbrace{6\pi\eta\left(1+\frac{R}{\delta}\right)}_{b_i}u + \underbrace{3\pi R^2\sqrt{\frac{2\eta\rho}{\omega}}\left(1-\frac{2R}{9\delta}\right)}_{M_i}\frac{du}{dt}, \quad \delta = \sqrt{\frac{2\eta}{\omega\rho}}, \tag{1}$$

where R is the sphere radius, ω the angular frequency, and δ the depth of penetration of the acoustic wave. The terms b_i and M_i represent the additional damping of the cantilever and the added mass due to the surrounding liquid. Considering the bending actuator as an oscillator immersed in a liquid and driven by a harmonic force, the differential equation for the motion u in axial direction is

$$\left(M_e + M_i\right)\frac{d^2u}{dt^2} + \left(b_e + b_i\right)\frac{du}{dt} + Ku = F_0 e^{-j\omega t}, \tag{2}$$

where M_e and b_e are the effective mass and the intrinsic damping of the cantilever, K is the spring constant and F_0 and ω are the driving force's amplitude and angular frequency. Based on the oscillating sphere model, a more generalized model for the relationships between $\omega_n = 2\pi f_n$, D and η, ρ was deduced, given by

$$\omega_n = \omega_{n,AIR}\sqrt{\frac{1}{1+c_1\rho+c_2\sqrt{\eta\rho}}} \quad \text{and} \quad \frac{D}{\omega_n{}^2} = \frac{D_{AIR}}{\omega_{AIR}{}^2}\left(1+c_3\eta+c_4\sqrt{\eta\rho}\right). \tag{3}$$

The model parameters c_1, c_2, c_3, and c_4 were obtained by curve fitting to the equations to the measured data. Figure 2 elucidates that the resonance frequency is dominantly influenced by the liquid's density, whereas the damping is mainly determined by the viscosity. However, there is a "spread" in these straightforward bilateral relations which indicates a cross-sensitivity to the respective other liquid parameter and is properly described by the model (3).

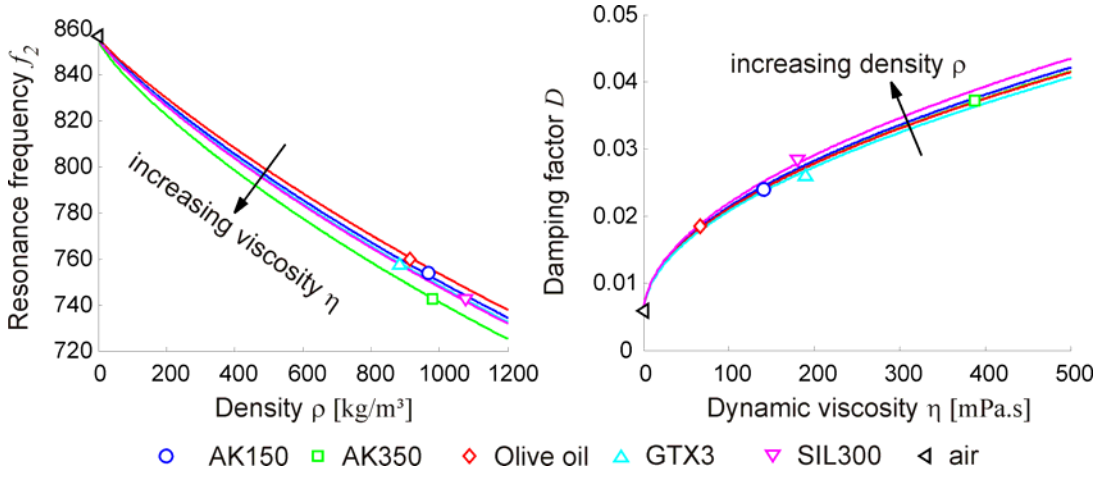

Fig. 2: Measured values (markers) and fitted curves for the respective fluids. These measurements have been obtained with tip A, dipping depth 4 mm.

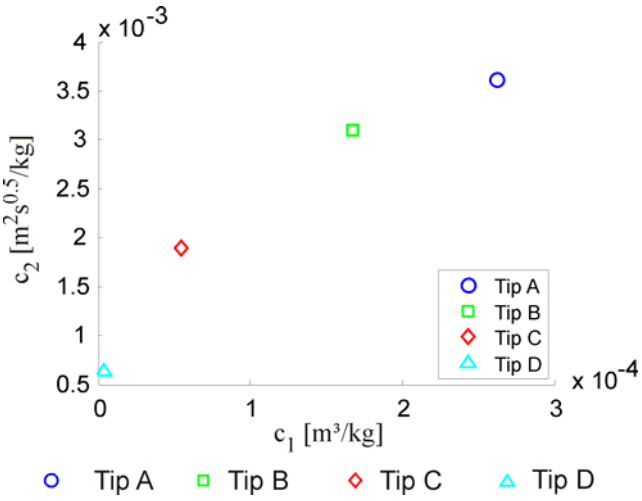

Fig. 3: Fit parameters c_1 and c_2 (associated with $f_n(\eta, \rho)$) for the different tip geometries (Fig. 1(b)).

Figure 3 depicts the dependence of the fit parameters c_1 and c_2 on the kind of tip used. It turns out that the sensitivity of the resonance frequency to the density (determined by c_1) can be steadily increased by increasing the tip width, whereas its sensitivity to the viscosity-density product tends to saturate for increasing widths. This can be explained by the fact that larger amounts of liquid must be moved by the oscillating tip with in-

creasing tip width, whereas the influence of the viscosity is concentrated to the edges of the tip.

Micromachined Doubly Clamped Bridge

Motivated by the applicability for viscosity and density measurement of the PZT cantilevers, effort is being made to miniaturize the sensor with the aim of a sensing device in silicon technology. A precise modeling of the solid-liquid interaction and the measurement of the frequency response enables the measurement of the density and the rheological behavior of liquids [4] in a way comparable to the PZT cantilevers.

A SEM micrograph of a prototype which consists of a doubly clamped beam structure carrying a conductive path is shown in Fig. 4. The beam structure is exposed to a permanent magnetic field and a sinusoidal current through the conductor results in a sinusoidal Lorentz force causing the time-harmonic vibration.

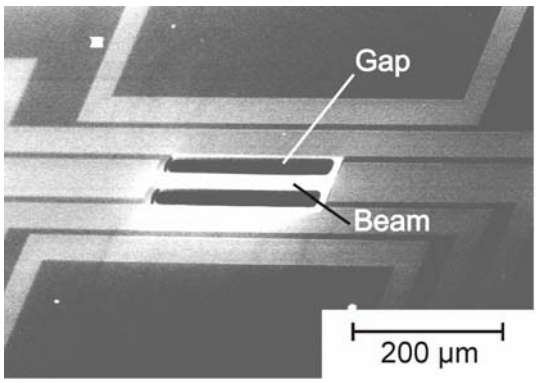

Fig. 4: SEM micrograph of the micromachined sensor element. The cross-sectional dimensions of the Silicon nitride beam are 40x1.3 µm; beams of different lengths ranging from 240 µm to 720 µm were fabricated.

The mechanical deformation (of pure transverse vibration modes) is described by the Bernoulli-Euler beam equation considering an intrinsic normal force N, an additional mass m_f and a viscous damping parameter α both resulting from the flow field around the beam:

$$EJ\frac{\partial^4 w}{\partial x^4} - N\frac{\partial^2 w}{\partial x^2} + \left(\rho A + m_f\right)\frac{\partial^2 w}{\partial t^2} + \alpha\frac{\partial w}{\partial t} = q(x,t)$$

where w is the deflection, E the Young's modulus, J the geometrical inertia, ρ the mass density of the beam material, and x the spatial coordinate along the beam, $q(x,t)$ is the driving force per unit length.

The additional mass per unit length m_f and the viscous damping coefficient α were calculated from a semi-numerical method based on Green's function in the spatial spectral domain. The simulation of the two-dimensional flow field around the rectangular cross-section yields the dependency of the resistance force on the liquid's mass density ρ_f and viscosity μ shown in Fig. 5.

The readout of the vibration amplitude can be carried out optically, with the integration of piezoelectric materials, or as done here, by measuring the impedance of the excitation circuit over the appropriate frequency range. The electrical equivalent circuit of the vibrating beam in an external magnetic field is depicted in Fig. 6.

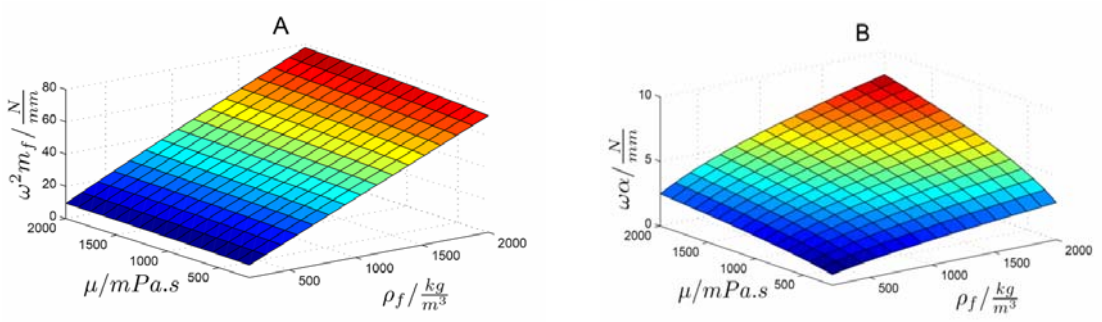

Fig. 5: Results of the semi-numerical analysis of the flow field around the rectangular cross-section of the beam. A: Dependency of the resistance force (per unit length) due to the added mass on both viscosity μ and liquid's density ρ_f. B: Force due to the viscous damping parameter α.

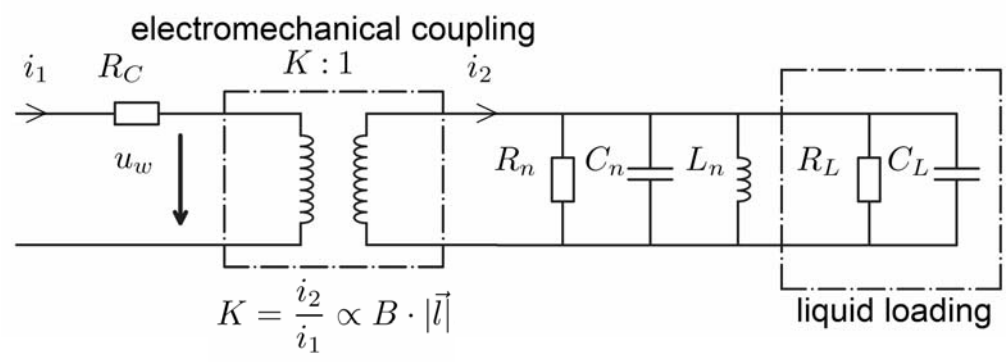

Fig. 6: Electrical equivalent circuit of the vibrating structure. R_C represents the resistance of the excitation path. The parallel resonance circuit on the secondary side of the transformer represents the lumped element approximation of the mechanical system, valid for one specific mode of vibration, and the fluid dependent elements R_L and C_L.

Using the equivalent circuit model it is possible to determine the liquid loading and thus the fluid properties from a measurement of the impedance spectrogram:

$$Z(\omega) = R_C + K^2 \frac{1}{\frac{1}{R_n} + \frac{1}{R_L} + j\omega(C_n + C_L) + \frac{1}{j\omega L_n}}$$

where R_n, C_n, and L_n are the resonance parameters of mode n in air and R_L and C_L represent the change of the behavior when the structure is immersed in a liquid due to additional damping and additional mass respectively.

Conclusion

In the paper we have investigated two different types of resonant cantilevers for the measurement of liquid properties. The resonance frequency as well as the damping of the cantilevers are influenced by the surrounding liquids. The relationships between the

cantilever's frequency response and the liquid parameters were described by models, allowing for separate determination of liquid viscosity and density.

Acknowledgements

This work was supported by the Austrian Science Fund (FWF) Project L103-N07.

References

[1] B. Jakoby, M. Scherer, M. Buskies, H. Eisenschmid: "Microacoustic Viscosity Sensor for Automotive Applications", Proc. IEEE Sensors, 2002, pp. 1587–1589.

[2] A. Agoston, C. Ötsch, B. Jakoby: "Viscosity sensors for engine oil condition monitoring – Application and interpretation of results", Sens. Actuators A, Vol. 121, 2005, pp. 327–332.

[3] A. Agoston, F. Keplinger, B. Jakoby: "Evaluation of a vibrating micromachined cantilever sensor for measuring the viscosity of complex organic liquids", Sens. Actuators A, Vol. 123–124, 2005, pp. 82–86.

[4] L. F. Matsiev: "Application of Flexural Mechanical Resonators to Simultaneous Measurements of Liquid Density and Viscosity", 1999 IEEE Ultrasonics Symposium, 1999, pp. 457–460.

[5] W. Y. Shih, X. Li, H. Gu, W.-H. Shih, I. Aksay: "Simultaneous liquid viscosity and density determination with piezoelectric unimorph cantilevers", J. Appl. Phys., Vol. 89 (2), 2001, pp. 1497–1505.

[6] L. D. Landau and E. M. Lifshitz: "Fluid Mechanics", Pergamon Press, London, 1959.

A Non Coaxial Sheath Flow Device for Micrometer Sample Stream Profiles

G. Hairer, G.S. Pärr, P. Svasek, A. Jachimowicz, and M.J. Vellekoop

Institute of Sensor and Actuator Systems,
Vienna University of Technology, Vienna, Austria

In this paper we present a novel non coaxial sheath flow device with channel dimensions of 50 µm in square at the focusing region. The device is suitable for one-by-one cell or particle detection near the channel bottom, in for example a Coulter Counter or for optical near field detection. The device comprises a silicon-glass sandwich with SU-8 resist in between. Analyses of the adaptable sample flow are carried out where the focusing limitation and its profile variations are shown using confocal microscope measurements. A comparison of the sample flow height inside the channel and its relative fluorescence intensity is highlighted.

Introduction

In a non coaxial sheath flow device a sample flow is hydrodynamically focused between three sheath flows. At the fourth side the sample flow is moving along the channel bottom, where sensors for characterizing small particles, cells or biological molecules are integrated. The position, the size and the profile of the sample flow can be dynamically adapted, as shown in [1]. This hydrodynamic focusing technique is an attractive way to achieve a small sample flow in microfluidic devices which prevents channel clogging, because of the relatively large channel size. Hydrodynamic focusing is typically used in flow cytometry, e.g. FACS (fluorescence activated cell sorting) and Coulter Counter. A review of different flow cytometer systems is listed in [2], where optical and impedance analysis has been described in the field of disease diagnostics, cell/molecular biology and genetics.

For characterizing particles or cells in the dimensions of a few microns or smaller a sample stream in the same range is needed. Experiments on focusing limitation of the sample flow in a non coaxial sheath flow device have been presented in [3] where a stream of 10 µm in width was achieved by a channel width of 160 µm. One way to achieve smaller sample diameters is to reduce the dimensions of the microfluidic device. In this paper a novel down scaled non coaxial sheath flow device is described, which allows a sample flow in the dimension of a few micrometers to analyze particles or cells in the same range. The focusing limitation of the sample flow of this device is shown. Additionally, a comparison of the sample flow height inside the channel and its fluorescence intensity is highlighted.

Device Description

Fabrication and Design

The non coaxial sheath flow device is manufactured with a planar microfabrication process using photolithography, combined with anisotropic silicon etching, photoresist structuring and adhesive low temperature bonding technique. The whole fabrication and clean room logistics were carried out on 100 mm wafers. The chip consists of a

silicon-glass sandwich with SU-8 resist in between. In Fig. 1 a photograph of the fabricated chip is depicted. The access holes through the 360 µm thick silicon wafer were anisotropically wet etched with a KOH water solution. The channel structure was defined by the 50 µm thick lithographically processed epoxy resist SU-8. As a cover plate an optical transparent PYREX glass wafer (200 µm thick) was used. The silicon wafer and the glass wafer were thermally bonded at 150°C [4]. Finally the bonded wafers were diced with a conventional wafer saw.

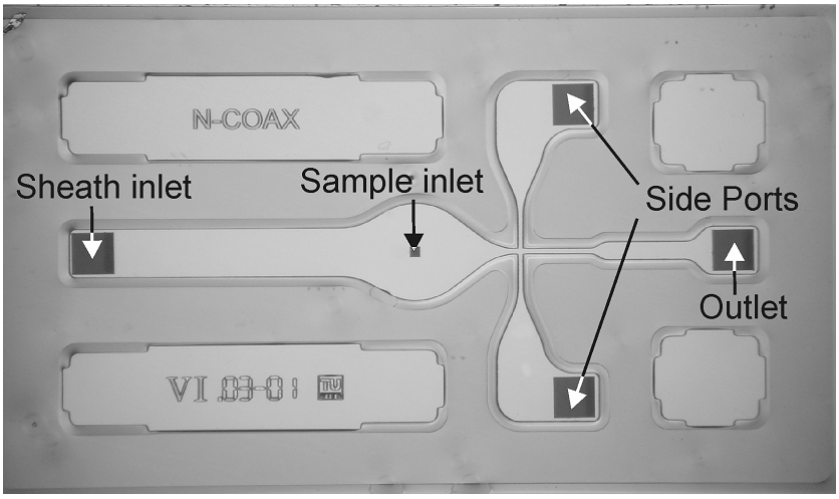

Fig. 1: Photograph of the non coaxial sheath flow device (chip dimensions: 6 x 9 mm^2); Sheath inlet, side port inlets, and outlet: 330 x 330 μm^2; sample inlet: 80 x 80 μm^2; channel dimensions after the focusing section: 50 x 50 μm^2.

At the sample inlet the sample is injected, which flows along the channel bottom. The sample is first focused by the taper. By controlling the flow rates of the sheath inlet and the side ports relatively to the sample flow rate the sample profile and its size can be varied.

Measurement setup

For experiments the non coaxial sheath flow device is fixed on a custom made holder to achieve fluidic connections to syringes. Syringe pumps (kdScientific model 200 series) define the flow rates at the different inlets. A diluted fluorescent dye (acridine orange) is used for the sample flow and the sheath flow is deionized water. During the experiments the chip is positioned in a confocal laser scanning microscope (Confocal C1 TE300, Nikon). This microscope not only allows to capture vertical images of the device with a digital still camera (D100, Nikon) for quantitative analysis but it also permits to measure the precise profile of the sample flow inside the channel. These two analysis techniques allow comparing the relative fluorescence intensity of the sample flow to the real sample height inside the channel.

Experiments

Focusing Limitation

The width of the sample flow is optically analyzed by taking a photo with a digital reflex camera. The concentration of the emitted fluorescent dye is evaluated. The width of the sample flow is defined as the width of the sample at 50 % of the maximum dye inten-

sity. The measured focusing limitation of this device is a 2.5 µm wide sample flow at a channel width of 50 µm. The flow rate at the inlet ports are held at 2 µl/min (sheath inlet), 0.1 µl/min (sample inlet) and 30 µl/min (side ports). The focusing limitation of this device is depicted in Fig. 2. The image presents the emitted green color of the fluorescent dye (wavelength of 520 nm). The reason of the focusing limitation is the low velocity of the pressure driven parabolic flow near the channel bottom.

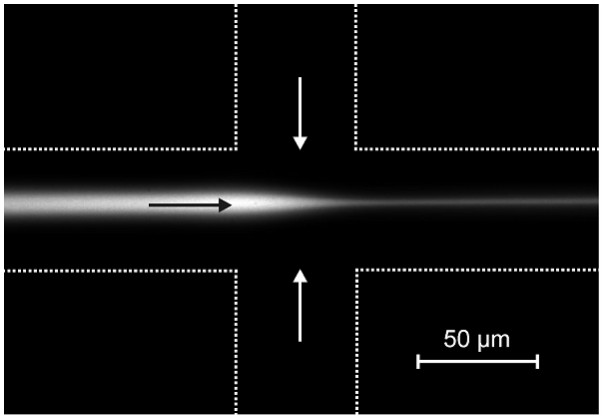

Fig. 2: Focusing limit of the sample flow in a non coaxial device (The edges of the channels are outlined with a dotted line for reference and the arrows indicate the flow direction): The smallest width of the sample flow amounts to 2.5 µm.

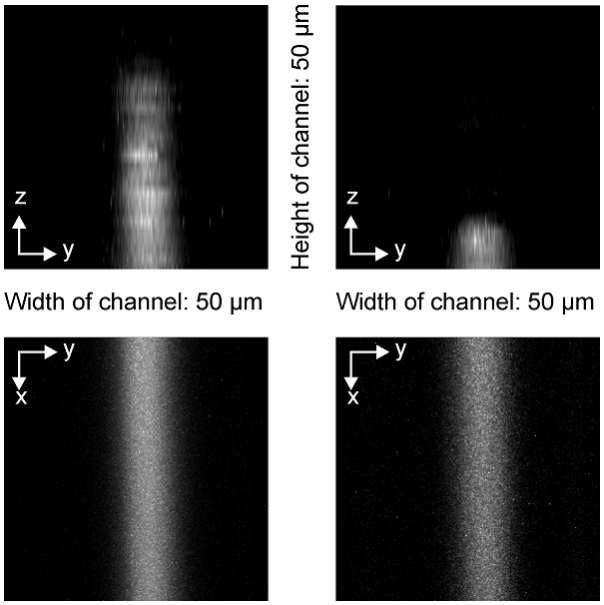

Fig. 3: Top: Confocal images of the sample flow profile inside the channel;
Bottom: Photos of the fluorescence concentration of these sample flows.

Confocal Images vs. Intensity Measurements

Measurements with the confocal laser scanning mode of the microscope are constituted in order to get the precise profile of the sample flow inside the channel. In Fig. 3 top left and top right measured profiles of the sample flow are depicted. The flow rate at

the sheath inlet is set to 10 µl/min and at the side ports there is no flow. At the top left and bottom left images the sample flow rate is held at 2 µl/min (sample height of 35 µm) and at the top right and bottom right at 0.05 µl/min (sample height of 8 µm). The two bottom images of Fig. 3 show a vertical section of the whole channel.

The height of the sample flow can be determined by comparing the intensity of the sample flow with the intensity of a sample flow reaching the channel ceiling. This assumption is valid while the green color of the camera is not in saturation. For this experiment, the flow rate of the sheath flow is constantly set to 10 µl/min and on the side ports there is no flow. The flow rate of the sample flow is varied: 0.05 µl/min, 0.1 µl/min, 0.5 µl/min, 1 µl/min, and 2 µl/min. The fluorescence concentration increases by increasing the flow rate of the sample flow. The fluorescence concentration relatively to the reference curve allows determining the sample height inside the channel.

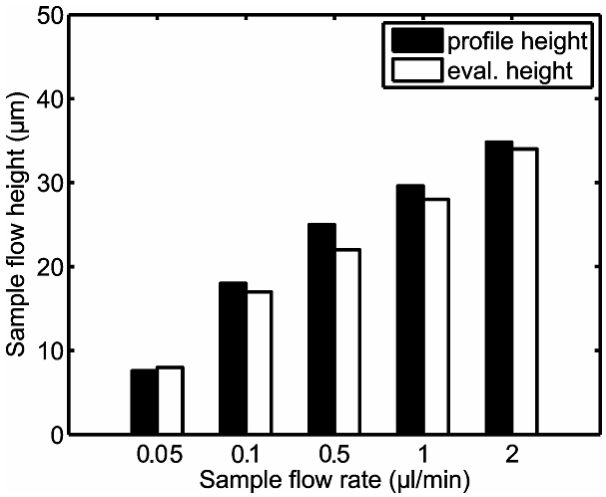

Fig. 4: Comparison of the measured sample profile height (black bars) in the channel and the evaluated sample flow height (white bars) over the fluorescence intensity. Flow rates: 10 µl/min (sheath inlet), 0 µl/min (side ports).

Fig. 4 compares the sample height measured by the confocal microscope and the calculated sample height found from the relative fluorescence intensity. The confocal images were performed at 0.5 µm per *z*-sectioning step over the 50 µm channel height. The results are in good agreement, so it is possible to determine the height of the sample stream using intensity measurements inside a micro channel. Taking top viewed fluorescence photos of the sample stream inside the micro channel the width and the height of the stream can be determined over color intensity. The precise shape of the sample flow can still not be determined.

Conclusion

In this paper, investigations of a novel scaled-down non coaxial sheath flow device with a channel cross-section at the focusing area of 50 x 50 µm^2 have been shown. The experimental determined focusing limitation of the sample flow is highlighted and amounts to 2.5 µm in width. This micro-scaled sample flow can be used to characterize particles or cells in the same order of magnitude. To get information of the sample profile inside the micro channel confocal laser scanning microscope measurements were constituted. The confocal measured heights of the sample profile are compared with the sample flow heights calculated from the fluorescence intensity of the sample. The results show good agreement. This analysis shows that without using extensive and

high priced confocal laser scanning measurement equipment the sample height can be estimated by taking top viewed fluorescence photos of the sample stream inside the micro channel. The sample height will be determined over the color concentration, although the shape of the sample flow is still unknown.

Acknowledgements

The authors gratefully acknowledge USTEM from the Vienna University of Technology for providing the possibility to carry out measurements with the confocal laser scanning microscope. We thank E. Pirker of the Institute of Sensor and Actuator Systems (ISAS) from the Vienna University of Technology for the fabrication of the chip-holder and the custom build mold.

References

[1] J.H. Nieuwenhuis, J. Bastemeijer, P.M. Sarro, and M.J. Vellekoop, “Integrated flow-cells for novel adjustable sheath flows”, *Lab Chip*, vol. 3, pp. 56-61, 2003.

[2] D. Huh, W. Gu, Y. Kamotani, J.B. Grotberg, and S. Takayama, “Microfluidics for flow cytometric analysis of cells and particles”, *Physiol. Meas.*, vol. 26, pp. R73-R98, 2005.

[3] G. Hairer and M.J. Vellekoop, “Experiments on hydrodynamic focusing of non coaxial sheath flows”, in *IEEE Sensors*, Daegu, October 22-26, 2006, p. 123.

[4] P. Svasek, E. Svasek, B. Lendl, and M.J. Vellekoop, “Fabrication of miniaturized fluidic devices using SU-8 based lithography and low temperature wafer bonding”, *Sens. Actuators A*, vol. 115, pp. 591-599, 2004.

On-chip Cytometric Detection of Single Biological Cells Using Integrated Photodiodes

S. Kostner, M. J. Vellekoop

Institute of Sensor and Actuator Systems
Vienna University of Technology, Gusshausstrasse 27-29
1040 Wien

In this contribution we present the principle and measurement results on cytometric detection of single biological cells using integrated photodiodes. The sensing element is built into a microfluidic flow cell that allows for positioning the cells directly over the sensor. Additionally to results with calibrated polystyrene beads we show sensor readings for yeast cells. Experiments show that those cells actually act like lenses, focusing the incoming light to the sensor.

Introduction

Cytometry is a measurement process in which physical or (bio-) chemical information about single cells is obtained [1]. Several methods can be found in literature like optical and impedance based techniques which are used to determine parameters like cell size/shape, protein content, electric conductivity and viability. Measuring single cells yields statistical information from a given sample that is usually hidden when the sample is measured in suspension. For obtaining this statistical information tens of thousands of particles have to be measured in a relatively short time period (for instance 10^6 events/second).

A typical optical setup for flow cytometry consists of a light source, a test volume, and one or more sensing elements. Usually the reflected, transmitted and/or absorbed light fraction is of interest and can be related to a physical parameter of the test substance. Very often the relation between wanted parameters and physical sensor readings is found in an empiric way by experiment.

Using microfabrication techniques the volume of the test channel can be made small enough so that suspended objects like small particles or biological cells can be detected as single events. The natural limitation to the miniaturization of these optical systems is diffraction: the size range of particles and photosensitive area cannot be much smaller than the wavelength used.

Compared to other systems our approach for gaining optical information about the cells is different in the sense that we place the photosensitive element directly into the analysis channel, thus sensing in the optical near field of the particle. This allows for obtaining information about the particle that is usually hidden for systems that pick up the far field only (like FACS systems).

Sensor Design and Technology

In order to produce repeatable sensor readings it is necessary not only to have a proper sensor layout but also to have means to control how the particles are being de-

livered to the sensor. Therefore a flow cell was designed that provides position control in 3D for the particles that move over the sensor [2]. This is achieved by generating a non-coaxial sheath flow that can be controlled by applying different flow rates to the fluidic ports of the device.

Figure 1 shows the principle of the sensor that consists of a strip photodiode (2 µm x 50 µm) that is arranged perpendicular to the flow channel which has a width of 150 µm. The device is a sandwich consisting of a bottom silicon wafer (with the integrated photodiodes; 1 µm standard bipolar process) and a top glass slide which are bonded together by an intermediate SU-8 layer (height: 70 µm) forming the fluidic structure [3]. The through-holes for the fluidic connection of the chip were etched in Si from the bottom.

When a particle moves over the sensor a change in the photocurrent or voltage can be measured that is proportional to the shadow area produced by the particle [4].

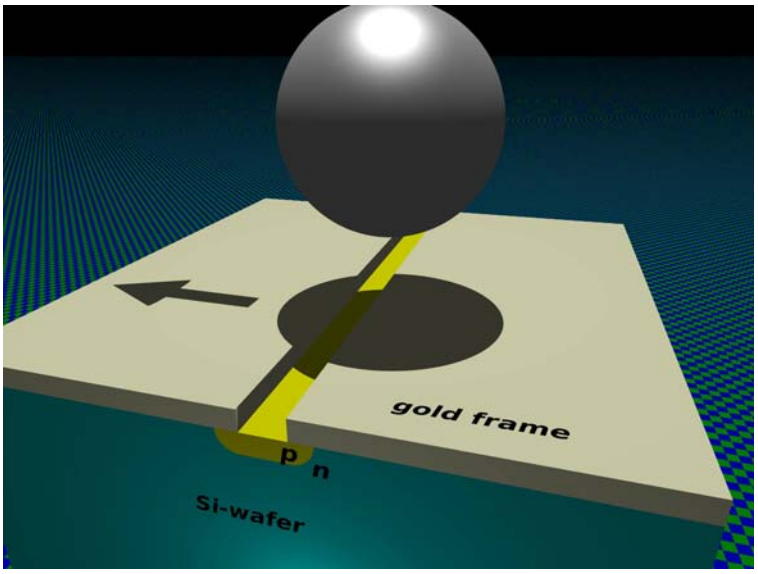

Fig. 1: Principle of the sensor with the integrated photodiodes. The arrow indicates the flow direction. The non-transparent particle produces a shadow on the light sensitive area which causes a signal drop.

Experimental Setup

The chip was clamped onto a custom made device holder that provides the electrical and fluidic connections. Syringe pumps with carefully chosen flow rates were used to apply a sheath flow to force the particles/cells closely over the photosensitive area. A modulated green laser source (592 nm, Roithner Lasertechnik GLMC1-10) was used to illuminate the chip from the top through the cover glass slice. The sensor signal (photodiodes in photovoltaic mode) was measured and demodulated with a lock in amplifier (Signal Recovery 7280). The demodulated signal was recorded with a digital storage oscilloscope. The whole setup was mounted on a solid construction in order to suppress vibrations in the optical path.

Results and Discussion

First experiments with polystyrene test particles of 20 µm and 24 µm diameter were carried out for the calibration of the sensor and published in [5]. In this contribution we show the use of the same system for the detection of yeast cells suspended in physiologic solution.

Figure 2 (left) shows sensor readings from experiments with polystyrene beads. The silver coated particles generate a negative pulse in voltage as expected since the shadow of the particle covers part of the photodiode. The transparent particles (plain polystyrene) show an increase in the sensor signal which can be explained by a "lens effect" where the particle actually focuses the light to a bright spot on the sensor area (Fig. 2 right).

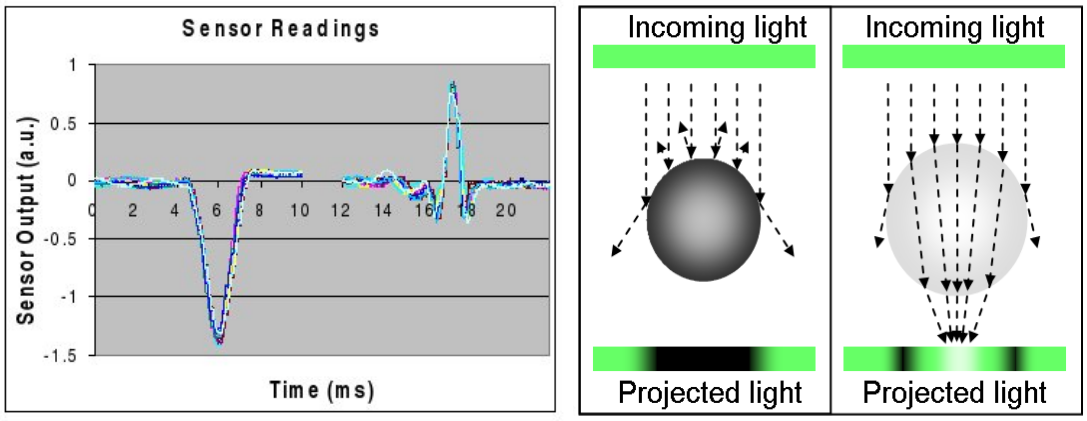

Fig. 2: Sensor readings from experiments with polystyrene beads (left). Silver coated particles cause a signal drop, while transparent plain particles show a signal increase. This behavior can be explained by a lens effect where a transparent particle focuses the incoming light to a bright spot, thus increasing the light intensity in the center of the projection (right) [5].

Because of this lens effect the intensity of the projected light depends on the height at which the particle passes the sensor. For repeatable results it is very important to keep this height constant.

With the polystyrene particle measurements as a reference, the sensor was now operated with suspended yeast cells. These measurements are more difficult because the cells are much smaller (about 3 – 5 µm diameter) and there is variation in some properties compared to calibration beads: the variation in size causes uncertainties, also the shape is not perfectly spherical and the surface is not well defined. As a result the focused beam has uncertainties in the focal length (caused by shape and size variation) and the intensity (absorption and diffraction at the irregular surface).

Measurement results are shown in Fig. 3. The cells are very well detectable but the SNR in the system is lower compared to measurements with the large polystyrene particles. Very interesting is the fact that those cells cause a positive peak which indicates their transparent character.

Conclusions

We have successfully demonstrated the optical detection of yeast cells in a projection cytometer. In our current setup we were able to detect particles down to the size of

yeast cells with the sensor (photodiode) placed in the near field of the particle. Non-transparent particles produce a drop in the sensor signal as expected due to their shadow. In the case of (semi-) transparent particles an increased sensor signal was observed which is explained by a lens effect. Measurements with yeast cells showed a similar sensor output (positive peaks) which indicates their transparent character.

We conclude that this analysis method can be used to distinguish different types of cells by their optical transmission and absorption properties.

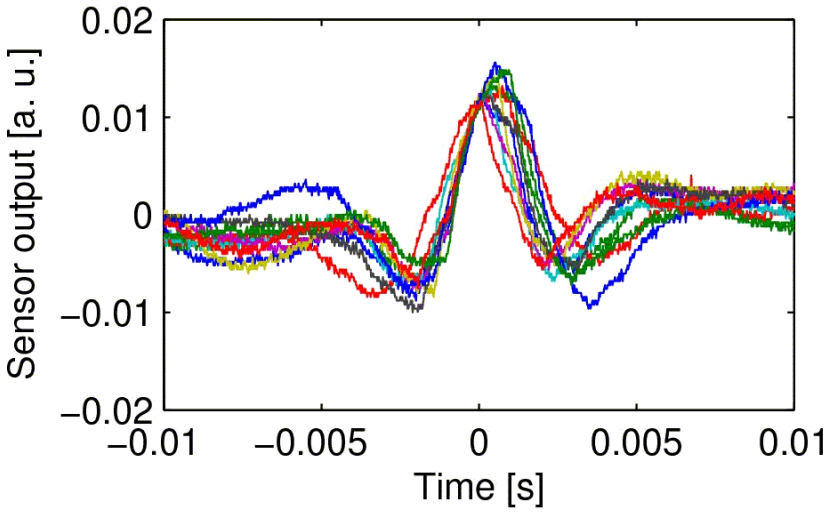

Fig. 3: Measurement results from experiments with yeast cells. The positive peak indicates the transparent character of the cells.

Acknowledgement

The chips were made in cooperation with the Delft University of Technology and co-funded by the Technologiestichting STW (project DPC.5521).

References

[1] H. M. Shapiro, “Practical Flow Cytometry”, 4th ed., 2003, Wiley & Sons

[2] J.H. Nieuwenhuis, J. Bastemeijer, P.M. Sarro, and M.J. Vellekoop, “Integrated Flow-Cells for Novel Adjustable Sheath flows”, Lab on a Chip, vol. 3, pp.56-61, 2003

[3] P. Svasek, E. Svasek, B. Lendl, and M. Vellekoop, “Fabrication of miniaturized fluidic devices using SU-8 based lithography and low temperature wafer bonding”, Sensors and Actuators A, vol. 115, pp. 591-599, 2004

[4] J.H. Nieuwenhuis, J. Bastemeijer, A. Bossche, and M.J. Vellekoop, “Near-Field Optical Sensors for Particle Shape Measurements”, IEEE Sensors Journal, vol. 3, pp. 646-651, 2003

[5] J.H. Nieuwenhuis, P. Svasek, P.M. Sarro, and M.J. Vellekoop, “Particle Discrimination with an Improved Projection Cytometer”, Proc. of μTAS 2004, Malmö, Sweden

Particle and Cell Detection using a DVD Pickup Head

S. Kostner, M.J. Vellekoop

Institute of Sensor and Actuator Systems, Vienna University of Technology
Gusshausstrasse 27-29, 1040 Wien

In this report we present an optical detection system for single biological cells that utilizes a standard DVD pickup head. In a feasibility study we have shown the detection for different plain and silver coated polystyrene particles and cells (yeast) suspended on a platinum mirror. For these experiments the integrated magnetic actor of the pickup was used to simulate the particle movement and we found a remarkable sensitivity. Then a flow cell with integrated mirror has been designed to be able to measure particles in a cytometric setup. First measurement results are given that show the high sensitivity and a good repeatability for polystyrene beads.

Introduction

Flow cytometry is a process where physical or biochemical characteristics of single biological cells are gained as the cells pass through the device in a fluid flow [1]. These systems are usually based on optical or impedance measurements where commercially the optical flow cytometers are the most important ones. Parameters like cell size, viability, and cytoplasm conductivity can be measured electrically by impedance changes, but more complex parameters like DNA content and the presence of certain biomolecules are only accessible by optical methods using fluorescent markers. Hereby a laser is used for excitation and the filtered fluorescent response from the cell is measured as a function of the angle (fluorescent activated cell sorting).

If one is interested in having information about the cell concentration in a suspension a less complex system is sufficient where every single cell generates a counting peak and the total number of peaks is the output of the instrument.

In this project we follow a low-cost approach using a DVD pickup head for detection of cells. Measurements with particles in a microchannel were performed to show the principle.

The Sensor System

The optical part of the system consists of a DVD pickup head (Sanyo SF-HD68V) which is explained in Fig. 1.

A laser diode is used to generate a beam that is reflected by a beam splitter to a lens and focused to a small spot of ca. 0.65 µm size. The lens position is controlled by two voice coil motors (VCMs) such that the focus of the beam can be adjusted to a reflective surface. The reflected beam propagates back to a four quadrant photodiode array. An astigmatic distortion in the optical path causes the beam profile at the photodiode array to be spherical only when the beam is reflected in the focal point. If the reflection is out of focus, the profile becomes elliptic with the principal axis depending on the sign of the focus error (Fig. 1, Beam Profiles). A focus error signal can be generated by summing up the photocurrents as follows: FE = A + D – B – C. In a typical DVD appli-

cation this signal is used to control the VCM such that the focus error becomes zero. The sum of all four photocurrents corresponds to the total reflected intensity.

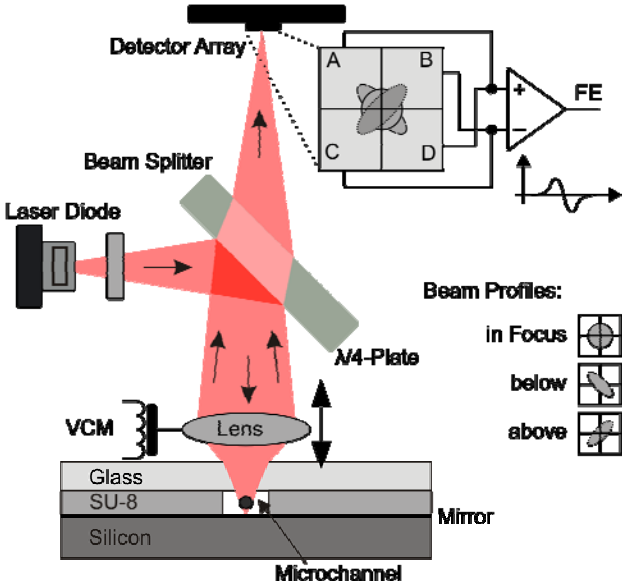

Fig. 1: The DVD pickup head in cytometric setup.

Compared to conventional optical cytometers where the light beam is coupled through the flow cell our system includes a mirror that is used to reflect the light back to the sender. The internal photodiodes of the pickup can be utilized which has several advantages: first the alignment between sender (laser diode) and receiver (photodiodes) is not critical because both are integrated in the pickup. Second, the VCM can be used to correct for alignment errors between the fluidic chip and the pickup head and third, the total cost of system is comparatively low because the whole high precision optical system is integrated in a mass product.

When a particle enters the detection region in the microchannel it influences the optical path and the reflected signal changes.

Flow Cell

The flow cell (Fig. 2) consists of a silicon glass sandwich with an intermediate layer of SU-8. The through holes for the fluidic interface were KOH-etched and the surface of the silicon is coated with titanium which acts as the mirror. The SU-8 layer defines the fluidic geometry of the microchannel and is also used to form a tight bond to the top glass wafer. At the detection region the channel has a cross section of 50 µm by 50 µm.

The chip was clamped to a device holder that provides O-rings to seal the liquid connections.

Measurements

In a first attempt different objects (spherical silver coated and plain polystyrene beads) were distributed on a platinum mirror and the reflected intensity signal was measured while a second VCM was used to simulate the movement of the cell with a speed of ca. 5 m/s. The results are shown in Fig. 3(a) and (b). The non-transparent particles (20 µm

diameter) cause an intensity drop while the transparent plain particles (15 µm diameter) cause a signal with a peak that exceeds the unperturbed reflected intensity which is labeled with 100%. In a cytometer the measuring speed would only be limited by the bandwidth of the pickup.

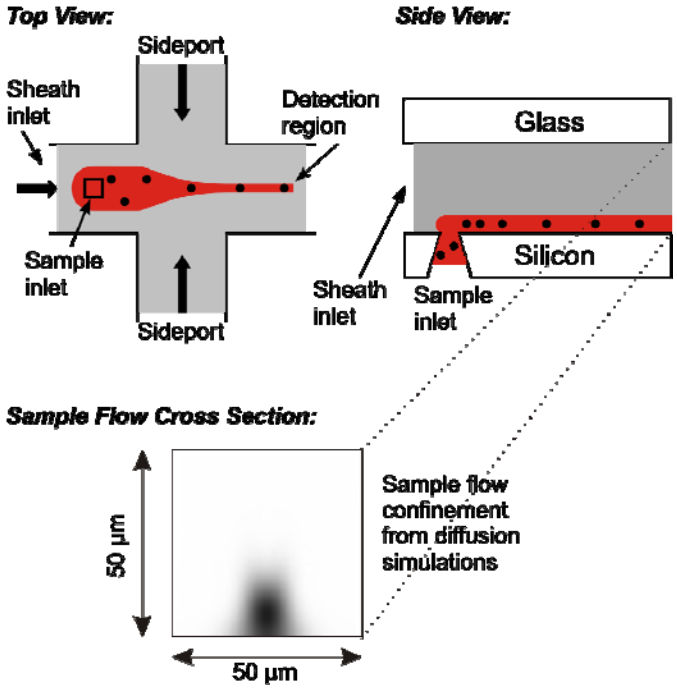

Fig. 2: Flow cell for non-coaxial sheath flow.

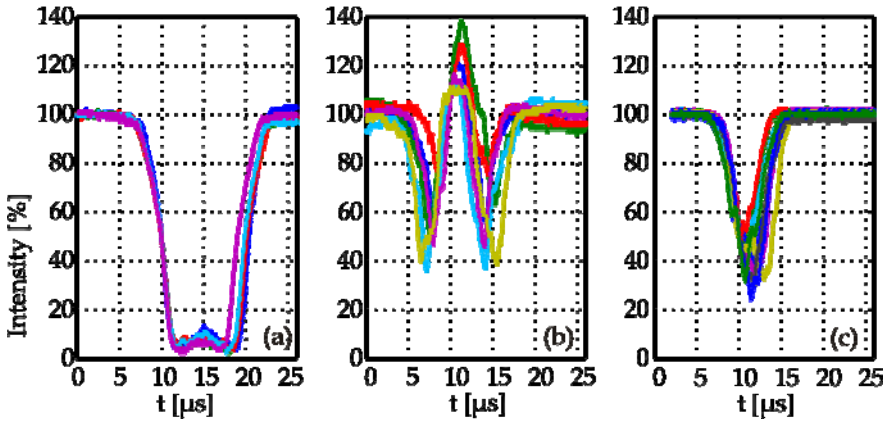

Fig. 3: Sensor response for three different particle types suspended on a platinum mirror: 20 µm silver coated polystyrene (a), 15 µm plain polystyrene particles (b), yeast cells (c). Note that the plain particles cause an intensity rise to more than 100% which is a higher response than produced by a mirror in the focal point.

To estimate the potential of the system for detection of other particles, also yeast cells have been tested. The cells were taken from a suspension and distributed on the mirror. The results (Fig. 3(c)) show a signal drop of between 50% and 70% which is a re-

markably high sensitivity. This indicates that even smaller cell types can be measured in the system.

In the next step a flow cell has been used to generate a non-coaxial sheath flow to move the particles through a microchannel. To obtain a high sensitivity the sample flow has to be very close to the mirror. Syringe pumps have been used to apply the necessary flow rates.

First measurement results using plain polystyrene beads (8 µm diameter) are given in Fig. 4. The graph shows 10 consecutive measurements and demonstrates the good repeatability of the process. The intensity drops to less than 40% when a particle passes by. The variation of the amplitude of the signal is within a range of ± 4.3 %.

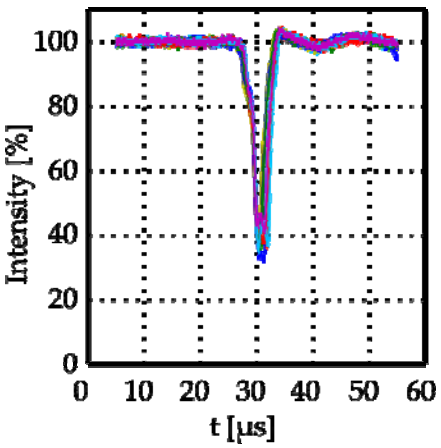

Fig. 4: Sensor response from measurements in the flow. Plain 8 µm particles (Micromer). The intensity drops to less than 40% due to the presence of a particle. The variation in amplitude is in a range of ± 4.3 %.

Conclusions

We have successfully shown the principle of a low cost cell detection system that utilizes a DVD pickup head. First measurements using a mirror instead of microfluidic channel indicate the ability to detect yeast cells from their optical reflection pattern. We have also performed measurements with polystyrene particles in a microfluidic channel that showed a good repeatability and a remarkably high sensitivity.

We conclude that our system will allow for detection of biological cells with different optical properties (fast viability tests, stained cells).

References

[1] H..M. Shapiro, “Practical Flow Cytometry”, 4th ed., 2003, Wiley & Sons

[2] J.H. Nieuwenhuis, J. Bastemeijer, P.M. Sarro, and M.J. Vellekoop, “Integrated Flow-Cells for Novel Adjustable Sheath flows”, Lab on a Chip, vol. 3, pp.56-61, 2003

PCR Microsystem for Fast Cycling

G. Hairer[1], M.H. Mansfeld[2], C. Nöhammer[2], M.J. Vellekoop[1]

[1] Institut für Sensor- und Aktuatorsysteme, Technische Universität Wien, A-1040 Wien

[2] Molekulare Diagnostik, ARC Seibersdorf research GmbH, A-2444 Seibersdorf

In this paper we present the design, fabrication and test of silicon-glass based PCR chips which amplify specified DNA strands. The design of the chip was optimized to ensure a fast PCR process in terms of thermal cycling speed, biocompatibility, size of reaction chamber and simplicity of fabrication. First tests using a conventional setup for thermocycling show successful DNA amplification in the micro PCR chip.

Introduction

A lot of effort is put into the development of integrated microsystems for analyzing blood and especially DNA. The aim of the integration is to design small devices for fast and cost efficient analysis. Polymerase Chain Reaction (PCR) is a proven technique for amplifying DNA. This method allows multiplying a single DNA molecule up to a billion times. The DNA of the target gene is copied leading to an exponential increase of the number of the gene. The whole process consists of 20 to 50 heat cycles. One PCR cycle contains three different temperature steps. First, the double stranded DNA is heated up to 95 °C to break up the hydrogen bonds (denaturation) and separate the two DNA strands from each other. Next, at a temperature of approximately 55 °C (annealing) gene-specific oligonucleotide primers, which flank the DNA region to be amplified, hybridize to the single strands. Finally these DNA strands are extended in the presence of the thermostable Thermus aquaticus polymerase (Taq) and deoxynucleotide triphosphates (dNTPs) at a temperature of 72 °C (extension) [1].

After first tests on a silicon-glass PCR chip where the filling ports were fabricated in the silicon part, in this paper a modified design of silicon-glass PCR chips is demonstrated and tested. The PCR chip is a single chamber chip with filling ports through the glass. The realization of the filling ports through glass has the advantage that a heating unit can be attached on the silicon side, which improves the thermal behavior of the device and simplifies the injection and extraction of the PCR sample from the chip. Practical issues related to chip design, fabrication process and PCR tests will be discussed in the next sections.

Concept and Design

Several different PCR microsystems have been published [2], which are generally grouped into two principles; (i) the continuous flow PCR microsystems and (ii) the micro chamber PCR systems. In the continuous flow PCR microsystems the reaction mixture is moved between three well-defined temperature zones. The mixture is transported in rotary, serpentine or back and forth motion. In the micro chamber PCR systems the reaction mixture is kept stationary, while the temperature of the reaction chamber is cycled between three different temperatures. Advantages of the chamber PCR are the freedom in the number of cycles to be made and the possibility to test the

device in a conventional thermocycler. This allows first PCR tests of the device without any heating and sensing elements on chip and the conventional PCR results can be compared with those of the PCR chip. Therefore, we decided in favor for the chamber PCR concept. To achieve high recovery of the PCR sample the chamber has to be constructed like a channel, where the filling ports are located near the chamber walls. In Fig. 1 on the left hand side the designed PCR chip is shown. The chamber consists of a (wide) channel with funnel shape at the side of the filling ports. The volume of the chamber is 25 µl. The chip dimensions are 15 x 20 mm and the distance between the two filling ports is about 13 mm. The access holes are drilled in the Pyrex glass with a diameter of 1 mm. The reason for realizing the filling ports through glass is that a heating unit can be attached on the silicon side for thermocycling the chamber, which, because of the better thermal conductivity of silicon compared to glass, improves the thermal behavior of the device.

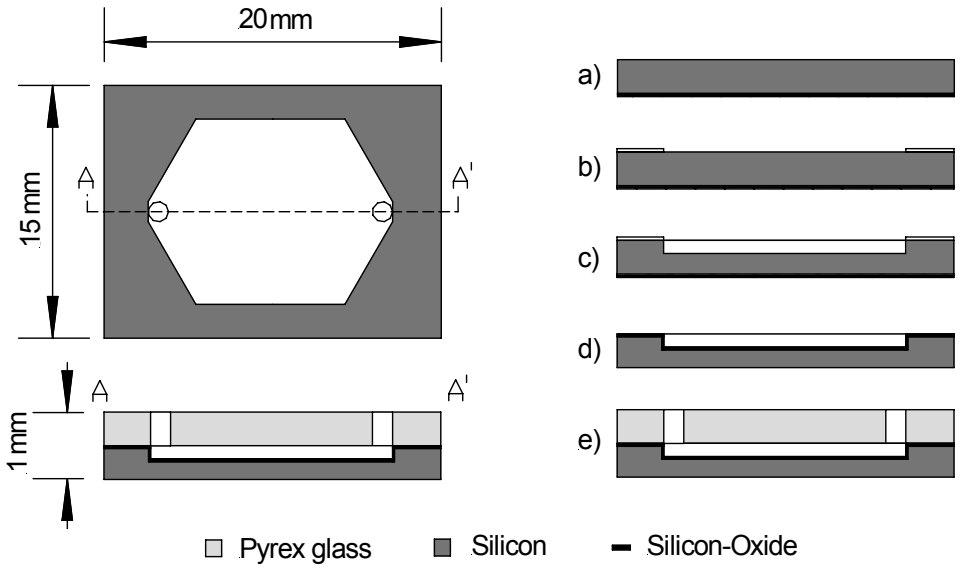

Fig. 1: Design of the PCR chip (top view and cross section) with a reaction volume of about 25 µl (left); Fabrication process of the PCR chip (right)

For fast thermocycling on chip the device has to be small, so that less thermal mass has to be heated and cooled. As a further term the material has to have a high thermal conductivity and a low heat capacity. Silicon fulfills both criteria and additionally, it has excellent structuring characteristics. The heating unit will be realized on the silicon side of the PCR microsystem. As lid a Pyrex glass is used, which has the advantage of allowing insight into the chamber and the possibility of irreversible anodic bonding to the silicon. It can also be machined (through-holes).

Surface chemistry plays a dominant role in PCR reactions within a micro fabricated environment due to the high surface-to-volume ratio. Silicon as such is not very well compatible with DNA and Taq polymerase, since it provokes adhesion effects that can inhibit standard PCR reactions. An oxidized surface however was shown to give consistent amplification that is comparable to those performed in conventional PCR tubes [3]. Thus an oxide layer will be thermal grown on the silicon side in the chamber.

Fabrication Process

The PCR chip is fabricated using photolithography, combined with DRIE (deep reactive ion etching) process, glass drilling and glass-to-silicon dioxide anodic bonding (Fig. 1, right hand side). We used double side mirror polished silicon wafers (100 mm diameter, 525 µm thick, <100>, n-type) coated with an insulating layer consisting of 250 nm thermally grown silicon dioxide and 70 nm LPCVD (low pressure chemical vapor deposition) silicon nitride on one side (a). To fabricate the cavities for the chamber the positive photoresist AZ6624 was coated and patterned on the silicon side of the wafers (b). The reaction cavities were plasma etched to the depth of 180 µm using a DRIE reactor (SF_6/O_2, so called Bosch process) (c). Afterwards a silicon oxide layer with the thickness of 40 nm was thermally grown on the side of the reaction cavities to achieve biocompatibility. The oxide and nitride layers were removed from the wafers with RIE in order to achieve electrical contact during anodic bonding (d). Holes with 1 mm in diameter are drilled in the 500 µm thick Pyrex 7740 glass wafers. Afterwards the wafer is anodically bonded with the silicon wafer to cap the cavities (e). Finally the wafers were diced with a conventional wafer saw.

Fig. 2: Photo of the fabricated PCR chip

Proof of Functionality

The functionality of the PCR chip is tested by placing it into a thermocycler (PTC-200 slide cycler from MJ research). For the thermal cycling a standard PCR program can be run. The temperature of the hot air in the cycler is set at 95 °C for denaturation, 55 °C for primer annealing and 72 °C for extension. Each step is performed for 1 min and to achieve a high yield of DNA amplification 50 cycles are carried out. A standard PCR mastermix is used, where gene-specific primers, deoxynucleotide triphosphates (dNTPs), Taq polymerase and E. coli DNA are included.

The ready-made mastermix is manually injected into the PCR chamber with a conventional pipette. At one port the mastermix is filled in whereas at the other port the air escapes. Before the chip is placed into the thermocycler the filling ports are sealed properly with the PCR tape “ARseal 90404” from Adhesives Research. This prevents gradual evaporation of the sample at denaturation temperature and avoids generating undesired air bubbles in the chamber.

After running the PCR in the conventional cycler the detection of the amplified DNA product is performed off chip. For this the amplified DNA sample is pulled out from the chip with a conventional pipette and afterwards analyzed on an agarose gel. The volumes of the recovered PCR product and the mastermix initially applied to the chip are almost identical due to the chip design. Only tiny amounts of the DNA sample remain at the corners of the reaction chamber.

Figure 3 shows the result of the on chip DNA amplification.

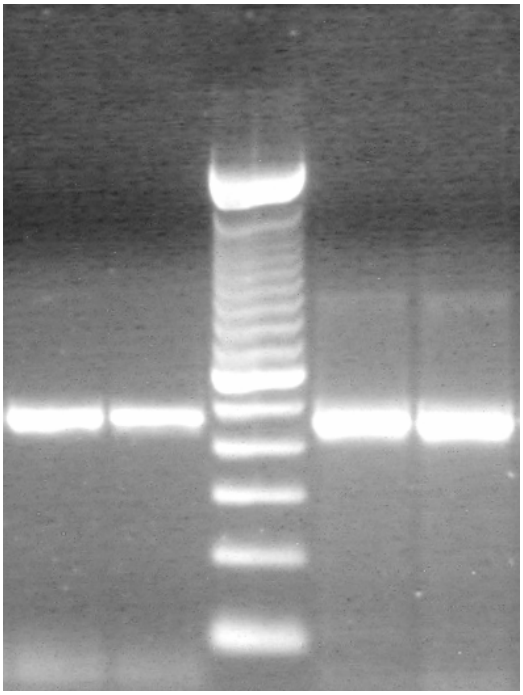

Fig. 3: Agarose gel electrophoresis of 16S rRNA PCR product (497 bp fragment) amplified from E. coli DNA; Lane 1 and 2: single chamber design; in comparison to conventional PCR reaction tubes (Lane 4 and 5). Lane3: 100bp ladder

Discussion

The design of PCR chips with filling ports through the glass has been presented and the functionality of the PCR of these devices has been successfully proven. The device promises miniaturized, fast and effective PCR performance. As a next step a heating unit and thermal sensing elements will be added on the chip to achieve a standalone PCR microsystem.

Acknowledgements

For fabrication of the devices and technical support we thank Dr. A. Jachimowicz, E. Svasek and P. Svasek (ISAS, Vienna University of Technology, Austria) and the Research Centre of Microtechnology at the University of Applied Sciences Vorarlberg, Austria.

References

[1] C.R. Newton, A. Graham: “PCR. Introduction to Scientific Techniques”, BIOS Scientific Publishers Ltd., Oxford 1997, ISBN 1872748821

[2] P.-A. Auroux et al.: “Miniaturised nucleic acid analysis”, Lab Chip, 2004, 4, 534-546

[3] M.A. Shoffner et al.: “Chip PCR. I. Surface passivation of microfabricated silicon-glass chips for PCR”, Nucleic Acids Research, 1996, Vol. 24, No. 2, 375-379

Sensitive Measurement of Flow Velocity and Flow Direction Using a Circular Thermistor Array

F. Keplinger, J. Kuntner, A. Jachimowicz, F. Kohl

Institute for Sensor and Actuator Systems
Vienna University of Technology, A-1040 Vienna

Eight highly sensitive amorphous germanium thermistors (TCR = -1.8%/K) are the sensitive part of the micromachined sensors for flow velocity and flow direction. Carried by a 1.3 µm thick diaphragm they measure temperature differences generated by the sample flow and a heater (430 µW). This allows gas flow measurements in the range from 0.025 m/s to about 3 m/s with a sensitivity of up to 30 mV/(m/s). Two orthogonal pairs of opposed thermistors feature a sensitivity of 150 µV/°. An increase in sensitivity (50%) is gained by using two 90° rotated thermistors situated in the downstream position.

Introduction

Measurement of fluid velocity combined with the acquisition of flow direction is a challenging task in different fields of research. Especially miniaturized sensors are suitable for investigation of flows with high spatial resolution which are not accessible for mechanical anemometers. The current miniaturized cutting-edge devices are based on the thermal anemometer principle allowing the simultaneous measurement of flow direction and velocity [1]. The application of amorphous germanium thermistors for flow sensor [2] with their high resistive temperature coefficients (TCR) initiated the design of extremely sensitive flow direction sensors. Moreover, a further increase in sensitivity of the direction measurement was expected by the use of four additional thermistors.

Sensor Principle

Basis of the sensor is the so-called ‘calorimetric’ measurement principle where a thin diaphragm supported by a micromachined silicon frame is flush mounted with the wall surrounding the flow channel. A thin-film resistor (heater) at the centre position of the diaphragm generates a symmetric temperature distribution on the diaphragm as long as the flow velocity is zero. When a tangential flow occurs, the thermal symmetry is broken. Two thermistors, placed symmetrically in respect to the heater and parallel to the flow, are used to measure the temperature difference. More heat is transported to the downstream thermistor than to the upstream ones, a difference signal is generated which is a measure for the velocity. Applying more than one thermistor pair on the diaphragm being rotated appropriately compared to the first one, the direction of the flow within the diaphragm plane can be measured.

For high sensitivity the diaphragm has to have a high thermal resistance. The heat should be transported mainly by the sample flow and not by thermal conduction within the diaphragm. Therefore the diaphragm has to be as thin as possible making it very fragile.

Experimental

Sample Preparation

The sensor structures (Fig. 1) are evaporated on a <100>-Si wafer, passivated on both sides with 250 nm SiO_2 and 70 nm Si_3N_4. A chromium meander (300 µm x 5 µm x 130 nm, 580 Ω) serves as heater. The thermistors consist of amorphous germanium (250 nm, 75 µm² x 5 µm, 320 kΩ). Amorphous germanium was chosen as thermistor material because its resistivity is highly sensitive to temperature changes [2]. It exhibits a TCR of about -1.8%/K being almost five times higher than the corresponding value of platinum. The thermistors are contacted by an interdigital sandwich structure consisting of 50 nm titanium (at the germanium side), 100 nm gold and 30 nm chromium.

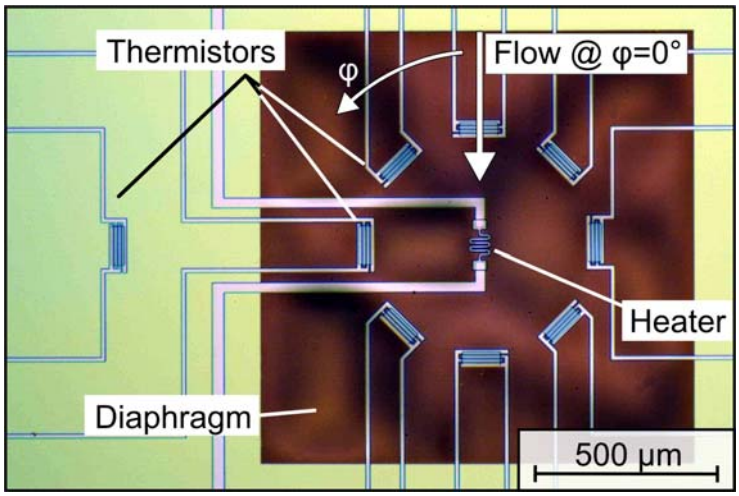

Fig. 1: Micrograph of the flow sensor consisting of eight thermistors on the 1.3 µm thick diaphragm and one on the surrounding Si-frame to measure the ambient temperature. φ denotes the direction of the flow in respect to the N-S-direction. Due to the buckling of the diaphragm it is irregularly shaded.

The metal layer and the Ge layer are evaporated and patterned with an image reversal photo resist. The complete structure is isolated by 1 µm thick LPCVD silicon nitride. Finally, the diaphragm is generated by anisotropic etching with a 30 wt% potassium hydroxide solution at 80 °C. The etching process is stopped by the silicon oxide layer of the wafer. The diaphragm features a size of 1.2 x 1.2 mm^2 and an overall thickness of 1.3 µm. It is an inherent property of the anisotropic etching process of a <100>-Si-wafer that the boundaries of the etched cavity are formed by {111}-planes [3]. Therefore the cavity is a truncated pyramid, bounded by a rectangular silicon nitride membrane.

Measurement Setup

The sensor is positioned flush with the wall of a flow channel (rectangular cross-section of 12 mm x 1 mm) and can be rotated 360° as indicated in Fig. 1. Filtered nitrogen is used as fluid and controlled by a flow controller allowing a maximum velocity of 2.8 m/s. The central Cr resistor is heated up by 430 µW in the constant voltage mode (over-temperature of approximately 5 K). The thermistors resistances are measured by applying constant voltage (5 V) and current-to-voltage converters (120 mV/µA) based on the ultralow noise BiFET OpAmp AD743. Their output voltages are recorded by a PC-controlled data acquisition board (Fig. 2).

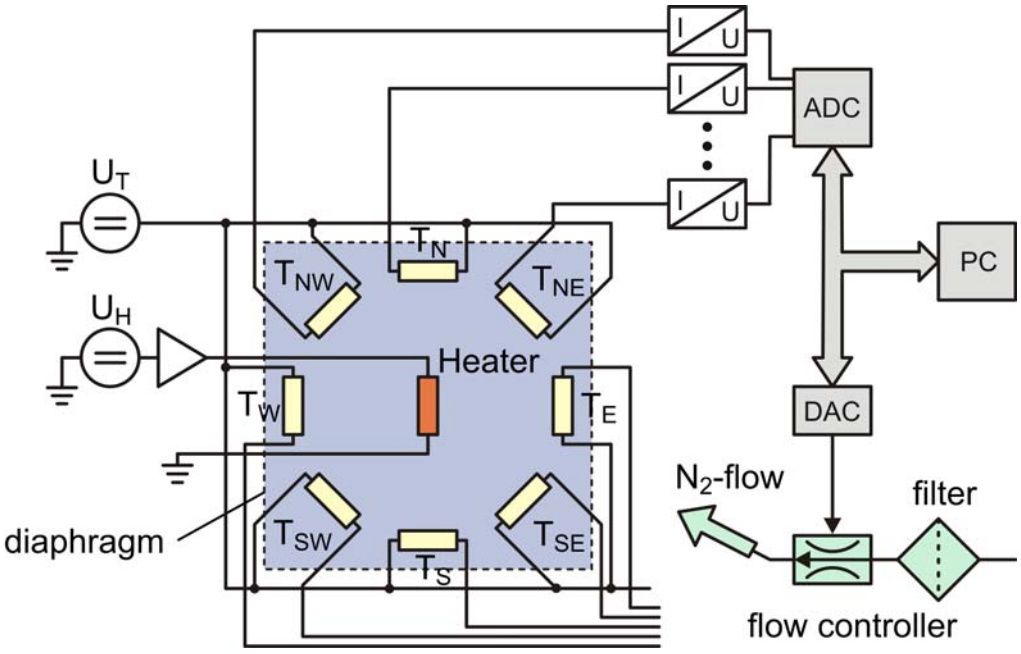

Fig. 2: Schematic measurement setup. Thermistors T_N, T_{NE}, T_E, … T_{NW}, U_T thermistor voltage, U_H heater voltage.

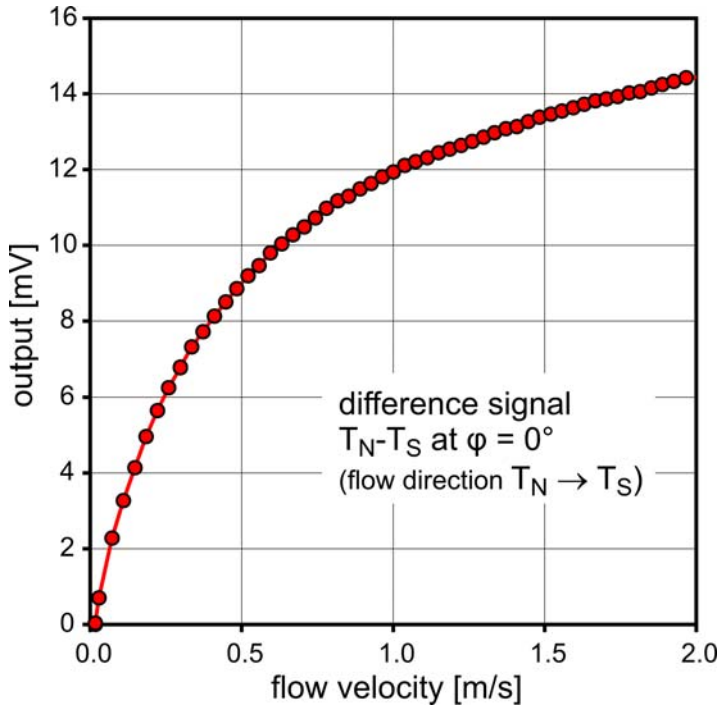

Fig. 3: Difference signal ($T_N - T_S$) of the thermistors at the north and south position versus flow velocity. The channel is oriented in parallel to the connecting line of the thermistors. Heating power: 430 µW.

Measurements

As an example, the measured difference signal of the north/south thermistor pair (Fig. 3) emphases the high sensitivity of the sensor for flow velocities. The gas flows parallel to N-S-direction, the heater is operated in the constant heating power mode. For low velocities the sensitivity is 30 mV/(m/s). At higher velocities the overtemperature of the upstream thermistor vanishes. Also the downstream sensor gets less and less heated because more and more gas has to be heated up. Beyond a velocity of 3 m/s the temperature difference decreases with increasing flow rate.

The dependence of the difference signal of opposed sensors versus flow direction is plotted in Fig. 4 (thick lines). The direction sensitivity for flow with an angle smaller than 60° in respect to the connecting line is about 150 µV/°. Evaluating the signal difference of 90° rotated thermistors (e.g., S-E) the directional sensitivity can be improved by approximately 50%, when the thermistor pair is near the downstream position.

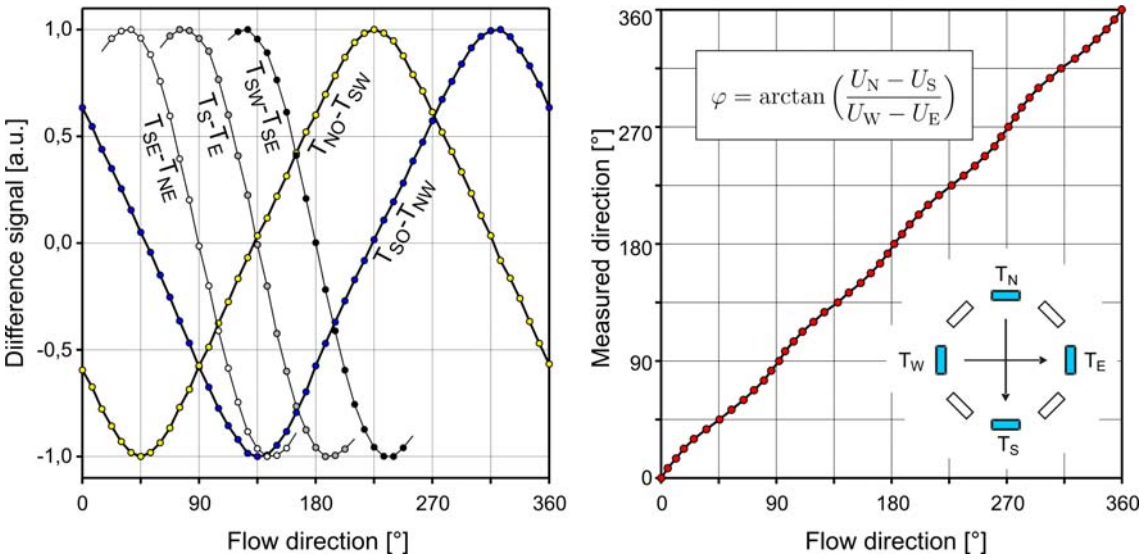

Fig. 4: Left: Measured and normalized difference signals of opposed (thick lines) and of 90°-rotated thermistors (thin lines). Right: Measured flow direction assuming sinusoidal characteristic of the difference signals of opposed sensors (N-S and W-E).

The value of the angle of the flow direction can be determined using the difference signals of two thermistor pairs: $\varphi = \arctan\left[(U_N - U_S)/(U_W - U_E)\right]$ taking into account the signs of the individual differences to decide the quadrant. The function assumes a sinusoidal response of the difference signal to the flow direction. The deviations from this are mainly responsible for the nonlinearity in the measured direction of Fig. 4.

Conclusion

The application of amorphous germanium enables the development of highly sensitive sensors for flow velocity and flow direction measurement. By applying eight thermistors the angular resolution can be increased by about 50%. The directional characteristic of a single thermistor deviates significantly from a sinusoidal function. A very high accuracy is achievable using all available thermistor signals and more sophisticated evaluation schemes. Additionally, improved sensor designs are feasible to take full advantage of the superior properties of the thin-film thermistors.

References

[1] S. Kim, S. Nam and S. Park: “Measurement of flow direction and velocity using a micromachined flow sensor”, Sens. Actuators A, vol. 114, 2004, pp. 312–318.

[2] F. Kohl, R. Fasching, F. Keplinger, R. Chabicovsky, A. Jachimowicz and G. Urban: “Development of miniaturized semiconductor flow sensors”, Measurement, Vol. 33, 2003, pp. 109–119.

[3] M. Elwenspoek and H. Jansen: “Silicon Micromachining”, Cambridge University Press, Cambridge, England, 1998.

Advanced Thermal Flow Sensors

J. Schalko[1], F. Kohl[2], F. Keplinger[1], R. Beigelbeck[2], A. Talic[2], S. Cerimovic[2], J. Kuntner[1], A. Jachimowicz[1]

[1] Institute of Sensor and Actuator Systems, Vienna University of Technology, A-1040 Vienna

[2] Research Unit for Integrated Sensors Systems, Austrian Academy of Sciences, A-2700 Wr. Neustadt

Miniaturized flow sensors composed of a thin membrane supporting appropriately positioned heating resistors and temperature sensors were studied by computer-numeric analysis. Significant improvements of steady-flow transduction characteristics as well as responses to step-like changes of the dissipated power are feasible by design modifications and new transduction schemes.

Introduction

Calorimetric flow sensors are preferable devices for limited space applications in mass products like cars or domestic appliances. They are well-known for ruggedness, sensitivity, and fast response, each of which may be achieved using MEMS technologies. After a brief description of state of the art designs, we discuss new concepts enabling faster response, enhanced transduction efficiency, improved durability as well as means for in-service monitoring of the functionality.

Theory

Calorimetric flow sensors rely on flow dependent heat transfer altering the temperature distribution close to a small heat source. The temperature field is probed at a few preselected sites. Based on these recordings, a representative characteristic of the flow field is determined using suitable calibration information. The cross sectional view depicted in Fig. 1 is typical for the majority of micromachined versions of calorimetric flow sensors.

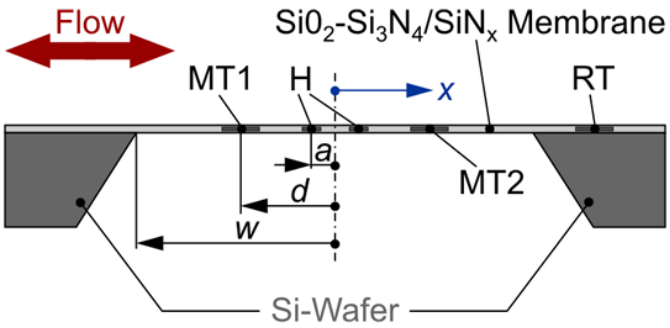

Fig. 1: Schematic cross section of a typical calorimetric flow sensor design

The heating resistor H generates a temperature profile in the membrane and the surrounding fluid. Due to convective heat transport, the profile is altered if the fluid flows along the membrane surface as indicated. Local changes of the temperature profile are probed using the thermistors MT1 and MT2. Flow related information can be derived from variations of their temperature difference $T_{MT1}-T_{MT2}$ wherein the subscripts indicate the measuring site. In contrast to hot-wire and hot-film anemometers, calorimetric sensors offer flow direction information in principle.

More refined structures employ larger one-dimensional arrays of temperature sensors to optimize the sensitivity over a wide measuring range [1], whereas two-dimensional arrangements of these components are used to gain directional resolution [2]. To achieve high sensitivity and fast response, all essential components are made by thin-film technology, and they are embedded in an extremely thin membrane.

Experimental

Sample Preparation

Figure 2 depicts the usual placement of thin-film components on the membrane which measures 1 mm in length and 0.5 mm in width. A KOH based anisotropic wet etch process and backside lithography is used to shape this membrane. A closer examination of the pattern reveals a 10 µm misalignment caused by the backside lithography step. Further details of the technology and key specifications of such sensors can be found elsewhere [3], [4].

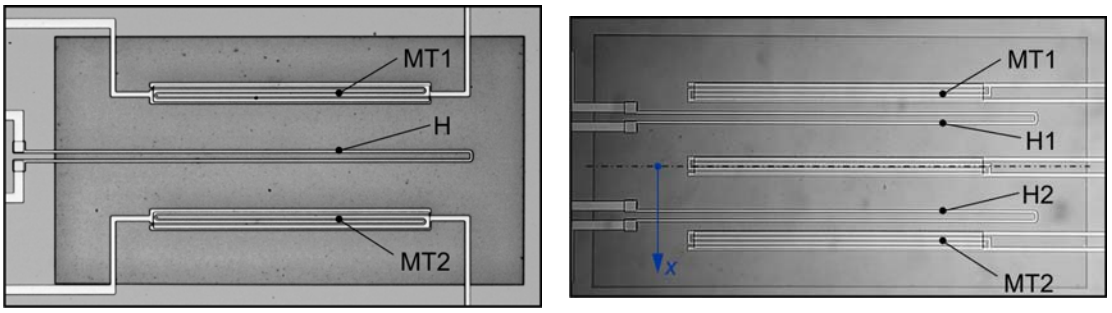

Fig. 2: Top view of the membrane area of a flow sensor featuring a common layout (left) and alternative design (right). The latter uses two equal-valued heating resistors together with the top and bottom thermistors. Highest sensitivity is achieved for flows in ± *x*-direction.

With an alternative arrangement of components on the membrane shown in Fig. 2, the specifications and monitoring capabilities can be significantly improved. For comparison, equally sized membranes, series connection of heating resistors, and only MT1 and MT2 are used. We investigated the progress achievable by these design improvements using finite element (FE) computations. The analysis is based on a two-dimensional (2D) FE model corresponding to the cross section shown in Fig. 1. The results presented below were obtained using COMSOL Multiphysics. Based on the Navier-Stokes equations for incompressible fluids, air-flow velocity fields were calculated approximately. The temperature dependencies of fluid viscosity, density, heat capacity, and thermal conductivity were not considered. Thus the effects of natural convection were neglected throughout the model. To reduce the computational effort, a uniform flow profile was assumed at the model inlet, which is situated 0.5 mm upstream

of the heater. Due to the sticking of the fluid at the sensor surface, typical flow boundary layers emerge. However, this simplification ignores the fluid displacement due to the finite thickness of the sensor chip, which would inevitably occur if the bare flow sensor chip was inserted into a homogeneous flow field. All computed FEM results are in good agreement with experiments [3], [4]. Hence, the 2D FEM analysis is an appropriate tool to predict the behavior of new sensors designs.

Four main areas of significant improvement of the performance of common calorimetric flow sensors were identified, which can be achieved by design modifications and modified transduction schemes, i.e., without any change of technological processes.

These fields are (i) improved sensor dynamics, (ii) reduction of the thermal stress acting on the sensor membrane, (iii) improvement of existing tools and new possibilities for in-service operability checks, and (iv) removal of the saturation of the transduction characteristics at very high flow velocities.

Common Design versus Alternative Approach

Constant excess temperature operating modes are based on closed loop control of temperature(s) at specific site(s) on the membrane by means of the heating resistor. Actually, the mean excess temperature of the membrane thermistors $\Delta T = T_{MT1}+T_{MT2}$ is controlled (enhanced CT mode). Figure 3 shows computed temperature profiles of the enhanced CT mode for the indicated set of free-field air velocities. All curves of the diagram are normalized to $\Delta T = 1$. In case of high flow velocities and a standard design, the temperature response to variations of the heating power becomes very small at the site of MT1 and the thermal output at very high flow rates saturates at $|T_{MT1}-T_{MT2}| \rightarrow 2 \bullet \Delta T$. Thus, an in-service check of the functionality of the upstream temperature sensor is hindered considerably. The improved design provides a much larger excess temperature at the upstream thermistor site. Thus the functionality of MT1 can easily be monitored during sensor operation. Moreover, this marked improvement is obtained in spite of the moderate maximum excess temperature of $2.3 \bullet \Delta T$.

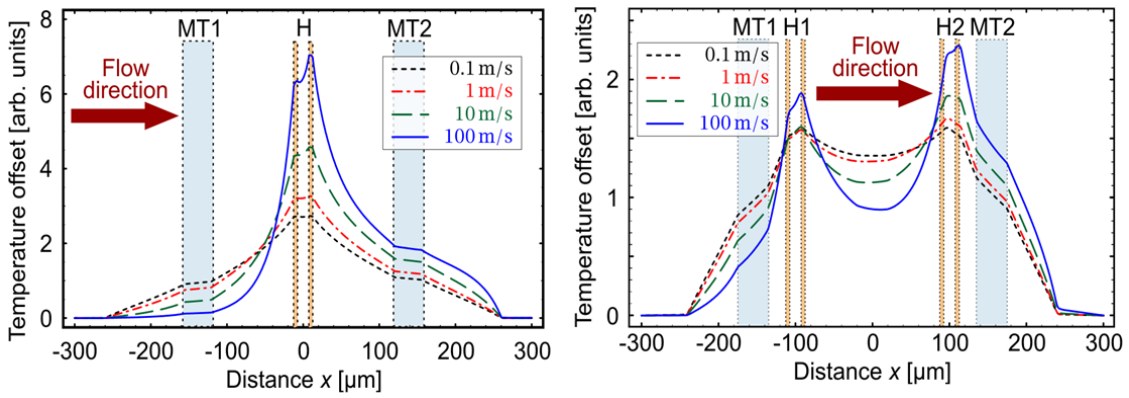

Fig. 3: Temperature profiles across the membrane region of flow sensors (left: standard design, right: alternative design) when operating in the enhanced CT mode.

It can be seen that the maximum of the temperature offset is located near the downstream heater trace. It grows with rising flow velocity by a factor of three up to the sevenfold of ΔT. Compared to the standard CT mode, the enhanced CT mode offers a higher thermal output $|T_{MT1}-T_{MT2}|$ by the same factor.

The thermal delay between heater and membrane temperature sensor limits the achievable performance of the control loop employed by the enhanced CT operational mode. The calculated responses to step-like changes of the heating power are shown in Fig. 4 for both designs.

Due to the smaller distance between heater and adjacent thermistor, the new sensor design exhibits significantly lower delays. For the enhanced CT operation mode, a much faster response to sudden flow changes can be achieved with the new design.

The sensor characteristics of the standard and the advanced design are also shown in Fig. 4 for both, the CP and the enhanced CT mode. The characteristics of the new design are shifted up by a factor of two approximately to coincide with those of the standard design at low flow velocities. The reduced useful transduction range of the CP mode due to the non-monotonous characteristics becomes obvious. As outlined above, the transduction characteristic of the standard sensor design saturates at high flow velocities even in the enhanced CT mode. Due to the closer spacing of heater and neighboring temperature sensor, the saturation of the transduction characteristic of the improved design occurs beyond the investigated flow range. In terms of resolution at high flow velocities the new design outperforms the conventional device significantly.

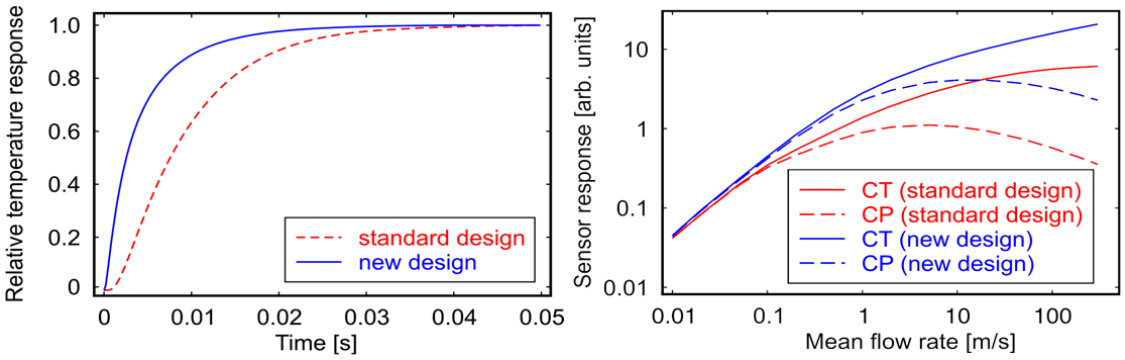

Fig. 4: Left: Zero-flow temperature sensor response to step like changes of the power dissipated by the neighboring heater. Right: Flow responses calculated for each sensor design and two operating modes

Conclusion

FEM analysis of calorimetric flow sensors proved that faster response, extended measuring range, reduced thermal load, and improved in-service functionality monitoring is obtainable at the same time through more sophisticated arrangements of heat sources and temperature sensors on the sensor membrane.

Acknowledgements

We greatly acknowledge financial support by the Austrian Science Fund, FWF.

References

[1] N. Sabaté, J. Santander, L. Fonseca, I. Gràcia, C. Cané: “Multirange silicon micromachined flow sensor”, Sensors and Actuators A. Vol. 110, 2004, pp 282–288.

[2] S. Kim, S. Nam, S. Park: “Measurement of flow direction and velocity using a micromachined flow sensor”, Sensors and Actuators A, Vol. 114, 2004, pp 312–318.

[3] A. Glaninger, A. Jachimowicz, F. Kohl, R. Chabicovsky, G. Urban: “Wide range semiconductor flow sensors”, Sensors and Actuators A, Vol. 85, 2000, pp 139–146.

[4] F. Kohl, R. Fasching, F. Keplinger, R. Chabicovsky, A. Jachimowicz, G. Urban: “Development of miniaturized semiconductor flow sensors”, Measurement, Vol. 33, 2003, pp 109–119.

ISBN: 978-3-901578-18-2